Generator design for, and modelling of, small-scale wind turbines

Stannard, Nick

Generator Design for, and Modelling of, Small-scale Wind Turbines

Nick Stannard

School of Engineering
Durham University

A thesis submitted in partial fulfilment of the requirements of the Council of the University of Durham for the Degree of Doctor of Philosophy (PhD)

2008

Generator Design for, and Modelling of, Small-scale Wind Turbines

Nick Stannard

2008

Abstract

This thesis explores the design and manufacture of permanent magnet (PM) axial-flux generators for micro wind and water turbines, and the impact these generators have on the operation and performance of the turbine system. It also considers the limitations of the axial-flux topology and how these limitations can be overcome by moving to a novel radial-flux configuration for higher power applications. The research shows that above power ratings of approximately 20kW at 100-200rpm – corresponding to a generator diameter of about 1m – the axial flux configuration becomes increasingly difficult to manufacture due to the large magnetic closing forces, and it is appropriate to switch to a radial flux layout.

A novel PM radial-flux generator is designed and constructed using 0.5mm diameter mild steel wire in place of traditional stator laminations to preserve the simple manufacturing process. The prototype generator produced a power output within 5% of predicted values and had an acceptable core loss of about 7% at rated power.

A number of small-scale wind energy conversion systems (WECSs) are also modelled using MATLAB/SIMULINK. A turbulent wind model is developed to examine how the turbines can be better controlled to aid stability and energy capture. The research showed that certain symmetrical blade profiles can become unstable when the system is used for grid connection.

Acknowledgements

I would like to thank my Supervisor, Jim Bumby, for all his support and encouragement during my time at Durham. I would also like to thank the many technicians who have lent their advice and expertise during the practical parts of this research, in particular David Jones, Paul Jarvis and Tony Collinson for their excellent work on the prototype generators.

Declaration

I hereby declare that this thesis is a record of work undertaken by myself, that it has not been the subject of any previous application for a degree, and that all sources of information have been duly acknowledged.

Contents

List of Figures

List of Tables

Nomenclature

a	Outer radius of applied pressure, m
a_w	Cross-sectional area of wire strand, m^2
A	Swept area, m^2
A_{active}	Active area of generator, m^2
A_c	Surface area of armature coil, m^2
A_{core}	Cross-sectional area of test core, m^2
$A_{o/p}$	Output wind turbulence amplitude, m/s
$A_{i/p}$	Input wind turbulence amplitude, m/s
A_{return}	Area available for magnetic return path, m^2
A_w	Winding area, m^2
B	Beta function
$\hat{B}$	Magnetic loading, T
B_g	Air gap flux density, T
B_{ma}	Maximum flux density at armature, T
B_{rem}	Remnant flux density, T
c	Running clearance, m
C	Weibull scaling factor
C_P	Energy capture coefficient
$C_{P(\max)}$	Maximum energy capture coefficient (mechanical)
$C_{P(\max)e}$	Maximum energy capture coefficient (electrical)
C_{WB}	Windy Boy capacitance, F
d_w	Wire diameter, m
D	Rotor diameter, m
D_{mean}	Mean diameter of generator, m
D_C	Duty cycle of DC-DC boost converter
D_{gen}	Generator diameter, m
E	Young's modulus, Pa
f	Frequency, Hz
F_i	Frequency domain amplitude of i^{th} harmonic, m/s
$F_{mag\ pair}$	Force between opposing magnet pairs, N
GR	Gain ratio of DC-DC boost converter
h	Coil height, m
h_s	Surface heat transfer coefficient, $W/K/m^2$
H	Rotor height (VAWT), m
H_{hub}	Turbine hub height, m
H_{ref}	Reference height, m

H_z	Height, m
I	Current, A
I_c	Current into capacitor, A
I_d	Terminal DC current, A
$I_{d\,in}$	Input current to DC-DC boost converter, A
$I_{d\,out}$	Output current to DC-DC boost converter, A
I_{dump}	Current through dump load, A
I_{gen}	Current from generator, A
I_{link}	DC link current, A
I_w	Current into Windy Boy, A
J	Current density, A/m^2
$\hat{J}_n$	Equivalent current source density, A/m^2
J_r	Turbine inertia, kg/m^2
k	Generator constant, V/(rad/s)
k_{bob}	Thermal conductivity of acetal bobbin, W/K/m
k_{eddy}	Power loss constant (due to Eddy currents), W/kg
k_{hyst}	Power loss constant (due to hysteresis), W/kg
k_{wind}	Thermal conductivity of winding, W/K/m
k_σ	Turbulence intensity factor
K	Generator constant, V/rpm
$\hat{K}$	Current loading, A/m
K_F	Gain constant
l_{inner}	Inner axial length of coil, m
l_{mean}	Mean turn length, m
l_{outer}	Outer axial length of coil, m
l_{return}	Length of magnetic return path, m
L	Turbulence length scale, m
L_{coil}	Coil inductance, H 、
L_{gen}	Generator length, m
L_m	Radial length of magnet, R_{mo}-R_{mi}, m
L_{self}	Self-inductance, H
m	Number of phases
m_1	Nichita transfer function constant
m_2	Nichita transfer function constant
M_{coil}	Mass of coil, kg
n	Weibull shape factor
n_c	Number of armature coils
n_h	Harmonic number
n_{pall}	Number of armature coils connected in parallel

n_{series}	Number of armature coils connected in series
n_{rpm}	Generator speed, rpm
n_{sp}	Number of wire stands in parallel per coil
N	Rated speed, rpm
N_c	Number of turns per coil
N_{cur}	Number of turns of current carrying coil
N_{emf}	Number of turns of current EMF coil
p	Number of pole pairs
P_{Eddy}	Power loss due to Eddy currents, W
P_{elec}	Electrical power output, W
P_{gain}	Power gain
$P_{generator}$	Generator power, W
P_{Joule}	Joule loss in armature, W
P_{hyst}	Power loss due to hysteresis, W/kg
P_{iron}	Power loss in stator iron, W
$P_{\lim it}$	Maximum power of Windy Boy, W
P_{load}	Power to load, W
P_m	Magnet pressure, Pa
P_{norm}	Normalised power
$P_{turbine}$	Turbine power, W
P_{rated}	Rated power, W
r	Internal battery resistance, Ω
r_c	Mean radius of test core, m
r_i	Inner radius of armature coil, m
r_o	Outer radius of armature coil, m
r_m	Mean generator radius, m
R	Turbine blade radius, m
R_c	Reluctance at centre of coil, turns/H
R_{coil}	Coil resistance, Ω
R_{dump}	Dump resistance, Ω
R_L	Load resistance, Ω
R_{mi}	Inside radius of magnet, m
R_{mm}	Mean magnet radius, m
R_{mo}	Outside radius of magnet, m
R_{over}	Overlap resistance, Ω
R_{phase}	Phase resistance, Ω
R_r	Reluctance of magnetic return path, turns/H
s	Laplace operator

s_w	Wind shear factor
S	Apparent power, VA
S_v	Power in turbulent wind signal, W
t	Plate thickness, m
$t_{binding}$	Binding tape thickness
t_c	Armature coil thickness, m
t_m	Magnet thickness, m
t_0	Time of initial sample, s
T	Temperature, ºC
$T_{electrical}$	Electrical torque, T
T_F	Time constant, s
$T_{mechanical}$	Mechanical torque, T
T_s	Sample period, s
T_0	Total sampling time, s
V	Voltage, V
V_{batt}	Battery voltage, V
V_{cut-in}	Cut-in wind speed, m/s
$V_{cut-out}$	Cut-out wind speed, m/s
V_d	Terminal DC voltage, V
V_{dc}	DC voltage, V
V_{diode}	Diode voltage drop, V
$V_{d\,in}$	Input voltage to DC-DC boost converter, V
$V_{d\,out}$	Output voltage from DC-DC boost converter, V
V_{mean}	Mean wind speed, m/s
V_{phase}	Phase voltage, V
V_{rated}	Rated wind speed, m/s
V_{rect}	Voltage at output of rectifier, V
V_{ref}	Reference wind speed (at height H_{ref}), m/s
V_{TH1}	Threshold voltage 1, V
V_{TH2}	Threshold voltage 2, V
V_{turb}	Wind speed at turbine, m/s
V_w	Wind speed, m/s
V_z	Wind speed at height H_z, m
V_1	Voltage at which Windy Boy starts transferring power, V
V_2	Voltage at which Windy Boy transfers full power, V
w	Winding width, m
w_{inner}	Inner circumferential width of coil, m
w_{outer}	Outer circumferential width of coil, m
W_{AV}	Disc averaging transfer function

x	Beta function variable
X_{phase}	Phase reactance, Ω
y	Beta function variable
Y_{eff}	Effective air gap, m
Y_m	Magnet thickness, m
λ	Tip speed ratio
ω	Angular speed, rad/s
ω_{gen}	Angular speed of turbine, rad/s
ω_{elec}	Electrical frequency, rad/s
ρ	Air density, kg/m^3
ρ_c	Resistivity of core material, Ωm
ρ_{cu}	Resistivity of copper, Ωm
ρ_0	Resistivity of copper at 0°C, Ωm
η_{dc}	DC generator efficiency
$\eta_{measured}$	Measured efficiency
$\eta_{predicted}$	Predicted efficiency
η_{WB}	Windy Boy efficiency
λ	Flux linkage, Wb-turns
$\hat{\lambda}_{bore}$	Flux linkage through coil bore, Wb-turns
$\hat{\lambda}_{coil}$	Flux linkage through coil, Wb-turns
$\hat{\lambda}_{total}$	Total flux linkage through coil, Wb-turns
σ_i	Span across inside of coil, rad
σ_m	Coil span, rad
σ_o	Span across outside of coil, rad
σ_v	Standard deviation of turbulence, m/s
μ_{rec}	Recoil permeability, H/m
μ_0	Permeability of free space, H/m
γ_s	Decay factor
ε	Armature coil packing factor
δ	Deflection, m
υ	Poisson's ratio
ϕ	Flux, Wb

Chapter 1

Background and introduction

1.1 Introduction

The research in this thesis is primarily concerned with the design and manufacture of permanent magnet (PM) axial-flux generators for micro wind and water turbines, and the impact these generators have on the operation and performance of the turbine system. It also considers the limitations of the axial-flux topology and how these limitations can be overcome by moving to a novel radial-flux configuration for higher power applications such as large wind, water or tidal stream turbines.

The following chapter will examine the context in which this work sits and its relevance to the challenges facing future power generation in the UK. It will show there is an urgent need to develop new sources of renewable energy in the light of the increasingly precarious position of the UK's energy supply and the possible catastrophic effects of climate change. Against this gloomy backdrop the government has signalled that small-scale embedded generation can make an important contribution to meeting part of the UK's energy needs. Having established the context of the research, the Chapter will detail the structure of the research and explain how the different the aspects of the work fit together.

1.2 Climate change

Our understanding of the climate has improved greatly over the past three decades as we have moved from simple models of the climate system in the mid-1970s,

accounting for the effects of solar heating, rain fall and CO_2, to highly detailed models that account for many aspects of the real world including the interaction of vegetation and atmospheric chemistry [1]. Although the models have become more precise, climate science is still in its infancy and there is still a considerable amount that we do not understand. For example, the role that clouds and aerosols play in reflecting and absorbing heat from the sun and earth are very complex and poorly understood at this time [2], as is the possible fragility of the North Atlantic Conveyor which brings warm water from the tropics to Northern Europe [3, 4]. These and other uncertainties could produce unpleasant surprises for us in the future if the many positive feedback mechanisms vaunted by scientists produce a rapid and catastrophic runaway warming effect.

This thesis is not concerned with a detailed discussion of the science behind climate change, however, save to say that the past debate over the exact cause and extent of planetary warming has been replaced in recent years by a scientific consensus. This consensus is articulated by the International Panel on Climate Change (IPCC), whose most recent report states that global warming is real and lays the blame squarely in human hands:

> *"Global atmospheric concentrations of carbon dioxide, methane and nitrous oxide have increased markedly as a result of human activities...Warming of the climate system is unequivocal, as is now evident from observations of increases in global average air and ocean temperatures, widespread melting of snow and ice, and rising global average sea level"* [1].

One method of mitigating the effect of climate change is to reduce our dependence on fossil fuels by producing more electrical power through renewable sources, and the ultimate aim of the research contained within this thesis is to further that goal.

1.3 Energy Security

Besides the obvious need to reduce greenhouse gas (GHG) emissions, producing more energy locally from renewable sources will also improve security of supply, and make the UK less dependent on unstable energy exporting countries and long supply pipelines.

In the past the UK has been in the enviable position of generating its power from a mix of sources. These were split roughly evenly between nuclear, coal, and gas, with the domestic production of coal and gas making our energy supply one of the most secure in the world. In 1985 the UK began to consume more coal then it produced [5] following the closure of many collieries after the miners' strike of 1984, and in 2004 the UK became a net importer of natural gas because of dwindling North Sea supplies [6]. To make matters worse many nuclear power stations in the country are now coming to the end of their design life with over 60% of the installed capacity due to be decommissioned by 2020 [7]. If no action is taken the UK will become increasingly dependent on imported gas, as shown by Figure 1-1. This will put the country in a precarious position, with long gas pipelines being highly susceptible to terrorist attack. In addition, many EU countries will increasingly be in competition to secure supplies from a re-emergent Russia in order to meet future pollution reduction targets.

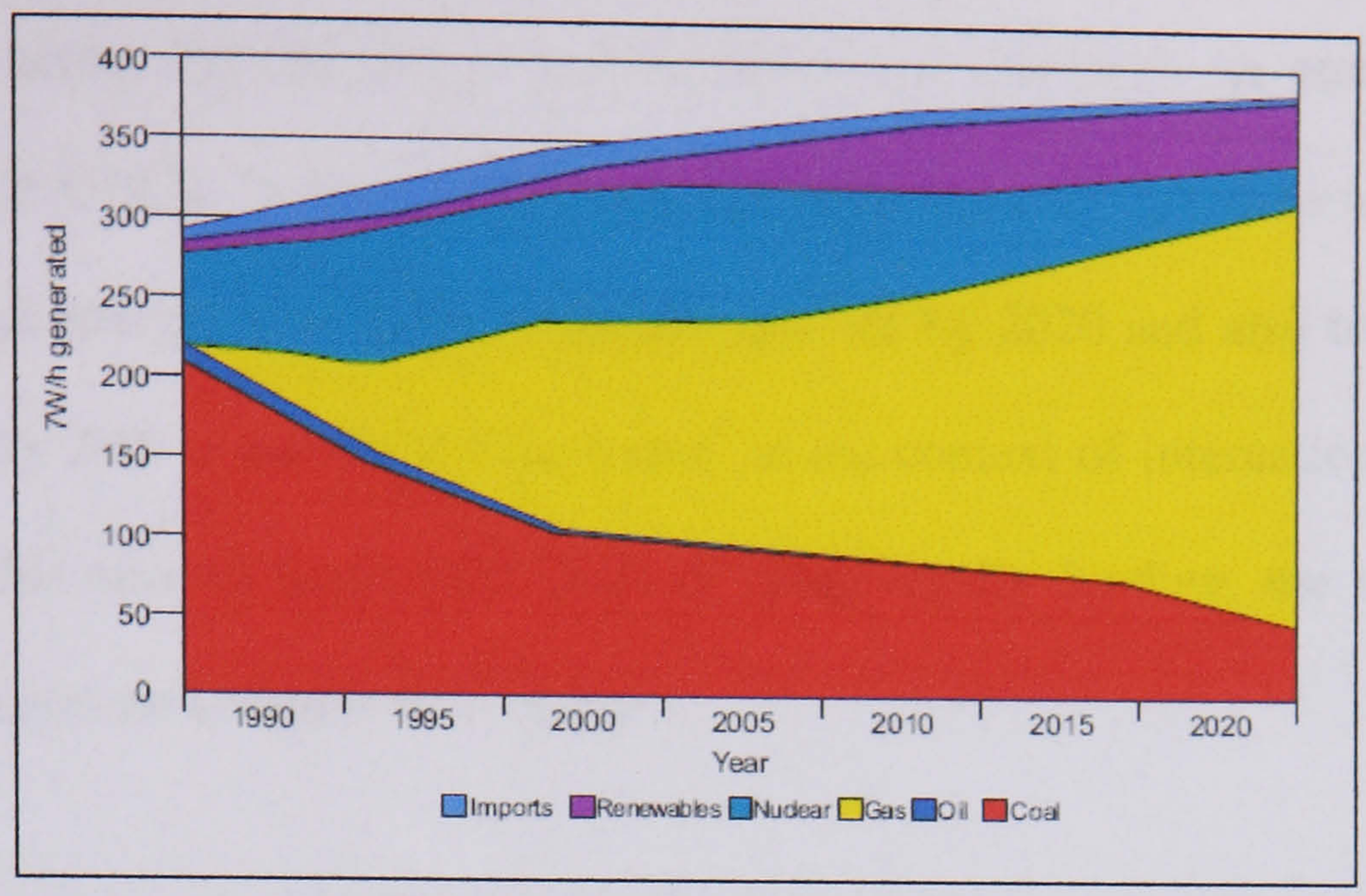

Figure 1-1. Past and future UK electricity generation mix [8]

Despite the increased use of natural gas to generate power – particularly in the UK – it is worth noting that some sources have suggested it has no benefit over coal in mitigating climate change, and indeed may make matters worse. This is because 2-4% of the methane leaks into the atmosphere during the pumping and distribution process, where it produces a warming effect 24 times greater then CO_2. When this effect is factored in, natural gas is, at best, equally as bad as burning coal and at worse, twice as bad [9].

1.4 Response to climate change and energy security

World leaders are now beginning to accept that urgent action has to be taken to tackle climate change. Generating electrical power from renewable sources is perhaps one of the simplest methods of doing this, and is popular with politicians because it is thought to stimulate growth in new technology. The energy supply sector is also ripe for improvement; the IPCC recently pointed out that the largest growth in GHG emissions between 1970 and 2004 came from the energy sector, which increased 145% [10].

Politicians across Europe and in the UK have now started to set binding targets for reductions in GHGs. In March 2007, the European Council agreed to meet 20% of the EU's overall energy needs from renewable sources by 2020 and also to decrease GHG emissions by 20% in the same time frame 'in the context of international action' [11]. Although this second target falls short of being legally binding, the rhetoric coming from the European Union is still robust:

"When the current international commitments are renewed in 2012, the EU will push for developed countries collectively to reduce their emissions of greenhouse gases by an amount in the order of 30% by 2020 compared to 1990. Irrespective of what other countries do, the EU has made a firm independent commitment to achieve a reduction of at least 20% by 2020" [11].

In the UK the political climate is slightly less bullish but still optimistic. The energy white paper of 2003 announced the 'ambition' to cut CO_2 emissions by 60% from 1990 levels by 2050, with the 'aim' of producing a 10% reduction in emissions by 2010 and the need to make 'real progress' by 2020 [12], although the only binding target is a 5% reduction by 2012 under the Kyoto Protocol [13].

In order to make these proposed reductions a reality there has been much interest in the idea of moving away from centralised power generation and towards Distributed Generation (DG) by using a large number of small or micro generators spread over a large area. Adopting this strategy also has the added benefit of delaying or negating grid reinforcement [14], reducing transmission losses [14] and providing ancillary services to the network operators [15]. A 2003 study by the Government [16] found that building mounted wind turbines could make a useful contribution to providing DG, and

enthusiasm for this technology was reaffirmed in the 2006 Microgeneration strategy which stated:

"Microgeneration technologies have the potential to make a significant contribution to our energy policy goals of tackling climate change [and] ensuring reliable energy supplies..." [17].

However, it is important to sound a note of caution as the UK's track record on emissions reductions is not particularly impressive. Despite the Government's continual reminders that the UK will be one of the few countries to meet its 2012 emissions targets under the Kyoto Protocol, the actual quantity of new renewable generating capacity that has been installed in recent years is tiny. From 2002 to 2006 a total of 2GW of new wind turbine capacity – by far the most economically viable form of renewable power – was installed out of total generating capacity of 76GW, with a further 1.6GW under construction and 11.4 GW planned [7]. In total the UK has increased its renewable electricity generation from 1.8% to 4% in this period [7]. The reduction of GHG emissions since 1990 has largely been due to the replacement of many coal-fired power stations with gas-fired CCGT plants in the 1990s.

If the UK Government is serious about meeting its 2010 target, approximately 10 GW of additional DG will have to be connected to distribution networks [18]. DBERR (formerly the DTI) suggest that up to half of this can be provided by wind energy [19], while a study focussing on the use of small-scale embedded generation in the built environment has suggested that the widespread installation of micro-generation could meet 60% of our electricity needs and cut carbon emissions by 15% by 2050 [17]. Numerous studies [14, 17, 20, 21] have also shown it is entirely feasible for distributed

micro-generation to make a significant contribution to the future UK energy mix. The work presented in this thesis is therefore of real relevance if the UK is to meet its emissions reduction targets. The following section describes the structure of the thesis in more detail.

1.5 The structure of the thesis

The remainder of this thesis is predominantly devoted to the development of electrical generators for micro wind and water turbines, and to the modelling and control of these systems. By way of an introduction into this field, Chapter 2 discusses three types of commonly used micro wind turbines and examines how they can be integrated into an efficient Wind Energy Conversion System (WECS). The Chapter also introduces a PM axial-flux generator that has been developed at Durham over several years, and examines how different WECSs employing this generator can be modelled in MATLAB/SIMULINK.

Micro and small-scale WECS will only help contribute to the Government's target of installing 10 GW of DG capacity by 2010 if suitable economic conditions exist to drive their uptake, and this topic is examined in Chapter 3. A Weibull probability analysis of wind speed distribution is introduced to provide an estimate of the annual energy yield of a selection of micro turbines placed in different wind regimes. By investigating the cost of the system, government subsidies and inducements, and the monetary value of the electricity generated, the economic attractiveness of micro turbines can be assessed. A review of recent research in this area reveals that there may be serious question marks over the viability of roof-level turbines in the urban environment [22, 23].

Chapters 4-7 focus on different aspects of modelling WECSs using MATLAB/SIMULINK. Chapter 4 introduces a wind turbulence model based on a spectral analysis of real wind data. In chapter 5 this model is used in conjunction with the model of an H-type Darrius turbine, introduced in Chapter 2, to investigate potential stall problems that can arise when the turbine is connected to the grid via a Windy Boy grid-tie inverter. It is found that these problems can be mitigated, at least to some extent, by the inclusion of a DC-DC converter on the front end of the Windy Boy inverter. Chapter 6 extends the concept of modelling a single WECS by considering the consequences of aggregating the output powers form a number of turbines together. Aggregation at AC and DC are both examined and it is shown that DC aggregation, where the outputs of a number of turbines are channelled through a single inverter, produces a more cost effective system, although at a slightly lower efficiency.

In Chapter 7 the focus shifts back to modelling an H-type Darrieus turbine in turbulent wind, however now the annual energy yield rather then the stability of the turbine is considered. The turbulent wind model developed in Chapter 4 is again combined with the Darrieus model of Chapter 2 to investigate the effect of turbulence on the energy capture coefficient, C_p, of the turbine. By combining this information with the Weibull wind speed distribution introduced in Chapter 3, a more realistic assessment of the annual energy capture can be made. Chapter 7 then extends this analysis to look at ways of improving energy capture in turbulent wind and shows that a simple control system, which uses a braking resistor to slow the turbine during wind gusts, can considerably improve annual energy capture.

Although the air-cored axial flux generator introduced in Chapter 2 has been integrated into two turbine systems, little work has been done on its optimisation and this is the

subject of Chapter 8. The 1kW, 300rpm machine which is used for much of the modelling in Chapters 2 and 6 is used as a case study to investigate the design process of the generator. By experimentally verifying the thermal model of the machine it is possible to investigate how the stator thickness affects the output power, current density, active weight and efficiency of the generator, and by doing this an optimised design can be produced.

Having considered the optimisation of a small axial-flux machine in Chapter 8, Chapter 9 considers the practicalities of extending this generator concept to larger power ratings. The Chapter looks at switching from a round to a trapezoidal generator topology and also discusses the structural problems facing large diameter axial-flux generators, which arise due to the increasingly large magnet closing forces. Methods of increasing the generator power, such as using an epicyclic gearbox and moving to a stacked rotor-stator configuration, are also investigated.

An important conclusion from this work is that at large power rating (>20kW, 100rpm) the axial-flux concept becomes untenable, and it is advantageous to move to a radial-flux topology because this allows the large magnet forces to be managed more easily. Chapter 10 extends this concept by examining the radial flux topology in some detail and specifically focuses on manufacturing techniques that can be adopted by small Mechanical Engineering companies with little experience of electrical machines. The radial flux generators considered here follow the simple manufacturing philosophy of the axial-flux concept but allow larger machines to be constructed, and these could be used for hydro or tidal stream turbines. For this application, a number of novel stator materials are considered in place of the electrical steel laminations which require specialist equipment to produce. Of the materials tested, a 0.5mm mild steel wire was

shown to provide the best magnetic and loss properties, and so was chosen for a prototype machine which was constructed to test the accuracy of the design process. In addition, a similar air-cored generator was also constructed to benchmark the performance of wire-wound stator machine and also to explore other simple manufacturing methods.

The design, manufacturing, test and evaluation of the wire-wound stator machine and the air-cored machine are the subject of Chapter 11. It is shown to be feasible to construct simple, large diameter machines using novel manufacturing techniques and materials that perform predictably and with acceptable losses.

The final chapter of this thesis draws together the conclusions of the research and examines where further work should be done.

1.6 Conclusions

This Chapter has shown that securing the UK's electricity supply and the threat of global warming are two of the main drivers behind the current interest in distributed generation. The government has already signalled a willingness to adopt renewable sources of energy generation with embedded micro-generation being tipped as an important contributor. The government's own research has highlighted the usefulness of micro wind turbines in this respect and so the research covered in this thesis must be considered apposite.

Chapter 2

Introduction to micro and small-scale wind energy conversion systems

2.1 Introduction

The following chapter will examine the operation of a basic wind energy conversion system. Section 2.2 introduces the three components of the system: the turbine, the generator and the load, and examines how these must be matched to produce efficient energy conversion. A permanent magnet air-cored axial flux generator, which has been developed at Durham, is also introduced in this section.

AC and DC equivalent circuit representation of the wind energy conversion system are developed in sections 2.3 and 2.4, and this allows the load characteristic and turbine characteristic to be combined to define a steady-state operating point for the system. Section 2.5 details how a 300W Savonius wind energy conversion system (WECS) can be modelled in MATLAB/SIMULINK, while section 2.6 deals with the validation of this model by comparing the predicted performance with measurements taken on an identical generator-load system in the laboratory.

2.2 The Micro Wind Energy Conversion System

Micro (0-5kW) and small-scale (5-25kW) wind energy conversion system consists of three components: the turbine, the generator and the load. Efficient energy conversion only occurs in a narrow band of speeds that vary according to the wind speed and because of this all three components must be well integrated to ensure effective

operation. Sections 2.2.1- 2.2.3 will examine each component to see how this can be done.

2.2.1 The Micro Wind Turbine

There are three generic types of micro turbine that are used for electricity generation and these are shown in the figure below.

(a) (b) (c)

Figure 2-1. Micro wind turbines: (a) HAWT [24] (b) Darrieus type VAWT [25] (c) Savonius type VAWT [26]

Figure 2-1(a) shows the most well-recognised type of turbine, the Horizontal Axis Wind Turbine (HAWT) which generates rotational force through aerodynamic lift. Figure 2-1(b) shows an H-type Darrieus Vertical Axis Wind Turbine (VAWT), sometimes known as an 'egg beater' due to an alternative design where the blades are attached at the top and bottom of the rotor. This device also operates through aerodynamic lift. Figure 2-1(c) shows a Savonius type VAWT, named after its inventor. The Savonius turbine is a drag operated device and so cannot spin faster then the wind speed; it is also less efficient then the two other turbines.

Vertical axis turbines are attractive for use in the built environment as they can accept wind from any direction, and anecdotal evidence has suggested they may provide better energy capture in the highly turbulent urban environment. However, there are some drawbacks to aerodynamic Darrius type VAWTs: they cannot be turned out of the wind (furled) in high wind speeds and so are prone to over-speeding (this is discussed in more depth in Chapter 7), and some turbine designs will not self-start [27], requiring the generator to be run as a motor which provides extra complexity. By contrast the Savonius turbine has a high starting torque and does not need to be protected against over-speeding since, as a drag operated device, it cannot spin faster then the wind speed. This may make it attractive for urban applications despite its poor efficiency.

Power is extracted from the wind by the turbine according to:

$$P_{turbine} = \frac{1}{2} C_P(\theta, \lambda) \rho A V_w^3 \qquad [2\text{-}1]$$

C_p is the energy capture coefficient and is a function of the turbine blade's pitch angle, θ, and a dimensionless group known as the tip-speed ratio, λ. For the turbines examined in this thesis, however, the turbine blades are fixed and so C_p can be considered a function of λ only.

λ is defined as the tip speed of the turbine blades divided by the oncoming wind speed:

$$\lambda = \frac{\omega R}{V_w} \qquad [2\text{-}2]$$

By plotting C_p as a function of λ, a performance curve for the turbine may be produced.

C_p-λ curves for the three types of turbine shown in Figure 2-1 are presented below.

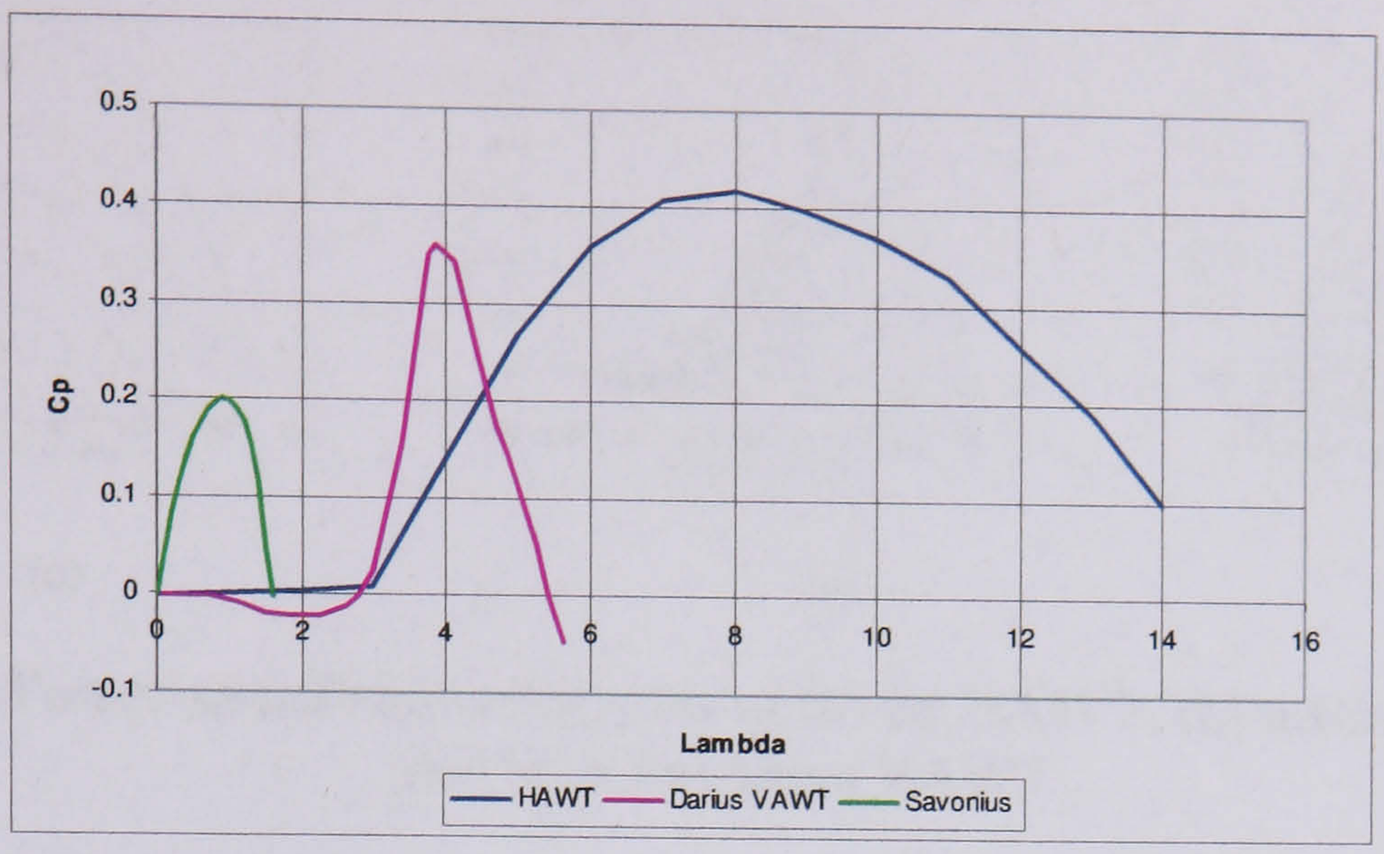

Figure 2-2. Typical performance curves for a Savonius type VAWT [26], a HAWT [28] and a Darrieus type VAWT [29]

Figure 2-2 shows the Darrius turbine will not self-start due to the negative C_p value at low λ, and has a much narrower peak then the HAWT or Savonius turbine, implying the WECS must be more carefully controlled to keep an optimal value of λ as the wind speed changes. This control strategy will be discussed in more detail in Chapter 5. Being a drag operated device, the Savonius turbine operates at much lower values of λ (the maximum being slightly over 1), and the peak C_p is also significantly lower then either of the aerodynamic turbines.

The power produced by a turbine through its rotational speed range may be plotted, for a given wind speed, by combining the C_p-λ curve with equation [2-1]. If this is done for a series of wind speeds, the resulting family of curves can be used to predict the power available from the turbine at different wind speeds and rotational speeds. The power curves corresponding to the three C_p-λ curves shown in Figure 2-2 are presented in Figure 2-3 (the turbine dimensions are shown in Table 1). The turbines achieve different powers because of the difference in physical size between the turbines and because of

the different maximum C_p values.

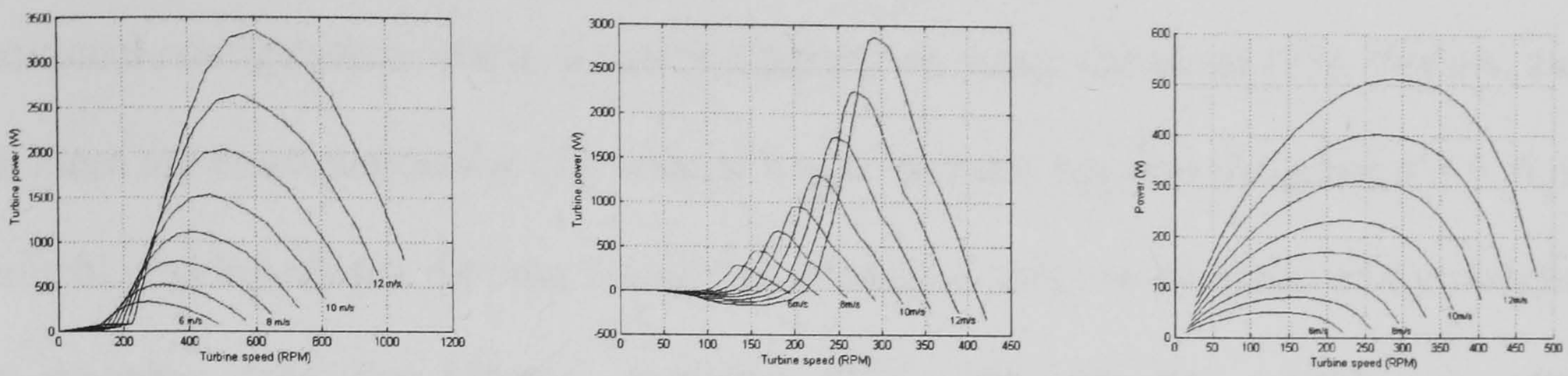

(a) (b) (c)

Figure 2-3. Power-speed characteristics of (a) an HAWT, (b) a Darrieus VAWT and (c) a Savonius VAWT

Turbine type	Swept Area (m^2)	Turbine rating (kW)	$C_{p(max)}$
HAWT – Figure (a)	6.6	3.0	0.420
Darrieus VAWT – Figure (b)	6.6	2.5	0.362
Savonius VAWT – Figure (c)	1.90	0.5	0.200

Table 1. Turbine dimensions

The turbine characteristics shown in Figure 2-3 (b) and (c) have been used for the extensive modelling work described in Chapters 5, 6 and 7.

In all three characteristics the maximum power available from the turbine occurs at a specific rotational speed for a given wind speed. As the wind speed increases, so the turbine speed must increase to maintain the turbine at the maximum power point. The ideal relationship between turbine speed and output power is cubic as can be seen by combining equations [2-1] and [2-2].

2.2.2 The Micro Generator

In the past some small-scale wind turbines manufactures have used 'off-the-shelf' induction generators with gearboxes to supply power [30] but these have largely been superseded by specially built direct-drive permanent magnet machines. Most generators use a radial flux topology with a slotted stator and concentrated windings, and

employ an 'inside out' design where the 'magnet can' rotates around the coils [24] [31] [32]. Some manufactures have used a radial flux topology but opted for a more traditional configuration where the rotor magnets lie inside the stator [33]. Vertical axis machines are characterised by low starting torque and this requires the generator to have minimal cogging torque. For the radial flux generators this can be achieved by skewing the magnets, (see the 'Turby' generator [32]), although this topology is often challenging to build, especially for small companies with limited specialist manufacturing capabilities[1].

An alternative design which offers a much simpler manufacturing route is the axial-flux configuration. A toroidally wound axial-flux machine with a strip wound iron core has been developed at Durham [34] for use with diesel generating sets and has been adapted for use with wind turbines. It was found that the iron core added a significant weight penalty and the high magnetic forces were also awkward to manage during assembly. In addition, the structural flexing of the turbine during wind gusts tended to be transmitted through the generator, causing damage to the armature windings. An alternative solution that retains the axial-flux topology is to use an air-cored armature structure with concentrated armature coils [35]. Such a generator is simple to construct, highly robust and, by removing the stator iron, also fairly lightweight.

This generator concept has proved successful during field trials with two turbine manufactures [25] [26] and so has been used as the basis for much of the simulation

---

[1] A further discussion of generator configuration can be found in Chapter 10

work in Chapters 4-7. Because of this, the generator will be discussed in some detail below.

The generator comprises two mild steel rotor discs sandwiching a non-magnetic, non-conducting stator containing armature coils. Rare earth (NdFeB) permanent magnets are arranged circumferentially around the two rotor discs in an N-S-N-S pattern such that the N on one disc faces the S on the other (Figure 2-4).

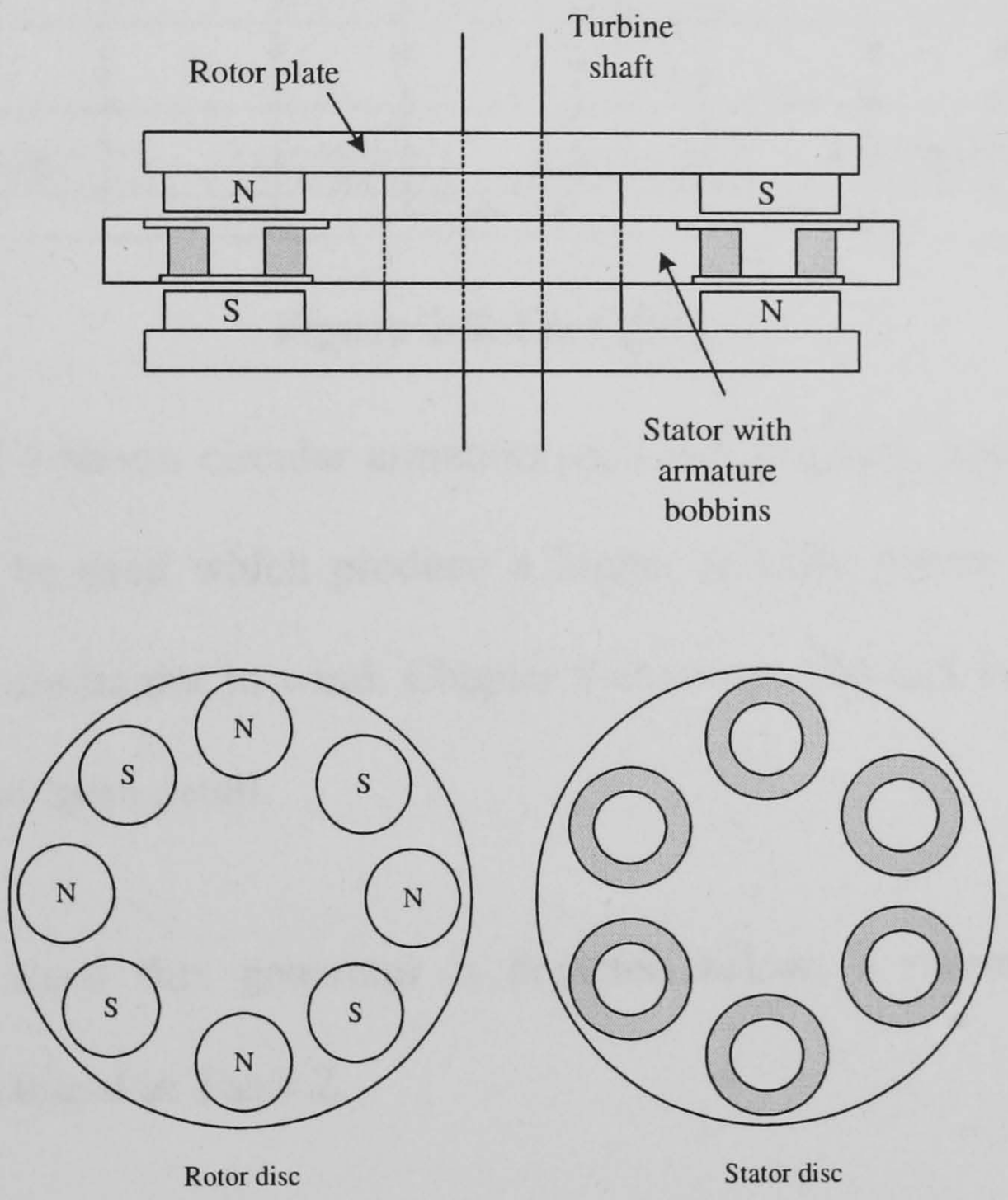

Figure 2-4. Generator concept

The concentrated armature windings can be wound on bobbins or directly potted into the stator to protect the coils from contact with the rotor. Reference [36] shows that this type of concentrated windings structure can have a similar performance to an overlapping coil configuration. The stator is made from a non-magnetic, non-conducting material such as PVC or Tufnol, which reduces weight, lowers the magnetic

closing forces and, perhaps most importantly for VAWTs, ensures the generator has no cogging torque.

The flux travels from the N of one magnet across the air gap to the S of the opposing magnet before turning 90° to travel circumferentially within the rotor plate by one pole pitch. It then completes the return path across the air gap as shown below.

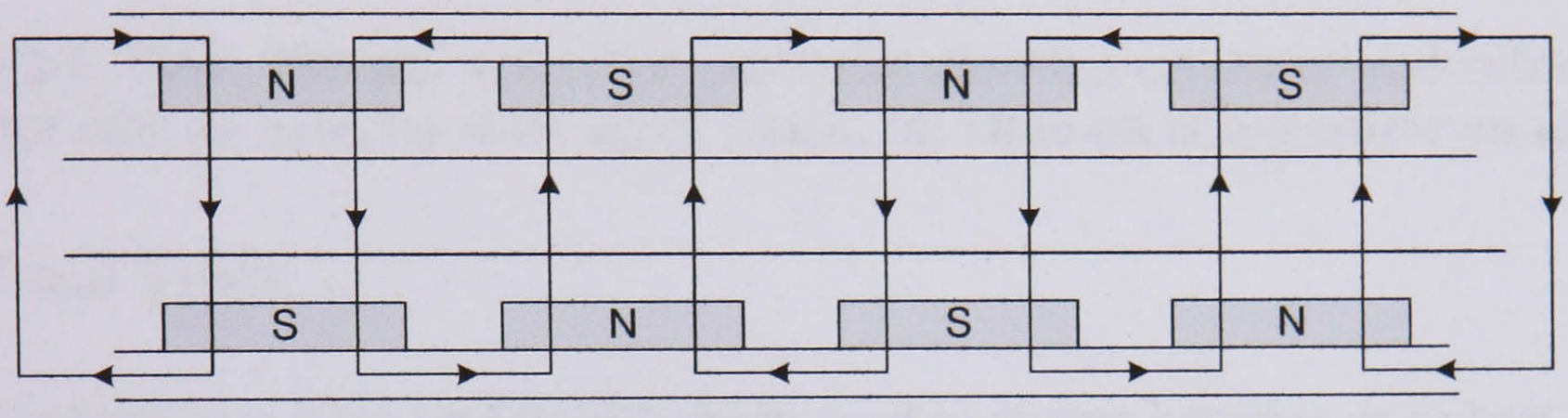

Figure 2-5. Flux path

Although Figure 2-4 shows circular armature coils and magnets, trapezoidal coils and magnets can also be used which produce a higher specific power in the generator, although the coils are harder to wind. Chapter 9 examines the link between coil shape and output power in more detail.

A 1kW, 300rpm axial flux generator is depicted below; a summary of generator dimensions can be found in Table 2.

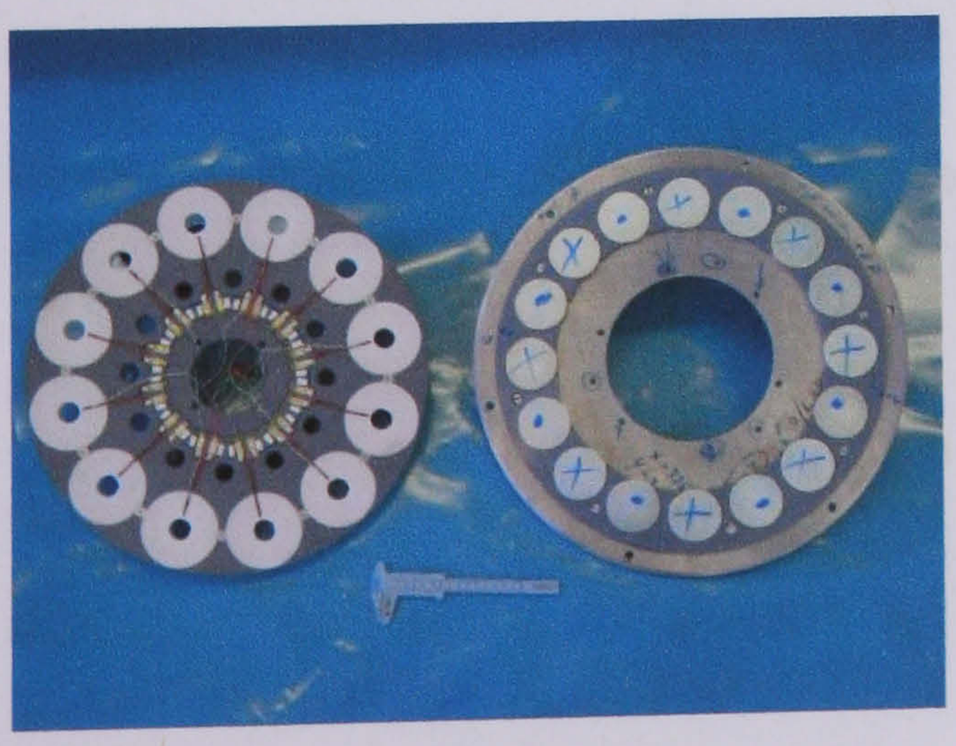

(a)

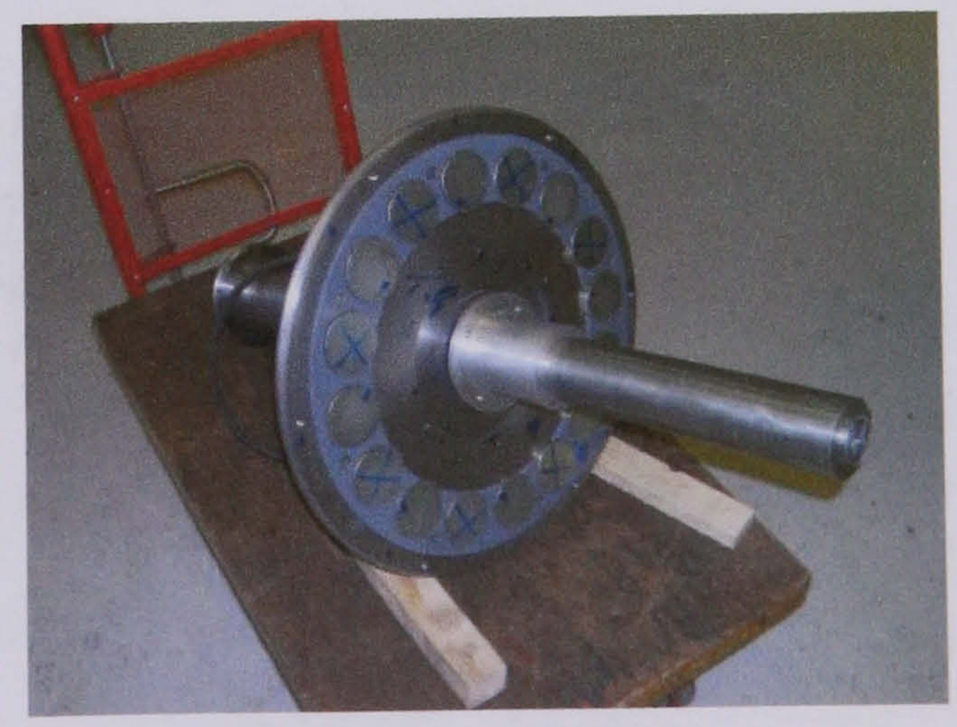

(b)

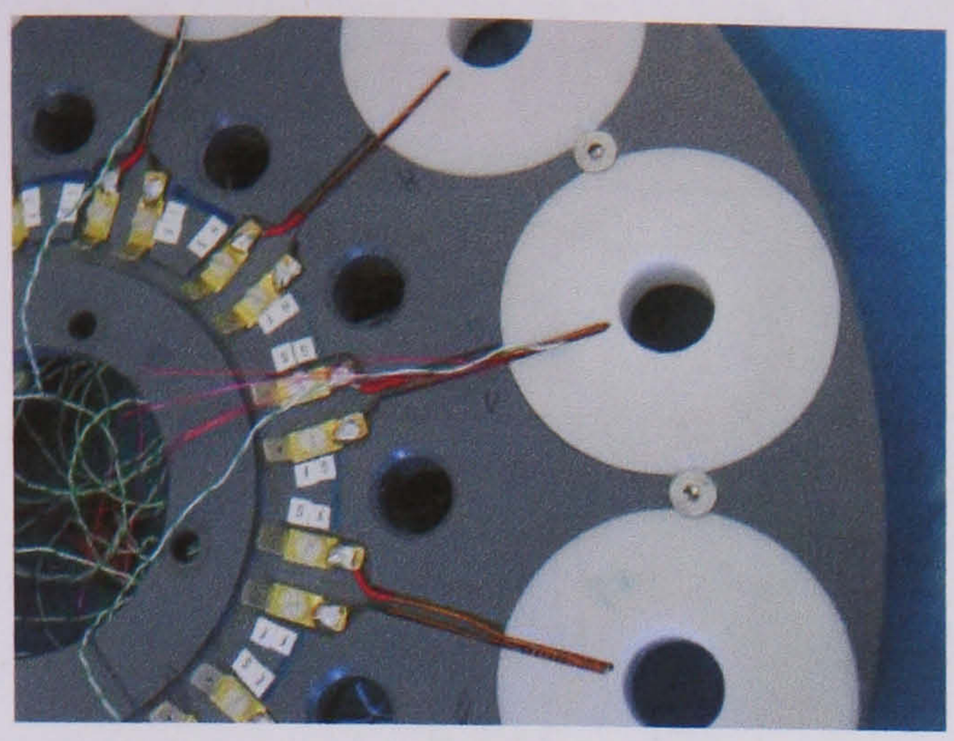

(c)

(d)

Figure 2-6. 1kW, 300rpm axial flux generator showing (a) stator and rotor discs, (b) rotor disc on axle, (c) close-up of stator, (d) close-up of generator on turbine

2.2.3 Load Types

Micro wind turbines have traditionally been used to charge batteries or to heat water in off-grid applications and are now also used for grid connection via a suitable grid-tie inverter. An inverter that is compliant with the G83 grid code and is fast becoming the industry standard for such applications is the SMA WindyBoy inverter [37], (this is considered in detail in Chapter 5). For battery charging and grid connection, the 3-phase AC is converted to DC using a simple passive rectifier, although this is not necessary for heating applications if a 3-phase resistive load is used. The three basic load types are shown schematically in the figure below.

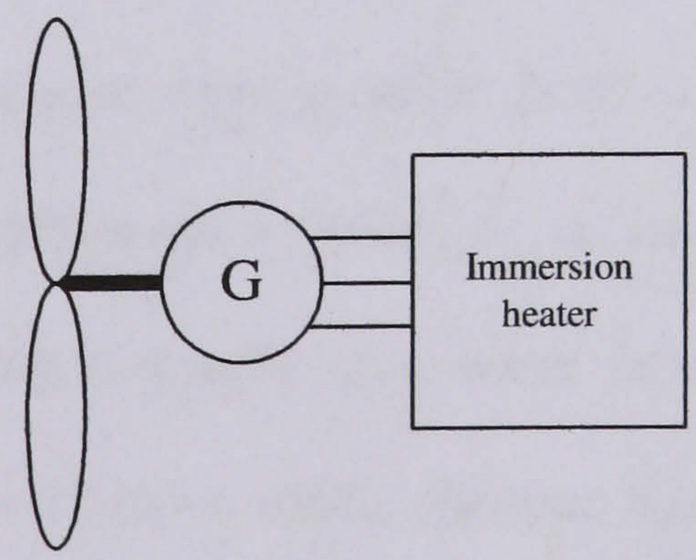

(a)

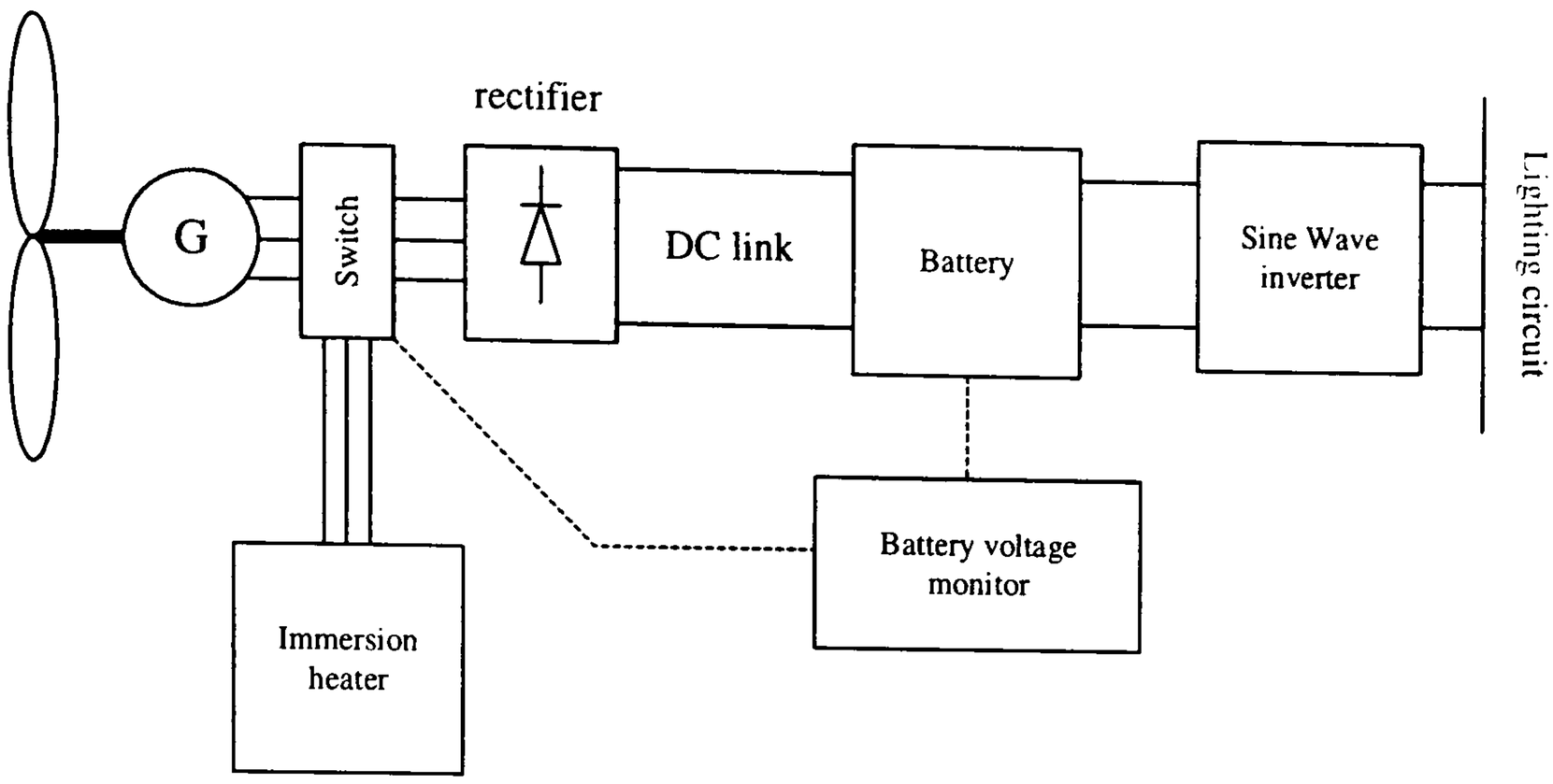

(b)

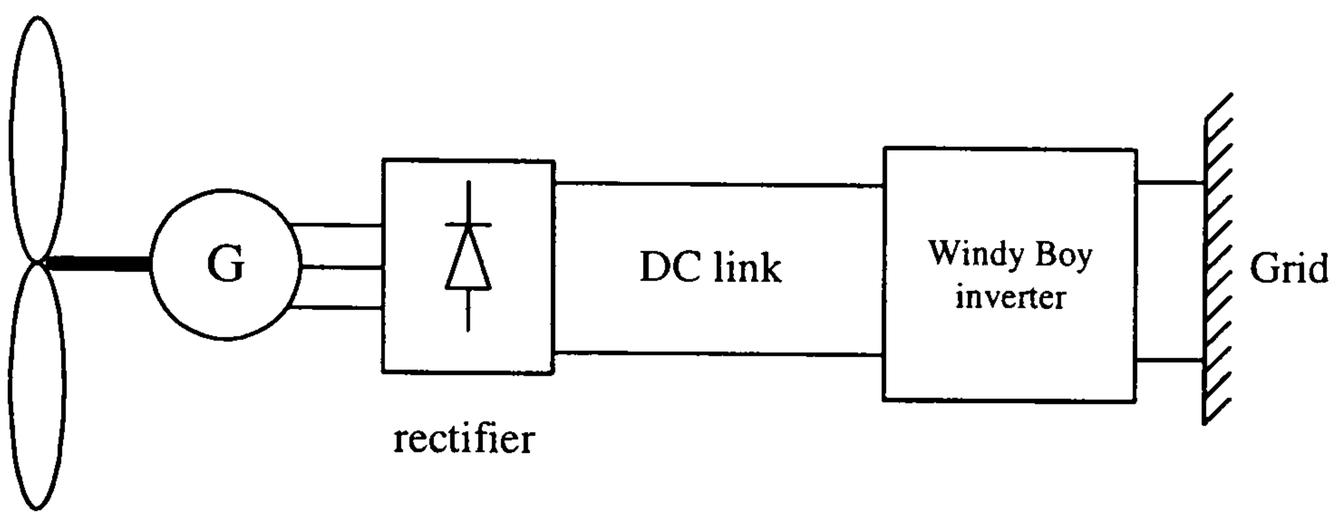

(c)

Figure 2-7. Schematic connection diagrams for (a) resistive heating, (b) battery charging and (c) grid connection

Figure 2-7 (a) represents the simplest way of using power generated from the wind, by simply dumping it into a resistive load and using the energy to heat water. In Figure 2-7 (b) the energy is stored in a battery and used to power the lighting circuit of a domestic home via a 230V single phase sine wave inverter. A device to monitor battery voltage is also included to divert the generator's power to an immersion heater if the battery becomes fully charged. Using a simple sine wave inverter to supply power to the domestic side of the grid interface is much cheaper then using a grid-tie inverter to export power back to the grid, as in Figure 2-7 (c). A full study of the economics of WECS is given in the following Chapter.

Each type of load imposes its own operating characteristic on the turbine. For a resistive load, the power dissipated is proportional to the square of the voltage across the load and this produces a quadratic power transfer characteristic if power is plotted against turbine speed. This is because the synchronous PM generator produces a terminal voltage in proportion to rotational speed, neglecting the voltage drop across the resistance and reactance of the armature.

The Windy Boy inverter contains software which synchronises the AC waveform created by the inverter with the grid waveform at the required amplitude and power angle. The power angle is controlled so the power exported increases as a linear function of the DC input voltage (and therefore turbine speed), as shown in the figure below.

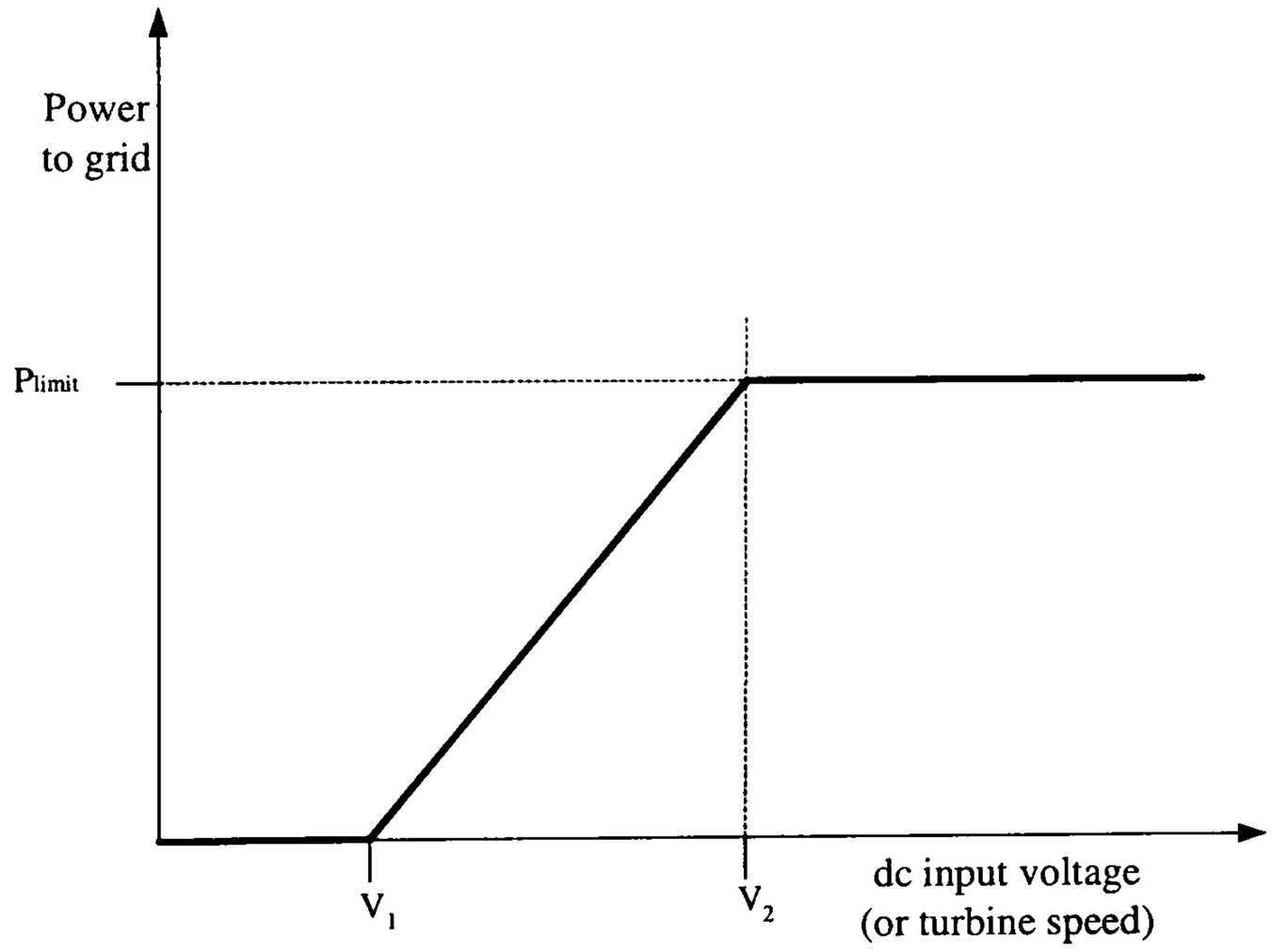

Figure 2-8. Windy Boy characteristic

P_{limit} is fixed by the inverter; parameters V_1 and V_2 maybe chosen by the operator to best fit the turbine's power curves.

Battery charging imposes a near vertical power transfer characteristic onto the turbine since the battery voltage is essentially fixed (hence constant turbine speed), and only deviates due to the slight voltage drop caused by the battery's internal resistance, the generator's resistance and reactance, and the cable resistance.

These three types of characteristic are shown in detail in Figure 2-18, Figure 2-19 and Figure 2-20. For the purpose of illustration, however, a generic turbine and grid-tie inverter characteristic are presented below.

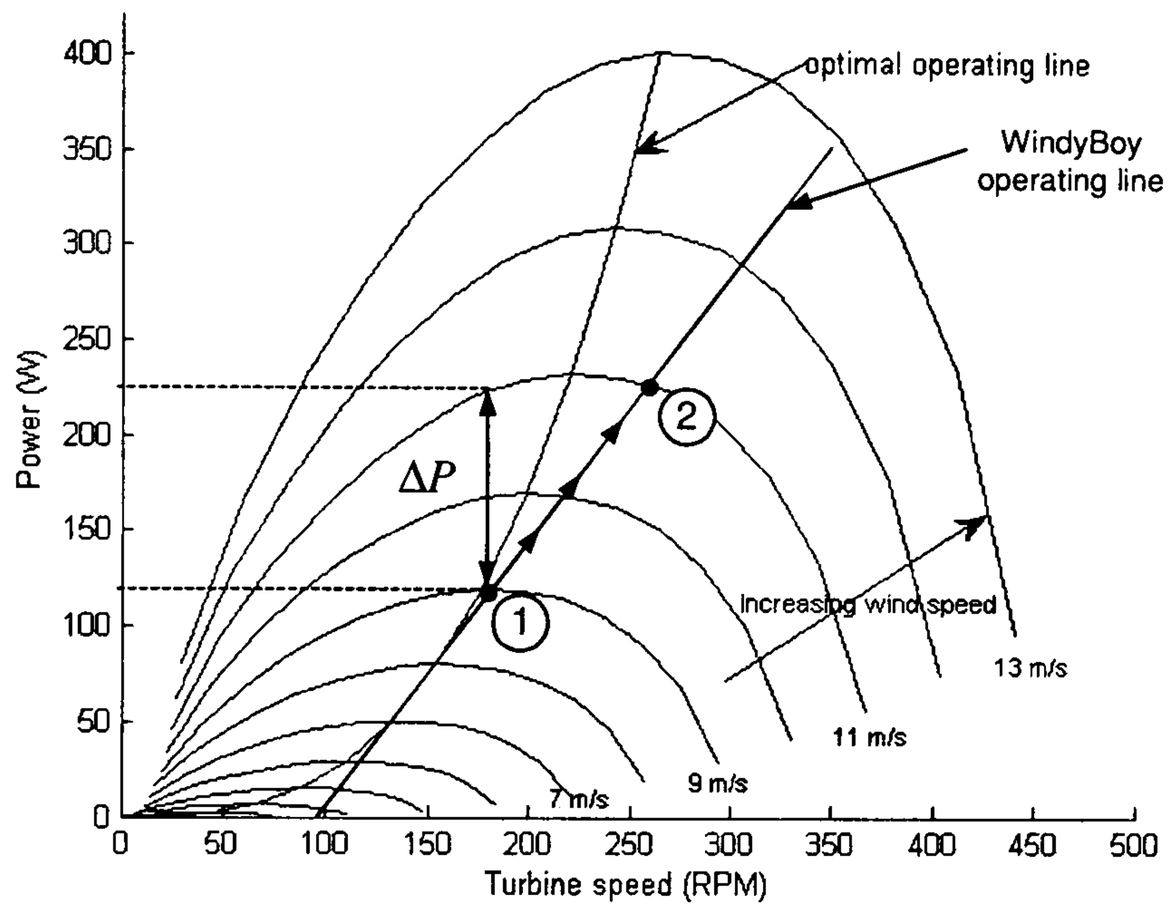

Figure 2-9. Operating characteristic

Although the wind speed determines which power curve the turbine may be operating on at any one moment, it is the electrical load that determines its rotational speed, and this produces a unique operating point that will change as the wind speed changes. For example, if the turbine is operating at position (1), in a steady wind of 9 m/s, and the wind speed abruptly changes to 11m/s, the turbine suddenly produces a quantity of surplus of mechanical power, ΔP. This produces an accelerating torque that shifts the turbine's operating point to position (2) along the inverter's operating line. The speed of this transition depends on the turbine's inertia. The same mechanism operates in reverse

if the wind speed drops.

2.3 AC equivalent circuit representation

The wind energy conversion system shown in Figure 2-7 (a), in which the energy is dumped into an AC resistive load, can be represented by an equivalent circuit and phasor diagram shown in Figure 2-10 and Figure 2-11. By using circuit analysis, the performance of the system can be converted into a series of analytical expressions which in turn can be implemented in SIMULINK to produce a model of the system, as described in section 2.5.

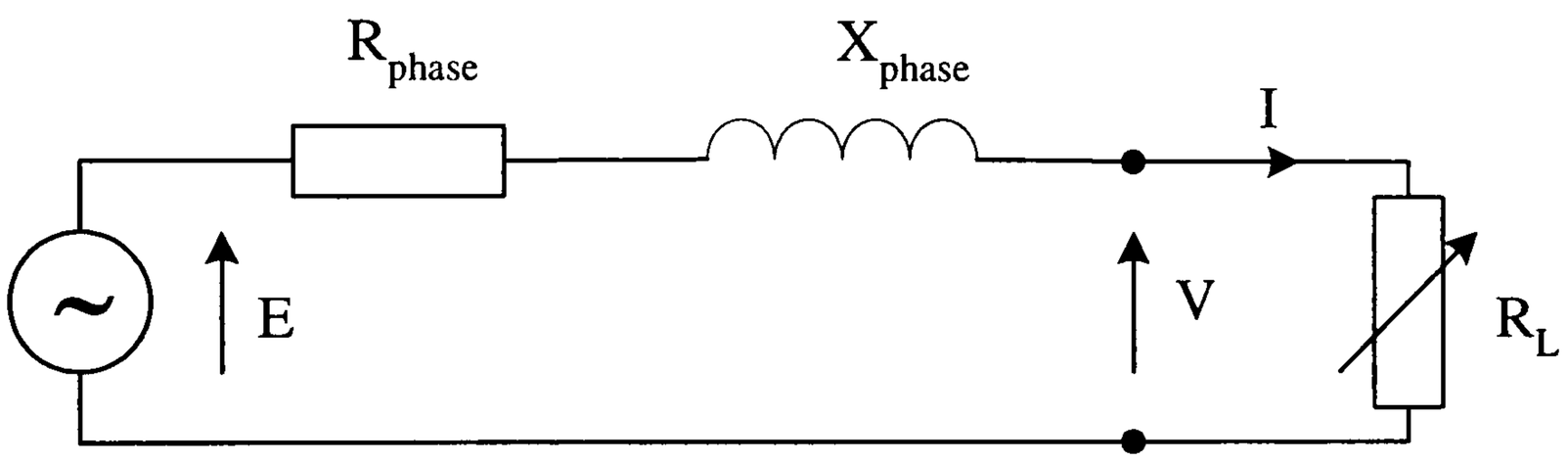

Figure 2-10. Per phase equivalent circuit

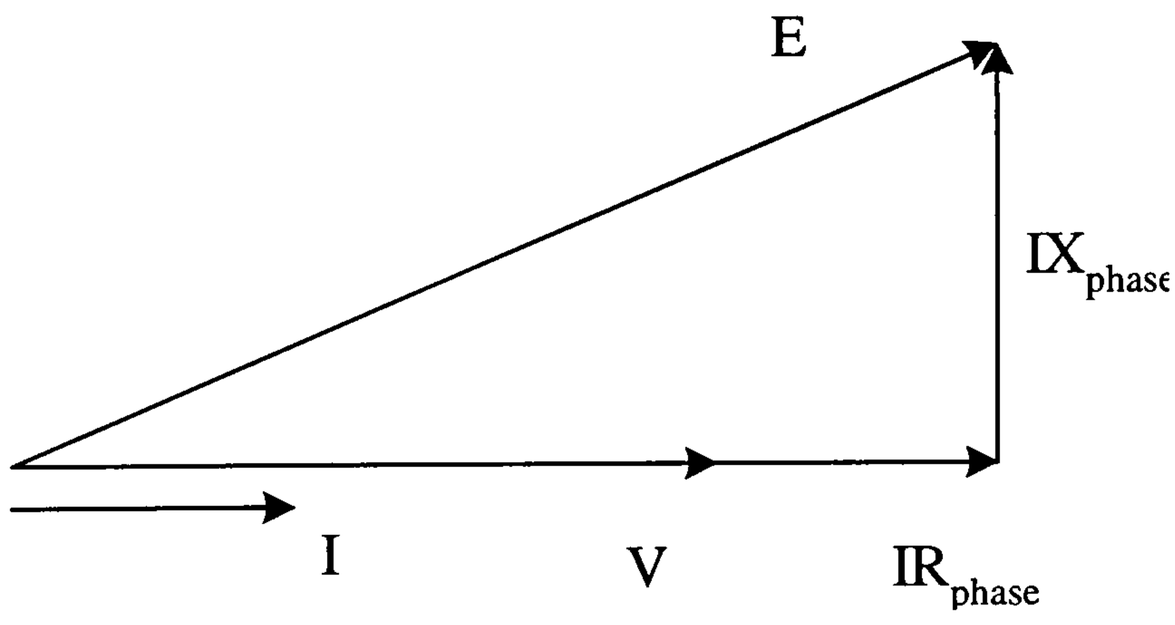

Figure 2-11. Phasor diagram

In the equivalent circuit the generator is represented as an ideal voltage source which produces an EMF in proportion to turbine speed, (equal to $k\omega$), connected in series to a resistor and inductor to account for the armature coil windings.

As the mutual inductance is small, the reactance per phase is given by:

$$X_{phase} = \omega_{elec} \frac{n_{series}}{n_{pall}} L_{coil} \qquad [2\text{-}3]$$

and $$R_{phase} = \frac{n_{series}}{n_{pall}} R_{coil} \qquad [2\text{-}4]$$

The phasor diagram is shown in Figure 2-11. Applying Pythagoras gives

$$V = \sqrt{E^2 - (IX_{Phase})^2} - IR_{Phase} \qquad [2\text{-}5]$$

Further,

$$I = \frac{k\omega}{\sqrt{(R_L + R_{Phase})^2 + X_{Phase}{}^2}} \qquad [2\text{-}6]$$

$$P_{load} = 3VI \qquad [2\text{-}7]$$

$$T_{electrical} = \frac{P_{load} + 3I^2 R_{Phase}}{\omega_{gen}} \qquad [2\text{-}8]$$

2.4 DC equivalent circuit representation

2.4.1 Battery charging

The Wind Energy Conversion System shown in Figure 2-7 (b) and (c) can be represented by an equivalent DC circuit viewed from the DC side of the rectifier [38]. The equivalent DC circuit for battery charging is shown below.

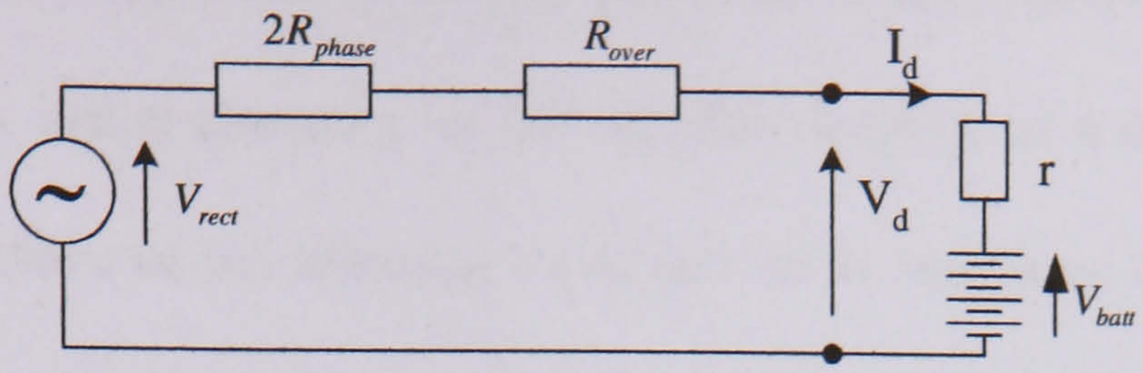

Figure 2-12. DC equivalent circuit for battery charging

The battery is represented by an ideal voltage source connected in series with a small internal resistance, '*r*'.

The average DC voltage at the output of the rectifier related to the AC phase voltage by [39]:

$$V_{dc} = \frac{3}{\pi}\sqrt{6}V_{phase} \cong 2.34V_{phase} \qquad [2\text{-}9]$$

However, there is a small voltage drop across the diodes of the rectifier (≈ 2-3V) which must be included, giving:

$$V_{rect} = 2.34V_{phase} - V_{diode} = 2.34k\omega_{gen} - V_{diode} \qquad [2\text{-}10]$$

Twice the phase resistance is used in the DC equivalent circuit since the current passes through two phase of the generator at any one time, as depicted in Figure 2-13.

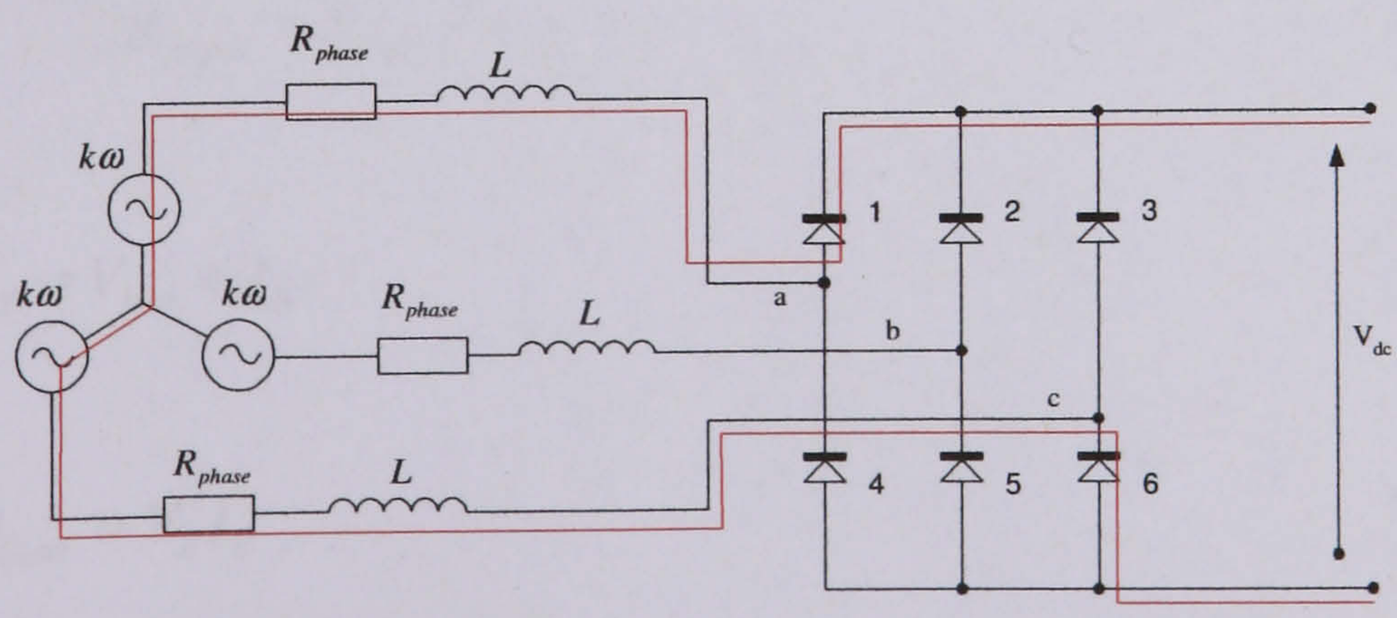

Figure 2-13. Current path through rectifier

The effect of commutation overlap is also included in the equivalent circuit. Ideally, commutation occurs instantaneously in the rectifier leading to a constant DC current. However, the inductance of the armature coils acts as an inertia to the changing flow of current, slowing the rate at which the diodes can be energised. The voltage drop per diode each time commutation occurs is given by the product of the current, I_d, and phase inductance, L_{phase}. Since all six diodes conduct during one cycle, the total averaged voltage drop is given by:

$$V_{drop} = 6fL_{phase}I_d \qquad [2\text{-}11]$$

$$\text{where } f = \frac{\omega_{elec}}{2\pi}$$

Commutation overlap may thus be modelled as a resistance which produces a voltage drop but no energy dissipation. The value of the resistance is given by:

$$R_{over} = \frac{3}{\pi}L_{phase}\omega_{gen}p \qquad [2\text{-}12]$$

Circuit analysis of Figure 2-12 gives:

$$I_d = \frac{V_{rect} - V_{batt}}{2R_{phase} + R_{over} + r} \qquad [2\text{-}13]$$

$$V_d = V_{batt} + I_d r \qquad [2\text{-}14]$$

$$P_{Load} = V_d I_d \qquad [2\text{-}15]$$

$$T_{electrical} = \frac{P_{Load} + I_d{}^2(2R_{Phase})}{\omega_{gen}} \qquad [2\text{-}16]$$

The equations shown above were implemented in SIMULINK, as described in section 2.5.

2.4.2 Windy Boy grid-tie inverter connection

The DC equivalent circuit for Windy Boy grid-tie inverter connection is shown in Figure 2-14.

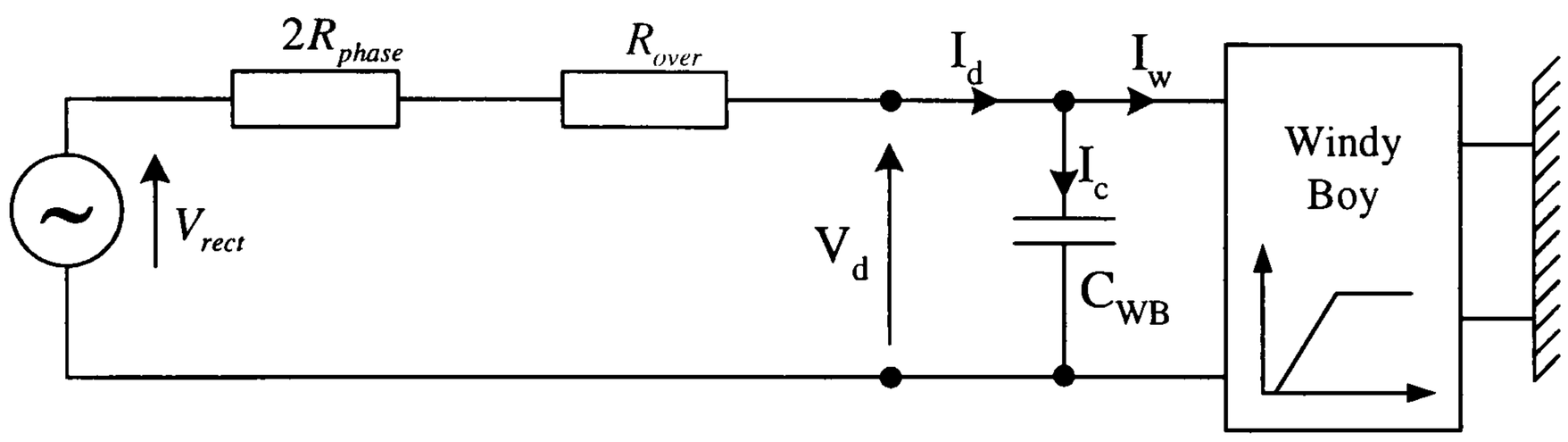

Figure 2-14. Equivalent dc circuit for WindyBoy connection

The WindyBoy inverter is represented by a simple look-up table which varies the exported power as a function of the DC link voltage (Figure 2-8) at a constant efficiency of 94%. The Windy Boy has a shunt capacitor connected across the input terminals which is also included in the equivalent circuit. Circuit analysis gives:

$$I_w = I_d - I_c \qquad [2\text{-}17]$$

$$I_w = \frac{P}{\eta_{WB} V_d} \qquad [2\text{-}18]$$

$$I_d = \frac{V_{rect} - V_d}{2R_{phase} + R_{over}} \qquad [2\text{-}19]$$

$$V_d = \frac{1}{C_{WB}} \int I_c dt \qquad [2\text{-}20]$$

$$\Rightarrow V_d = \frac{1}{C_{WB}} \int \frac{V_{rect} - V_d}{2R_{phase} + R_{over}} - \frac{P_L}{\eta_{WB} V_d} dt \qquad [2\text{-}21]$$

$$T_{electrical} = \frac{(2.34k\omega_{elec})I_d}{\omega_{gen}} \qquad [2\text{-}22]$$

The equations shown above can be implemented in SIMULINK, as described in the following section.

2.5 MATLAB/SIMULINK modelling

The wind energy conversion system can be modelled in SIMULINK by considering it as two separate parts: the mechanical (or aerodynamic) torque created by the turbine, and the electrical torque created at the generator by the load. Since the turbine and generator are mechanically connected, any imbalance between these torques will cause the system to accelerate according to:

$$J_r \frac{d\omega_{gen}}{dt} = T_{mechanical} - T_{electrical} \qquad [2\text{-}23]$$

$$\omega_{gen} = \frac{1}{J_r} \int (T_{mechanical} - T_{electrical}) dt \qquad [2\text{-}24]$$

2.5.1 Turbine torque

The turbine can be modelled to convert an initial wind speed into a mechanical torque at a given rotor speed. This can be done by considering the turbine power equation:

$$T_{mechanical} = \frac{P_{turbine}}{\omega_{gen}} \qquad [2\text{-}25]$$

where $$P_{turbine} = \frac{1}{2} C_P(\theta, \lambda) \rho A V^3 \qquad [2\text{-}26]$$

Since all turbines considered in this thesis use fixed blade geometry, C_p is a function of λ only and so can be implemented in SIMULINK using a look-up table, as shown in the schematic below.

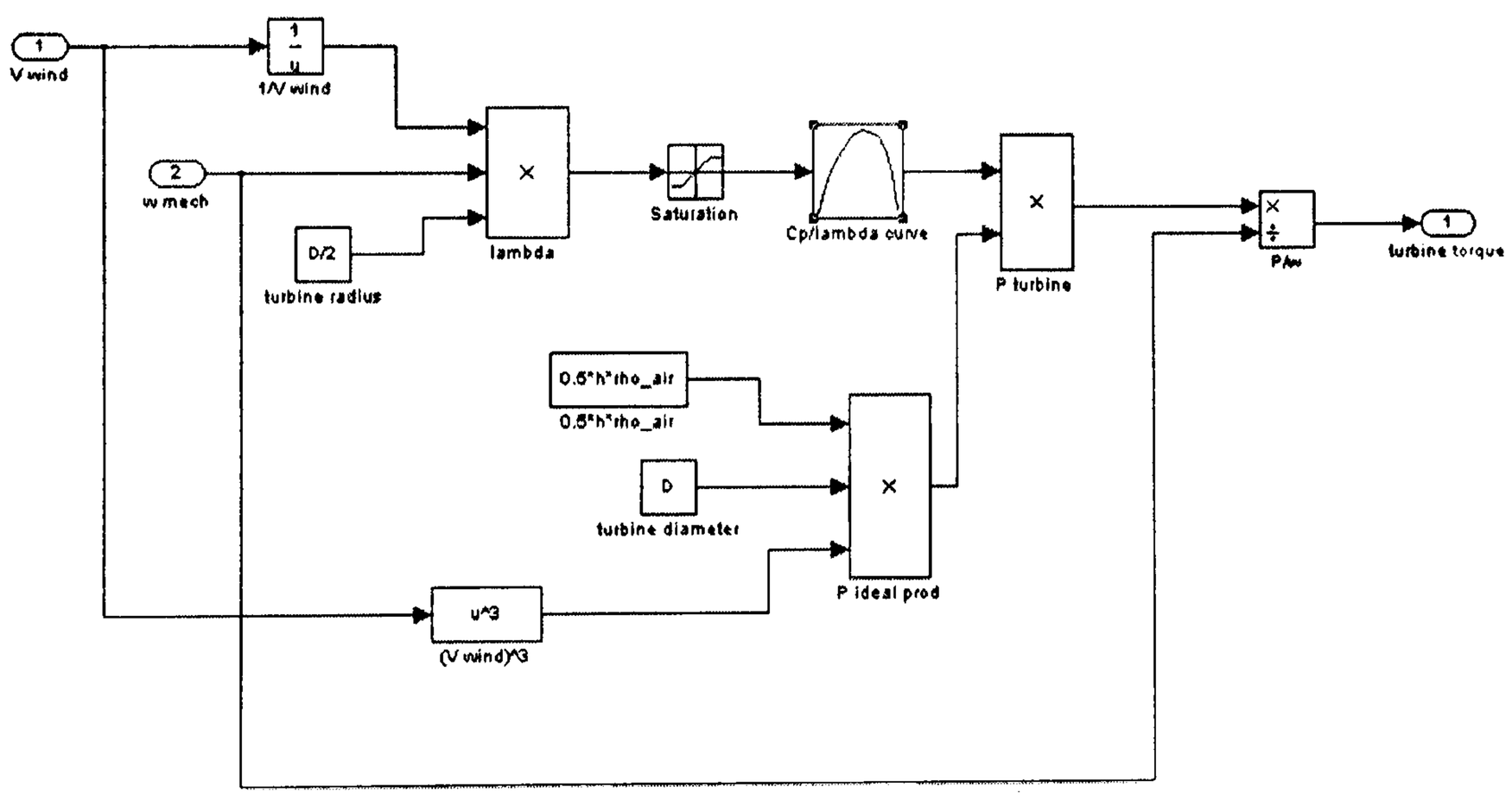

Figure 2-15. Turbine model

2.5.2 Generator torque

The electrical reaction torque generated at the armature windings can be calculated in a similar way for each electrical load. Circuit analysis can be used to calculate the total

power produced by the generator and this can be related to the electrical torque by:

$$T_{electrical} = \frac{P_{generator}}{\omega_{gen}} \qquad [2\text{-}27]$$

The whole model is shown in the block diagram below. Values for the generator EMF, overlap and phase resistances, and equivalent DC current are calculated in the 'gen, rectifier, load' block, and passed to the 'power and torque' block where the electrical torque is calculated according to the above equations. The difference between the turbine torque and the electrical torque is then calculated and integrated according to equation [2-24] to provide a value for rotor speed.

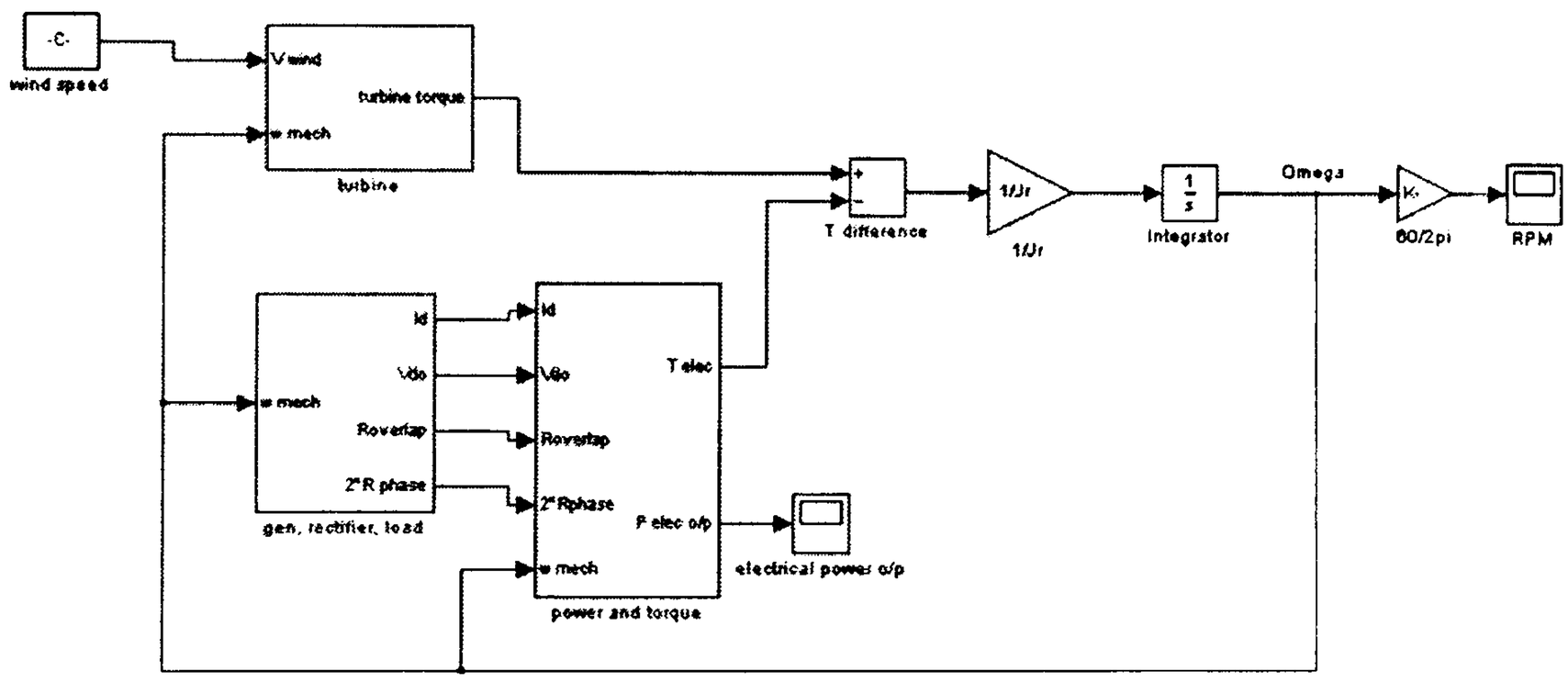

Figure 2-16. Turbine and generator model

Thus, by defining the wind speed and electrical load, the system's dynamic response can be found. The process of verifying the model against experimental measurements is discussed in the next section.

2.6 Experimental verification of the model

An experimental test rig was constructed comprising of a 1kW, 300rpm PM axial-flux

generator coupled to a variable speed induction motor to act as the prime mover. The prototype generator was identical to that used in the Savonious turbine depicted in Figure 2-1 (c) and this allows the SIMULINK model of the Savonius system to be verified. Details of the turbine and generator used for the comparison are given in the table below and the test rig is shown in Figure 2-17.

Savonius Turbine	**Symbol**	**Value**
Rotor Height (m)	H	2.438
Rotor Diameter (m)	D	0.780
Swept Area (m^2)	A	1.902
Rotor Inertia (kg/m^2)	J_r	5.292
Cut-in wind speed (m/s)	$V_{cut\text{-}in}$	2.5
Rated wind speed (m/s)	V_{rated}	12.5
Energy capture coefficient (max)	$C_{p(max)}$	0.2
Savonious Generator		
Rated power (W)	P_{elec}	1000
Rated speed (rpm)	N	300
Rated frequency (Hz)	f	40
EMF per coil @ 300 rpm (V)	E	33.6
Number of phases		3
Number of pole pairs	p	8
Number of armature coils		12
Machine constant (V/rpm/coil)	K	0.11
Coil resistance (Ω)	R_{coil}	1.205
Coil Inductance (mH)	L_{coil}	4.74
DC Efficiency (%)	η_{dc}	92
Generator diameter (m)	D_{gen}	0.462
Generator active mass (kg)	M_{act}	20.1

Table 2. Parameters of Savonius Turbine and 1kW, 300rpm generator

Figure 2-17. 1kW, 300rpm generator test rig

The test rig allowed the generator's output power to be used for resistive heating via a 3-phase load bank, battery charging via four 12V deep-cycle batteries connected in series, and grid connection via a 2.5kW Windy Boy grid-tie inverter. All three loads were modelled in SIMULINK and a comparison between the predicted and measured performance is shown in the three figures below. In each case the power transfer characteristics are plotted on top of the Savonius turbine's power curves to give an idea of how the WECS would behave in different wind conditions.

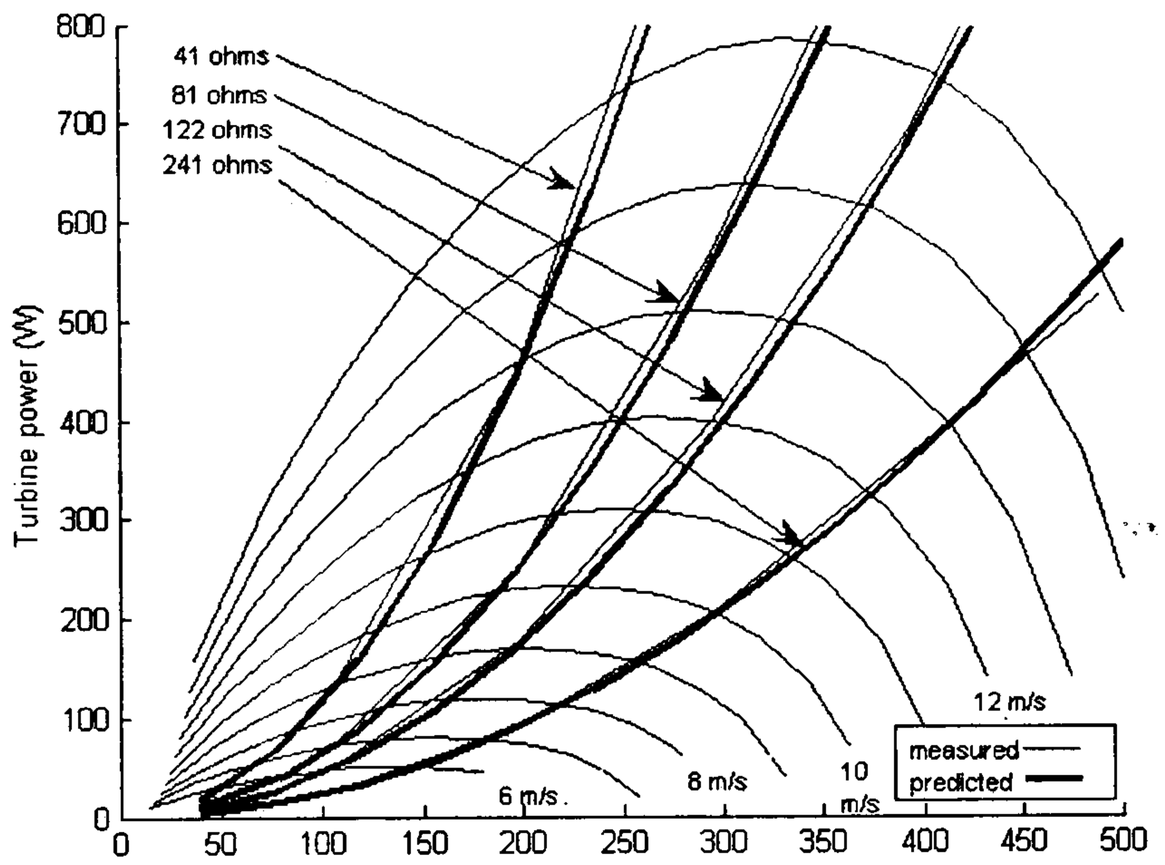

Figure 2-18. 3-phase AC resistive load characteristic

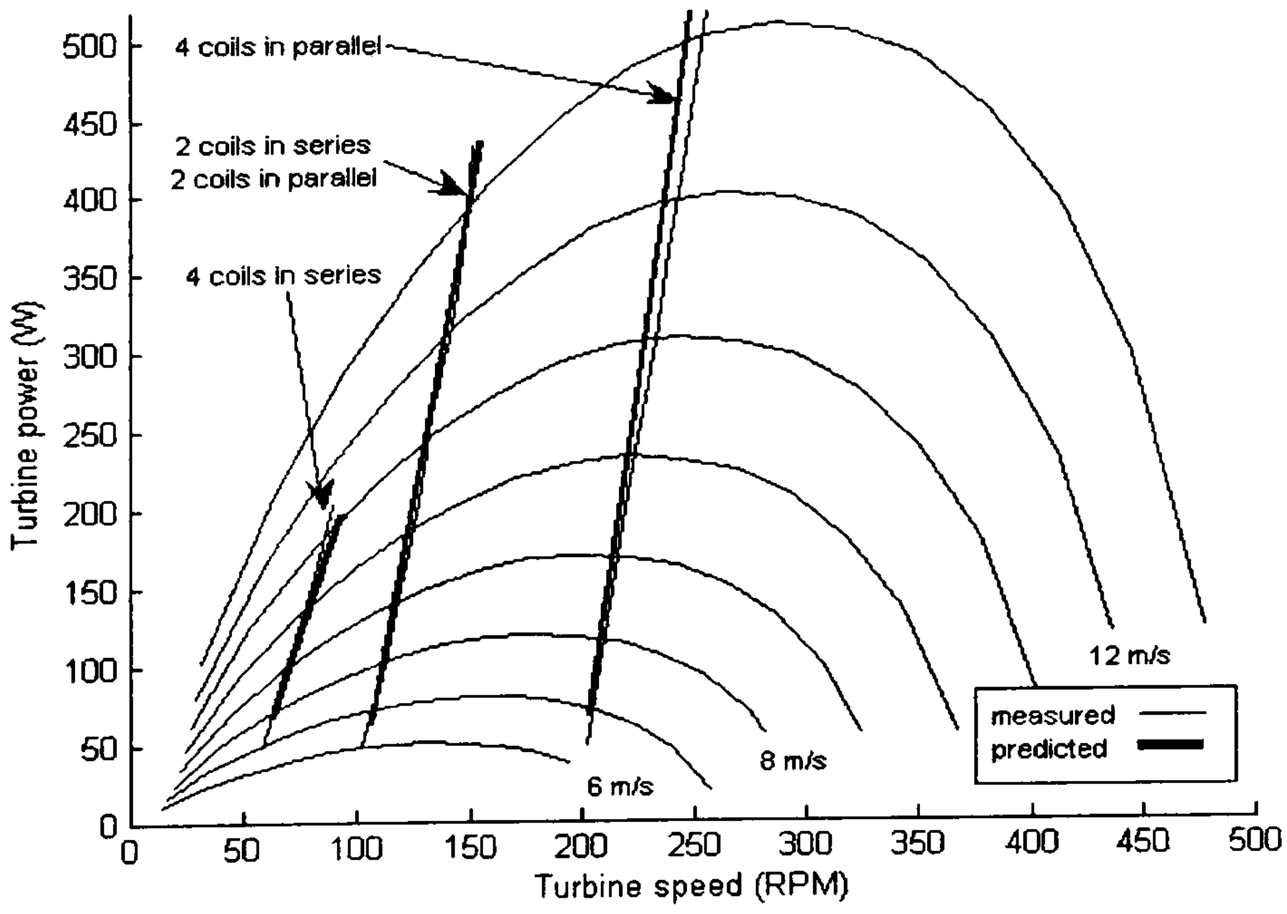

Figure 2-19. 48V battery charging characteristic

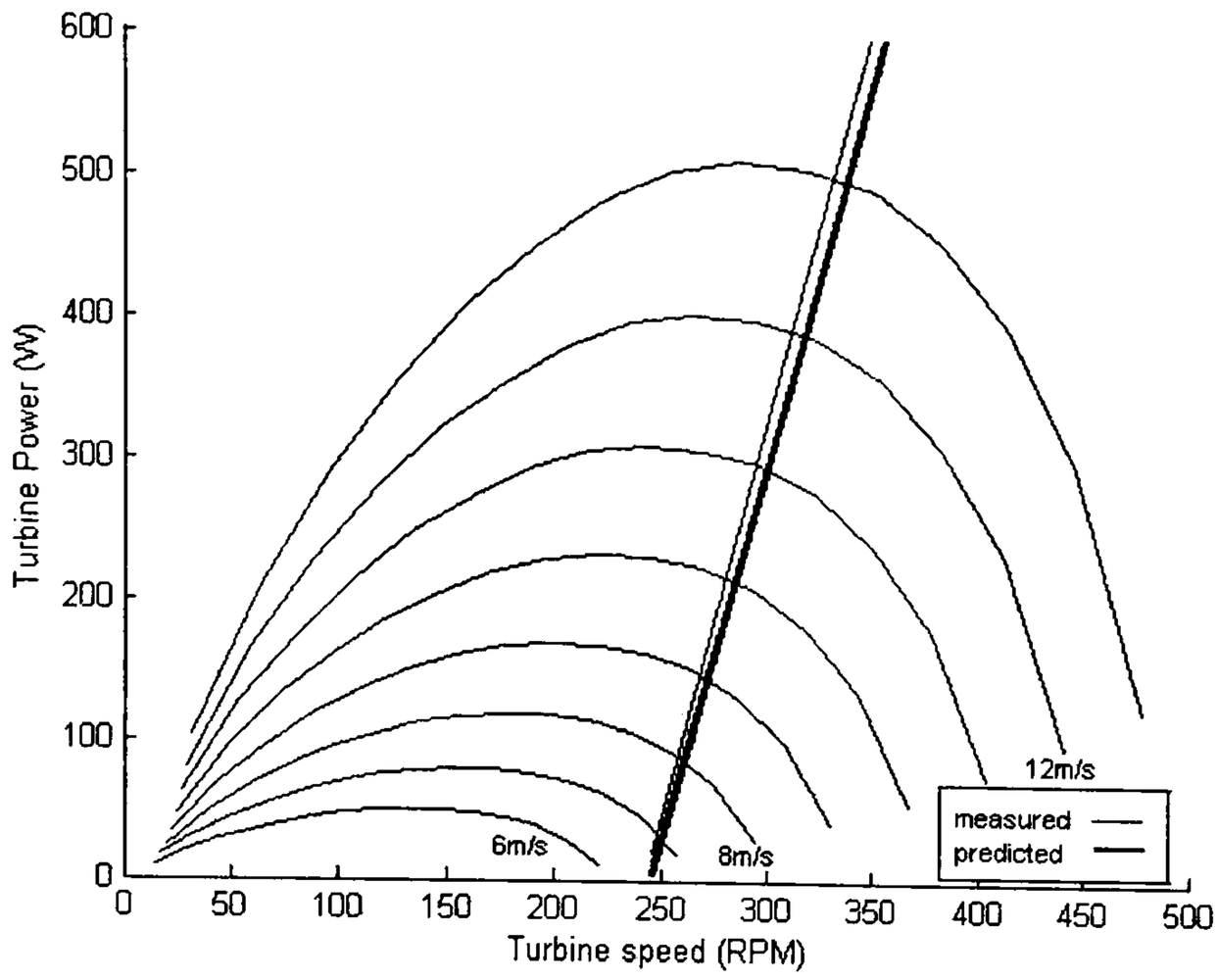

Figure 2-20. Windy Boy load characteristic

Figure 2-18 - Figure 2-20 shows the predicted values from the SIMULINK model are in close agreement with measured values, with a discrepancy of less then 3%. The figures also convey important information about the behaviour of the WECS under different loads. Resistive loads produce quadratic power transfer characteristics which, with the correct value of load impedance, can be made to fit the ideal cubic power transfer characteristic relatively closely.

Battery charging produces a near vertical power transfer characteristic which leads to poor energy capture in most wind conditions, although this problem may be overcome by switching the coil connections as the wind speed increases. The 1kW, 300rpm axial flux generator examined here is a 3-phase device with four armature coils per phase. These can be connected in three configurations: all four coils in series, all four coils in parallel, or two coils in series and two in parallel, and the power transfer characteristics of each is shown in Figure 2-19. At low speeds it maybe necessary to connect the armature coils in series to boost output voltage, and then, as the wind speed increases, switch to a parallel connection to achieve better energy transfer. An alternative strategy

would be to use a DC-DC converter in the DC link to boost the voltage at lower speeds and this is discussed in Chapter 6.

Figure 2-20 shows there is a relatively poor match between the power transfer characteristic of the Windy Boy inverter and the Savonius turbine. Although the characteristic of the inverter may be set by the user, this facility does not provide sufficient flexibility to produce efficient power conversion in the system. In the tests the inverter parameters V_1 and V_2 were set to 250V and 599V, to produce the largest power transfer gradient possible. However, Figure 2-20 shows that this gradient is not a good approximation to the optimal turbine characteristic, especially at low speed. This is because the inverter has a much larger power rating than the turbine (2.5kW compared to 300W) and so its power transfer characteristic appears much steeper when plotted on the same scale as the turbine power curves. For more efficient power transfer, a lower rated inverter (such as a 700W Windy Boy) could be used or the outputs of several turbines could be aggregated together, as discussed in Chapter 6.

2.7 Conclusions

There are three main configurations of micro wind turbine that are currently on the market: lift operated horizontal axis turbines, drag operated vertical axis turbines (Savonius), and lift operated vertical axis turbines (the Darrieus or 'egg-beater' type). The turbines are generally used with an electrical generator to provide power to three types of load: resistive heating, battery charging and grid connection through an inverter.

An air-cored PM axial flux machine has been developed at Durham for use with direct-

drive micro turbines, and this has been modelled in SIMULINK as part of a larger wind energy conversion system comprising of a Savonius turbine and the three electrical loads. The modelling process was validated by comparison with an identical generator system on test in the laboratory, and the predicted performance was found to be in good agreement with the measurements, with an error of under 3%.

The modelling process showed that to get efficient energy transfer between a wind turbine and a load, the power demanded from the load must be carefully controlled to enable the turbine to operate at its most efficient speed. This optimal speed varies with the strength of the wind to produce a locus of points along which an ideal operating line may be drawn. The locus follows a cubic relationship when turbine power is plotted against turbine speed. Unfortunately, electrical loads impose their own power transfer characteristics, leading to non-optimal energy transfer.

A number of strategies may be employed to better match the load characteristic with the turbine characteristic. In the case of AC resistive loads, the power transfer characteristic is quadratic and so by carefully choosing the value of dump resistance, a reasonably efficient energy transfer system can be produced.

Battery charging is more problematic since the constant battery voltage forces the turbine to operate at a near-constant speed. The coil connections may be changed at low speeds to boost the generator's voltage or, alternatively, a DC-DC converter may be used to augment the power transfer characteristic, as discussed in more detail in Chapter 6.

The power transfer characteristic of a Windy Boy inverter operates as a linear function

of the DC link voltage and may be adjusted to suit individual turbines, although in many cases it does not produce an ideal power transfer characteristic. Because of the high DC link voltage required by the Windy Boy, a generator designed for use with this inverter is incompatible for use as a battery charger.

Chapter 3

The economic case for micro wind turbines

3.1 Introduction

Before considering the technical challenges facing the designers of micro wind turbine systems, it is first necessary to address the economic drivers behind the technology. This chapter will briefly look at the history of small-scale turbines before examining the costs and savings associated with the current technology. In order to assess this, the cost of the system, the annual energy production of the system, and the value of the energy produced must all be known. A Weibull probability analysis is introduced in section 3.3 to model an average annual wind speed distribution, and this is combined with the power characteristics from a series of generic wind turbines to calculate their average annual energy yield. This analysis is used in section 3.4 to provide indicative figures for energy yield, income and level of CO_2 abatement for various sizes of small-scale wind turbines.

Section 3.5 examines whether turbine manufacturers' claimed performance, which are often based on a similar Weibull analysis, are accurate. It will consider the evidence from the limited number of field trails that have been carried out on micro turbines and will also assess whether the wind resource in an urban environment is accurately represented by manufactures.

Finally, the economic attractiveness of micro and small-scale turbines will be assessed in light of the current grant and incentive schemes available from the government. The

payback period for three turbines in different wind regimes, and when their energy is used in different ways, is presented in section 3.7.

3.2 Commercial history of Micro Wind Generation

The development of small-scale wind turbines began in the mid 1920s in the Midwestern Great Plains, where companies such as Parris-Dunn and Jacobs Wind-electric manufactured small turbines (c 1-3kW) that were connected to DC generators to provide battery charging facilities in off-grid rural homesteads [40]. The electricity was used for low voltage lighting and to power crystal radio sets. The advent of rural electrification in the late 1940s and 50s effectively destroyed the American 'wind-charging' industry, and interest in the technology was not rekindled until the 1970s when successive oil shocks caused the price of energy to rise sharply. Initially much of the technology in this period was simply 1930s equipment that had been refitted or rebuilt, however it soon became clear that further research and development work was needed and in 1976 a federal research centre was established at Rocky Flats, Colorado [41]. The R&D program proved successful and much expertise was gained about small-scale devices; several 1-3kW and 6kW small-scale turbines were commercialised and the knowledge gained during this period was used by every major small-scale turbine manufacturer in the US. Despite the success of this program, funding was withdrawn by the incoming Reagan administration in 1981 in favour of tax breaks for the industry. This move proved to be disastrous for the wind industry as most of the technology was not yet mature enough to be commercialised, which led to a large number of ill-conceived wind turbine designs being constructed that later proved unreliable [40].

In Europe small wind turbines driving induction generators were adopted in many

countries such as Denmark, Germany, and the Netherlands from the 1970. Experimenters and hobbyists designed systems to supplement electricity from the local utility, and the wind turbines gradually grew in size to reach 50 kW by 1982. This grassroots effort complemented national research programs into larger turbines that started after the second world war when a shortages of coal caused the price of energy to remain high until the 1960s [42].

In the UK two large wind turbines were tested in the early 1980s, a 3.6MW two bladed design at Bargur Hill in Orkney and a 1MW three bladed design at Richborough in Kent. The large Bargur Hill turbine proved to be over-complicated, expensive and highly unreliable and was ultimately demolished. However, the Richborough machine, which was developed as a collaboration between James Howden, a Scottish Engineering company, and the CEGB, produced reasonably good results for a prototype machine but was not developed further because of the availability of cheap North Sea gas [43].

After the oil price collapsed in the early to mid 1980s, the economic attractiveness of small-scale wind decreased sharply and the industry declined on both sides of the Atlantic. It has only begun to remerge from this slump in recent years because of the resurgent oil price and because of fears over global warming. The ultimate driving force behind this current resurgence, however, is the economic attractiveness of the product, and this will be explored in the rest of the chapter.

3.3 Calculating turbine energy yield

Central to assessing the economic attractiveness of current micro and small-scale wind turbine technology is the need to predict the annual energy yield of the devices, and in

this section a Weibull probability function is introduced for this purpose. The Weibull function is used to model the annual wind speed distribution, based on a mean annual wind speed, which can then be combined with the turbine's power-wind speed characteristic to provide an estimate of energy yield.

3.3.1 Wind speed distribution

The annual wind distribution of a given site may be measured by recording the number of hours per year that the wind speed falls within certain defined ranges, known as 'bins'. However, it is often expensive and cumbersome to monitor the wind speed over an entire year (or even several years), and may even be impossible in certain situations (for example at sea). Because of this, the annual wind distribution can be estimated from the mean annual wind speed (MAWS) of the site by using a Weibull probability distribution. The mean annual wind speed can be found from a meteorological wind map such as Figure 3-1, or by reference to the DTI's NOABL wind speed database for the UK [44].

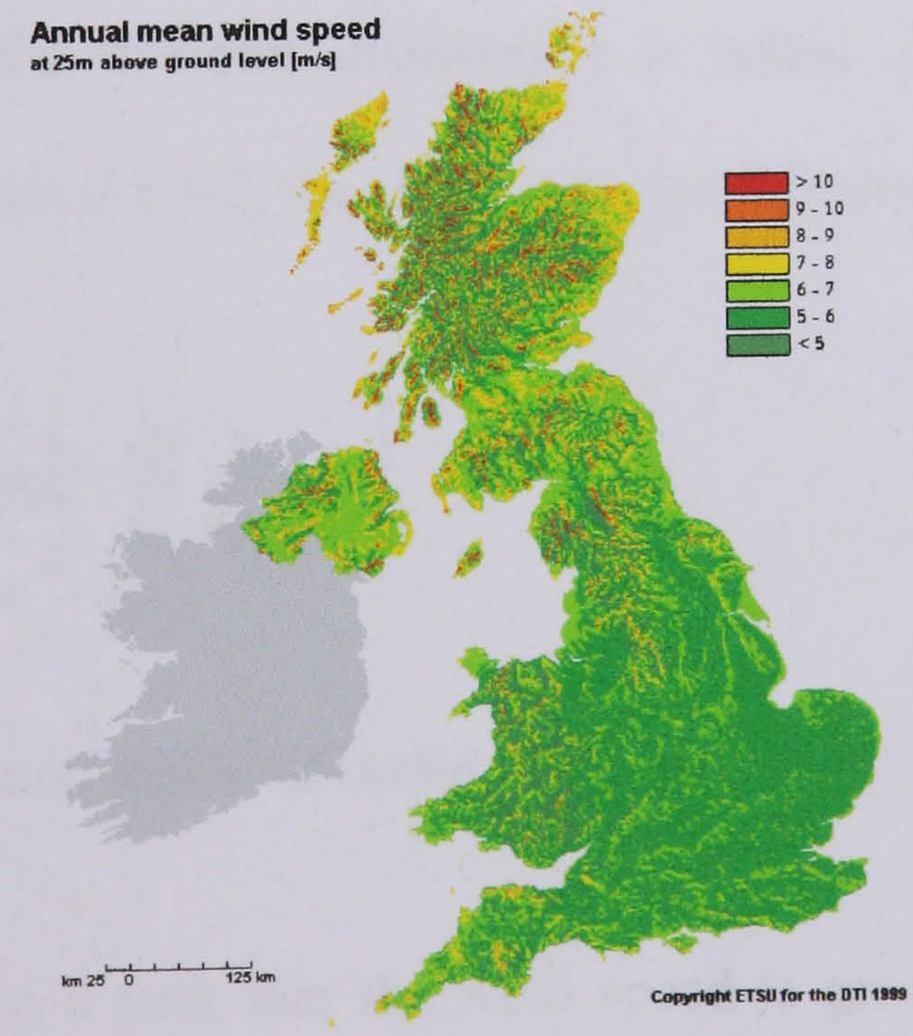

Figure 3-1. Wind map showing MAWS of the UK [45].

As can be seen in the figure, the wind resource improves towards the north of the country and is better on high, open ground. The wind resource in the built environment is generally worse then that shown in the figure because of the high level of turbulence created by buildings, as discussed in further detail section 3.5.

3.3.2 Weibull distribution

The probability, $F(V_w)$, that the wind speed is greater then value, V_w, is given by [46]:

$$F(V_w) = \exp\left[-\left(\frac{V_w}{C}\right)^n\right] \qquad [3\text{-}1]$$

Where C is the scaling factor and n is the shape factor (determined by the roughness of the site topology).

Choosing the correct shape and scaling factors is not a trivial task. Their values can shift subtly over the months and seasons, and much research has been carried out to model them, [47-49]. For flat terrain in Western Europe a shape factor of 2 is generally used. This special case of the Weibull distribution is called the Rayleigh Distribution. Reference [46] shows that if n = 2, the above equation becomes:

$$F(V) = \exp\left[-\frac{\pi}{4}\left(\frac{V_w}{V_{mean}}\right)^2\right] \qquad [3\text{-}2]$$

Where V_{mean} is the mean annual wind speed of the site.

The number of hours in a year that the wind speed is greater than value, V, can be calculated by multiplying this probability by the total number of hours in a year, as

shown by the equation below:

$$hrs = 8760 \exp\left[-\frac{\pi}{4}\left(\frac{V_w}{V_{mean}}\right)^2\right] \qquad [3\text{-}3]$$

This function is shown in Figure 3-2 for V_{mean} = 6.0 m/s.

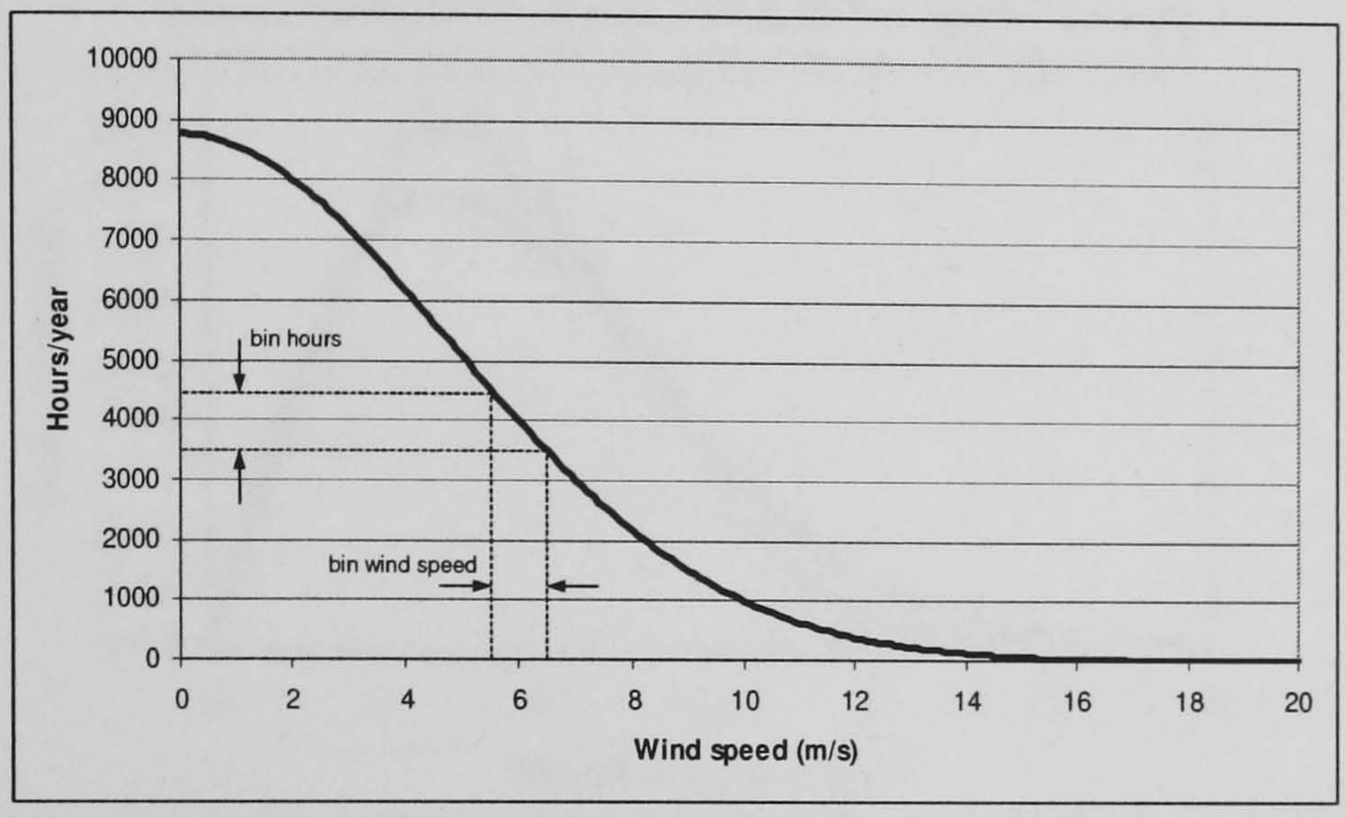

Figure 3-2. Weibull distribution (MAWS = 6.0 m/s)

The annual wind distribution can be constructed from the Weibull function by tallying the number of hours that the wind speed falls within each 1 m/s 'bin', as shown in Figure 3-2 for the 6 m/s 'bin'. This distribution is shown in Figure 3-3.

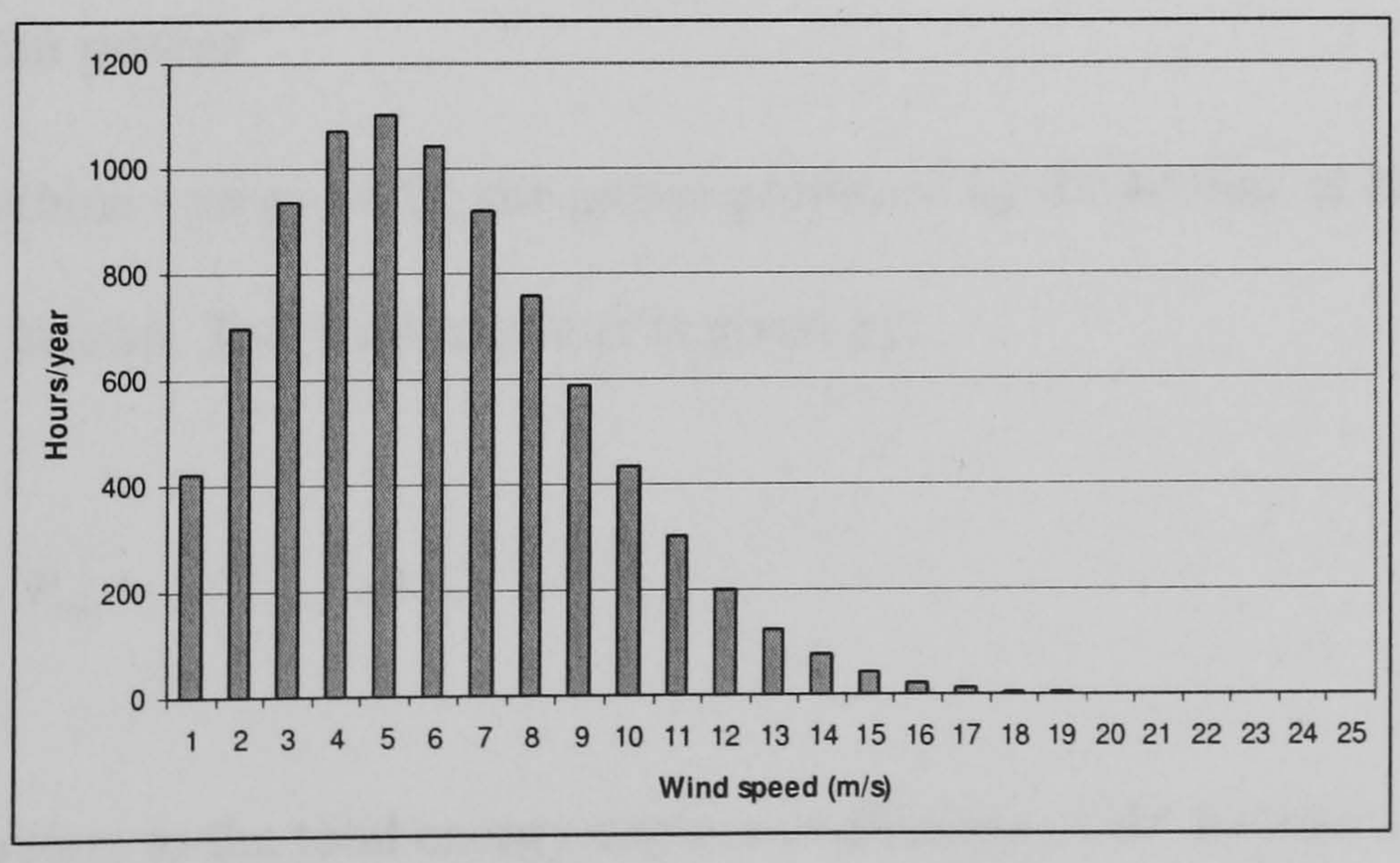

Figure 3-3. Annual wind distribution for a generic site (MAWS = 6.0 m/s)

Although a probabilistic approximation will never offer an exact representation of the real world, the Wiebull distribution does provide a useful guide when predicting wind turbine energy yields, as has been shown in [47] and [50]. The discrepancy between the Weibull prediction and values measured at the Horns Rev off-shore wind farm near Denmark is shown below.

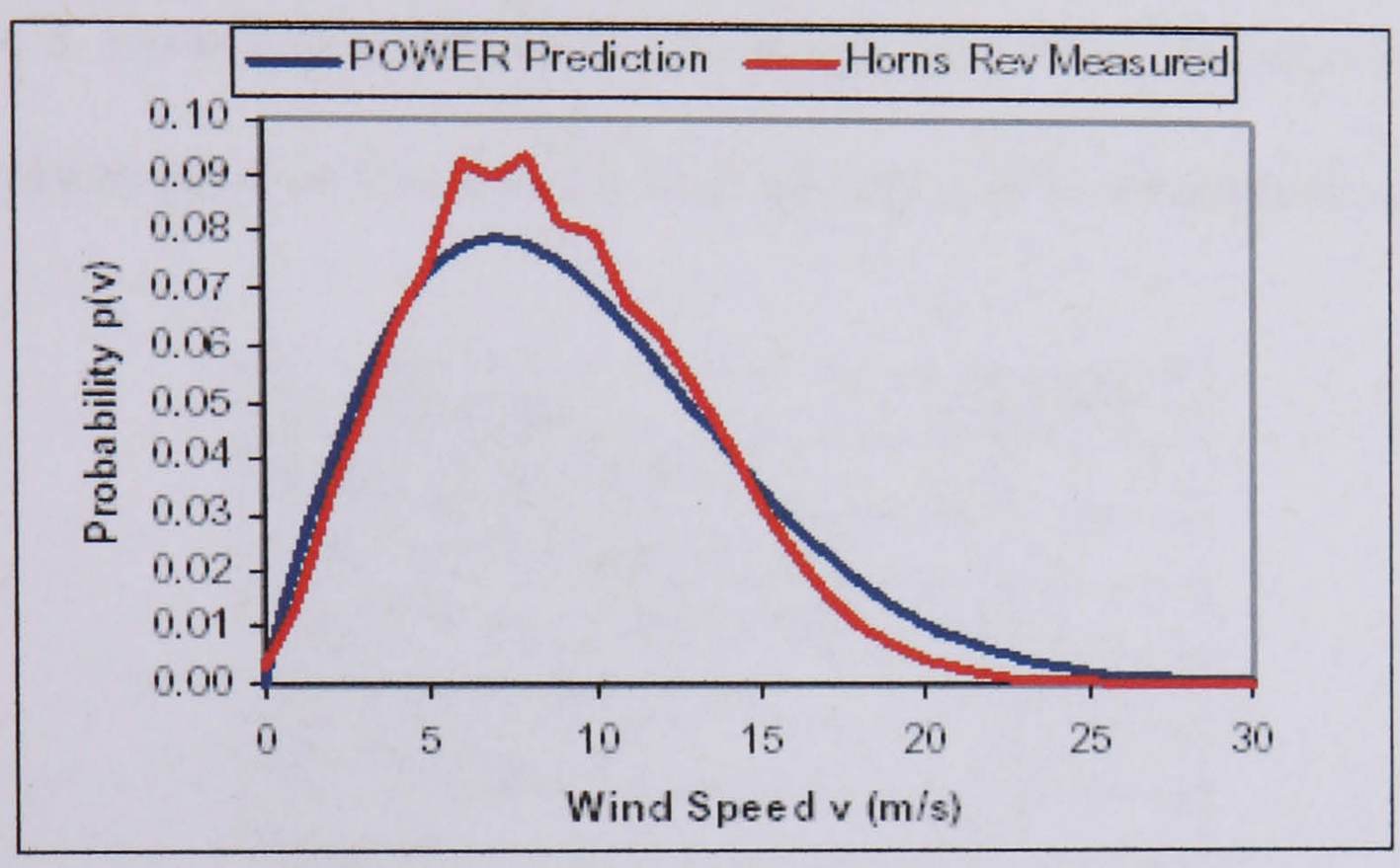

Figure 3-4. Comparison of Weibull and a measured wind speed distribution [50]

Although Figure 3-4 shows a general Weibull distribution rather then the special case Rayleigh distribution, it nevertheless demonstrates the power of the Weibull statistical method.

3.3.3 Turbine power

To calculate turbine energy yield, the power produced by the turbine at each 'bin' wind speed must be known. The turbine power is given by:

$$P_{\max} = \frac{1}{2} C_{P(\max)e} \rho A V_w^3 \qquad [3\text{-}4]$$

Here, $C_{p(max)e}$ refers to the total energy capture coefficient of the turbine and generator –

i.e. the energy capture coefficient of the turbine multiplied by the generator efficiency.

All small-scale wind turbines incorporate a mechanism to limit the output power in strong winds. This prevents the generator from operating above its rated power limit, which in most cases corresponds to a wind speed of 12.5 m/s. An idealised turbine characteristic is shown in Figure 3-5 for a 10kW turbine; the turbine parameters are given in Table 3. However, it should be noted that the power characteristic of real wind turbines is rarely as good as this and the discrepancy will be examined in section 3.5.

Turbine type	HAWT
Rated power (kWe)	10
Cut-in wind speed (m/s)	3
Rated wind speed (m/s)	12.5
Turbine diameter (m)	5.96
Swept area (m^2)	27.9
$C_{p(max)e}$	0.3

Table 3. Generic turbine parameters

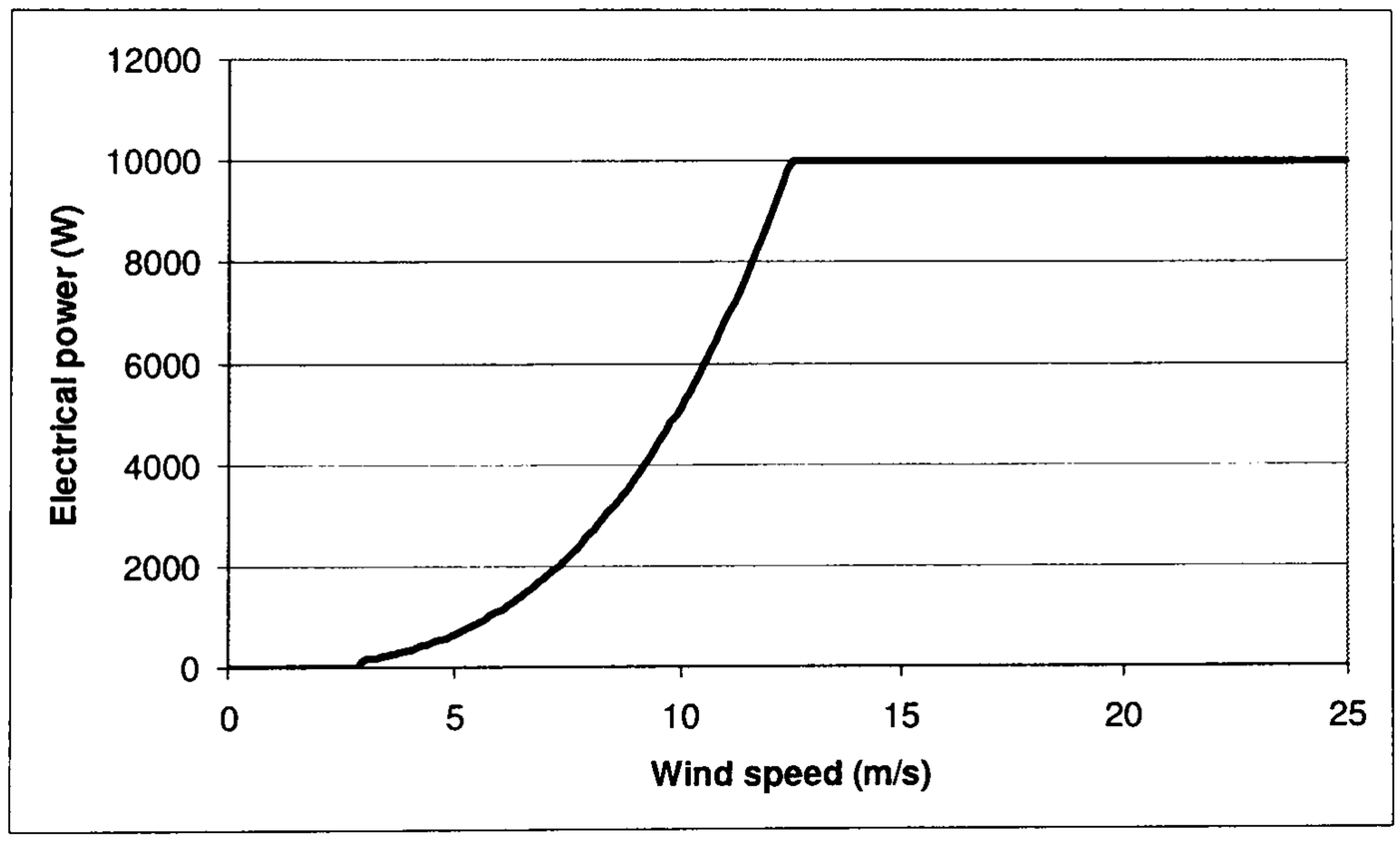

Figure 3-5. 10kW Turbine output power

The annual energy yield produced at each discrete wind speed is calculated by multiplying the 'bin hours' (Figure 3-3) by the turbine power at each 'bin' wind speed (Figure 3-5). This analysis has been carried for the generic 10kW turbine shown above,

sited in a 6 m/s MAWS and is shown in Figure 3-6.

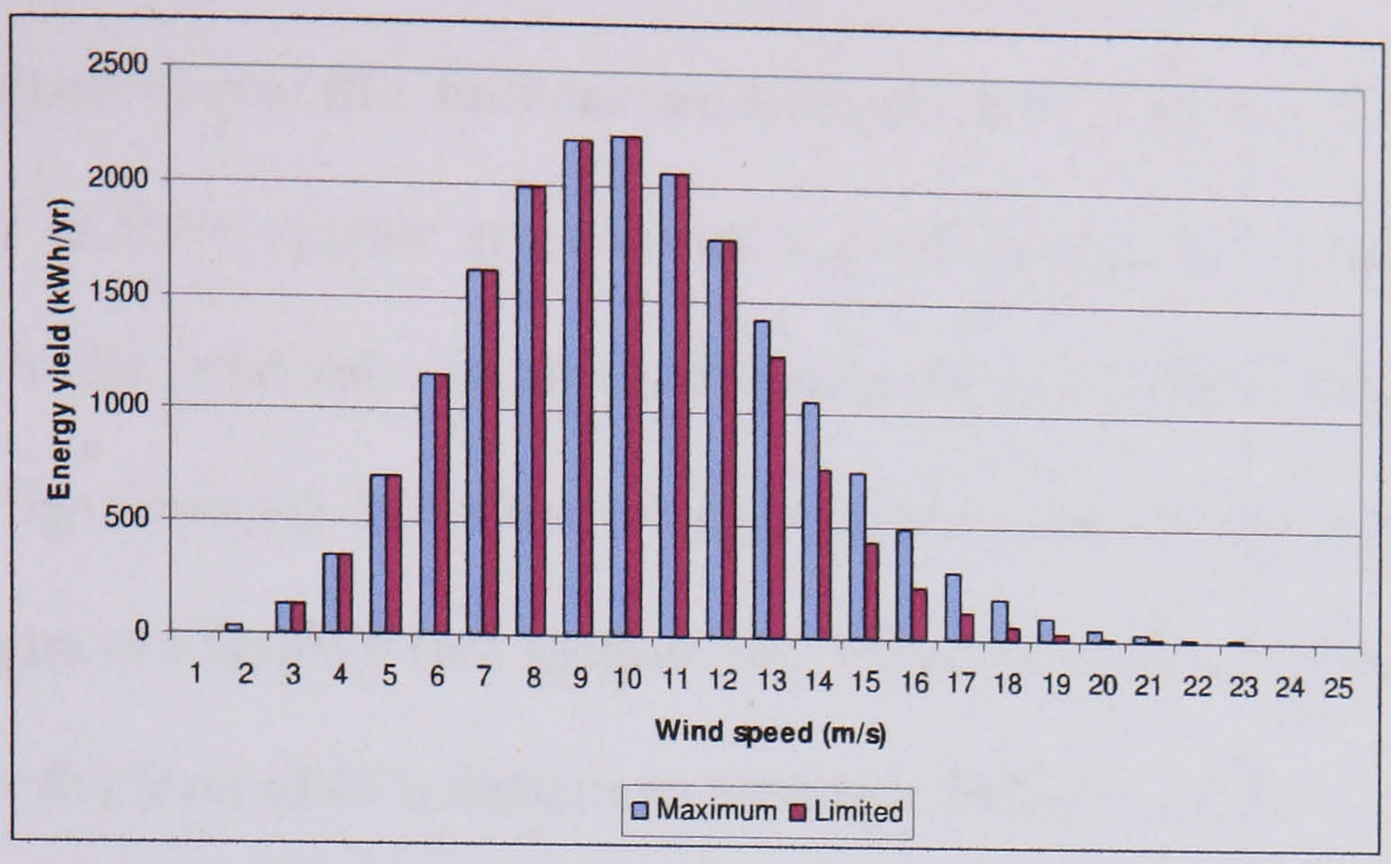

Figure 3-6. Energy yield as a function of discrete wind speed (10 kW turbine; MAWS = 6.0 ms)

The annual energy yield for each 'bin' wind speed is shown as the 'limited' bars in Figure 3-6. By summing the energy contribution of each 'bin', the total annual energy yield can be calculated, in this case 17081 kWh/yr. The maximum possible energy yield is shown alongside the 'limited' value, and is based on a 0 m/s cut-in speed and an infinitely rated generator. As can be seen, there is very little difference between these two sets of bars. Since the maximum possible energy yield is 18592 kWh/yr, the extra energy gained by rating the generator above 12.5 m/s would not justify the increased manufacturing cost.

3.4 General turbine performance

The analysis outlined above will now be extended by considering the effect of MAWS on annual energy yield, income, level of CO_2 abatement and capacity factor for a family of ideal generic micro and small-scale turbines to gain an insight into the potential of such devices to reduce emissions and generate income.

3.4.1 Annual energy yield, income and CO_2 abatement

Figure 3-7 (a) & (b) show the annual energy yield in kWh/yr based on the Weibull analysis described above, (the turbines are considered to have a cut-in speed of 3m/s, rated speed of 12.5m/s, operate at a constant C_p of 0.3, and have a mechanism to limit output power to the rated value in all wind speeds above 12.5m/s); Figure 3-7 (c) & (d) are the same figures as (a) & (b) but with a rescaled y-axis to show income generated based on a figure of 15p/kWh (see section 3.6); Figure 3-7 (e) & (f) have been similarly scaled to show the level of CO_2 abatement based on 430g of carbon dioxide released per kWh of energy generated [51]. The figure of 430g/kWh is compiled by the British Wind Energy Association and is created by proratering the CO_2 emissions from the various types of generating plant in the UK. It does account for the carbon footprint of the turbine itself, and assumes the penetration of micro-generation is low enough to offset the base load supply, equating to a direct saving in CO_2 for every kWh of energy generated.

A recent study [52] showed that in windy locations such as Wick in Northeast Scotland, the carbon dioxide released in manufacturing an average wind turbine would be paid back in 1 year. However, if the turbine was sited in Manchester, the carbon outlay would not be recouped over the lifetime of the turbine and hence the device would contribute to global warming. A second recent study put the carbon payback period for a Swift wind turbine as 10-39 months [53].

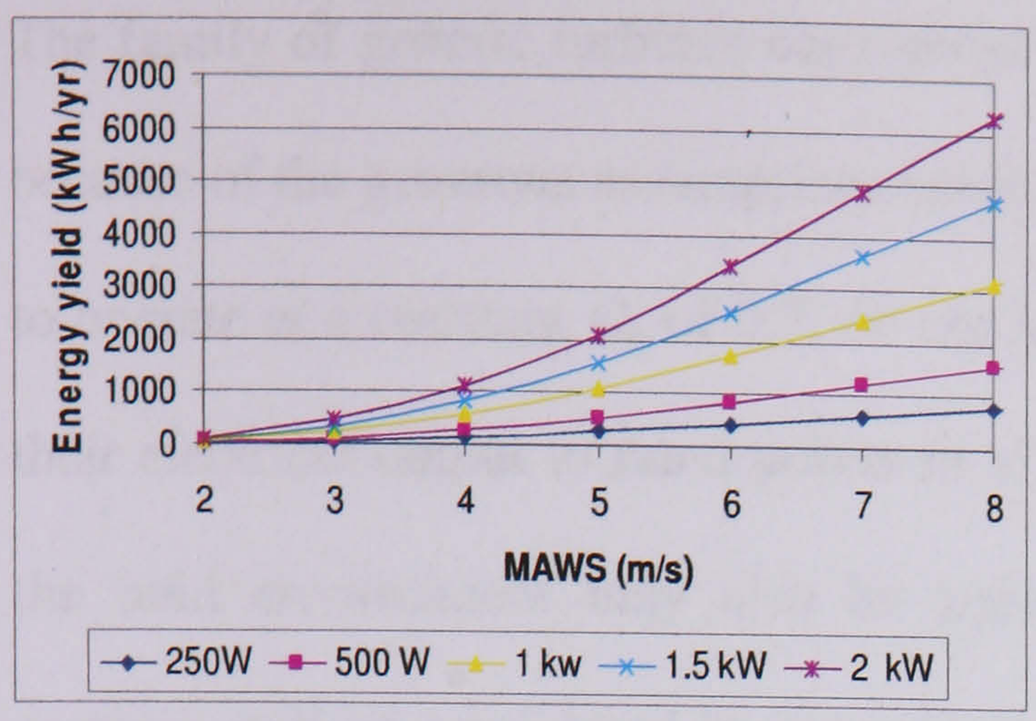

(a)

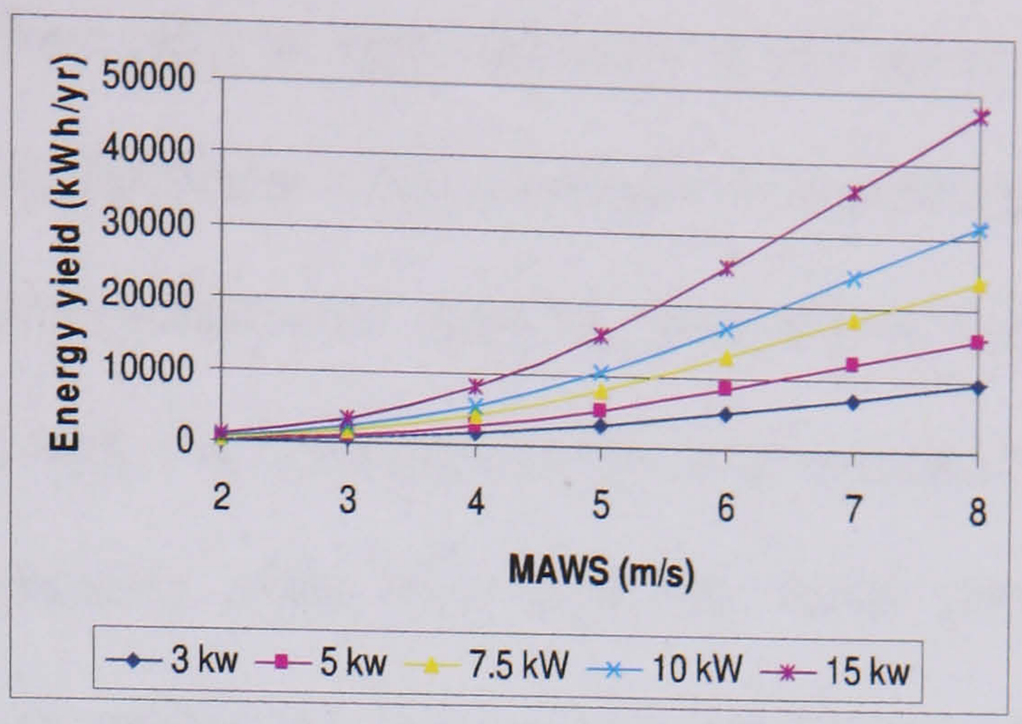

(b)

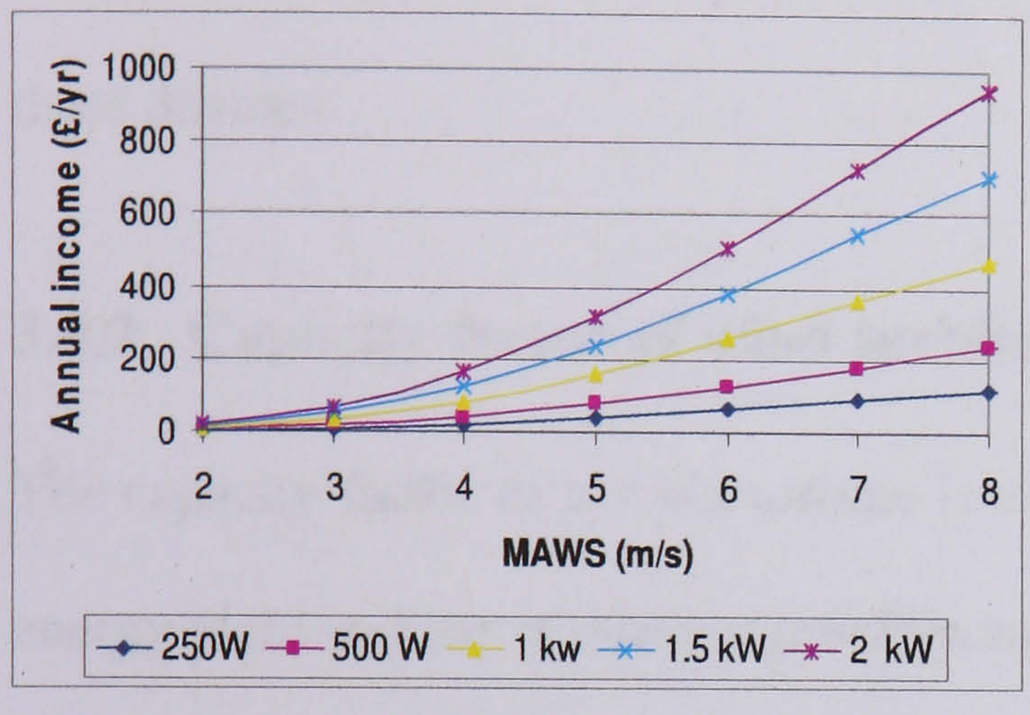

(c)

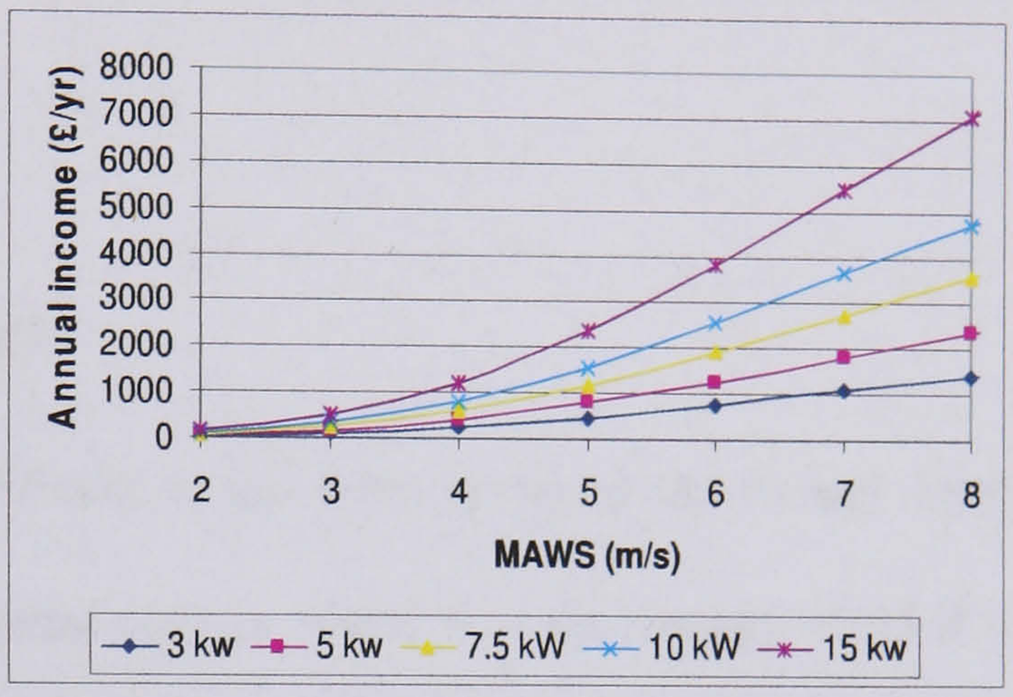

(d)

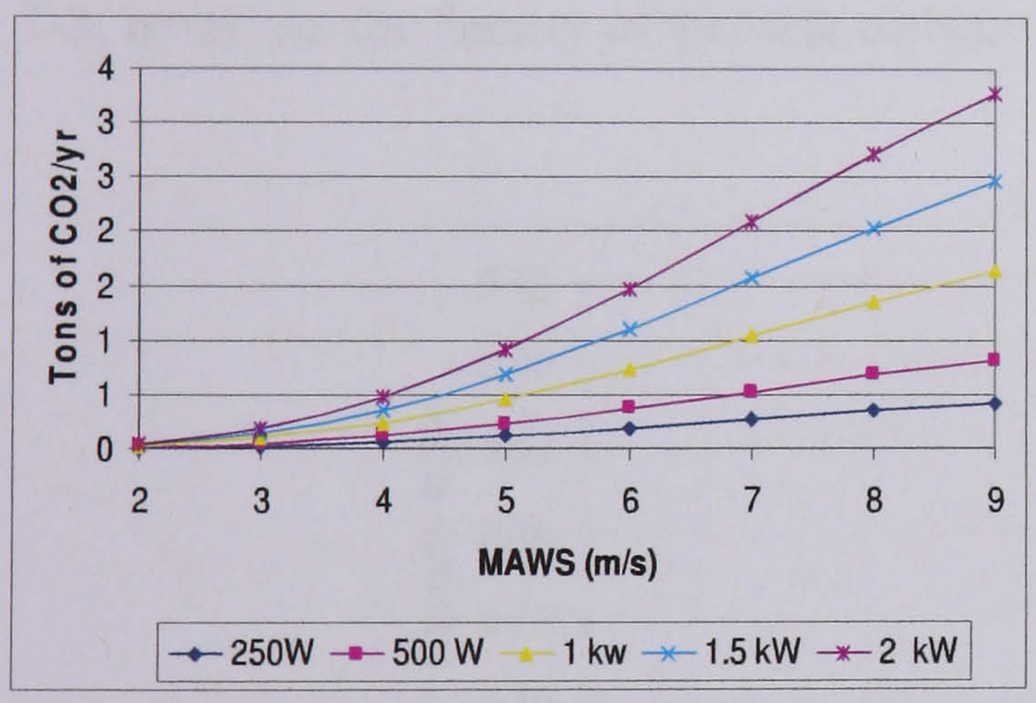

(e)

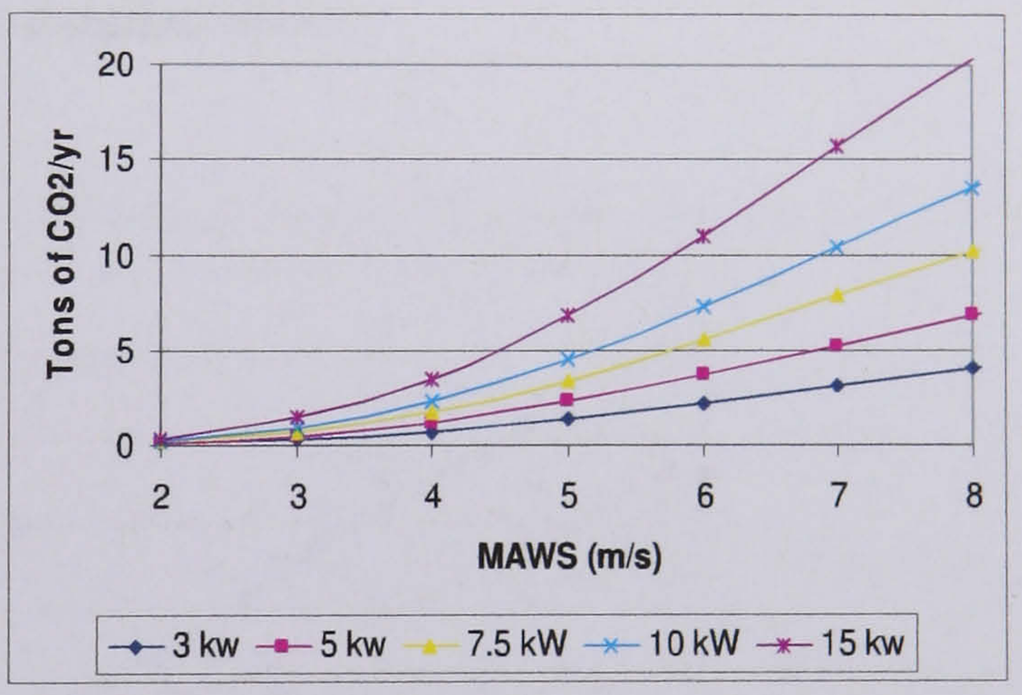

(f)

Figure 3-7. Mean annual wind speed versus (a) (b) annual energy yield, (c) (d) annual income, (e) (f) annual CO_2 abatement

Figure 3-7 shows that a small increase in the mean annual wind speed (MAWS) of the site can produce dramatic improvements in energy yield, and therefore the location of the turbine is critical.

The family of generic turbines considered here offer an upper estimate of performance because of the generous assumptions made in the analysis. Most turbines do not manage to operate at a constant C_p of 0.3, do not have perfect over-speeding protection to limit their electrical output to rated power in all high wind conditions; the wind resource in the built environment may also be significantly lower then expected. These short comings will be considered in more depth in section 3.5, however for the purposes of illustration, Figure 3-7 does provide useful general information on the performance of these devices.

3.4.2 Capacity factor of wind turbines

The capacity factor of a wind turbine is defined as the ratio between the actual annual energy yield and the maximum possible annual energy yield, (i.e. the energy yield if the wind blows at rated speed all year). This value is shown for varying MAWS in Figure 3-8, based on the family of generic turbines detailed above.

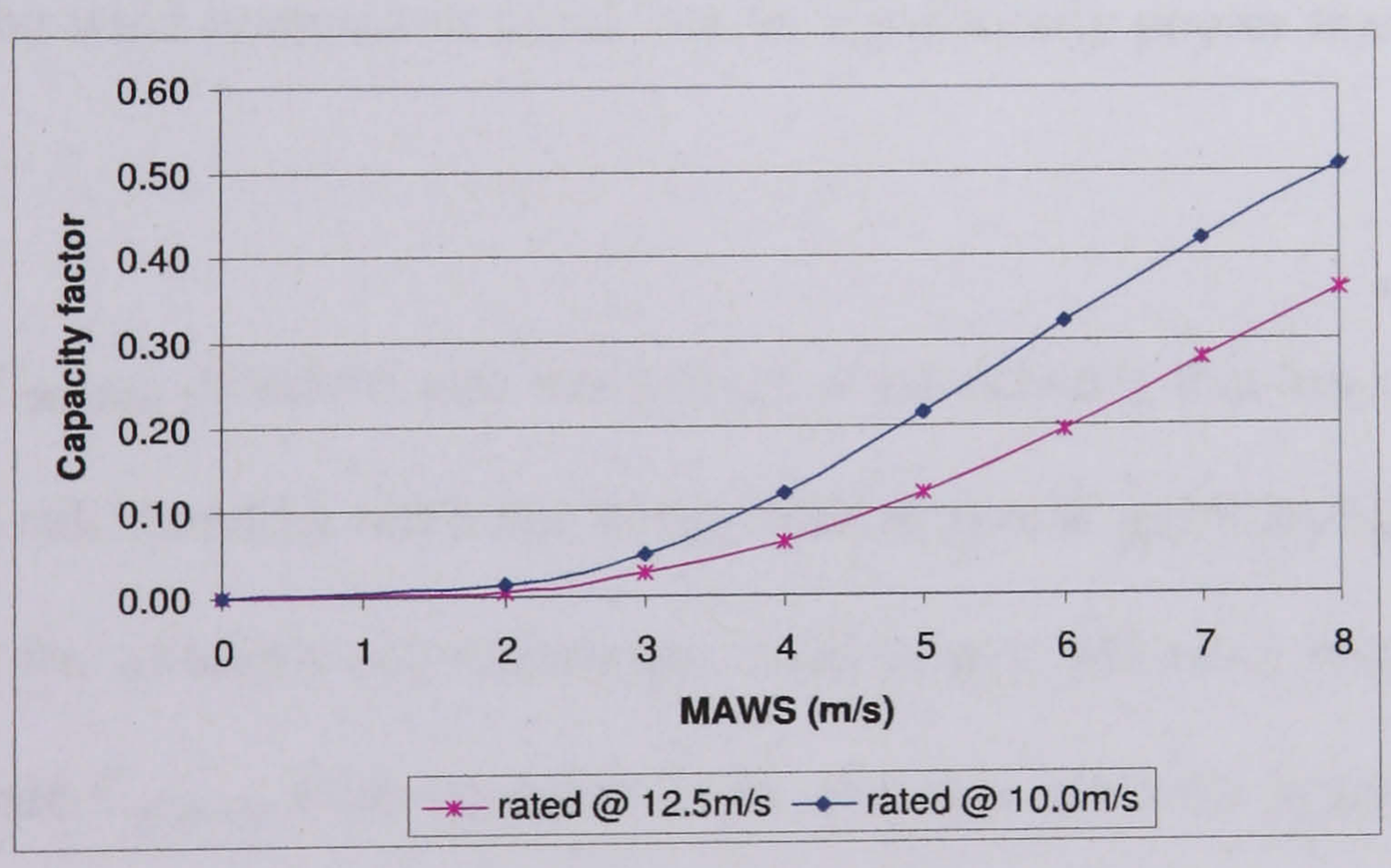

Figure 3-8. Capacity factor

To some extent the capacity factor shown in the figure above is an arbitrary quantity as it is based on the turbine being designed for an arbitrary rated wind speed. For large turbines sited in windy locations, a rated wind speed of 12.5 m/s is generally used

since the cost of building a wind turbine to cope with a higher wind speeds would not be re-cooped by the extra energy generated (as shown by Figure 3-6). However, the designer may argue that a lower value of rated wind speed should be used to reflect the poorer wind resource in the built environment, and this has the effect of improving the capacity factor as shown above.

3.5 Behaviour of real wind turbines in the built environment

The analysis of turbine performance carried out in the previous section focussed on a family of generic turbines with favourable operating characteristics, however there are a number of reasons why a prospective buyer should be sceptical about the claims that certain manufacturers makes about their devices. Firstly, unlike their large-scale counterparts, manufacturers of small scale turbines are under no legal obligation to certify that their device will produce the power claimed, and in tests many turbines significantly under perform, as discussed below. Secondly, and perhaps more importantly, the wind resource in cities can be significantly poorer than manufacturers assume.

The claimed $C_{p(max)e}$ of micro and small-scale wind turbines that are currently on the market can be calculated by reference to the manufacturers' published specifications. A knowledge of the turbine's rotor diameter, rated power and rated wind speed can be used to calculate $C_{p(max)e}$ from equation [3-4], and this is shown against rated turbine power in the figure below. It should be noted that $C_{p(max)e}$ represents the total energy capture coefficient for the system, i.e. the energy capture coefficient of the turbine multiplied by the generator and inverter efficiencies. A full list of manufacturers is

given in Appendix A.

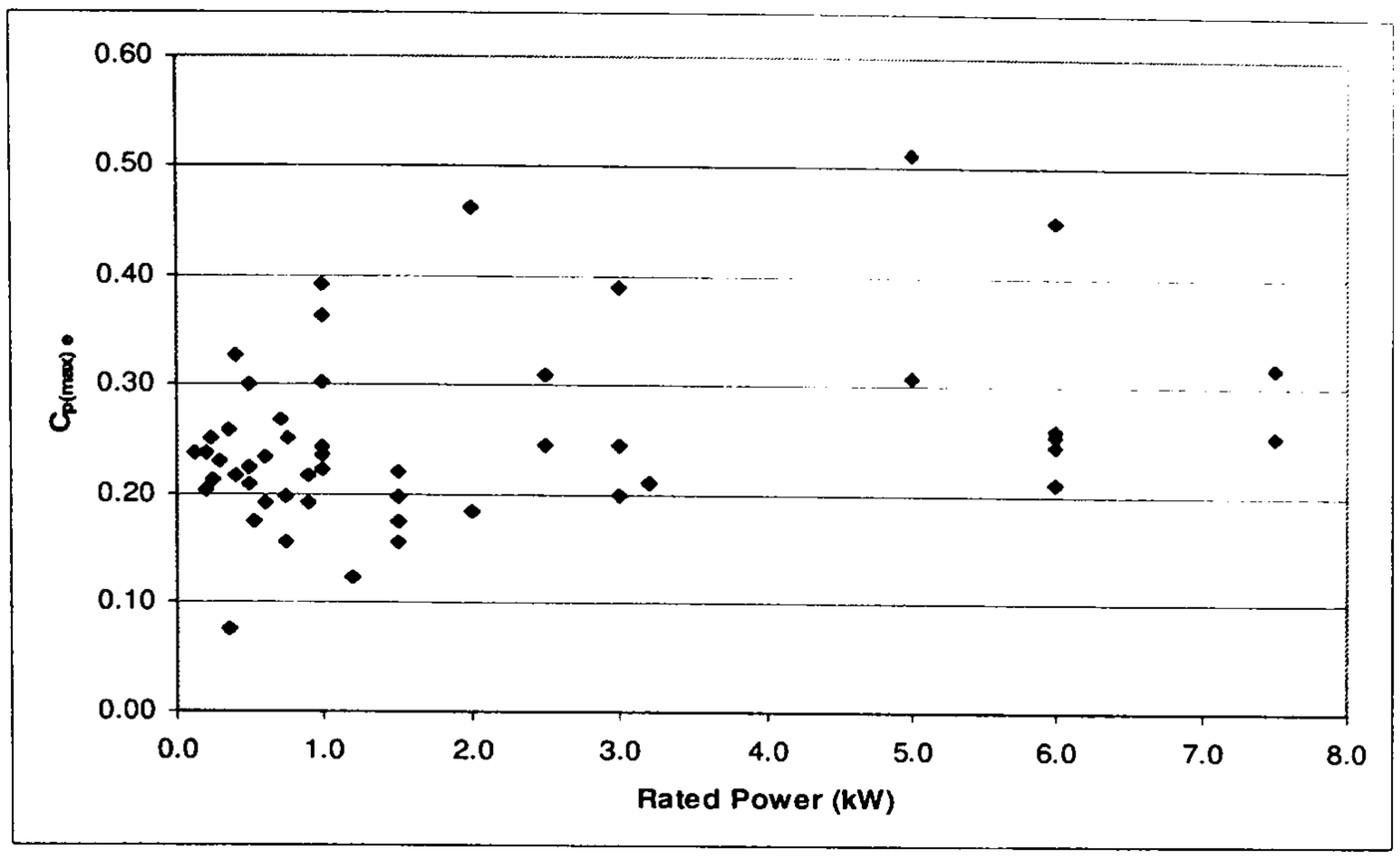

Figure 3-9. Manufacturers' claimed $C_{p(max)\,e}$

Figure 3-9 shows there is a large spread of claimed values for $C_{p(max)\,e}$ across different turbine ratings. However, these figures should not always be taken at face value. The maximum possible energy capture coefficient, known as the Betz limit, is 0.596 [54] and represents an upper ceiling for turbine efficiency. Modern large-scale turbines with carefully designed blades achieve a $C_{p(max)}$ of around 0.42 [28] and if this is multiplied by a nominal generator efficiency of 85%, a reasonable $C_{p(max)e}$ of 0.357 might be expected. Little independent data has been collected on the performance of micro and small-scale turbines, although what work has been done suggests their performance is significantly worse then their large-scale counterparts.

In the US the National Renewable Energy Laboratory tested a number of turbines near Boulder, Colorado [55] [56]; further tests were also carried out at Wulf Flats test facility in Southern California and the results appeared in the WindStats Newsletter in 2000 [57].

Turbine	Power Rating (kW)	Claimed $C_{p(max)e}$	Measured $C_{p(max)e}$	Reference
Bergey S/60	10	0.223	0.149	[55]
Whisper H40	0.9	0.217	0.167	[57]
Whisper H40	0.9	0.217	0.127	[56]
Air 403	0.4	0.328	0.287	[57]
Air X	0.4	0.328	0.08	[57]

Table 4. Measured and claimed turbine performance characteristics

Perhaps the more important constraint on wind turbines in the built environment is the poor wind resource. Wind maps such as the NOABL online service run by DBERR (formerly the DTI) [44] frequently quote MAWS in urban environments as 5-6 m/s, although the point is rarely made that this wind speed refers to a hub height of 10m above ground level (agl). Companies that make roof mounted turbines such as Swift [58] and Windsave [59] calculate their turbine's energy yield based on this 10m hub height rather then on the real wind speed at roof level. Little data has been collected about wind speed at roof level in real urban environments, however the studies that have been done suggest the wind speeds are much lower.

One recent study developed a computer model of monthly average wind speed in the built environment based on a 10m agl figure for a flat grassy field, and then corrected to allow for near-ground turbulence and wind shadow effects [60]. The study predicted a MAWS of 4.0m/s for a domestic dwelling in Aberdeen and 2.9 m/s for a similar property in Coleshill, West Midlands, although the study acknowledges the paucity of data with which to verify the model. A study carried out by Simon Watson at Loughborough University acknowledges the NOABL database is a poor resource for predicting mean annual wind speed, and also used CFD to show that the average capacity factor of a turbine in an urban site is likely to be less then 5% [61]. Of the studies done on real houses, Scoraig Wind Electric [23] measured wind speeds at roof

level on a house in Edinburgh for an entire year, and Warwick University has installed similar measurement equipment on 10 houses in Warwick [22], although only monthly average wind speeds on one house from May 06 – March 07 have been published. In both cases the anemometers were placed similar locations to where a roof mounted wind turbine would be sited, as shown in the figure below. The results of the studies are shown in Table 5.

(a) (b)

Figure 3-10. Wind measurements in the built environment for (a) Scoraig Wind Electric [23] and (b) Warwick Wind Trails [22]

Study	Predicted MAWS (m/s) (from NOABL database [44])	Measured MAWS (m/s)
Scoraig Wind Electric	5.6	1.7
Warwick Wind Trails	4.9	1.4

Table 5. Measured and predicted wind speeds in the built environment

When these lower values of MAWS are used to calculate turbine energy yield, the entire concept becomes much less attractive, as will be discussed in section 3.7 .

Increasing the speed of air through the turbine is not a trivial task. Increasing the hub height to 10m would allow a useful amount of energy to be generated but may not be politically acceptable. As shown in the figure below, a 10m tower is a sizable structure, and to erect a significant number would make a large visual impact on the urban landscape, not to mention the safety implications if the tower or turbine blades failed.

Figure 3-11. 1kW Bergey turbine on a 10m tower [24]

An alternative strategy is to use the building themselves to focus the oncoming wind. This can either be done by integrating the turbine into the design of the new building, such as the new Bahrain World Trade Centre or (on a smaller scale) by retro-fitting a new roof structure, such as the Aeolian Roof Wind Energy System shown below. Although the Aeolian roof system has not been tested, research at the Rutherford Appleton Laboratories on large building augmented structures shows that by channelling air through a large twin towered structure, the annual energy yield can be increased by 25% over a free standing yawing HAWT [62].

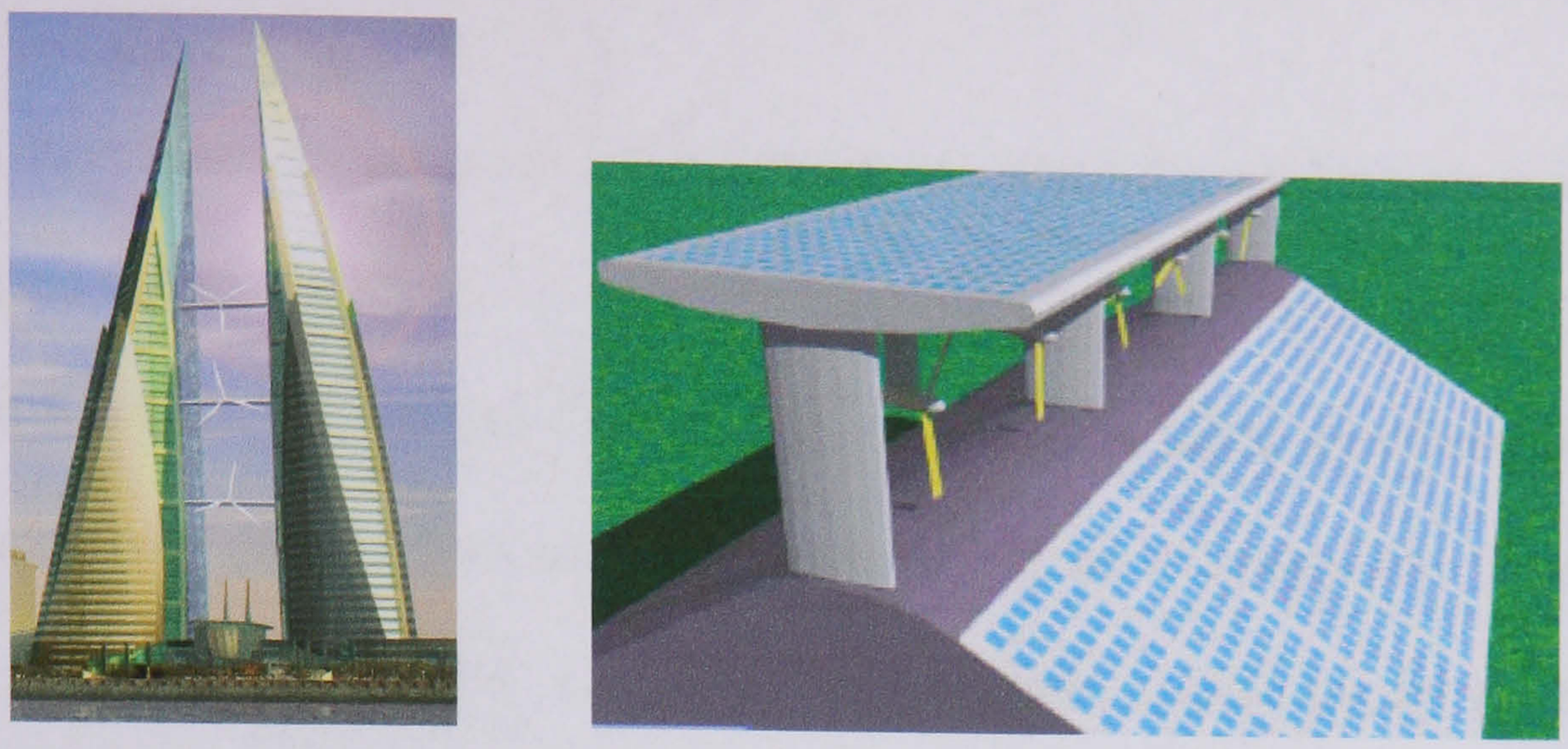

(a) (b)

Figure 3-12. Building Integrated Wind Turbines: (a) Bahrain World Trade Centre [63] (b) Aeolian Roof Wind Energy System [64]

There is also the possibility to increase the flow through the turbine by using a ducted fan arrangement such as the one developed at Strathclyde University in the late 1970s, shown below. The system was installed in the Lighthouse building in Glasgow in 1999 as part of a refurbishment that included the installation of a series of micro-renewable technologies [65].

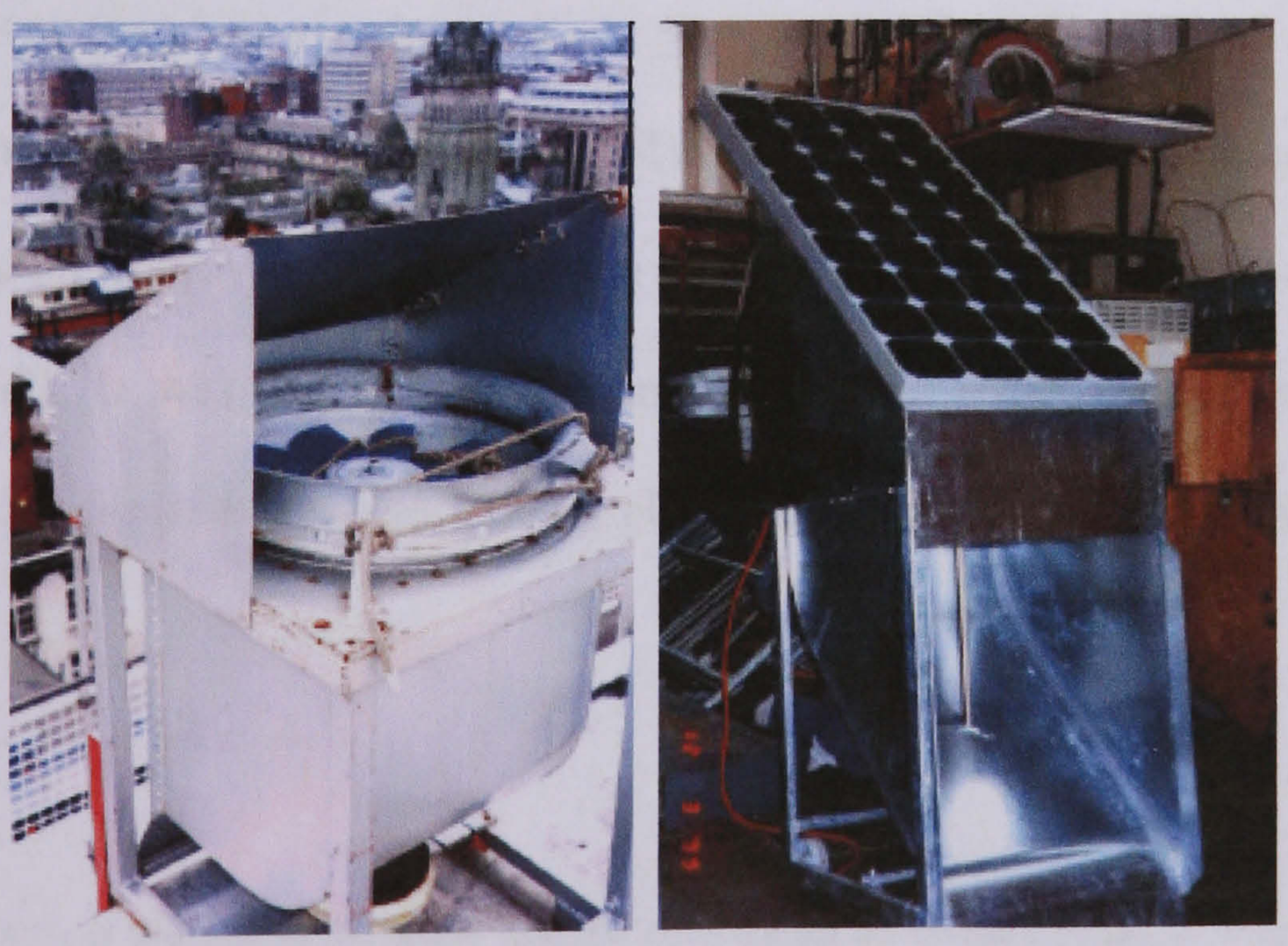

Figure 3-13. Strathclyde ducted fan system [16]

Apart from a small number of high profile building integrated wind turbines that have been constructed, the smaller scale, retro-fit type devices remain at the prototype stage.

Some studies have also shown it may be possible to boost the output power of a building mounted turbine by siting it in the 'sweet spot' of the air flow over a roof. CFD modelling that has been carried out for the DTI has shown a speed up effect as air passes over a shallow pitched roof of 40% at approximately 1.5 times the building height [16]. These findings were confirmed by research conducted at Durham University which used CFD – verified by wind tunnel tests – to model different roof shapes in a selection of wind directions [66]. The research found there was a speed up effect of approximately 20-30% at around 1.5 times the building height. A third study carried out at Delft University showed that wind speed increased by 20% at approximately 1.5 times the building height over a flat roof. It also showed that an H-type Darrieus turbine performed better then traditional HAWTs when subjected to a skewed wind profile[2] when sited on the windward edge of a flat roof. Indeed an angle of skew of 25° produced an *increase* in energy capture of approximately 30% during wind tunnel tests compared to a decrease in energy capture for a HAWT of approximately 10% [67]. Subsequent development of the Turby VAWT at Delft confirmed this finding by measuring an improvement in the energy capture coefficient of 35% at a skew angle of 25-30° [68]. It was found that the angle of skew increased as building height increased and decreased as the surface roughness upwind of the site was increased.

---

[2] The angle of skew is defined as the angle that the velocity vector of the oncoming wind makes with the horizontal as it passes upwards over the building.

3.6 Costs and income of micro wind turbines

The following section will move away from the details of turbine energy yield and focus more generally on the economics of micro and small-scale turbines. The annual energy yield of small turbines will be revisited in section 3.7 when a selection of turbines in different wind regimes will be analysed to calculate their payback periods.

When calculating cost and benefits of the wind energy conversion system it is necessary to consider the initial capital cost of the installed system, the grant and incentive schemes on offer from the government, and also the income that can be generated from the device. This depends on how the energy is used – whether it is sold back to the grid, stored and used to offset the consumer's electricity bill or used to heat water, which offsets the consumer's gas bill. These aspects will be examined in the following section.

3.6.1 Capital cost of micro and small-scale turbines

The cost of a micro wind turbine system is currently around £2000-5000/kW installed [69] [70]. Specifically, the cost of a 2.5kW turbine is approximately £10,000-12,000 [69], although a 1kW roof mounted turbine can be as cheap as £1,799 [59] but a figure of £3000 is more typical [70] [22].

3.6.2 Low Carbon Building Programme Grant

To reduce this capital cost, the government has introduced a grant scheme known as *The Low Carbon Building Programme* (formerly Clear Skies), which was launched in 2006 and is administered by the DBERR (formerly the DTI) through the Energy Saving Trust. At the time of writing the Programme had funds of £18m to provide grants for the installation of micro generation technologies in homes and for community projects [70].

For micro wind turbines, the grant offered is a maximum of £1,000 per kW installed, up to a maximum of £5,000 subject to an overall 30% limit of the installed cost (exclusive of VAT) [71].

As well as a grant scheme, the government also offers two further inducements to encourage the uptake of renewable generation: the Climate Change Levy and Renewable Obligation Certificates and these are both discussed below.

3.6.3 Climate change levy

The Climate Change Levy (CCL) was introduced in 2001 to encourage energy efficiency in business and the public sector by taxing carbon emissions. The tax has caused non-domestic electricity bills to rise by an average of 8-10%, although this income has been given back to employers through a reduction in employer's NI of 0.3% to prevent UK businesses from being competitively disadvantaged. The CCL is not paid on any energy generated locally by a renewable device, and so gives an inducement to the installation of micro generation. The CCL is not paid by domestic consumers, however, and so offers no encouragement for home owners to adopt micro turbines [45].

3.6.4 Selling electricity and Renewable Obligations Certificates

Renewable Obligation Certificates (ROCs) were introduced by the government in the Utilities Act (2000) and came into force in April 2002, although it has only been since 2004 that small-scale producers could claim ROCs payments. The act forces power companies to generate a certain proportion of their energy from renewables, rising every year from 3% in 2003 to 15% by 2015. Companies who generate less renewable power than their quota must buy ROCs from companies who generate more, leaving market

forces to establish the price. At the time of writing, ROCs were worth 3.0p/kWh, although they had in the past been as high as 4.7 p/kWh [45].

To sell electricity back to the grid or claim ROCs payment, a special Import/Export meter is required at a cost of £75 [72]; to sell electricity the producer must also register with National Grid at a cost of £54.75 p.a.. Once registered, the producer is then free to establish a deal with an electricity supplier to sell surplus electricity or ROCs or both. There are many different tariffs and rates available from suppliers, with some unwilling to offer the market rate for ROCs because of the prohibitive administrate cost associated with small producers. Ofgem is currently trying to streamline this process in order to encourage further uptake of micro generation technologies, however [73]. Despite the extra cost there are some suppliers willing to deal specifically with small-scale generators and offer a premium for green electricity. Their prices on 3/4/07 are shown in the table below.

Company	Exporting electricity (p/kWh)	ROCs payment (p/kWh)	Importing electricity (p/kWh)	Importing gas (p/kWh)
Green Energy [74]	4.0	3.0		
Good Energy [75]	-	4.5	11.5	
EDF Energy [76]	-	-	10.5	2.7

Table 6. Electricity and gas prices on 3/4/07

If the consumer wanted to sell all electricity produced by a wind turbine to the grid, the highest price offered is 4.0 p/kWh for the electricity plus 4.5 p/kWh for the ROCs payment. This total of 8.5 p/kWh for selling electricity is greater then the price for using the electricity to heat water (offsetting the consumer's gas bill), which equates to 4.5 p/kWh for the ROCs payment plus 2.7 p/kWh for the offset gas bill (a total of 7.2 p/kWh). However, it should be noted that to sell electricity to the grid, an annual grid

registration charge of £54.75 is levied which may take a significant proportion of the income generated.

3.6.5 Offsetting rather then selling

The most cost effective way of using electricity generated by a micro wind turbine, however, is to consume it locally rather then sell it to the grid. By adopting this strategy, the electricity is worth the market rate of 10.5 p/kWh [76] and, with the addition of a ROCs meter, a further 4.5 p/kWh in ROCs payments [75]. The figure of 15p/kWh has been used to calculate the annual income generated from micro and small-scale turbines in section 3.4.1.

A battery storage system similar to that described in Figure 2-7 (b) would be required to gain the full benefit from the intermittent wind resource. Some manufactures claim the cost and complexity of this system is prohibitive [59, 77], however this is more than compensated for by the favourable rate for offsetting and by the fact a grid-tie inverter and grid registration are no longer required. The Windy Boy 2500W inverter, for example, can be a significant proportion of the total capital outlay (50% of the system cost or 12% of the total installed cost for a 2.5kW turbine [78]).

3.7 Actual income and payback periods

A simple method to establish the cost effectiveness of current micro wind turbines is to consider the payback period on the initial capital investment. The 1kW Windsave turbine and the1.5kW Swift turbine have been chosen for study as these are currently the only two commercialised mass-produced roof mounted turbines. In each case a 'favourable' scenario and a 'realistic' scenario have been examined. The 'favourable'

scenario assumes the turbine operates at a $C_{p(max)e}$ of 0.3 in a MAWS of 4.5m/s; the 'realistic scenario' assumes a $C_{p(max)e}$ of 0.2, based on the evidence in Table 4, and a MAWS of 2.0m/s, based on the evidence in Table 5. The $C_{p(max)e}$ of the turbines considered here are based on a rated wind speed of 12.5 m/s. The turbines are treated as if they had been installed according to the manufactures' recommendations; the Swift is used for both hot water heating and electricity generation, while the Windsave is just used for electricity generation. It is assumed that all generated electricity can be used by the house and none 'slips' back on to the grid, giving it a value of 10.5p/kWh. For both turbines full ROCs payments of 4.5p/kWh are claimed and the full 30% Low Carbon Building Programme grant is available.

A third generic turbine is also considered based around technology that is currently on the market [25] [79]. This device is a 2.5kW turbine with a $C_{p(max)e}$ of 0.2, mounted on a 10m tower to provide an air stream of MAWS = 5.5m/s; all generated energy is stored and used to offset the household electricity bill and all grant and ROCs payments are claimed as before.

In a fourth scenario the same generic turbine is mounted on top of a 20m office block with a MAWS of 6.8m/s. This has been calculated according to the wind sheer power law equation below:

$$V_{turb} = \left(\frac{H_{turb}}{H_{ref}} \right)^{s_w} V_{mean} \qquad [3\text{-}5]$$

Where a V_{mean} of 5.5 m/s is assumed at a reference height H_{ref} of 10m, and the wind shear s_w is taken to be 0.3 (rather then the more usual $^1/_7$) due to the roughness of the

urban environment [80]. It is assumed that the energy generated from this turbine is used to offset the building's electricity bill at 10.5 p/kWh, the grant and incentive schemes are claimed as before, and the generated energy is exempt from the Climate Change Levy (a 10% tax on imported energy), making the energy relatively 10% more valuable.

The study does not consider any interest payments made on the initial capital investment or secondary costs such as planning permission (which can be in the region of £3000 [22]). The results are shown below:

Turbine	WindSave 1kW	WindSave 1kW	Swift 1.5kW	Swift 1.5kW	Swift 1.5kW	Generic 2.5kW	Generic 2.5kW
Scenario	Realistic	Favourable	Realistic	Favourable	Favourable	10m tower	20m office roof
MAWS (m/s)	2.0	4.5	2.0	4.5	4.5	5.5	6.8
$C_{p(max)e}$	0.2	0.3	0.2	0.3	0.3	0.2	0.2
Installed cost (k£)	1.8	1.8	2.0	2.0	2.0	10.0	10.0
Energy yield (kWh/yr)	33	669	47	963	963	3413	5724
Energy use	Offsetting electricity	Offsetting electricity	Offsetting gas	Offsetting gas	Offsetting electricity	Offsetting electricity	Offsetting electricity
Value of energy (£/yr)	3*	100*	1†	69†	144*	512*	853‡
Percentage of household power generated (%) §	1	15	1	21	21	76	-
Design life (yrs)	10	10	20	20	20	20	20
Payback period (yrs)	**385**	**13**	**1162**	**21**	**14**	**14**	**8**

Table 7. Cost analysis for small-scale wind

* (Energy yield)*(offsetting electricity price + ROCs)
† (Energy yield)*(offsetting gas price + ROCs)
‡ (Energy yield)*(offsetting electricity price*CCL + ROCs)
§ Based on an average household consumption of 4500kWh/yr (BWEA)

The table above shows the most cost effective scenario is to mount a turbine on a large office block and this is simply because of the better wind resource. Roof mounted wind turbines are not currently economically feasible in most scenarios, although this may change in the future if energy prices continue to rise or if high volume production reduces the capital cost of the devices. However, the early research has thrown up a serious worry concerning the wind resource at roof level in the urban environment, and no matter how cheap the turbines become, their energy yield may always be diminutive. As the interim report from the Warwick Wind Trails puts it:

"The (very early) data we have suggests urban wind will deliver tens to hundreds of kWh per year on typical urban sites rather than the hundreds to thousands optimistically forecast in the early stages of market development." [22]

Urban turbines may still find favour when sited in a good location, for example by the sea or on the edge of an urban conurbation; in cities may also be mounted on towers, in the 'sweet spot' on roofs, on office blocks or incorporated into the structure of a building. However, if manufacturers continue to make unrealistic claims for their turbines, such as Windsave's statement that their turbine can *'save up to 30% off the average annual electricity bill'* [59] with a payback period of around *'5 to 7 years'* [59], there is a serious risk of damaging the credibility of not only the small-scale wind industry but also the large-scale wind industry as well. Indeed the number of recent newspaper articles that have reported the poor performance of urban wind turbines [81-83] may be testimony to this.

3.8 Conclusions

The annual energy yield from small-scale wind turbines can be estimated by combining a Weibull wind speed distribution with the turbine's power characteristic. However, it is necessary to have accurate turbine characteristics and wind speed data - both of which appear to have been overstated by manufacturers who are keen to sell their products and are under no legal obligation to be truthful (unlike the manufacturers of large-scale turbines). There is currently little data on the performance of small-scale turbines in the built environment or on the wind resource at roof level, although what evidence there is suggests the performance of roof mounted turbines has been grossly exaggerated. This could have serious implications for the whole of the wind industry if the public become disillusioned with the technology.

By siting micro and small-scale turbines carefully, for example on designated towers, in the 'sweet spot' of air flow over a roof, on tall office blocks or as an incorporated part of the structure, these devices could generate significant quantities of energy. Of these concepts, siting turbines on office blocks or as an integrated part of the building's structure shows the most promise, although more research is need to assess their viability.

The correct economic incentives are also critical to the uptake of micro and small-scale turbines and it is questionable whether this has been achieved in Britain. In Northern Ireland a 50% (rather then 30%) grant scheme is available, in the US a 'net metering' system is used to give generated power the same market value as imported power without the need for battery storage, and in Germany an inflated tariff is offered to producers of renewable energy which is guaranteed for a period of time (usually 20

years). These systems appear far simpler and more accessible to the consumer then the complicated ROCs payment and free market tariff system that exists in the UK.

The analysis has shown that with the current incentive schemes it is only economically viable to mount turbines on tall office block. However, even with a lack of further government aid, it is still likely that micro wind power will become more attractive in the future as the cost of the technology decreases as production volumes become larger. Energy prices may also continue to rise and carbon taxes/trading schemes may be introduced to better account for the environmental impact of fossil fuel power generation.

A final point with regard to the benefits of micro-wind turbines in the urban environment is in the less tangible effect it has on people's attitude towards energy efficiency and energy saving. Studies have shown that people become more interested in saving energy and tackling climate change when they are exposed to renewable micro-generation technologies. Such exposure allows them to take ownership of the climate change problem in a way that makes them feel they can make a difference and it also encourages them to change other aspects of their lives such as car use [16] [84].

Chapter 4

Spectral method of modelling turbulent wind

4.1 Introduction

Chapter 2 introduced a micro wind energy conversion system which was modelled using MATLAB/SIMULINK. Although the model provided accurate predictions of steady state performance that could be verified by experimental measurement, it took no account of the turbulent nature of the wind, and this topic will be discussed in the following chapter.

In section 4.2 the nature of energy transfer in the wind is examined and from this a spectral method of modelling wind turbulence is developed in section 4.3. The Von Karman power spectrum is shown to be a good approximation of real wind turbulence and a method of modelling this spectrum is developed in sections 4.5 and 4.6. The SIMULINK implementation of this model is discussed in section 4.7 and the accuracy of the resulting wind profile is also examined. Finally, the effect of turbulence on real wind turbines is discussed in section 4.8.

Although spectral models of wind turbulence have been examined before [85-88], it is generally with large-scale wind turbines in mind. The implementation of this approach in SIMULINK in this chapter, and the investigation of the dynamic response of small-scale turbines in the following chapters, is novel (see references [89] and [90]).

4.2 Modelling of turbulent wind

Wind energy is an indirect form of solar energy resulting from an imbalance between the solar radiation incident at the poles and at the equator. This imbalance sets up large-scale convection currents that circulate throughout the atmosphere. In the free stream, several thousand meters above the earth's surface, the wind is essentially stable, however in the boundary between the free stream and the earth's surface, known as the Ekman layer, the wind speed is continually fluctuating. The level of turbulence generally decreases with altitude and is highly dependent on surface topology at near-ground levels, as shown in the figure below.

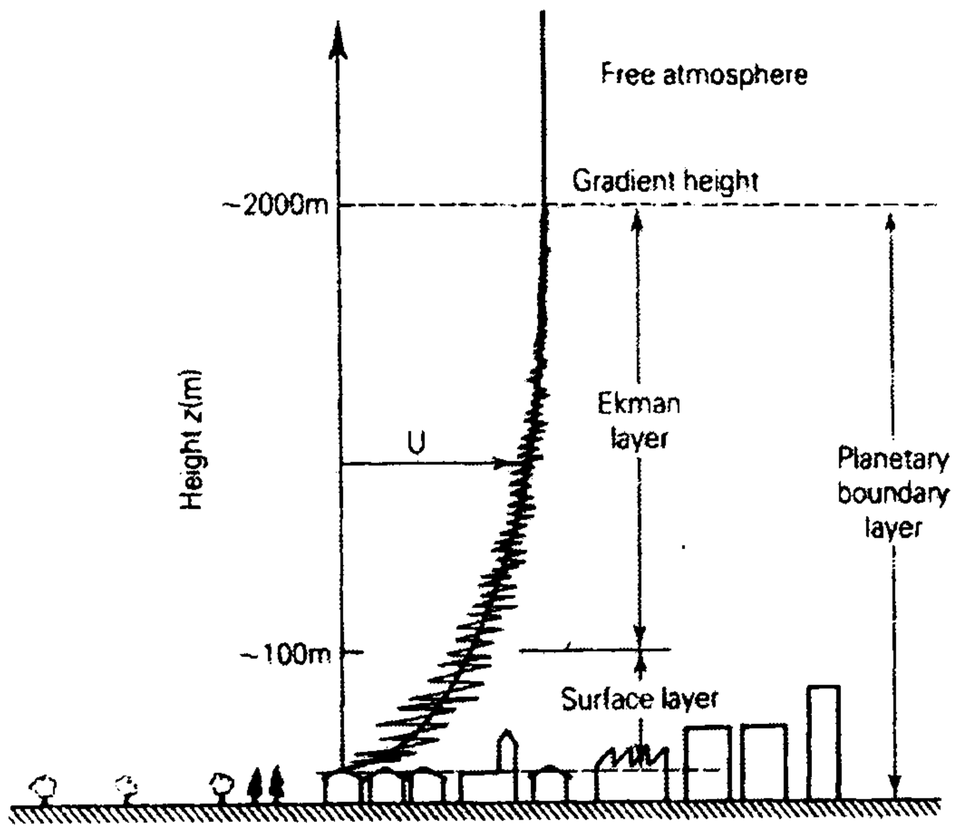

Figure 4-1. The atmospheric boundary layer

In 1957 Isaac Van der Hoven showed that energy carried in the wind is transferred at discrete frequencies [91], as shown in Figure 4-2. Three major energy peaks occurring at approximately 100 hours, 12 hours and 1 min, caused by the passing of large-scale weather systems, diurnal variations and atmospheric turbulence, respectively. On longer timescales, seasonal variations are important for determining the generating potential of a given site, and over such timescales a probabilistic analysis of wind speed,

(as described in Chapter 3), must be adopted.

However, in this chapter it is the short term fluctuations caused by atmospheric turbulence that are of interest. These fluctuations, with time periods in the order of seconds and minutes, can have significant implications for the control of the turbine and on the system's energy conversion efficiency, (these subjects will be addressed in Chapters 5 and 7).

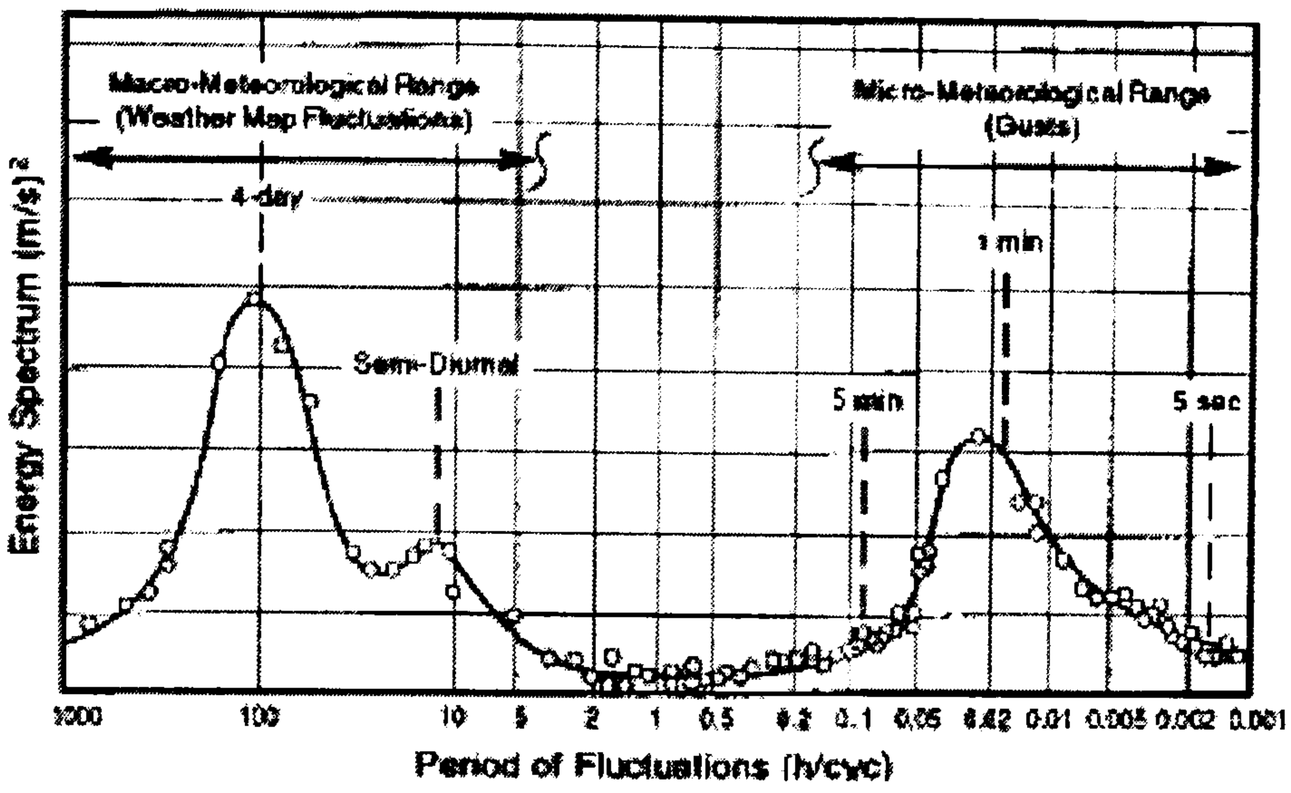

Figure 4-2. The Van der Hoven Power Spectrum

4.3 Spectral model of wind turbulence

In this section a method of modelling ground level turbulence is developed using spectral analysis, which allows an accurate representation of the wind to be reconstructed from a handful of parameters that can be measured on a site location.

A schematic representation of the turbulent wind model is shown in Figure 4-3 and central to this is the random number generator which produces normally distributed white noise; this acts as the basis for the turbulent wind component. Since the wind speed cannot (for physical reasons) change instantaneously, the white noise must be smoothed using a carefully designed signal-shaping filter in order to achieve the correct

spectral distribution. The shaping filter must be chosen to best characterise the true spectrum of the wind and there are a number of candidates for this task, (this is dealt with in the section 4.4). The gain and time constants of the filter are chosen to ensure the standard deviation of the filtered output is equal to 1. This normalised coloured noise can then be multiplied by the respective wind-speed-dependent standard deviation, σ_v, to provide a turbulent wind component with the correct standard deviation. By adding the base wind speed, V_{mean}, to the turbulent component, a turbulent wind profile can be generated.

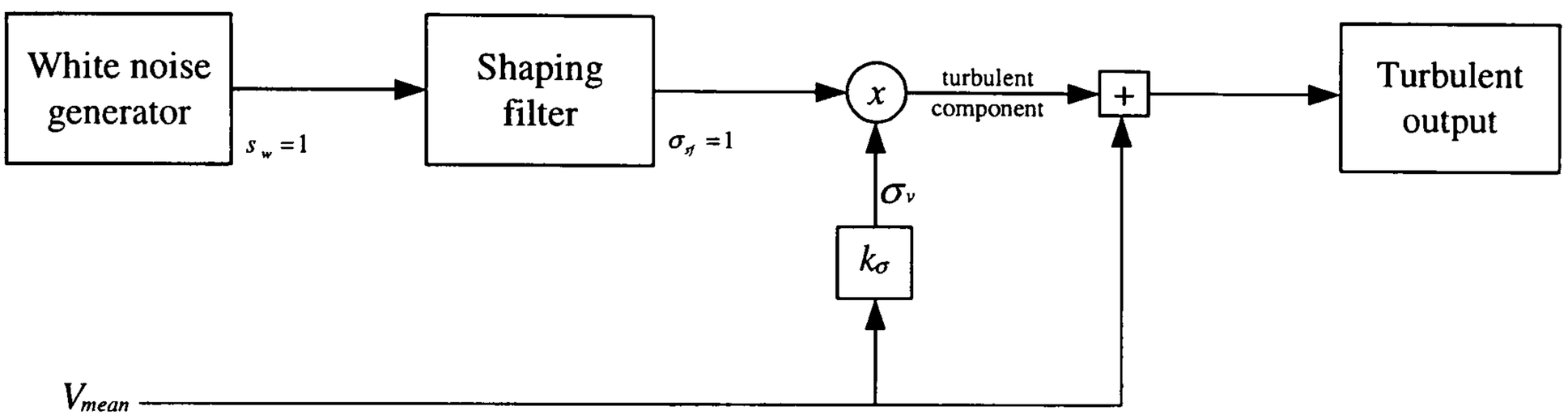

Figure 4-3. Schematic representation of the turbulent wind model

4.4 Von Karman spectrum of turbulent wind

A number of attempts have been made to model the power spectrum of turbulent wind [92-94], although the most widely used is the Von Karman power spectrum [95] which is considered here.

For an average wind speed, V_{mean}, Von Karman states the power spectrum of turbulent wind, $S_v(\omega)$, may be represented by equation [4-1].

$$S_v(\omega) = 0.475\sigma_v^2 \frac{LV_{mean}^{-1}}{\left[1 + \left(\omega LV_{mean}^{-1}\right)^2\right]^{\frac{5}{6}}} \qquad [4\text{-}1]$$

In the equation above, L is the turbulence length scale and can be considered as the typical length of eddies in the free stream, while σ_v is the standard deviation of the wind turbulence, which gives a measure of the turbulence's intensity and will be discussed in more detail in section 4.6. The turbulence length scale is determined by the terrain conditions and is independent of turbine rating. Although this quantity is difficult to measure, a good approximation is given by Frandsen [96], who approximates it as linearly proportional to hub height, such that:

$$L = 6.5H_{hub} \qquad [4\text{-}2]$$

Where H_{hub} is the hub height.

A comparison between the Von Karman power spectrum and the power spectrum generated by 200 seconds of real wind data taken from an 18m mast in open country [97] is shown in Figure 4-4 .

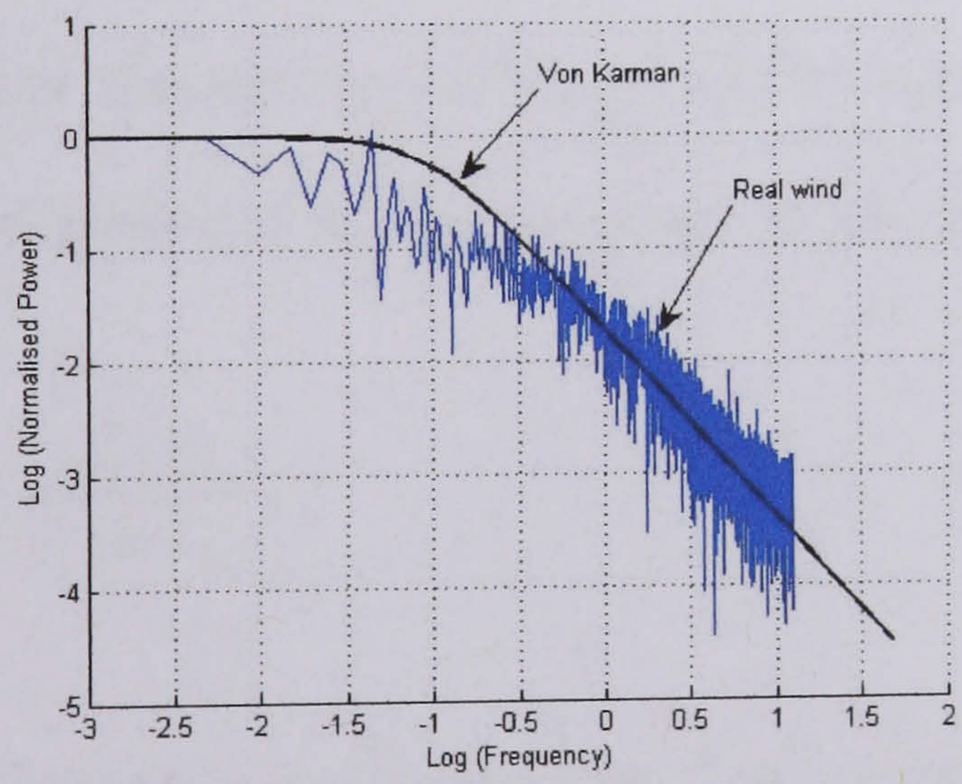

Figure 4-4. Comparison between the Von Karman spectrum and real wind data

This comparison has been made in the following manner: Parseval's theorem states that,

for a periodic signal, the normalised power in the Fourier domain can be equated to the normalised power in the time domain according to [98]:

$$P_{norm} = \sum_{i=-\infty}^{\infty} |F_i|^2 = \frac{1}{T_0} \int_{t_0}^{t_0+T_0} p(t)dt \qquad [4\text{-}3]$$

Although the wind signal is not periodic, it can be considered so over the short time interval that the signal is sampled. Such an assumption allows a Fast Fourier Transform (FFT) to be taken of the normalised power signal which is shown as the blue line in Figure 4-4. The power signal from the wind data can be normalised according to equation [4-4], such that the signal amplitude is divided by the mean amplitude, which is calculated using a simple MATLAB script. The FFT can be generated using MATLAB's FFT routine.

$$P_{norm} = \left| \frac{V_w}{V_{mean}} \right|^2 \qquad [4\text{-}4]$$

The Von Karman power spectrum can be normalised by dividing the power at a given frequency by the power present in the DC component of the wind, i.e.:

$$P_{norm} = \frac{S_v(\omega)}{S_v(\omega_{T\to 0})} \qquad [4\text{-}5]$$

In order to make a valid comparison between the Von Karman power spectrum and the real wind data, the same values of mean wind speed, V_{mean}, and turbulence length scale, L, must be used. Although V_{mean} has been calculated from the real wind data, L is unknown and must be estimated from Frandsen's equation (equation 4-2). The numeric

values of these variables are given in the table below along with the standard deviation of the wind turbulence and the ratio of mean wind speed to standard deviation which will be discussed in more detail in section 4.6.

Mean wind speed, V_{mean} (m/s)	10.74
Turbulence length scale, L (m)	117
Standard deviation on wind, σ_v (m/s)	1.95
σ_v / V_{mean} $(=k_\sigma)$	0.18

Table 8. Values calculated from wind data

Figure 4-4 shows the Von Karman spectrum is a good approximation to real wind turbulence and Frandsen's equation is a fair approximation of the turbulence length scale.

4.5 Modelling the Von Karman Spectrum

Turbulence can be created by passing white noise through a signal shaping filter to produce coloured noise of the same spectral distribution as the Von Karman spectrum, as this has been shown to be a good representation of real wind. References [87] and [88] show that this spectrum can be represented by the 5/6th order transfer function shown below.

$$G(s) = \frac{K_F}{(1 + sT_F)^{5/6}} \qquad [4\text{-}6]$$

Where K_F and T_F are the gain and time constant of the filter. (An explanation of how this is equation is linked to the Von Karman power spectrum is given in Appendix B.)

However, in order to implement this transfer function in SIMULINK, a rational form of the denominator must be used. Nichita et al states in [87] that a close approximation can

be made by the second order transfer function:

$$G_{Nichita}(s) = K_F \frac{(m_1 T_F s + 1)}{(T_F s + 1)(m_2 T_F s + 1)} \qquad [4\text{-}7]$$

Where: $m_1 = 0.4$; $m_2 = 0.25$

The time constant, T_F, is related to turbulence length scale, L, and mean the wind speed, V_{mean}, by [87, 88]:

$$T_F = \frac{L}{V_{mean}} \qquad [4\text{-}8]$$

As mentioned previously, the standard deviation of the coloured noise coming from the output of the filter must be equal to 1, and this criteria is met if the gain of the filter is [87, 88]:

$$K_F \approx \sqrt{\frac{2\pi}{B(x,y)} \cdot \frac{T_F}{T_s}} \qquad [4\text{-}9]$$

T_s is the sampling period and $B(x,y)$ designates the beta function:

$$B(x,y) = \int_0^1 t^{x-1}(1-t)^{y-1}\,dt \qquad [4\text{-}10]$$

The value of the Beta function must be selected so that the standard deviation of the coloured noise output is equal to 1. Prudnikov, *et al,* [99] show mathematically that with a sample time of 1s the beta function parameters x and y must equal ½ and ⅓, i.e. $B(x,y) = B(\frac{1}{2}, \frac{1}{3}) = 8$. In the model presented here, a much faster sampling frequency

is used (T_s=0.04 seconds), and so to ensure the standard deviation remained at $1, B(x, y) = 11.1$, to give:

$$K_F \approx \sqrt{\frac{2\pi}{11.1} \cdot \frac{T_F}{0.04}} \qquad [4\text{-}11]$$

4.6 Estimation of the standard deviation of turbulent wind

The schematic in Figure 4-3 shows that white noise is passed through a spectral filter (given by the transfer function in equation [4-4]), which provides the correct frequency profile of the desired wind at a standard deviation of 1. The amplitude of the turbulent component must then be scaled by the correct standard deviation (i.e. intensity) of the turbulent wind, σ_v.

Being able to accurately predict the standard deviation, σ_v, of the wind turbulence is obviously a critical aspect of the modelling process. This quantity is fairly easy to estimate, however, since the standard deviation is linearly proportional to the wind speed, i.e. the stronger the wind, the greater the variation in its turbulence, such that:

$$\sigma_v = k_\sigma V_{mean} \qquad [4\text{-}12]$$

This relationship is shown in Figure 4-5 for two sites in Germany: Heroldstatt and Nordholz, [88], where the mean wind speed has been plotted against the standard deviation of the turbulence. The data was collected from an 18m mast in flat open countryside and averaged in 10 minute segments over periods of 720 and 80 hours. Values of k_σ of 0.16 and 0.13 were recorded for the two sites and these are similar to the value of 0.18 which was calculated from the wind data obtained in section 4.4. This

wind data was recorded in a similar location to the German data - from an 18m meteorological mast in open country.

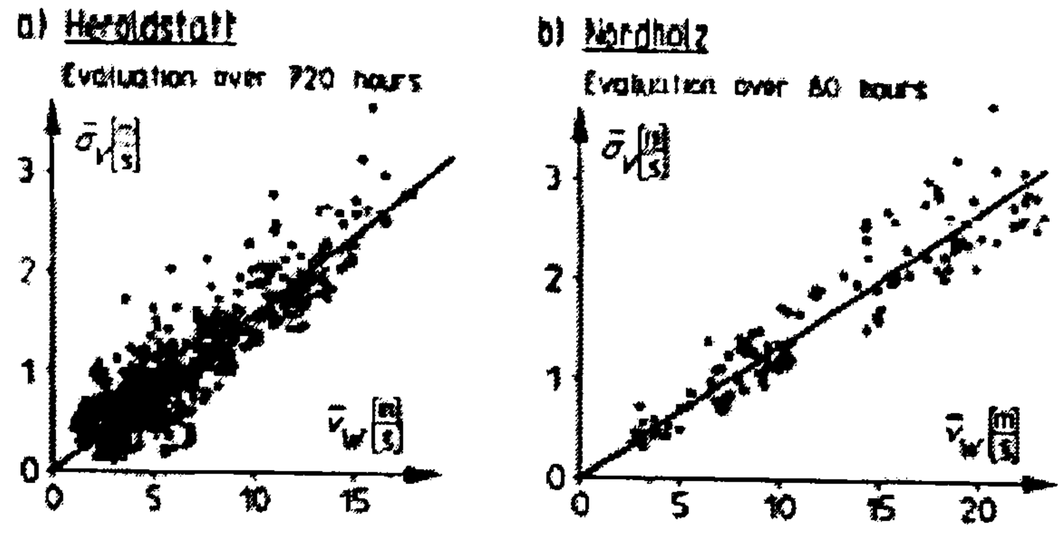

Figure 4-5. Dependence of standard deviation on wind speed [88]

Where detailed measurement cannot be taken, however, values of k_σ can be estimated from generic landscapes such as those given in Table 9.

Terrain type	K_σ
Coastal areas	0.123
Lakes	0.145
Open	0.189
Built up areas	0.285
City centres	0.434

Table 9. Values of k_σ for various terrains at a height of 10m [100]

4.7 SIMULINK implementation

The SIMULINK implementation of the model is shown in Figure 4-6. The base wind speed, V_{base}, turbulence length scale, L, and the standard deviation dependency constant k_σ (shown as k_sigma in the figure) are entered in a MATLAB program that runs behind the simulation, and are used to calculate values for T_F and K_F. The output of the model is returned to MATLAB at two points to allow checks to be made on the signal: *filter_out* allows the standard deviation of the coloured noise to be confirmed as unity, while *wind_out* allows turbulent output to be compared to real wind data, as discussed below.

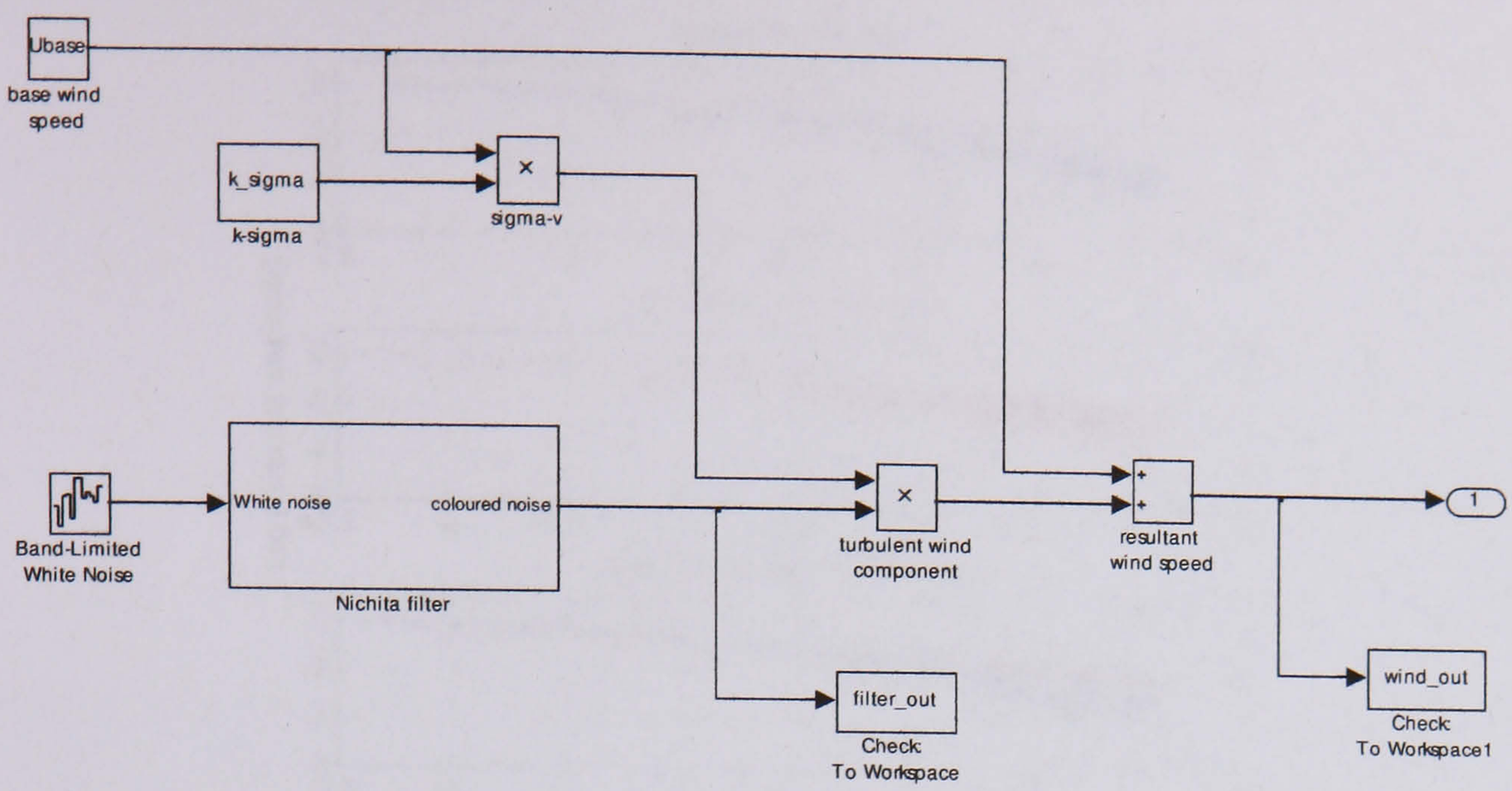

Figure 4-6. Turbulent wind model

Turbulent wind profiles can now be generated in the time domain for any given mean wind speed. To verify the model, a simulated wind profile is compared with a recorded wind profile in the time domain, Figure 4-7. The real wind profile [97] provides a visual check that the generated turbulence is of similar magnitude and frequency to the actual wind; a more satisfactory check is to compare the spectral distribution of the two wind profiles, as shown in Figure 4-8.

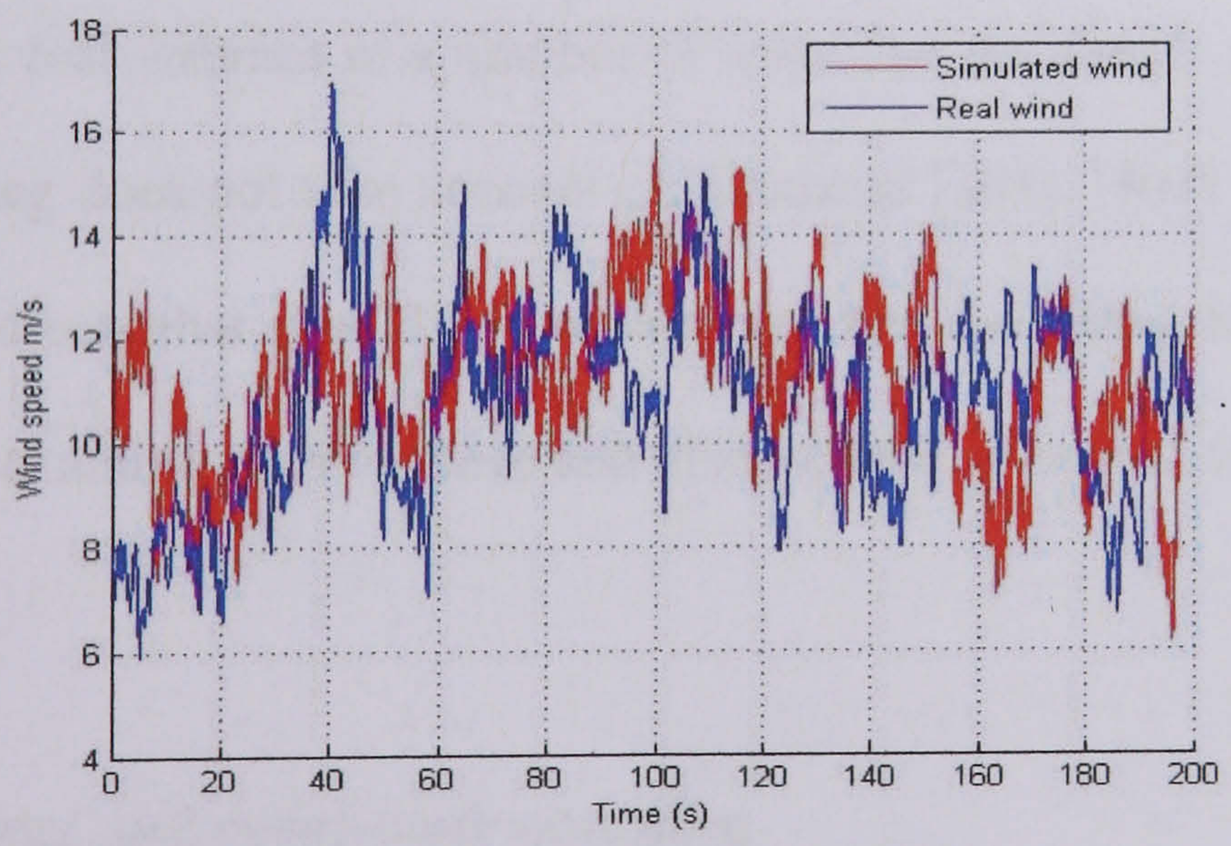

Figure 4-7. Comparison between simulated wind and real wind in the time domain (U_{mean} = 11.4; L=65; k_σ=0.18)

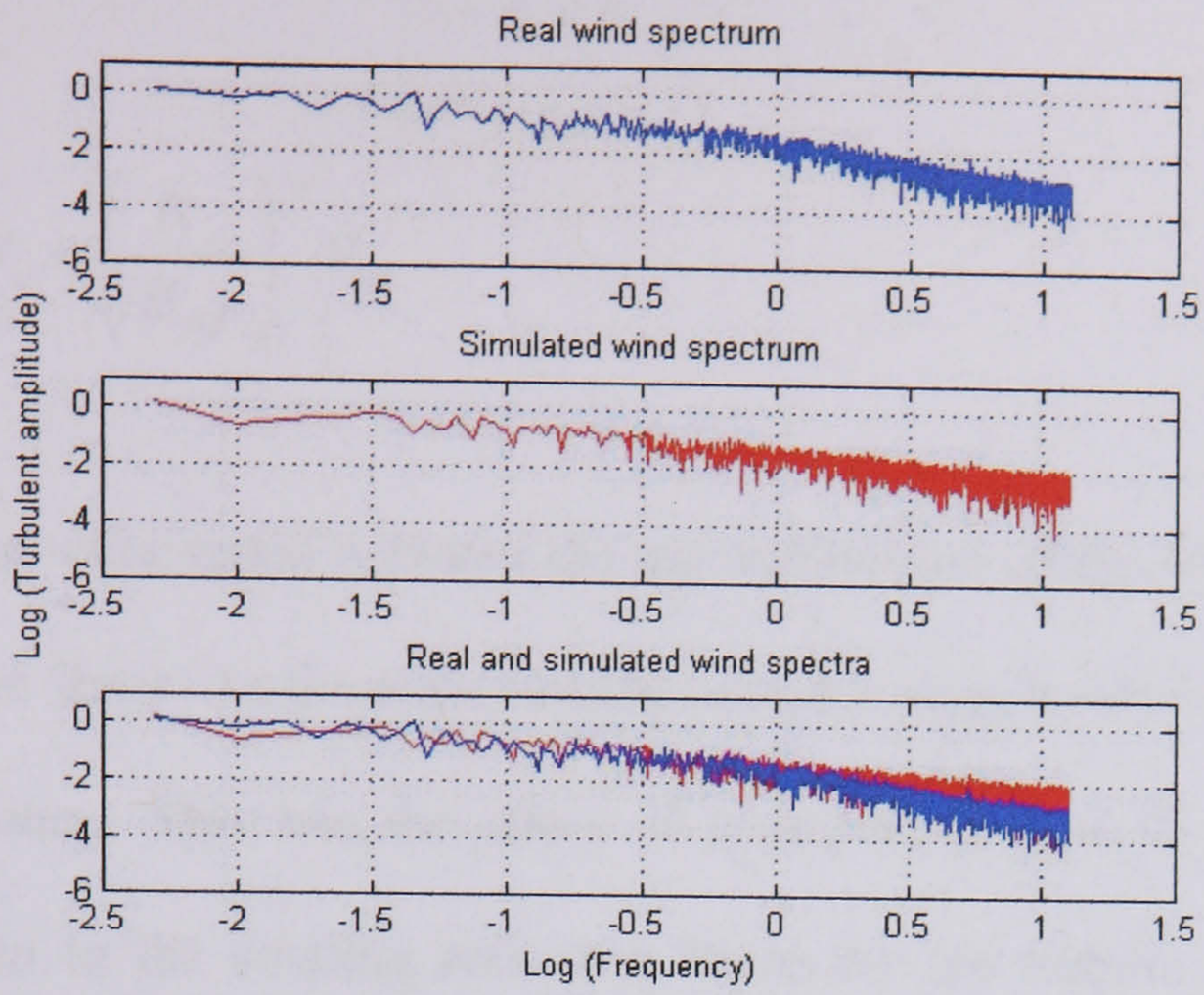

Figure 4-8. Comparison between simulated wind and real wind in the frequency domain (U_{mean} = 11.4; L=65; k_σ=0.18)

Although the spectra in Figure 4-8 agree closely with each other there is some disparity due to the unknown turbulence length scale of the real wind and the fact that the Nichita transfer function is an approximation to the Von Karman transfer function, which is itself an approximation to the real wind spectrum.

4.8 Effect of turbulence on real turbines

Real wind affects real turbines in a number of ways that the simple spectral method of turbulent modelling does not take account of. Leithead [101], [102] and Westlake [85] identify several effects that should be considered when modelling real-world turbines. This section will examine each of these and discuss their relevance to micro and small-scale turbines.

4.8.1 Wind shear and rotational sampling

As shown by Figure 4-1, the wind speed increases in the boundary layer between the

surface of the earth and the free stream according to the power law:

$$V_z = \left(\frac{H_z}{H_{ref}} \right)^{s_w} V_{ref} \qquad [4\text{-}13]$$

The difference in wind speed between the top and bottom of the swept area of a turbine is known as wind shear. As the wind turbine rotates it samples the wind shear field at its rotational frequency. This has the effect of introducing spectral peaks into the wind spectrum as seen in the rotating reference frame by the turbine blades. The spectral peaks, caused by the blades sampling a regularly changing wind speed, occur at the rotational frequency and higher harmonics [103]. However, this effect is only significant for large turbines with diameters of many tens of metres. For small rotor diameters located close to the ground, the effect of ground level turbulence dominates over the free stream power law.

4.8.2 Tower shadow

Tower shadow effects can be neglected as they do not occur with vertical axis turbines (which are chosen for study in subsequent chapters), and even on horizontal axis machines the effect is thought to be negligible at small-scales.

4.8.3 Disc averaging

As the turbine rotates it experiences an average of the turbulence passing through its blades, and this smoothing effect can be modelled by a spatial filter of the form [101]:

$$W_{AV}(s) = \frac{\left(\sqrt{2} + \mu s\right)}{\left(\sqrt{2} + \sqrt{0.55}\mu s\right)\left(1 + \frac{\mu s}{\sqrt{0.55}}\right)} \qquad [4\text{-}14]$$

μ is given by the following expression:

$$\mu = \frac{\gamma_s R}{V_w} \qquad [4\text{-}15]$$

γ_s is a decay factor and is taken to be 1.3 [101].

Since the disc averaging effect is dependent on mean wind speed rather then on the turbine geometry, it must be included in the model of a small-scale turbine. The transfer function shown above can be implemented in SIMULINK using a simple user-defined transfer function block which can be used to modify the output of the turbulent wind signal in Figure 4-6. The effect of disc averaging on a 3m diameter wind turbine is shown in Figure 4-9.

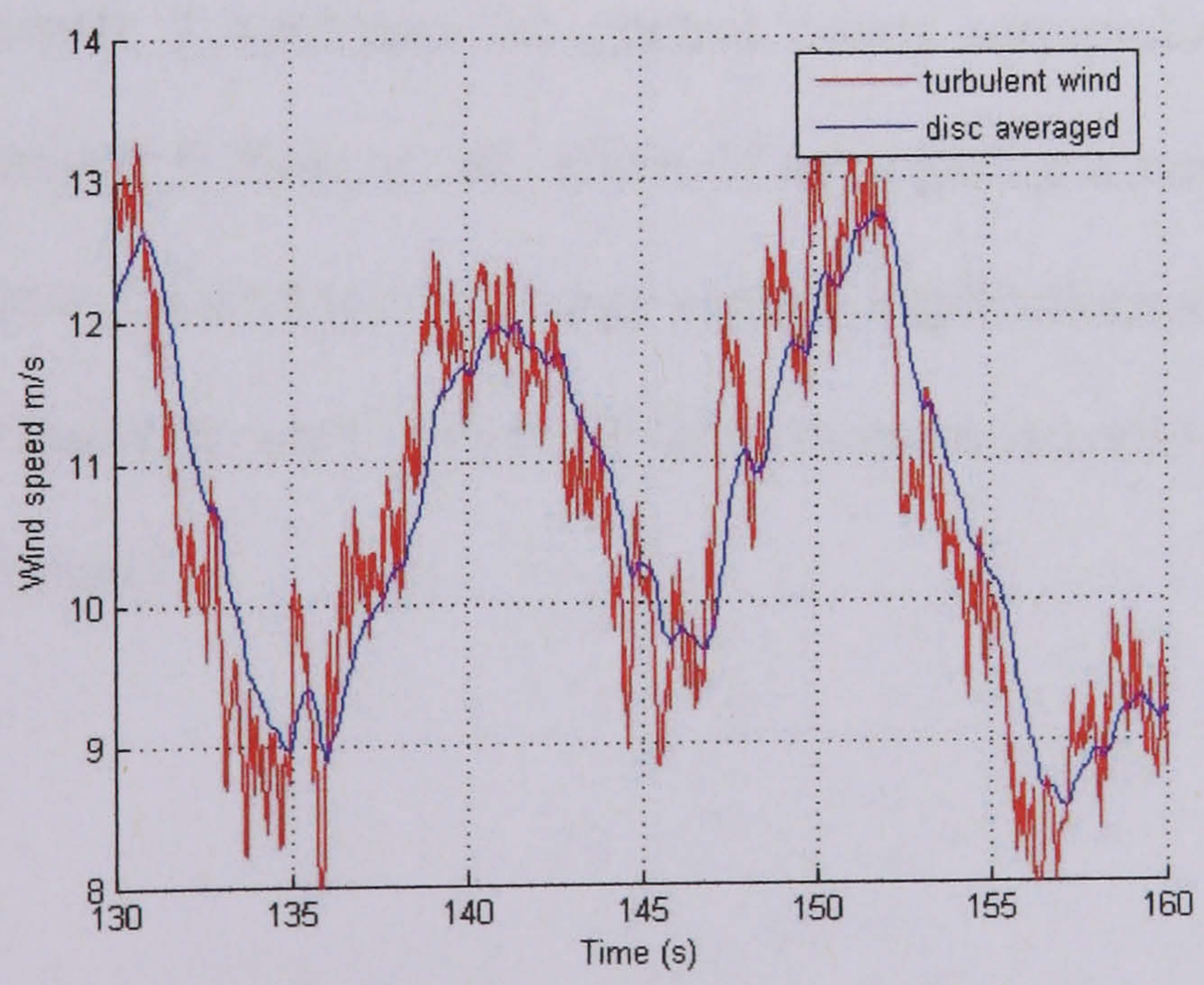

Figure 4-9. Effect of the disc-averaging filter in the time domain

4.9 Conclusion

The wind transfers energy on a number of different timescales, however it is the high frequency component, typically with time periods of seconds and minutes, which is important when assessing the dynamic performance of a small-scale wind turbine.

To model this type of high frequency turbulence, a spectral method base on the filtered output of random white noise has been employed and implemented in SIMULINK. The Von Karman power spectrum has been shown to be a good representation of real wind, and by using an appropriate signal shaping filter, it has been shown that turbulence of a similar spectral distribution to real wind can be generated. The interaction between the wind turbulence and the turbine blades has also been accounted for in the model.

The turbulent wind model outlined in this chapter is a powerful design tool as it allows a variety of turbulent wind conditions to be reconstructed using a handful of parameters that can either be measured at a real site location or estimated from data tables. The effects of turbulence on small-scale wind energy conversions systems are discussed in Chapters 5-7. Chapter 5 considers the control issues surrounding mains-connected turbines, while Chapter 6 looks at the effect of aggregating a number of small-scale turbines, and Chapter 7 addresses the energy capture implications associated with wind turbulence. The simulation work in each of these chapters is novel in its application to small-scale wind turbines.

Chapter 5

Potential control issues for mains connected H-type Darrieus micro VAWTs

5.1 Introduction

The previous chapter introduced a turbulent wind model based on the spectral distribution of real wind. In this chapter that model is combined with the turbine, generator and inverter model developed in Chapter 2 to investigate the effect of turbulent wind on the behaviour of an H-type Darrieus turbine when connected to a grid-tie inverter.

The effects of two different blade profiles are evaluated to assess their impact on the stability of the system: a symmetrical NACA0015 blade section and a cambered S1210 blade section [29]. Two wind regimes are also examined with two levels of turbulence corresponding to open terrain and the built environment.

In section 5.2 a wind energy conversion system is described, comprising of a 2.5kW H-type Darrieus turbine, 2.5kW, 250rpm axial flux generator and 2.5kW Windy Boy grid-tie inverter. Although this system is used as the basis for the simulation study, a cubic power transfer characteristic is also modelled to investigate its impact on turbine stability. A cubic power transfer characteristic can be created by the inclusion of a DC-DC boost converter in the DC link – on the front end of a Windy Boy inverter – to boost the DC voltage at low turbine speeds. Section 5.3 deals with the modelling of this converter in SIMULINK and with the construction of a prototype that was used to

validate the simulation.

The use of a turbulent wind model to assess the effect of turbine stability when connected to a grid-tie inverter is novel (see reference [89]).

5.2 SIMULINK modelling of H-type Darrieus wind energy conversion system

A 2.5kW, 250rpm H-type Darrieus turbine of similar construction to that depicted in Figure 2-1(b) has been modelled using the wind energy conversion system model introduced in Chapter 2.

Two turbulent wind regimes are also modelled corresponding to open countryside and the built environment. Full details of the turbine and generator parameters are given in Table 10, while the parameters used to generate the turbulent wind are given in Table 11.

Turbine	
Configuration	H-type vertical axis
Blade height (m)	2.0
Blade diameter (m)	3.3
Number of blades	3
Swept area (m^2)	20.7
Turbine inertia (kg/ m^2)	18.0
Generator Type	3-phase; PM; axial flux
Rated speed (rpm)	250
Rated power (W)	2500
Number of coils	12
Number of magnets	16
Generator constant (V/rpm/coil)	0.819
Coil resistance (Ω)	11.5
Coil inductance (mH)	101
Coil connection	coils connected in parallel
Number of turns/coil	945

Table 10. Turbine and generator modelling parameters

	Wind regime 1 (open country)	Wind regime 2 (built environment)
Base wind speed (m/s)	10.0	10.0
k_σ	0.16	0.40
Turbulent length scale (m)	65	65

Table 11. Turbulence modelling parameters

Two blade profiles have also been modelled to assess their effect of the stability of the system. The NACA0015 is a symmetrical blade, similar to the type used by many vertical axis turbines [68], [79], [27]. Conventional wisdom considers a symmetrical blade profile superior since the angle of attack changes from positive to negative during one revolution of the turbine. However, research carried out for a PhD thesis at Griffith University in Australia [29] claims that mathematical modelling shows a cambered blade profile has a superior self-starting capability and does not perform worse then a symmetrical blade during operation. This is because the poor lift created during the portion of the revolution when the angle of attack is negative is more then made up for by the extra lift created when the angle of attack is positive. The reference recommends using an S1210 profile which has been specially designed for use on model aeroplanes to provide a high lift/drag ratio at low Reynolds numbers. The C_p/λ performance curves are shown in Figure 5-1 for these two blade sections.

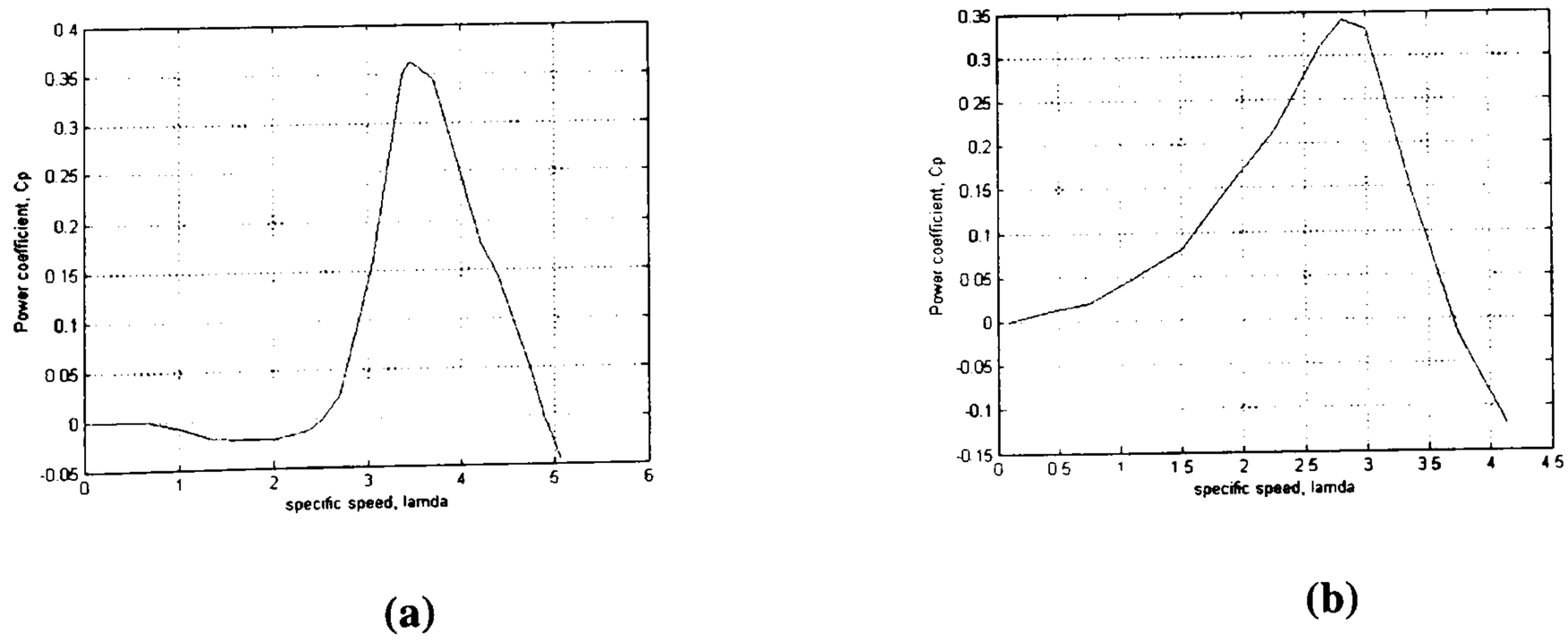

(a) **(b)**

Figure 5-1. C_p-λ characteristic for (a) NACA0015 and (b) S1210 [29]

The two turbine characteristics shown in Figure 5-1 convey important information. The negative C_p value at low values of λ for the NACA0015 in Figure 5-1(a) implies that at low rotational speeds the turbine power is negative, i.e. it requires power to drive it, meaning it will not self-start. In contrast, when the turbine is equipped with the cambered S1210 blades, C_p is always positive, and although the available torque at low rotational speeds is low, the turbine will self-start providing the generator has no cogging torque.

The model of the 2.5kW, 250rpm generator and 2.5kW mains-connect inverter, introduced in Chapter 2, has been verified by experimental measurement and was found to give an accurate prediction of power transfer with an error of less that 5%, as can be seen in the figure below.

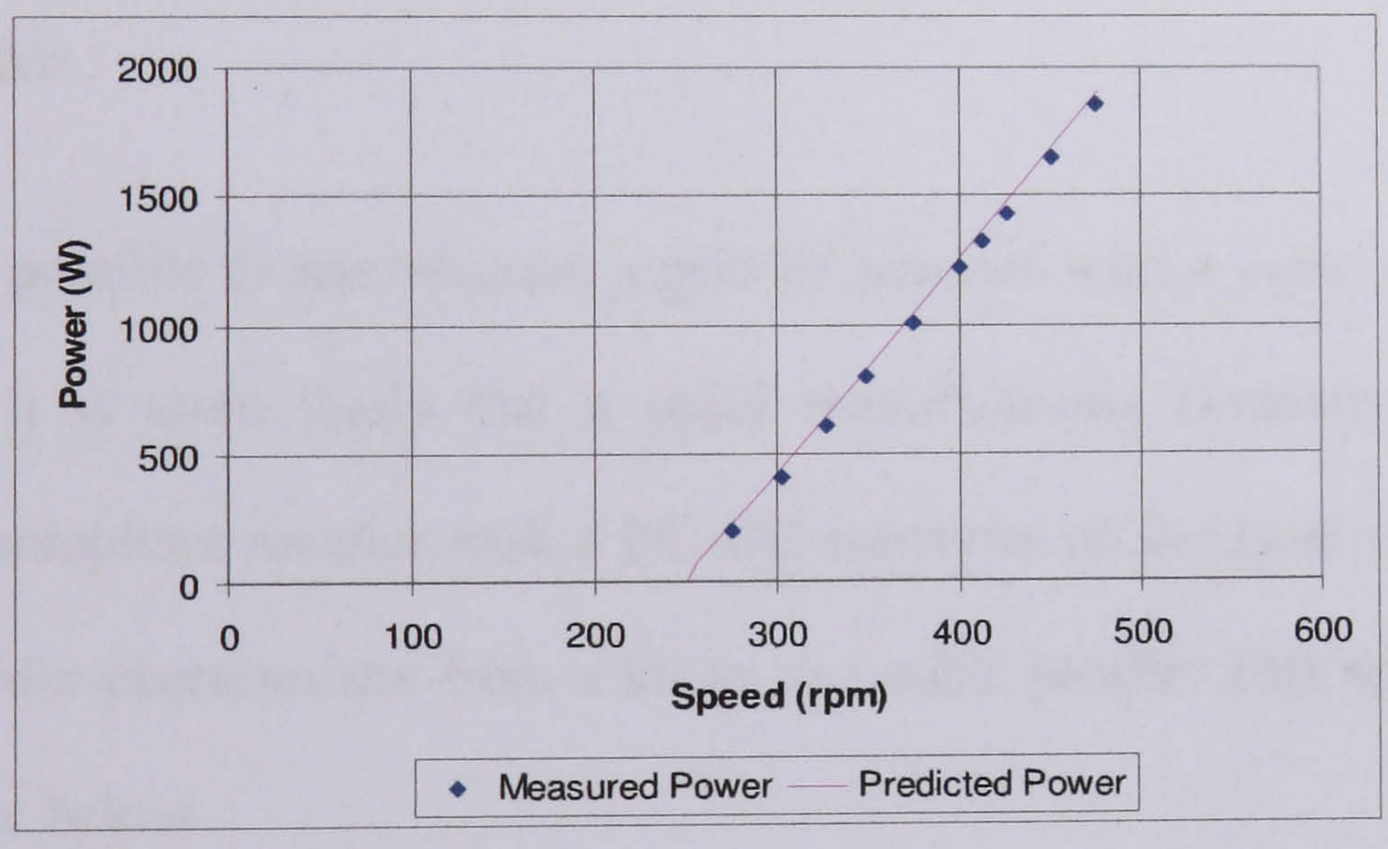

Figure 5-2. Windy Boy load characteristic

In the modelling process, the generator design has been matched to the turbine characteristic to produce the linear power transfer characteristics, shown in Figure 5-3, for the two different blade sections. A cubic power transfer characteristic has also been modelled for the NACA0015 blade section to examine whether this improves the stability of the system. The next section examines how a cubic power transfer

characteristic may be implemented using a DC-DC boost converter placed on the front end of the Windy Boy.

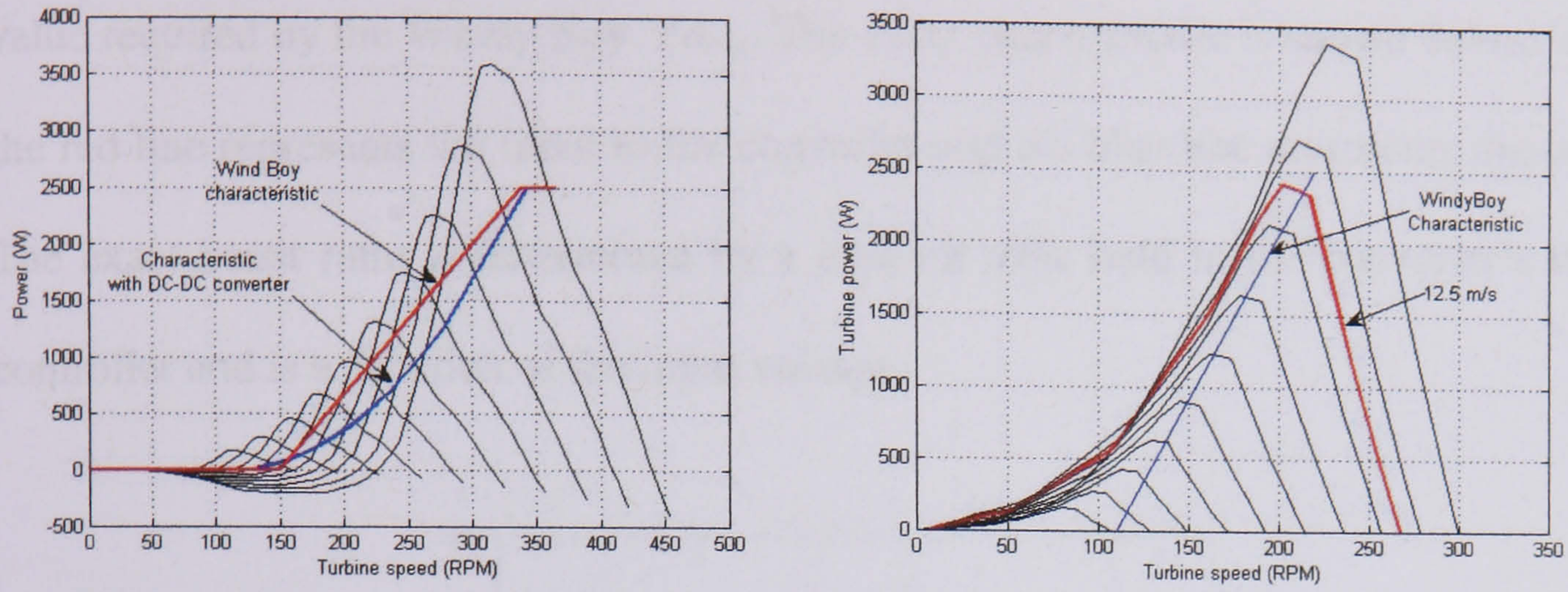

(a) (b)

Figure 5-3. Power-Speed characteristic for the (a) NACA0015 and (b) the S1210 at increasing wind speeds from 5-14 m/s

5.3 Cubic power transfer characteristic using a DC-DC boost converter

Although it is possible to manufacture a grid-tie inverter with a cubic power transfer characteristic, it is more likely that a small manufacturing company would use a standard G83 compliant inverter with a DC-DC converter on the front end to augment the power transfer characteristic from a linear to a cubic profile. This system is shown in the schematic below.

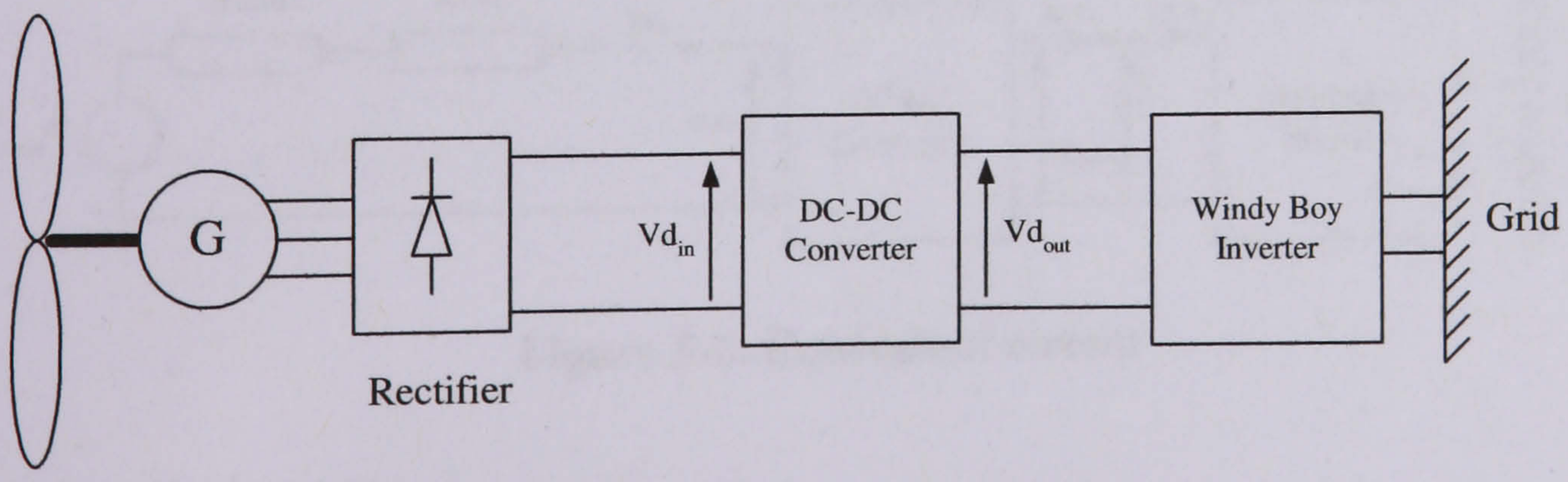

Figure 5-4. Electrical connection of DC/DC converter

The DC-DC boost converter operates at low turbine speeds (i.e. low DC voltages) and switches out when the DC input voltage exceeds a predetermined value. When operating, the converter steps up the DC voltage provided by the rectifier, Vd_{in}, to the value required by the Windy Boy, Vd_{out}. The exact characteristic is shown below, where the red line represents the input to the converter and the blue line represents the output. The exact boost ratio is determined by a look-up table held in the converter's micro-controller and is a function of the input voltage.

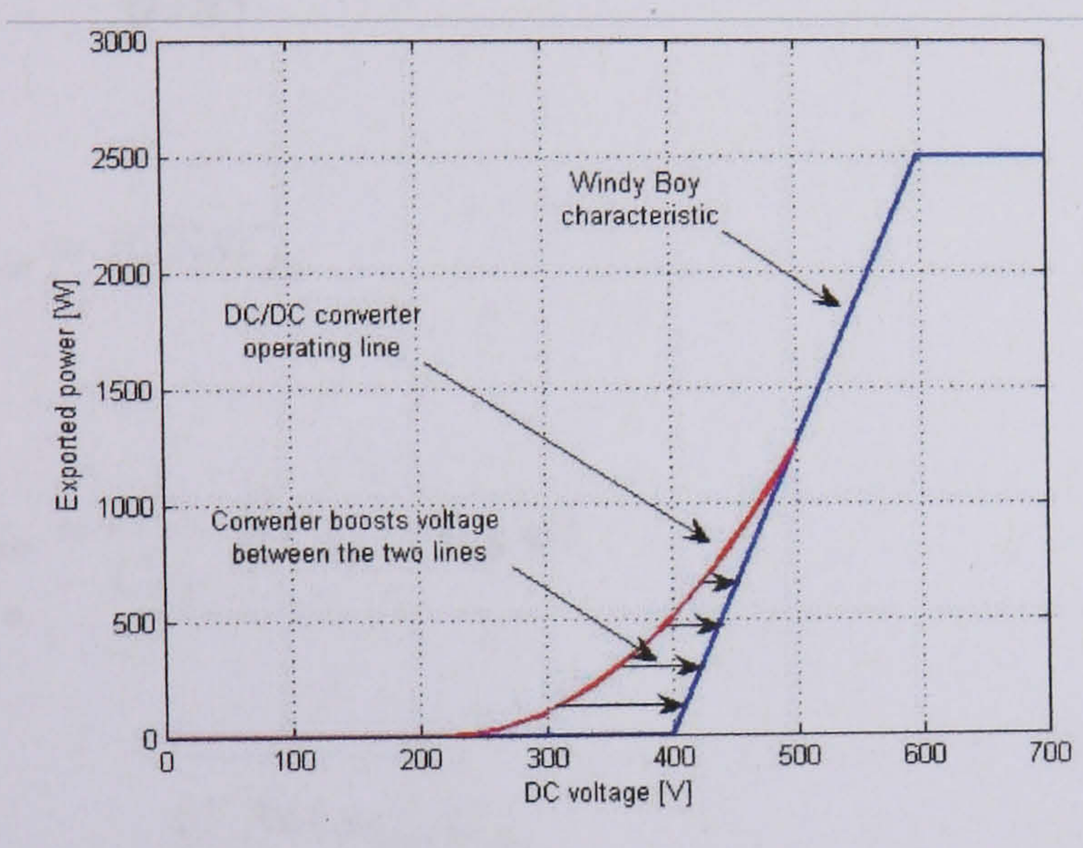

Figure 5-5. Power-DC voltage characteristic of converter

5.3.1 Modelling the DC-DC converter

The equivalent circuit for the system as seen from the DC side of the rectifier is shown below.

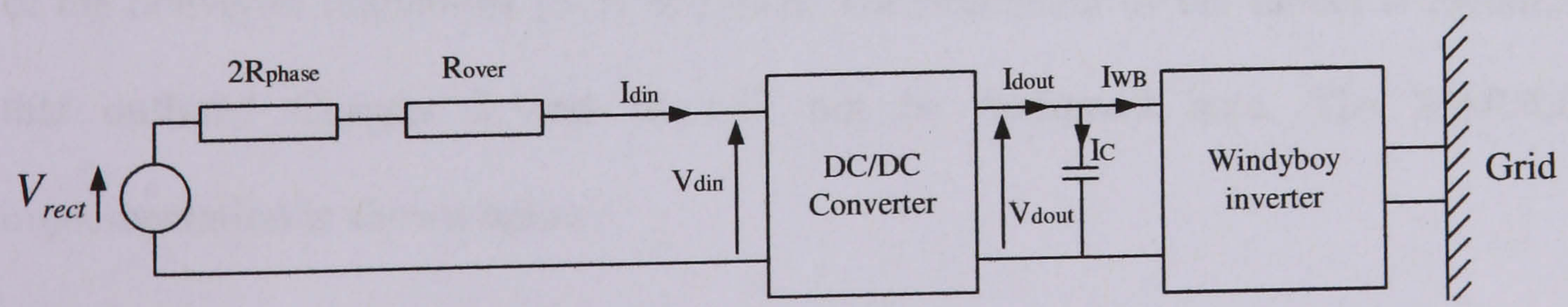

Figure 5-6. Equivalent circuit

Circuit analysis gives:

$$I_{din} = \frac{V_{rect} - V_{din}}{2R_{phsae} + R_{over}} \quad [5\text{-}1]$$

$$I_{WB} = I_c - I_{dout}$$

$$I_{WB} = \frac{P_{export}}{\eta_{WB} V_{dout}} \quad [5\text{-}2]$$

$$I_{dout} = \frac{I_{din}}{(GR)} \quad [5\text{-}3]$$

$$V_{dout} = (GR) V_{din} \quad [5\text{-}4]$$

$$V_{dout} = \frac{1}{C_{WB}} \int (I_{dout} - I_{WB}) dt \quad [5\text{-}5]$$

$$T_{electrical} = \frac{(2.34 k \omega_{elec}) I_{din}}{\omega_{gen}} \quad [5\text{-}6]$$

Where *GR* is the gain ratio of the DC-DC boost converter. The converter can be implemented in SIMULINK by using a look-up table to provide *GR* as a function of V_{dout}. The gain ratio can then used to calculate the voltage and current on the input side of the converter (equations [5-3] & [5-4]). The remainder of the model is identical to that outlined Chapter 2 and so will not be discussed here. The SIMULINK implementation is shown below.

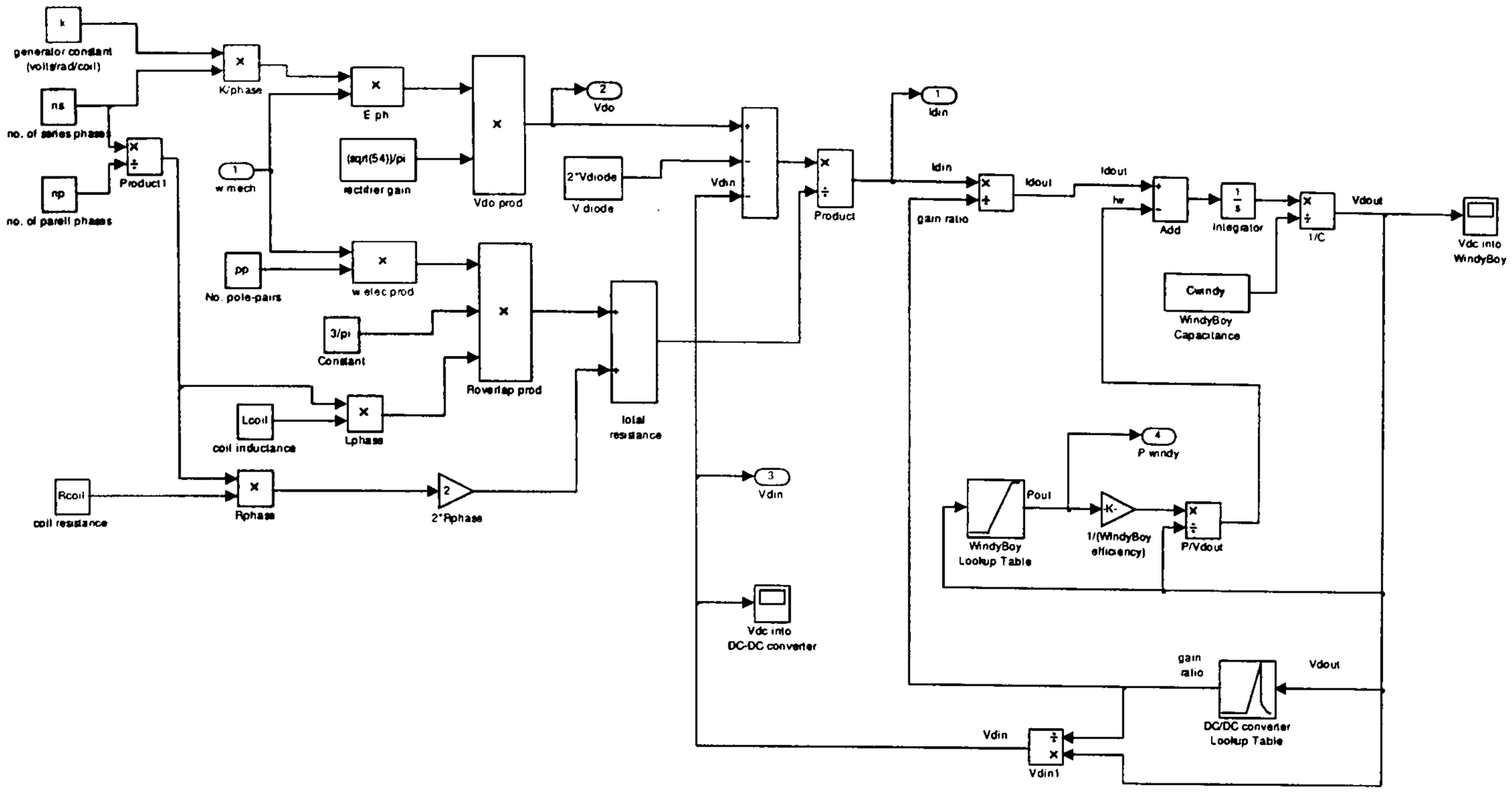

Figure 5-7. SIMULINK implementation

5.3.2 Validation of SIMULINK model

A simple DC-DC boost converter, as shown in the figure below, can be constructed to test the validity of the SIMULINK model[7]. The boost converter was placed in the DC link between the 1kW, 300rpm axial flux machine and the 2.5kW Windy Boy inverter (Figure 5-4), and measurements were taken at a number of different turbine speeds to test the simulation predictions.

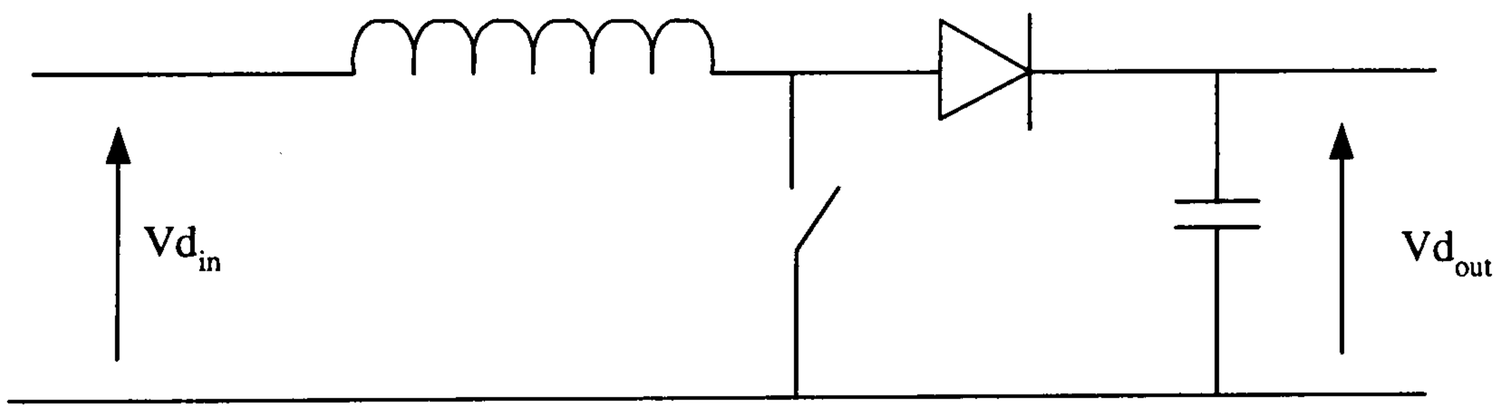

Figure 5-8. DC-DC Boost converter circuit diagram

---

[7] This device was constructed on a 'bread board' and controlled directly from SIMULINK using a D-space interface module. This work was carried out by Chong Ng.

The boost converter operates in the following manner: when the switch is closed, current flows through the inductor and energises it. When the switch is opened a back EMF is produced which is greater then Vd_{out}, and this allows the stored energy to be released through the diode, which otherwise prevents current passing from the high voltage output to the low voltage input. The capacitor acts to smooth voltage fluctuations on the output side of the converter. By varying the duty cycle, D_C, a variable boost ratio can be achieved such that [38]:

$$\frac{Vd_{out}}{Vd_{in}} = \frac{1}{1 - D_C} \qquad [5\text{-}7]$$

The duty cycle can be controlled through a D-space PC interface which allows easy implementation of the control algorithm - in this case a simple look-up table equating the duty cycle to the input voltage.

A comparison between the SIMULINK model predictions and experimental measurements are shown in the figure below, which shows the DC voltage at the input and output of the converter as power is exported through the Windy Boy.

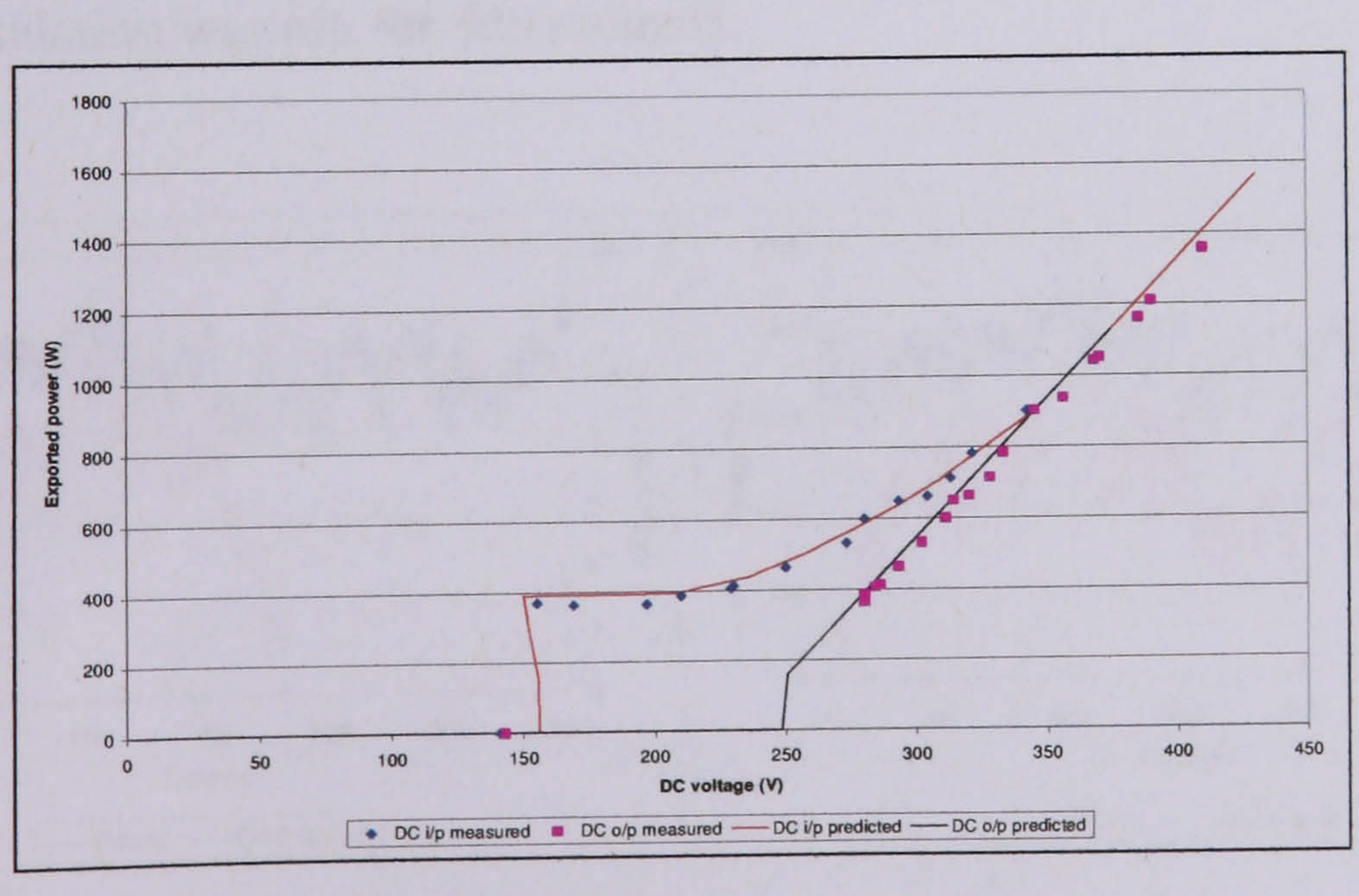

Figure 5-9. Predicted and measured values of the DC-DC converter

The model shows a good correlation with the measured data, with the maximum error being no more then 6%.

As stated previously, the function of the DC-DC converter is to modify the Windy Boy's power transfer characteristic from a linear to a cubic relationship. The power transfer characteristic used in the stability study (section 5.4) can be seen in Figure 5-3 (a), which shows the Windy Boy's linear power transfer characteristic along side the load profile created by the inclusion of the DC-DC boost converter.

5.4 Discussion and results of the stability study

The turbine must transfer power through the inverter to the mains, and the simulation results presented in Figure 5-10 show how the turbine will perform in the two wind regimes when equipped with the two different blade sections, and when transferring power through a Windy Boy inverter with a linear power transfer characteristic. The simulations were carried out at a mean wind speed of 10 m/s rather then the more usual 12.5 m/s as this is more representative of the poorer wind resource encountered in the urban environment. The generator output power is plotted alongside the turbulent wind input; the simulation was run for 300 seconds.

(a)

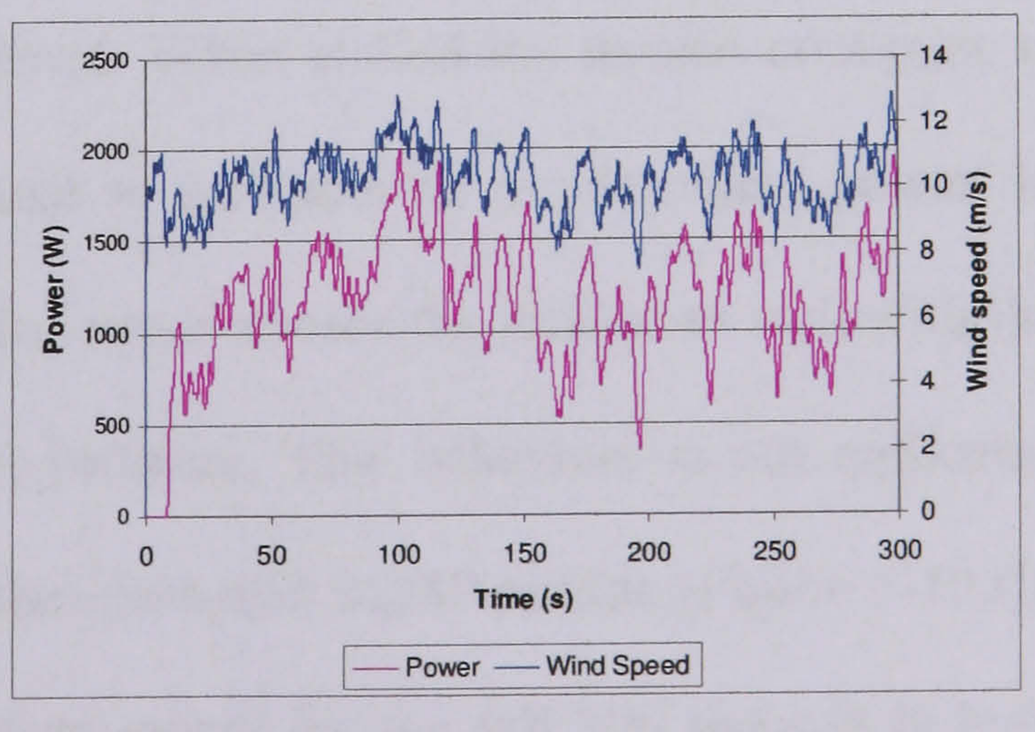

(b)

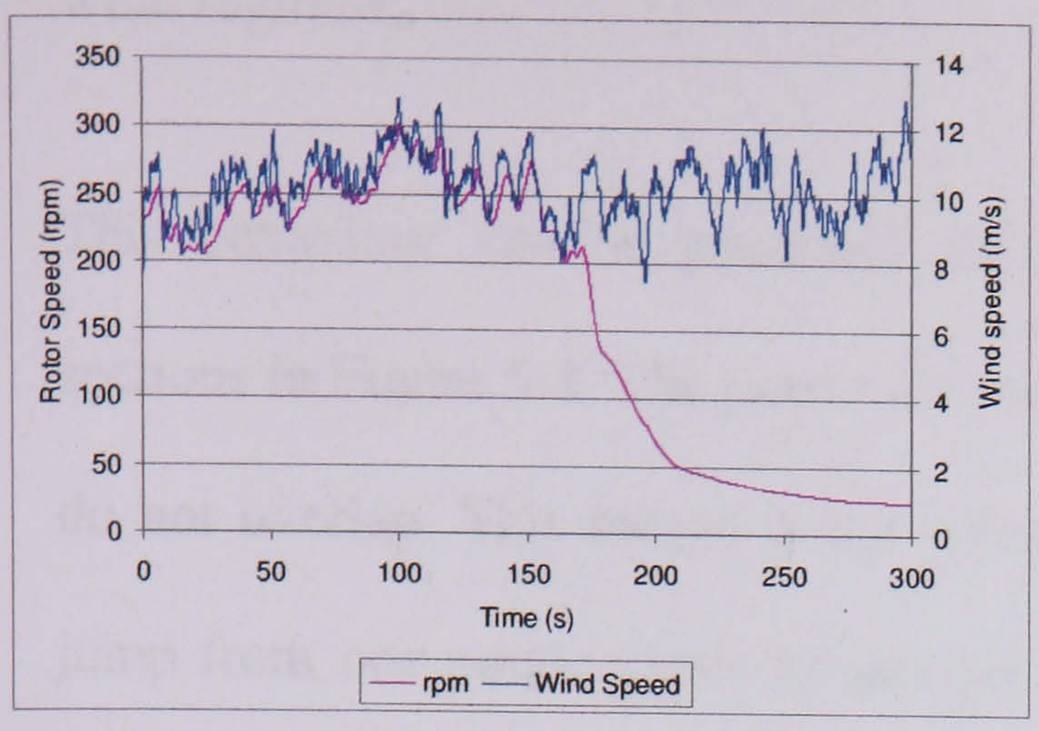

(c)

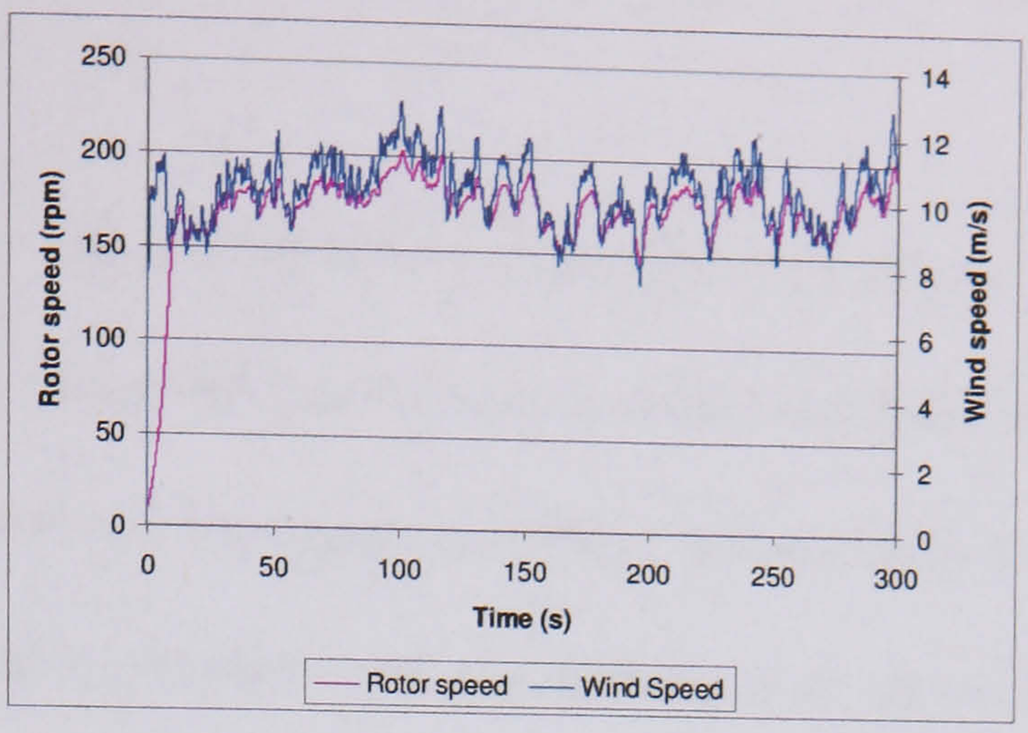

(d)

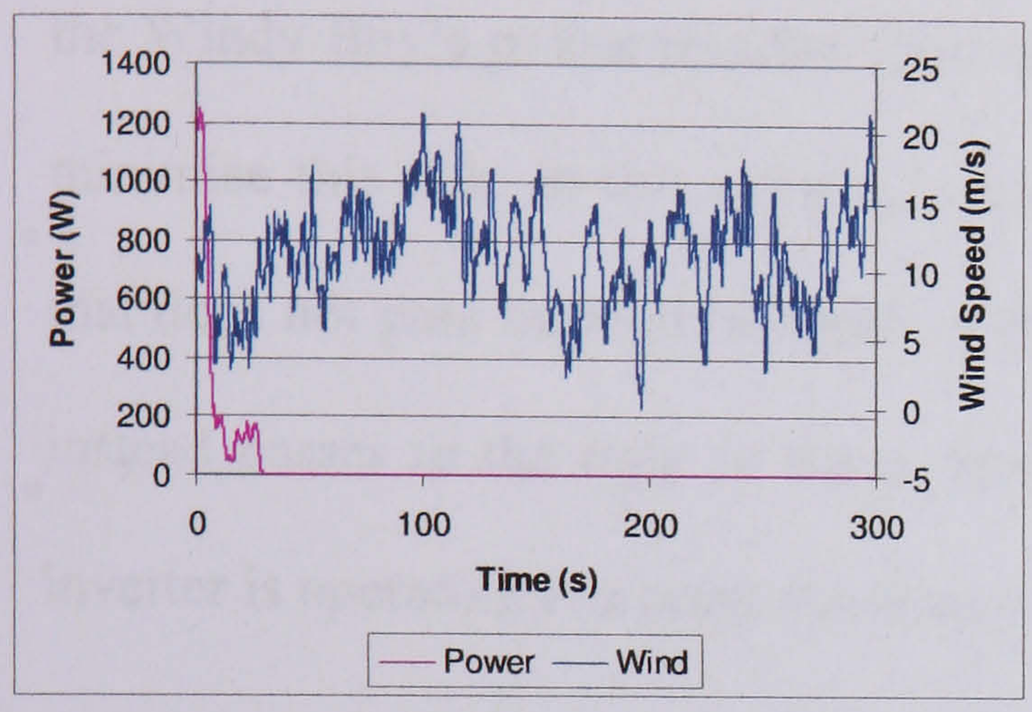

(e)

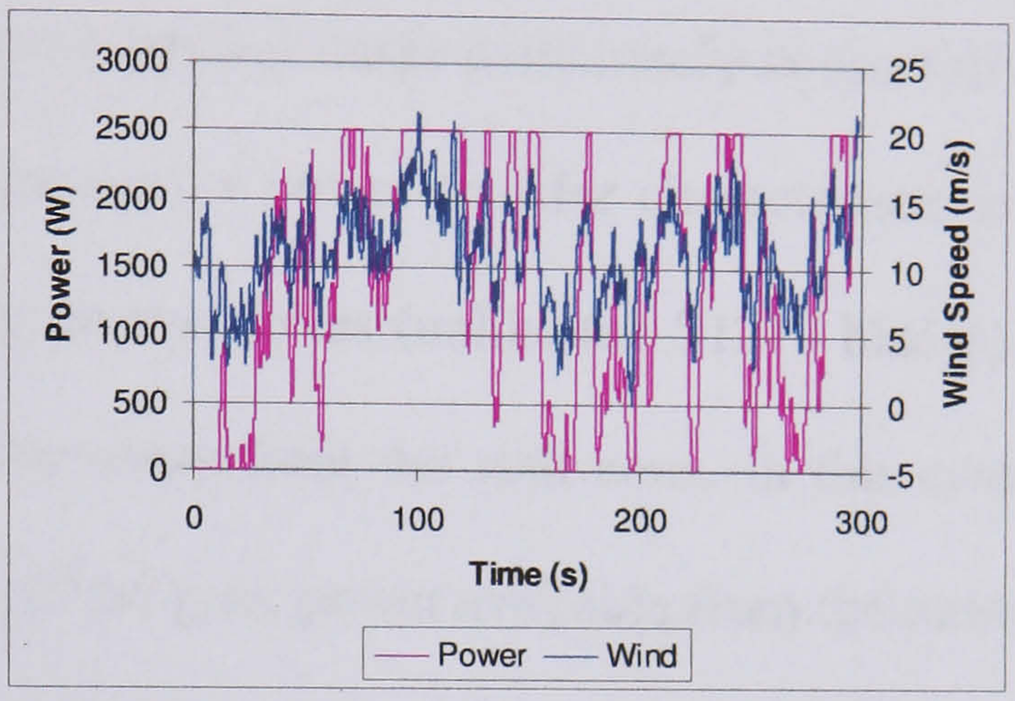

(f)

Figure 5-10. Performance for the turbine with a linear power transfer characteristic (a) Power output from the NACA0015 blade section in low turbulence, (b) Power output from the S1210 blade section in low turbulence, (c) Rotor speed from the NACA0015 blade section in low turbulence, (d) Rotor speed from the S1210 blade section in low turbulence, (e) Power output from NACA0015 in high turbulence, (f) Power output from the S1210 in high turbulence

Figure 5-10 (a) and (c) show that the turbine with the NACA0015 blade section stalls after approximately 160 seconds when subject to low level turbulence, and after 10 seconds when subject to high level turbulence. When stalled the turbine continues to rotate in drag mode rather then lift mode and so produces no usable output power. In both wind regimes a sudden increase in wind speed causes the turbine to stall with the higher turbulence level causing the greater problem. This behaviour is not replicated when the turbine blades are replaced with the cambered S1210 section (Figure 5-10 (b) and (d)), and the turbine continues to produce power for the full 300 seconds in both

wind regimes.

This behaviour can be predicted from the power-speed characteristics of the two sections in Figure 5-3. The power curves of the NACA0015 section are very narrow and do not overlap. This means if the wind speed increases suddenly, corresponding to a jump from one power curve to another at constant speed, the turbine may move from the peak of one curve to the stall zone of the next. Indeed, this behaviour occurs despite the Windy Boy's power transfer characteristic being made deliberately conservative to minimise this risk. In this context, a conservative power transfer characteristic is one that does not pass through the peak of the power curves (unlike the S1210 blades), but instead passes to the right of them, further away from the stall zone. In this case the inverter is operating at a point some way off the peak power available from the turbine.

The power curves of the S1210 section *do* overlap, and because of this a more aggressive Windy Boy characteristic can be adopted without risking stall, Figure 5-3 (b), since sudden changes in wind speed will not force the turbine into the stall zone.

The effect of replacing the Windy Boy's linear load characteristic with a cubic power transfer characteristic, created by the inclusion of a DC-DC boost converter, was also examined. Figure 5-11 shows the results of the simulation for a turbine equipped with the less stable NACA0015 blades in the two wind regimes. As can be seen, using a DC-DC converter with a cubic power transfer profile, which better fits the turbine's power curves, has the effect of stabilising the turbine in low turbulence but is unable to prevent stalling when the turbulence is increased.

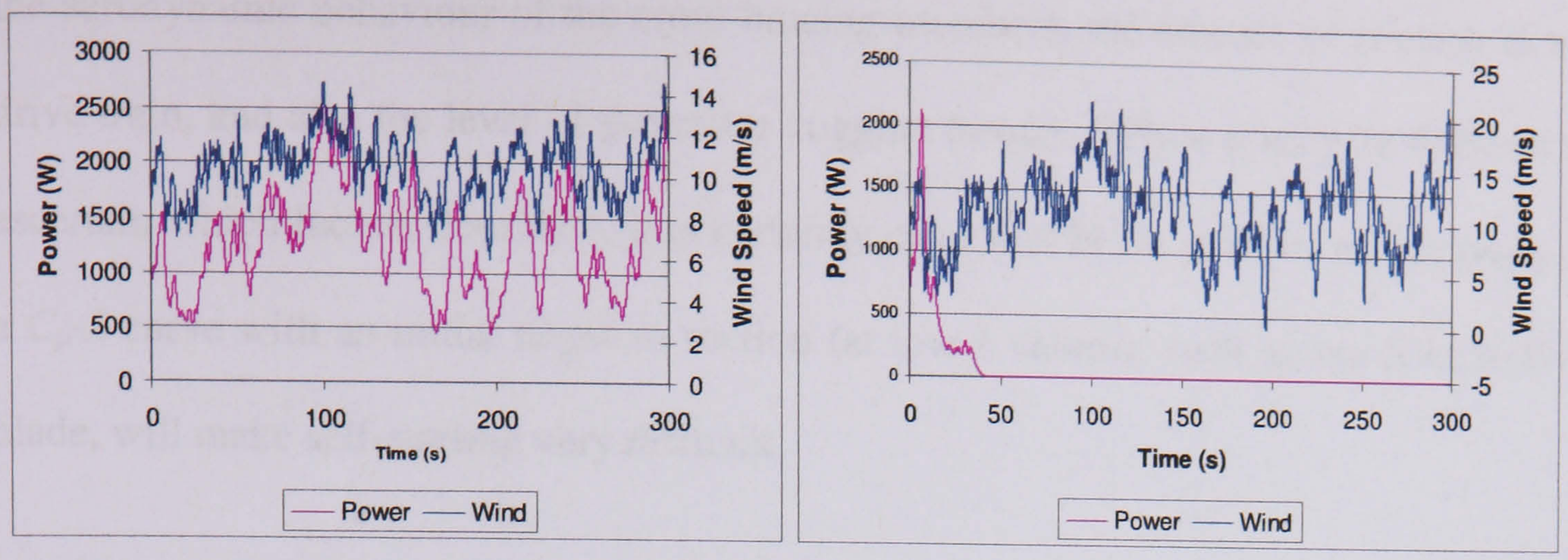

(a) (b)

Figure 5-11. Performance for the NACA0015 blade section when a DC-DC converter is used in (a) low turbulence and (b) high turbulence

5.5 Conclusion

Applying the turbulent wind model to a small-scale wind turbine model allows the turbine's dynamic performance to be assessed. This procedure has been carried out for two blade sections – symmetrical and cambered – and of these the symmetrical NACA0015 profile was found to make the system highly unstable in turbulent wind. The cambered S1210 blade was stable in all wind conditions because the peak of its C_p-λ curve was spread over a wider range of λ values, allowing the power curves to overlap and hence reducing the risk of stall.

The use of a DC-DC converter to provide a cubic inverter power transfer profile, which better fits the turbine's power curves, has the effect of stabilising the turbine in low turbulence but is unable to prevent stalling when the turbulence is increased.

Reference [29] favours the cambered blade section over a symmetrical section because it aids self-starting, however it has been shown that turbines with symmetrical blades *do* self-start [25], [68] despite what is sometimes claimed in the literature [104] . Many factors influence the self-starting ability of a turbine such as the level wind turbulence,

the aerodynamic behaviour of the cross-bracing members, the amount of friction in the drive train, and also the level of generator cogging torque. While it may be difficult to ascertain which factors dominate, it is certainly clear that blade profiles which produce a C_p-λ curve with an initial negative section (at low λ values), such as the NACA0015 blade, will make self-starting very difficult.

The work carried out in this chapter shows that a cambered blade section may be favoured over a symmetrical one, not only because of their superior starting capabilities, but because cambered blades also produce a more stable wind energy conversion system.

Chapter 6

Aggregation of micro wind turbines

6.1 Introduction

Chapter 5 introduced some of the technical challenges facing the control of a single VAWT in turbulent wind. The following chapter will extend this idea by considering the effect of aggregating the output of multiple turbines, both on the turbine performance and on the output power quality.

Aggregating the output of several small turbines may be more appropriate then installing a single large turbine. This may occur for practical reasons, for example on the roofs of buildings where the possibility of structural reinforcement is limited, or for aesthetic reasons - to limit the visual impact of the devices. Aggregation may also have additional financial benefits since a more predictable source power is produced, which may be valued more highly by network operators.

The outputs of multiple turbines may be aggregated on the AC or DC side of the converter. If the grid system is 'stiff', as has been assumed here, aggregation at AC permits each turbine to behave independently and in a predictable manner. Aggregation at DC produces a much more complex control problem than aggregating the turbines at AC, and this is discussed in detail in section 6.4. These problems may be solved to some degree by employing a DC-DC boost converter on the front end of the WindyBoy, as discussed in Chapter 5, and this is addressed in detail in section 6.5.

The quality of the aggregated power at AC and DC will also be examined in terms of the smoothing of power fluctuations that can be achieved by combining turbines. This is of particular relevance to planners of embedded generation systems.

6.2 AC and DC aggregation

As discussed in Chapter 5, small-scale wind turbines are usually connected to the mains through a power electronic converter comprising a passive rectifier and main-connect inverter (such as the Windy Boy). Aggregation of the outputs of a number of such systems can be achieved on either the AC side or the DC side of the mains connected inverter as shown in Figure 6-1. Aggregation at the AC side represents the normal situation where a number of customers each install a single wind turbine each with a dedicated power electronic interface. It is generally acknowledged that the aggregation of the output from several wind turbines in this way is less variable than that of a single wind turbine, and that the variability decreases as the number of wind turbines aggregated increases [105]. However, the effect of aggregating several small-scale wind turbines on the DC side of the inverter, so as to share the same inverter and so reduce power conversion cost, is much less clear. Such an approach to aggregation could well appear attractive where, for example, a commercial building or block of flats installs a number of wind turbines which share the same inverter.

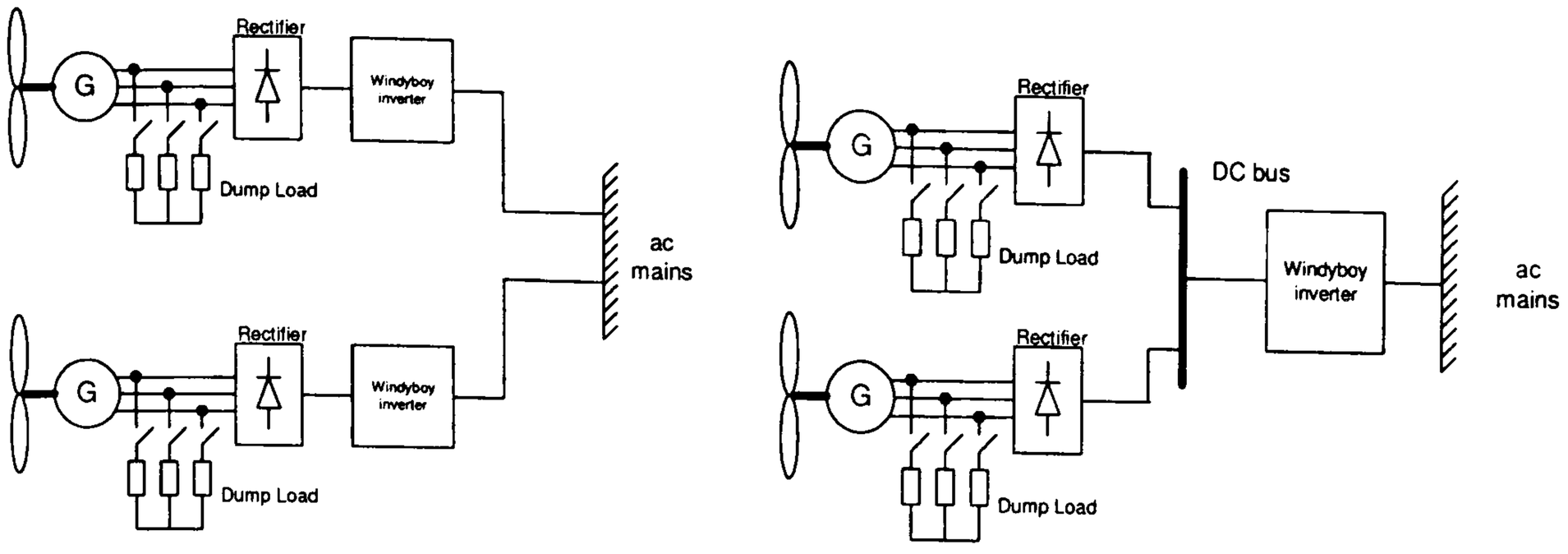

Figure 6-1. Aggregation at (a) AC and (b) DC

The following sections describe an aggregation case study at AC and DC. The impact aggregation can have both on the net power generated and the performance of the wind turbine itself are then compared and evaluated.

6.3 Small scale wind turbine models

The 500W Savonius turbine described and modelled in Chapter 2 has been chosen for this simulation study because of its robust operating characteristic. Data for the turbine and axial flux generator is shown in Table 2. Such sized machines naturally lend themselves to the use of a number of turbines aggregated at dc and connected to the mains through a single inverter. With such a connection, and the use of a passive rectifier, the inverter will control the power transfer from the group of turbines rather than from each individual turbine. Larger turbines, of a few kW rating, would tend to be connected through a dedicated inverter allowing control of individual turbines. However, in order to obtain a direct comparison between the two connection systems, the same 500W turbine system is used to study aggregation effects on both the AC and the DC side of the mains connected inverter. It is recognised that ac aggregation is more suited to larger power turbines, but not exclusively so.

Figure 6-2 shows the SIMULINK implementation at AC and DC and central to this is the *Savonius* block, which consists of the 500W savonious turbine, rectifier and, in the case of AC aggregation, a Windy Boy inverter that are described in Chapter 2. In the case of DC aggregation power is conveyed to a common Wind Boy inverter and so this is not included inside the *Savonius* block. These models are identical to those described in detail in Chapter 2 and so will not be discussed here.

The study assumes each wind turbine is spaced far enough apart for the turbulence at each turbine to be independent from its neighbour so that a separate turbulent wind, but with the same mean wind speed, can be used as the input for each turbine; an average wind speed of 10 m/s is used. The turbulent wind for each turbine is therefore different, but by using the same "seed" in the turbulent wind model, can be repeated to allow effective performance comparison. The turbulent wind input data is given in the table below. (N.B. highly turbulent wind has been assumed throughout the aggregation study.)

Mean wind speed (m/s)	10.0
Turbulence intensity, k_σ	0.4
Turbulent length scale, L (m)	65

Table 12. Wind turbulence parameters used in aggregation study

When aggregating at AC, the outputs from each Windy Boy inverter can simply be summed since it is assumed that the generated power will have negligible effect on the AC grid voltage i.e. a stiff ac system is assumed. When aggregating at DC, a common DC bus voltage is assumed which must be fed back to each generator/turbine module.

The global implementation of these aggregation methods is shown in Figure 6-2.

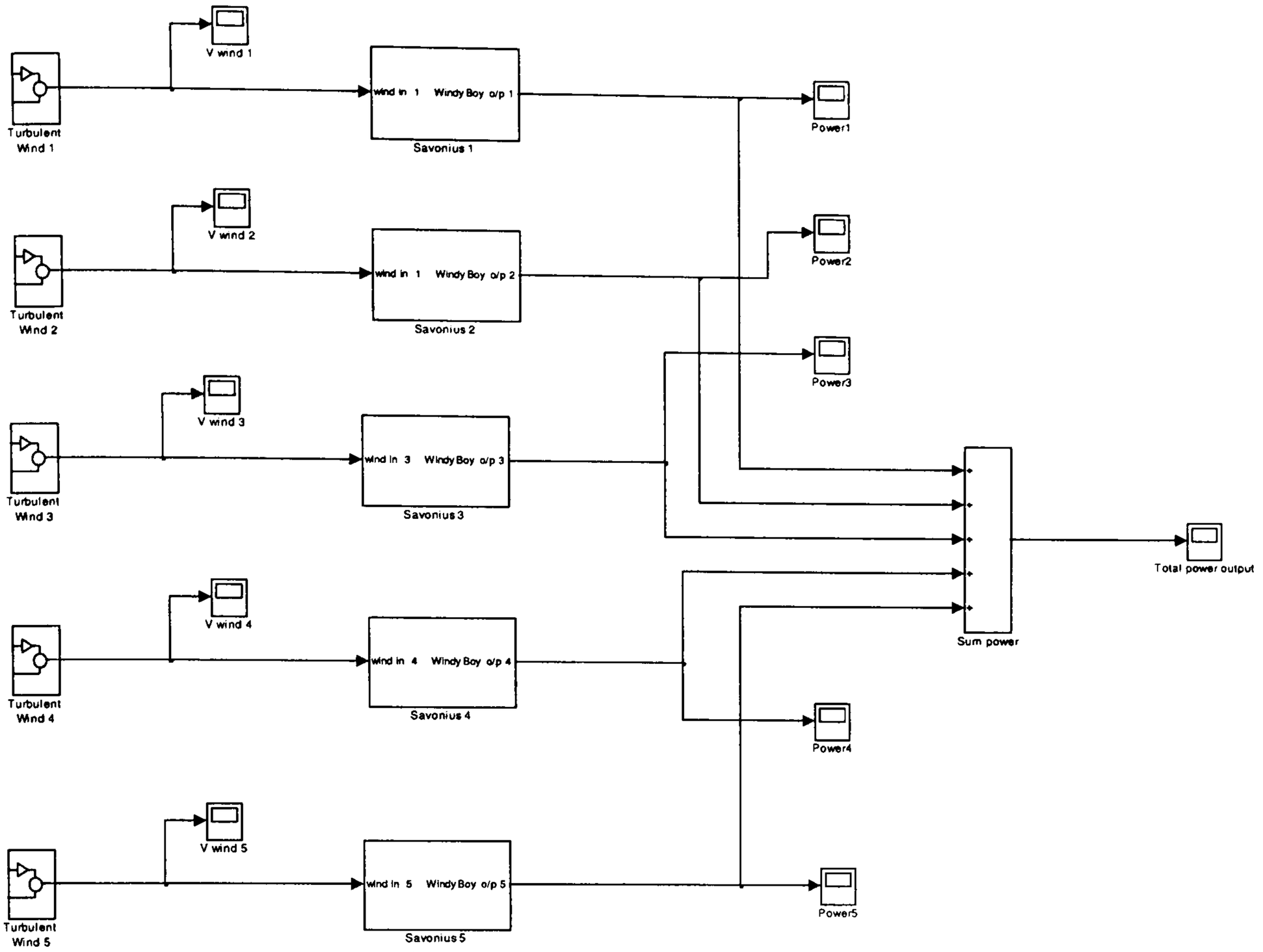

(a)

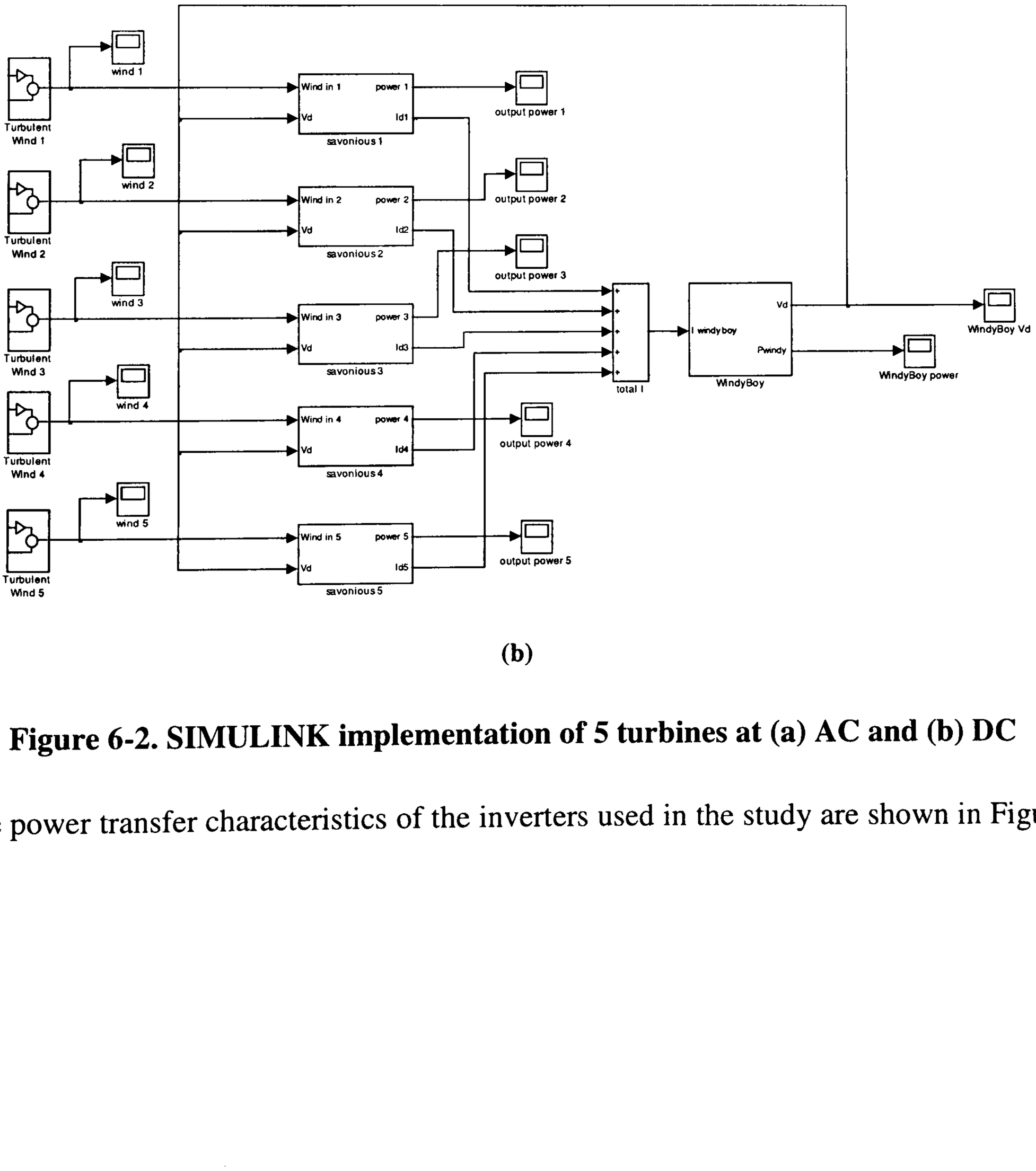

(b)

Figure 6-2. SIMULINK implementation of 5 turbines at (a) AC and (b) DC

The power transfer characteristics of the inverters used in the study are shown in Figure

6-3.

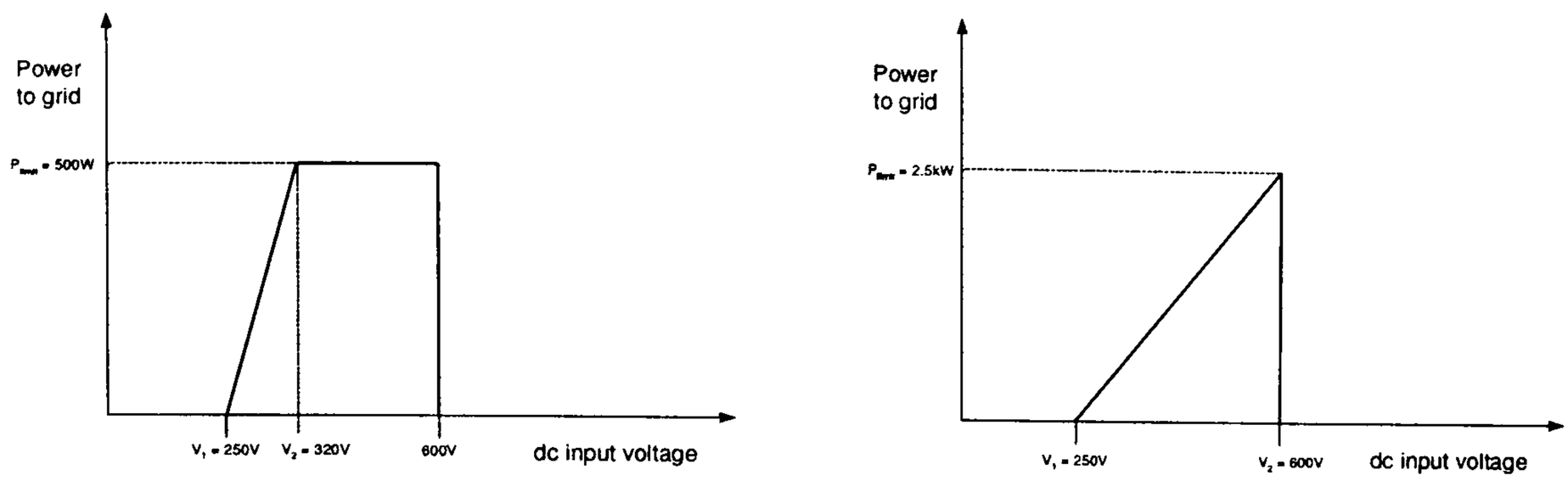

(a) **(b)**

Figure 6-3. Windy Boy Power-dc voltage characteristic (a) for AC aggregation of 500W turbines (b) for DC aggregation of five, 500W turbines

Figure 6-3 (a) shows the power transfer characteristic of a 500W inverter used in the AC aggregation study and Figure 6-3 (b) the characteristic of the 2500 W inverter used in the DC aggregation study. The inverter power transfer characteristics have been chosen to best match the Savonius turbine's power curves. As described in detail in Chapter 2, the inverter transfers power as a linear function of the dc link voltage from V_1 to V_2, when the maximum power, P_{limit}, of the inverter is reached, (in this case 500W or 2500W).

6.4 Results of aggregation study

The aggregation of five wind turbines is shown in Figure 6-4; Figure 6-4 (a), (c) and (e) show the power output, speed and dc link voltage of individual turbines whilst Figure 6-4 (b), (d) and (e) show the same but for DC aggregation. Figure 6-4 (g) shows the effect of aggregating the outputs of the five turbines. In both cases aggregation is seen to have a significant effect on power smoothing. At time zero all the turbines are at rest and take about 15 seconds to reach operating speed. Power is not produced until about

10 seconds after the start as the turbine speed, and hence dc link voltage, is less than the minimum required for the inverter to operate, Figure 6-3.

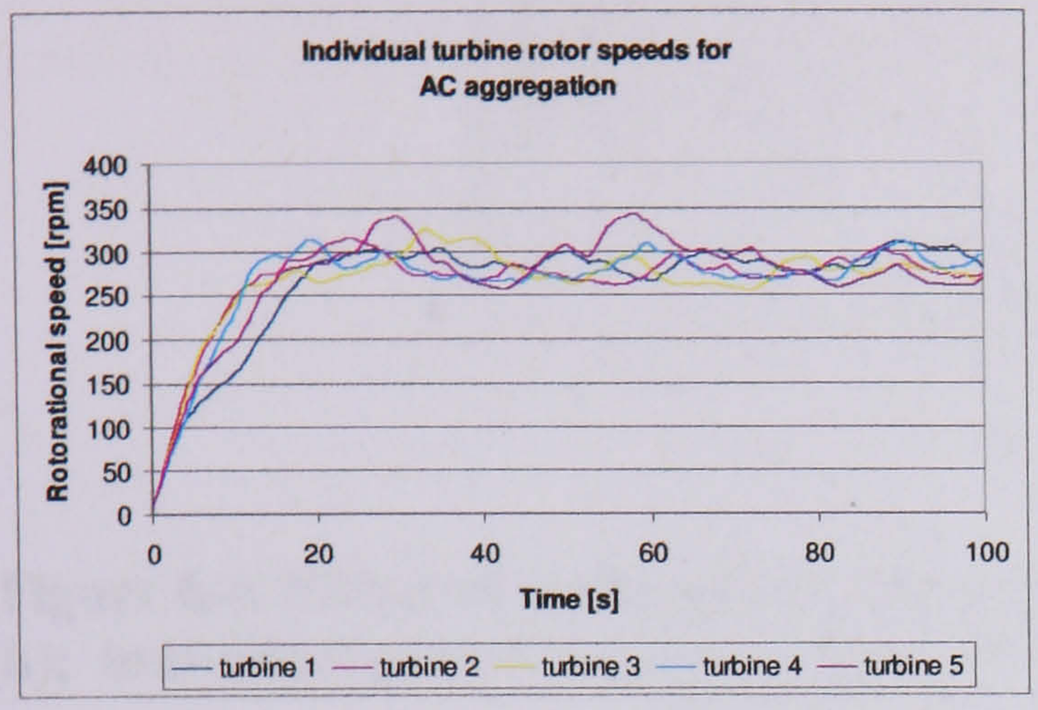

(a)

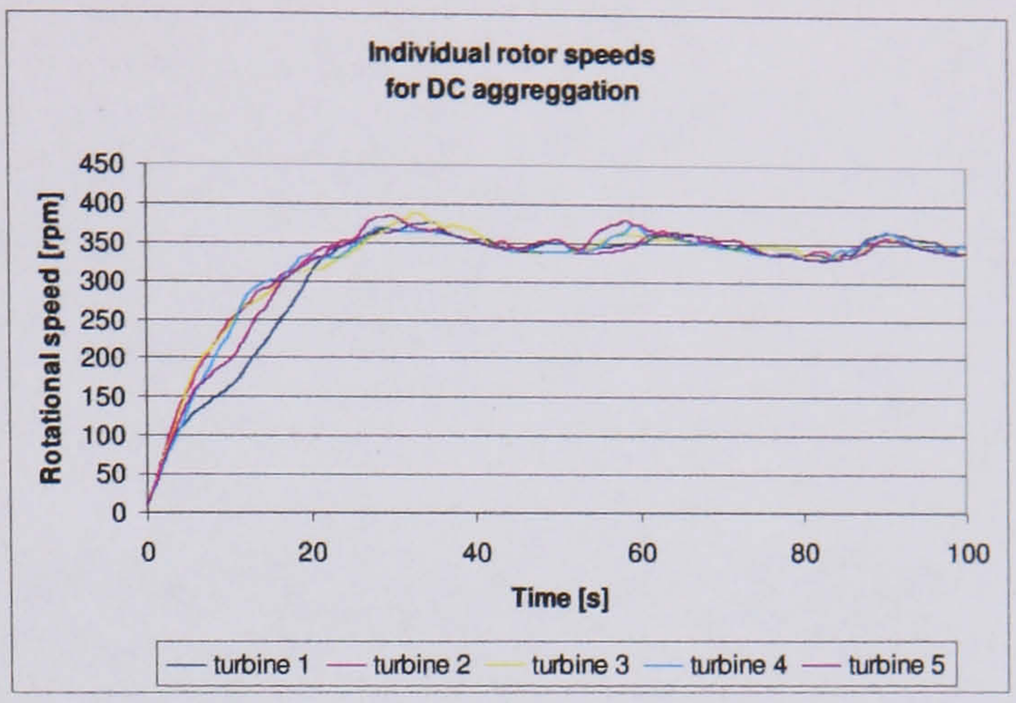

(b)

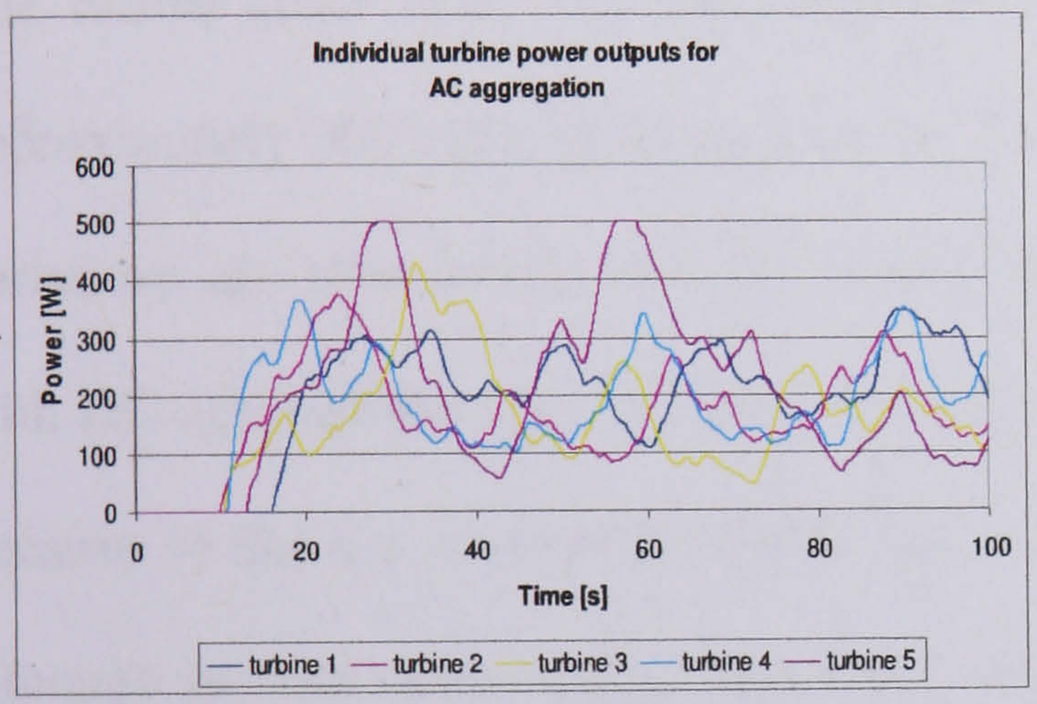

(c)

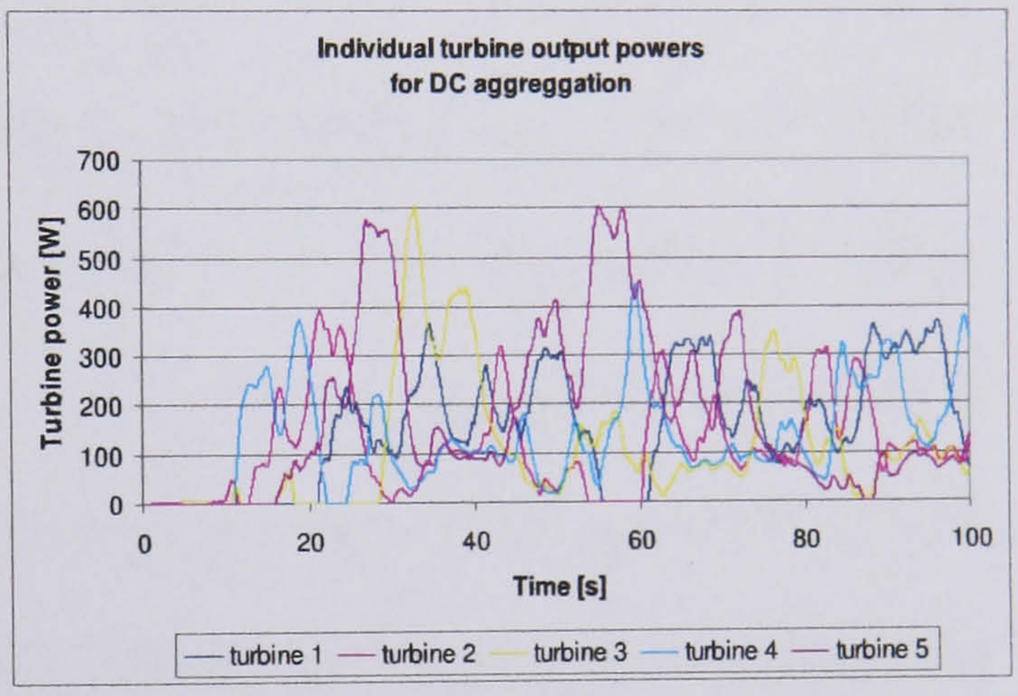

(d)

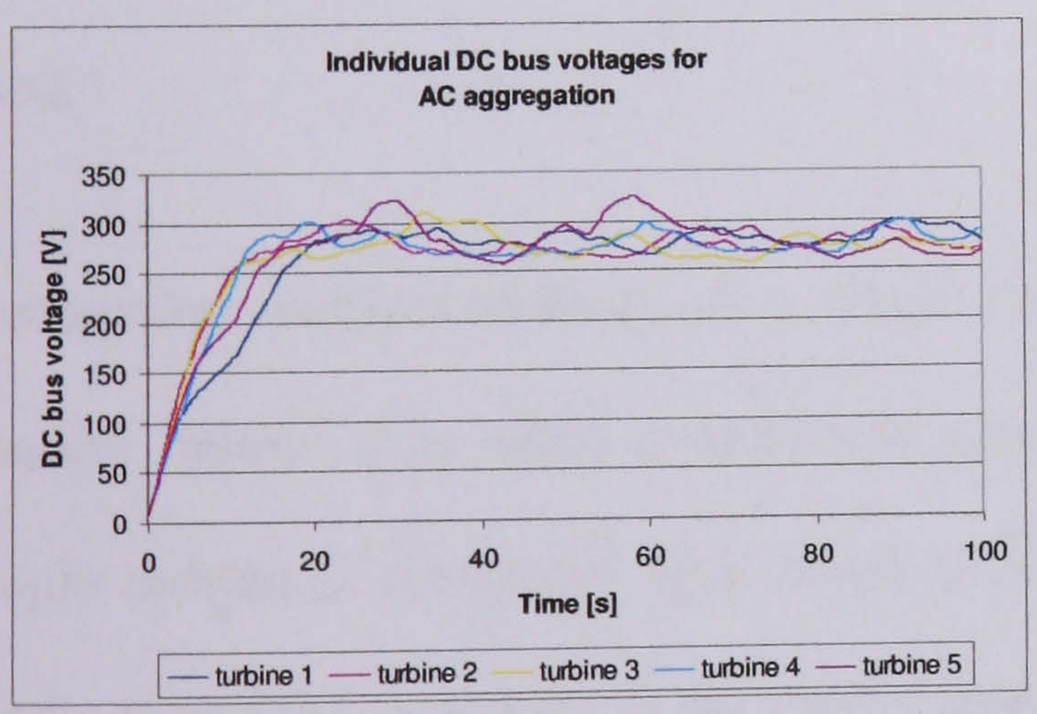

(e)

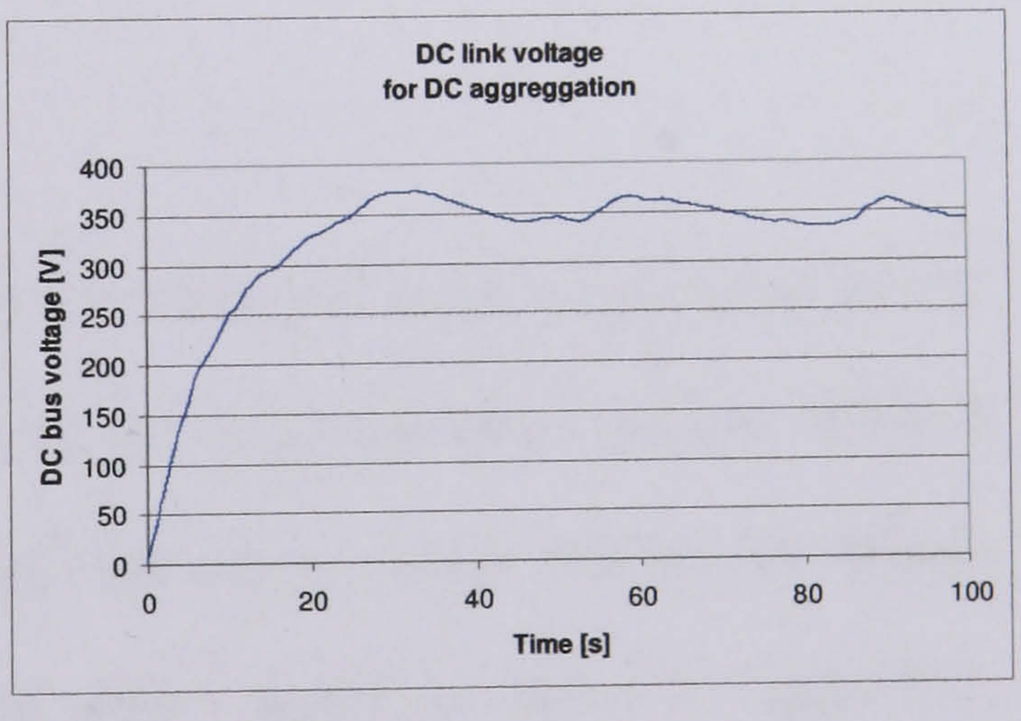

(f)

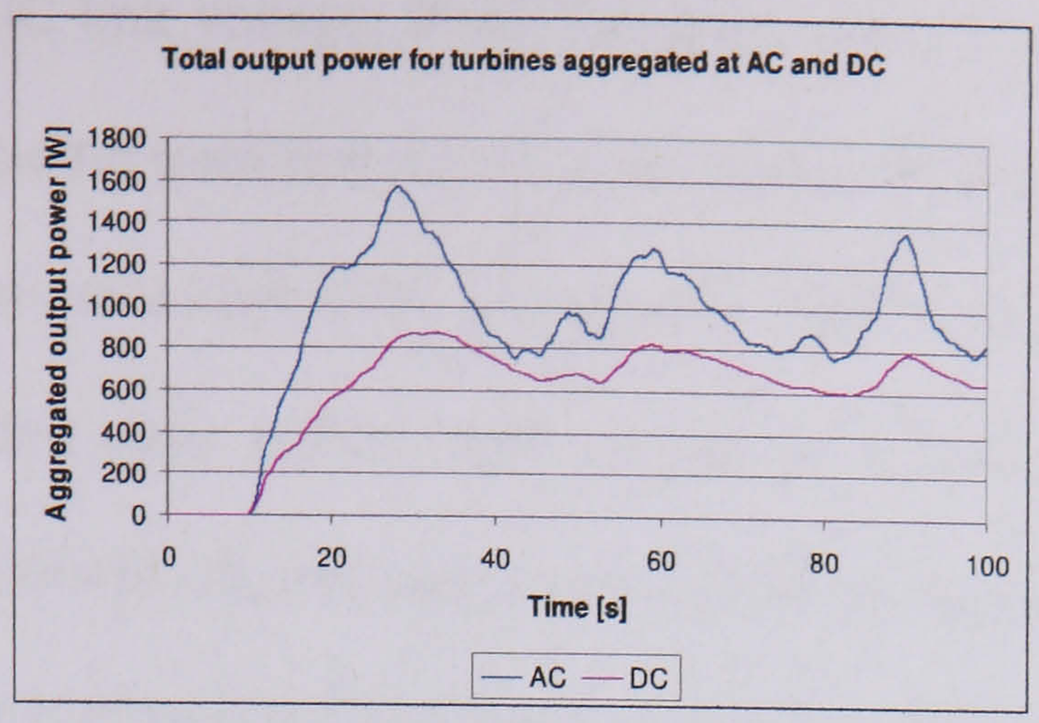

(g)

Figure 6-4. Effect of aggregation at ac and dc: individual speeds at ac (a) and dc (b); individual power outputs at ac (c) and dc (d); dc link voltage at ac (e) and dc (f); (g) power aggregation.

The results show that with AC aggregation the turbines operate at a lower speed, approximately 300 rpm, compared to DC aggregation, approximately 350 rpm. Speed variations are also greater with AC aggregation. Similarly, DC link voltage is higher with DC aggregation than AC (there is only one DC link voltage with DC aggregation because of the use of a common DC bus). It is also notable from Figure 6-4 (g) that although in both cases aggregation leads to substantially smoother power delivery the power delivered using DC aggregation is substantially less than when AC aggregation is used.

Connecting multiple turbines to a single inverter creates a more complicated power transfer system than using a dedicated inverter for each individual turbine. When a single turbine is connected to a single inverter the power output follows the Windy Boy's load line according to the instantaneous turbine speed, as shown in Figure 6-3, since turbine speed and the DC link voltage are tightly linked. With several turbines connected to the inverter, the turbine's power output becomes decoupled from the Windy Boy's operating line, since now the individual turbine speeds and DC link voltage are set by the group. Consider Figure 6-5 which shows the power transfer as

a function of the DC link voltage. If all 5 turbines were producing the same power P then the power converter must transfer 5P to the mains. This can only be achieved if the DC link voltage rises to a higher DC voltage, V_5. This in turn corresponds to a higher turbine speed so that each turbine will operate at a higher speed than if it were transferring power individually through its own dedicated power converter. This has the effect of shifting the turbine operating curve to the right, Figure 6-6 (a).

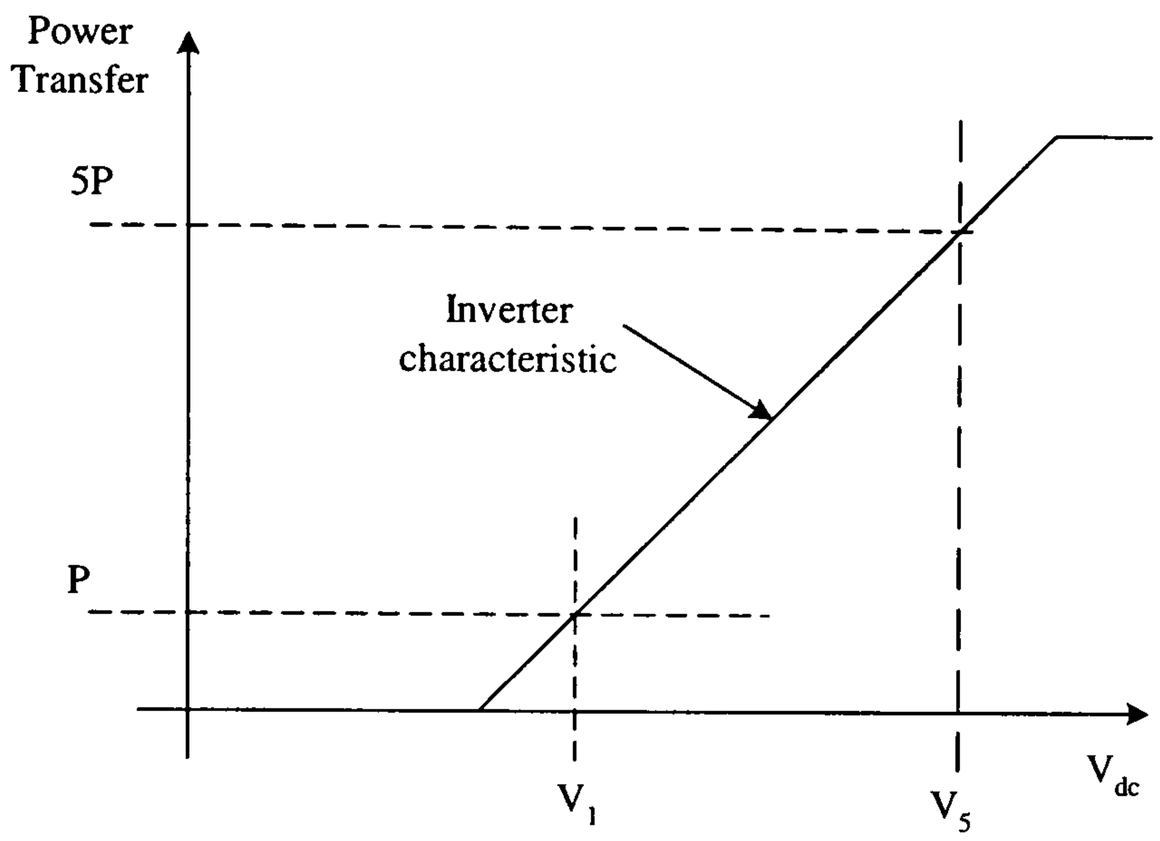

Figure 6-5. Windy Boy characteristic showing how dc voltage determines total exported power

The impact of this behaviour is well demonstrated in Figure 6-6 (a) by simulating each of the 5 wind turbines operating at constant wind speeds of 9, 10, 11, 12 and 14m/s; this is shown as 'operating line 1' in Figure 6-6 (a)[8]. As the DC voltage is set by the total power transfer, all 5 turbines operate at higher rotational speeds than if they were controlled separately. This new common operating line intersects the operating points of the 5 individual turbines, shown as circles in the figure. The power transfer mechanism is further complicated as the common operating line shifts along the x-axis depending

[8] This operating line would be vertical if each generator was ideal, i.e. it had no armature resistance or inductance. In this situation all 5 generators would run at the same speed.

on the average wind speed across the group of turbines. This can be seen by modifying the 5 wind speeds to 9.5, 10, 10.5, 11 and 12 m/s respectively, and is shown as 'operating line 2' on Figure 6-6 (a).

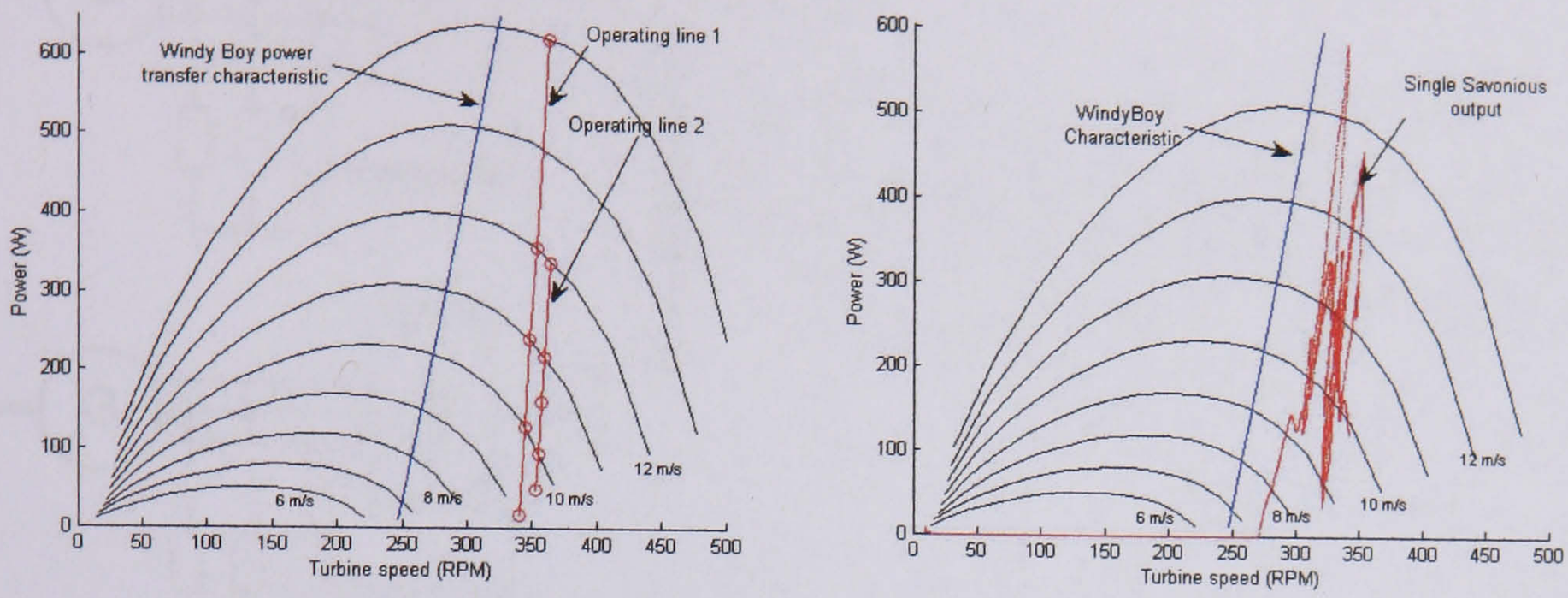

(a) (b)

Figure 6-6. Output of Savonius VAWT (a) Multiple Savonius operating characteristic and (b) Output of 1 Savonius turbine

When turbulent wind inputs are used, the average wind speed fluctuates with time, and has the effect of shifting the common operating line back and forth along the x-axis. The power output of a single turbine moves up and down the common operating line as the wind speed at the *individual* turbine fluctuates due to turbulence, while the common operating line moves back and forth along the x-axis as the *average* wind speed fluctuates. This behaviour is shown in Figure 6-6 (b) where the output power and speed of one Savonius turbine from the model has been plotted during the 100 seconds that the simulation was run.

6.5 DC-DC converter augmentation

It has been shown in Chapter 5 that a DC-DC converter placed in the DC link can augment the power transfer characteristic of the Windy Boy inverter to produce a cubic rather then a linear profile. In this section the same method is used to shift the group

operating point of the turbines back towards a more optimal location on the turbine's power curves. A schematic of the system including a DC-DC converter is below.

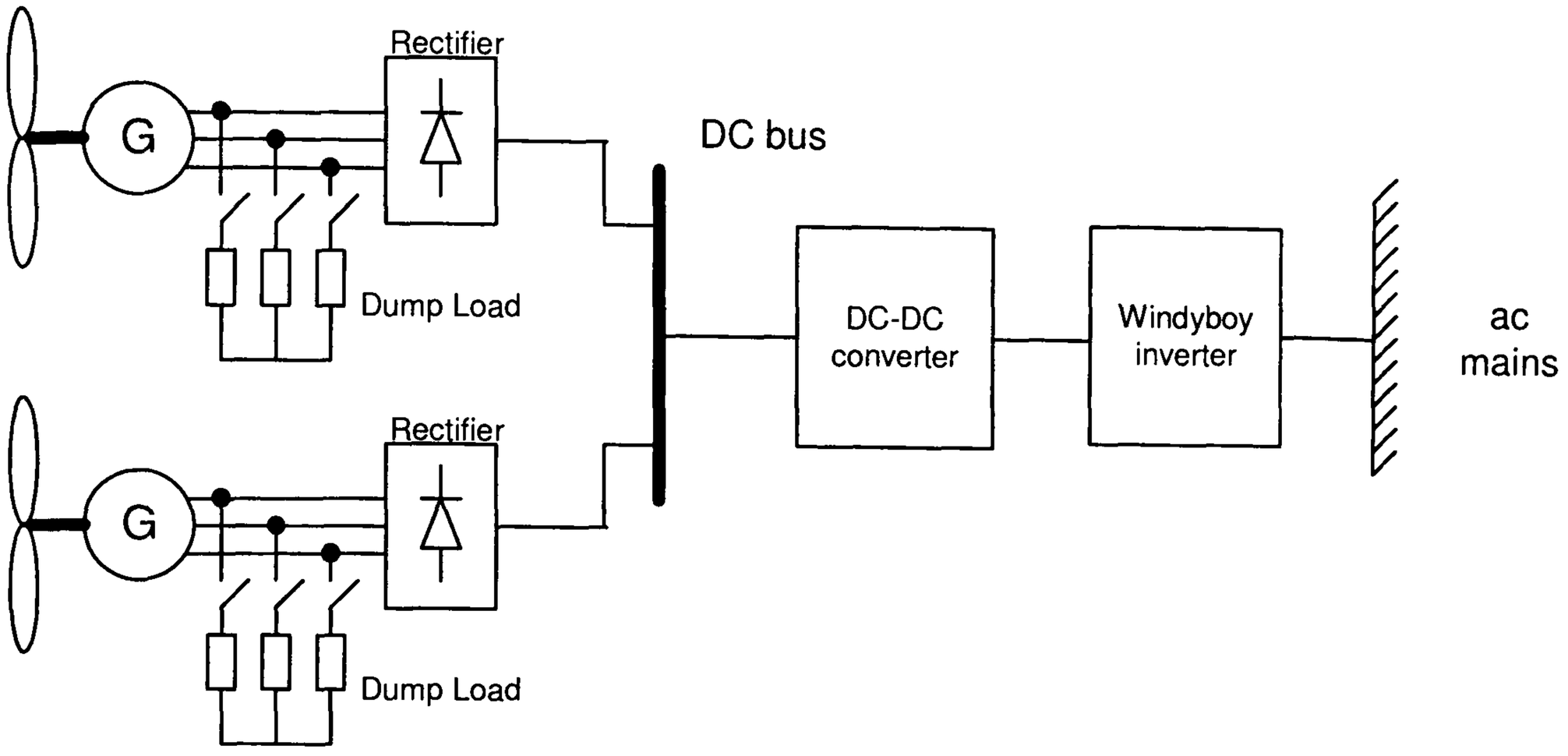

Figure 6-7. Schematic of DC aggregation using a DC-DC converter

Since the five turbines push power through a single inverter, the DC link voltage must rise to meet the increased power demand, and this forces the turbines to over-speed, leading to a reduction in efficiency. To prevent this, a DC-DC converter can be used to boost the DC bus voltage to the level that the Windy Boy requires to export the necessary power.

The figure below shows the Savonius turbine's power curves with the ideal operating characteristic shown in pink. Also shown is a scaled version of the Wind Boy's power transfer characteristic in which the power output from the inverter has been divided by the number of turbines in the aggregation (in this case 5), so that the maximum inverter output is 2500W/5 = 500W. The gain ratio of the DC-DC converter can then be adjusted to boost the DC voltage from one characteristic to the other and this allows the turbines to operate at their ideal speed while transferring the correct level of power to the inverter. Scaling the inverter characteristic in this way takes account of the fact the 5

turbine output powers must be summed by the aggregation.

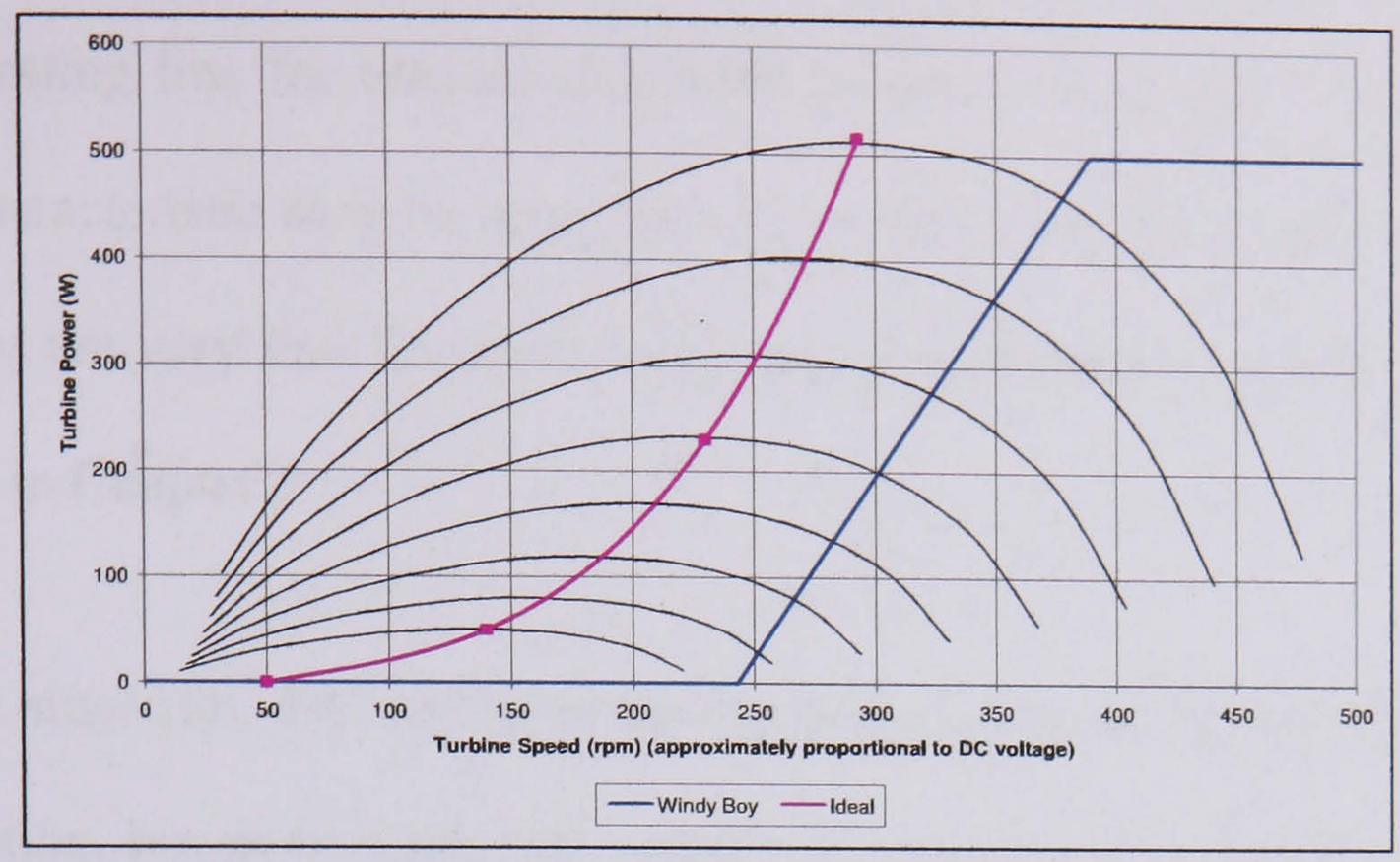

Figure 6-8 Turbine speed versus power for wind speeds from 6-13 m/s

The results of the simulation are shown in the figure below. For clarity, the operating points of two of the five turbines are tracked during the 100 second simulation run. A mean wind speed of 10m/s and a high level of turbulence ($k_\sigma = 0.4$) were used in the simulation; the optimal operating line is also shown as the black cubic.

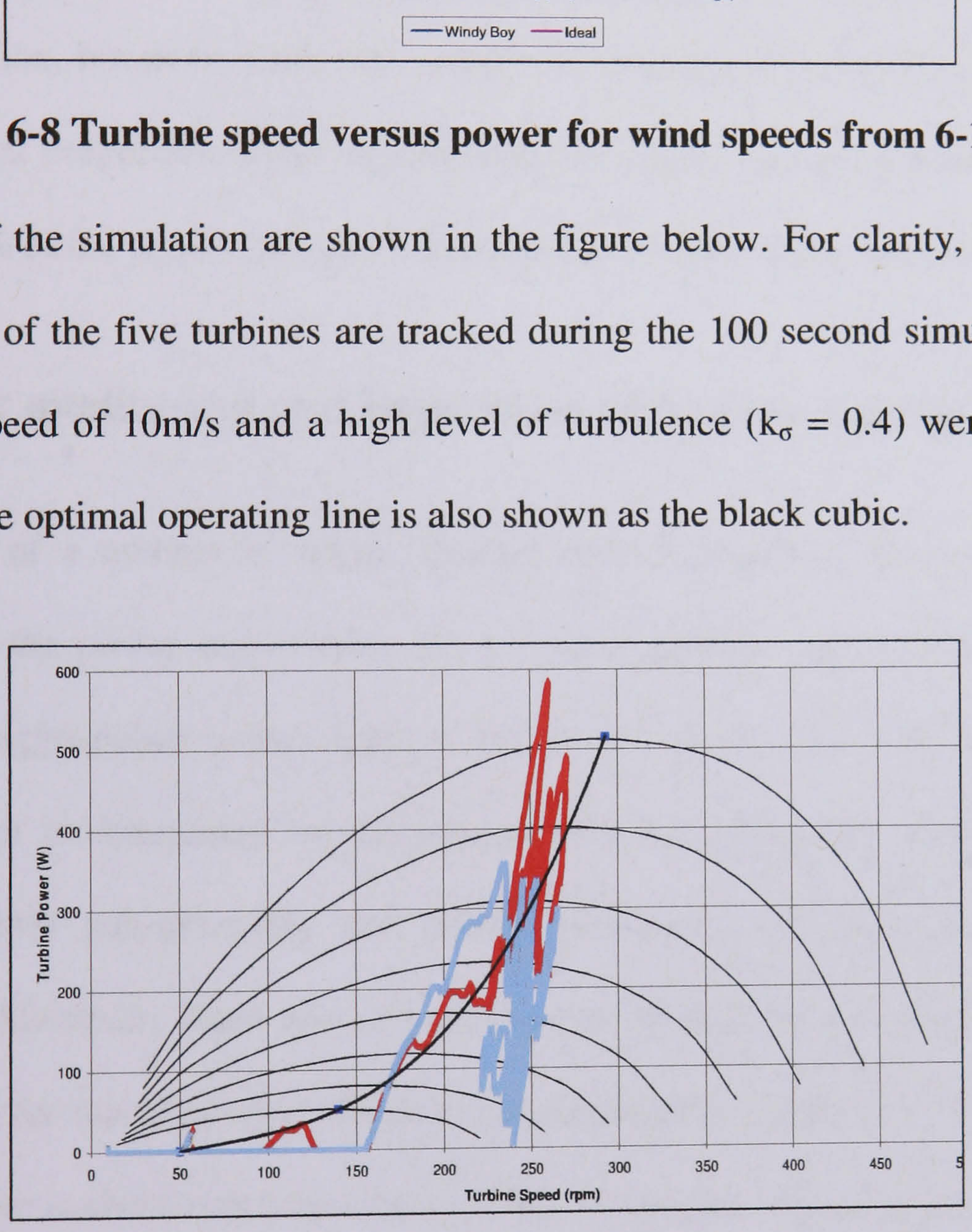

Figure 6-9. Operating points of 2 of the 5 turbines; wind speed curves from 6-13m/s

By comparing Figure 6-9 with Figure 6-6 (b), it is clear that the use of a DC-DC converter can indeed move the group operating point to the left, so as to promote more

efficient energy transfer when aggregating at DC. Although the average operating point of the 5 turbines now lies within the power curves, individual turbines still follow a near vertical operating line for reasons discussed in section 6.4. Such an uncompromising operating characteristic may be acceptable for a drag operated Savonius turbine, whose power curves are very flat, however it may cause stall problem for the H-type Darrieus turbine seen in Chapter 5.

The use of a single DC-DC converter on the front end of the Windy Boy is still worthy of consideration, however, since the cost of G83 compliant power electronic interfaces is a significant proportion of the overall costs for small scale wind generation systems; typically 50% of the turbine and generator cost (or 15-20% of the installed cost).

6.6 Power quality and cost implication of turbine aggregation

Aggregation of a number of wind turbines rapidly smoothes the net power output compared to the power output from an individual turbine. This is true regardless of whether the aggregation is performed at AC or DC. However, in DC aggregation the power transfer is determined by the behaviour of the group of turbines so that each turbine operates sub-optimally and power transfer is not as great as with AC aggregation. However, there are cost savings to be had by using a single inverter. Current costs for mains connect inverters are tabulated in Table 13 [78]. The cost of a 2500W inverter is about twice the cost of a 700 W inverter so that aggregating 5x500W turbines through one 2500W inverter reduces the cost from 5x£686 to 1x£1244; a cost saving of £2186. Further, by aggregating at DC the power variation the inverter must now cope with has been reduced; in the case of dedicated inverters each inverter may be called upon to transfer 500W, Figure 6-4 (c), whilst the DC aggregated maximum is

under 1000W (even the AC aggregated is less than 1500W). This means that either more turbines could be connected to the inverter or the inverter rating could be reduced to, say 1700W, further reducing cost, Table 13.

Rating (W)	Cost (£)	Cost/W (£/W)
700	686	0.98
1700	943	0.56
2500	1244	0.50

Table 13. Cost of Windy Boy inverters [78]

The smoothing effect aggregation has at both AC and DC is shown in Figure 6-10, where the variation in power output as a fraction of the average power output is plotted. The variation is calculated using equation [6-1] with the analysis performed for a single turbine and for the aggregated outputs of 2, 3, 4, 5, 6, and 7 turbines. As the variation in power output is dependant on the exact nature of the turbulent wind profile, Figure 6-4 (c) and (d), the model was run over ten different random turbulent wind profiles and the results averaged in order to obtain a meaningful result. In all cases the same mean wind speed was used.

$$Power\ Variation = \frac{(Max.Power - Min.Power)/2}{Average\ Power} \qquad [6\text{-}1]$$

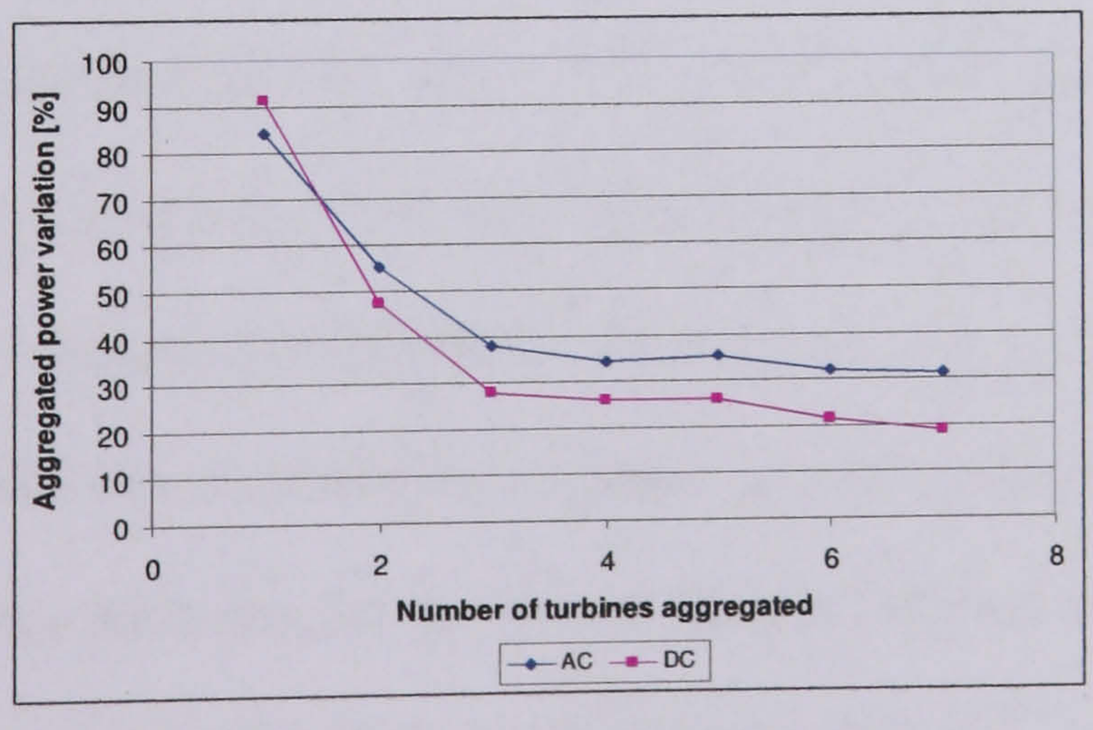

Figure 6-10. Power output variations for different numbers of wind turbines aggregated

Figure 6-10 shows that the variations in power decrease, from approximately 90% to about 20% of the average power, as the number of turbines aggregated increases to 7. It is clear that aggregation quickly smoothes the power output. Figure 6-10 also suggests that better power smoothing is achieved with DC aggregation as the turbines are constrained to operate in a much narrower speed range for reasons described above. It is reasonable to assume that the reduction in variability will increase as more and more turbines are aggregated.

6.7 Conclusion

Aggregation at AC produces a predictable power output profile, consisting of the sum of the individual turbine contributions. Each turbine can be controlled independently by a designated inverter to produce optimal energy capture. The drawback to this system is the significant financial penalty that must be paid for the 5 separate inverters – typically 50% of the turbine and generator cost (or 15-20% of the installed cost).

Aggregation at DC provides a much cheaper solution as now only a single power converter is required. However, controlling individual turbines becomes much harder since the power transfer characteristic of the turbines becomes decoupled from the inverter's load characteristic and is set by the average performance of the group. This difficulty can be eased by using a DC-DC converter on the front end of the inverter to effectively shift the common operating line to the left, towards the peaks of the turbine power curves. It should be noted that the common operating line is nearly vertical, and this may cause stability problems for the type of Darrius turbine discussed in Chapter 5. The Savonius turbine used in this study is ideally suited for DC aggregation because its 'flat' power curves allow it to operate efficiently despite the uncompromising power

The Savonius turbine used in this study is ideally suited for DC aggregation because its 'flat' power curves allow it to operate efficiently despite the uncompromising power transfer characteristic imposed by DC aggregation. Some horizontal axis devices may also be suitable for this application.

Aggregation of a number of wind turbines rapidly smoothes the net power output compared to an individual turbine. This is true regardless of whether the aggregation is performed at the AC or DC side of the system, although aggregating at DC produces more smoothing because the turbines are electro-mechanically coupled. Smoothing power fluctuations in this way has important implications for designers of embedded generation systems, as it allows a more predictable power output to be generated.

Chapter 7

Turbine energy capture from turbulent wind

7.1 Introduction

Chapter 5 introduced the idea that wind turbulence can have an important effect on the stability of a mains connected Darrieus-type VAWT. This chapter will extend that concept by considering the effect of turbulence on the annual energy capture of a similar small-scale turbine.

The analysis of energy yield described in Chapter 3 used a Weibull probability function to estimate the annual wind speed distribution, which was then filtered through the turbine power-wind speed characteristic to produce a figure for the annual energy yield. This analysis was simplistic in that a constant and maximum value of C_p was assumed throughout. As Chapter 4 has shown, in real wind conditions the turbine does not always operate at an optimal value of C_p and must also be shut down in strong winds, which can have an important effect on energy capture. To explore this phenomenon a unidirectional fluctuating wind profile is used to generate a more representative power-wind speed characteristic. In this work no account has been taken of the effect of the changing wind direction since a VAWT can accept wind from any direction.

Sections 7.2 and 7.3 explore the methods of over-speed protection in HAWTs and VAWTs and describe the system that is used in the H-type Darrieus turbine shown in Figure 2-1 (b). It is likely that this system will be widely adopted in the market place. Section 7.4 shows how this system can lead to a reduction in energy capture due to the voltage protection system being tripped in highly turbulent wind conditions. The

following two sections outline possible solutions: an increase in turbine inertia and the use of a dump load to slow the turbine during wind gusts. Both solutions are modelled using SIMULINK and the results, presented in section 7.6.2, show that actively controlling the speed of the turbine using a dump resistor provides the greater energy capture.

7.2 Over-speed protection for micro and small-scale turbines

The manufactures of most horizontal axis wind turbines protect against over-speeding by using a furling mechanism to turn the rotor out of the wind, as shown in the diagram below [24, 106, 107]. Alternative strategies include the blade furling mechanism adopted by *Proven* [79] and the blade pitching mechanism used by *Ampair* [108], although these have proved less popular.

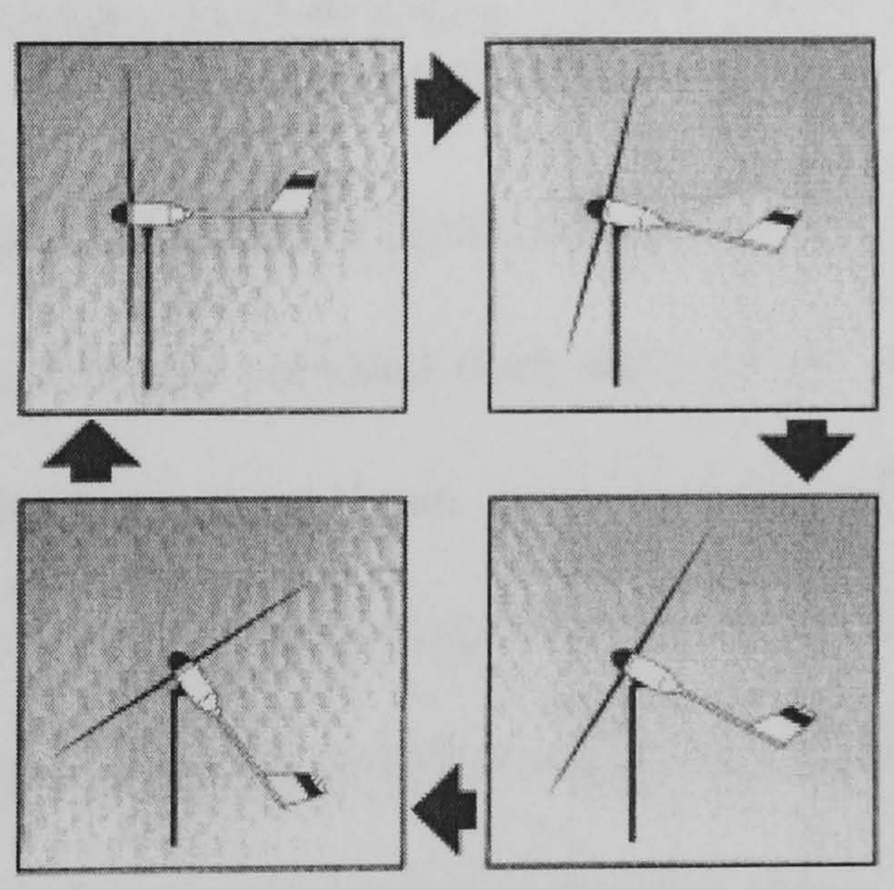

Figure 7-1. Ubiquitous furling mechanism for HAWTs [107]

With vertical axis devices it is not possible to furl the turbine as it cannot be turned out of the wind. The manufactures of most Savonius VAWTs overcome this problem by simply building their turbines strongly enough to survive high winds without being shut down [26]. This is possible because their high solidity factor allows an inherently sturdy

structure to be constructed, and since they are drag operated devices, their maximum speed is limited to a little over the maximum wind speed. Some Darrieus VAWTs have also adopted this 'over-engineered' approach, most notably the Italian built *Ropetec* [109] shown in the figure below alongside the more slender *Carbon Concepts* turbine [25].

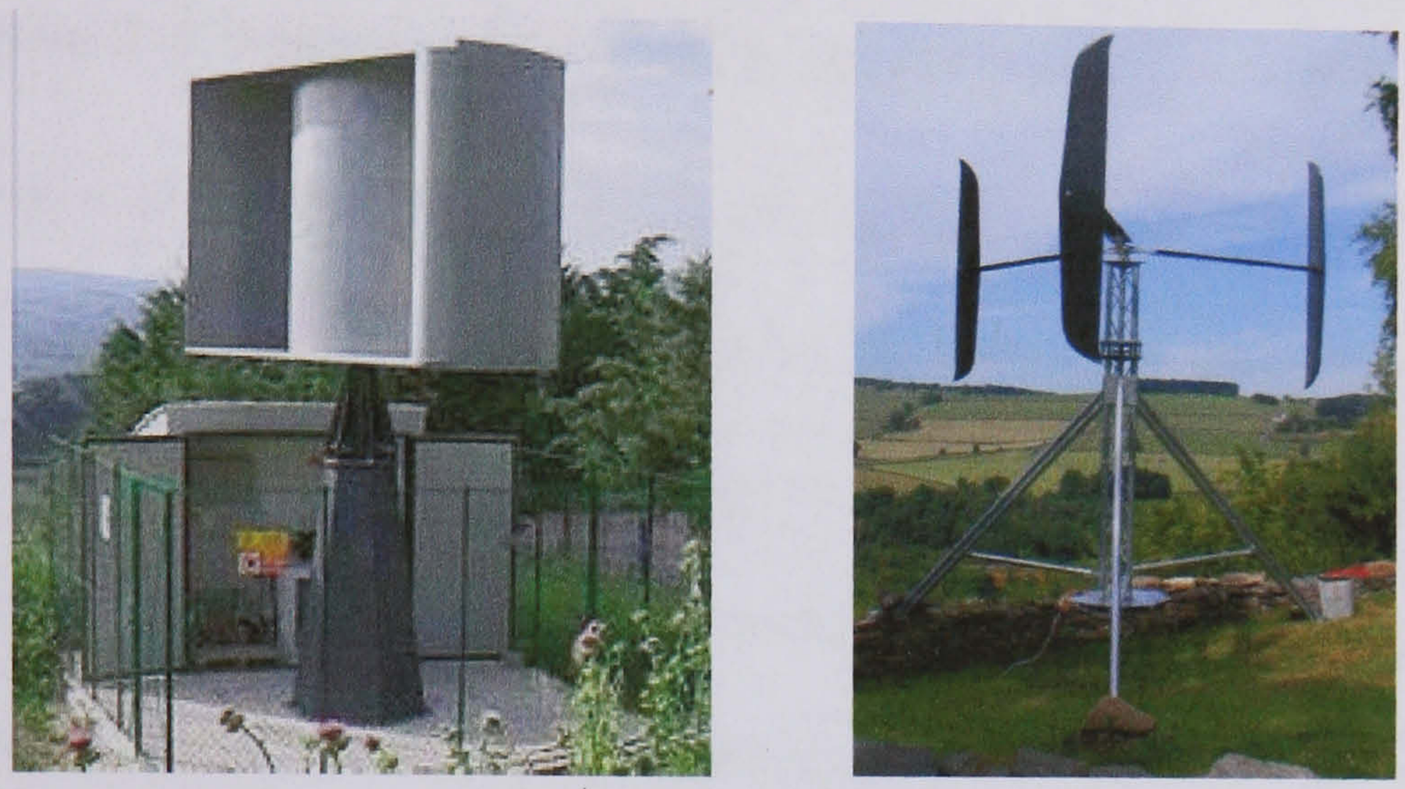

(a) **(b)**

Figure 7-2. (a) Over-engineered Ropatec VAWT [109]; (b) Slender H-type Darrieus [25]

A quick search through any major patent database reveals many types of variable pitch VAWTs that have been tested and patented over the years to accommodate some kind of over-speed control, although none have been commercialized to any significant extent. The figure below shows a promising design by PJ Musgrove from Reading University who patented the design in 1976 [110]. Unfortunately the prototype proved unreliable because a large downward bending moment was created on the supporting arms each time the blades were feathered, which eventually caused the arms to fail [29].

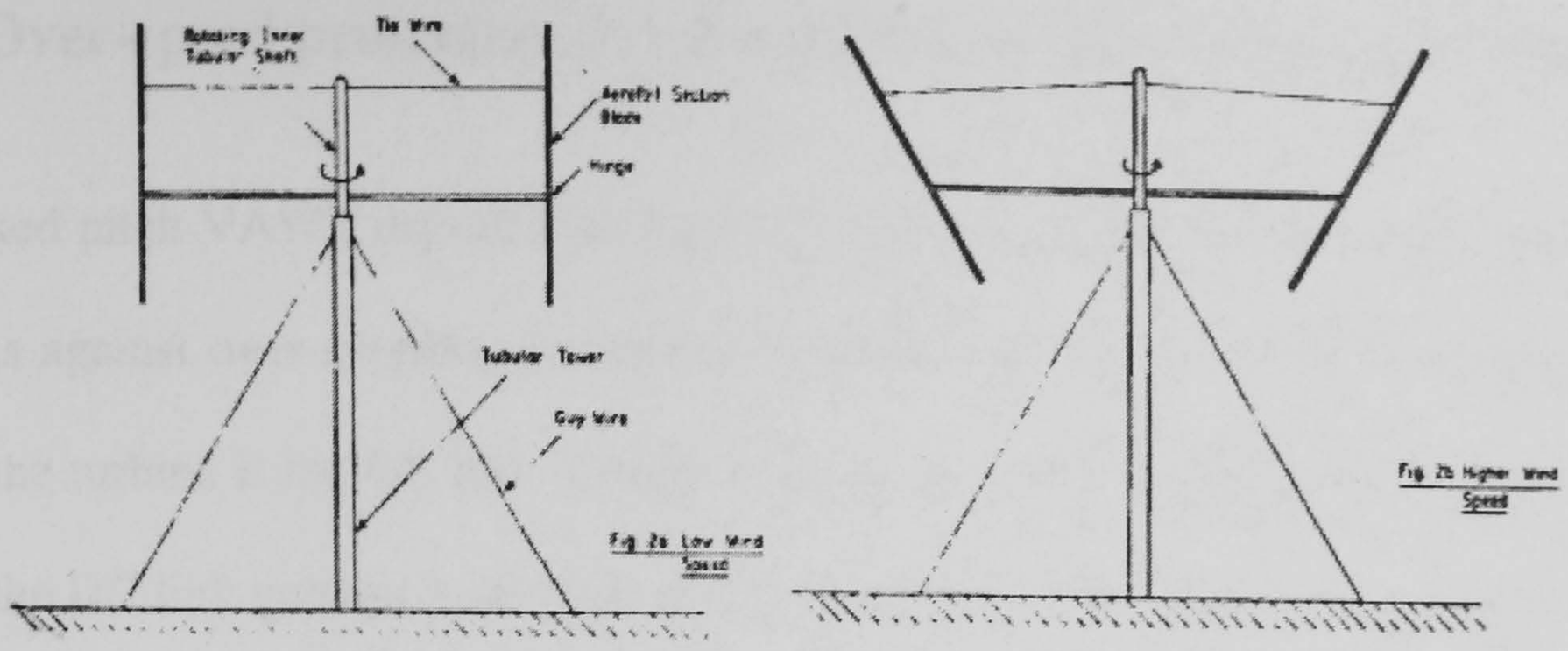

Figure 7-3. Musgrove's patented variable geometry VAWT [110]

Figure 7-4 shows an alternative design which was patented in 1980. Here, the tendency of the blades to pivot outwards in response to the generated lift is counteracted by tie rods (numbered 50 in the diagram) which are connected to a central junction (#54). The junction is free to move upwards on a rod mechanism (#58) against the force of a spring (not shown) as the lift force from the blades increases. At high rotor speeds (high lift) the blades are progressively stalled as the junction boss approaches its fully raised position (depicted in the figure).

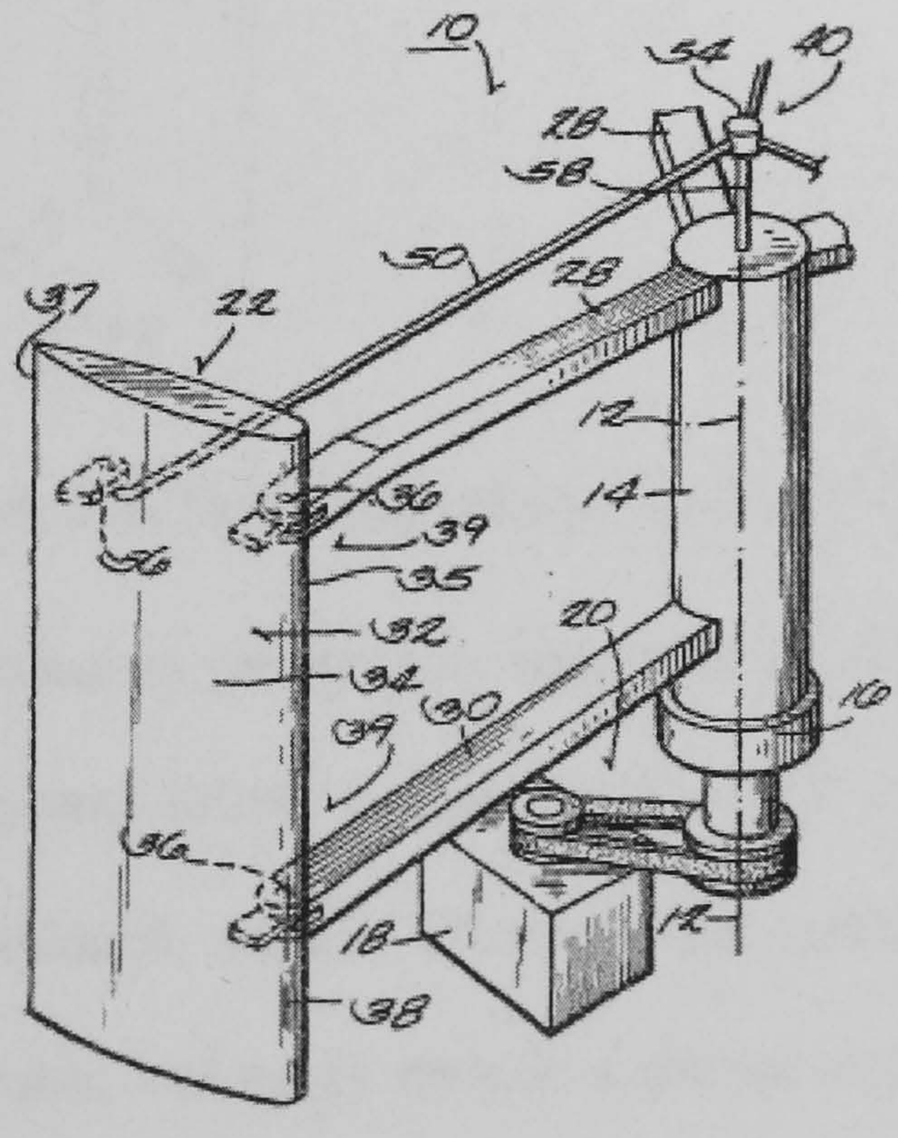

Figure 7-4. Variable pitch VAWT [111]

7.3 Over-speed protection in a fixed pitch H-type Darrieus turbine

The fixed pitch VAWT depicted in Figure 7-2 (b), and which has been modelled here, protects against over-speeding by means of a braking resistor which is switched in to brake the turbine if the DC link voltage rises above a set threshold, for example 550V. Since the DC link voltage is proportional to rotor speed (neglecting voltage drops in the armature), this places a limit on the speed of the rotor and also protects the Windy Boy from DC voltages over 600V, which is a requirement of the inverter. A schematic representation of the braking system is shown below. The voltage detection device operates a 3-phase relay to switch in the braking resistors at a preset DC link voltage.

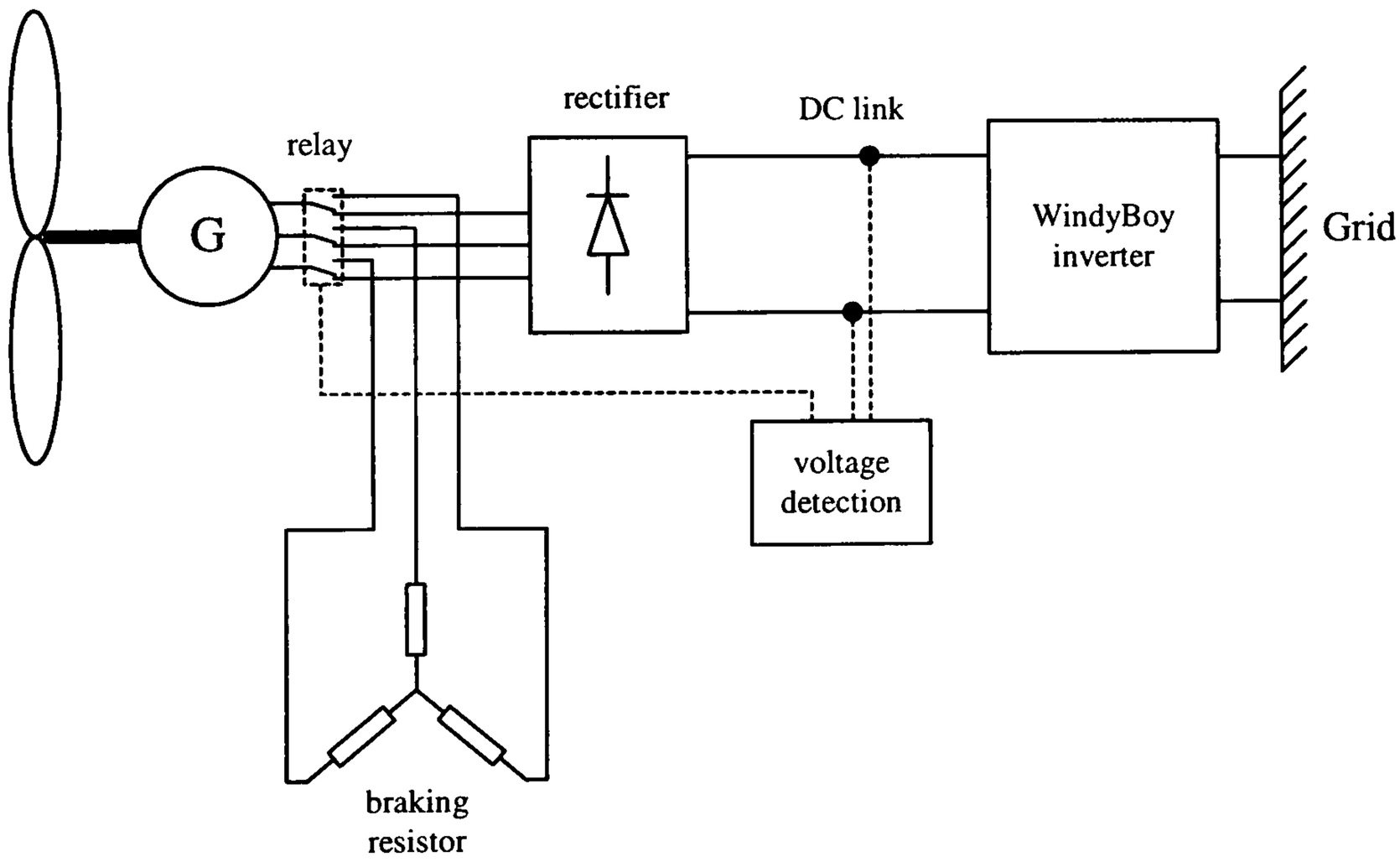

Figure 7-5. Schematic of speed control system

This type of braking system is particularly suited for a permanent magnet generator since in the event of a power failure a magnetic flux will still be present, enabling a braking torque to be produced. Almost all micro and small-scale turbines employ a permanent magnet generator, and many include a similar braking system [27, 79, 107] because of its simplicity and ruggedness, and because it is one of the only simple

systems available to designers of fixed pitch VAWTs.

The effect on the turbine of switching in the braking resistors is shown in Figure 7-6, which shows turbine power as a function of DC link voltage rather then speed, although as described in Chapter 2, the two terms are almost proportional. Suppose the wind speed increases steadily from 5 to 12 m/s; as the turbine speed increases, so the DC link voltage rises and the inverter exports an increasing amount of power. This corresponds to the operating point moving upwards along the sloped blue 'Windy Boy characteristic' line until it reaches position (1). If the wind speed increases above 12 m/s, the DC link voltage will rise above 550V and the over-speed voltage relay will be tripped, the braking resistors switched in, and the operating point will move to position (2) on the braking resistor characteristic line. As can be seen, now 3250W are being dissipated through the braking resistors, although only 2250W are being supplied by the turbine. This causes the turbine to stall and the operating point descends down the braking resistor characteristic line until position (3) is reached when the turbine is at rest. The turbine will not produce further power until the voltage trip relay is reset, in this case by the operator when wind conditions have become more benign.

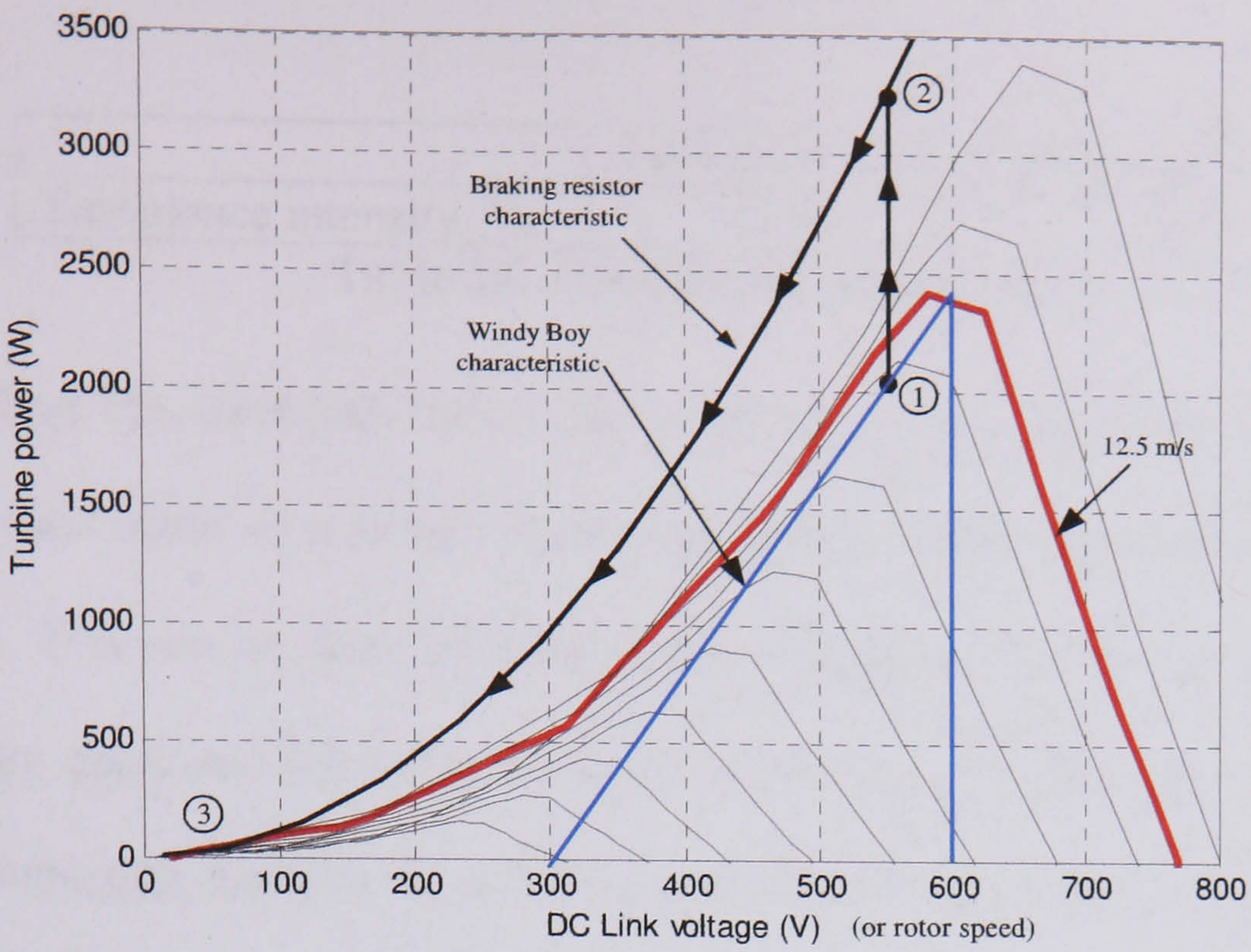

Figure 7-6. Effect of braking resistance on turbine behaviour (wind speeds from 5-14 m/s)

Problems can arise with this mechanism in turbulent wind, however. If a sudden gust causes the turbine speed to increase such that the over-voltage relay is tripped, the turbine will be shut down. This has obvious implications for long term energy capture in highly turbulent wind regimes.

7.4 Modelling of over-speed protection system

In this section the turbine and generator system described above, and which has been modelled in Chapter 2 and Chapter 5, is again modelled to assess the effect of wind turbulence on energy capture. In the simulation, the turbine is equipped with the more stable S1210 blades (as described in Chapter 5), and power is transferred to the mains using a grid-connected inverter with a power transfer characteristic set up to optimise the turbine's performance as described in the previous chapter and shown in Figure 5-3 (b). Two wind regimes are investigated corresponding to high and low levels of turbulence (parameters are given in the table below).

	Low turbulence	High turbulence
Turbulence intensity, k_σ	0.16	0.40

Table 14. Turbulence parameters

By recording the electrical output power of the grid-tie inverter in response to a turbulent wind input of a known mean wind speed, the average output power can be calculated. This can be done by numerically integrating the power signal to find the total energy generated (ignoring the start-up period), and dividing by the simulation time. By repeating this process at increasing increments of mean wind speeds, a new power-wind speed characteristic can be produced which is more representative of the H-type Darrieus turbine sited in real wind.

To model the over-speed protection system, the DC link voltage in the simulation can be monitored to see if it rises above the trip voltage at any point during the simulation run. If this event occurs the system is deemed to have shut down and the turbine would not have contributed to the annual energy capture in such a wind regime. A plot of the DC link voltage during the simulation is shown below when the turbine is subject to a 10.0 m/s mean wind speed and a high level of turbulence (k_σ=0.4).

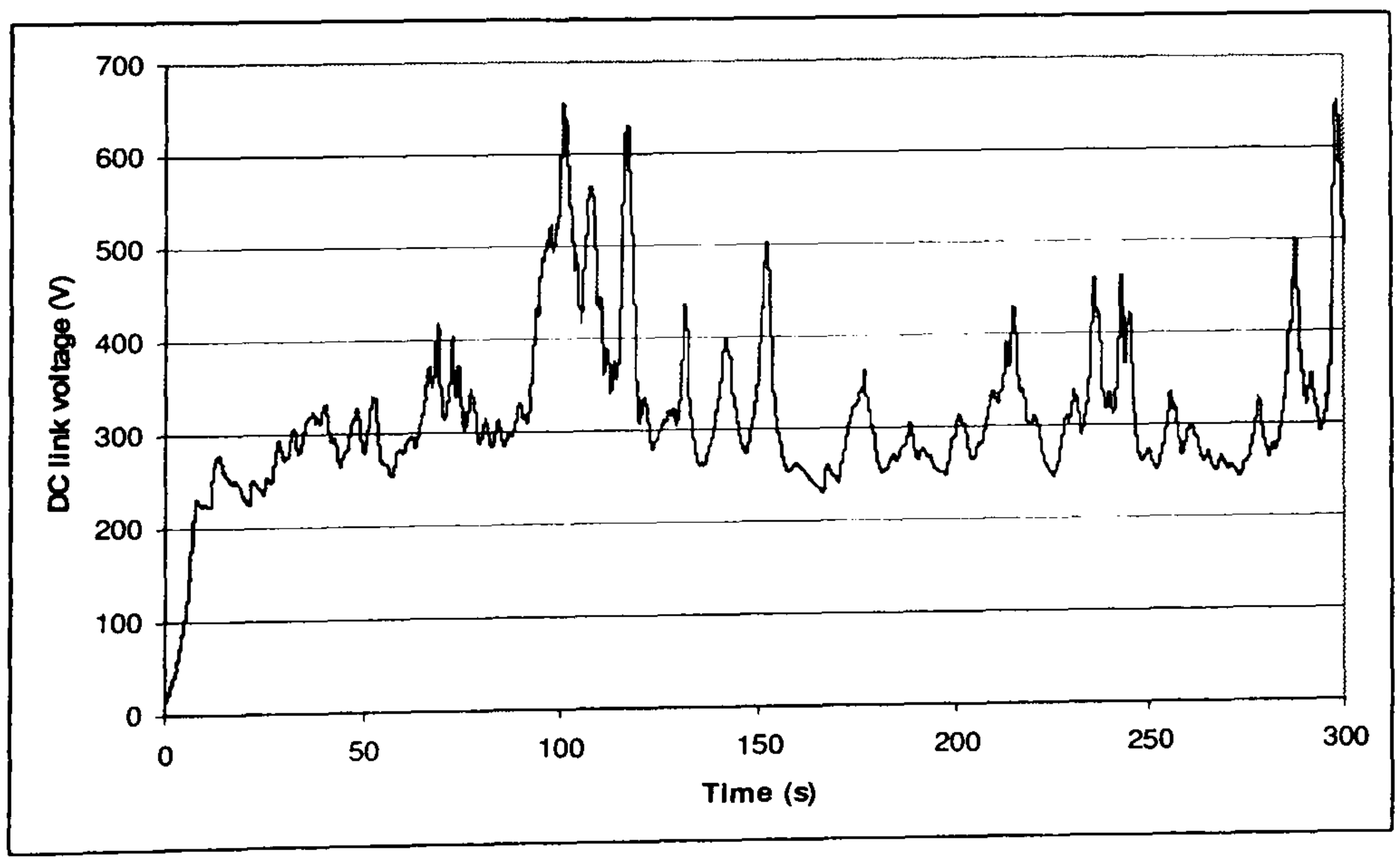

Figure 7-7. DC link voltage

As can be seen, the DC link voltage rises above 550V on three occasions during the simulation run. The turbine is therefore assumed to have shut down in a 10.0 m/s highly turbulent wind regime. By repeating this process for different wind speeds, a new power-wind speed characteristic can be drawn, as shown in the figure below. A constant wind speed characteristic is also included for comparison.

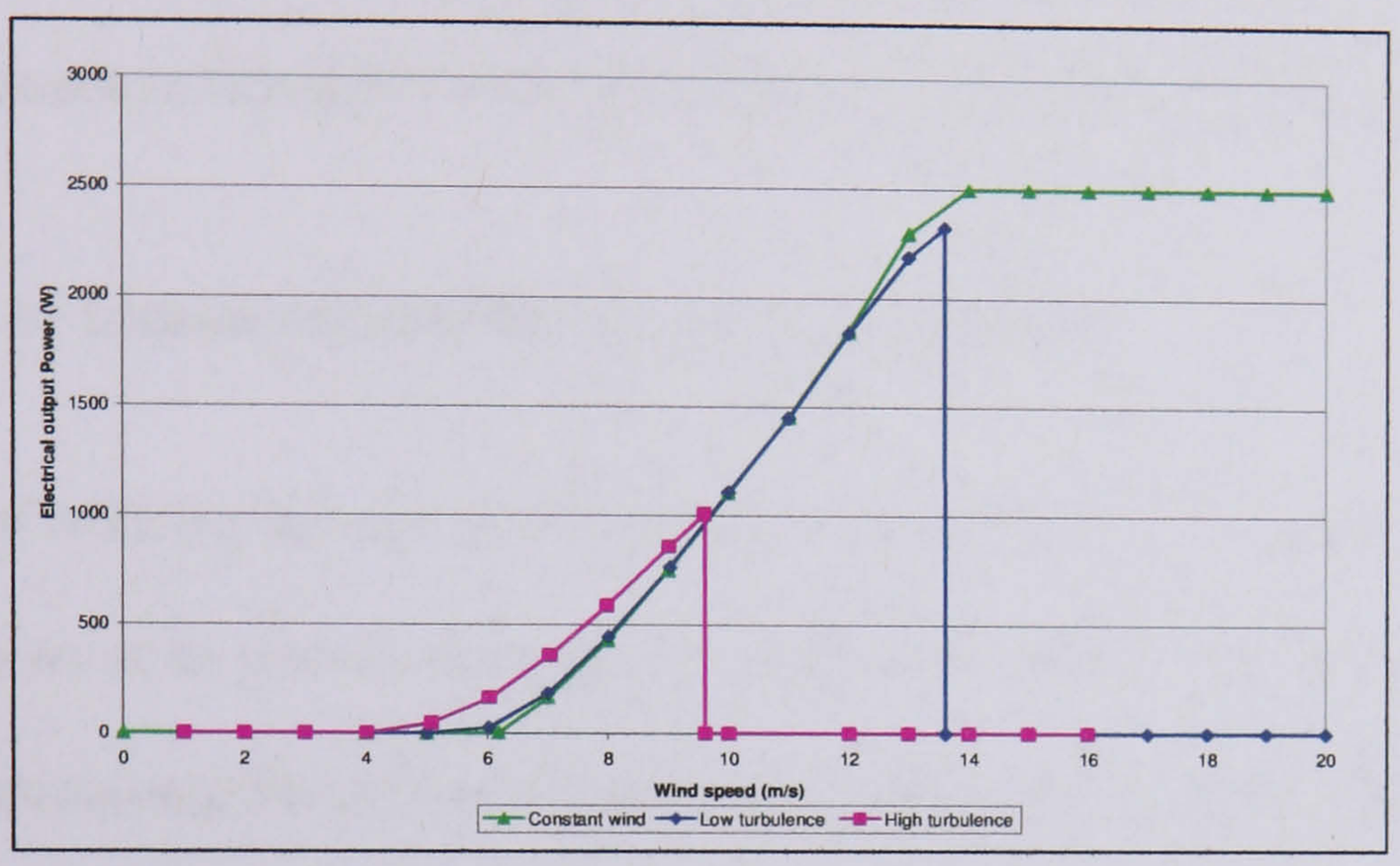

Figure 7-8. Power-wind speed characteristic for different levels of turbulence

Figure 7-8 shows that in highly turbulent wind the power characteristic is curtailed at high wind speeds because the over-voltage trip is activated. It is also interesting to note that the highly turbulent wind produces a slightly more favourable power characteristic at lower wind speeds. This is because for a given wind speed fluctuation ΔV, there is more power available if the wind speed increases from its mean value than if it decreases, since the power available is proportional to the cube of the wind speed.

The annual energy yield from the turbine was calculated for the three power characteristics shown above by using the Weibull analysis described in Chapter 3. These are shown in the table below, based on a Mean Annual Wind Speed (MAWS) of 5.0 m/s; also shown is the maximum wind speed the turbine can operate in without

causing an over-voltage trip.

	Constant wind	Low turbulence	High turbulence
Trip wind speed [m/s]	15.3	13.6	9.6
Annul energy yield [kWhr/yr]	1442	1417	1212

Table 15. Annual energy capture in different levels of turbulence (MAWS = 5.0m/s)

Table 15 shows that operating the turbine in highly turbulent wind curtails the power-wind speed characteristic significantly which lowers the annual energy yield.

7.5 Effect of increased inertia on energy capture

One method of reducing the risk of shut down occurring in gusty wind is to increase the turbine inertia so as to smooth rotor speed fluctuations. Figure 7-9 and Table 16 show the effect of increasing the turbine's inertia on the power-wind speed characteristic, trip voltage and energy capture. The simulation was run in highly turbulent wind ($k_\sigma = 0.4$) for turbine inertias of 18, 54, 108 and 162 kg/m2, corresponding to the actual turbine inertia (18 kg/m2), and then multiples of 3, 6 and 9 times this inertia.

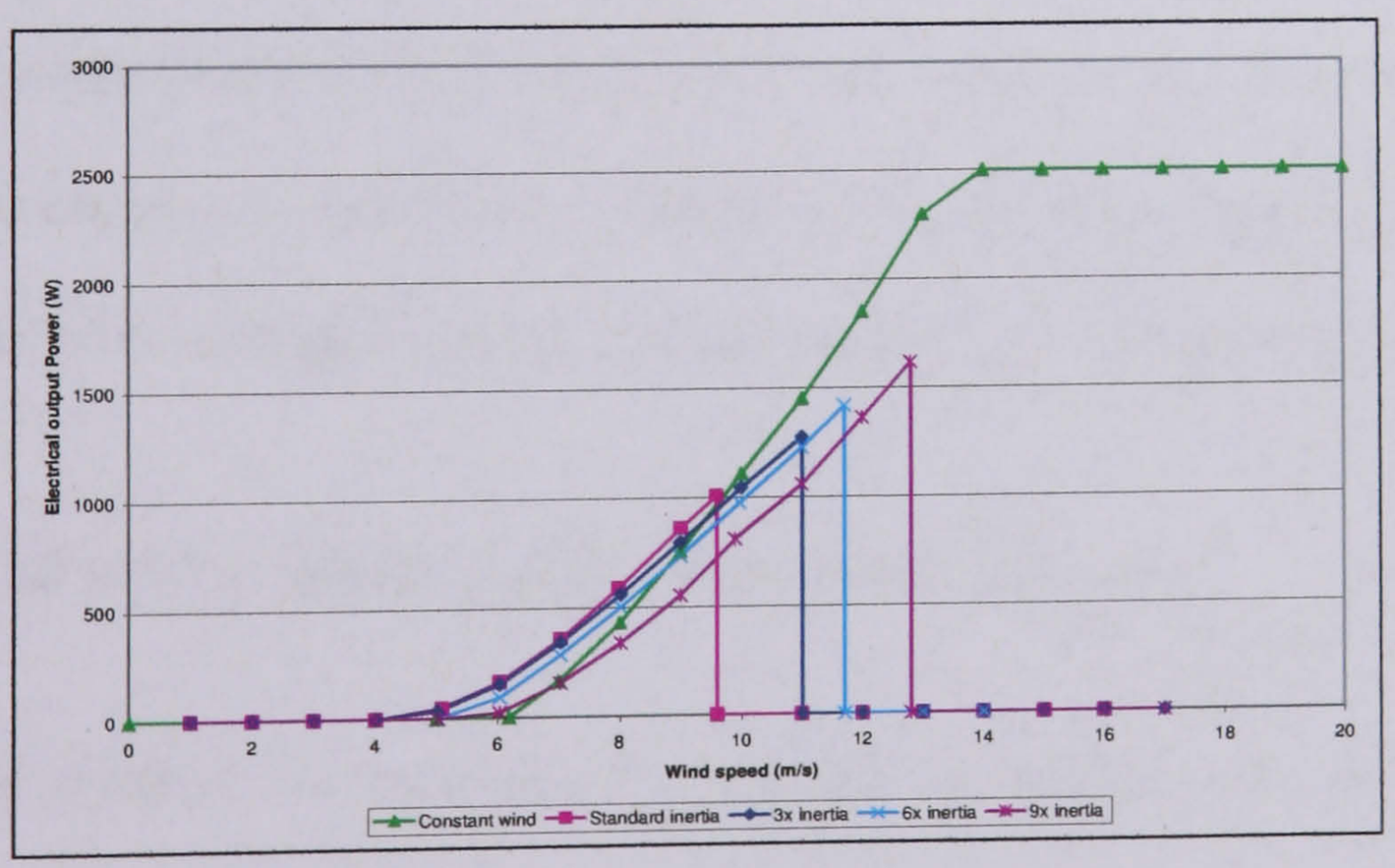

Figure 7-9. Effect of inertia on power characteristic

Figure 7-9 shows that at higher turbine inertias the system is indeed able to cope with

higher wind speeds without tripping out, which has a favourable effect on the annual energy capture of the system. However, the increased inertia prevents the turbine from following the changing wind speed which adversely affects energy capture. This is because if the turbine rotates at a constant speed while the wind speed increases by ΔV, it will lose out on more power then would be gained if the turbine remained at a constant speed while the wind speed dropped by ΔV (since $P \alpha V^3$). The net result of these two competing factors is shown in the table below, where the effect of increasing turbine inertia on energy capture is initially beneficial and then subsequently detrimental. The effect of a constant wind speed is also included for comparison.

Multiple of turbine inertia	1 (in constant wind)	1	3	6	9
Trip wind speed [m/s]	15.3	9.6	11.0	11.7	12.8
Annual energy yield [kWh/yr]	1442	1212	1304	1078	874

Table 16. Effect of increased inertia on trip wind speed and annual energy yield (Energy yield figures based on MAWS = 5.0 m/s using the Weibull analysis described in Chapter 3. A highly turbulent wind regime is assumed)

Although increasing the turbine inertia appears to promote energy capture, it is clear that a better system would maintain the turbine's low inertia, so as to follow wind speed fluctuations as closely as possible, but incorporate a method of speed control to reduce the instances of over-voltage tripping. Such a method is discussed in the next section.

7.6 Effect of active speed control on energy capture

An alternative method for reducing the number of turbine shut downs in highly turbulent wind is to use a second dump resistor as an extra electrical load. If a suitable hysteresis lag is used, the dump resistor can be switched in to slow the turbine during strong wind gusts, and then switched out when the wind speed drops, allowing the

turbine to accelerate again. This behaviour is shown in the figure below.

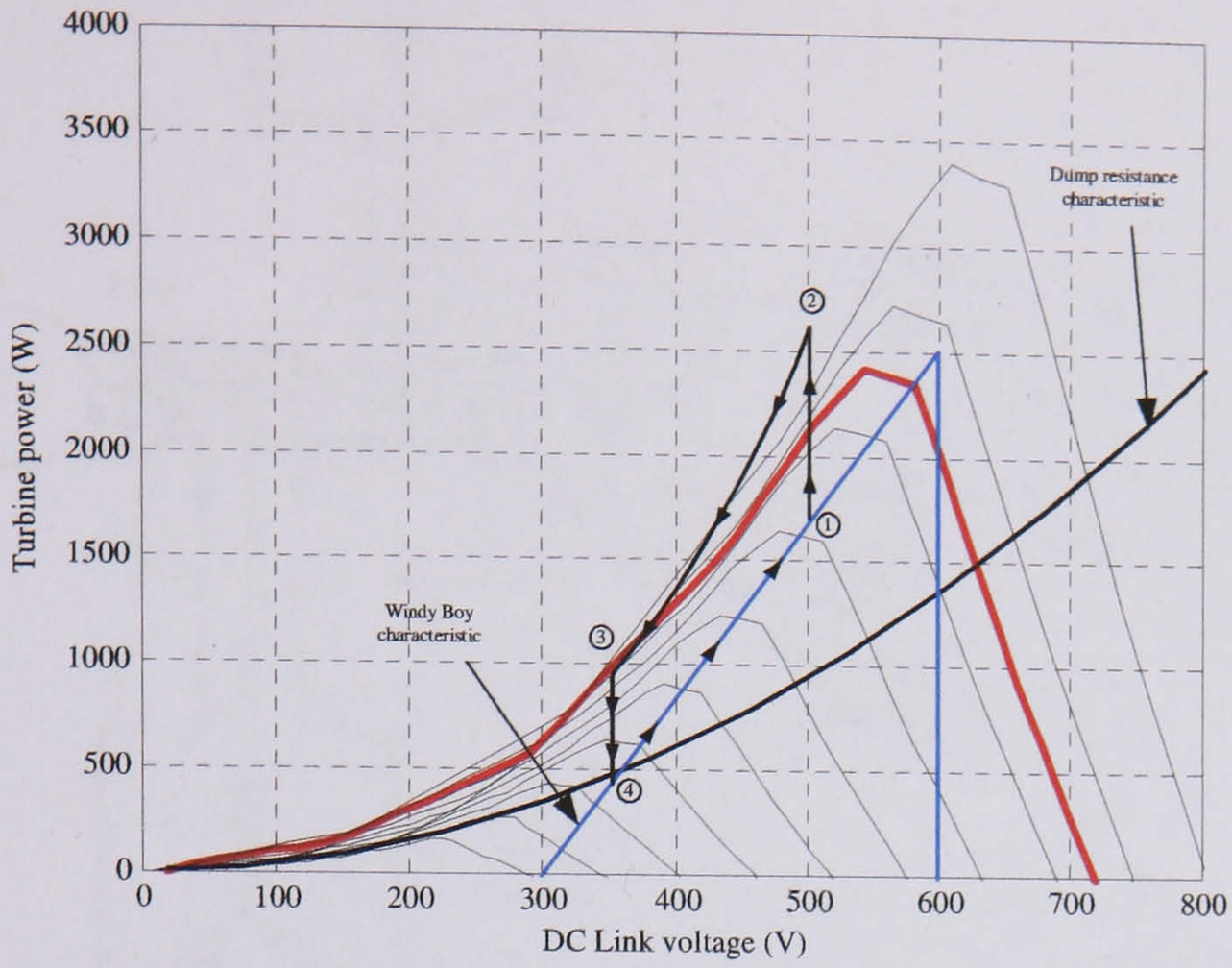

Figure 7-10. Behaviour of active speed control

Figure 7-10 shows that as the wind speed increases, an increasing amount of power is exported until position (1) is reached, when the DC link voltage is 500V. At this point the dump resistor is switched in and the operating point jumps to position (2), which is the sum of the output power from the Windy Boy and the extra power dissipated in the dump resistor at 500V. Although the inverter is still exporting approximately 1600W, the dump resistance adds a further 950W to the generator load. Since the turbine is only supplying a little over 1600W, the turbine stalls and the rotor speed slows until the DC link voltage falls below 350V, position (3). At this point the resistors are switched out, position (4), and if the wind is still strong the turbine will accelerates back towards position (1). The dump resistors contribute a lower load then the braking resistors because when they are switched in, power is still being exported through the grid-tie inverter. The system is shown schematically below.

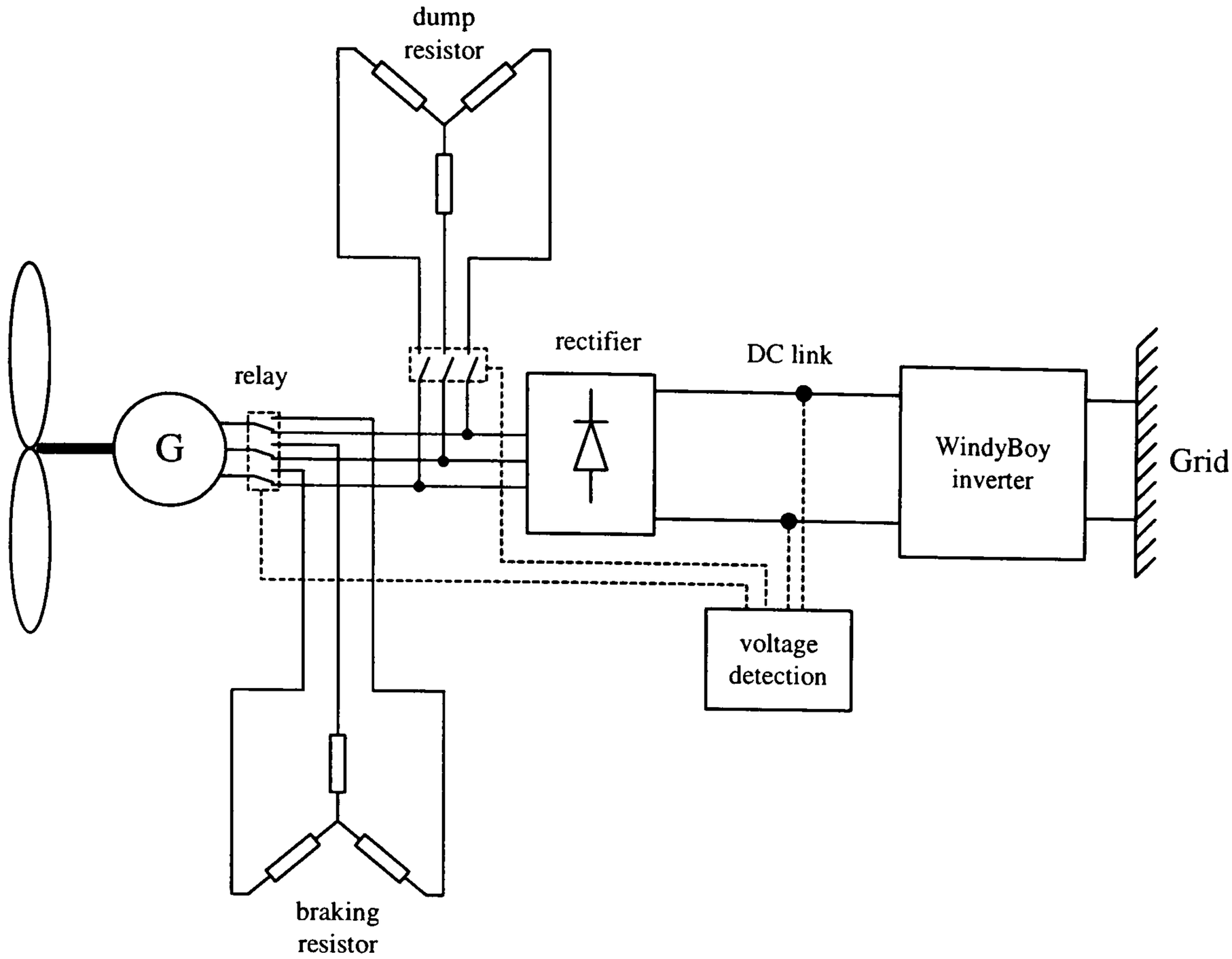

Figure 7-11. Over-speed protection system schematic

By using this strategy, the turbine can be held around the maximum power point for an increased range of wind speeds. However, if the wind speed is very high, so that even with the dump resistor switched in the turbine still accelerates, the braking resistor will eventually be activated as before, when the DC voltage passes the safety threshold (550V).

7.6.1 Modelling the speed control system

The speed control system described in the previous section can modelled in SIMULINK by assuming the dump resistance is situated on the DC rather then AC side of the rectifier, as shown in the equivalent circuit below.

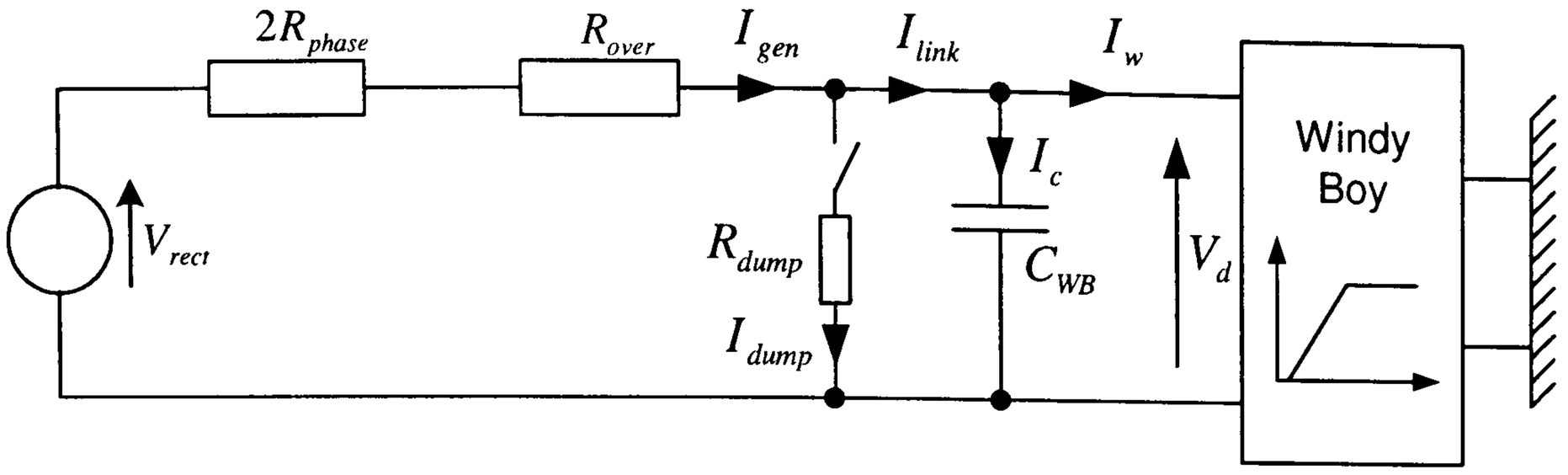

Figure 7-12. DC equivalent circuit

The dump resistance is switched in when the turbine spins fast enough to raise the DC link voltage, V_d, above a threshold voltage, V_{TH1}. A hysteresis loop can be used in SIMULINK to ensure the dump resistance remains switched in until the turbine slow sufficiently for the DC link voltage to fall below a second threshold voltage, V_{TH2}, at which point the dump resistance is switched out. Details of the modelling parameters are given in the table below. Apart from the inclusion of the dump resistance the system is otherwise identical to that modelled in Chapter 5 and described by the parameters in Table 10.

Turbine type	H-Darrieus
Blade profile	S1210
Windy Boy voltage V_1	250
Windy Boy voltage V_2	340
Dump resistance (ohms)	30
V_{TH1} (V)	340
V_{TH2} (V)	270
Turbulence intensity, k_σ	0.40
Mean wind speed (m/s)	11.0

Table 17. Modelling parameters

At low turbine speeds when the dump resistance is switched out, the system is identical to that described in Chapter 2 by equations [2-17] – [2-22]. With the dump resistance switched in, circuit analysis of Figure 7-12 gives:

$$V_d = \frac{1}{C_{WB}} \int I_c dt \qquad [7\text{-}1]$$

$$I_w = \frac{P_{out}}{\eta_{WB} V_d} \qquad [7\text{-}2]$$

$$I_{dump} = \frac{V_d}{R_{dump}} \qquad [7\text{-}3]$$

$$I_{gen} = \frac{V_{rect} - V_d}{2R_{phase} + R_{over}} = I_{link} + I_{dump} \qquad [7\text{-}4]$$

$$V_d = \frac{1}{C_{WB}} \int \left(\frac{V_{rect} - V_d}{2R_{phase} + R_{over}} - \frac{V_d}{R_{dump}} - \frac{P_{out}}{\eta_{WB} V_d} \right) dt \qquad [7\text{-}5]$$

$$T_{electrical} = \frac{(2.34 k \omega_{elec}) I_{gen}}{\omega_{gen}} \qquad [7\text{-}6]$$

7.6.2 Results of modelling

The figure below shows the operating point from the simulation as it travels around the hysteresis loop in response to the turbulent wind input.

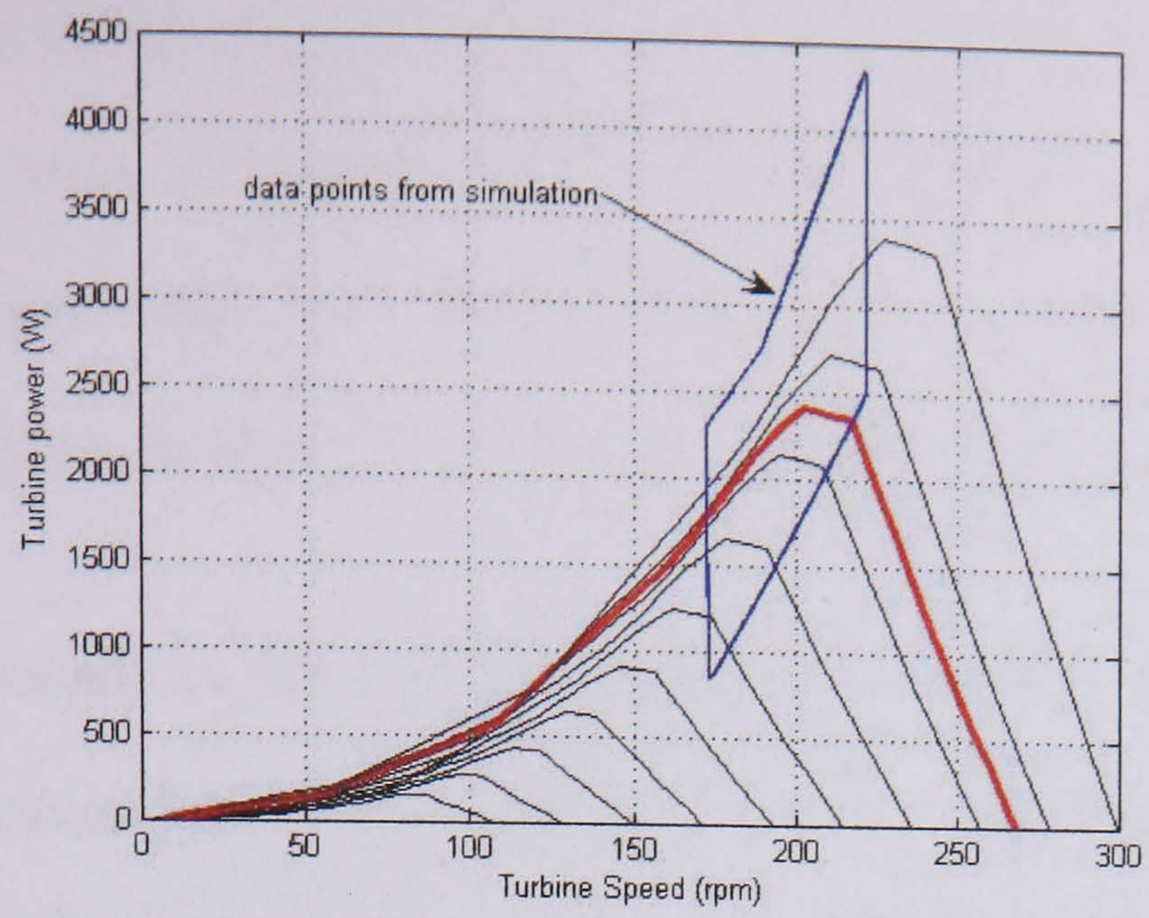

Figure 7-13. Operating point hysteresis loop (wind speeds from 5-14 m/s)

This behaviour is consistent with that described in the previous section. When the dump resistance is switched in the increase in generator load causes the rotor speed to fall until the DC link voltage decreases below its trigger threshold, at which point the dump resistance is switched out and the turbine accelerates.

The concern with this type of speed control system is that the extra power drawn by the dump resistance will draw an unacceptably large current from the armature windings. The graph below shows how the coil current increases when the dump resistor is switched in.

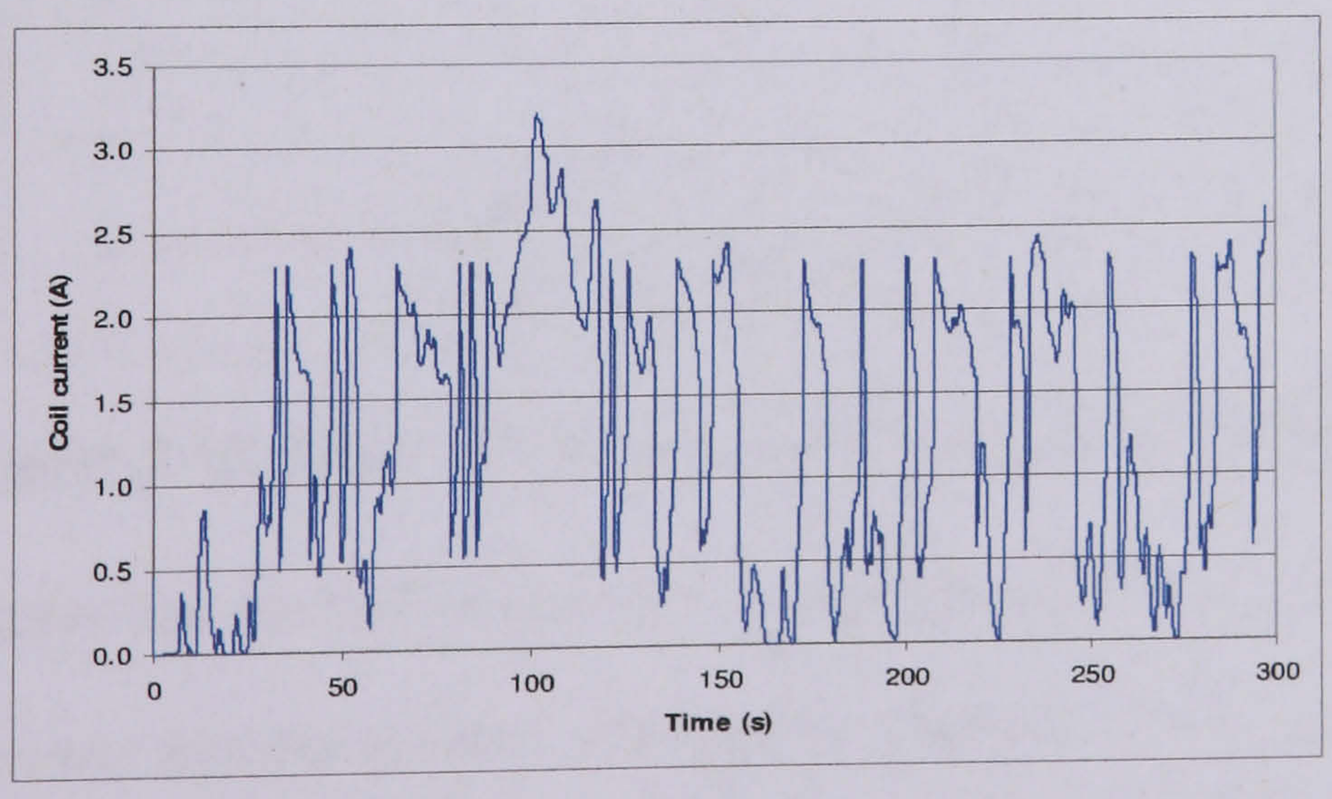

Figure 7-14. Behaviour ofcoil current when speed control is used (U_{base} = 11m/s)

Figure 7-14 shows that the highly turbulent wind creates spikes in the armature coil current of approximate magnitude 2.3A compared to the design current of 1.5A, although occasionally, when the wind speed is sufficient, a peak current of 3.2A is recorded. These spikes occur at a duty cycle (mark-space ratio) of 43%.

The effect of coil current on the winding temperature in the air-cored axial flux machine is specifically examined in Chapter 8, and it is shown that using a fully potted coil construction can increase the operating temperature of the coil significantly. It is therefore likely that the axial flux generator that has been modelled here would be able to survive such currents without serious harm. The design has also proved to be highly robust in tests.

The effect of the active speed control on the turbine's power-wind speed characteristic is shown in the figure below.

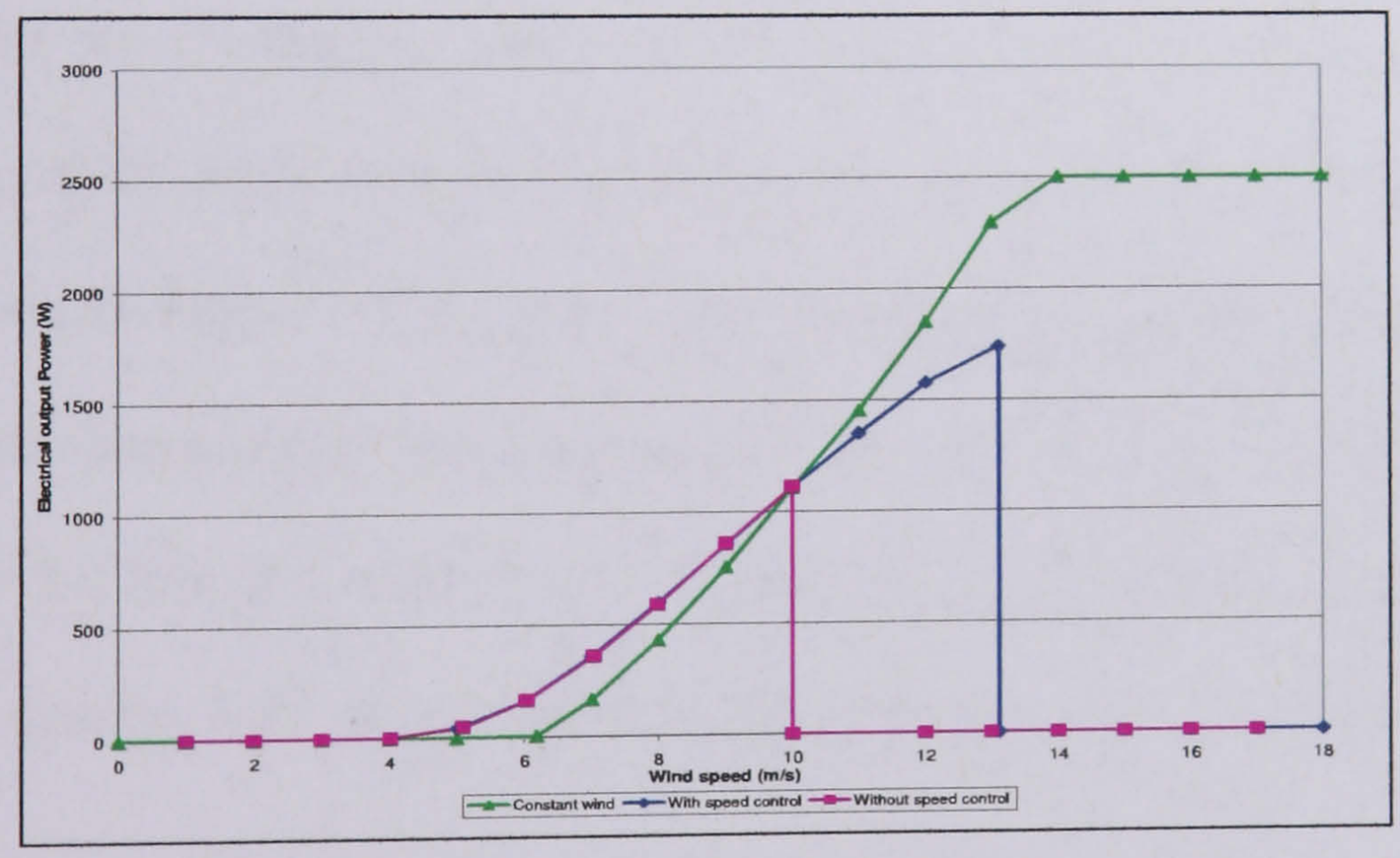

Figure 7-15. Effect of speed control on power characteristic

Figure 7-15 shows that the turbine trips out at a higher wind speed while continuing to achieve good power transfer at lower wind speeds. There is a lower power transfer then would be expected at high wind speeds (compared to constant wind) due to the turbine

would be expected at high wind speeds (compared to constant wind) due to the turbine being unable to follow the highly fluctuating wind (recall that turbulence intensity is proportional to wind speed). The net effect is to produce a significantly improved energy capture figure compared to increasing the turbine inertia, as shown in the table below.

Speed control system	No speed control	No speed control	3x Inertia	Dump resistance
Wind regime	Constant wind	High turbulence	High turbulence	High turbulence
Multiples of Turbine inertia	x1	x1	x3	x1
Trip wind speed (m/s)	15.3	9.6	11.0	13.1
Energy yield (kWh/yr)	1442	1212	1304	1836

Table 18. Effect of speed control on trip voltage and Energy yield (based on MAWS=5.0m/s)

The table above shows that the active speed control system produces greater energy capture in turbulent wind than is achieved by the benchmark case of a system with no speed control in a constant wind field. This is because the power-wind speed characteristic of the active speed control system is more favourable at low wind speeds, as can be seen in Figure 7-15. (This arises because there is more power available in turbulent wind than constant wind for reasons given in section 7.5.) For a wind regime of MAWS = 5.0 m/s, the wind speed will be low for large parts of the year and this favours the system with active speed control, so producing greater annual energy capture.

7.7 Conclusions

Over-speeding is a problem particular to vertical axis turbines due to the fact they cannot be turned out of the wind. To prevent over-speeding in strong winds causing

voltages in excess of 600V, a voltage protection relay is required to shut the turbine down by connecting a braking resistance across the generator output. However, such a system can be triggered by wind gusts which can significantly affect the annual energy capture of the turbine.

It was found that increasing the turbine inertia smoothed out the wind speed fluctuations, and this allowed a higher average wind speeds to be accepted by the turbine without tripping. However, a turbine with increased inertia is less able to follow the fluctuating wind speed and this has a detrimental effect on energy capture.

A second, more effective method of speed control is to introduce a dump load which can be switched in as the turbine approached rated speed, and switched out once the turbine has slowed. The simulation shows that this strategy can increase the annual energy capture over a turbine without a speed control system by 51%. Although the armature coil current (and therefore heat) increases as the extra load is switched in, the axial flux design allows greater power capacity to be accommodated easily by simply making the generator larger.

Chapter 8

Stator thickness optimisation of the air-cored axial flux machine

8.1 Introduction

The MATLAB/SIMULINK modelling described so far has considered a single generator which employs an air-cored axial flux topology. This topology lends itself to direct-drive applications because it allows large diameter multi-pole machines to be constructed without the need for specialist manufacturing materials such as electrical steel laminations. Although the generator has been integrated with two turbine systems [25, 26], little work has been done to verify the thermal model used in the design process or to examine where the optimal stator thickness or optimal armature current density may lie. In this chapter the 1kW, 300rpm generator depicted in Figure 2-6 is used as a case study to investigate these boundaries.

Section 8.2 examines the design process and describes how a comparison of different designs may be made using a design spreadsheet, while the case for using a thinner stator in the generator is laid out in section 8.3.

The heat transfer mechanism inside the axial flux machine is examined in section 8.4. The thermal conductivity of the armature winding and acetal bobbin, and the surface heat transfer coefficient from the bobbin to the air, are also measured by experiment and used to verify the thermal model.

The thermal model is used in sections 8.5 - 8.6 to examine how the efficiency, output power, current density and active weight of the generator are affected by stator thickness. An alternative coil construction to a bobbin winding is examined in section 8.7 which allows a higher operating temperature to be reached, and conclusions are drawn in section 8.8 as to whether such a construction may be useful.

8.2 Optimisation rationale

Optimising the axial flux topology for different sizes of machine is highly complex due to the interplay between the many design parameters. The process is further complicated by the fact that a given design may be optimised in different ways depending on what the application demands. For example, a design may be optimised for cost, efficiency, reliability, output power, weight, stiffness, etc., depending on how the generator is to be integrated with the turbine and how much confidence the designer has in the reliability of the WECS. The level of confidence in the device will tend to increase as the product moves towards commercialisation and more hours of field testing are clocked up, and this allows refinement of the design as practical problems come to light.

Although many of the generator's dimensions are constrained by practical requirements, such as the size of magnets that can be easily handled or the ease with which coils can be wound and fitted into the stator, one aspect of the design is essentially unconstrained: the stator thickness. This topic will be examined in the following chapter using the 1kW, 300 rpm machine as the basis for a design case study. The 1kW machine is considered here because a designated test rig had previously been constructed which allowed the design predictions to be verified.

The global dimensions for a 1kW, 300 rpm axial flux generator with round coils and magnets can be generated using the design equations detailed in reference [35], and these can be arranged in a design spreadsheet format to allow easy manipulation. A design comparison can be made by duplicating this spreadsheet many times and allowing only one of the independent design variables to vary between copies - in this case, the stator thickness. The other independent design variables relating to the geometry of the generator, such as the diameter of the machine or the size of the magnets etc., are held constant while the dependent design variables, such as the air gap flux density or the generated EMF per coil are allowed to vary (further details of the spreadsheet design process are given in Appendix D). This allows the relationship between the stator thickness and quantities such as the specific power, efficiency and active weight of the generator to be isolated.

8.3 The case for a thinner stator

There are a number of arguments for using a thinner stator in the generator construction. Firstly, the rotor plates can be brought closer together, so increasing the flux density at the armature coil windings. This higher magnetic loading increases the specific apparent power of the generator and hence leads to a more compact machine. The second advantage concerns heat transfer within the stator coils. Most electrical machines are limited by the operating temperature of their coil windings. By reducing the stator thickness, heat generated in the winding has a shorter path to the bobbin surface and this leads to a lower winding temperature (or allows a higher current density to be imposed for the same winding temperature). Figure 8-1 shows how the flux density and current density can be increased at lower stator thicknesses. The flux density is taken at the

centre of the armature coil; the current density is based on a maximum winding temperature of 90 °C (this assumption is discussed in more detail in section 8.4).

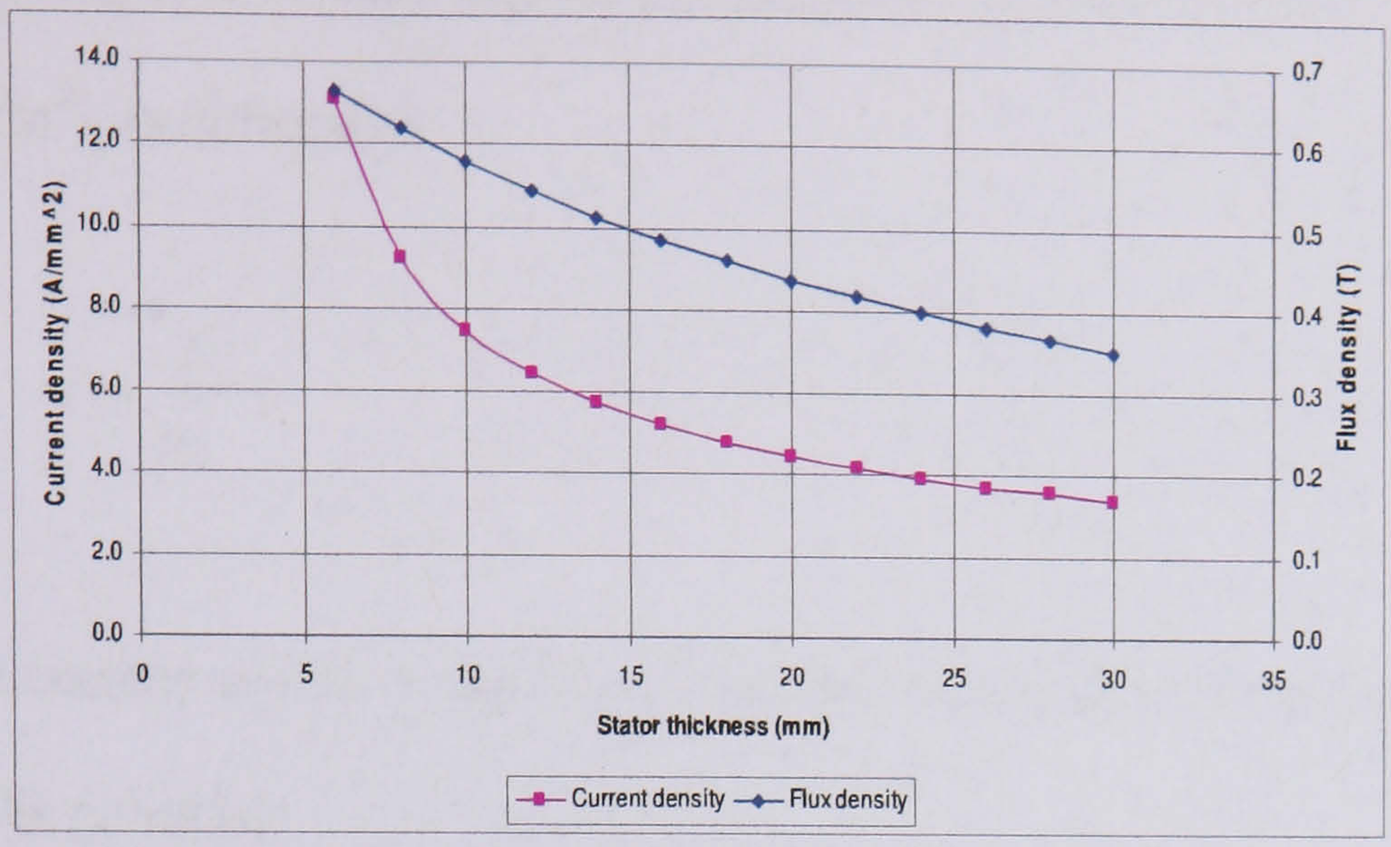

Figure 8-1. Stator thickness versus flux density and current density for a constant armature temperature

Of course reducing the stator thickness also results in less copper being present in the machine and this will have a detrimental effect on output power. It is therefore important to examine whether the increase in magnetic loading and current density will compensate for the low copper content. Put formally, the apparent power, S, of the generator is given by:

$$S = k\hat{B}\hat{K}\left(D_{gen}^2 L_{gen}\right)n_{rpm} \qquad [8\text{-}1]$$

Where k is the machine constant, $\hat{B}$ is the magnetic loading, $\hat{K}$ is the current loading, D_{gen} and L_{gen} are the diameter and length of the generator, and n_{rpm} is the speed. The current loading, $\hat{K}$ (A/m), gives a measure of the quantity of current that can be fitted into the active area and is given by:

$$\hat{K} = \frac{n_c I(2N_c)}{\pi D_{mean}} \qquad [8\text{-}2]$$

where n_c is the number of coils and N_c is the number of turns per coil. Since the current density, J (A/m^2), is defined as:

$$J = \frac{I}{a_w} \qquad [8\text{-}3]$$

where I is the current and a_w is the cross-sectional area of the wire strand, the number of turns per coil is given by:

$$N_c = \frac{(r_o - r_i)t_c \varepsilon}{a_w} \qquad [8\text{-}4]$$

where r_o and r_i are the outer and inner coil radii, t_c is the coil thickness and ε is the coil packing factor. The current loading can then be described as:

$$\hat{K} = \frac{2n_c \varepsilon (r_o - r_i) J t_c}{\pi D_{mean}} = k' J t_c \qquad [8\text{-}5]$$

By substituting equation [8-5] into [8-1] an expression for the apparent power of the generator in terms of stator thickness, current density and magnetic loading can be found:

$$S = k' \hat{B} J t_c \left(D_{gen}^2 L_{gen}\right) n_{rpm} \qquad [8\text{-}6]$$

As the stator thickness, t_c, is reduced, the quantity $\hat{B}Jt_c$ may increase because the higher

current density, J, and magnetic loading, $\hat{B}$, may off-set the effect of reducing the coil thickness, t_c.

However, although reducing the stator thickness may seem advantageous in terms of reduced material costs, it comes at the expense of lowering the efficiency. This is because Joule loss per unit volume in the armature windings is given by:

$$P_{joule} \alpha \ J^2 \rho_{cu} A_{active} t_c \qquad [8\text{-}7]$$

where ρ_{cu} is the resistivity of the copper winding and A_{active} is the active area. As the stator thickness is reduced the current density can be increased and this allows the J^2 term to dominate over the effect of reducing t_c.

8.4 Heat transfer in an axial flux machine

In order to assess the impact of reducing the stator thickness, the heat transfer mechanism inside the armature windings must first be understood as this allows the maximum armature current density to be calculated. The following section will address this topic.

The axial-flux generator comprises two rotor discs containing magnets, spinning above and below a stator disc containing the armature coils. Heat is generated in the windings due to Joule loss and Eddy current loss (mainly Joule loss), and is removed by cooling air passing over the stator surface. The air flow is driven by the motion of the rotor magnets which act like fans, as shown schematically in Figure 8-2.

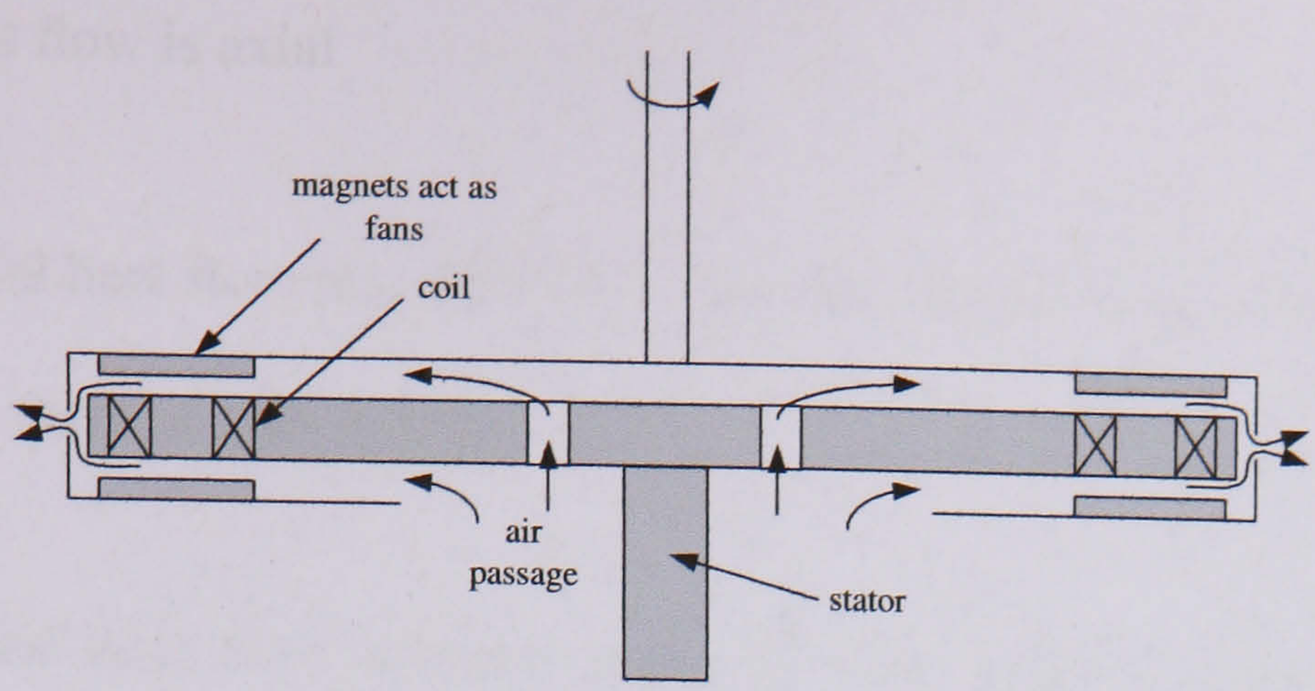

Figure 8-2. Schematic of the axial flux cooling system

8.4.1 Thermal model of the heat transfer problem

An armature bobbin winding from the generator is shown in the figure below. The copper wire is wound onto an acetal bobbin which is dropped into a PVC stator (shown in Figure 2-6 (c)).

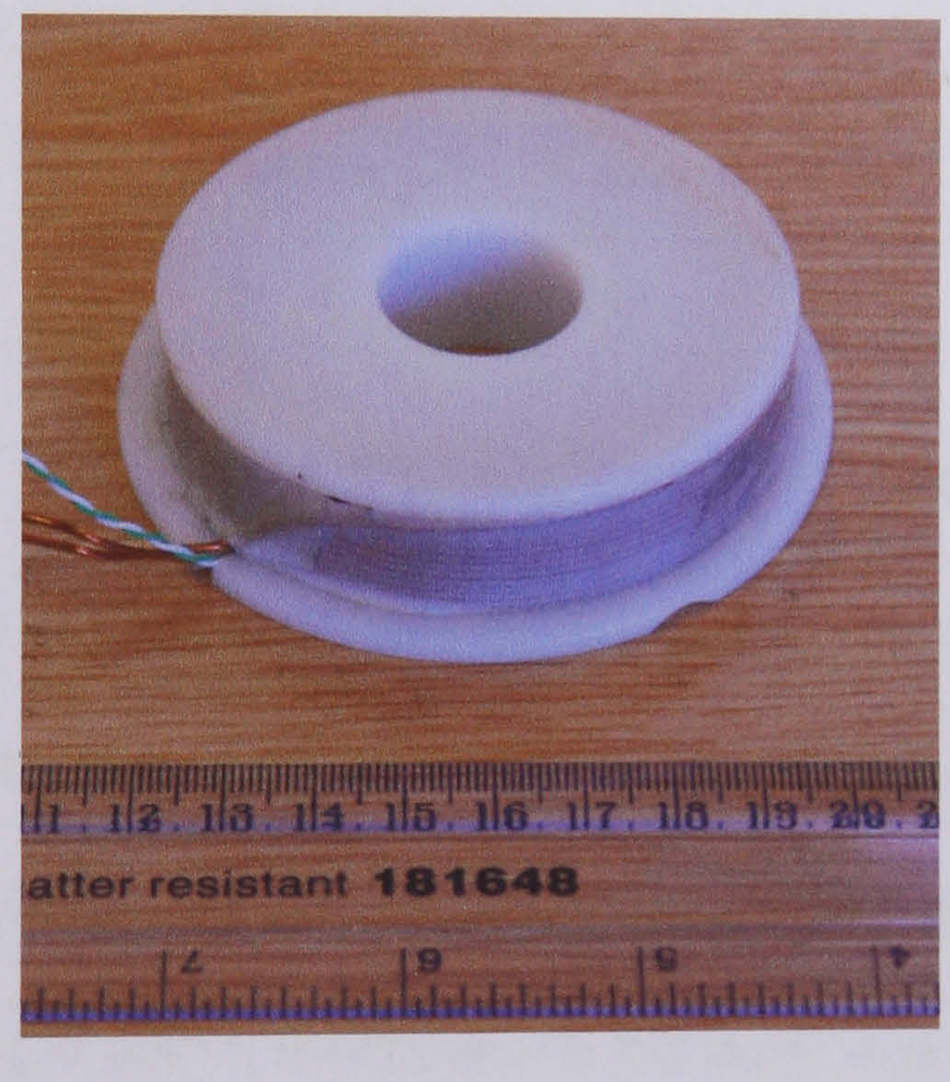

Figure 8-3. Armature bobbin winding

A lumped parameter thermal model of the heat transfer process can be constructed by considering the heat flow through a cross-section of the bobbin between discrete nodes, as depicted in Figure 8-4. The model assumes:

1. All heat flow is axial

2. No radial heat flow into the PVC – the PVC has a very low thermal conductivity and the thermal path is long

3. No radial heat flow into the centre of the bobbin – there is very little heat transfer since very little cooling air gets to this surface.

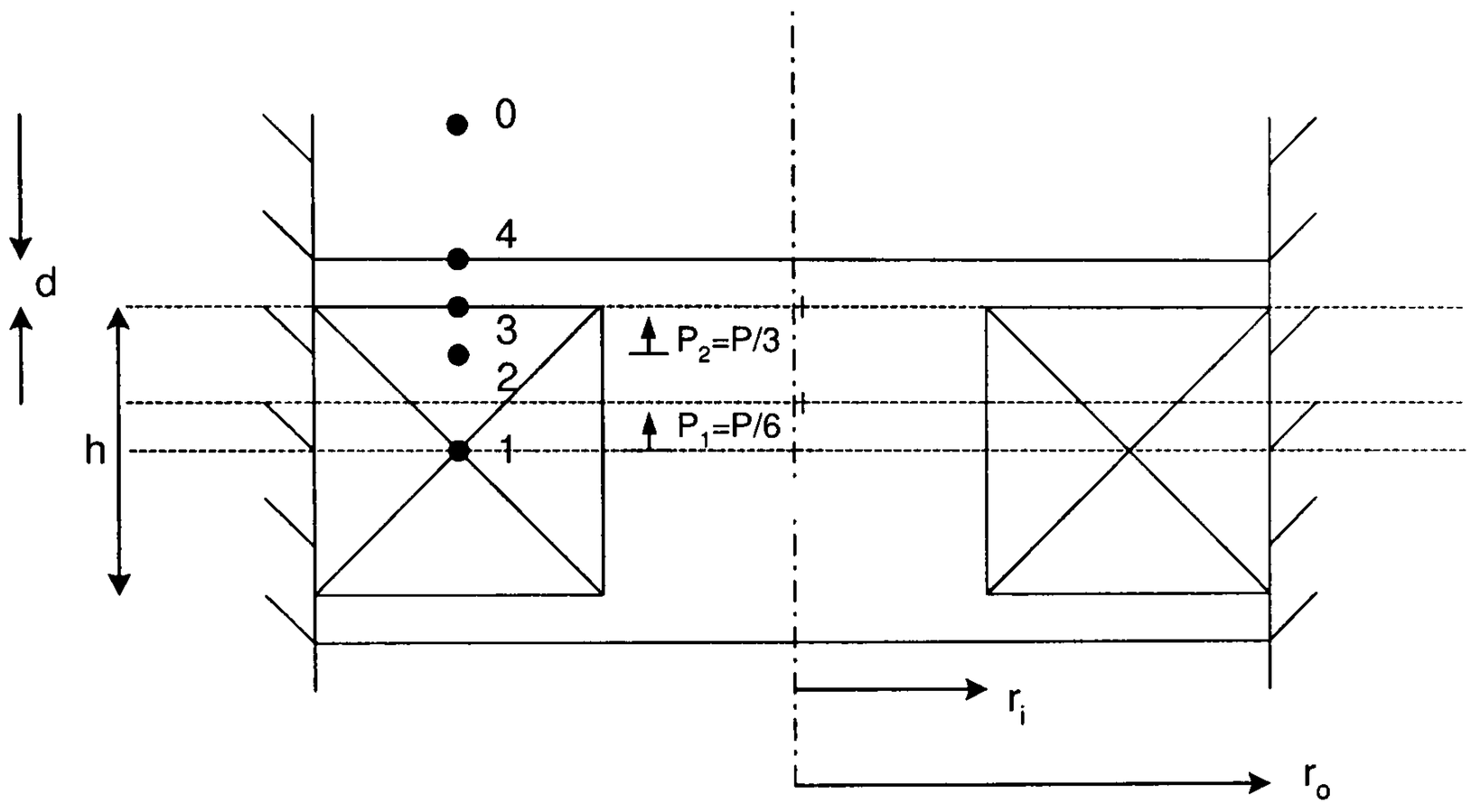

Figure 8-4. The heat transfer model

The copper winding is divided into three segments with the heat loss divided equally between each segment. Heat can travel only axially up and down. The problem is symmetrical. Heat is assumed concentrated at nodes 1 and 2. At node 1 heat can flow in both directions so half the power dissipated at this node will flow upwards. Between each node is a thermal resistance the value of which depends on the distance between nodes, the thermal area and the material thermal conductivity. Heat transfer from node 4 to the cooling air is by convection. By symmetry the thermal resistance between node 2 and 3 will be half that between node 1 and 2.

The thermal model can be represented as the electrical analogy depicted in Figure 8-5

where the thermal resistances are given by:

$$R_{12} = \frac{h}{3}\frac{1}{k_{wind} A_c} \qquad [8\text{-}8]$$

$$R_{23} = \frac{1}{2} R_{12} \qquad [8\text{-}9]$$

$$R_{34} = \frac{d}{k_{bob} A_c} \qquad [8\text{-}10]$$

$$R_{40} = \frac{1}{h_s A_c} \qquad [8\text{-}11]$$

where: $A_c = \pi(r_o^2 - r_i^2)$, k_{wind} is the effective thermal conductivity of the copper/varnish/air that makes up the winding, k_{bob} is the thermal conductivity of the bobbin, and h_s is the surface heat transfer coefficient.

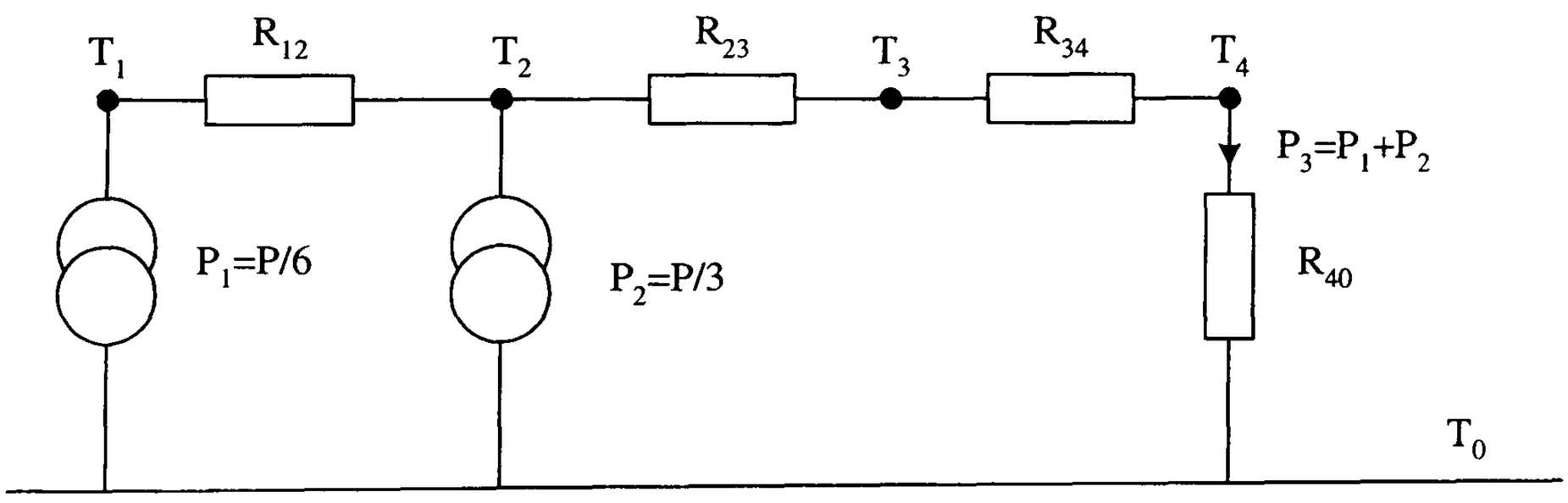

Figure 8-5. Thermal model

Basic circuit analysis shows that:

$$T_4 = P_3 R_{40} + T_0 \qquad [8\text{-}12]$$

$$T_3 = P_3 R_{34} + T_4 \qquad [8\text{-}13]$$

$$T_2 = P_3 R_{23} + T_3 \qquad [8\text{-}14]$$

$$T_1 = P_1 R_{12} + T_2 \qquad [8\text{-}15]$$

Although the thermal conductivity of copper is high, the heat must also travel through the varnish surrounding the wire and across any air space between the wires, which significantly reduces its value. The surface heat transfer coefficient depends on the air flow across the bobbin surface and will improve with rotational speed. Although the thermal conductivity of the acetal bobbin is known, the effective thermal conductivity, which takes account of non-axial heat flow, is unknown and must be found by experiment. This is also true for the surface heat transfer coefficient of the bobbin and thermal conductivity of the winding, and this is the subject of the following sections.

8.4.2 Experimental measurement of thermal conductivity of the bobbin and winding

By constructing a small wind tunnel, the heat transfer mechanism in a test armature coil can be examined in isolation to obtain values for the thermal conductivities of the acetal bobbin, k_{bob}, and armature winding, k_{wind}. The wind tunnel is depicted in Figure 8-6 without its lid.

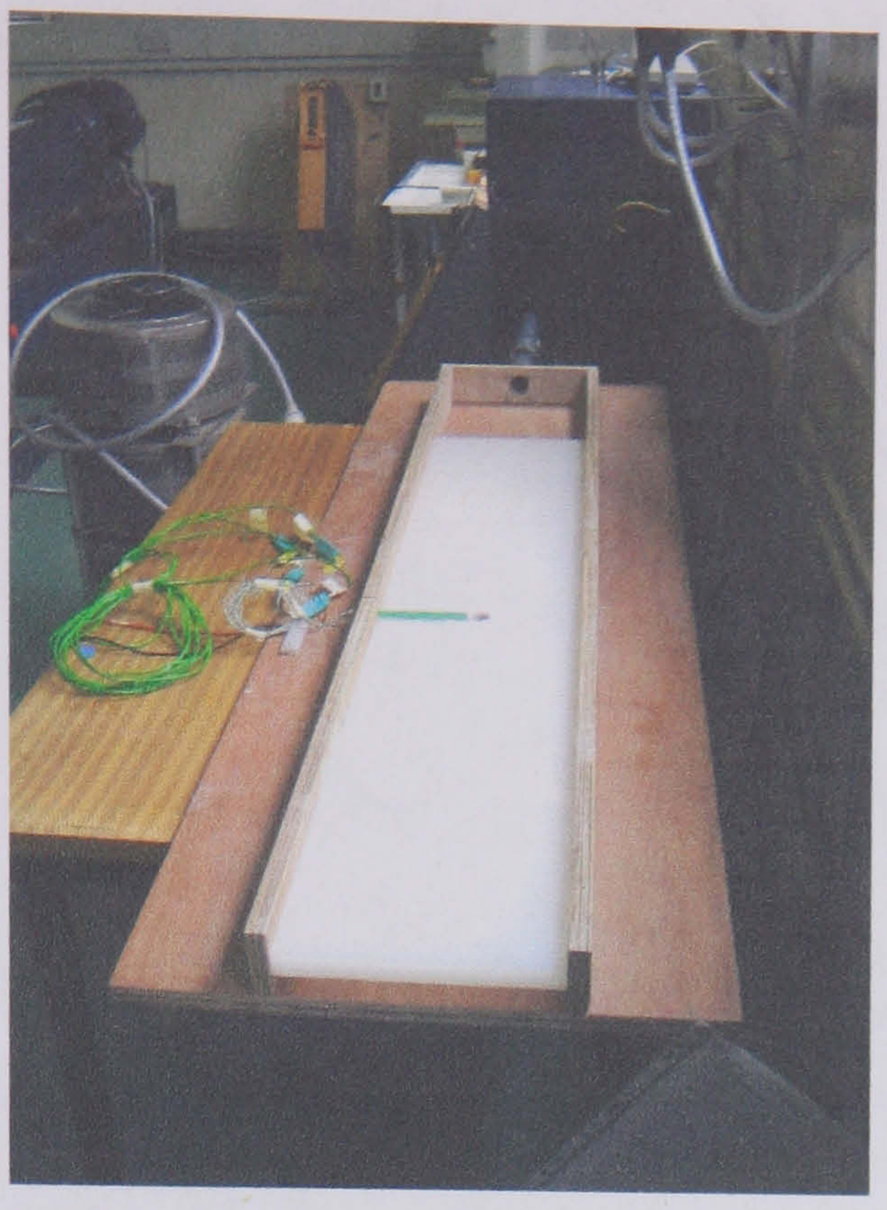

Figure 8-6. Wind tunnel

The top surface of the test bobbin can be seen in the centre of the image (the white disc). The bobbin was mounted in the centre of a plastic panel which serveed to replicate the generator's stator. The panel was elevated to allow cooling air to pass over the top and bottom surface of the coil to mimic the cooling in the generator; the cooling air was generated by a suction device mounted at the far end of the wind tunnel (this can be seen at the top of the image). A constant DC current was passed through the coil and the temperature measured using thermocouples located at the three nodes shown in the lumped parameter model in Figure 8-4. The locations of the thermocouples are shown in the figure below, which shows a cross-section though the bobbin winding. A fourth thermocouple was used to measure the ambient air temperature.

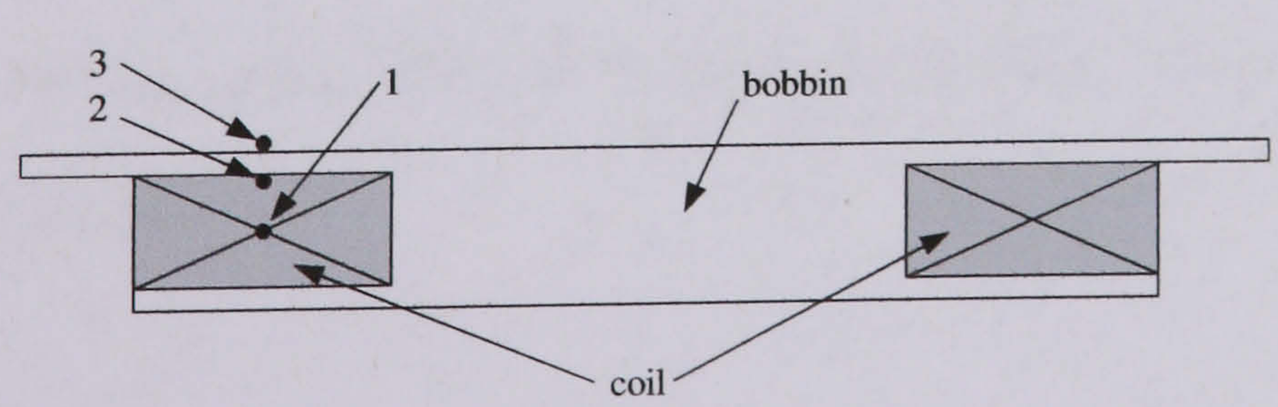

Figure 8-7. Location of thermocouples in bobbin

The temperature measured at each of the thermocouples is shown in the figure below as a function of air speed.

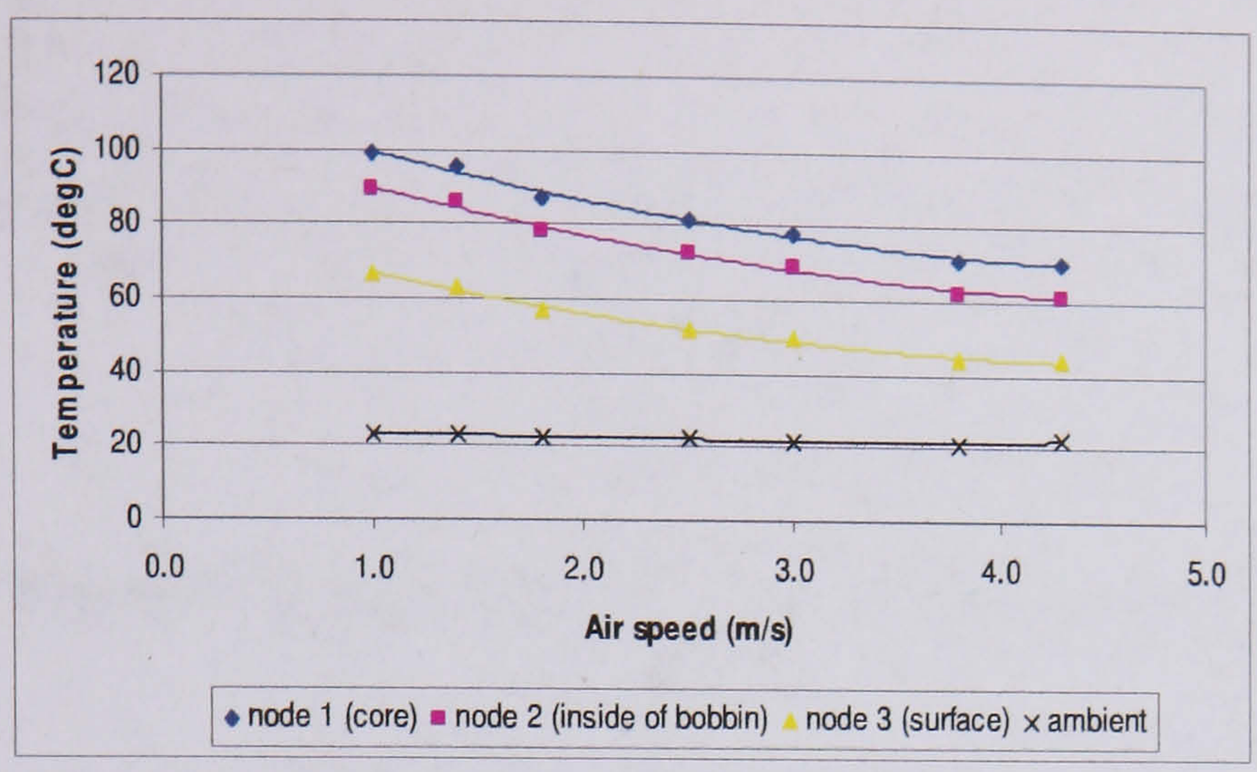

Figure 8-8. Coil node temperatures as a function of air speed

Equations [8-14] and [8-15] can be combined to eliminate T_2, and thus obtain an expression for k_{wind} in terms of T_1 and T_3 only. A similar manipulation can be used to find an expression for k_{bob}, as shown below.

$$k_{wind} = \frac{5}{36}\frac{hP}{A(T_1 - T_3)} \qquad [8\text{-}16]$$

$$k_{bob} = \frac{1}{2}\frac{dP}{A(T_3 - T_4)} \qquad [8\text{-}17]$$

The temperature differences T_1-T_3 and T_3-T_4 can be obtained from the difference in temperatures between thermocouples 1 & 2, and 2 & 3.

Values for k_{wind} and k_{bob} calculated from the above expressions are shown in Figure 8-9 for a range of air speeds.

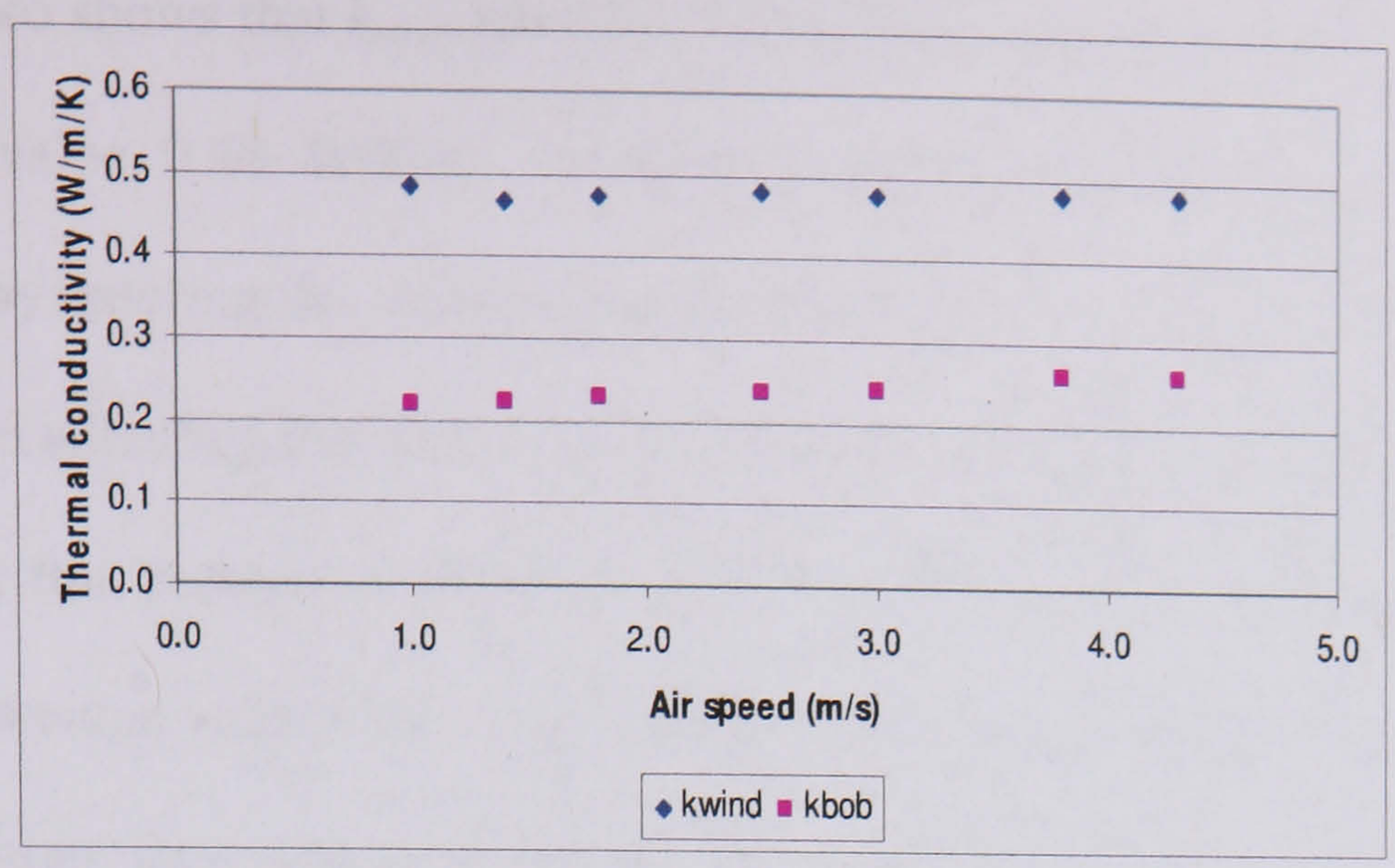

Figure 8-9. Thermal conductivity of bobbin winding (at current density of 4.2A/mm^2)

Figure 8-9 shows that k_{bob} increases slightly with air speed and that the average value of 0.24 W/K/m is similar to that quoted in the datasheet for acetal of 0.23-0.31 W/K/m [112]. The slight increase in k_{bob} with respect to air speed is most likely due to non-axial heat flow, as shown below.

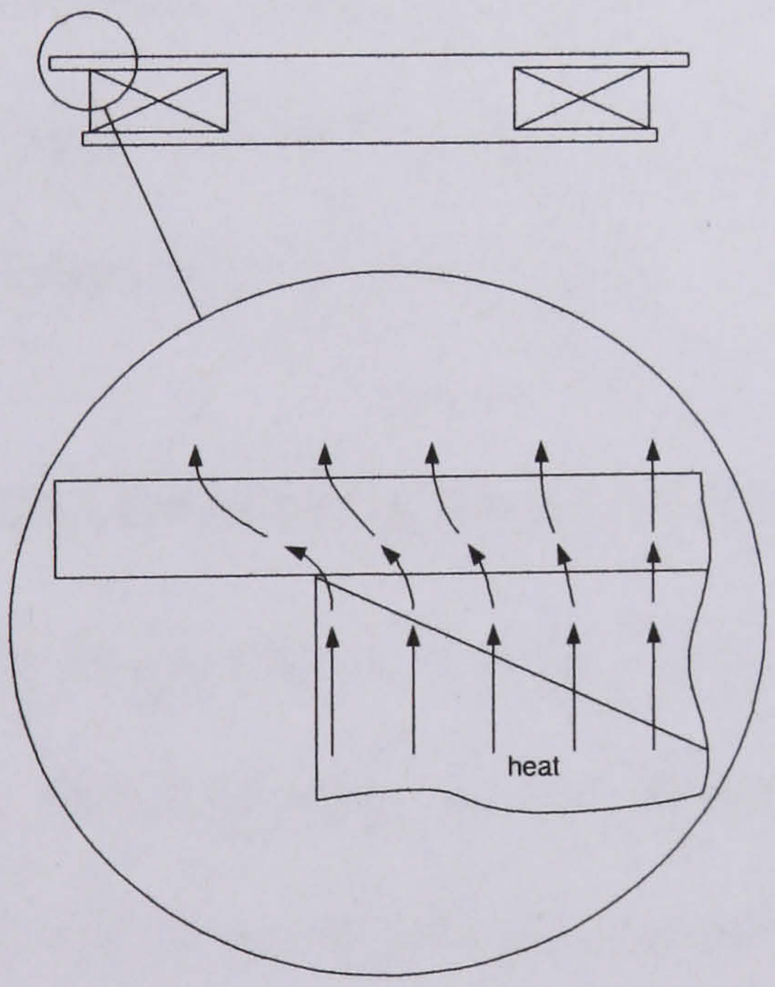

Figure 8-10. Non-axial heat flux

For the purposes of this study, however, an effective value of k_{bob} of 0.24 W/K/m^2 has been assumed.

Figure 8-9 also shows that k_{wind} remains constant throughout the air speed range, giving an average value 0.48 W/K/m. A check can be made on k_{wind} using the design spreadsheet by entering the values of rotor speed and coil current used in the generator tests, and then adjusting the values of k_{wind} to achieve the observed winding temperature. By repeating this process at different load conditions and cooling regimes (see next section), an average value for k_{wind} of 0.44 W/K/m was calculated. This value is likely to be more accurate then that produced by the wind tunnel experiment since it has been calculated by averaging the thermal properties of many armature coils in a real generator, and so this value has been used in the study.

The thermal conductivity of the winding is low compared to that of, say, pure copper (390 W/K/m) and this could be improved by using vacuum impregnation to remove air pockets between the wire strands. Although such a construction would aid cooling, the heat transfer mechanism is dominated by the surface heat transfer coefficient and so the improvement would be slight. The measurement of the surface heat transfer coefficient in the test generator is discussed in the next section.

8.4.3 Experimental measurement of surface heat transfer coefficient

The surface heat transfer coefficient, h_s, of the bobbin can be measured in the test generator by mounting thermocouples at the bobbin surface and recording the temperature difference between the bobbin and the ambient air. A value for h_s can then be calculated according to the equation below.

$$\frac{1}{2} P = h_s A_c \Delta T \qquad [8\text{-}18]$$

The surface heat transfer coefficient depends on the level of cooling air permitted to

circulate through the generator and three cooling regimes (shown below) have been considered.

(a) (b) (c)

Figure 8-11. Three cooling regimes

In cooling regime (a) the holes in the plastic retaining ring have been obstructed by tape to prevent the flow of cooling air. In regime (b) the cooling holes are fully exposed to allow some air to circulate. In regime (c) the entire plastic retaining ring has been removed to allow air to circulate without restriction. Of the two turbine systems that have adopted the axial flux generator, the 1kW, 300rpm Savonius turbine [26] used cooling regime (b) while the 2.5kW, 250rpm Darrieus turbine [25] used cooling regime (c).

The average surface heat transfer coefficient was calculated for the three cooling regimes and the results are shown below.

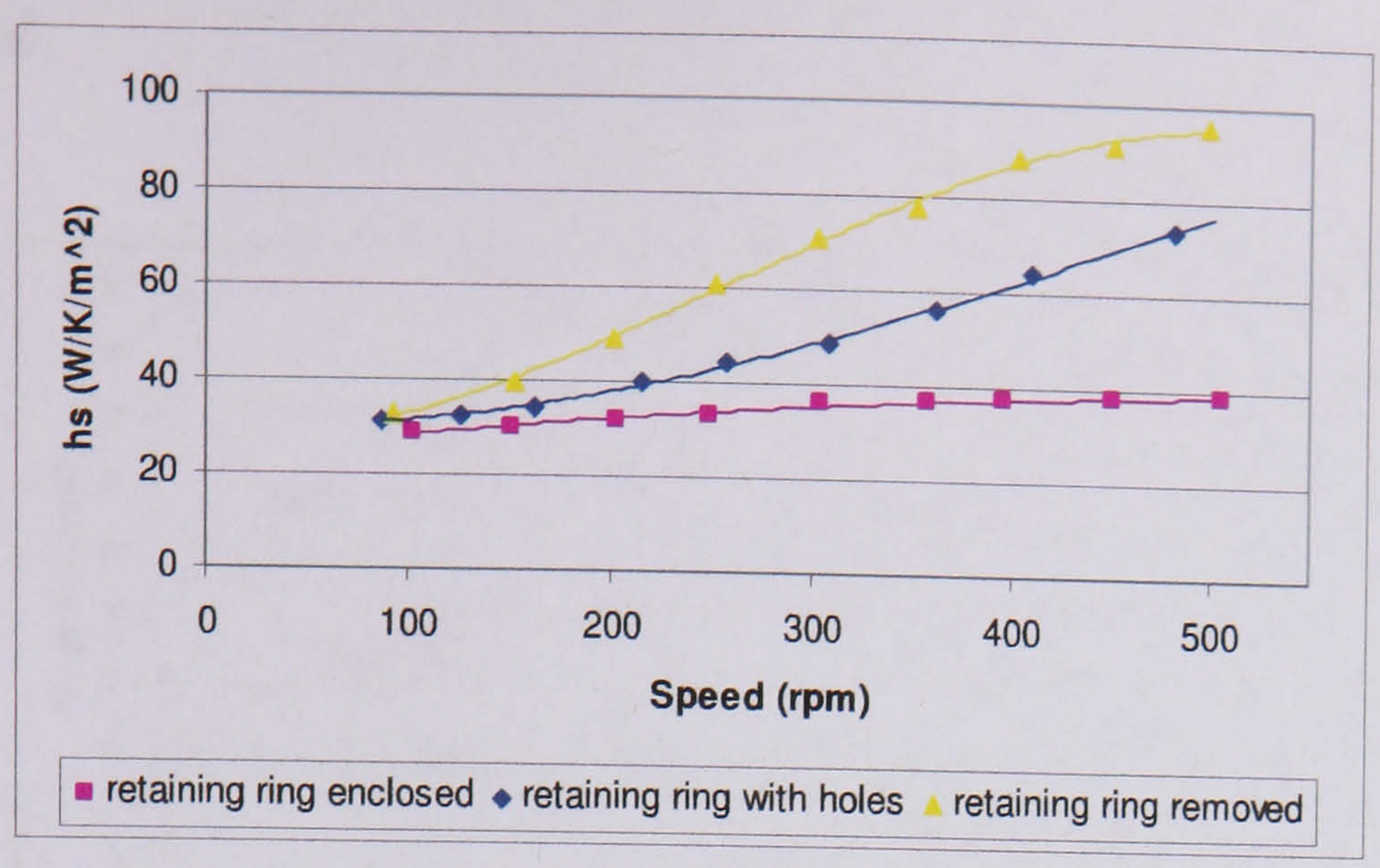

Figure 8-12. Heat transfer in armature coils for the three cooling regimes

Figure 8-12 shows that removing the plastic retaining ring significantly improves the surface heat transfer coefficient, especially at low speeds, and this would allow a higher current density to be imposed on the armature winding.

8.4.4 Validation of the lumped parameter model

A validation of the lumped parameter thermal model can be made by comparing the predicted coil temperature rises to those measured in tests. The values of k_{bob}, k_{wind} and h_s, which have been found by experiment, are summarised in the table below along with the generator's load conditions. The surface heat transfer coefficient is taken from cooling regime (b) (retaining ring with holes) at 500rpm.

Generator speed (rpm)	500
Generator power (kW)	2.0
Armature current density (A/mm^2)	4.15
k_{bob} (W/m/K)	0.24
k_{wind} (W/m/K)	0.44
h_s (W/m^2/K)	75

Table 19. Parameters used in the validation of the lumped parameter model

A comparison between the measured temperature rise at the centre of the winding and at the bobbin surface, and those predicted by the lumped parameter model, are shown in

the figure below.

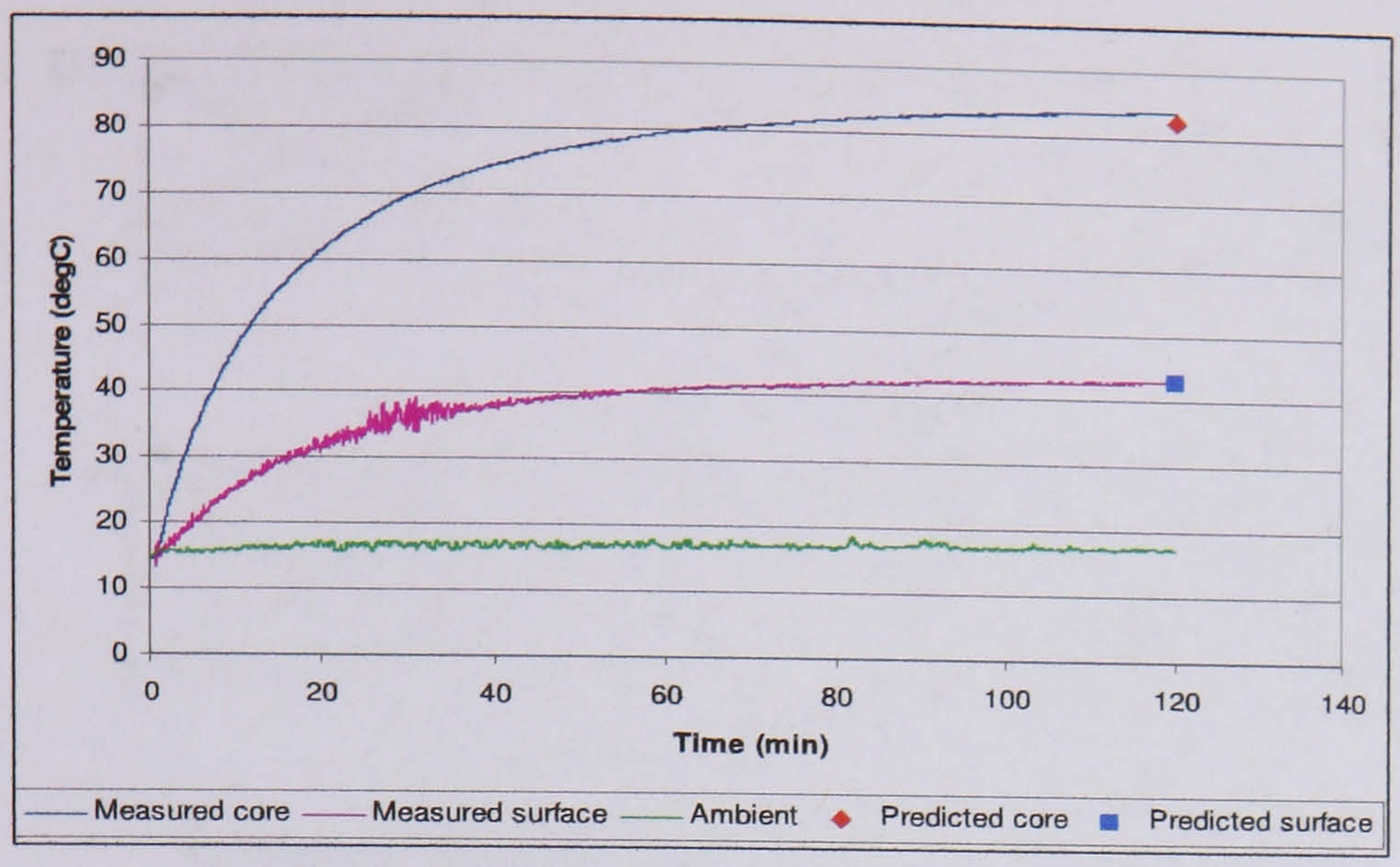

Figure 8-13. Comparison between measure and predicted values of temperature rise in coil core and at coil surface

Figure 8-13 shows that the steady-state temperature rise agree well with values predicted by the lumped parameter model, with an error of less then 3%. This gives confidence both to the model assumptions and to the values of the coefficients measured by experiment.

8.4.5 Maximum operating temperature

The lumped parameter model is an important design tool as it allows the armature winding temperature to be calculated within the design spreadsheet based on the coil current. Knowing the maximum operating temperature of the coil is therefore vital as it places a limit on the maximum allowable current, and this can be found by destructive test. Such a test found that at temperatures above 110ºC, the structural integrity of the bobbin was compromised, as shown in Figure 8-14, which lead to a maximum operating temperature of 90ºC being imposed on the bobbin winding. Through the thermal model, this can be equated to a maximum armature current density of 4.2 A/mm^2 at 300 rpm in cooling regime (b). The assumption that the current density is limited by a maximum

winding temperature of 90 ℃ has therefore been used throughout this study.

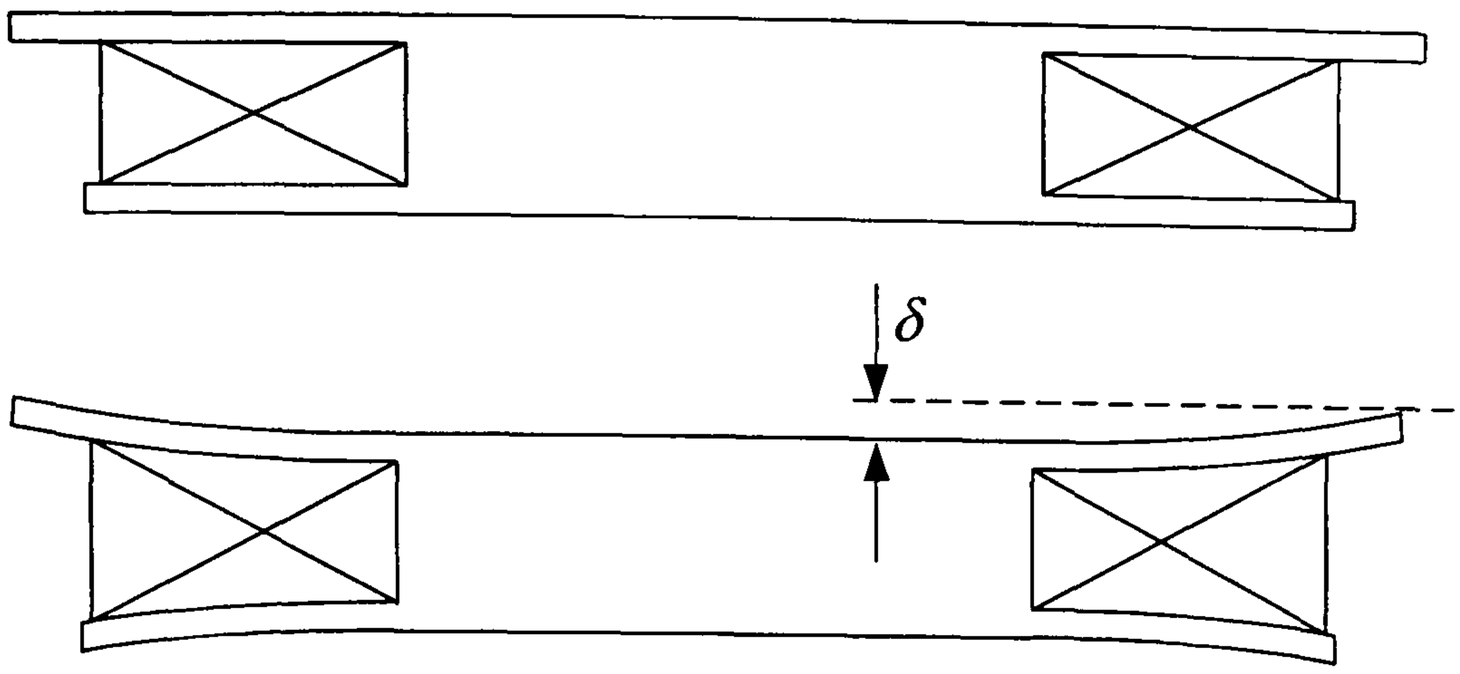

Figure 8-14. Destructive test on armature coil

In destructive testing the coil temperature was held at 110 ℃ for 20 minutes and this produced a deflection $\delta \approx 0.5$mm.

8.5 Effect of stator thickness on power and efficiency

The lumped parameter model developed in the previous section can be integrated with the design spreadsheet to examine how the generator's power and efficiency are affected by stator thickness. As stated, this analysis assumes the generator operates at a maximum winding temperature of 90°C, an assumption which can be implemented in the design spreadsheet by adjusting the current density until the desired temperature is reached. The predicted power and efficiency of the subsequent generator design can then be recorded, and this is shown in the figure below along with two experimental data points taken from the 1kW, 300rpm machine with a 20mm stator. As can be seen, predicted and measured values are in close agreement.

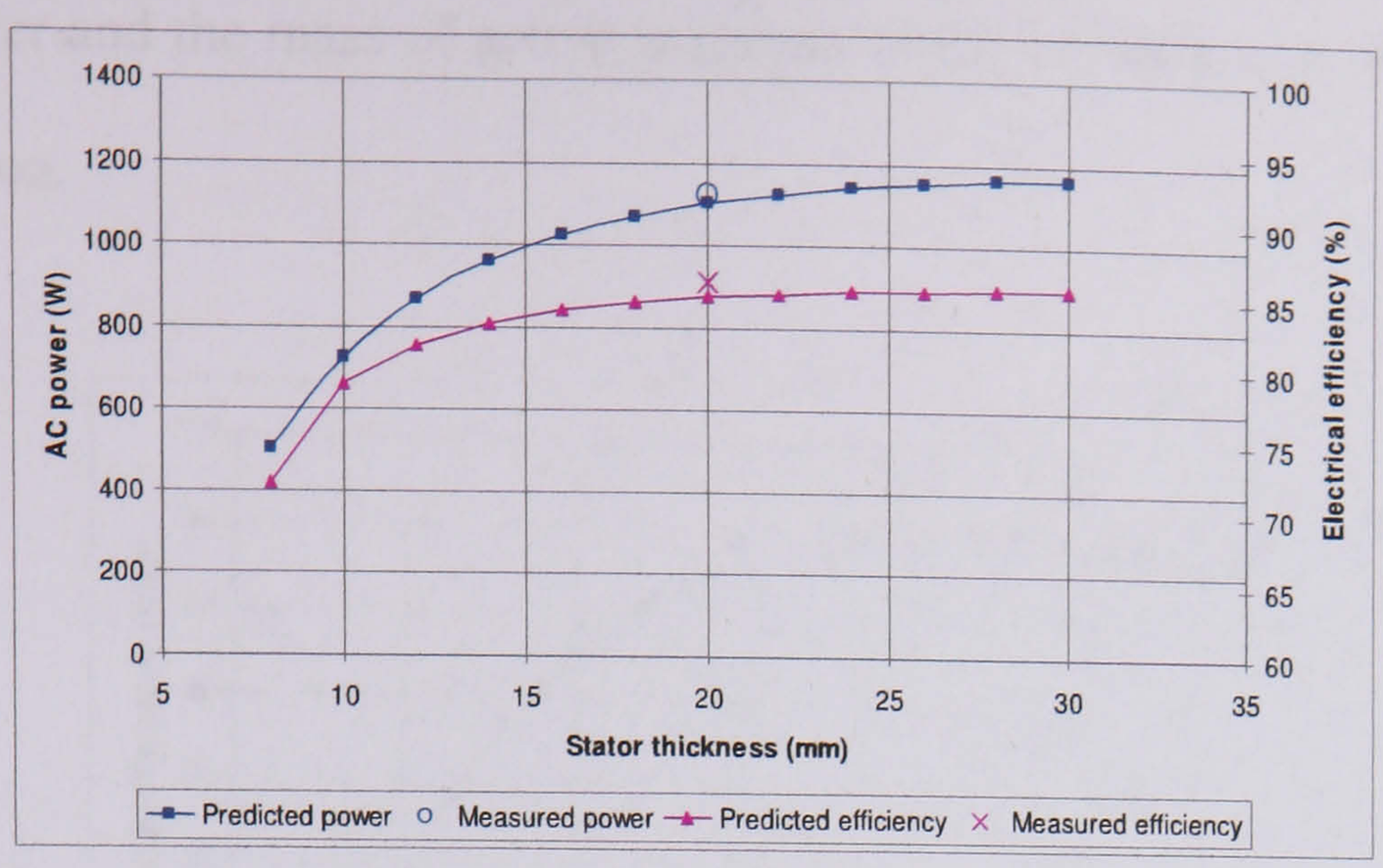

Figure 8-15. Stator thickness versus power and efficiency (300 rpm; 90°C winding temperature)

Figure 8-15 shows that there is no significant advantage in power or efficiency in constructing a generator with a stator thicker then 20mm (equating to a coil height of 14mm), and indeed such a design would incur a cost penalty due to the extra copper. As the stator thickness is reduced below 20mm the power begins to fall away more steeply. In terms of the generator power equation (equation [8-1]), the $\hat{B}Jt_c$ term in fact decreases rather then increases (as postulated in section 8.3) as the stator thickness is reduced. The effect of the increased magnetic loading and the increased current density is no compensation for the reduction in copper (i.e. fewer turns) in the stator.

The machine weight is another important design consideration, especially for smaller devices which would ideally be handled by no more then two men. Figure 8-1 shows that reducing the stator thickness leads to an increase in the magnetic flux density as the rotor plates are brought closer together, and this must be accommodated for by thickening the rotor back iron to prevent saturation. This represents an increase in machine weight which mitigates the effect of reducing the copper mass by thinning the stator. This relationship can be demonstrated by plotting active specific power against stator thickness, Figure 8-16. Here, active specific power is defined as the ratio between

output power and the mass of active material, which comprises of the magnets, copper and rotor iron.

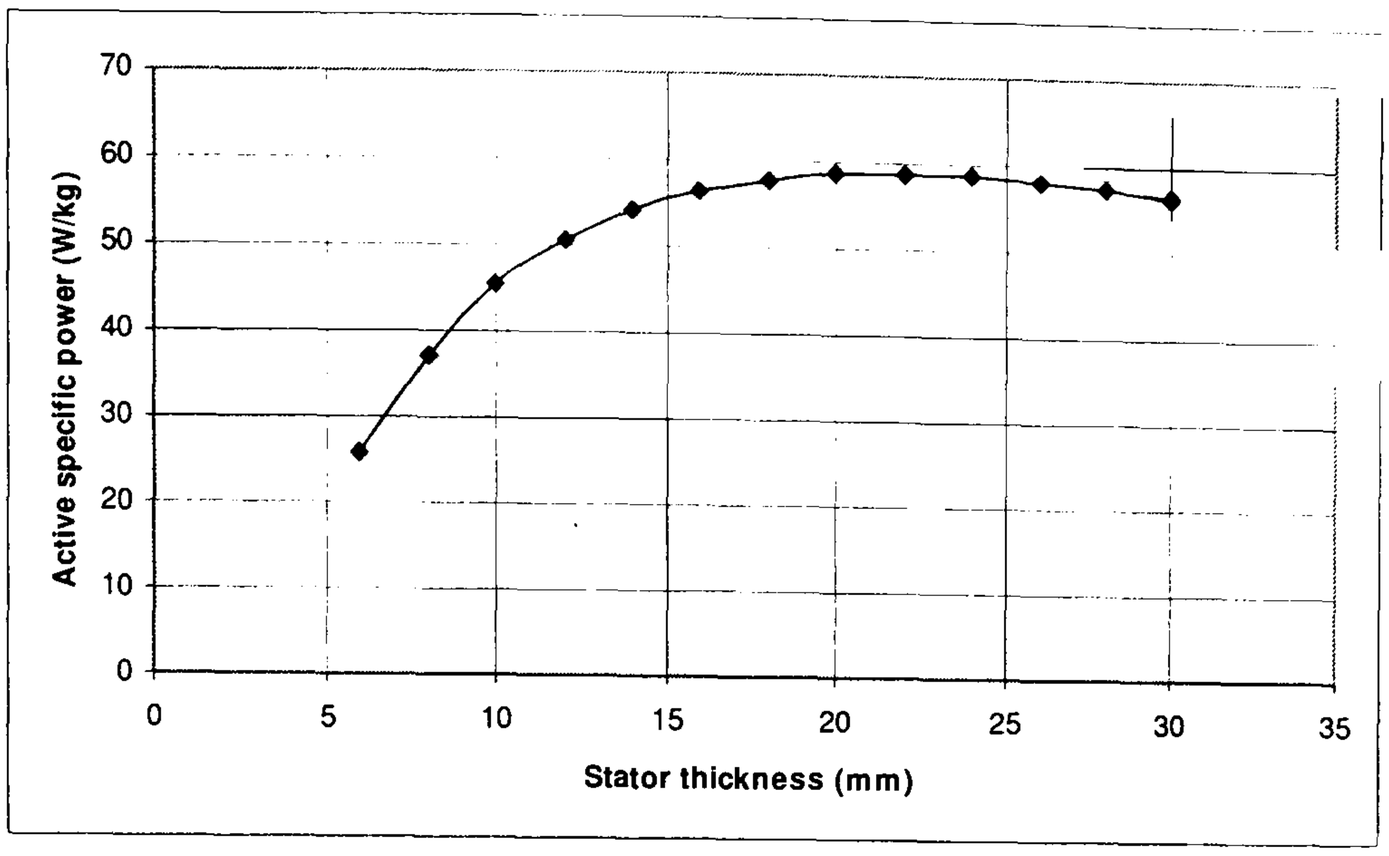

Figure 8-16. Active specific power versus stator thickness

As can be seen, the maximum active specific power occurs at a stator thickness of 20mm.

It should be noted, however, that the reduction in copper weight at lower stator thicknesses represents a genuine saving, whereas the reduction in rotor iron at higher stator thicknesses may be illusionary. This is because the back iron also plays an important role in resisting the high magnet forces between the rotor plates and it is therefore unlikely that a designer would wish to reduce its thickness significantly.

8.6 Impact of current density on efficiency

Although the power, efficiency and active weight of the generator appear optimal at a stator thickness of 20mm, it is still feasible to reduce the stator thickness to (say) 16 mm without incurring a significant penalty. The study carried out so far has assumed the designer wishes to use as high a current density as possible so as to operate the generator at the thermal limit of the winding, in this case 90 ℃. However, this may

not always be desirable since higher current densities result in higher Joule losses (I^2R) in the armature which impinge on the generator's efficiency. This is depicted in the figure below which shows generator efficiency and coil temperature as a function current density for a generator with a 20mm thick stator in cooling regime (b) (retaining ring with holes) at 300 rpm.

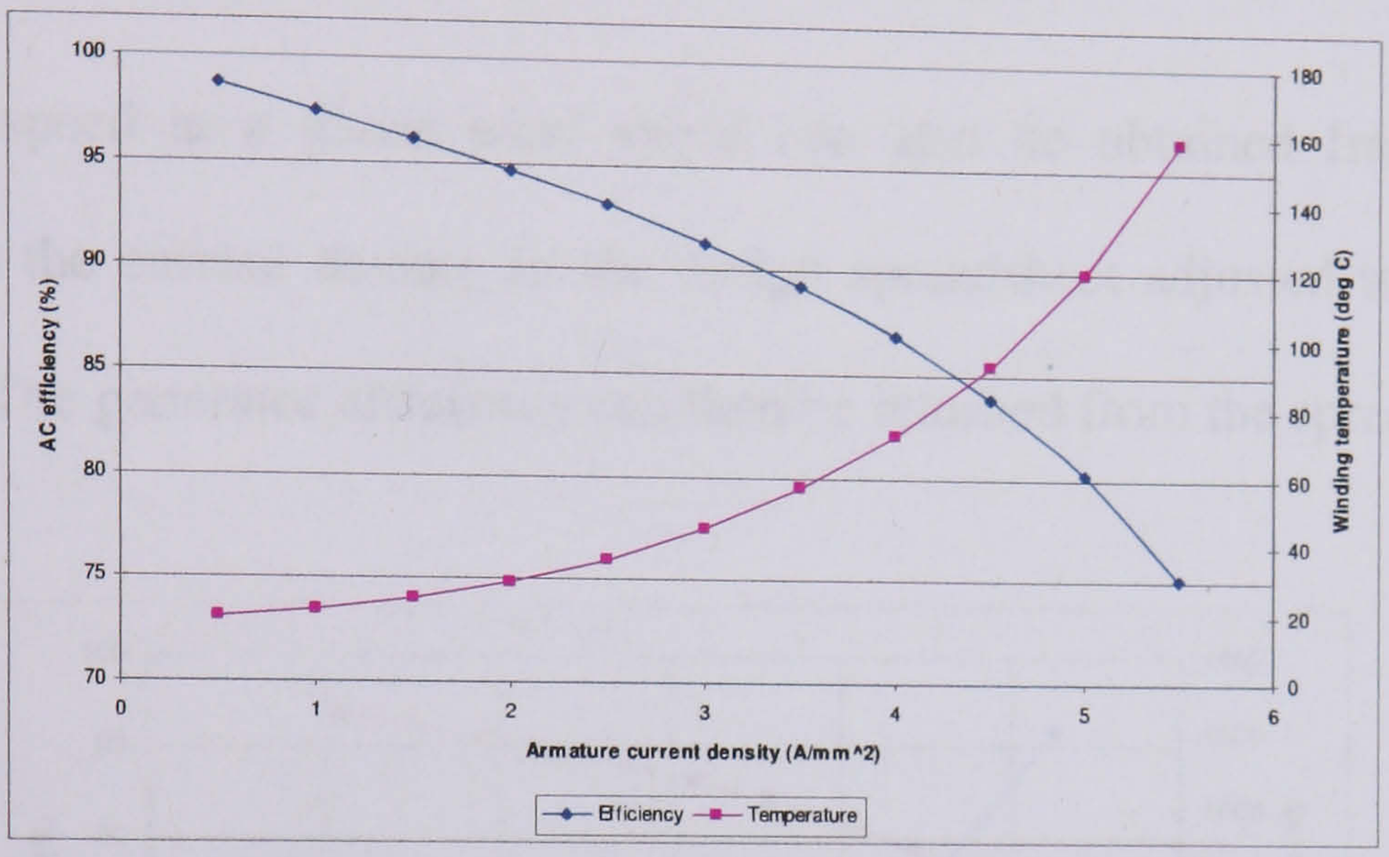

Figure 8-17. Dependency of efficiency and coil temperature on current

Figure 8-17 shows that as the current density is increased the efficiency of the generator decreases. A sensible design might therefore require a stator of reasonable thickness to achieve a minimum operating efficiency of (say) 90%. In the case of the 20mm stator shown in the figure above, an operating efficiency of 90% would impose a current density of 3.4 A/mm^2 on the winding and would produce a coil temperature of only around 60 °C – well below the 90 °C maximum.

However, it is likely that any practical wind energy conversion system would only require a high efficiency when the wind speed was low in order to gain the maximum possible benefit from what little energy was available. At times when the wind energy is abundant the designer would accept a lower efficiency for the maximum possible specific power. This concept is shown in Figure 8-18 which shows generator power and

efficiency as a function of wind speed. The blue line in Figure 8-18 can be created by assuming the turbine operates at constant λ and equating the power to the wind speed by:

$$\frac{P}{P_{rated}} = \left(\frac{\omega_{gen}}{\omega_{rated}}\right)^3 = \left(\frac{V_w}{V_{rated}}\right)^3 \qquad [8\text{-}19]$$

The rotational speed at a given wind speed can also be obtained from the above expression, and the current density in the design spreadsheet adjusted to produce the desired power. The generator efficiency can then be returned from the spreadsheet.

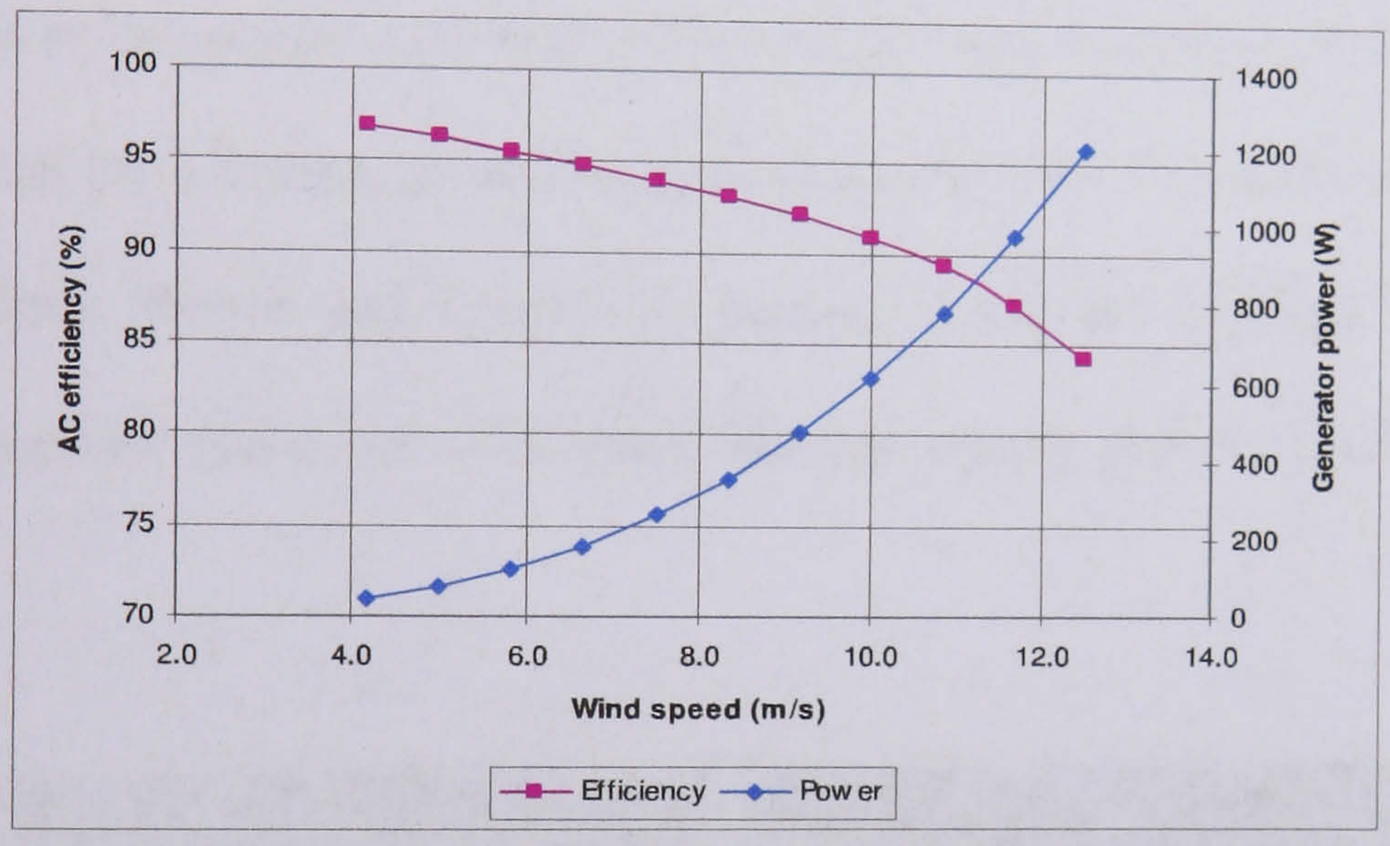

Figure 8-18. Power and efficiency as a function wind speed

Figure 8-18 shows that at low wind speeds the generator's efficiency is very high, leading to excellent energy capture. When the wind speed increases the efficiency falls, although since more power is being generated this becomes less important for most practical applications. This rationale leads to the conclusion that it is more appropriate for the generator's maximum power to be limited by the maximum possible winding temperature rather than by an artificially imposed minimum acceptable efficiency. The following section looks at a method of increasing the winding temperature by using an

alternative armature construction to the acetal bobbin.

8.7 Alternative armature coil construction

The maximum output power of most electrical machines is constrained by the thermal limit of the electrical insulation of the windings, typically 180 °C for an H-class insulator [113]. In the Savonious generator, however, the maximum operating point is limited by the temperature of the acetal bobbin which must not exceed 90°C.

To allow the generator to produce a higher specific power, the thermal limit of the winding can be increased by adopting an alterative winding construction. One such construction is to use a heat activated self-bonding copper wire to produce a solid coil without the need for a bobbin, as shown in the figure below. The coil can be wound on a separable bobbin former and heated by passing a current through it. The bonded winding can then be potted into the stator using an epoxy glue, as shown in the figure below.

(a) (b)

Figure 8-19. (a) Self-bonded coil, (b) Coil potted in stator

By using a self-bonded coil construction, the armature coils can operate at a higher

temperature and this increases the power of the generator, as summarised in the table below. This method of construction has the added benefit of allowing a slightly thinner stator to be used since the bobbin walls are no longer present and this allows the rotor plates to be brought closer together, leading to a slightly higher air-gap flux density.

Coil construction	Bobbin-wound	Epoxy-bonded
Max operating temperature (°C)	90	180
Rated Power (W)	1217	1307
Efficiency (%)	84.4	78.3
Current density (A/mm^2)	4.5	5.2
Air gap flux density (T)	0.430	0.481

Table 20. Operating parameters for different coil constructions (based on 20mm stator for bobbin-wound and 16mm stator for epoxy-bonded constructions)

8.8 Conclusion

Heat transfer in an air-cored PM axial flux machine can be modelled using a simple lumped parameter thermal model. The thermal conductivity of the acetal bobbin and winding of a 1kW, 300rpm machine can be found by testing an identical armature coil in a small wind tunnel. The surface heat transfer coefficient of the bobbin can be found by taking measurements of the bobbin's surface temperature inside a test generator in the laboratory, and by using these coefficients, an accurate prediction of steady-state coil temperature rise can be made. The measurements show that the thermal conductivity of the armature winding is low (0.44 W/K/m). This could be improved by vacuum impregnating the winding to remove air pockets. However, the heat transfer process is dominated by the surface heat transfer coefficient rather then by the thermal conductivity of bobbin or winding and so the advantage would be slight. Changing the level of cooling air circulating in the generator significantly alters the surface heat transfer coefficient and so has a large effect on cooling. Removing the plastic retaining

ring increases h_s from approximately 50 to 70 W/K/m^2 and hence increases the specific power of generator from approximately 1100 to 1200 W at 300 rpm. However, by removing the retaining ring the generator becomes more prone to damage from debris and from weathering, and although both types of construction would require an external cover, it remains unclear whether removing the retaining ring may compromise reliability in the long term.

The lumped parameter thermal model can be incorporated into the design process to allow the armature current to be equated to an armature temperature and by doing this the stator thickness can be optimised. If output power is plotted against stator thickness (see Figure 8-15), a 'saturation' type curve is produced. At low stator thicknesses the effect of reducing the amount of copper in the machine dominates over the improvement in magnetic loading and current density that can be achieved. At high stator thicknesses the power increase caused by a higher number of turns is balanced by the lower magnetic loading and current density, leading to little net improvement for the extra copper in the machine. An optimal design would aim for the knee of the curve which, in the case of the 1kW, 300rpm machine, occurs at a stator thickness of 20mm.

Chapter 9

Increasing the power rating of the axial flux topology

9.1 Introduction

The previous chapter considered the design optimisation of the stator thickness and coil design of a small axial flux generator (1kW, 300rpm). The following chapter considers the practicalities of extending the axial flux concept to larger generator diameters and to do this a number of different aspects of the design are examined. These include an examination of the magnet and coil shape, the structural constraints that may be encountered, and the impact of incorporating further mechanical complexity into the design.

Small axial flux generators (1kW) can be constructed most easily using round coils and magnets. However, as the generator power rating is increased it becomes advantageous to move to a trapezoidal topology as this produces a more compact design, boosting the power output for a given size of generator. The point at which this transition – from a round to a trapezoidal topology – takes place is discussed in section 9.2.

If the generator diameter is increased still further, the dominating constraint comes not from an inefficient use of space or from the difficulty of manufacture, but from the structural integrity of the mild steel rotor plates which must resist the increasingly large magnet forces. The rotor plate deflection mechanism is examined in section 9.3 and a structural finite element methodology is developed in section 9.4 to examine their stiffness. The predicted rotor plate deflections are compared to those measured in two

test generators in order to validate the finite element model, and the results are presented in section 9.5. Section 9.6 extends the finite element model to examine alternative designs for the rotor plate geometry of the 5kW generator and discusses strategies for building larger diameter axial flux machines. These include the incorporation of structural webbing elements to improve rigidity, the use of an epicyclic gearbox to increase rotational speed, and the move to a stacked rotor assembly to reduce the generator diameter. Finally, conclusions are drawn about the most appropriate design for a given power rating.

9.2 Round versus trapezoidal topologies

The PM axial-flux generators discussed so far may be constructed using circular or trapezoidal magnets and coils. While the magnets can be easily manufactured in any shape (by sintering), the coils must be wound using relatively inflexible copper wire and this places restrictions on the shapes that can be produced. Winding round coils is significantly easier then winding trapezoidal coils, especially if a large number of turns are required, as the trapezoidal shape trends to become circular with increased width, as shown in the figure below. In addition, a circular coil produces a readily definable geometry which allows the corresponding stator holes to be cut easily.

Figure 9-1. Trapezoidal coil

The active area of the axial flux generator consists of a ring in which the magnets and coils sit, as shown schematically in Figure 9-2. Reference [114] shows that the optimal ratio (to provide the greatest specific power) between the inside radius and the outside radius of the active area is $\sqrt{3}$. When round magnets and coils are used it is impossible to decouple the width of the active area, Δr, from the mean radius, r_m, and this leads to a less efficient design. When a trapezoidal geometry is used, a more compact, stiffer generator may be constructed and this becomes increasingly important at large diameters. It should be noted, however, that for most practical designs the optimal ratio $\frac{r_o}{r_i} = \sqrt{3}$ is rarely used since the magnets and coils become slightly too long (radially) to be handled easily. The coils become difficult to fit into the stator near their inner radii and the flux rings become heavier then would be wished.

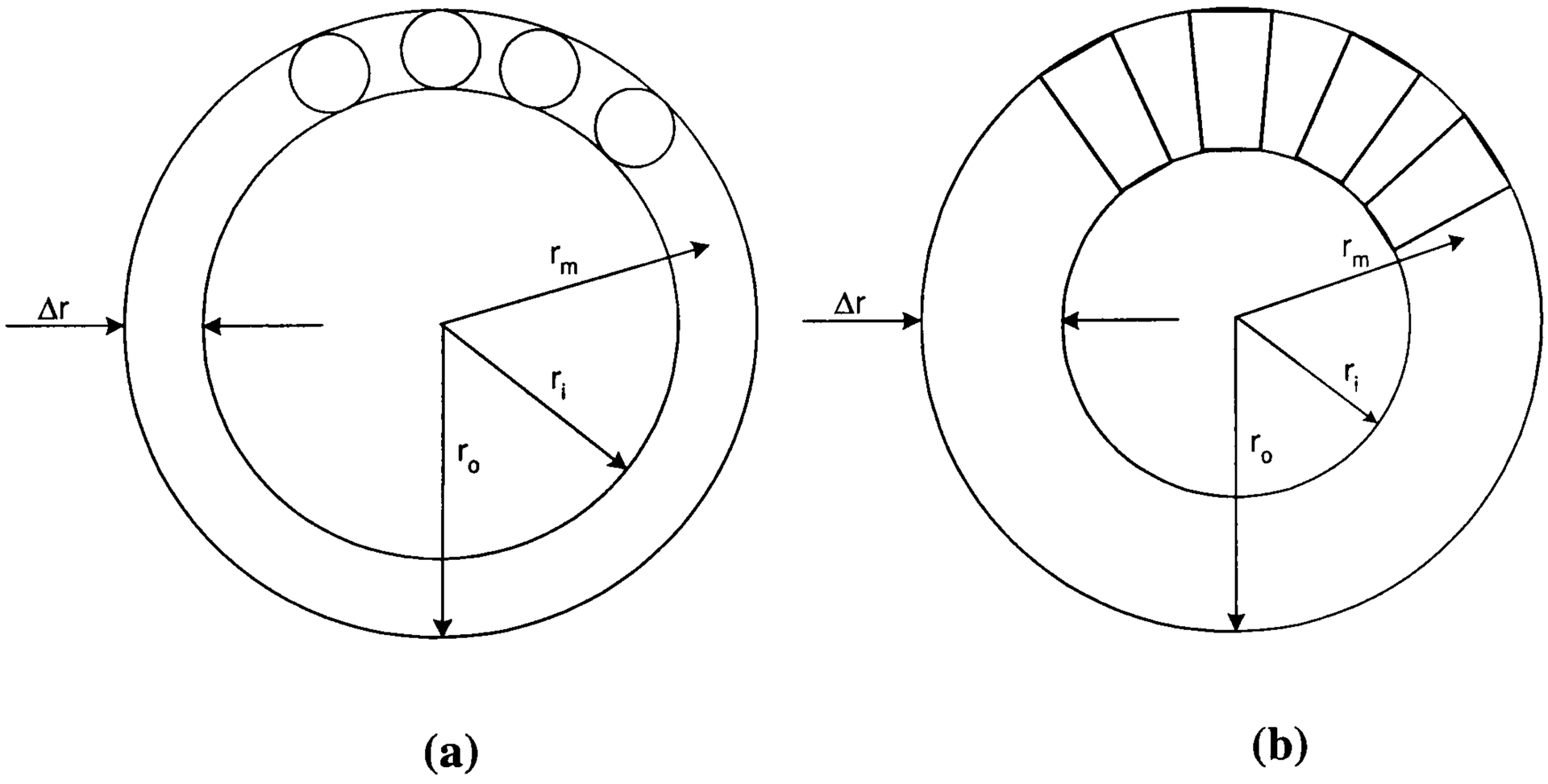

Figure 9-2. Active area of axial flux topology for (a) round and (b) trapezoidal topologies

When constructing small generators there is little benefit in using trapezoidal coils to make the device slightly more compact due to the added complexity of the manufacturing process. At large generator diameters, however, it makes sense to move

to a trapezoidal topology since the generator can be made significantly more compact for a given power rating. The point at which this transition takes place is somewhat of a grey area and will depend how the generator is integrated with the turbine: if space is at a premium in the nacelle it may make more sense to move to a trapezoidal topology at a lower power rating then if ease of manufacture is the only concern. An approximate power rating for this transition may be 3-5kW, 100-200 rpm, as demonstrated by Table 21 which shows two alternative designs for a 3kW, 160 rpm machine using circular and trapezoidal topologies. The circular design has a slightly larger outer diameter but is lighter, using less magnet material and rotor back iron.

Topology	Circular	Trapezoidal
Power (W)	3000	3000
Rated speed (rpm)	160	160
No. phases	3	3
Magnet type	NdFeB	NdFeB
Magnets per disc	16	16
Magnet Grade	N35	N35
Magnet length (diam) (mm)	70	100
Magnet thickness (mm)	12	12
No. armature coils	12	12
Frequency (Hz)	40	40
Approx OD (mm)	700	610
Magnet weight (kg)	10.9	16.2
Copper weight (kg)	13.0	13.2
Flux rings weight (kg)	19.5	23.4
Approx active wt (kg)	43.5	53.5
Min. flux ring thickness (mm)	7.8	8.8
Flux ring radial length (mm)	100	130
Stator thickness (mm)	20	20
Coil height (mm)	18	18
Running clearance (mm)	3	3
Armature wire diam. (mm)	0.85	0.85
Current density (A/mm^2)	4.0	4.0
Power at 160 rpm (W)	3573	3661
Electrical efficiency (%)	88.7	88.2

Table 21. Comparison between round and trapezoidal generator topologies

9.3 Rotor plate deflection mechanism

At larger generator diameters the most significant design constraint comes not from the use of materials or the difficulty of manufacture but from the large closing forces produced in the generator by the PM material. The following section examines these closing forces and the deflections they produce in the rotor plates of two test generators, depicted in Figure 9-3, by using a finite element analysis to assess the structural rigidity of the generator. For clarity the rotor plate assembly is shown schematically in Figure 9-4; the design parameters of both generators are given in Table 22.

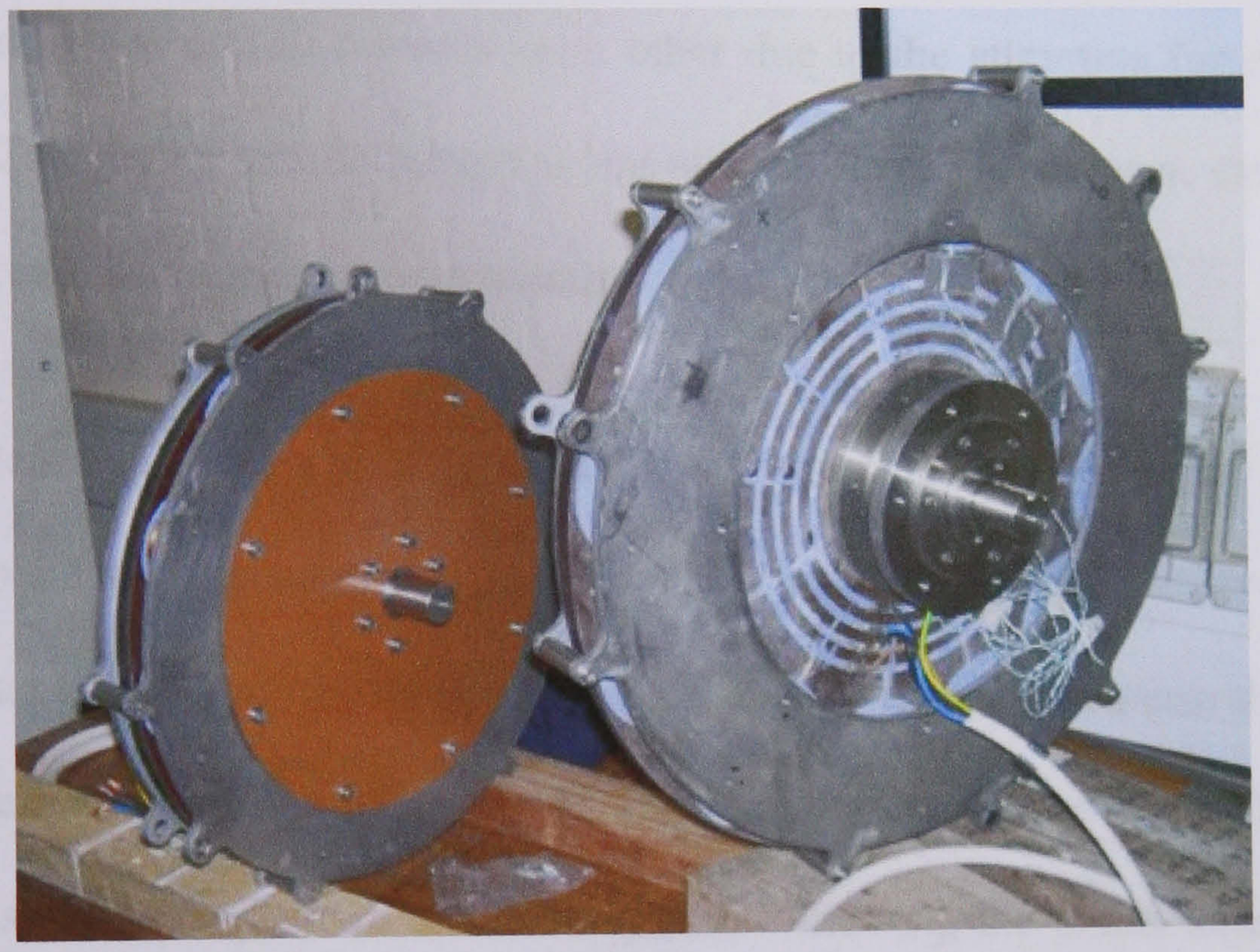

Figure 9-3. 2.5kW, 250rpm and 5kW, 200 rpm axial flux generators

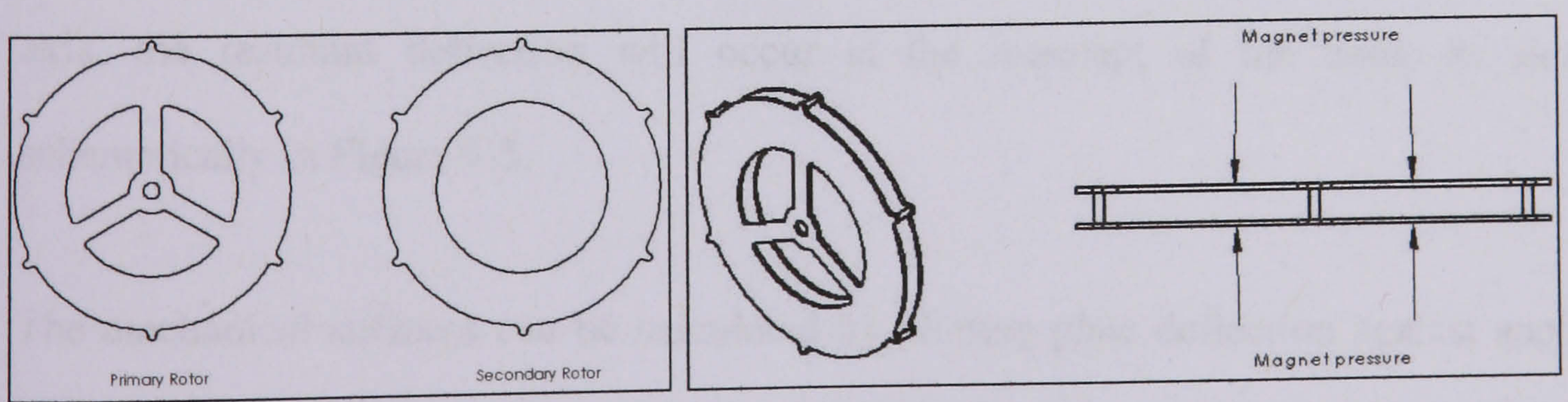

(a) **(b)**

Figure 9-4. Rotor plate schematic in (a) plan and (b) isometric and section

Generator Size	2.5kW, 250 rpm	5kW, 200 rpm
Rotor plate thickness (mm)	8	8
Rotor plate material	Mild steel	Mild steel
Plate separation (mm)	24	22
Number of magnets	16	24
Number of coils	12	18
Stator thickness (mm)	14	20
Magnet thickness (mm)	10	10
Magnet type	Round	Trapezoidal
Inner radius of annulus (mm)	181	210
Outer radius of annulus (mm)	281	310
Number of separating (anchor) pillars	6	6

Table 22. Design parameters of 5kW, 200rpm machine

Figure 9-3, Figure 9-4 and Figure 9-8 show the rotor plate assembly. The primary rotor plate is mounted to the central hub and the secondary disc is suspended from it by 6 pillars. The plates deflect towards each other due to the attractive forces between the magnets. Calculating this deflection is not straight forward, however, since the magnet forces increase as the plates come together.

This problem can be addressed by splitting the structural rigidity of the generator into two components: mechanical stiffness and 'magnetic stiffness'. The mechanical stiffness can be thought of as a negative feed back system in the sense that an increase in plate deflection causes an opposing restorative force in the plate. The 'magnetic stiffness' is akin to a positive feedback system – drawing the plates together increases the attractive force between them. If these two characteristics are plotted on the same axis, the resultant deflection will occur at the intercept of the lines, as shown schematically in Figure 9-5.

The mechanical stiffness can be calculated by plotting plate deflection against applied load, and this can be achieved using a finite element package [115]. The magnetic stiffness can be calculated by evaluating the Maxwell stress on an incremental area at the mean magnet radius, and then integrating over the magnet area, (a full description is

given in Appendix D). As the magnets come together the total air gap reduces, increasing the flux density and hence producing a greater attraction force between the plates. Plotting how the attractive force increases as a function of deflection describes the 'magnetic stiffness' of the structure.

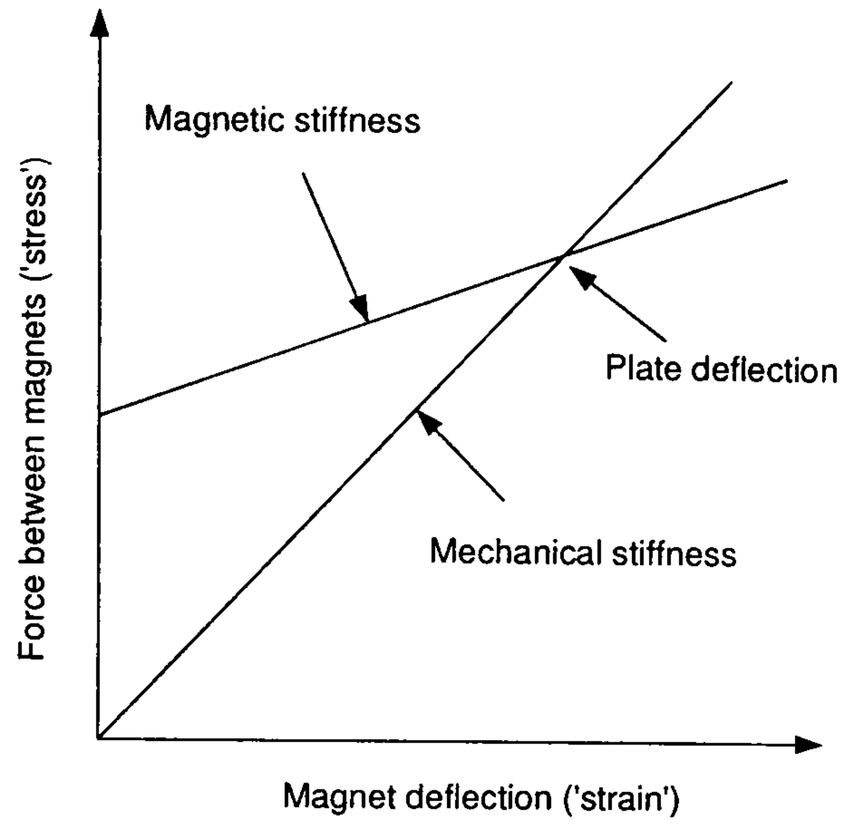

Figure 9-5. Mechanical and magnetic stiffness of axial flux generator

The rotor plates will fail if the gradient of the 'magnetic stiffness' is either greater or equal to the mechanical stiffness. Alternatively, the plate deflection can become significant if either the mechanical stiffness is too low or the 'magnetic stiffness' too high.

The large air gap in the axial flux machine serves to reduce the gradient of the magnetic stiffness such that it would not be a significant threat. However, ensuring an adequate mechanical stiffness is a significant challenge that will be discussed in the next section.

9.4 Finite Element Methodology

To assess the accuracy of the finite element (FE) mesh required, and to gain confidence in the FE analysis, the FE method can be compared to an analytical solution to a similar plate deflection problem. This type of analysis has been used in the past to calculate

rotor deflections in large-scale PM axial-flux machines [116]. Although this technique was found to give good approximations of the rotor and stator deflections, a more detailed approach is required here which accounts for the exact geometry of the rotor plates and support pillars. This can be accomplished using a finite element analysis, although the analytical solution still provides a useful verification.

The analytical problem, shown schematically in Figure 9-6, consists of an annulus ring, built-in around its outer edge and subject to a uniform pressure which is exerted from radius r_i to a.

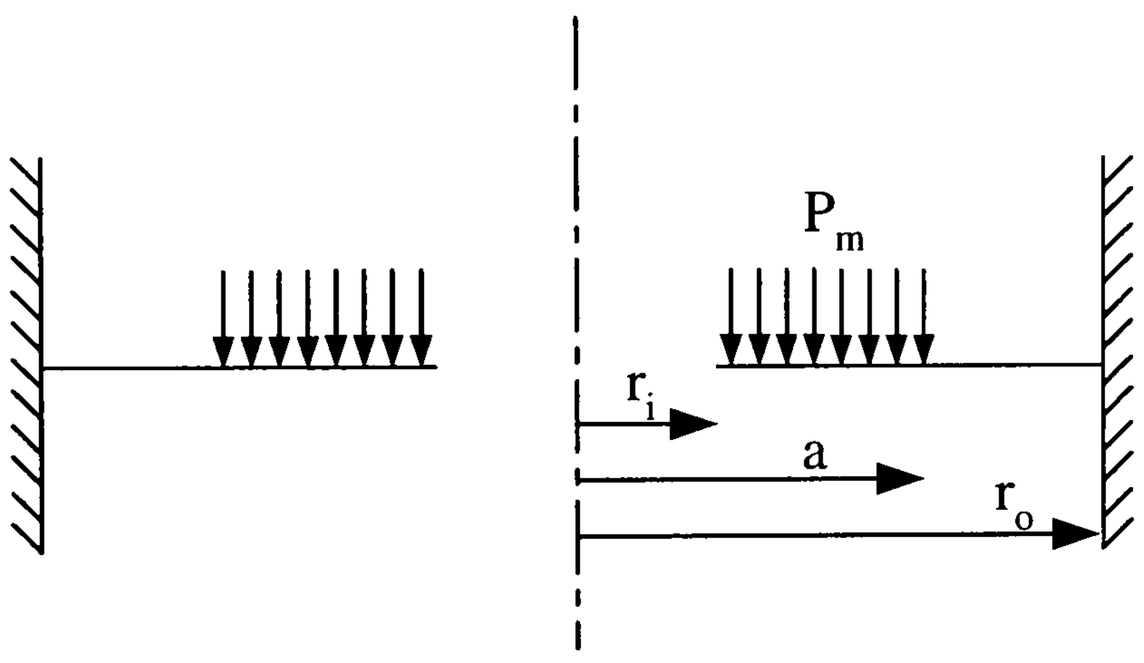

Figure 9-6. Analytical solution schematic

An analytical solution to this problem can obtained from reference [117], which shows that the deflection at the inner edge of the annulus is given by:

$$y_z = -\frac{P_m a^4}{D_1}\left(\frac{C_1 L_1}{C_2} - L_2\right) \qquad [9\text{-}1]$$

Where:

$$D_1 = \frac{Et^3}{12\left(1-\nu^2\right)} \qquad [9\text{-}2]$$

$$C_1 = \frac{1+\nu}{2}\frac{r_i}{a}\ln\frac{a}{r_i} + \frac{1-\nu}{4}\left(\frac{a}{r_i} - \frac{r_i}{a}\right) \qquad [9\text{-}3]$$

$$C_2 = \frac{1}{2}\left[(1+\nu)\frac{r_i}{a} + (1-\nu)\frac{a}{r_i}\right] \qquad [9\text{-}4]$$

$$L_1 = \frac{1}{16}\left[1 - \left(\frac{r_o}{a}\right)^4 - 4\left(\frac{r_o}{a}\right)^2 \ln\frac{a}{r_o}\right] \qquad [9\text{-}5]$$

$$L_2 = \frac{1}{64}\left\{1 + 4\left(\frac{r_o}{a}\right)^2 - 5\left(\frac{r_o}{a}\right)^2\left[2 + \left(\frac{r_o}{a}\right)^2\right]\ln\frac{a}{r_o}\right\} \qquad [9\text{-}6]$$

The geometrical parameters used in the comparison are given in Table 23 and are similar to the dimensions of the 1kW, 300rpm machine introduced in Chapter 2 The applied pressure, P_m, can be calculated by imagining the magnets are smeared out over an annulus ring of width $a - r_i$. The analytical solution can then be used to describe the deflection at the inner edge of the annulus as a function of the rotor plate closing force, Figure 9-7.

Inner annulus radius, r_i (m)	0.21
Outer annulus radius, r_o (m)	0.34
Outer radius of applied pressure, a (m)	0.31
Plate thickness, t (m)	8x10-3
Young's modulus, E (Pa)	2x1011
Poisson's ratio, ν	0.25

Table 23. Parameters used in analytical solution

Before embarking on a detailed study of the specific rotor plate bending problem, confidence can first be gained in the FE method by setting up an identical axi-symmetric plate bending problem in *Strand 7*, a structural FE package [115]. By using 7

different applied loads and recording the resulting plate bending in each case, a comparison can be made between the FE model and the analytical solution, Figure 9-7.

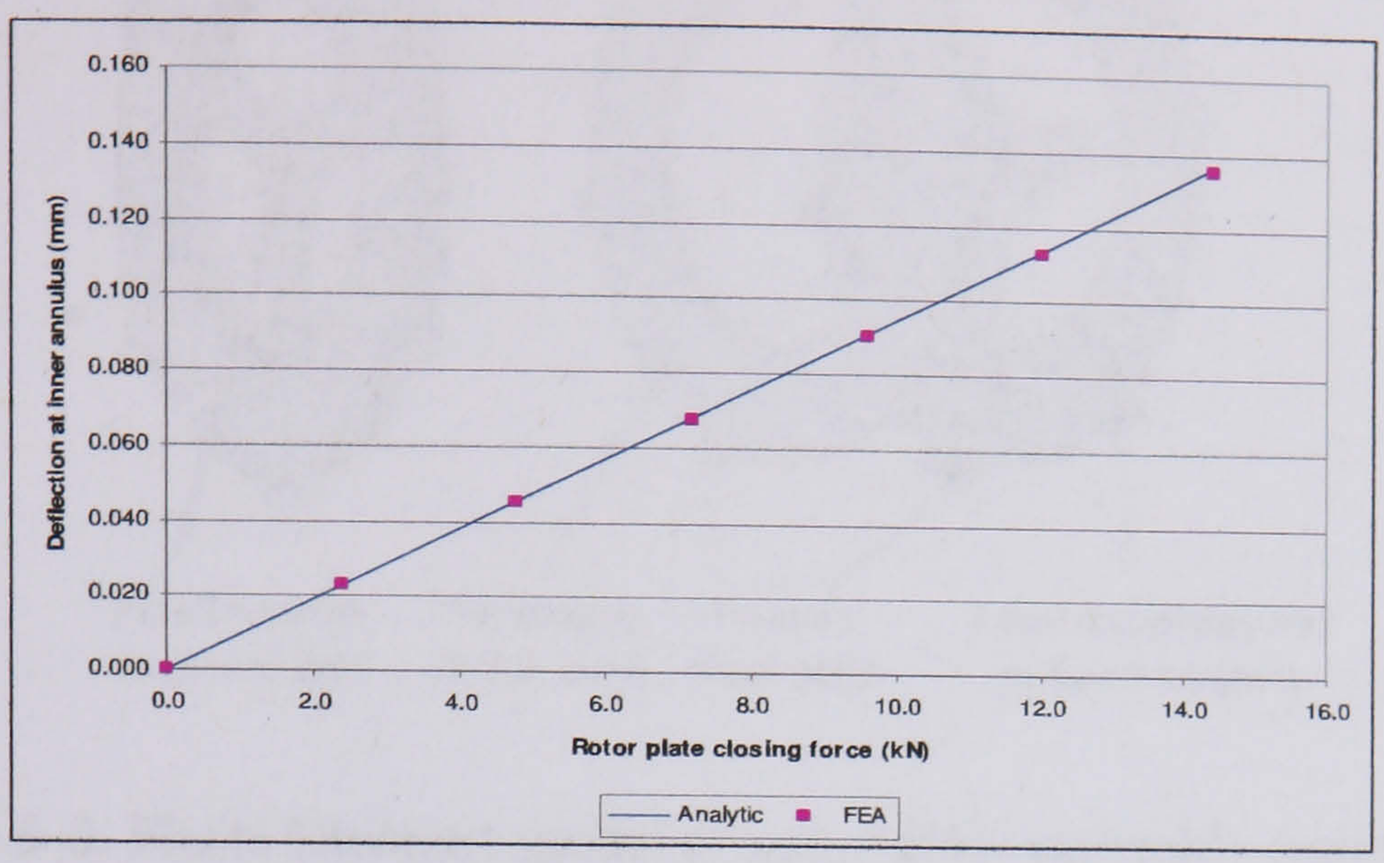

Figure 9-7. Comparison between FEA and analytical solution

A mesh size of 9mm was found to produce a FE solution that was within 1% of the analytical solution.

Having established the accuracy of the FE method, the analysis can be extended to consider the case of the 5kW generator introduced in section 9.3. An accurate finite element model of the generator can be constructed using dimensions and geometry taken directly from the generator's drawings, and this allows the predicted rotor plate deflections to be compared to the test generator.

The rotor plate assembly is shown in the figure below. To save computational time, the two flat rotor discs are modelled as two dimensional plates of known thickness which are separated by eight supporting pillars, modelled in three-dimensions. The primary rotor plate is supported from the central hub by a fixed support and discrete loads can be applied to both plates to mimic the attractive forces of the magnets.

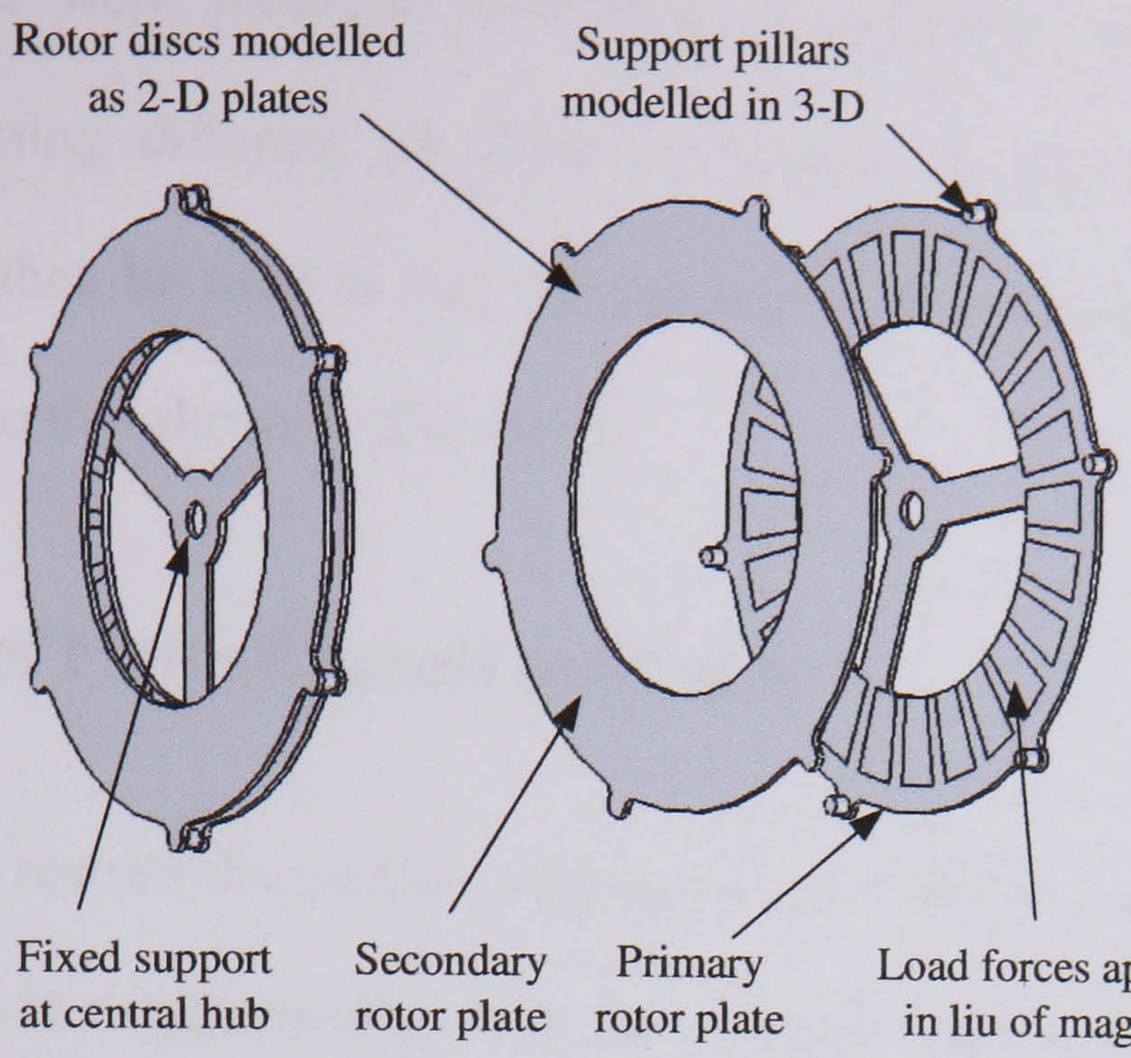

Figure 9-8. Finite Element model of rotor plate assembly (schematic)

Since the rotor disc assembly is symmetrical about a 30° segment of the generator, a significant simplification can be made by invoking symmetry and adopting the necessary boundary conditions at the edges of the segment, (zero translation in the θ direction, zero rotation in the r and z directions). The finite element mesh of this segment is shown in the figure below. A 9mm mesh size was used for the bulk of the model, although a finer 0.5mm mesh was used to gain better detail of the stress concentrations around the support pillar.

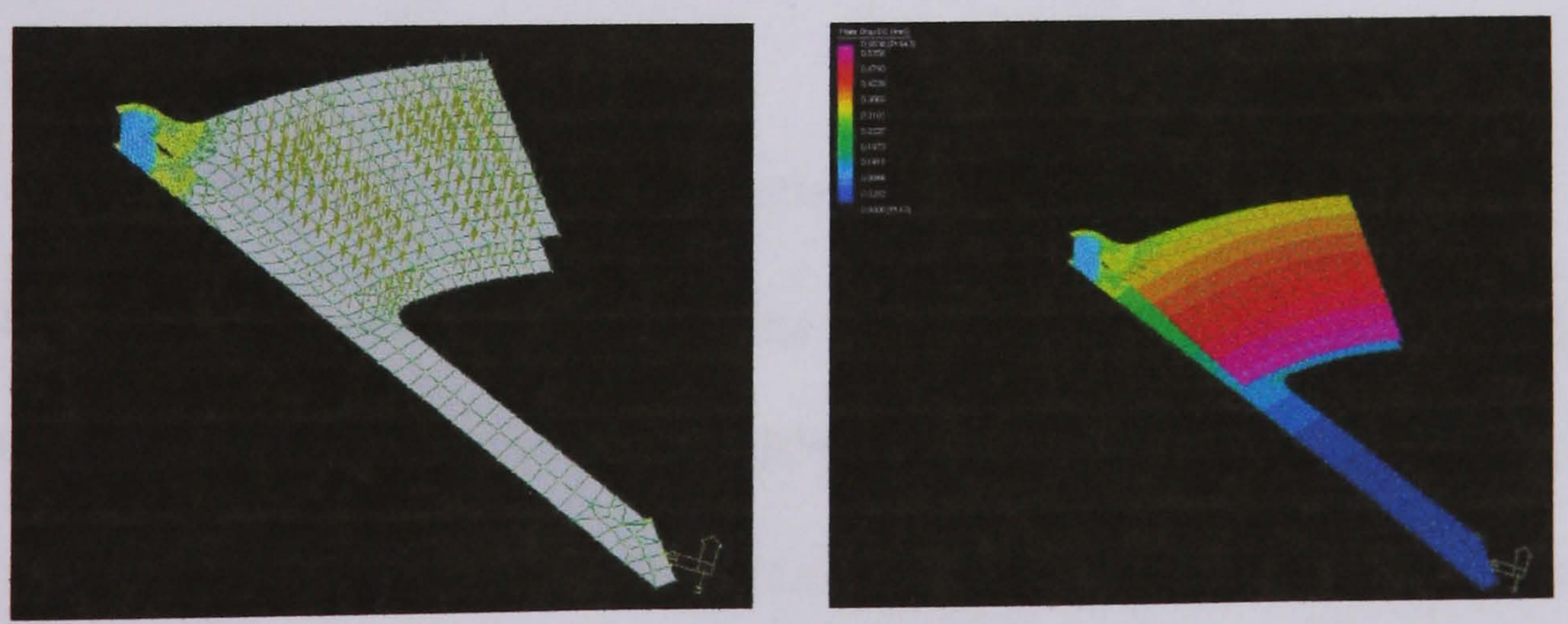

(a) **(b)**

Figure 9-9. A 30° segment rotor showing (a) the load case, and (b) the resulting z-axis deflection

Five load cases were modelled consisting of different levels of applied force – analogous to using different strengths of magnet in the generator. The resulting deflections can then be used to plot out the structural stiffness of the rotor plates in a similar manner to that shown in Figure 9-7.

9.5 Results of Finite Element modelling

The FE analysis reveals the primary and secondary rotor plates have different bending modes, as shown in exaggerated form in the schematic below. These bending modes are in line with the deflections observed the 2.5kW and 5kW machines, which gives confidence to the model.

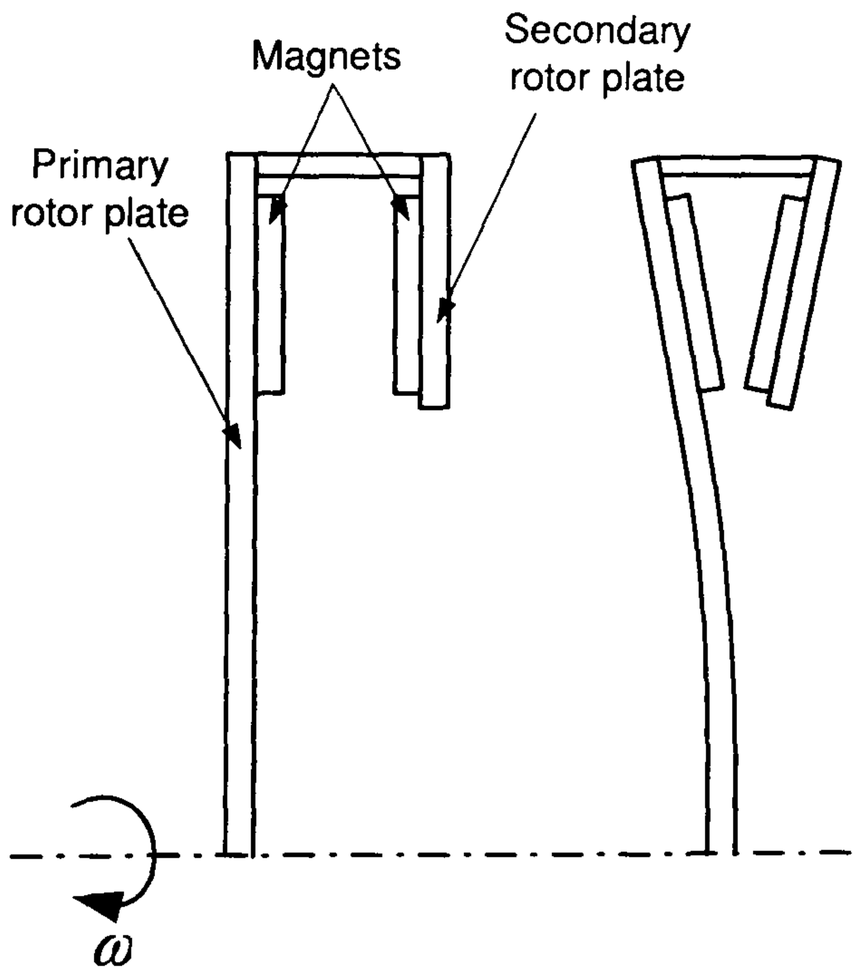

Figure 9-10. Bending mode of rotor assembly

Figure 9-11 shows the quantitive results of the analysis. As described in the previous section, the mechanical stiffness can be established by plotting the maximum rotor plate deflection (at the inner edge of the annulus) against the rotor plate closing force for the 5 load cases considered. This procedure can be carried out for both the primary and secondary rotor plate. The 'magnetic stiffness' is calculated using the method outlined in Appendix D and the two lines are plotted on the same axes in Figure 9-11, the

intersection giving the predicted rotor plate deflection. Also shown in the figure is the measured deflection of the secondary rotor plate of the test generator. (The measured deflection of the primary plate was 1.95mm, well outside the scale of the graph and so is not shown.)

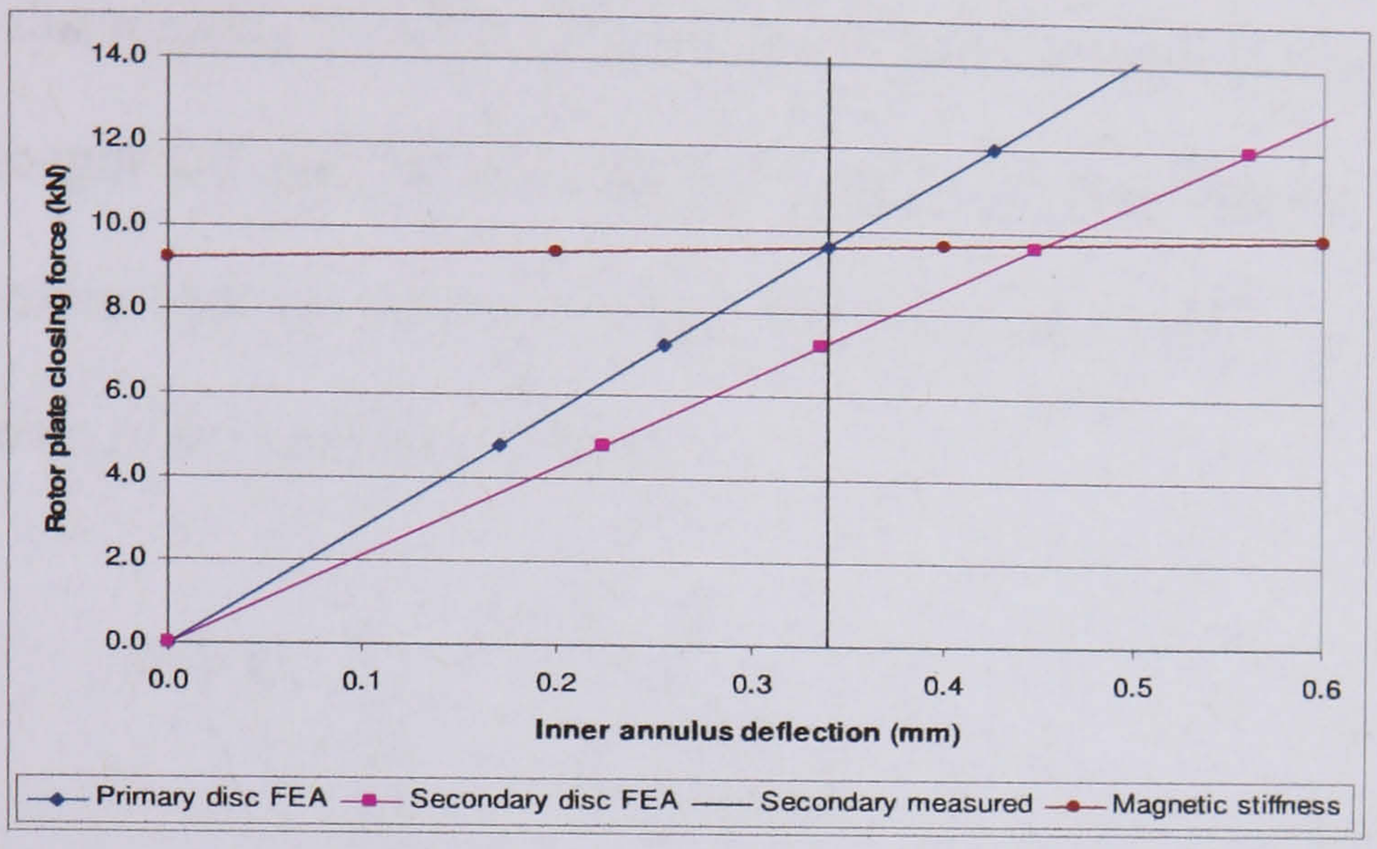

Figure 9-11. Comparison between predicted and measured deflections

The measured deflection of the secondary rotor plate (0.45mm) is close to the predicted value (0.34mm), although there is a large discrepancy between the predicted and measured values of the primary rotor plate. This information is summarised in the table below along with a similar finite element analysis on the 2.5kW, 240rpm generator.

It is also interesting to note that in Figure 9-11 the 'magnetic stiffness' of the generator is actually very flat. This is because the deflections of the rotor plates are a relatively small proportion of the total air gap and so make only a modest difference to the flux density.

Rotor plate type	Predicted (mm)	Measured (mm)
Primary of 2.5 kW generator	0.64	0.48
Secondary of 2.5 kW generator	0.64	0.45
Primary of 5.0 kW generator	0.34	1.95
Secondary of 5.0 kW generator	0.34	0.45

Table 24. Comparison between predicted and measured deflections

In comparing the predicted rotor plate deflections with those measured on the two test generators, Table 24 shows the finite element model is reasonably accurate. However, there is a notable exception: the primary rotor plate of the 5.0kW machine is significantly more deformed than would be expected.

Such a large discrepancy is mostly likely caused by the assembly process, when the two plates are brought together by jacking them down on three lengths of M12 studding (attached to extra lugs on the rotor plates which are not shown in Figure 9-4). This process is shown in the schematic below.

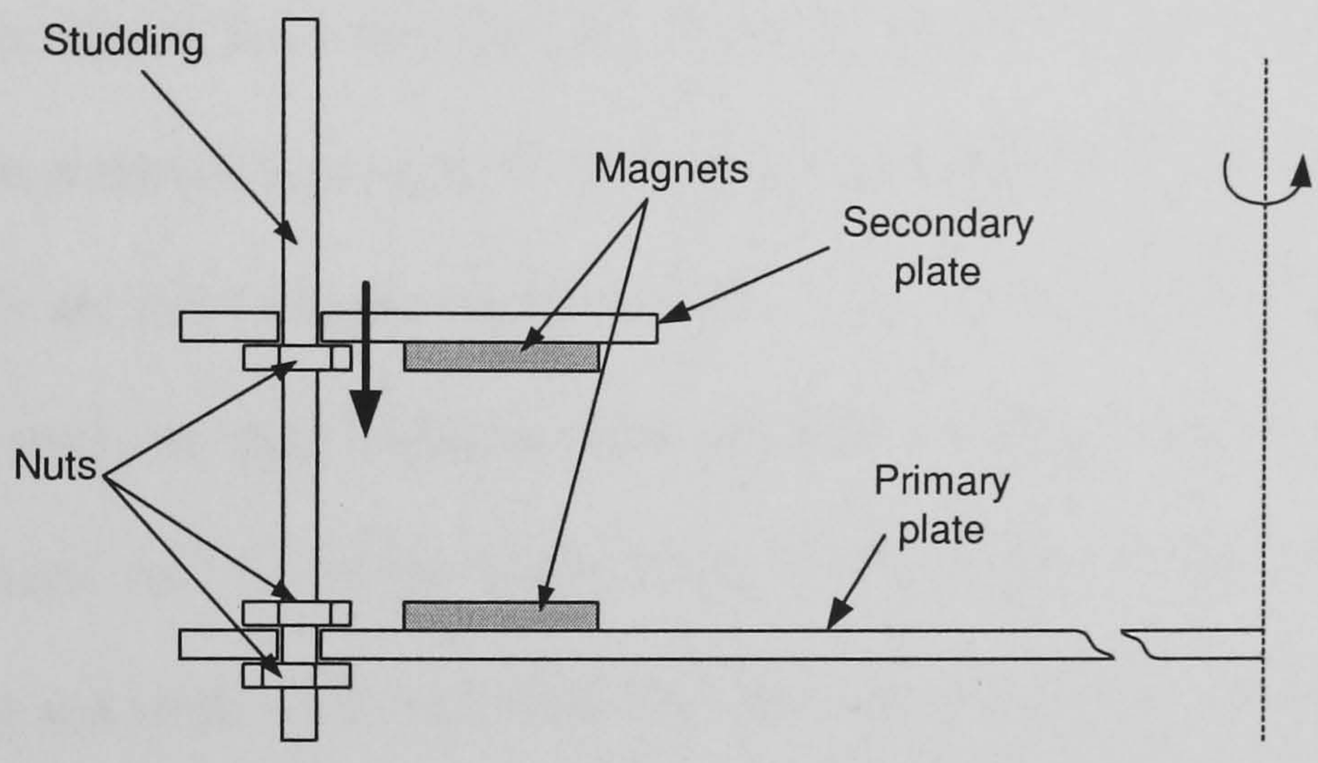

Figure 9-12. Rotor plate assembly process

It is possible that the high stress concentrations around the assembly lugs may have exceeded the yield strength of the material, causing plastic deformation. This may have occurred during the assembly process because 3 rather then 6 support points were used.

In order to assess this risk, the assembly lugs were modelled using the same method as before, although now symmetry dictates that a 60° segment of the generator be considered. Figure 9-13 shows the stress concentration around the jacking point.

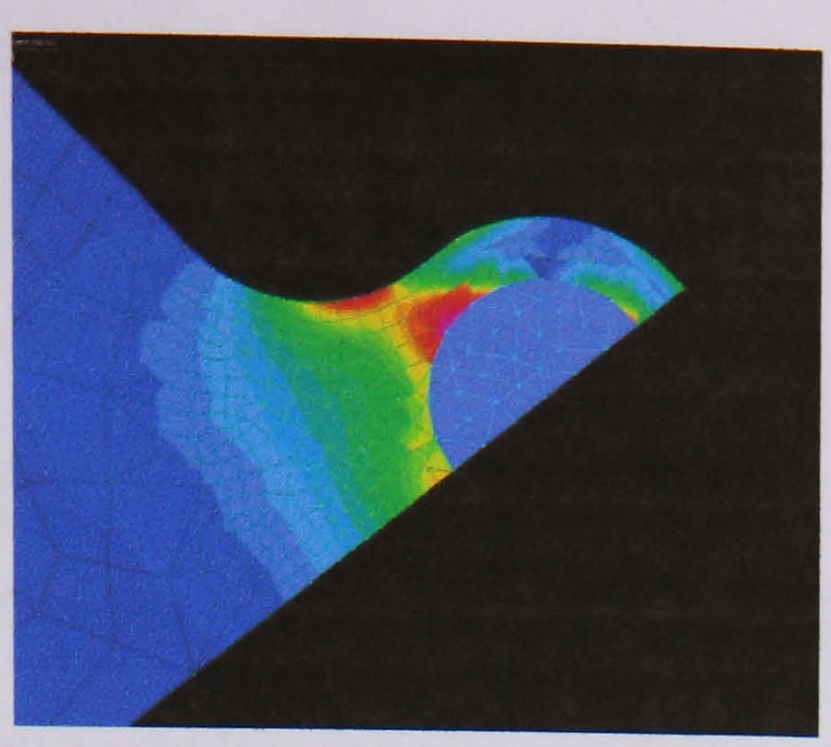

Figure 9-13. Stress concentration around the jacking point (Von Misses stress criteria)

The analysis shows a maximum plate stress of 22 MPa (using the Von Misses stress criteria) occurs during jacking, which is well below the yield stress of the material (240 MPa). However, it should be noted that the model presented here is highly simplistic and may not be an accurate representation of the jacking process. For example, during assembly the discs are not brought together uniformly - the three edges of the disc are each lowered in turn on their jacking nuts, perhaps leading momentarily to larger stresses being placed on one of the lugs. Also, the boundary conditions at the point where the jacking nut makes contact with the disc are not strictly as described in the model. The two pieces of material are not physically connected to each other, as could be assumed in the case where each disc is securely bolted through the six supporting pillars, but lie one on top of the other. The bending of the studding itself may also be significant during the assembly process, as may be the residual stresses in the rotor plates.

Investigating the detailed behaviour of the rotor plate during assembly is beyond the scope of this work, and the analysis carried out here very much represents a first step along this road. However, a number of important conclusions can be drawn from the modelling process:

1. The bending mode predicted by the model is in agreement with that observed in the generators.
2. Maximum stress occurs in the anchoring lugs and their design must be given special consideration.
3. The most significant plate deflection can occur during assembly not during operation, and because of this the number of jacking points, as well as their geometry, must be given special consideration.

9.6 Rotor plate design investigation

The finite element model developed so far has focussed on the 2.5kW, 240rpm and 5kW, 200 rpm generators, and has been validated against an analytical solution of the plate bending problem and by measurements and observations made on the test generators. Investigating the structural rigidity of the rotor plates in this way allows useful insights into the construction of larger generators to be gained, and with this in mind the analysis will now be extended by considering three factors which affect the rigidity of the rotor discs at larger generator diameters:

1. The number of supporting pillars which separate the two discs.
2. The precise design of the lug geometry used for jacking/bolting purposes.
3. The thickness of the rotor plates.

For the purposes of the design study a 2 dimensional representation of the rotor plate is considered which neglects any bending in the primary rotor plate or support pillar. This simplification allows a much more efficient use of time since the production of a detailed three dimensional model proved highly labour intensive. A comparison between the 2-D and 3-D models is shown in Figure 9-14.

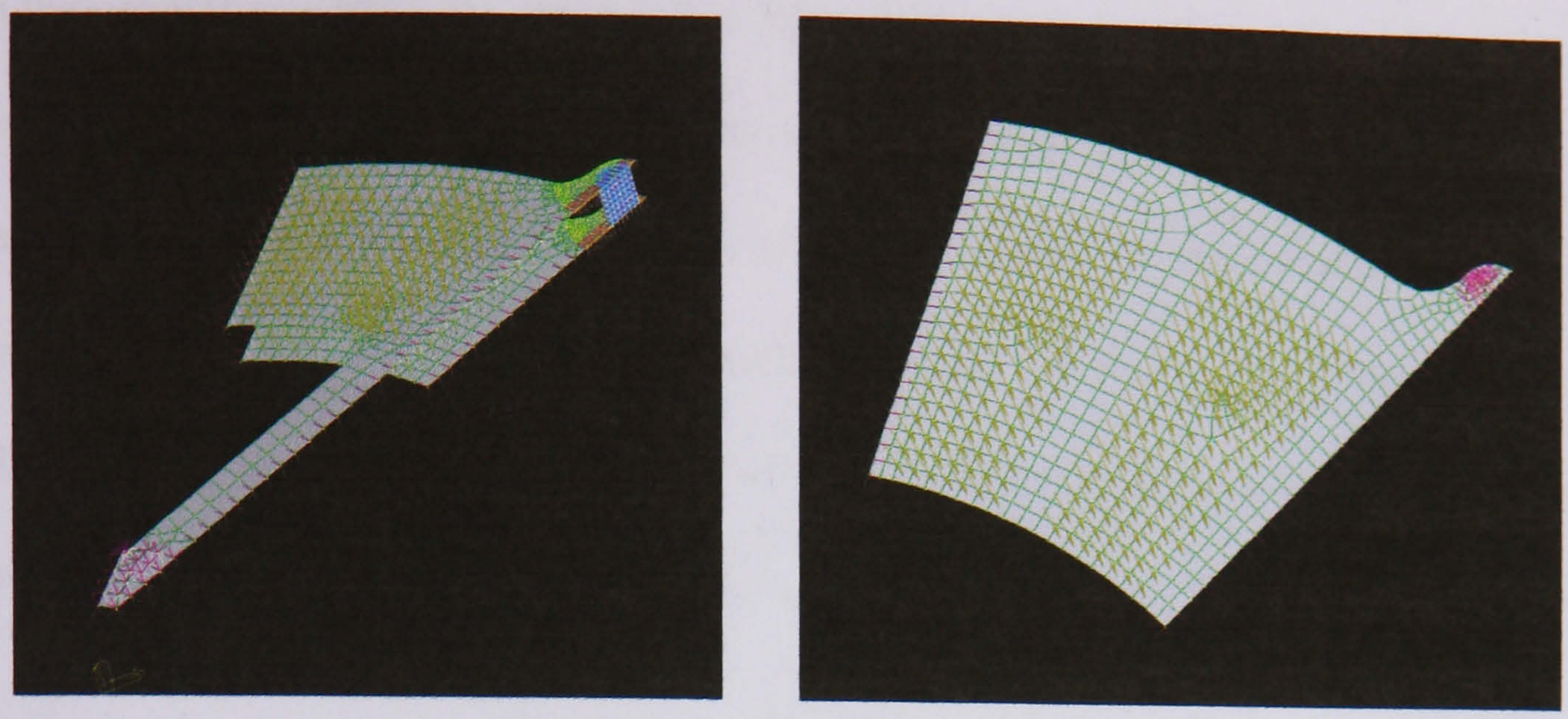

(a) (b)

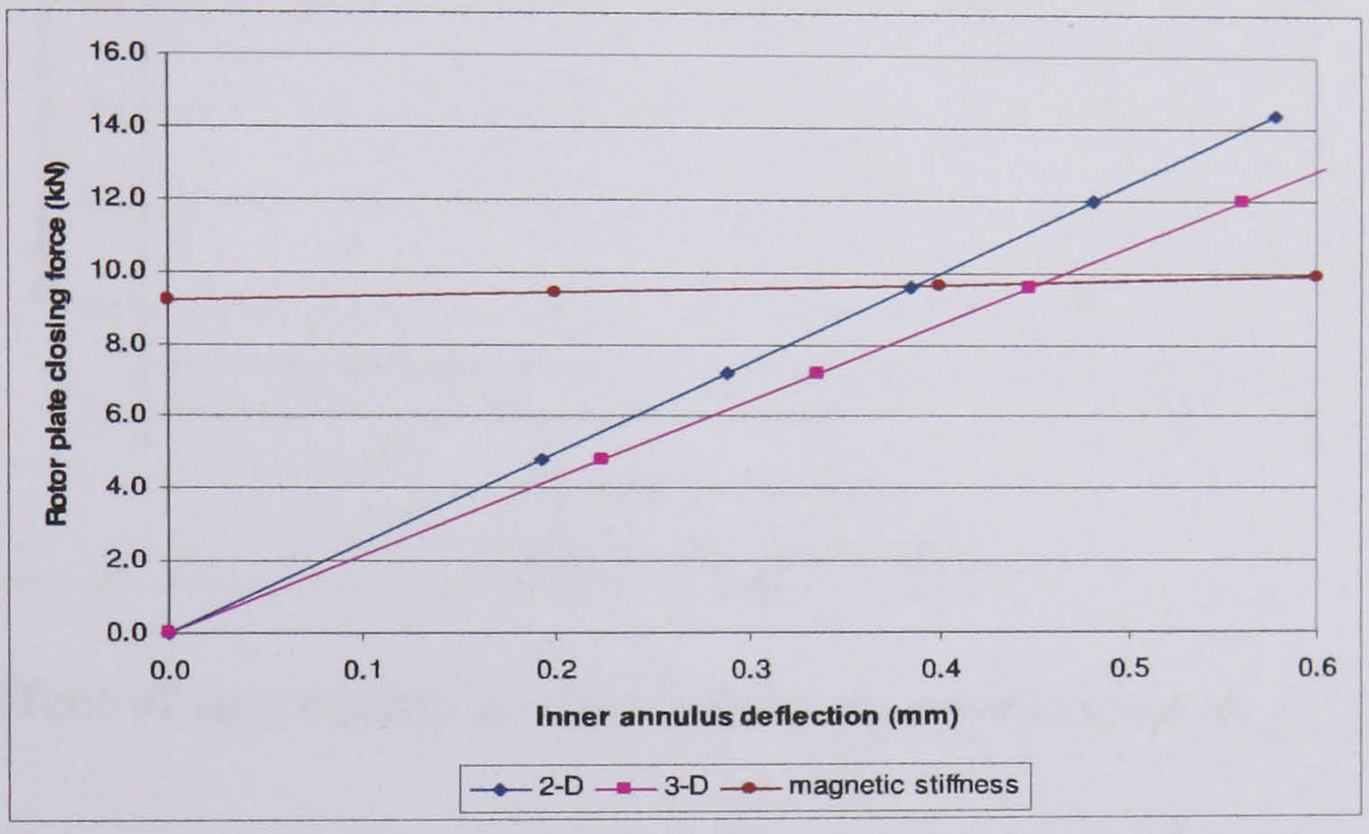

(c)

Figure 9-14. Finite element model of the rotor plate assembly of the 5kW, 200rpm machine in (a) 2-D, (b) 3-D; (c) shows a comparison between rigidities of the two models

Figure 9-14 (c) shows the 2-D simplification does not significantly decrease the accuracy of the model. As might be expected, neglecting bending in the primary rotor plate and support pillar makes the structure appear slightly stiffer, and this must be borne in mind when considering the results of the analysis.

9.6.1 Effect of number of anchor points

Figure 9-15 shows the structural rigidity of the rotor plate is affected by increasing the number of points at which the two rotor plates are held apart – either during jacking or

when the generator is fully assembled. The 5kW, 200rpm generator has 6 anchor points, although only 3 jacking points were used when the generator was assembled. Both these scenarios have been examined, along with effect of using 8, 10 and an infinite number of anchor points, i.e. the rotor plate is built-in around its outer edge. The structural rigidity of the plate is quantified in terms of the maximum deflection at the inner edge of the annulus ring.

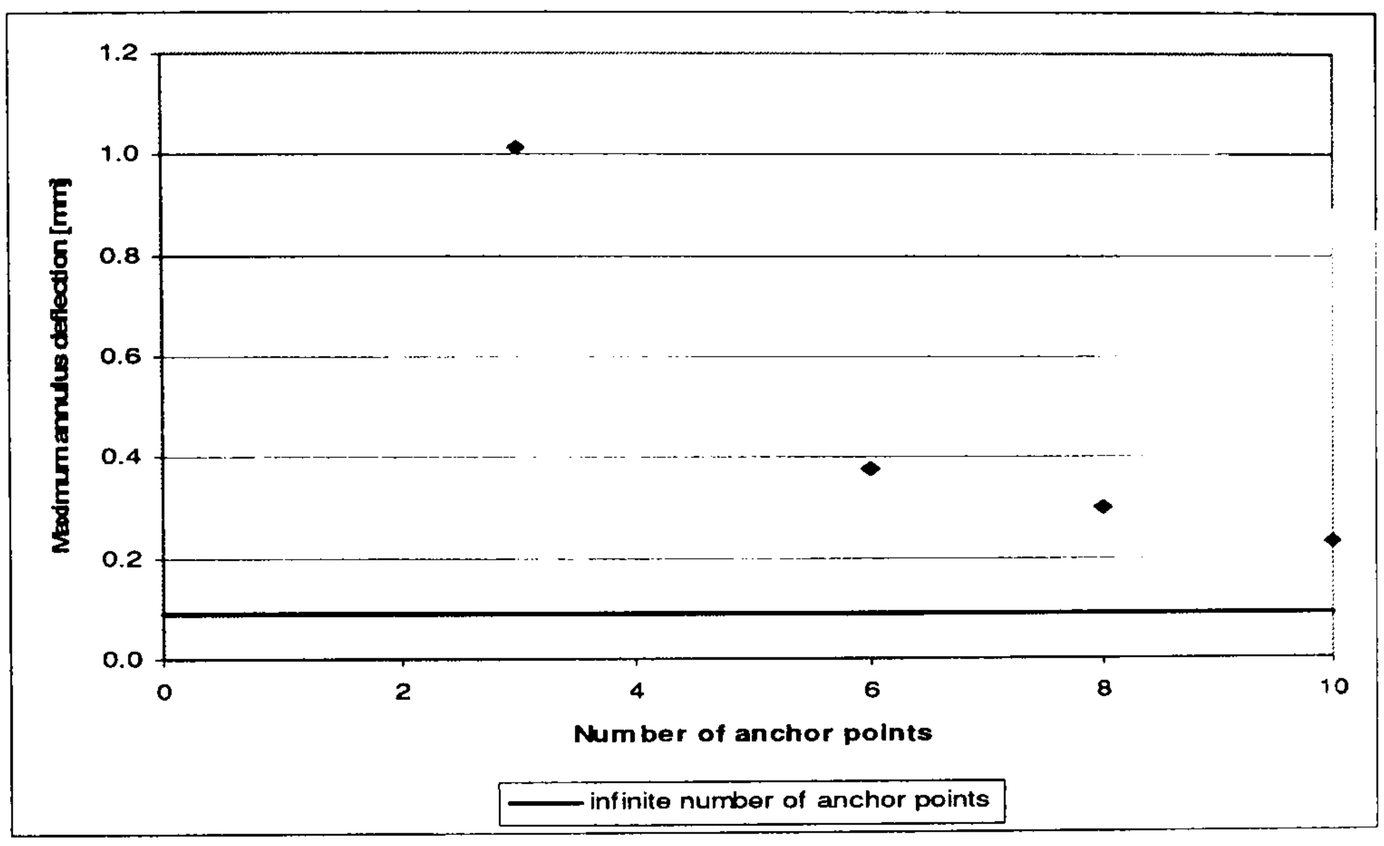

Figure 9-15. Effect of increasing anchor points on maximum rotor plate deflection

As can be seen, there is a small increase in stiffness when 8 or 10 (rather then 6) anchor points are used, although it is questionable whether this justifies the extra complexity. Using only three anchor points for assembly does severely compromise the rigidity of the structure, however, and a necessary design revision may be required for subsequent generators to avoid damage during assembly.

9.6.2 Effect of lug geometry

A second area of concern is the geometry of the rotor plates' mounting lugs as this may have an important effect on the stiffness of the structure. Four lug geometries, show in Figure 9-16, are considered for the rotor plate design of the 5kW, 200rpm machine, which comprises of two 8mm thick mild steel rotor plates separated by 6 supporting

pillars. The four alternative geometries examined include: the standard lug design used on the 5kW machine, a completely circular rotor disc design (i.e. no lugs for maximum stiffness), a hexagonal design with cropped corners, and a compromise design with wide angled lugs to increase stiffness without increasing weight.

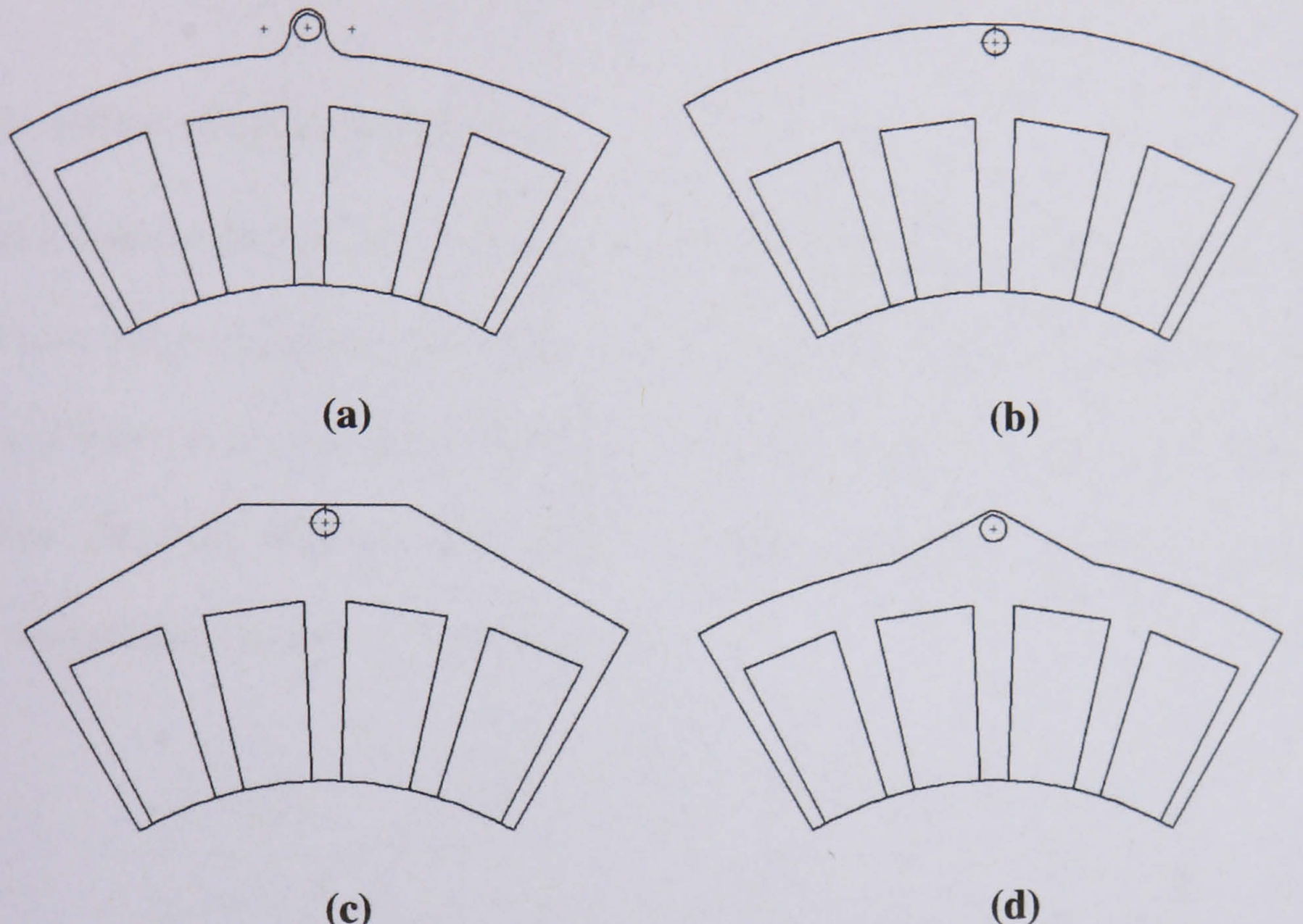

Figure 9-16. Lug geometries: (a) standard lug, (b) circular, (c) hexagonal, (d) wide lugs

The effect of these lug geometries on the rotor plate stiffness is shown in the figure below along with the 'magnetic stiffness' of the generator.

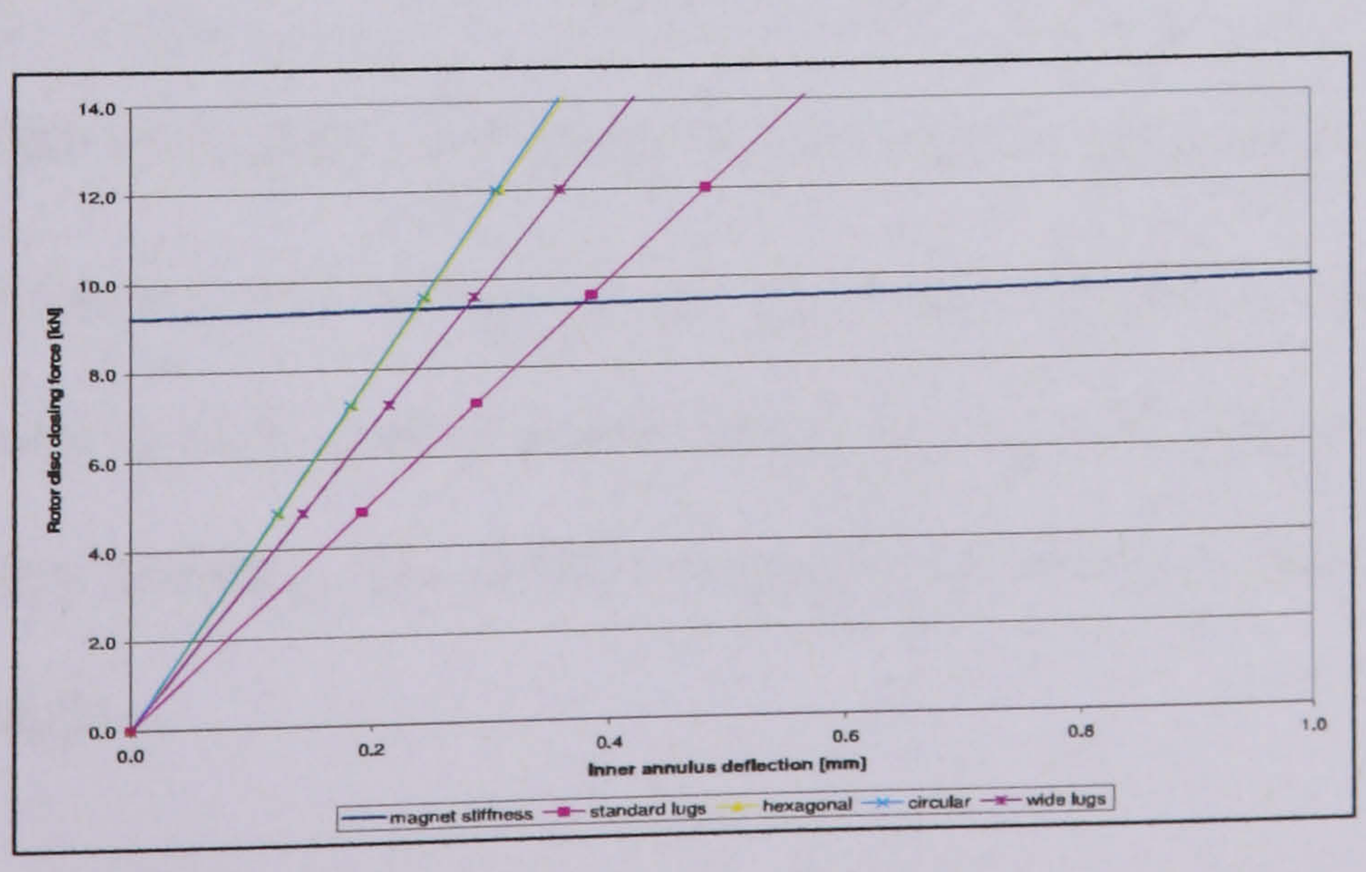

Figure 9-17. Effect of lug geometry on rotor plate stiffness

Figure 9-17 shows the cropped hexagonal and the wide lugged geometries are almost as stiff as the fully circular rotor plates, and that all three designs are significantly stiffer then the standard lug geometry which was used on the 5kW test machine. It is interesting that the compromise solution – comprising of wide lugs – performs almost as well as the circular geometry but with reduced mass.

9.6.3 Effect of plate thickness

A third method for increasing the rotor disc stiffness is simply to increase the plate thickness, although this comes at the cost of increased weight. Figure 9-18 shows the effect of increasing plate thickness on the maximum deflection at the inner edge of the annulus. The 5kW, 200 rpm test machine is again considered; (standard lug geometry with 6 supporting pillars are also assumed).

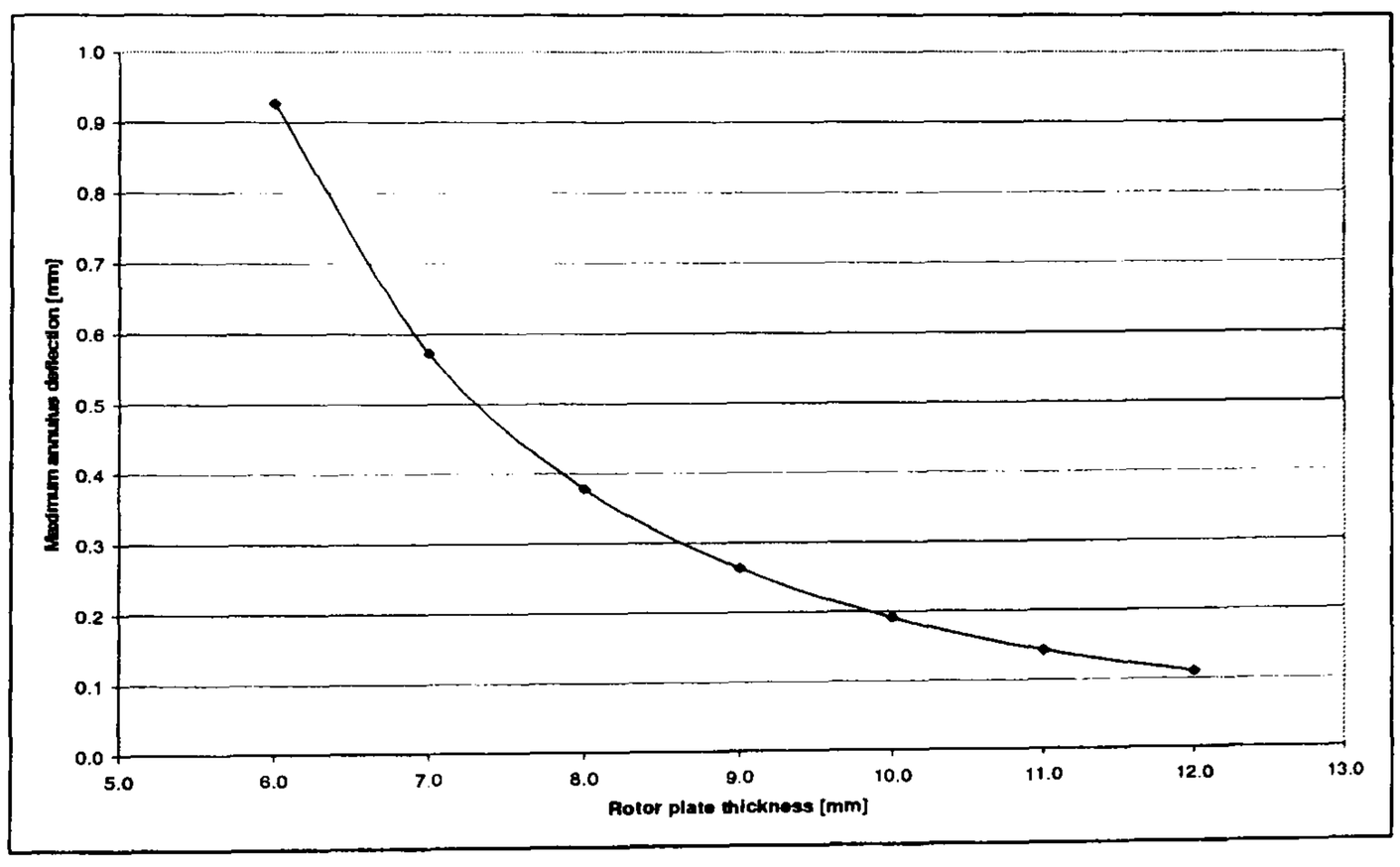

Figure 9-18. Effect of plate thickness on rotor plate deflection

Figure 9-18 illustrates that increasing the rotor plate thickness reduces the plate bending, but that it is a law of diminishing returns. In reality the plate must be at least 8 mm thick to carry sufficient flux without saturating and probably less then 10 mm to avoid excess weight.

9.7 Consideration of large diameter generators

The design case study in the previous section has shown the number of anchor points, the lug geometry, and the plate thickness all have an effect on the rotor plate stiffness, and all three factors must be considered when designing smaller machines. However, at large power ratings the design becomes increasingly constrained; weight saving becomes less important since the generator is already too heavy to be lifted by a single man, and because of this a circular rotor plate geometry with no lugs would probably be adopted to maximise stiffness. In addition, it is likely that no more then 8 supporting pillars would be used to separate the discs due to the complexity involved in accommodating the extra pillars and an equal number of extra jacking points. The following section will consider the case of a larger 20kW, 100rpm generator which is of similar construction to the 5kW, 200 rpm device but uses larger dimensions. A list of the general design parameters are given in the table below.

Generator power	**20kW**
Rated speed (rpm)	100
Number of magnets	32
Number of coils	24
Coil length (radial) (mm)	150
Coil height (mm)	18
Min rotor plate thickness (mm)	15
Mean diameter (mm)	1100
Magnet thickness (mm)	15
Magnet shape	Trapezoidal
Closing force between rotor plates (kN)	45.5
Active mass (kg)	265.1
Number of rotor plate anchoring pillars	8
Lug geometry	Round (i.e. no lugs)

Table 25. Design parameters for a 20kW axial flux machine

Figure 9-19 shows the structural rigidity of the rotor plate assembly when 15mm and 20mm thick mild steel rotor plates are used. It should be noted that a 15mm rotor plate is the minimum allowable thickness to carry the required flux.

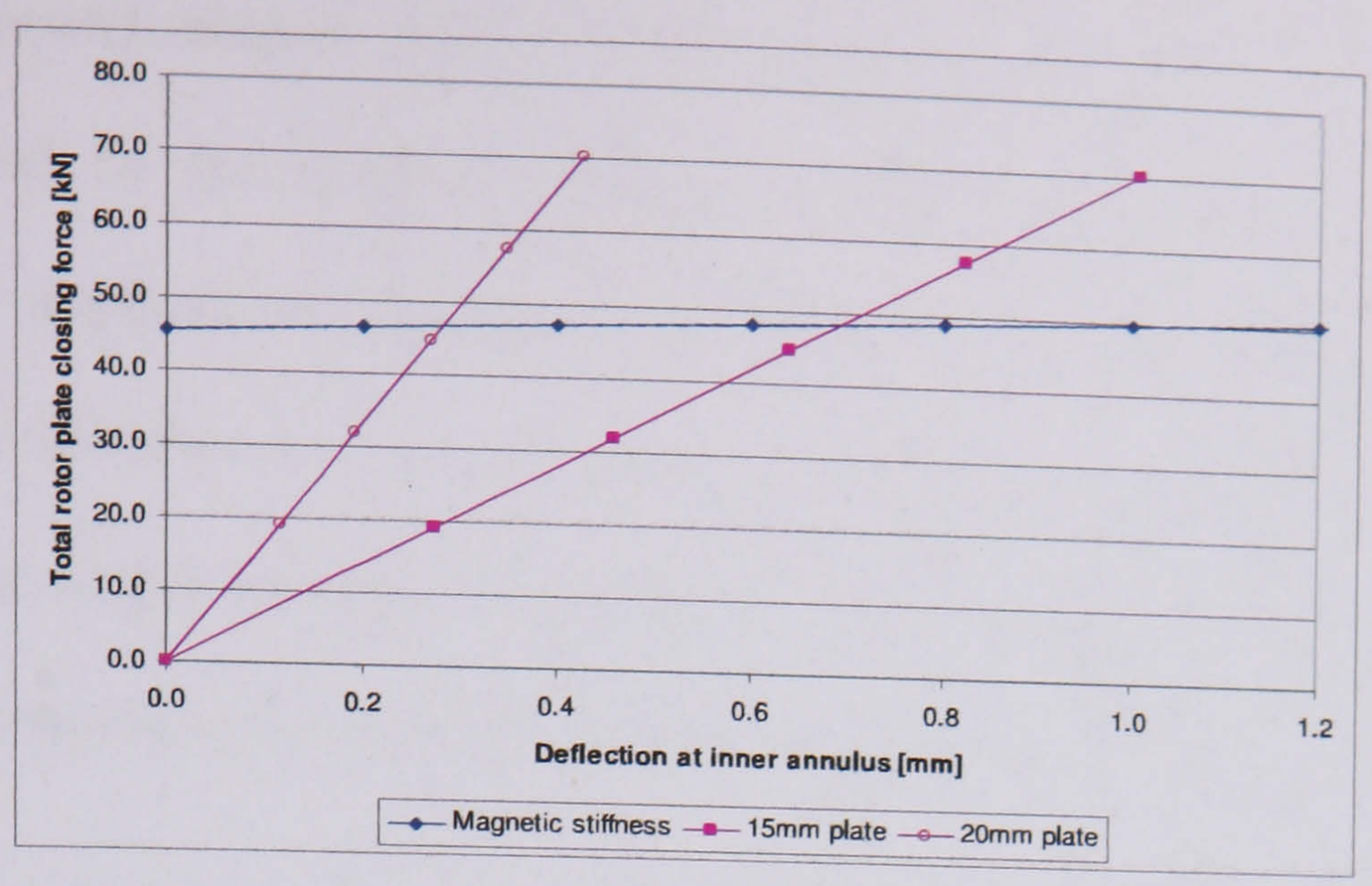

Figure 9-19. Deflection of 20 kW generator with 15mm and 20mm thick rotor plates and different rotor plate geometries.

Figure 9-19 shows that a 15mm plate thickness may push the design too close to the structural limit since this produces a rotor plate deflection of approximately 0.7 mm. A more conservative design using a plate thickness of 20mm might therefore be appropriate as this would produce a deflection of less then 0.3mm.

9.8 Alternative solutions to improved generator power

An alternative to using ever thicker rotor plates to counteract the large magnet forces is to use structural webbing elements to increase the rotor plates' stiffness without adding significant amounts of extra weight. However, such an approach would add considerable complexity to the design and probably require further finite element work which is beyond the scope of this study.

The inclusion of an epicyclic gearbox is another option for boosting the power output of the generator. Although a gearbox would increase the mechanical complexity of the system, it would also offer the possibility of building generators of several power ratings from the same component parts. Since the generator's shaft speed is proportional to power output, the inclusion of 3:1 gearbox on the 5kW, 200 rpm machine would effectively transform it into a 10kW, 133 rpm machine. Although this would equate to a

higher centripetal magnet force (166N compared to 40N), this could easily be accommodated by the magnet retaining ring. A greater concern might be in the maintenance implications associated with including a gearbox, as one of the great attractions of the direct-drive concept is that it is essentially maintenance free. However, as the power ranges increase, the application moves away from home owners and towards professional operators with properly administered maintenance schedules.

A further possibility is to move to a multiple rotor configuration by stacking two or more machines back-to-back, as shown in Figure 9-20.

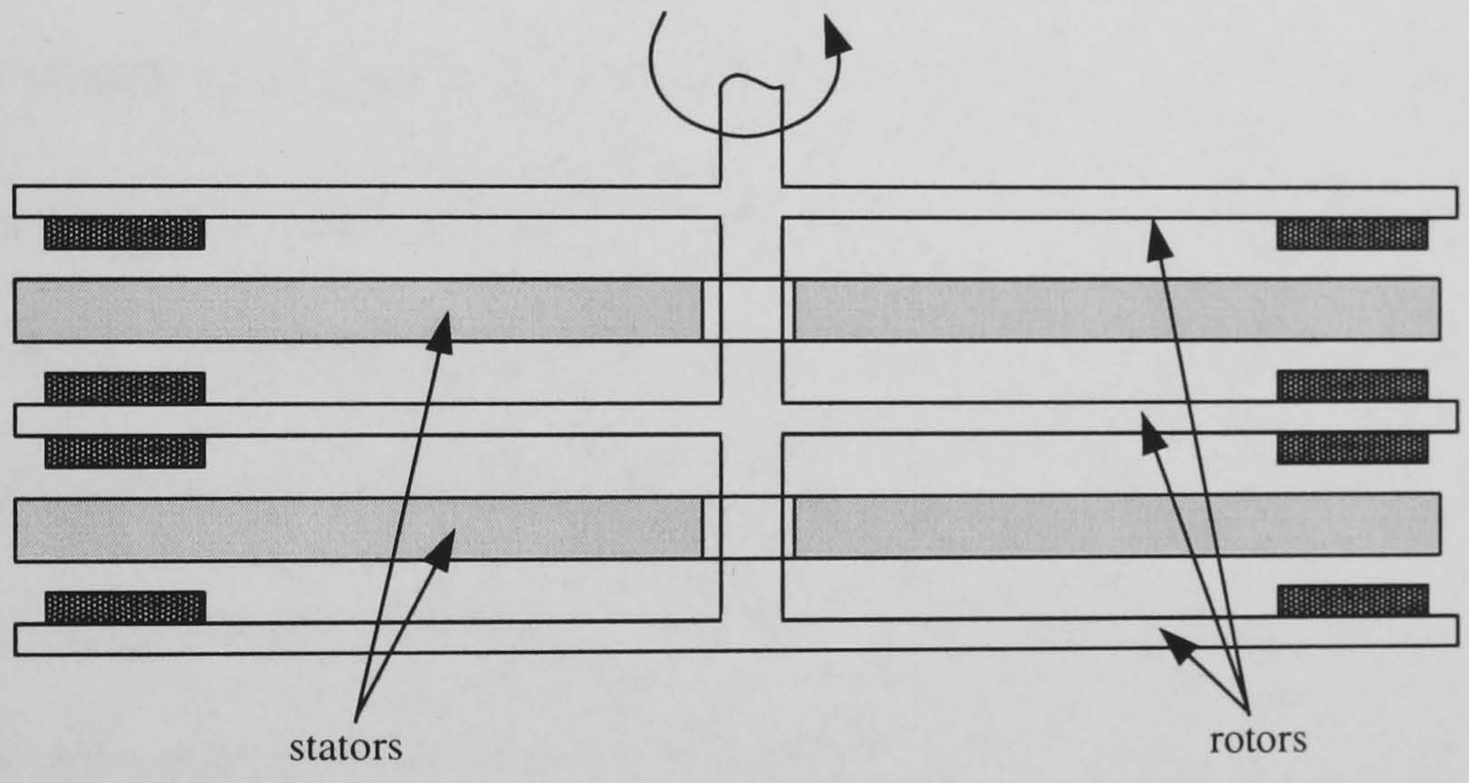

Figure 9-20. Multi-stage axial-flux machine

As with the epicyclic gearbox, this solution allows generators of multiple power ratings to be constructed from the same component parts. However, it is unlikely that this design offers significant improvements over large diameter machines in terms of specific power since, by effectively bolting two generators together, the active material is used less efficiently then if the diameter of the single generator has been increased slightly (since power α diameter^2). There is also a significant penalty in increasing the axial length of the machine since it becomes less rigid and may require further bearing supports. Much of the attraction of the axial flux topology is that the short axial length

allows it to be integrated directly into the turbine system without the need for extra bearings.

9.9 Conclusions

Several methods have been identified to increase the output power of a PM axial flux generator. At small generator diameters the output power maybe increased for a given machine size by moving from a round to a trapezoidal configuration as this produces a more compact design. To some extent the power rating at which this transition occurs is arbitrary as it depends on how the generator is to be integrated with the turbine.

As the rotor diameter is increased the structural rigidity of the rotor plates comes to dominate the design process. The finite element analysis developed in this chapter has made reasonably accurate predictions of the rotor plate deflections in two test generators. However, the study showed that the primary rotor plate of the 5kW, 200 rpm machine was significantly more deformed then would be expected in normal operation. This leads to the conclusion that a critical loading phase occurs during assembly when only 3 simple supports are used to separate the rotor plates, and it is therefore crucial to design an appropriate assembly process. This is an important conclusion of the work which has not been considered before.

The finite element study also shows that the specific design of the rotor plate lug geometry has an important effect on the stiffness of the disc. Using wide lugs improves the rigidity of the structure without a significant weight penalty, although at larger diameters a fully circular rotor plate geometry (without lugs) would most likely be adopted as weight saving becomes less important since the generator is too heavy to be lifted by a single man.

A number of methods have been identified for increasing the output power of the axial flux generator without resorting to ever-increasing rotor plate thicknesses to provide rigidity. The use of extra structural webbing elements or the incorporation of an epicyclic gearbox are both feasible solutions, although they would add significant complexity to the design. Alternatively, multiple rotors may be used on a single axle but this is unlikely to provide an optimal solution due to the lower material efficiency and poorer structural rigidity caused by the longer axial length. A more attractive method of producing higher power ratings may be to move to a radial flux topology as this does not have the large plate bending forces that are inherent in the axial flux configuration. This is discussed in greater detail in the next chapter.

The table below summaries the approximate power rating for the transition between different generator topologies.

Power rating	Topology
< 3-5kW	Round coils and magnets
> 3-5kW	Trapezoidal coils and magnets
> 20kW	Epicyclic gearbox, structural webbing, radial flux configuration

Table 26. Generator topologies at increasing power ratings

Chapter 10

The radial flux concept

10.1 Introduction

The advantage of the axial flux configuration is in its ease of manufacture, however this attraction becomes increasingly compromised as the power rating is increased. This topic was highlighted in the previous chapter, which examined the difficulties that arise when the diameter of the axial flux generator is increased. It showed that at power ratings above 20kW, 100-200rpm the axial flux topology has significant constraints and it becomes sensible to move to a radial flux configuration. However, since the radial flux topology is based on a 'round' rather then a 'flat' geometry, it is inherently harder to manufacture and the main benefit of the axial flux configuration is lost. Because of this, the following chapter will examine methods of constructing radial flux generators which retain the simplicity and ease of manufacture of the axial flux configuration.

Closing forces are a significant challenge in large diameter machines and section 10.2 examines different strategies for managing them, and shows that an air-cored structure may be appropriate in certain applications such as rim generators for ducted turbines. In other applications an iron-cored machine may be appropriate and sections 10.3 – 10.5 investigate novel stator materials and construction techniques that retain a simple manufacturing route. Judged by this criterion, the results of the material tests are presented in sections 10.6.and 10.7, and an analysis of the flux density in the stator iron for different stator materials is presented in section 10.8, along with the predicted power loss in the stator core. Finally, in section 10.9, conclusions are drawn about the most

appropriate configuration for a prototype machine and about the most attractive stator materials to use.

10.2 Managing high closing forces at large diameters

There are essentially two ways to manage the high attractive forces between the stator and rotor in an electrical generator as the machine size is increased: either the attractive forces themselves can be reduced or a more robust mechanical design can be chosen and, depending on the application, either strategy may be employed. Section 10.2.1 examines applications where the first of these two strategies might be used while section 10.2.2 examines the second, with specific reference to the construction of robust small-to-medium scale radial flux generators for wind turbines.

10.2.1 Reducing the magnetic forces

In certain applications it becomes increasingly important to reduce the magnetic closing forces between the stator and rotor of the machine. One such application is in large diameter direct-drive wind turbine generators. Reducing the closing forces allows a rigid machine to be constructed at large diameters by using a novel mechanical design such as a spoked structure akin to a bicycle wheel. Research carried out as Durham university [118] [119] has shown the feasibility of this concept on a 1.78m diameter machine depicted in Figure 10-1. The SLiM machine eliminates stator-rotor closing forces by using a fully air-cored configuration with no stator iron. This is shown alongside the 4.5MW direct-drive Enercon machine which uses conventional stator iron and so produces high closing forces which must be managed using an extremely robust and heavy structure. Although the inclusion of stator iron improves the specific power of the machine, it does so at a significant weight penalty as illustrated by the Enercon E-

112 machine whose top heavy mass (THM) exceeds 500 tons, compared to Vestas V110 4.2MW indirect drive machine whose THM is 214 tons [120].

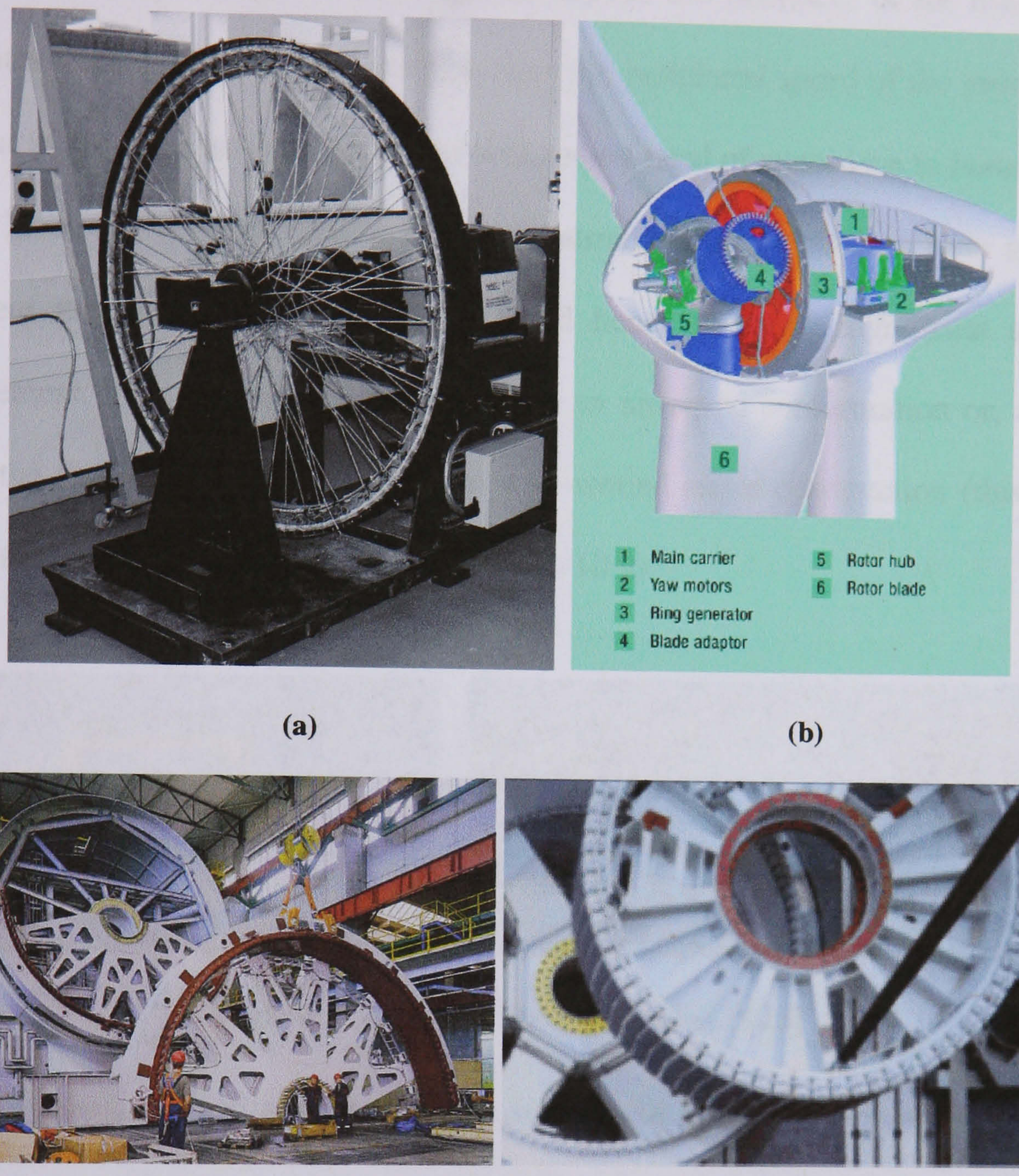

(a) (b)

(c) (d)

Figure 10-1. (a) Spoked Lightweight Machine (SLiM) [118], (b) the Enercon machine schematic [121] (c) the E-112 stator manufacturing process [122] and (d) the rotor and stator assembly [121].

Although it may seem inappropriate to compare a 1.78m diameter test machine with a large-scale 4.5MW turbine, the difference in structure of the machines is obvious. Reducing the magnet closing forces by using an air-cored configuration has a significant economic advantage in terms of material use.

A second application where stator-rotor closing forces must be reduced is in rim generator tidal stream turbines, such as Open Hydro's turbine shown in Figure 10-2. In this configuration the generator is integrated around the periphery of the rotor and an open water bearing is used. In a rim generator the peripheral speed of the rotor may be sufficient to produce the required power without the need of stator iron to boost the flux density. However, it is still vital to reduce the attractive forces between rotor and stator to prevent the machine from 'ovalising' and hence requiring significant structural reinforcement. This can be achieved by using an air-cored configuration or, as in the case of the Open Hydro turbine, using a wire-wound stator construction (this type of construction will be discussed in sections 10.3 - 10.9)

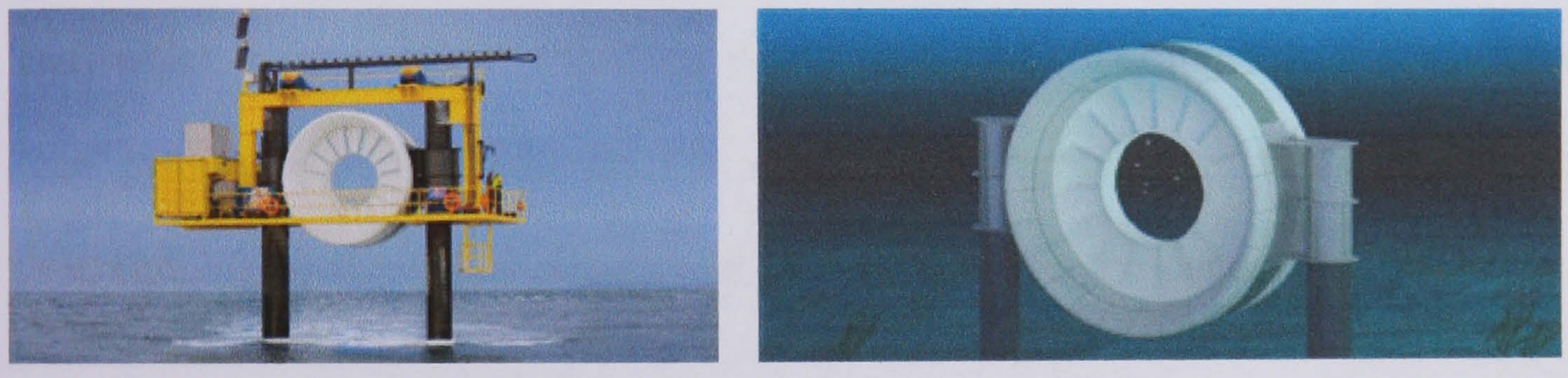

Figure 10-2. Open Hydro turbine [123]

In both of these applications reducing the stator-rotor closing forces has a significant advantage over increasing the mechanical stiffness of the machine in terms of weight saving. In the following section the alternative strategy of managing the magnet closing forces by increasing the stiffness of the structure will be examined. This strategy is particularly appropriate for small-to-medium scale wind turbines since the generator cannot be incorporated into the rim of the rotor, and so by boosting the magnetic flux by using electrical steel laminations, a smaller, more compact machine can be built.

10.2.2 Increasing machine rigidity

Chapter 9 highlighted the problems caused by the magnetic closing forces in the axial flux generator, which begin to become a significant constraint as the rated power approaches 20kW at 100-200rpm. This problem can be overcome by switching to a radial flux configuration as this does not have the plate bending geometry that lies at the heart of the axial flux topology's weakness. However, producing a rigid radial flux machine is not a trivial task, especially at large diameters, and the following section assesses different configurations in terms of their ease of manufacture.

Perhaps the most popular radial flux topology in the small-scale wind industry is the so called 'inside-out' design where the magnets are mounted on the inside of a 'magnet can' which rotates outside the coils, supported by two bearing. The structure of the 'can' provides rigidity to the rotor and allows the turbine blades to be mounted directly to it, simplifying the design and reducing the overall generator diameter, Figure 10-3.

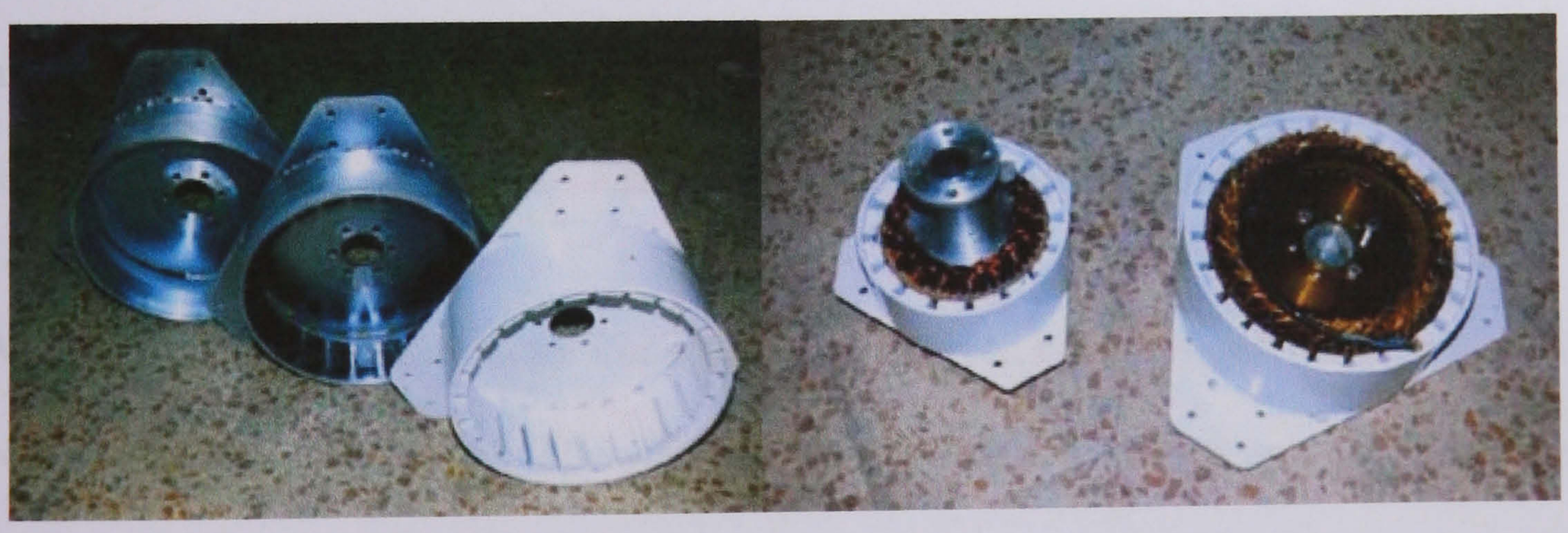

(a) (b)

Figure 10-3. Conventional radial-flux machine showing (a) the 'magnet can' and (b) the rotor with the stator [31]

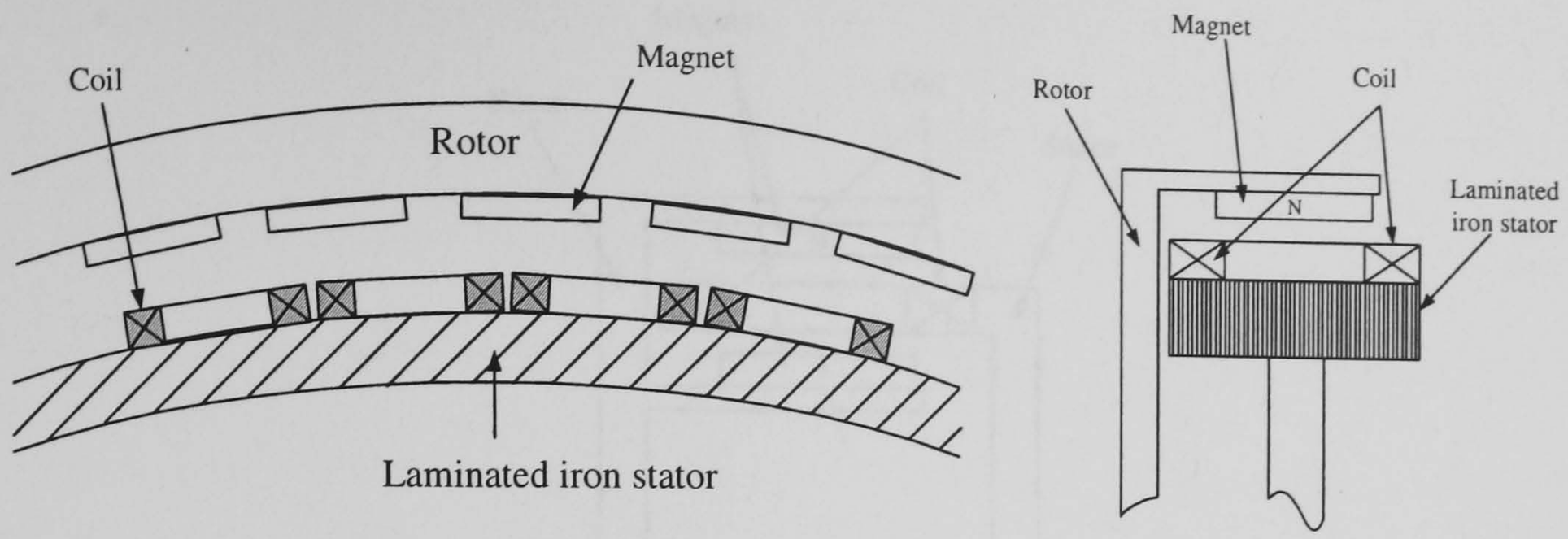

Figure 10-4. 'Magnet can' type construction showing (a) front view and (b) side view

Although this configuration is simple and rigid at small diameters, there are significant drawbacks as the diameter is increased. At large diameters it is no longer feasible to weld a single large plate to one side of the magnet can, as the rotor would need to be supported from two sides (much like the SLiM machine depicted in Figure 10-1 (a)), and by so doing a hollow central axle is required to allow the power to be tapped off. In addition, building a stator from electrical steel laminations at large diameters becomes increasingly untenable. This is because large diameter machines have high pole numbers and so carry low flux per pole, meaning the laminations become thinner (in the radial direction) and hence more flimsy, awkward, and time consuming to assemble.

A second possibility is to move away from the iron stator design and use an air-cored configuration, shown below. This design is essentially the axial-flux topology turned through 90°.

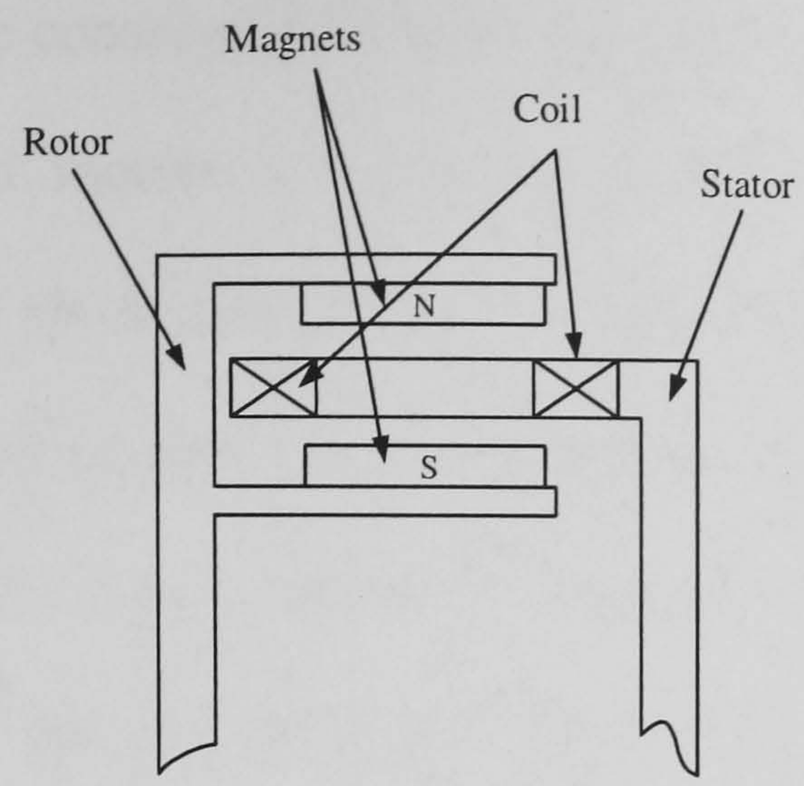

Figure 10-5. Air-cored radial flux configuration

Although it is possible to construct a generator using this configuration, there is an inherent fragility about the structure. The ring holding the stator coils must be made thin to maintain a narrow air gap and is only supported from one side. Conversely, in iron-cored radial flux machines the coils or magnets maybe firmly secured to the stator by means of thin binding tape. An alternative design uses the traditional rotor-inside-stator configuration, as shown in Figure 10-6. At medium generator diameters (1-1.5m) end plates can be used to provide rigidity to the structure, as shown in the Figure 10-6, which illustrates how two configurations might be integrated into a horizontal axis turbine system.

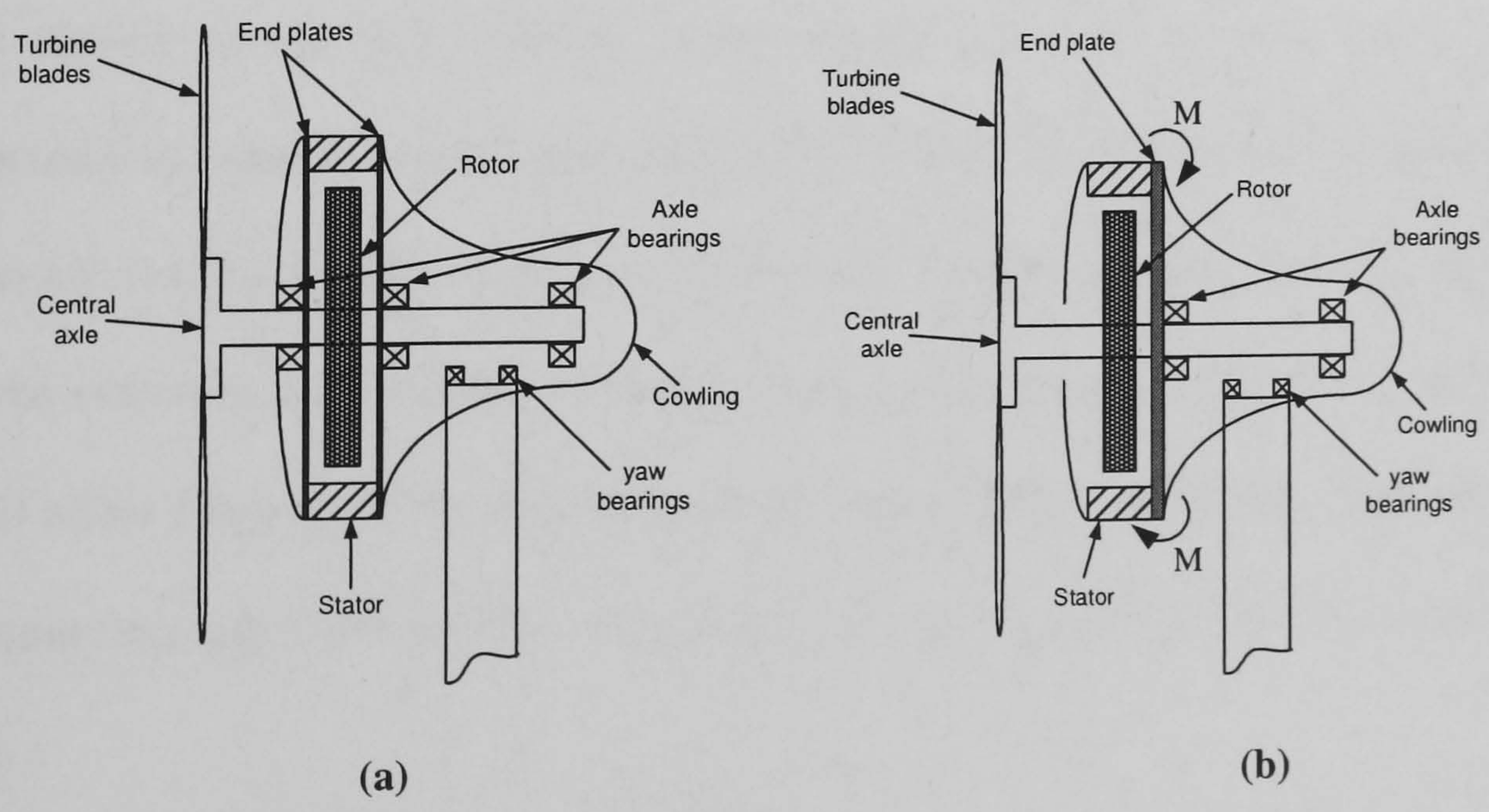

Figure 10-6. Two radial flux turbine configurations showing (a) single end plate and (b) double end plate

Configuration (a) is a more conservative design because it incorporates two end plates rather then one. It would require a third bearing support, however, which adds complexity. Using two end plates may be more important for larger diameter machines due the large bending moment created on the single end plate in configuration (b). To counteract this moment the plate would have to be exceptionally stiff, perhaps reinforced with webbing, and this problem becomes similar to the plate bending scenario of the axial flux machine.

For the purposes of a prototype machine, a conservative design has been chosen based on the configuration shown in Figure 10-6 (a). This configuration should allow simple manufacturing techniques to be tested which can then be scaled up to large diameter machines.

10.3 Consideration of stator material

Having chosen a generator configuration it is also necessary to identify appropriate materials with which to construct the stator and the stator back iron from. At one end of the spectrum the generator could adopt a fully air-cored topology in order to reduce magnet closing forces and simplify construction. Alternatively, the stator could be constructed from specially made electrical steel laminations which would provide a high flux density, but the machine would be heavy and complex to manufacture. In between these two extremes lie a number of novel stator materials and manufacturing processes that will allow large diameter machines to be constructed easily while still maintaining an adequate air-gap flux density. This topic will be the subject of the remainder this chapter.

10.4 Review of commercial magnetic materials

Before embarking on a detailed examination of the magnetic properties of potential stator materials, it is important to first consider the range of commercial magnetic materials currently available.

Magnetic materials are classed as either 'hard' or 'soft' depending on the area enclosed by their hysteresis loop. 'Hard' magnetic materials have large hysteresis loops and hence require a large amount of energy to magnetise them. They also have a high remnant flux density which makes them ideal for permanent magnets. The flux carrying components of an electrical machine, however, see a constantly changing magnetic field and so are continually being magnetised and re-magnetised. Because of this, they require a material with a low-loss hysteresis loop, known as magnetically 'soft', and are examined here.

For a good 'soft' magnetic material three things are required: a high relative permeability, a high magnetic saturation point and a low intrinsic coercivity. A high relative permeability (>10,000) results in a higher air gap flux density; a high saturation point allows the magnetic flux to be carried by less stator material, resulting in a more compact machine; a low intrinsic coercivity (<1kA/m) implies the material has a low-loss hysteresis loop which increases the machine's efficiency. Commercial magnetically soft materials are characterized by a high initial permeability, high saturation and a narrow, square hysteresis loop. A number of methods have been developed to produce materials with these characteristics and they are discussed below:

1. Alloying iron with nickel. 'Numetal', for example, is produced by careful heat treatment and minor additions of Cu and Cr. Such commercial alloys have

extremely high permeability (≈300,000), extremely low intrinsic coercivity ($0.4Am^{-1}$), and almost zero magnetostriction.

2. Process control. Hot and cold rolling stages are used to produce a 'textured' sheet with grains aligned in the direction of the magnetic flux, which increases the relative permeability of the material.

3. Iron annealed in hydrogen. The hydrogen atoms bind with spare oxygen atoms in the lattice structure to increase the relative permeability and decrease the intrinsic coercivity.

4. Iron alloyed with silicon (approx. 3-4%). This increases the resistivity of the material and so decreases Eddy current losses. The technique is used in most electrical steels.

5. Use of Iron oxide (Soft Ferrites). At high frequencies conventional magnetic materials suffer from high Eddy current losses. Soft ferrites, which consist of iron oxide combined with nickel, manganese or zinc, are ceramic insulators and so have good Eddy current properties.

6. Soft Magnetic Composites (SMC). SMCs comprise of high purity powdered iron, bonded under pressure using an organic compound as a matrix to produce a material with high electrical resistivity. The process allows more complicated stator structures to be built then would be possible with simple lamination and has recently been adopted in a number novel applications [124-127]. The material is characterised by high hysteresis loss and low permeability, and a

number of methods have been developed to improve both of these weaknesses, such as cyclic compaction and annealing [128, 129].

Table 27 compares the magnetic properties of some of these processes.

Material	Treatment	Initial μr	Max μr	Hc (A/m)	Br (T)	Ref
Iron, 99.8% pure	Annealed	150	5000	80	1.3	[130]
Iron, 99.95% pure	Annealed in hydrogen	10,000	200,000	4	1.3	[130]
Steel, 0.9% C	Quenched	50	100	5,570	1.03	[130]
78 Permalloy	Annealed, quenched	8,000	100,000	4	0.7	[130]
Iron oxide			720	100-300		[130]
SMC	Die pressed and annealed	130	150	250	0.25	[131]

Table 27. Magnetic material properties [130]

Of interest in Table 27 is the fact that small amounts of additives to pure iron, (e.g. 0.9% carbon in the case of steel), or changes in the heat treatment of the metal (e.g. annealing in hydrogen) can have large effects on the magnetic properties of the material. Both these effects have been highlighted during the development of SMC.

The techniques used to produce commercial magnetic material (points 1-4) are not appropriate for small-scale manufactures since conventional stator laminations require specialist punching equipment and become cumbersome at large diameters. Soft ferrites are only used for RF applications and SMC requires highly specialised equipment and procedures which are beyond the capabilities of small manufacturing companies.

10.4.1 Novel stator materials

In order to produce a viable stator that is easy to manufacture at large diameters, a number of criteria must be met. The material must be:

1. Sufficiently low energy loss

2. Have sufficient relative permeability

3. Easy to work with

Two manufacturing techniques which meet these criteria are described below:

1. A stator made of thin steel wire, wound onto a former and encapsulated in epoxy resin (see test core in Figure 10-8 (a)). In this approach the turns of steel wire act as laminations since the dimension perpendicular to the air gap flux path is narrow.

2. A stator ring made of steel shot in an epoxy matrix (see test core in Figure 10-8 (e)). Although such a material has similar (but inferior) mechanical and magnetic properties to SMC, it has still been considered because it requires no specialist manufacturing equipment.

10.5 Magnetic materials testing

The following section outlines an experimental testing procedure that can be used to measure the magnetic properties of prospective stator materials.

A small ring shaped core can be manufactured from each of the test materials and wound toroidally with two coils. One coil carries an AC current to provide an alternating flux in the core, while the second is used to measure an induced EMF. The set-up is shown schematically below, although in reality both coils are evenly distributed around the whole core, as depicted in Figure 10-8.

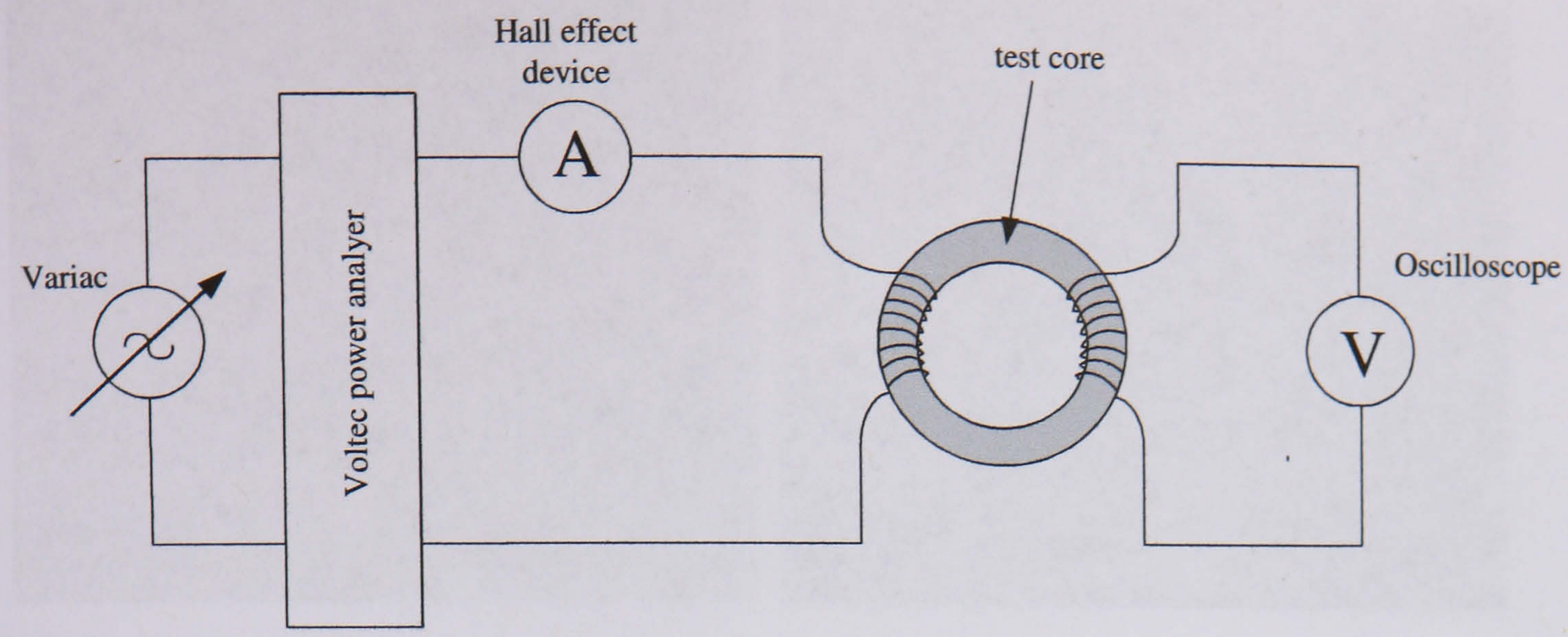

Figure 10-7. Schematic of testing arrangement

(a)

(b)

(c)

(d)

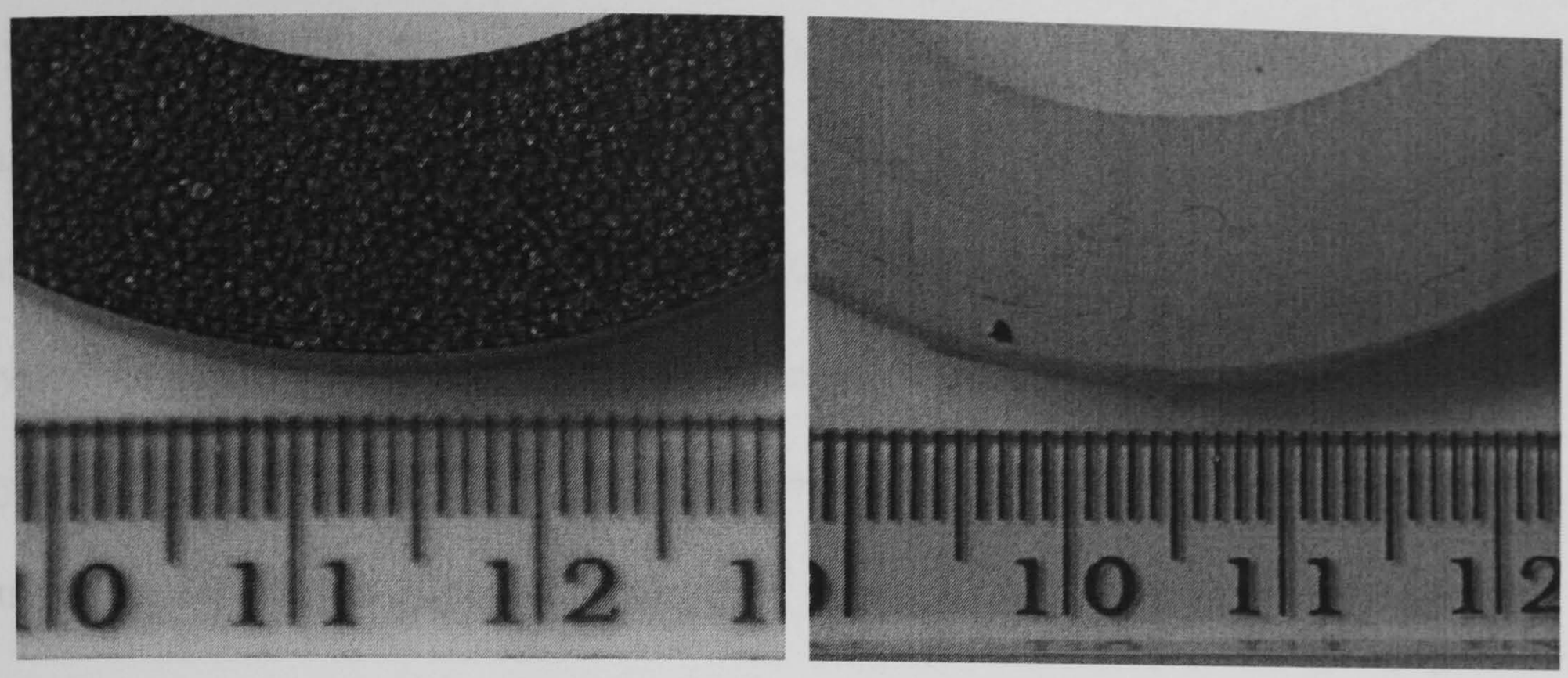

(e) (f)

Figure 10-8. Test cores showing (a) a steel wire wound core, (b) steel wire wound core with copper windings, (c) a shot composite core, (d) shot composite core with copper windings, (e) a close-up on a shot composite core and (f) a close-up of an epoxy core

The magnetic field intensity, H, can calculated instantaneously according to:

$$H = \frac{N_{cur} i}{2\pi r_c} \qquad [10\text{-}1]$$

Where N_{cur} is the number of current carrying turns, i is the instantaneous current and r_c is mean core radius.

The instantaneous flux can be calculated according to equation [10-2] by numerically integrating the measured EMF over time.

$$EMF = -N_{emf} \frac{d\phi}{dt} \qquad [10\text{-}2]$$

$$\Rightarrow \phi(t) = -\frac{1}{N_{emf}} \int (EMF) dt \qquad [10\text{-}3]$$

$$B(t) = \frac{\phi(t)}{A_{core}} \qquad [10\text{-}4]$$

By plotting instantaneous values of B against H over one cycle, a hysteresis loop for the material can be found. A full B-H characteristic can be measured by repeating this process many times using different levels of inducing current, to produce a family of hysteresis loops whose extremity points can be connected together. A selection of hysteresis loops for the materials tested are shown in Figure 10-9 and the full B-H curves are depicted in Figure 10-10.

A number of materials were tested for their suitability as stator back iron and these are listed in the table below.

Type	Material	Diameter /size (mm)	Fill factor	Notes
Wire composite	Bright mild steel	0.45	0.7	
Wire composite	Galvanised mild steel	1.45		
Wire composite	Galvanised mild steel	3.0		3mm rope wound from 49 strands of 0.3mm wire
Shot composite	G24 steel grit in MEKP resin	≈1.0	0.69	
Annealed shot composite	G24 steel grit in MEKP resin	≈1.0	0.69	Shot annealed before casting
Laminated core	Electrical steel	-	1	Strip wound
Solid epoxy ring	Epoxy	-	1	

Table 28. Properties of test cores

Wire composite cores can be manufactured by winding steel wire around a plastic bobbin, Figure 10-8 (a). A test winding was fully potted into the bobbin using MEKP resin to observe whether this made any difference to the core losses over a loose wound structure, but no measurable difference was found.

Steel shot (grade G21) in a MEKP fibre glass resin matrix was tested with and without annealing to assess whether annealing reduced hysteresis losses as had been suggested for SMC in reference [128].

A strip-wound laminated core from a commercial transformer and a pure epoxy ring were also tested to provide best and worst case scenarios with which to benchmark the test cores against.

10.6 Results of materials testing

The following section describes the results obtained from the material testing procedure in terms of relative permeability, saturation and power loss. Tests were conducted at 50 Hz.

10.6.1 Relative permeability and saturation

Hysteresis loops and full B-H characteristics for the wire composite materials are shown below. The area used in the calculation of the flux density is the total cross-sectional area of the core rather then the area of the steel strands.

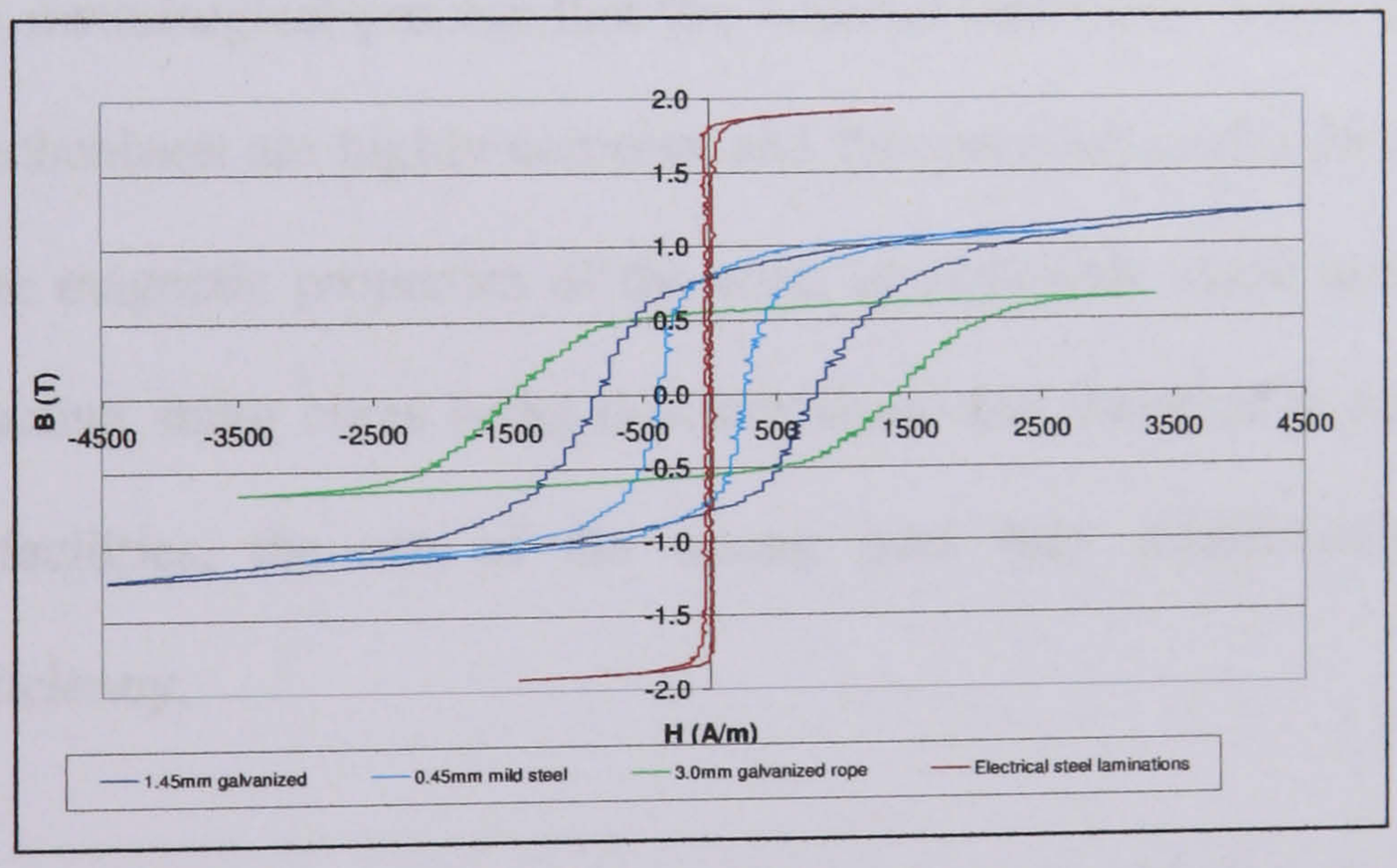

Figure 10-9. Hysteresis loops of wire-wound and laminated cores

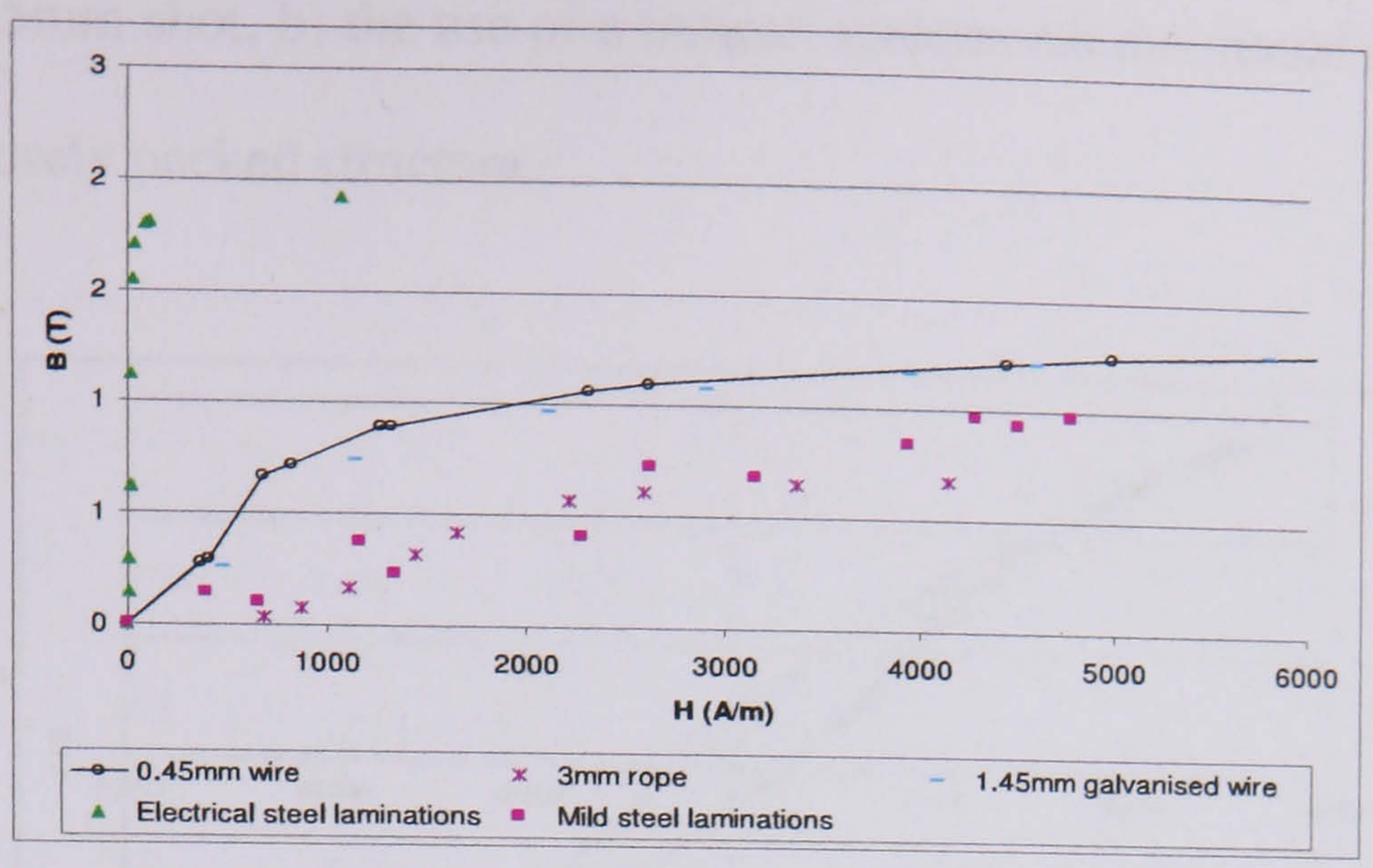

Figure 10-10. B-H curves for wire-wound and laminated cores

Figures 10-9 & 10-10 show the most attractive wire, in terms of the narrowest hysteresis loop and highest saturation point, is the 0.45mm diameter bright mild steel wire.

Figures 10-9 & 10-10 also show a range of magnetic properties between different grades of commercially available steel wire. This reflects the fact that the properties of ferromagnetic materials are highly dependent on the alloying constituents of the steel, as well as on the metallurgical process that the material underwent when it was formed. Both these mechanisms are highly complex and this prevents useful predictions being made about the magnetic properties of the wire. In situations where small companies maybe constructing stator cores using this technique, this variation is worrying since, without test facilities, the use of the wrong steel may significantly reduce the generator's efficiency.

Figure 10-11 shows a typical hysteresis loop for a shot composite ring. Tests on the shot composite revealed the importance of maximising the volume ratio of steel in the composite. Two methods were tested to improve the packing factor but neither showed significant promise. They were: a) sieving the (nominal) 1mm diameter balls to produce

a faction of 0.5mm shot, b) the use of a magnet underneath the mould to force the shot into a more closely packed structure.

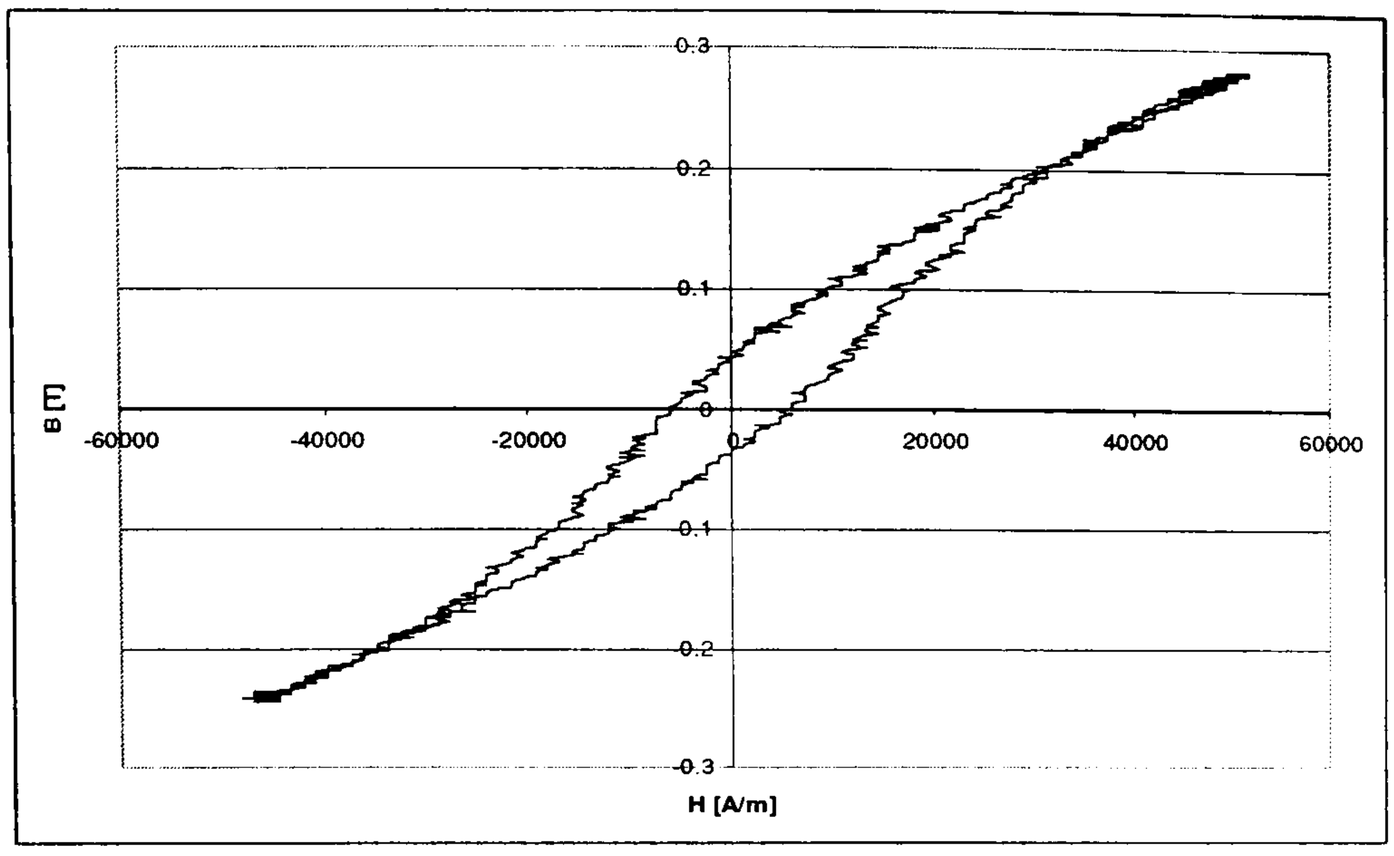

Figure 10-11. Hysteresis loop for G21 shot composite

It was not possible to measure a reliable B-H characteristic for the shot composites because the low relative permeability (c. 10) of the material made pumping flux around the core exceptionally difficult. It is not essential to know the exact B-H characteristic of the material, however, since the power losses were so large as to render the material impractical for this application, as discussed in the next section.

10.7 Results of materials testing - power loss

There are two main sources of power loss in electrical steel: Eddy current loss and hysteresis loss. Both are determined by the material properties of the steel and both are dependent on frequency and flux density such that:

$$P_{hyst} = k_{hyst} f B^{x} \qquad [10\text{-}5]$$

$$P_{eddy} = \frac{k_{eddy} d_{lam}^{2} f^{2} B^{2}}{\rho_{c}} \qquad [10\text{-}6]$$

Where the constants k_{hyst} and x depend on the molecular structure of the material (x is generally in the range 0.8 - 2.3 [132]). Due to the low generator frequency (c. <40 Hz) the hysteresis loss term dominates over the Eddy current loss. It can be found by integrating the area inside the B-H loop to give a value of energy loss per unit volume per cycle. Strictly the area inside the hysteresis loop also includes the magneto-striction[9] loss, although this effect is small and in any case it is not necessary to split the loss into its constituent parts.

The area enclosed by the hysteresis loop can be calculated by numerical integration. Alternatively, the power loss can be measured by subtracting the Joule loss in the coil from the total real power consumed:

$$P_{loss} = VI\cos\phi - I^2R \qquad [10\text{-}7]$$

Both methods of measuring power loss have been employed where possible to provide a method of checking the values obtained. However, it was found there was some uncertainty over the accuracy of Joule loss method at high coil currents because the loss was calculated as a small difference between two large numbers. At high currents the coil resistance (and therefore the current itself) changed rapidly as the coil heated up. This was particularly problematic when measuring the power loss in the shot composite materials since the low relative permeability demanded a high coil current to provide

[9] Magneto-striction occurs when the Young's modulus of a material changes in response to an applied magnetic field and this causes a lamination stack to vibrate at the excitation frequency, producing a characteristic 'transformer hum'.

sufficient flux. The power loss measured in the test composites is shown in Figure 10-12. These values were calculated using the numerical integration method.

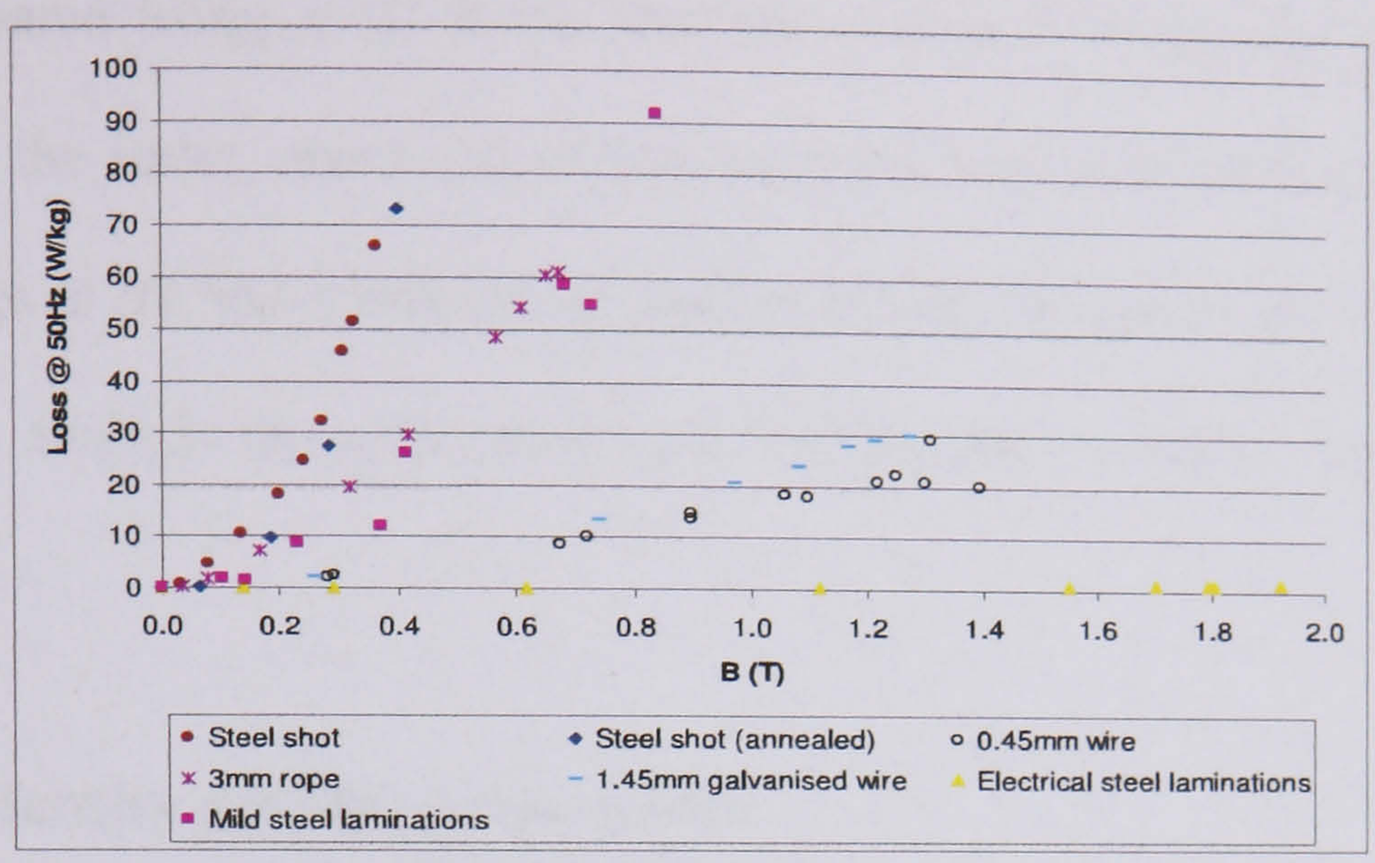

Figure 10-12. Power loss in wire composite materials at 50 Hz

Figure 10-12 shows that the 0.45mm bright mild steel wire has significantly better magnetic properties then the other materials tested. By comparing this wire to the shot composites, it is immediately obvious that the shot composites perform significantly worse. Table 29 summarises the magnetic properties of the materials tested.

Material	Packing factor	Saturation flux density (T)	Relative permeability	Power loss @ 0.5T, 50Hz (W/kg)
0.45mm steel wire	0.56	1.0	865	7
1.45mm galvanized steel wire	0.76	1.3	264	8
3mm galvanised rope	0.35	0.7	362	39
G24 steel shot composite	0.69	-	10	130
G24 steel shot composite (annealed)	0.69	-	10	130
0.6mm electrical steel laminations	1	1.9	50,000	0.08
Epoxy core	1	-	1	0

Table 29. Properties of test cores

10.8 Finite element analysis of radial flux machine

Having found the material properties through testing, prospective generator designs may now be compared using a 2D finite element package to determine the flux density profile across the stator, and hence the losses associated with each material. The flux density profiles in the stator and the air gap are discussed in sections 10.8.1 and 10.8.2, and from this analysis the total energy loss in the stator material may be calculated, section 10.8.3.

10.8.1 Flux density profiles in the stator

The primary role of the stator material is to provide a medium for the magnetic flux to travel in without incurring significant losses. Because of this, both the magnetic properties of the stator material and the likely behaviour of the flux density must be understood. This section examines how the flux density profile in the stator varies between the two types of materials considered. By coupling this information with the materials test results, a prediction can be made for the total power loss in the stator core.

The flux density profile in the stator can be examined using FEM, a 2-D finite element package [133]. A 2-D approximation is valid in the case of the radial flux configuration because the machine has sufficient axial length for the end effects to be considered small. A 2 kW, 200 rpm radial flux machine has been modelled and the general design parameters are listed in the table below. The dimensions have been created using the design procedure outlined in Appendix D.

Speed (RPM)	200
Power (W)	2000
Number of phases	3
Number of magnets	24
Number of armature coils	18
Frequency of induced voltage (Hz)	40
Magnet type	NdFeB
Magnet axial length (mm)	100
Magnet circumferential width (mm)	40
Magnet thickness (mm)	10
Pole pitch (mm)	65.0
Magnet pitch/pole pitch ratio	0.62
Outer Rotor diameter (mm)	514
Inner coil diameter (mm)	520
Running clearance (mm)	3
Stator wire thickness (mm)	15
Stator wire packing factor	0.70
Shot stator thickness (mm)	28
Shot stator packing factor	0.69
Pitch of armature coil (mech. deg)	20
Outer axial length of armature coil (mm)	140
Circumferential width of armature coil (mm)	94.0
Coil height (mm)	8
Coil width (mm)	25
Copper wire diameter (mm)	0.75
Number of turns/coil	230
Armature coil packing factor	0.68
Inner stator diameter (mm)	538
Outer stator diameter (mm)	635

Table 30. General design parameters of the 2kW, 200 rpm radial flux machine

Two stator constructions are modelled:

1. A wire composite structure consisting of 0.5mm diameter mild steel wire with a packing factor of 0.7. This was modelled in FEM by specifying that the stator was made of laminations of identical thickness to the steel wire, laminated in the z-θ plane (i.e. the laminations formed a horizontal stack in Figure 10-13). When specifying the lamination's fill factor, a value identical to the winding packing factor achieved on the test bobbin was used. The B-H characteristic for the material was inputted directly into the FE package and these values were taken from the test results shown in Figure 10-10.

2. A heterogeneous steel shot composite consisting of 1mm steel shot with a packing factor of 0.69 and a relative permeability of 10. This stator structure could be modelled in the FEA package by simply specifying that the magnetic material had a constant μ_r of 10 in all directions.

The results of the analysis are shown in Figure 10-13, while the flux density profile across the two stators is compared in Figure 10-14.

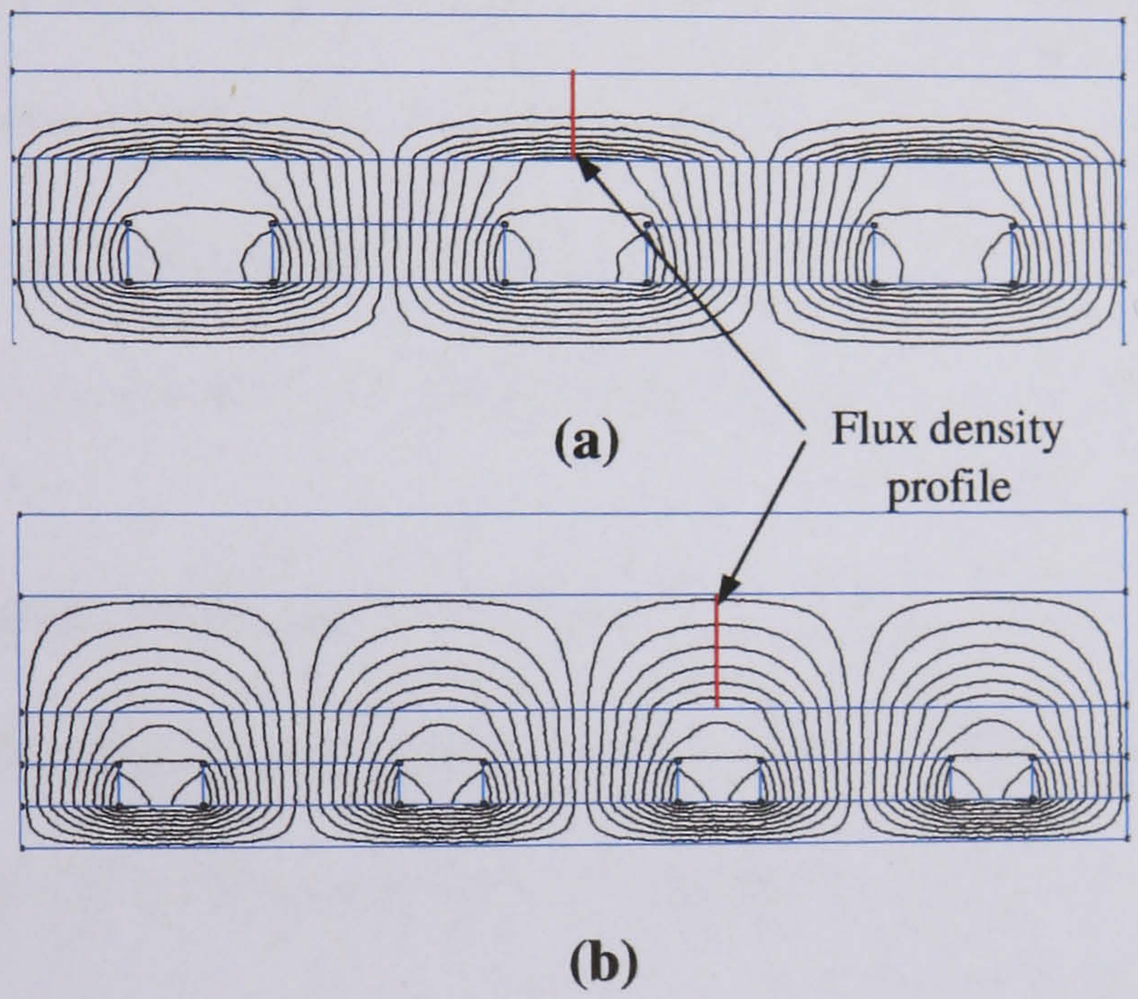

Figure 10-13. FEA of flux density in (a) wire wound stator and (b) steel shot composite

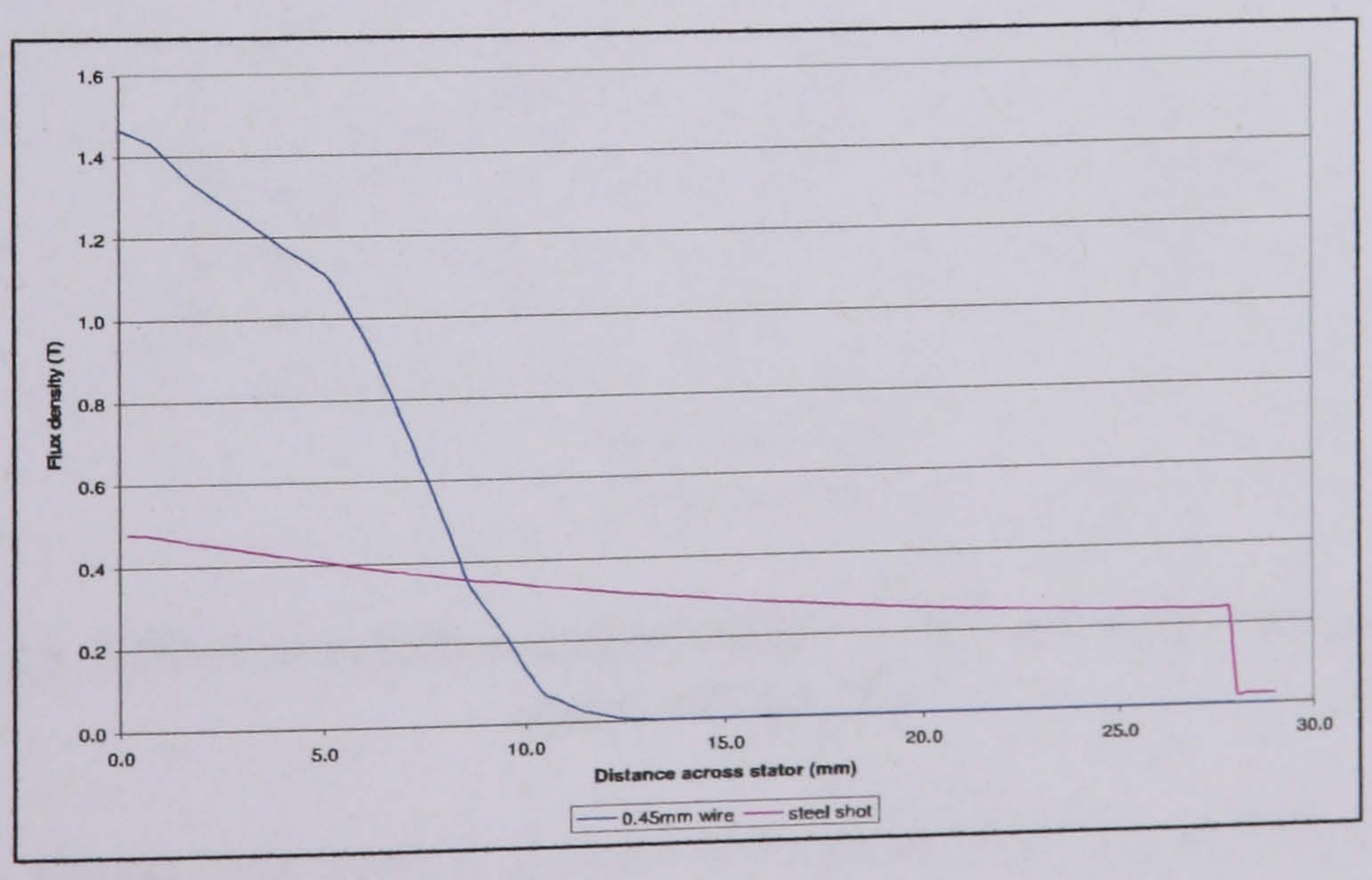

Figure 10-14. Comparison of flux density across stator for the two types of stator construction

Figure 10-14 shows the flux density profile across the stator varies significantly between the two stator types. Although the wire stators have a relative permeability which is an order of magnitude higher then the shot composite, they also have non-isotropic magnetic properties which lead to saturation occurring in the strands closest to the air gap. Conversely, the properties of the shot composite are uniform in all directions, which leads to a much flatter flux density profile. Because of this, the peak flux can be controlled by varying the thickness of the stator and this allows the designer the possibility of lowering the flux density to reduce losses, (although this comes at the expense of increased weight). In a wire-wound stator, the flux density and stator thickness are essentially decoupled - hence adding more turns of wire to the stator will not reduce saturation in the strands closest to the air gap.

Although the relative permeability of the shot composite is low, this need not necessarily compromise generator's output power. This is shown by Figure 10-15 which depicts flux density and power output as a function of relative permeability for a 5kW, 200rpm machine.

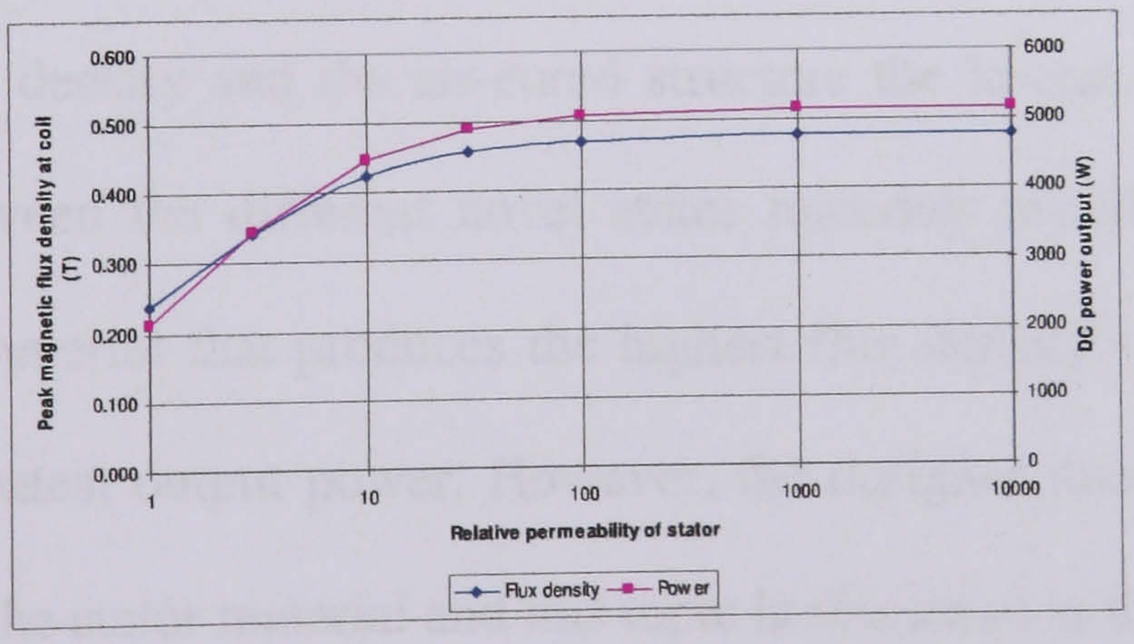

Figure 10-15. Effect of relative permeability on flux density and power (30mm stator thickness)

Figure 10-15 shows that even a modest permeability of 10 would not significantly reduce the output power.

10.8.2 Air gap flux density

Figure 10-16 shows the predicted flux density at the mid point of the armature coil for different types of stator construction. This information is summarised in Table 31.

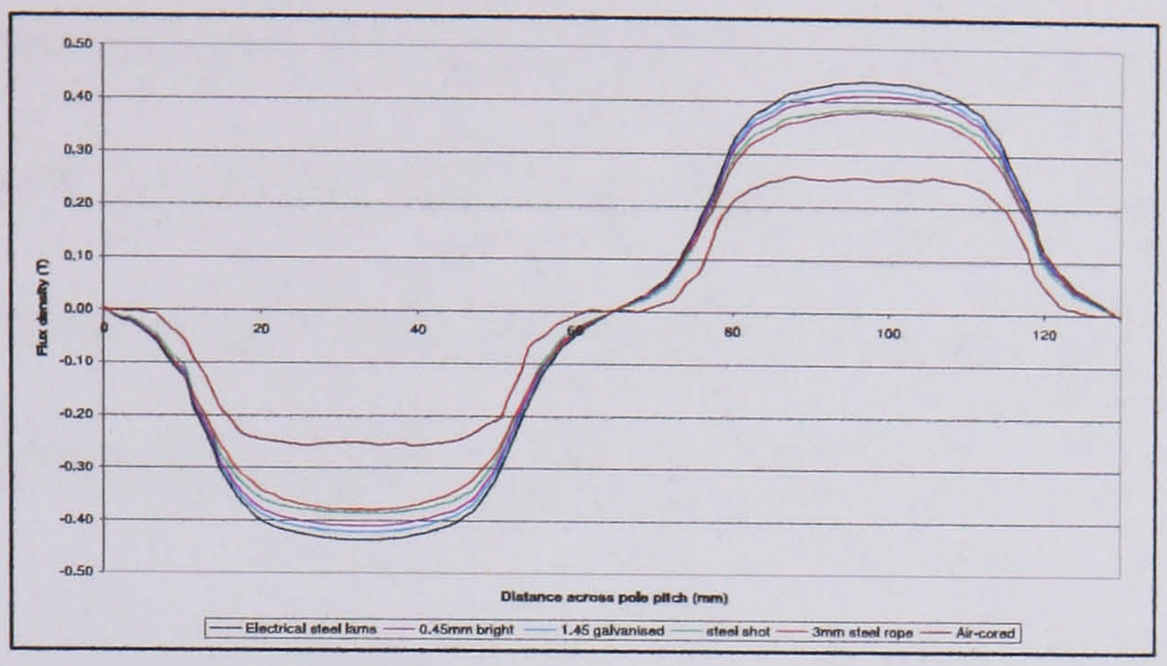

Figure 10-16. Air gap flux density measured half way through coil for different stator materials. Rotor made from 3.0mm wire rope.

Stator material	Peak flux (T)
Electrical steel laminations	0.437
0.45mm bright draw mild steel	0.411
1.45mm galvanised mild steel	0.423
1mm steel shot in resin	0.385
3.0mm galvanised steel rope	0.381
Air-cored	0.258

Table 31. Peak air gap flux density

Table 31 shows that, as might be expect, the electrical steel laminations produce the highest air gap flux density and the air-cored structure the lowest. However, there is little to choose between the different novel stator materials tested. It is tempting to simply choose the material that produces the highest flux density - assuming that this will produce the greatest output power. However, the designer must also consider the power dissipated in the stator material and this topic is discussed in the next section.

10.8.3 Power loss in stator material

The total power loss in the stator material can be calculated by combining the flux density profile across the stator, calculated using a finite element package in section

10.8.1, with the measured power loss per unit mass of the test cores, shown in Figure 10-12. To do this the stator may be split into a large number of thin concentric shells and the flux density found in each. By applying a quadratic line of best fit to Figure 10-12, the power loss per unit mass for a given flux density at 50 Hz can be calculated for each shell. This value can then be linearly scaled to fit the rated electrical frequency of the generator, which is 40 Hz, and then equated to an absolute power loss by multiplying by the mass of the shell. The power loss contribution of each shell can then be summed to give the total power loss in the stator.

This analysis has been carried out for the 2kW, 200 rpm generator described by the parameters in Table 30 and the results are summarised in the table below for a selection of stator materials.

Material	Relative permeability	Power loss in test core (W/kg @ 50Hz, 0.5T)	Predicted hysteresis loss in stator (W@ 40Hz)	Total measured machine power loss (W @ 40Hz)
Epoxy	1	0	0	0
0.45mm mild steel wire	865	7	166	178
1.45mm mild steel wire	264	8	338	
3.0mm steel rope	221	39	406	
G24 steel shot	10	130	1855	
0.7mm mild steel laminations	173	28	705	
0.6mm electrical steel laminations	50000	0.3	3	

Table 32. Predicted and measured power loss in the stator of a 2kW, 200rpm radial flux machine for a selection of stator materials

Table 32 shows that the 0.45mm steel wire composite material produces lowest total power loss in the stator, and for this reason the material has been chosen for the test machine which is described in detail in the following chapter. The measured power loss from that prototype generator is shown in the fifth column of the table and, as can be

seen, agrees to within 7% of the predicted value. More details about how this loss measurement was made can be found in Chapter 11.

10.9 Conclusion

This chapter has shown that, in certain applications, radial flux topologies employing air-cored and wire-wound stator structures can be advantageous in terms of manufacturing. These two stator designs have therefore been chosen for closer study, and this will be accomplished by constructing two prototype generators, as discussed in the next chapter. Constructing an air-cored machine will provide a useful benchmark for the lower end of the specific power range of the generator and will also allow the design process to be verified. The wire-wound stator construction employs a novel stator material and manufacturing process that can be usefully examined.

Although a number of different radial flux configurations have been adopted in the small-scale wind industry, for the purposes of a prototype machine a conservative configuration with the rotor inside the stator has been chosen.

In deciding which material to construct the stator from, a number of novel materials were tested and of these the 0.5mm mild steel wire was the most attractive due to its low losses. Although the 3mm galvanised steel rope had poor loss characteristics it was exceptionally easy to work with and so has been chosen for the rotor back iron, as this does not see a changing flux. It was found that the shot composite could be easily cast, at least on a small scale, however it too had poor loss characteristics and so was not considered for the stator material.

Finite element analysis of the air gap flux density at the mid point of the armature coil revealed there was little difference between the various wires that were tested. However, there were substantial differences between the predicted power loss in the core and for this reason the 0.5mm steel wire was chosen for the test machine.

Chapter 11

Design, Manufacture and Testing of the radial flux generator

11.1 Introduction

The following chapter discusses the manufacture, testing and evaluation of two prototype radial flux generators: a fully air-cored machine and a wire-wound stator machine. Sections 11.2 - 11.3 deal with the mechanical design of the generator and the design and manufacture of the rotor and stators, while section 11.5 compares the predicted performance of the generators, based on the design equations in Appendix E, with their measured performance in terms of voltage, power and efficiency. Section 11.6 discusses heat transfer within the generators and compares the measured temperature rise with a lumped parameter model and a finite element model. Finally, in section 11.7, conclusions are drawn about the performance of the two generators and the feasibility of the manufacturing processes.

11.2 Generator configuration

The generator dimensions were devised using the equations and procedure outlined in Appendix E. The following section describes the mechanical design of the generator.

The test generator is shown in exploded form in Figure 11-1 and is pictured on a Ward-Leonard test rig in Figure 11-2. Although this chapter describes tests performed on two generators, it is only the stators that are in fact different; the same rotor, end plates and bearing assembly were used for both generators. The generators consist of an epoxy

stator ring which is clamped between two end plates by eight lengths of stainless steel studding. The end plates contain bearings which locate the axle and allow the rotor to turn concentrically within the stator ring. Sections 11.4 and 11.3 discuss the manufacturing process of the stator and rotor in more depth.

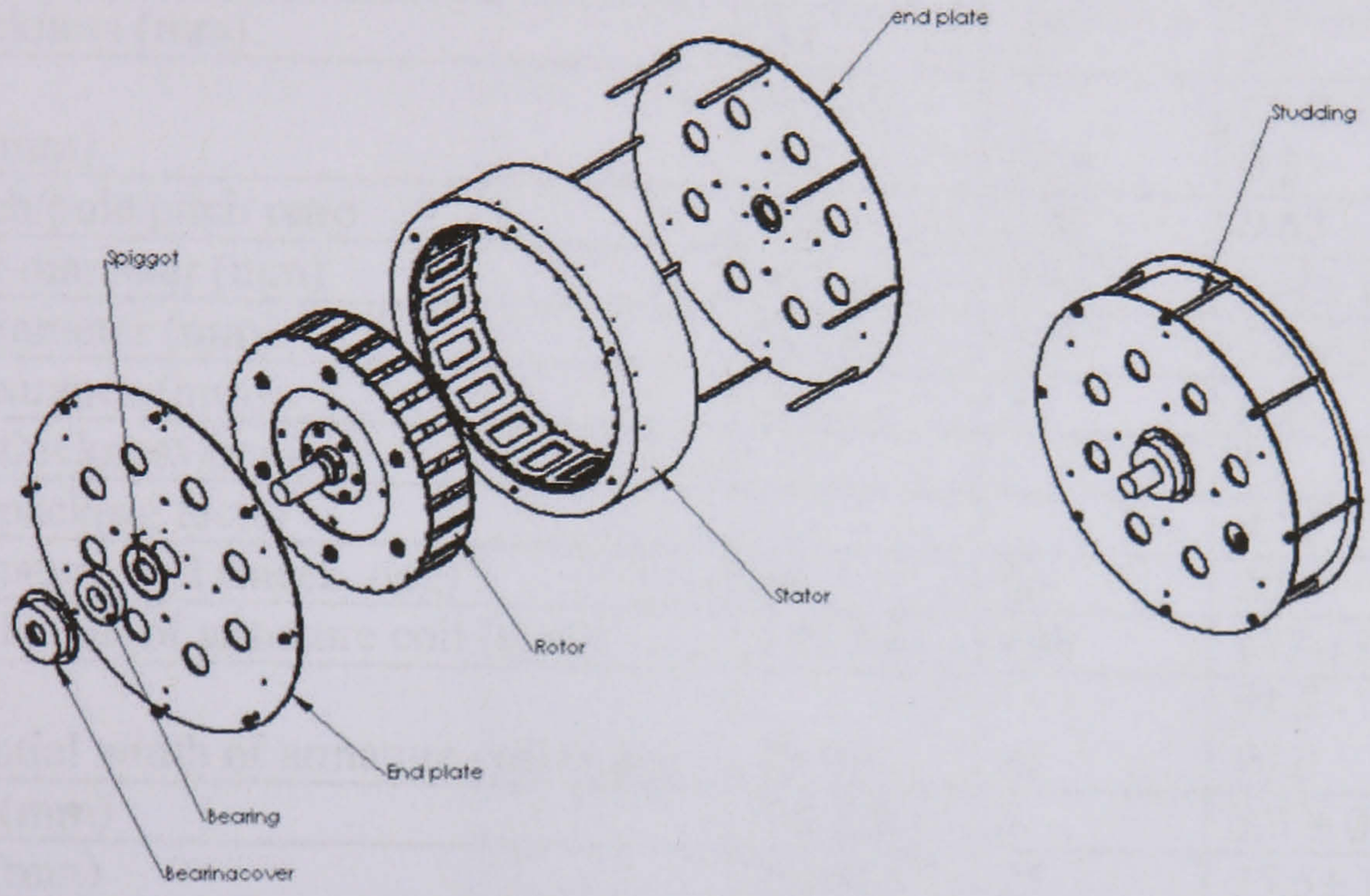

Figure 11-1. Generator assembly

Figure 11-2. Generator on test

The table below shows a summary of the generator dimension and highlights the difference between the designed and manufactured dimensions.

	Air –cored stator		*Wire wound stator*	
	Measured	*Designed*	*Measured*	*Designed*
Speed (RPM)	*200*	*200*	*200*	*200*
Number of phases	*3*	*3*	*3*	*3*
Number of magnets	*24*	*24*	*24*	*24*
Number of armature coils	*18*	*18*	*18*	*18*
Frequency of induced voltage (Hz)	*40*	*40*	*40*	*40*
Magnet type	*NdFeB*	*NdFeB*	*NdFeB -*	*NdFeB*
Magnet axial length (mm)	*2x50*	*100*	*2x50*	*100*
Magnet circumferential width (mm)	*40*	*40*	*40*	*40*
Magnet thickness (mm)	*10*	*10*	*10*	*10*
Pole pitch (mm)	*65.0 ± 0.5*	*64.6*	*65.0 ± 0.5*	*64.6*
Magnet pitch/pole pitch ratio	*0.62*	*0.62*	*0.62*	*0.62*
Outer Rotor diameter (mm)	*514± 1*	*514*	*514± 1*	*514*
Inner coil diameter (mm)	*520± 2*	*520*	*520± 2*	*520*
Running clearance (mm)	*3-4*	*3*	*0-2*	*3*
Stator wire thickness (mm)	*-*	*-*	*15*	*15*
Stator wire packing factor	*-*	*-*	*0.71*	*0.78*
Pitch of armature coil (mech. deg)	*20*	*20*	*20*	*20*
Outer axial length of armature coil (mm)	*139-140*	*140*	*137-139*	*140*
Circumferential width of armature coil (mm)	*89-91*	*91*	*91.5 - 94.0*	*93.5*
Coil height (mm)	*8.0 ± 0.1*	*8*	*8.5 ± 0.5*	*8*
Coil width (mm)	*25± 0.5*	*25*	*25.5± 1*	*25*
Wire diameter (mm)	*0.71*	*0.71*	*0.75*	*0.75*
Number of turns/coil	*300*	*300*	*230*	*271*
Armature coil packing factor	*0.60*	*0.60*	*0.51*	*0.60*
Coil resistance @ 20°C (Ω)	*4.43*	*4.58*	*3.10*	*3.21*
Coil inductance (mH)	*11.9*	*11.6*	*10.4*	*12.8*
Series/parallel coil connection	*3 series 2 para'l*	*3 series 2 para'l*	*3 series 2 para'l*	*3 series 2 para'l*
Inner stator diameter (mm)	*521*	*520*	*537*	*539*
Outer stator diameter (mm)	*636*	*635*	*637*	*635*
Active mass (kg)	*13.1*	*14.2*	*27.1*	*30.3*
Inactive mass (kg)	*59.2*	*-*	*70.0*	*-*

Table 33. Mechanical dimensions and electrical characteristics of the air-cored and wire-wound generators

11.3 Rotor design and construction

The rotor transfers torque from the central axle to the magnets which are placed at its periphery. Although it has no electrical connections and is structurally simple, the rotor must be rigid enough to resist transient wind gusts and must have a manufacturing

process that allows a round structure to be built at a large diameter without specialised workshop equipment. This can be achieved by using a sandwiched stack of 1" thick MDF discs, which can be cut with a router attached to a radius bar, allowing virtually any diameter to be constructed with an accuracy of ±1mm.

The rotor back iron was formed using successive layers of 3mm steel wire rope. Although the material tests outlined in Chapter 10 showed this material had high hysteresis losses, the back iron does not see a changing magnetic field and so can be made of a high loss material. The attraction of the 3mm steel rope is that it is extremely easy to work with and allows a reasonable thickness of steel to be laid down in relatively few turns. A finite element analysis of the flux density across the rotor iron (Figure 11-3) shows that an 11mm thick ring of steel rope could carry the required flux. This can be formed by winding 4 layers of 3mm diameter steel rope onto the MDF stack.

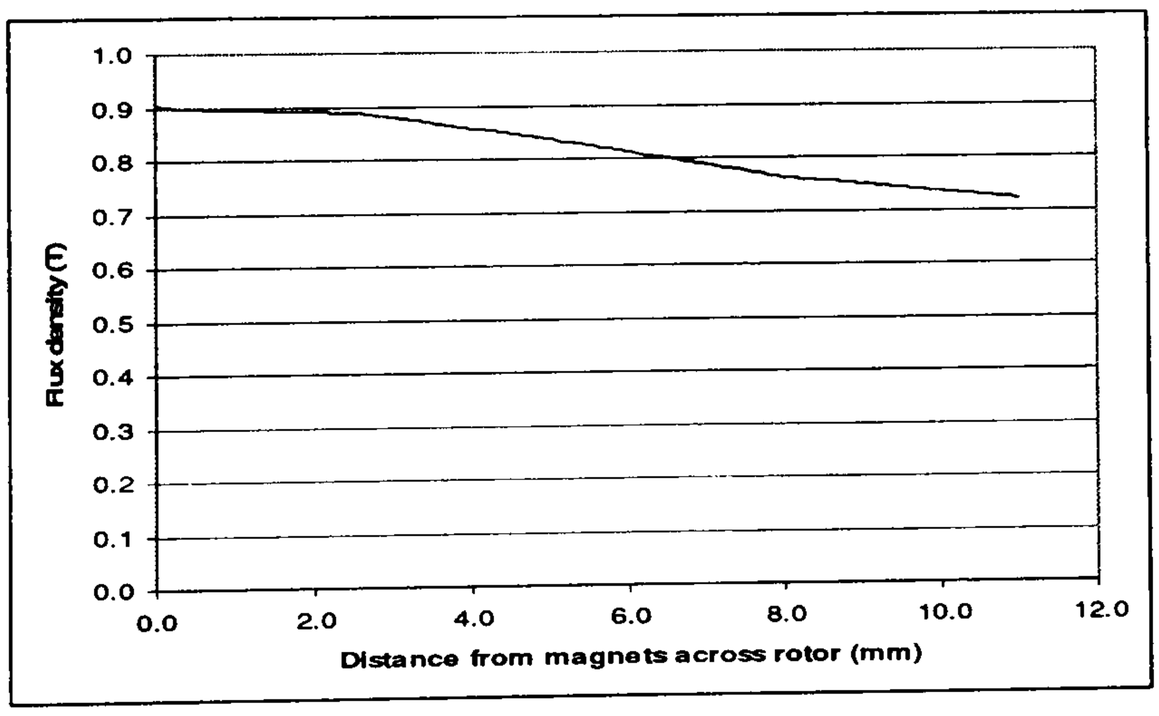

Figure 11-3. Flux density profile across the rotor back iron

Figure 11-3 shows that the steel wire strands nearest the magnets become saturated due to the non-heterogeneity of the wire composite material, just as with the wire-wound stator, although the flux remains high across the rotor because the thickness of wire

layer has been deliberately restricted.

The rotor construction is shown schematically in Figure 11-4 and pictorially in Figure 11-5.

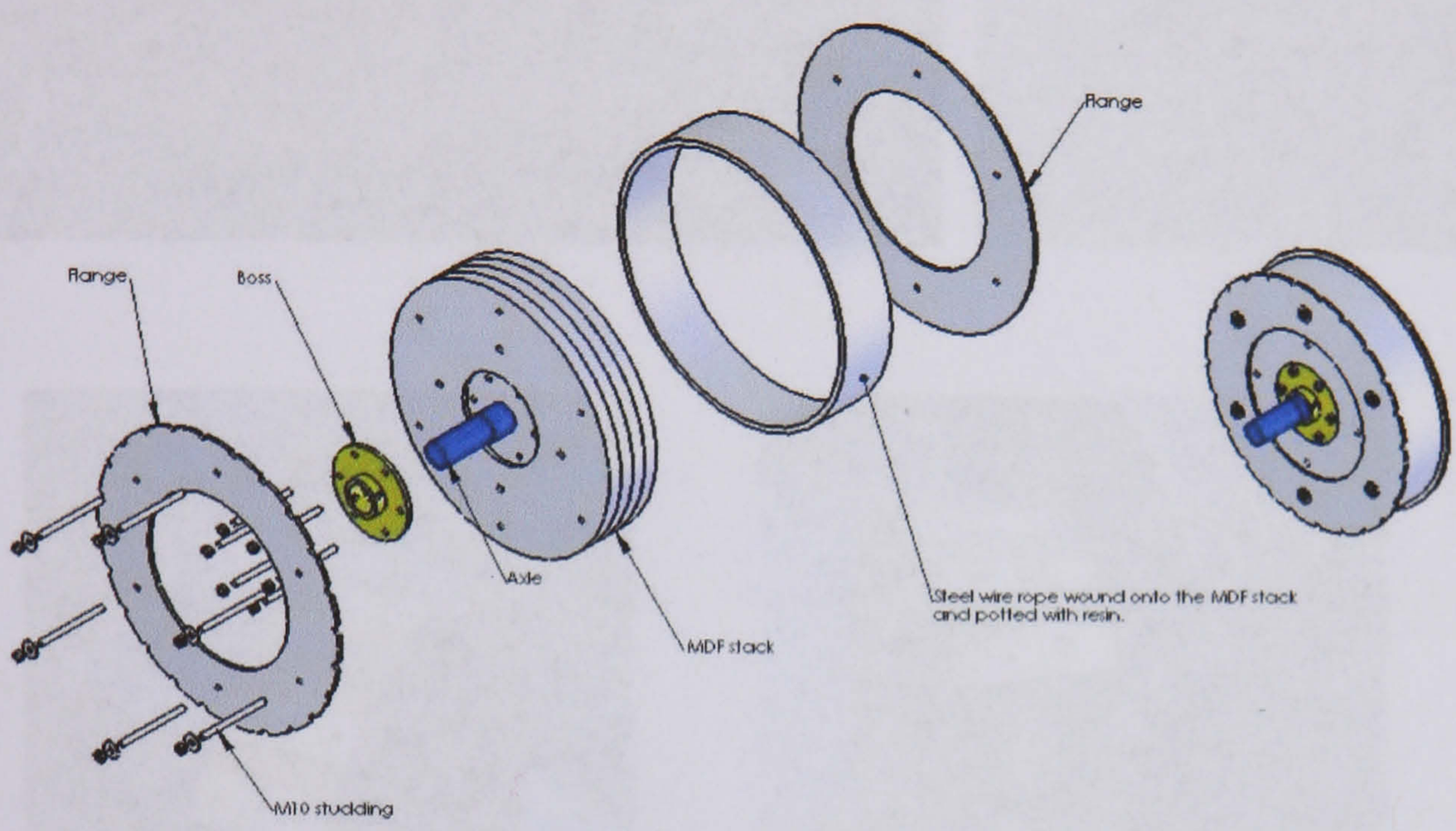

(a)

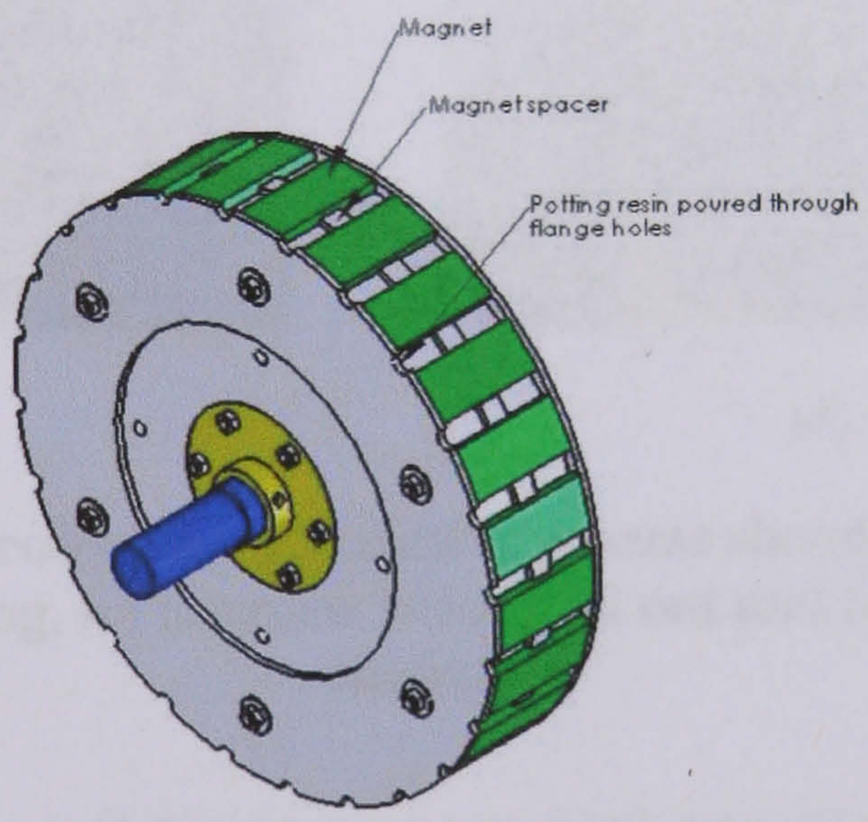

(b)

Figure 11-4. Rotor construction showing (a) the body assembly and (b) the rotor with magnets

(a)

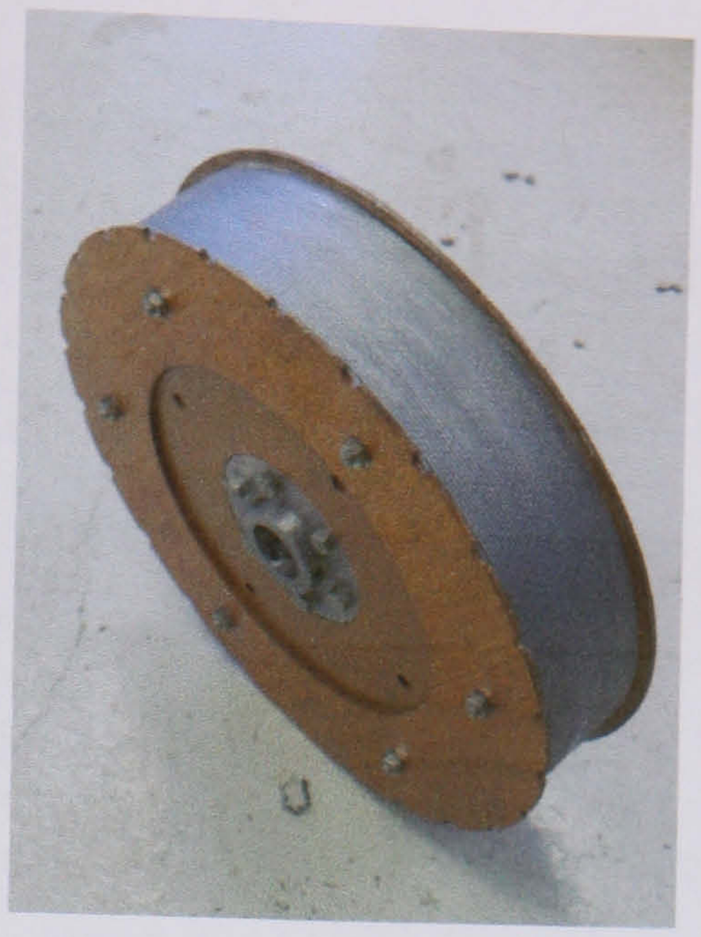

(b)

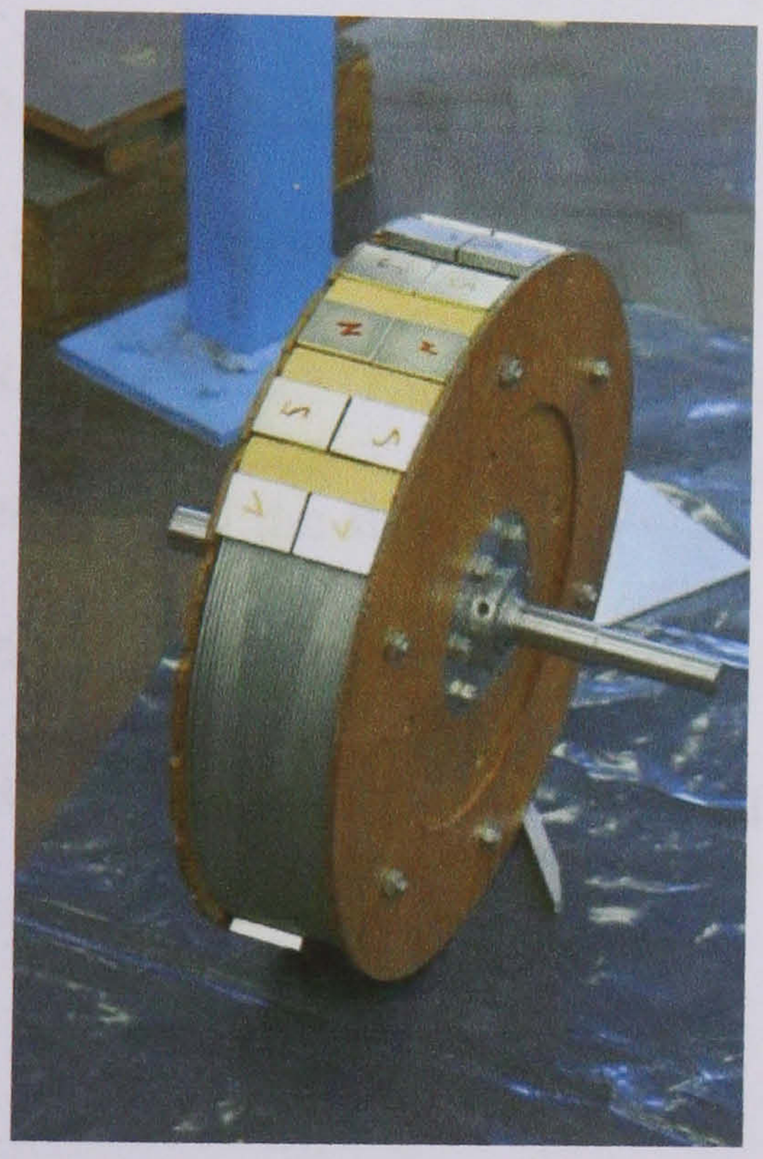

(c)

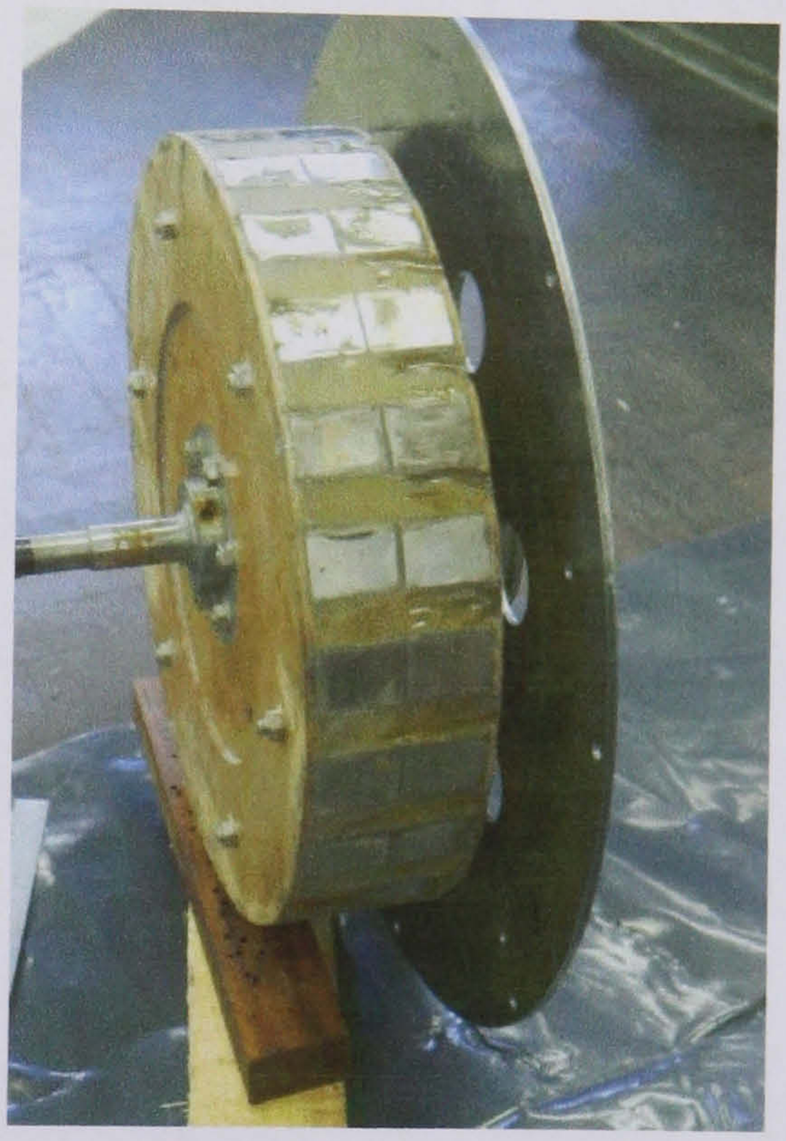

(d)

Figure 11-5. Pictures of rotor manufacturing process showing (a) the rotor former, (b) the wire rope winding, (c) magnets being laid out and (d) the magnets epoxied in place

Figure 11-5 shows the manufacturing process: steel rope was wound around a MDF former, cut from a stack of 1" boards. Wooden separators pieces were used to align the magnets so as to produce the desired magnet/pole pitch ratio, and the structure was then potted in epoxy.

11.4 Stator construction

As described in Chapter 10, two stators were chosen for examination: an air-cored structure and a wire-wound structure. Different construction methods have also been used for the two stators to assess their suitability for small manufacturing companies, and these are outlined in the following two sections.

11.4.1 Air-cored stator

The stator of the air-cored machine consists of a simple epoxy ring in which the coils are cast. A heat activated self-bonding copper wire was used to wind the armature coils, which allowed a flat, solid coil to be formed by heating the coil in the winding jig with an electric current. The coil is shown in Figure 11-6 (a). A separate harness was required to hold the flat coils in the correct location during the potting process as they could not be bent around the inner radius of the stator once the coils had been bonded. The coil harness is shown in Figure 11-6 (b) and the casting process is shown in Figure 11-6 (c)-(i).

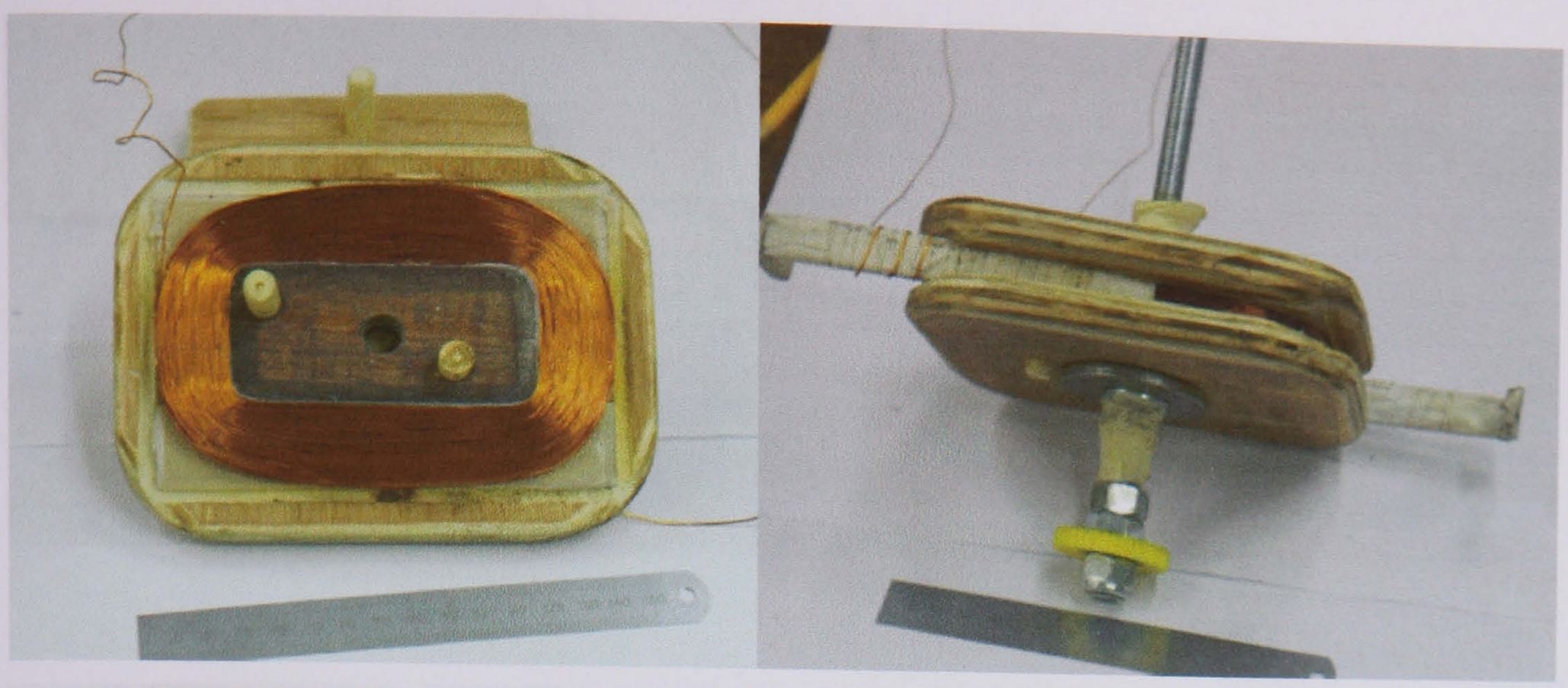

(a)

(b)

(c)

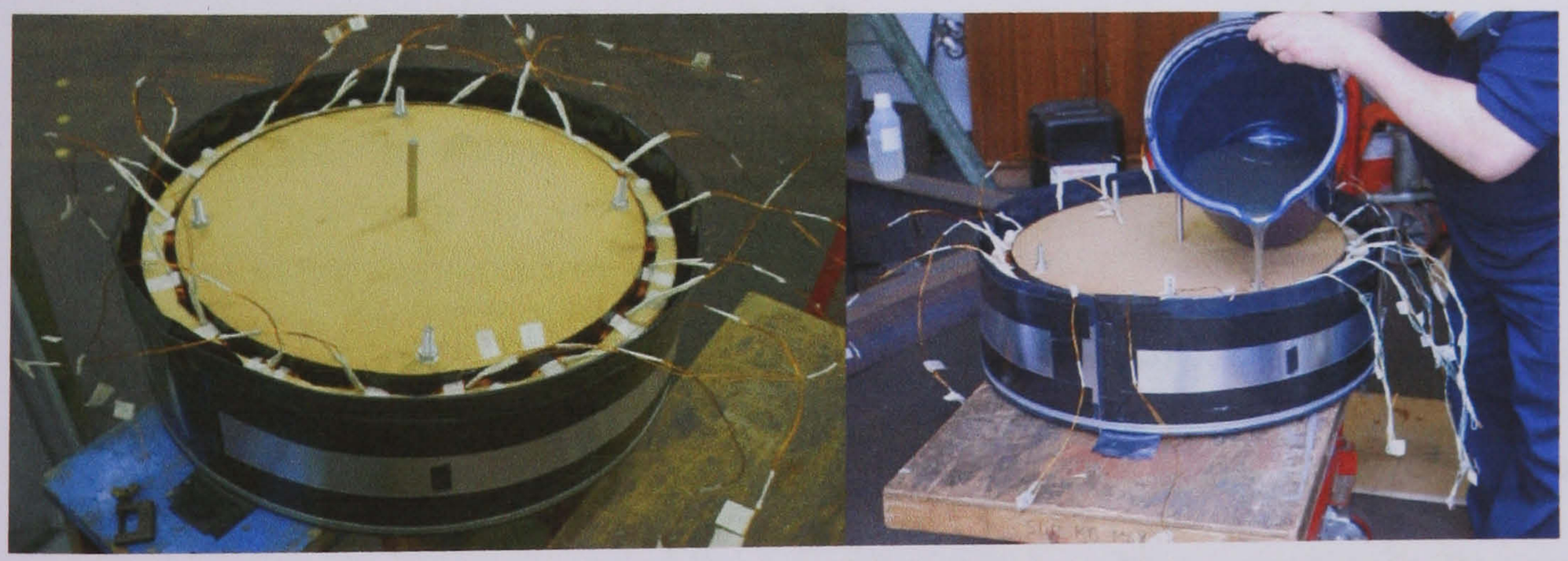

(d)

(e)

(f) (g)

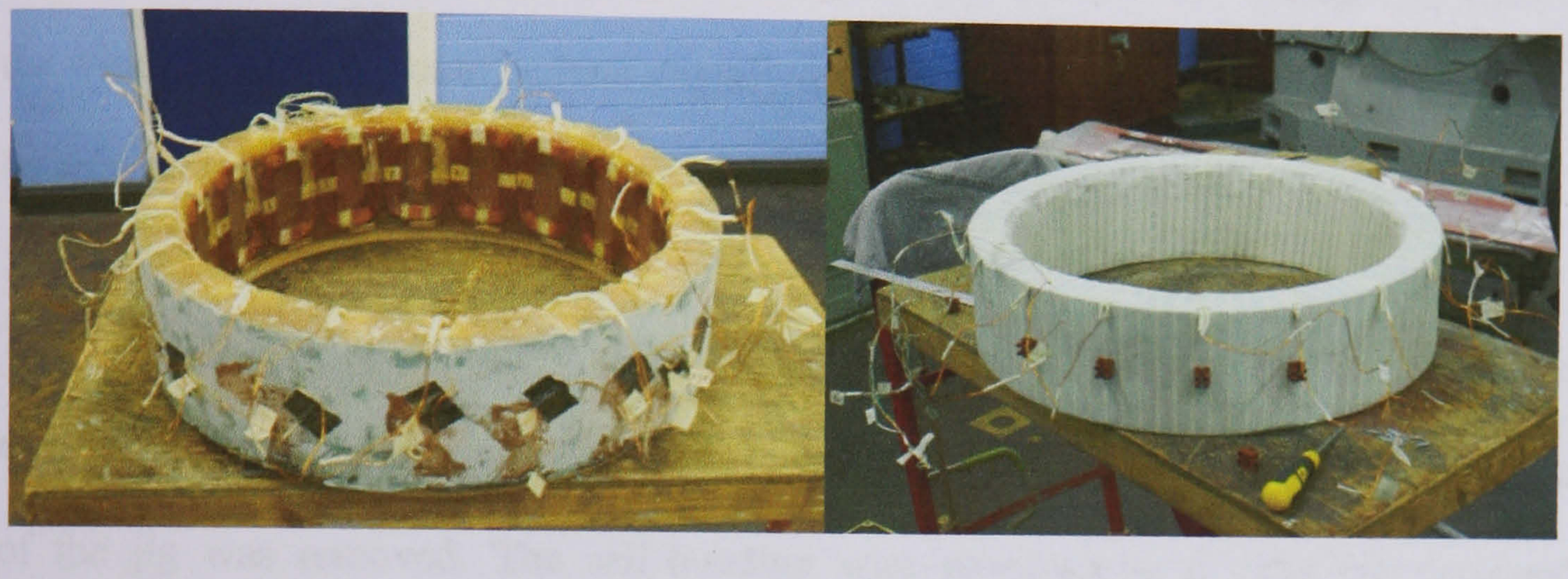

(h) (i)

Figure 11-6. Air-cored stator manufacturing process showing (a) the heat activated self-bonding wire coil on the air-cored machine, (b) the coils on the former, (c) the former in the mould without its aluminium edging strip, (d) the former in the mould with its aluminium edging strip, (e) pouring epoxy into the mould, (f) positioning the lid on the mould, (g) the cast stator ring before separation from the mould, (h) the coils cast in the epoxy ring and (i) the stator with glass tape around it

11.4.2 Wire wound stator

The second stator consisted of a wire-wound ring that was potted into a larger load bearing epoxy structure. Material tests described in Chapter 10 showed the most desirable material was 0.5mm diameter mild steel wire and this was used to create the stator back iron by winding it around an MDF former (Figure 11-7 (b)). During the winding process, Figure 11-7(c), the layers of wire were painted with epoxy resin to produce a rigid wire composite ring. This was then placed in a mould to form the load

bearing epoxy ring in an identical manner to the air-cored machine.

A second construction method was used for the armature coils of the wire-wound machine. Here the coils were wound in a jig using standard enamel coated copper wire; the top plate of the jig was removed and the coil held in place using brass clips while the long (axial) sides for the coil were covered in epoxy glue. The top plate of the jig was then replaced while the epoxy cured, Figure 11-6 (a). By only gluing two sides of the winding, the coil could be bent slightly in the circumferential direction to allow it to be secured on the inner surface of the stator, Figure 11-6 (d).

This construction method produced less uniform coils then the self-bonding wire method because the brass clips allowed some coil relaxation to occur when the top plate of the jig was removed. The self-bonding wire construction is therefore favoured. Although flat coils can be problematic to handle on small diameter machines, it becomes progressively easier to incorporate them as the diameter increases.

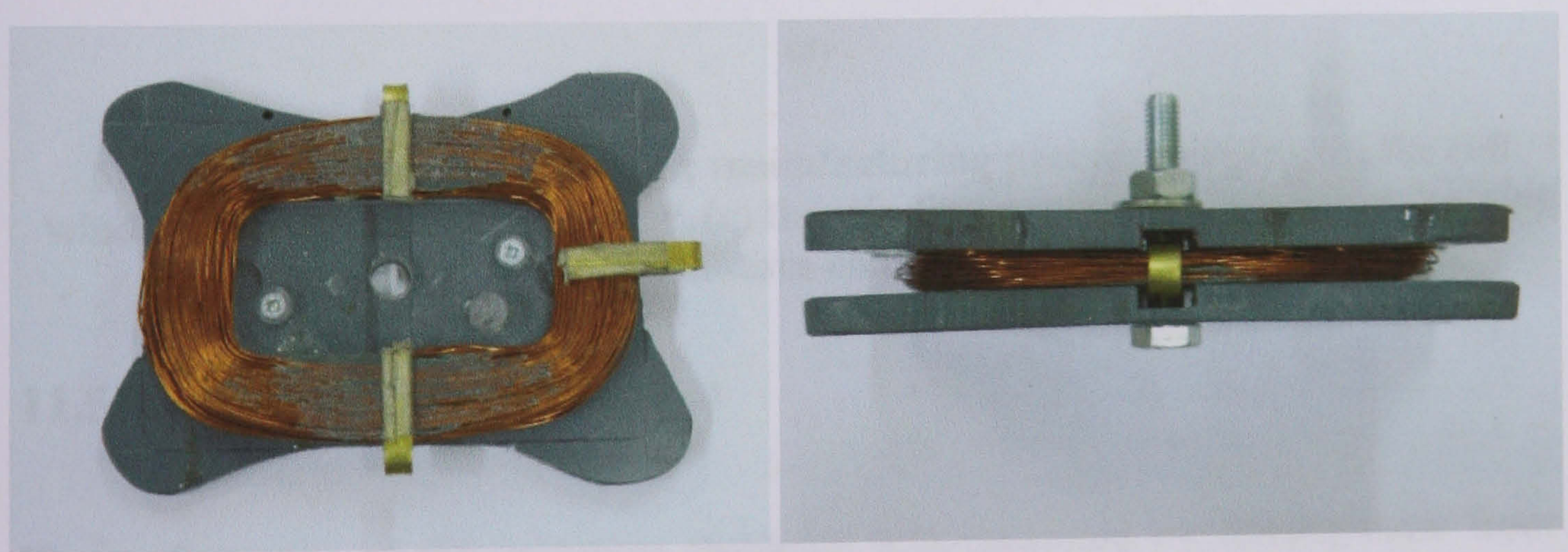

(a)

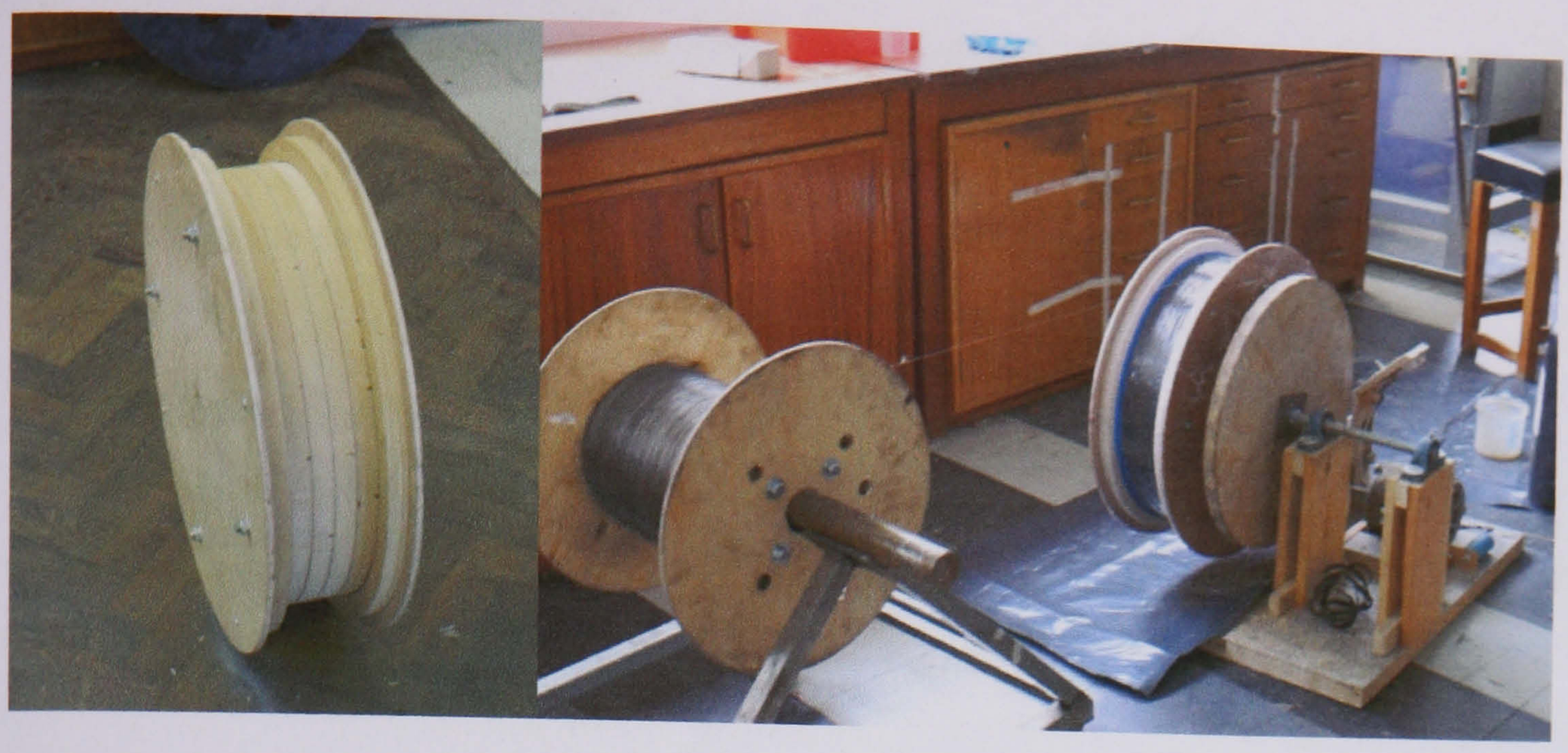

(b) (c)

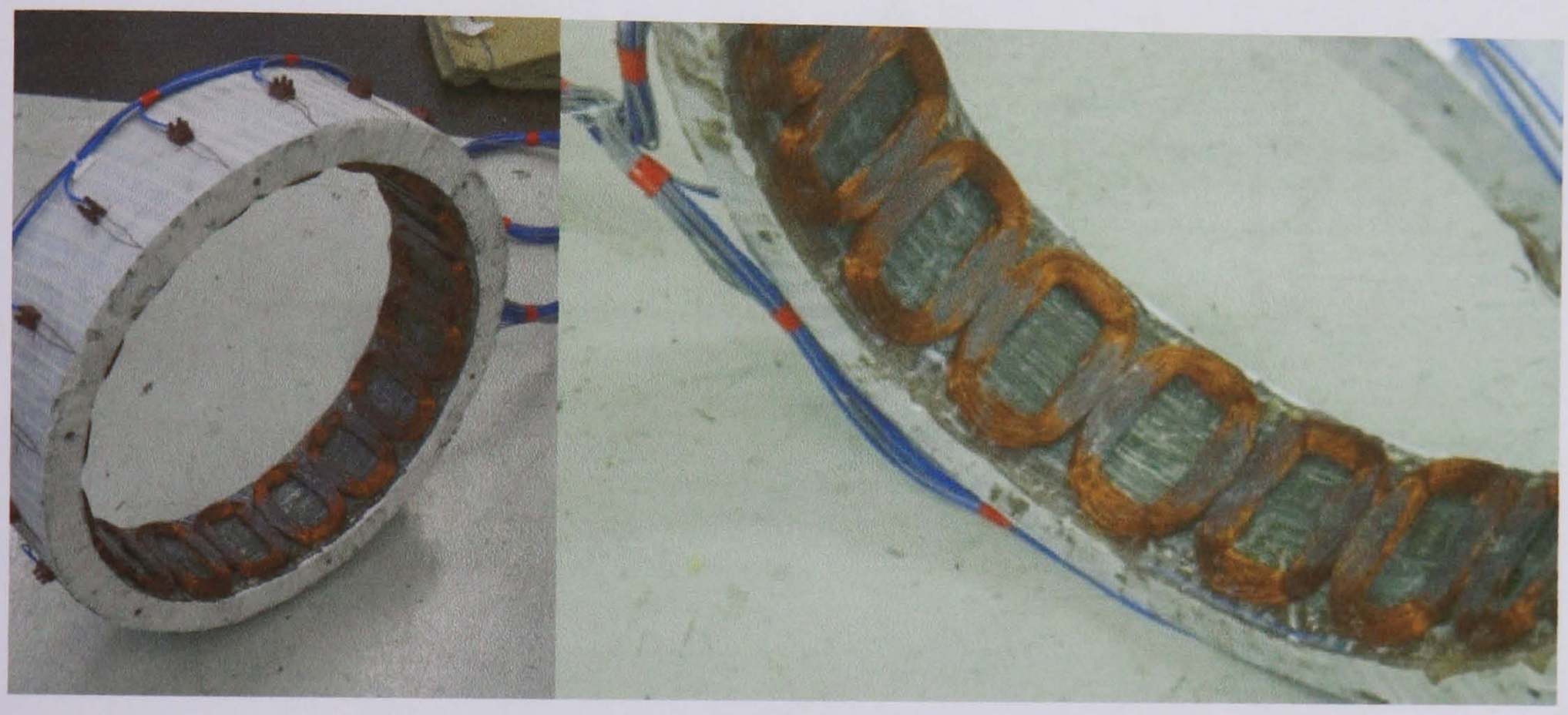

(d)

Figure 11-7. Wire-wound stator manufacturing process showing (a) the coil winding jig, (b) the stator former, (c) the winding process and (d) the stator ring with armature coils attached

11.5 Test results and discussion

The performance of the prototype machines was measured by driving them from a Ward-Leonard test rig (Figure 11-2) and dumping the generated power into a resistive load. The mechanical torque going into the generator was measured by a torque transducer situated just upstream of the generator, while the rotational speed was measured by a digital infrared tachometer. Currents, voltages, powers and harmonic

distortions of the power coming from the generator were monitored by a power analyser. The temperature of armature winding was monitored by thermocouples mounted on the surface of the coils.

11.5.1 Power and Voltages

The performance of the generator into a resistive load can be predicted from the equivalent circuit and phasor diagram shown in Figure 11-8.

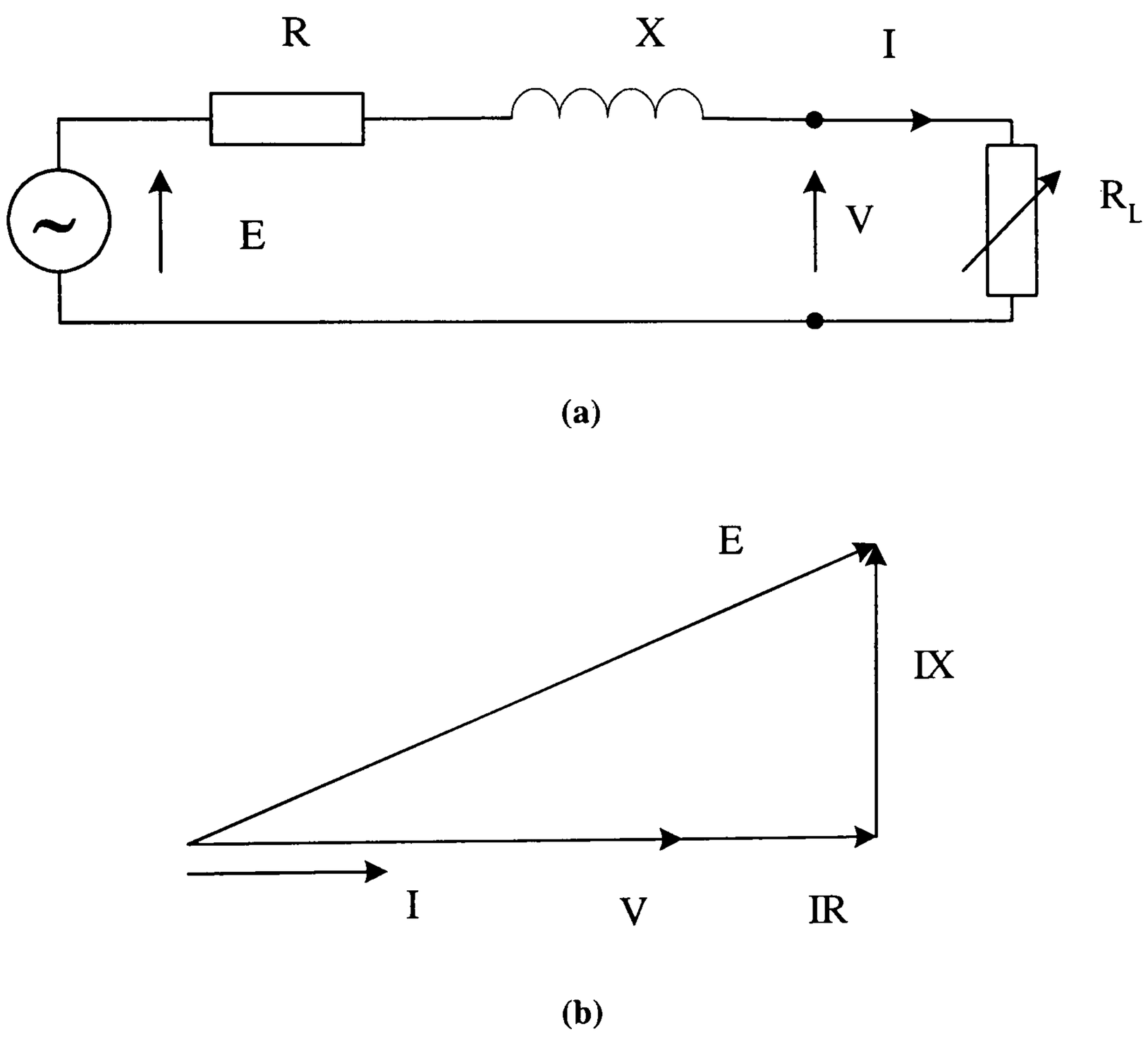

Figure 11-8. Resistive load showing (a) equivalent circuit and (b) phasor diagram

Where R and X are the phase resistance and reactance and are given by:

$$X = \omega \frac{n_{series}}{n_{pall}} L_{coil} \qquad [11\text{-}1]$$

$$R = \frac{n_{series}}{n_{pall}} R_{coil} \qquad [11\text{-}2]$$

Where L_{coil} and R_{coil} were found from the design equations outlined in Appendix D.

Applying Pythagoras to the phasor diagram in Figure 11-8 (b) gives:

$$V = \sqrt{E^2 - (IX)^2} - IR \qquad [11\text{-}3]$$

This allows generator performance to be determined for any defined current. The terminal power is given by:

$$P = mVI \qquad [11\text{-}4]$$

The measured and predicted open circuit voltages are shown in the figures below for the two stator constructions. These predictions were made using the design equations outlined in Appendix D and use values of air gap flux density taken from the finite element analysis described in Chapter 10. Figure 11-9 (a), which shows the induced EMF in the air-cored machine, also includes a theoretical line showing the predicted EMF of a wire-wound stator machine. This estimate cannot simply be transposed from Figure 11-9 (b) since the two machines have subtly different geometries which makes a direct comparison impossible[10]. A similar comparison has been made in Figure 11-9 (b)

---

[10] The air-cored machine used flat coils comprising 300 turns of 0.71mm diameter copper wire, where as the wire-wound machine used round coils comprising 230 turns of 0.75mm diameter wire.

which shows how much lower the induced EMF would be if the wire-wound machine had used an air-cored stator.

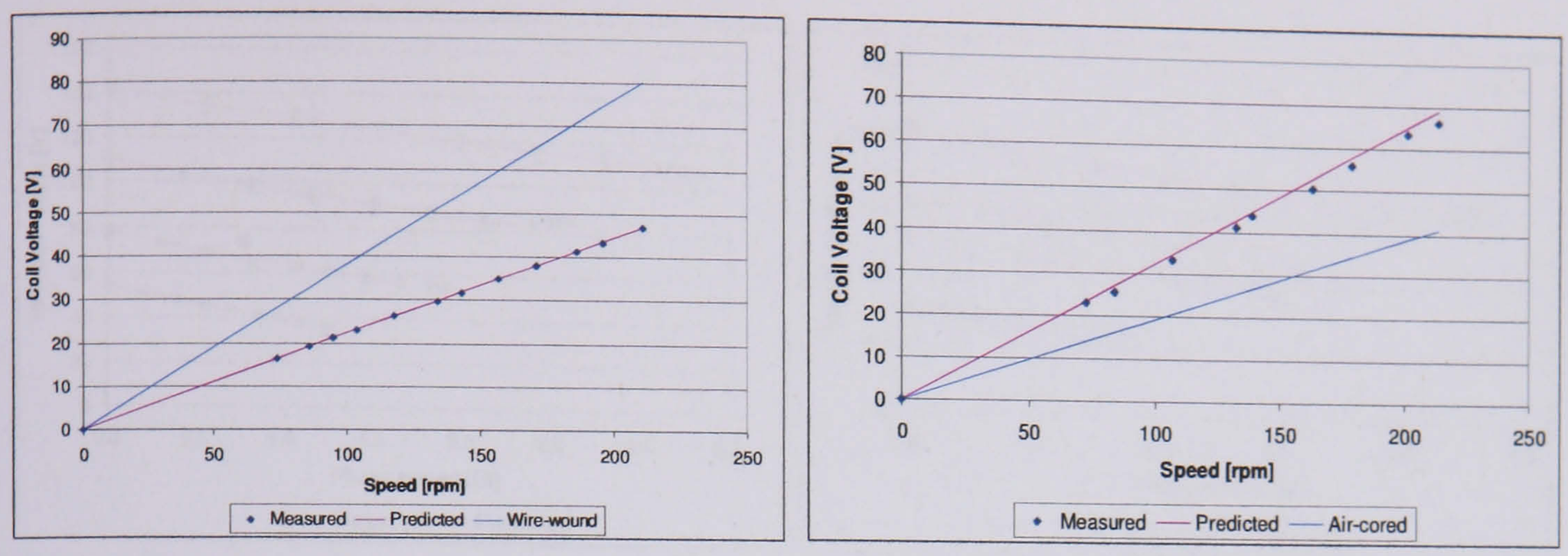

(a) (b)

Figure 11-9. Open circuit coil voltages for (a) air cored and (b) wire-wound stator machines

Figure 11-9 shows that an approximate 40% improvement in generated EMF (and therefore power) can be made by using a wire-wound structure.

The three phase open circuit waveforms are shown below; both traces are highly sinusoidal with a third harmonic distortion of less then 2%.

(a) (b)

Figure 11-10. 3-phase waveform for (a) air-cored and (b) wire-wound machines

Figure 11-11 and Figure 11-12 show the generators' performance in terms of terminal

voltage and power as a function of phase current. Also included are the predicted values from the design process.

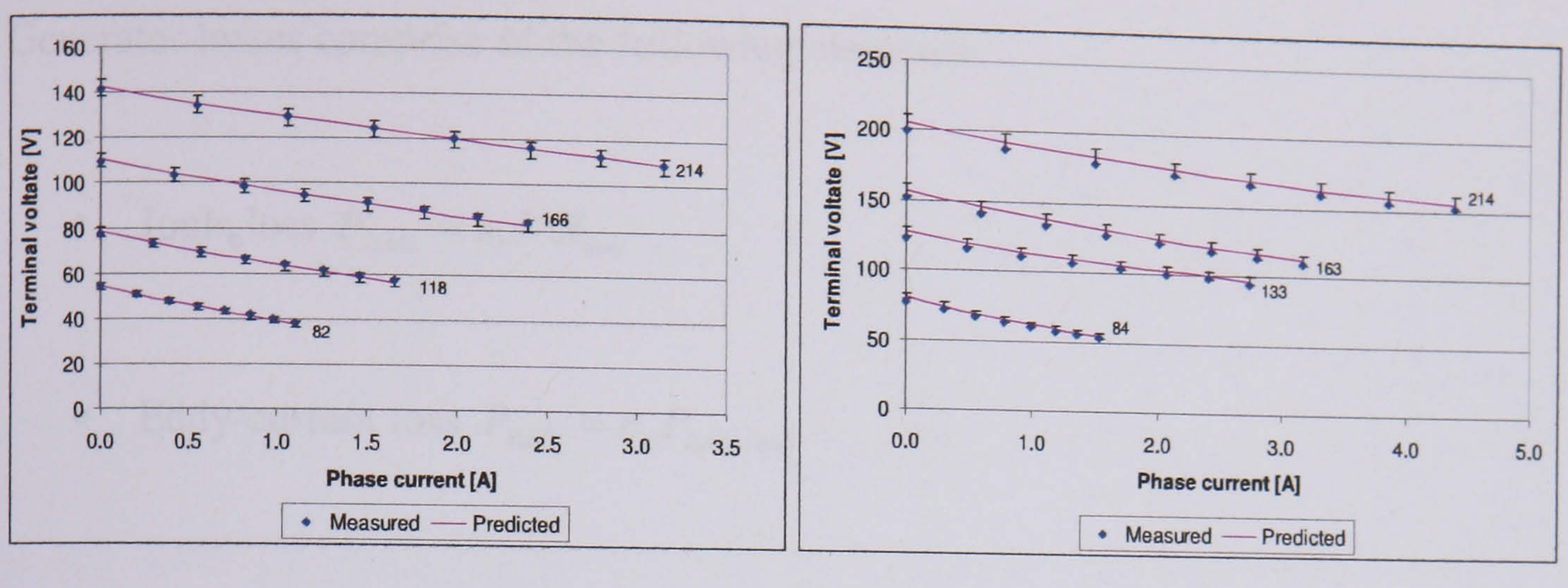

(a) (b)

Figure 11-11. Terminal voltage for (a) air-cored and (b) wire-wound machine

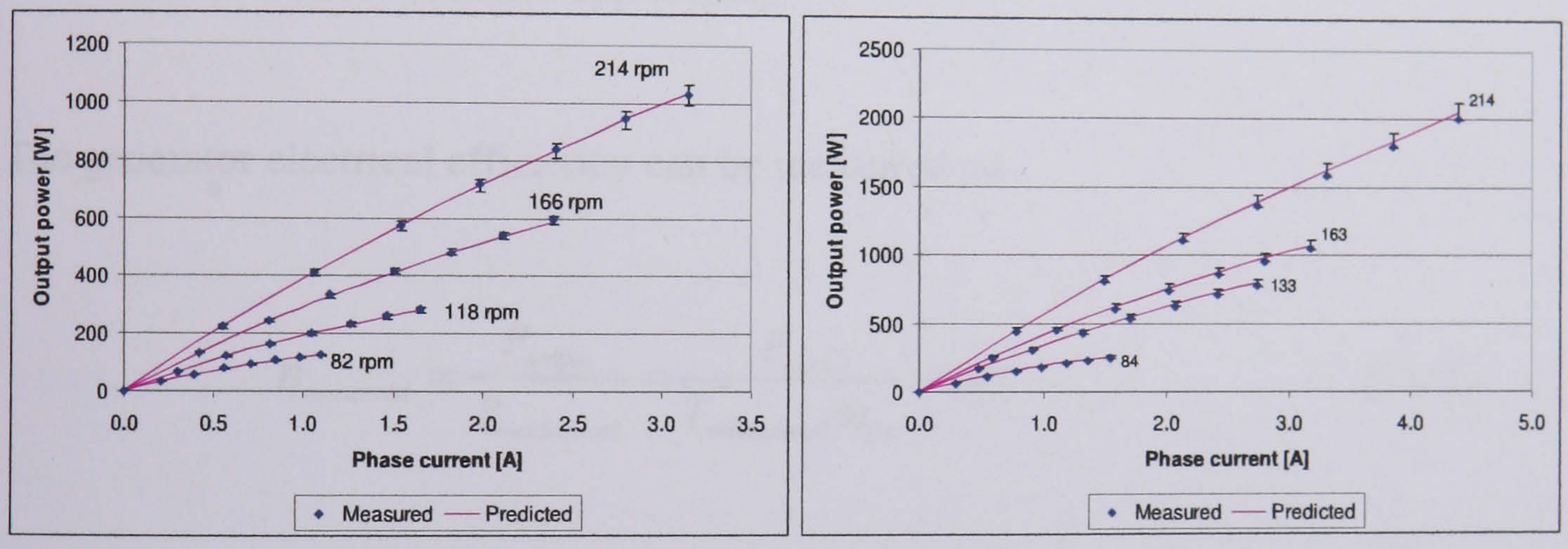

(a) (b)

Figure 11-12. Output power for (a) air-cored and (b) wire-wound machine

Error bars are shown in Figure 11-11 and 11-12 because the predicted values of terminal voltage are somewhat arbitrary due to the unknown value of the flux reduction factor, used to account for the drop in flux density towards the (axial) ends of the magnets (see Appendix D). Previous finite element work on axial flux machines [35] has shown the flux reduction factor to be between 0.9-0.95 and these have been used as the upper and lower bounds to the error bars. The value used in the predictions is 0.93

and is based on a finite element calculation described in Appendix D.

Efficiency and Power loss

Generator losses comprise of the following elements:

- Joule loss $P_{Joule} = n_c I^2 R_{coil}$
- Eddy-current loss $P_{Eddy} = n_c P_{Eddy/coil}$
- Friction and windage loss
- Stator iron loss (where applicable)

The generator electrical efficiency can be measured as:

$$\eta_{measured} = \frac{P_{output}}{P_{mechanical}} = \frac{P_{load}}{T_{mechanical}\omega_{gen}} x100 \qquad [11\text{-}5]$$

Figure 11-13 shows the measured efficiency of generators at a selection of speeds as the electrical load is increased. Also shown is the predicted efficiency which is calculated according to:

$$\eta_{predicted} = \frac{P}{P + P_{cu} + P_{eddy} + P_{iron}} x100 \qquad [11\text{-}6]$$

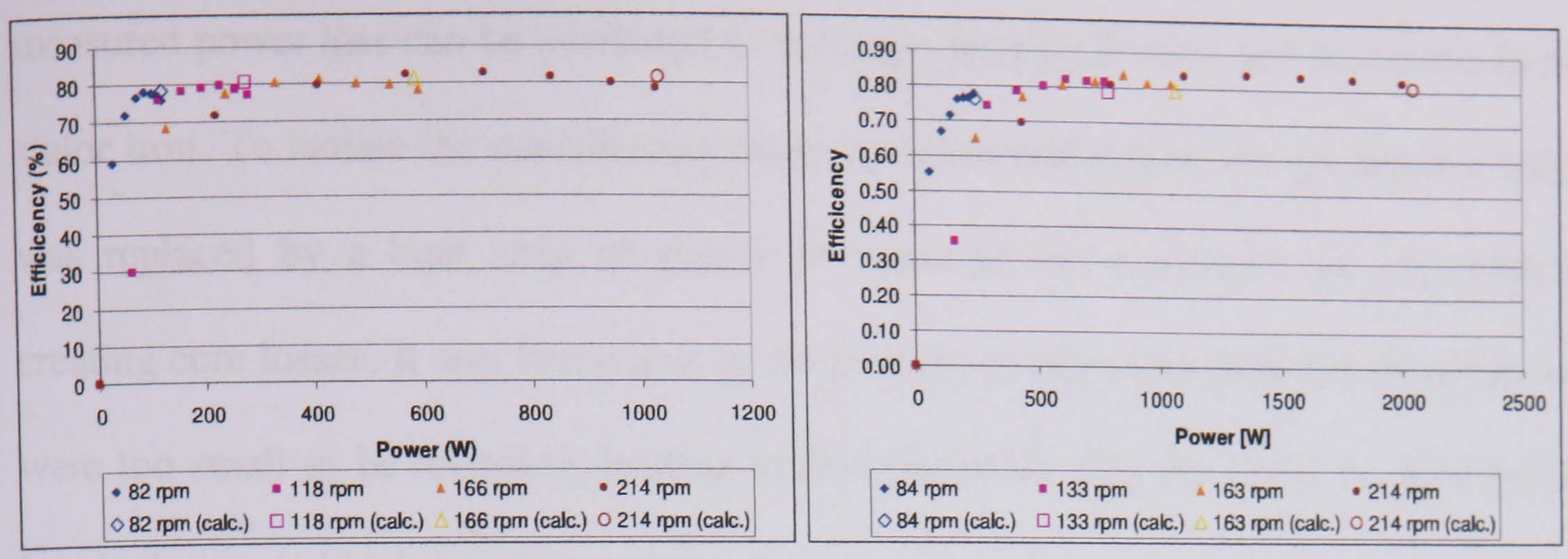

(a) (b)

Figure 11-13. Generator efficiency for (a) air-cored and (b) wire-wound stators

A maximum efficiency for the air-cored and wire-wound machines of 83% and 84% was achieved respectively. Although one might assume the air-cored machine would be more efficient since it has no iron losses, it also produces less power then the wire-wound machine. Since the Joule and Eddy current losses are almost identical, the lower output power will tend to decrease the machine's efficiency. The similar measurements of maximum efficiency would indicate that these two effects appear to be roughly balanced. The following section examines the loss mechanisms in the generators in more detail.

11.5.2 Power loss mechanisms

The loss mechanisms for the two generators are similar; each generator dissipates power due to bearing friction, windage, Eddy currents and Joule loss, although the wire-wound stator has an extra component associated with the iron core, and aspect will be discussed below.

Measurements of the power loss at no load for the wire-wound stator machine are shown in Figure 11-14 (these values were calculated by recording the input torque and speed of the generator). When no current is drawn from the generator, the entire

measured power loss can be attributed to windage, bearing friction and hysteresis in the stator iron. To isolate the contribution made by hysteresis losses, the generator's stator was replaced by a bent strip of plastic to maintain the machine's air gap without creating core losses. It was found that in the absence of any stator iron, the power losses were too small to be recorded, leading to the conclusion that the entire no load power loss is dominated by hysteresis.

Also shown in Figure 11-14 is the theoretical prediction of hysteresis loss which is based on a numerical integration of the power loss that occurs at each point of the stator. This calculation is described in detail in section 10.8.3.

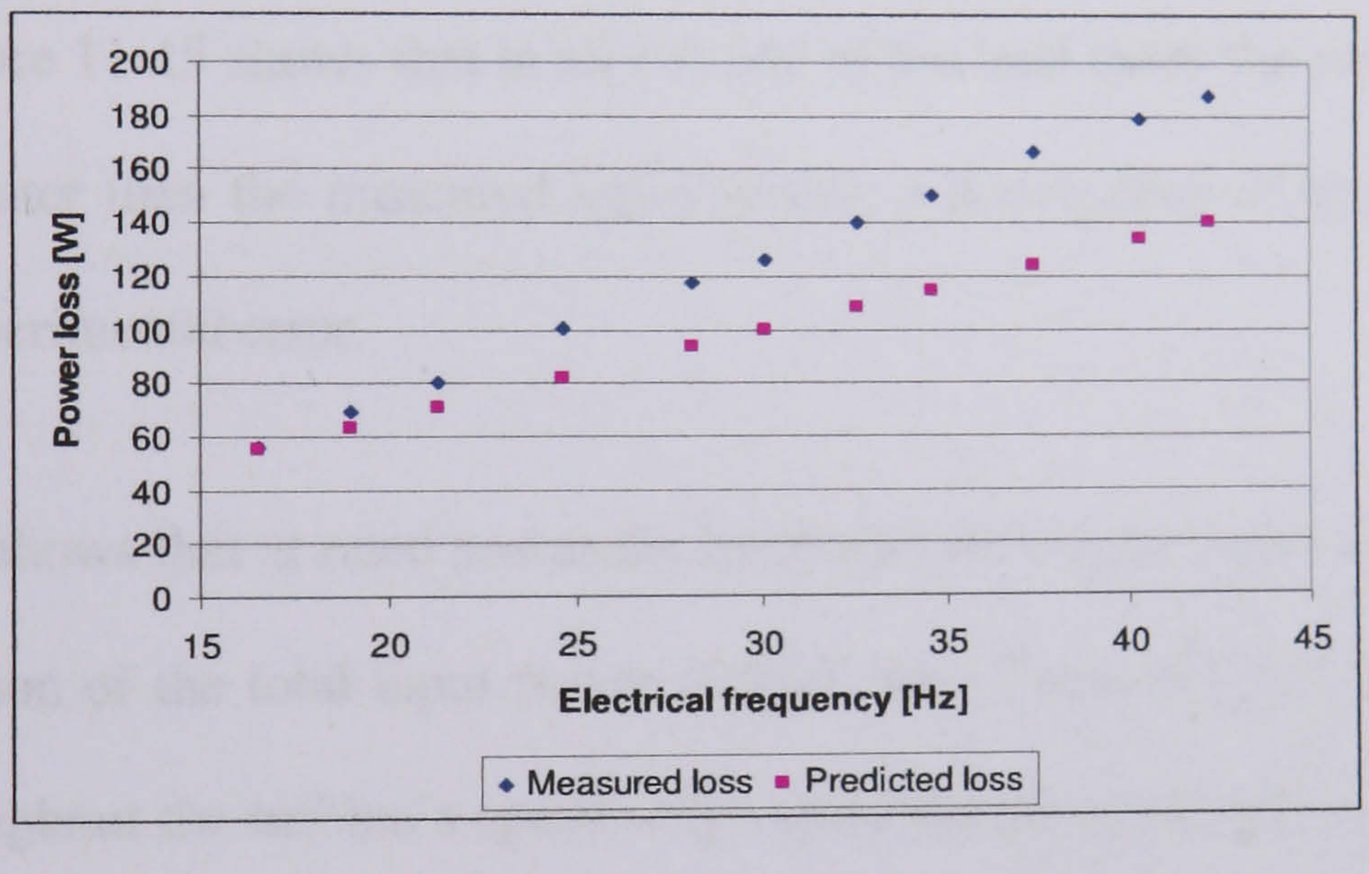

Figure 11-14. Power loss at no load

There is some discrepancy between predicted and measured values of hysteresis loss. This is likely due to uncertainties in the exact packing factor of the steel wire in the stator winding due to manufacturing problems.

Figure 11-15 shows how the mechanical input power is split between the electrical output power and the losses. This test was conducted at rated speed (214 rpm) for increasing loads (i.e. phase currents); rated power occurs close to 4.39 A/phase. The

electrical output power, mechanical input power and I^2R loss were measured directly, while the hysteresis loss is inferred from the no load tests shown in Figure 11-14.

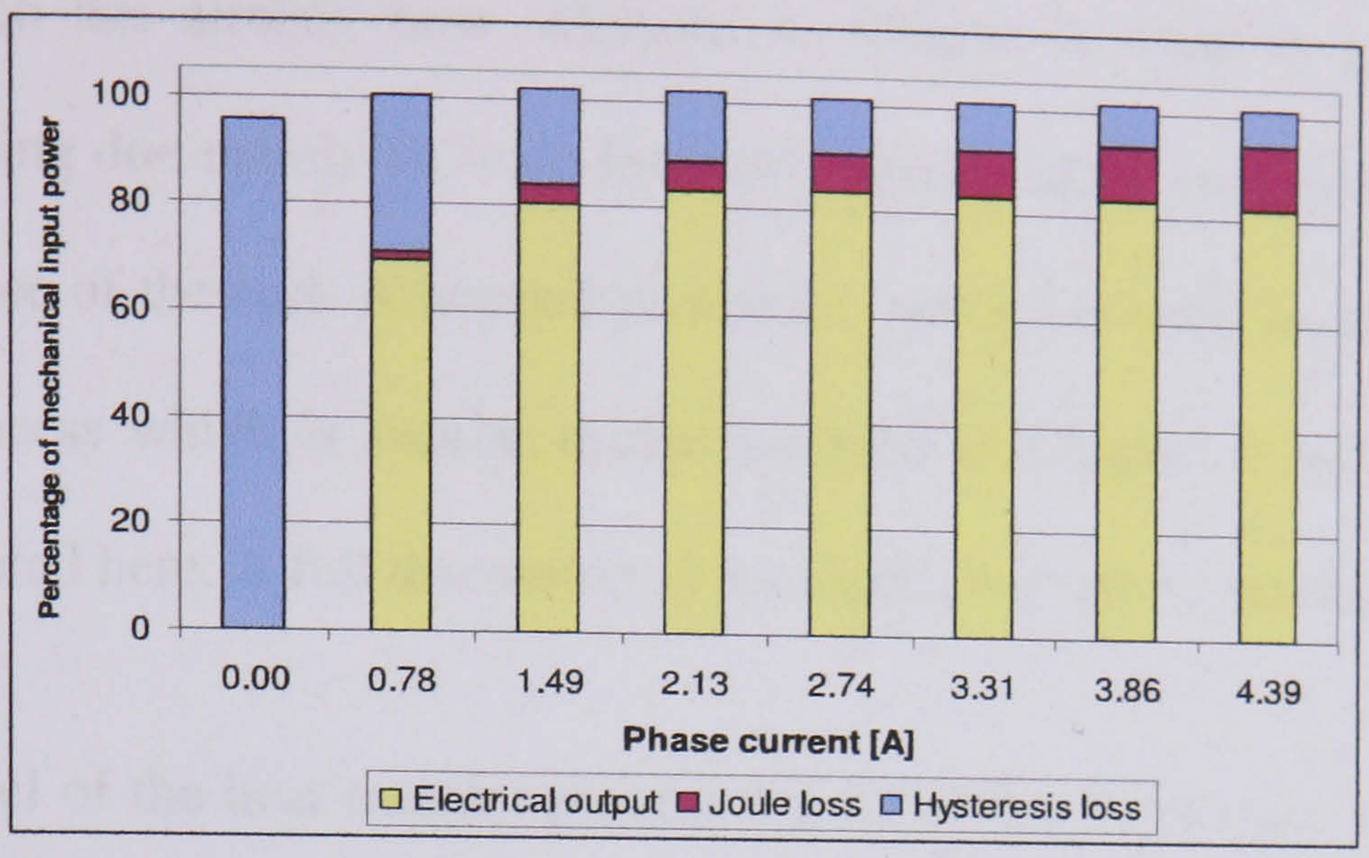

Figure 11-15. Breakdown of generator power

Although Figure 11-15 shows that in all but one of the load cases the sum of the output powers is greater then the measured input power, a discrepancy of under 2% is well within the experimental error.

Figure 11-15 shows that at rated power the hysteresis loss in the stator iron is actually a small proportion of the total input power (6.9%). This figure is likely to remain fairly constant throughout the turbine's speed range since the generator output power and the hysteresis loss are both linearly proportional to rotational speed.

The power loss in the air-cored machine is relatively straightforward to characterise as there is no iron loss to account for. Since the same rotor was used for the two machines, the windage and bearing loss is identical to the wire-wound machine (i.e. negligible). Eddy current loss is again small due to the low electrical frequency, which leaves I^2R dissipation in the armature winding as the dominant loss mechanism.

11.6 Heat transfer

The heat transfer problem in the radial flux machine is similar to that in the axial flux machine, which has already been analysed in Chapter 8. Heat is generated in the armature winding due mainly to Joule loss and is removed by cooling air passing over the inner surface of the coil. A lumped parameter model has been developed for use in the design process which is similar to that outlined in Chapter 8 and so will not be discussed in detail here. A full discussion of the model is given in Appendix E

A 2D FE model of the heat transfer process has also been developed and is discussed below. In the following sections the lumped parameter model is compared to the FE model and both are compared to temperature measurements taken on the test generators.

11.6.1 Finite element validation of heat transfer model

The heat transfer problem shown in Figure E-2 in Appendix E can be modelled using *Mirage*, a 2-D Finite Element package [134]. By doing this, the accuracy of the various assumptions made in the lumped parameter model can be assessed. However, in order to gain confidence in the FE method, the cooling problem can first be set up using the same geometry, thermal boundary conditions, thermal conductivities and power dissipation as the lumped parameter model. These values are shown in Table 34. A comparison between the temperature profiles across an armature coil in the radial direction can then be made, Figure 11-16.

Power dissipated in coil (W/m^3)	213148
Equivalent coil current density (A/mm^2)	4.0
Ambient temperature (°C)	18
Thermal conductivity of coil (W/K/m)	0.4
Height of coil (mm)	8
Circumferential length of coil (mm)	93
Width of winding volume (mm)	25
h_s of air gap side ($W/K/m^2$)	40
BC at stator side of coil	Insulated

Table 34. Modelling parameter for the lumped parameter-FEA comparison

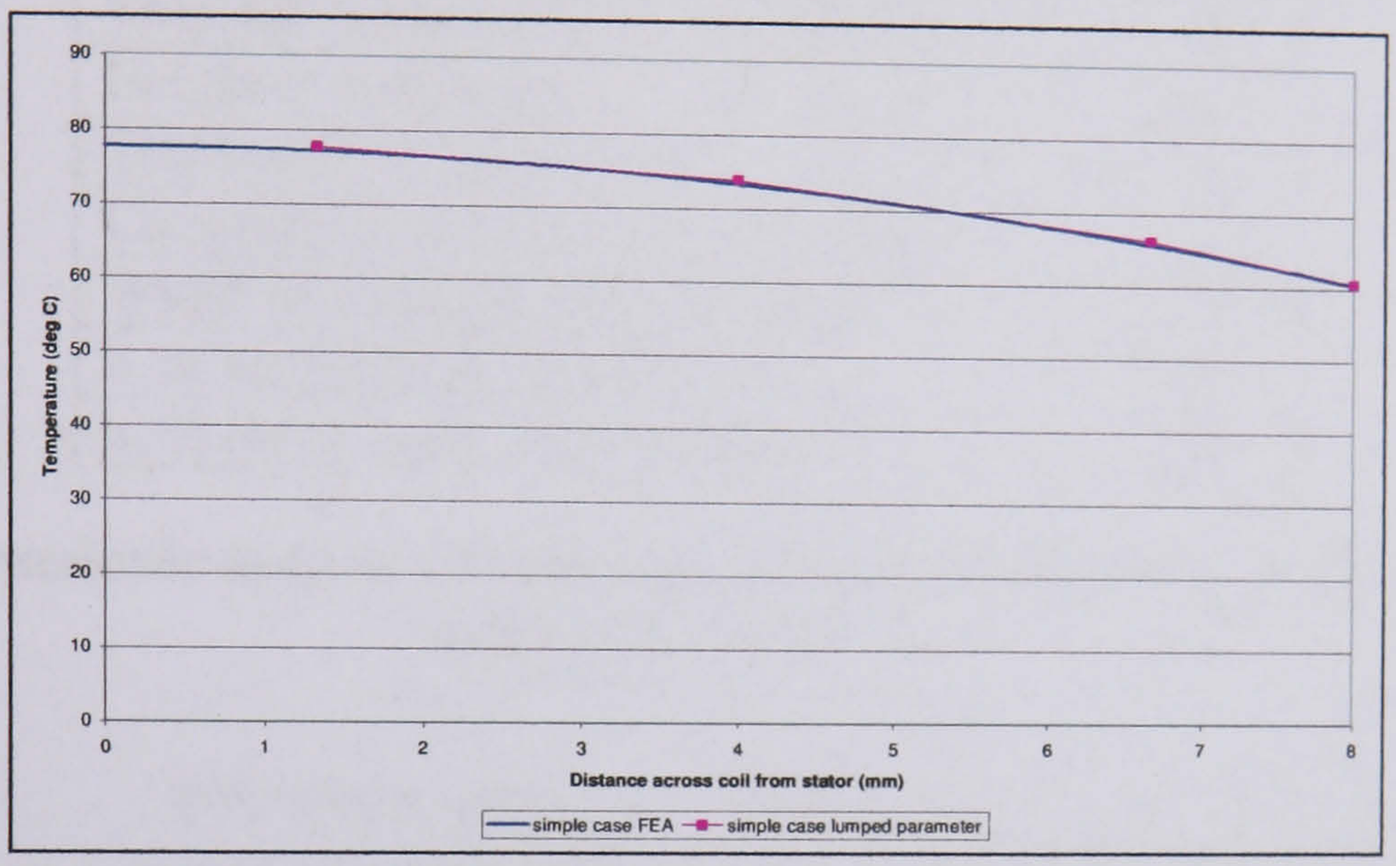

Figure 11-16. Simplified heat transfer problem and measurements on the air-cored machine

Figure 11-16 shows the lumped parameter model agrees well the FE analysis when all heat is assumed to travel radially and the stator side of the coil is fully insulated. The finite element method is now extended to consider a more realistic heat transfer picture.

As described in section 11.4, the two test generators use two alternative methods of attaching the coils to the stator: the coils in the air-cored machine are fully potted, as shown in Figure 11-6 (h), while the coils in the wire wound machine are simply attached to the stator with glue, Figure 11-7 (d). Both construction techniques have been modelled and the resulting analysis is presented in Figure 11-17, which shows a comparison between the heat transfer mechanisms in the two coils, and in Figure 11-18, which shows a comparison between the temperature profiles across the hottest part

of each coil. For the purposes of the comparison, identical coil geometries, surface heat transfer coefficients and coil power dissipations have been assumed (see Table 35). However, such an assumption cannot be made in the case of the test generators, which have different coil geometries and heat transfer properties.

Coil current density (A/mm^2)	3.0
Thermal conductivity of epoxy (W/K/m)	1.0
Thermal conductivity of air (W/K/m)	0.03
Thermal conductivity of coil (W/K/m)	0.4
Height of coil (mm)	8
Thickness of Stator (mm)	60
Circumferential length of coil (mm)	93
Width of winding volume (mm)	25
h_s of air gap side ($W/K/m^2$)	45
h_s of outer stator side ($W/K/m^2$)	20

Table 35. Parameters used in FE analysis (derived from heat transfer experiments outlined in Chapter 8)

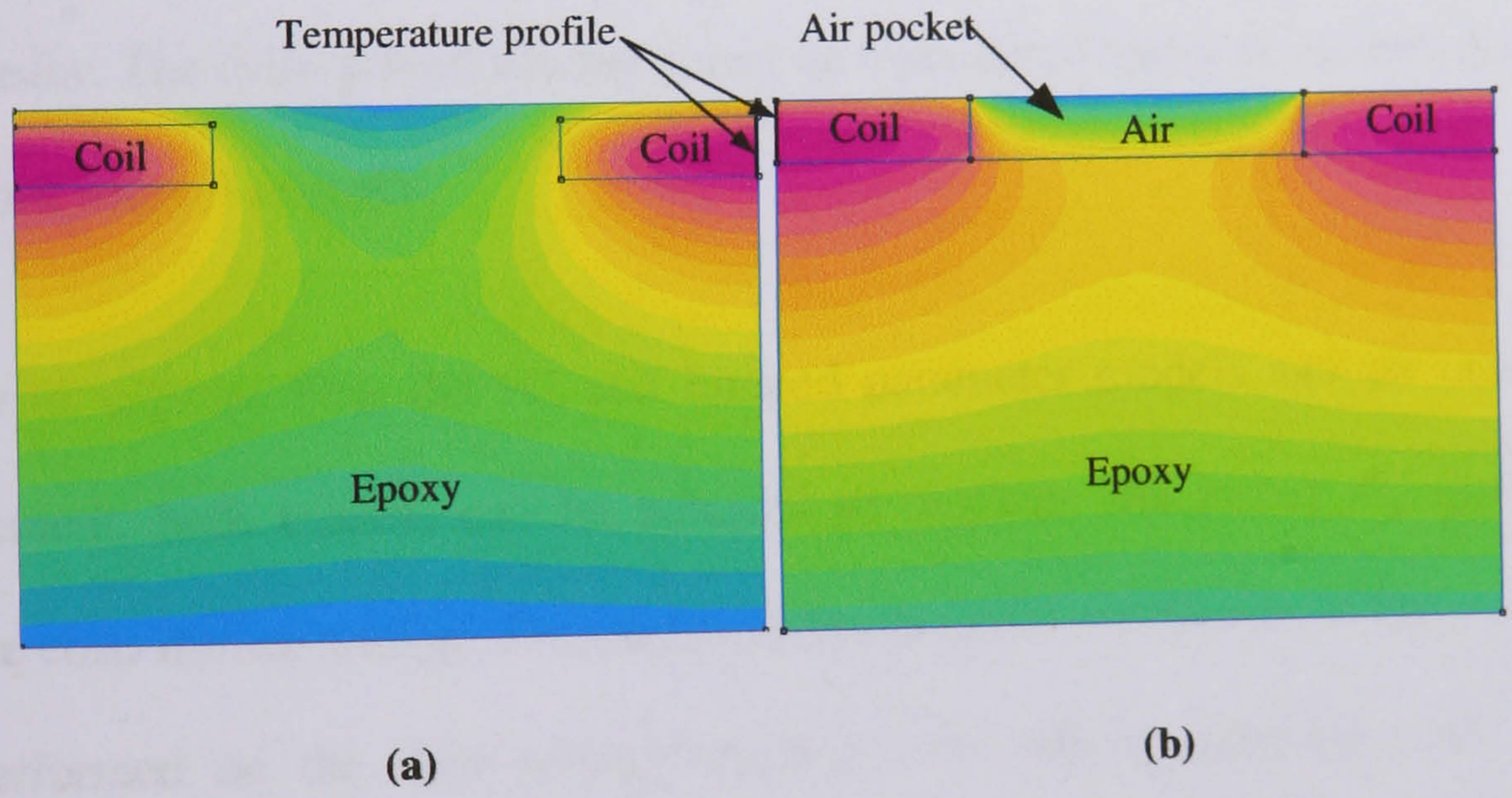

Figure 11-17. Temperature plot in (a) fully potted machine and (b) simply attached machine

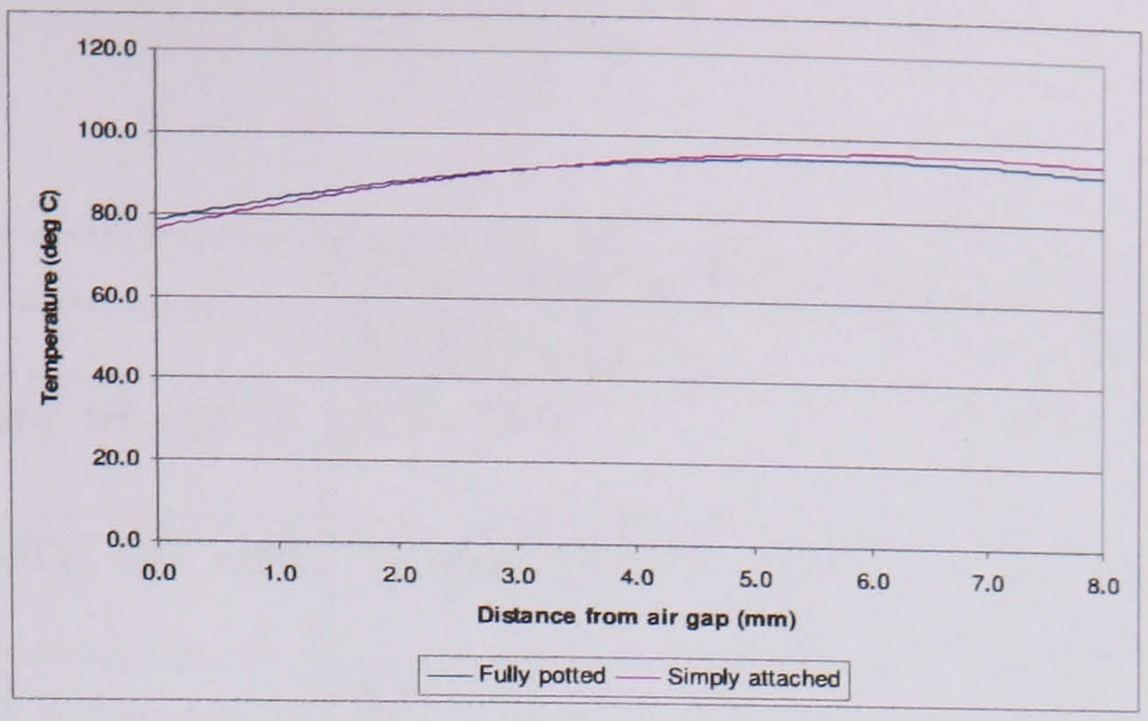

Figure 11-18. Comparison between heat transfer mechanism for different coil attachment methods

Figure 11-18 shows the two structures have similar heat transfer capabilities. The air pocket in the simply attached structure, shown in Figure 11-18 (b), acts as an insulator, inhibiting any non-radial heat transfer and this would tend to make the coil hotter. However, the winding is not significantly hotter than the fully potted structure and this is because the epoxy layer covering the coil of the fully potted structure also reduces heat transfer. The fully potted structure may be considered superior, however, due to its greater mechanical strength.

In order to validate both the FE and lumped parameter models against experimental measurement, both models can be adjusted to replicate the power dissipated in the armature coils during testing. The results of the analysis are shown in Figure 11-19 for tests performed on the wire-wound machine with simply attached coils. The coil geometries and test conditions of the two generators are shown in the Table below.

Machine type	**Wire-wound radial flux**	**Air-cored**
Coil type	Simply attached	Fully potted
Thermal conductivity of epoxy (W/K/m)	0.5 [135]	0.5 [135]
Thermal conductivity of coil (W/K/m)	0.4 (see section 8.4)	0.4 (see section 8.4)
Height of coil (mm)	8	8
Thickness of Stator (mm)	60	60
Circumferential length of coil (mm)	93	91
Width of winding volume (mm)	25	25
h_s of air gap side (W/K/m^2)	35 (see note 1)	35 (see note 1)
h_s of outer stator side (W/K/m^2)	20 (see note 1)	20 (see note 1)
Test conditions		
Speed (rpm)	189	207
Coil current density (A/mm^2)	3.03	2.45
Power output (W)	1832	905
Test time	120	180
Max temperature rise	72.4	69.9
Note 1. From measurements of h_s taken of the axial flux machine (Figure 8-12)		

Table 36. Parameters of test conditions

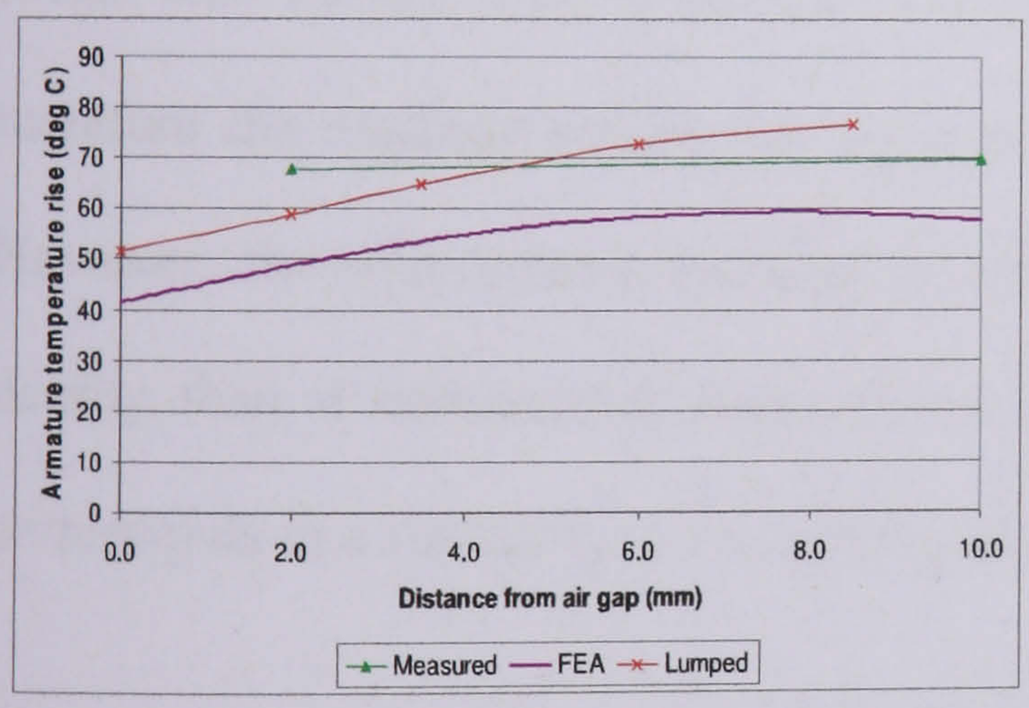

(a)

(b)

Figure 11-19. Comparison of modelling methods for (a) the air-cored machine which used fully potted windings and (b) the wire-wound machine which used simply attached coils

Figure 11-19 shows that the lumped parameter models for both stator constructions produces an over-estimate of temperature rise in the armature coils. This is because in reality heat can leave the coil through all available surfaces rather then just then one

facing the air gap, as has been assumed in the lumped parameter model. Although the FE analysis predicts temperature rise in the generator reasonably accurately, it is the lumped parameter model that is used in the design process and it is reassuring to note that this model is conservative in its predictions.

11.7 Conclusion

A novel permanent magnet radial flux generator was manufactured using two stator constructions: a wire-wound structure and an air-cored structure. It has been shown to be feasible to construct simple large diameter machines using a stack of MDF discs cut by a router on a radius arm to produce a former or mould. Narrow diameter steel wire can be used to form the stator back iron which has been shown to produce acceptable losses (6.9% at full load). If a large volume of generators were manufactured, the stator wire could be made from commercial grade electrical steel, which would reduce these losses still further. The inclusion of steel wire increases the generated EMF, and therefore the machine power, by approximately 40% over a fully air-cored structure. However, the wire-wound machine would have produced a 6% lower air gap flux density than if commercial grade electrical steel laminations had been used, which corresponds to a similar drop in output power.

Of the other materials considered for the generator, both the 3mm galvanised steel rope and the shot composite could have been adopted for the rotor, although the 3mm rope was chosen for its ease of manufacture. The rope produced a tight, homogenous structure to which the magnets could be easily bonded, and this technique can be regarded as a simple, lightweight and highly versatile method of manufacturing the

rotor back iron.

Two armature coil construction techniques were tested: the first used a heat activated self-bonding wire to form a solid, homogenous, but flat, coil; the second used standard enamel coated copper wire to produce a coil which could be epoxied along two edges to form a flexible structure that was secured directly onto the inside radius of the stator. It was clear that the self-bonding wire produced a much more satisfactory coil with a higher packing factor. At large diameters the flatness of the coil would not significantly increase the air-gap of the machine either, making this technique the clear choice. Fully potting the coil is also vital for producing a robust structure and by doing this the heat transfer mechanism is not significantly compromised. The favoured construction technique would therefore be to first pot the coils into an epoxy ring, which wound then be wound with steel wire to form the back iron, before being potted into a larger load bearing epoxy ring.

Tests on the two generators verified the design assumptions, with measured powers, voltages and efficiencies being within 3% of predicted values. Lumped parameter and finite element thermal models were compared to the temperature rises observed in both generators. It was found that the finite element model gave reasonably accurate predictions of temperature rise and that the lumped parameter model gave slight overestimates. Since the design process relies on the lumped parameter model, a slight overestimate of temperature rise is to be welcomed. The accuracy of both models has not entirely been established, however, due to the complex heat transfer mechanisms within the generator and the unknown surface heat transfer coefficients

Chapter 12

Conclusions and further work

12.1 Summary of the Research

The work in this thesis has introduced a number of micro wind energy conversion systems (WECSs) and has shown how these systems can be modelled. A wind turbulence model was created and combined with the WECS models to examine how wind turbines can be better controlled to aid stability and energy capture. The research also focussed on the development of an air-cored PM axial flux generator, which had previously been built as a prototype at Durham. The research looked at the optimisation of the stator and at how larger machines could be built without compromising the simplicity of manufacture, which is one of the main attractions of the axial flux configuration. The research showed that above power ratings of approximately 20kW at 100-200rpm – corresponding to a generator diameter of about 1m – the axial flux configuration becomes increasingly untenable due to the large magnetic closing forces, and it is appropriate to switch to a radial flux layout. Two radial flux generators were then constructed using novel materials and manufacturing techniques which aimed to maintain the simple construction methods of the axial-flux topology but with the potential to move to larger generator power ratings.

12.2 Main conclusions of the research

Research conducted on the economic attractiveness of micro turbines, presented in Chapter 3, has shown that there is a large question mark over the feasibility of building mounted devices in urban areas. This is partly due to structural considerations of the

building and, more crucially, due to the wind resource at roof level in urban environments. Little research has been done on this topic. Some CFD models have shown it may be possible to gain extra power from the wind due to the speed up effect as it passes over a building, although there is a paucity of experimental trials to establish whether this effect is real. The limited trials that have been carried out have shown there is little wind available at roof level in cities and that it is so turbulent as to seriously limit the performance of horizontal axis turbines. Despite government incentives there is still no economic case for the large scale up-take of micro turbines. However, this may change in the future if the devices become cheaper, energy becomes more expensive, or the government changes its incentive scheme. Many people will still be motivated to buy micro turbines even if there is no economic advantage, however, and for these consumers the government could make things easier by streamlining the application process for grants and for gaining ROCs.

Chapters 4 and 5 introduced a turbulent wind model based on the filtered output of random white noise, and this was used to assess the dynamic performance of a micro turbine when connected to the grid through a Windy Boy grid tie inverter. Two blade profiles were used in the simulation and of these the symmetrical NACA0015 profile was found to be highly unstable in turbulent wind. The cambered S1210 blade section did not stall and has been shown to have superior self-starting capabilities, and would therefore be the clear choice for a Designer if the experimental evidence verifies this result.

The use of a DC-DC converter in the front end of the Windy Boy can be used to provide a more sympathetic power transfer characteristic and this has the effect of stabilising the turbine in low turbulence but is unable to prevent stalling when the turbulence is

increased. Again, further work is needed to verify this result, although DC-DC converters employing MPPTs have been used in the past to provide better energy capture for battery charging applications.

The simulation work of Chapter 5 was extended in Chapter 6 to consider the effect of aggregating the outputs of many turbines together. Aggregation at AC and DC were both examined and it was found that aggregation at DC, where multiple turbines share a single inverter, produced smoother power flows and provided a more cost effective solution then aggregating at AC, where each turbine used a designated inverter. The research highlighted that DC aggregation, although cheaper, had the drawback of achieving lower overall efficiency in each turbine. However, this problem could to some extent be solved using a DC-DC converter on the front end of the Wind Boy inverter to augment the power transfer characteristic and hence move the group operating point to a more optimal location. The work presented here is in the early stages of development and it would be interesting to verify these results through experiment.

Over-speeding is a problem particular for vertical axis turbines due to the fact they cannot be turned out of the wind, and this subject was examined in Chapter 7 with reference to methods of electrical speed control. It was found that an effective method of speed control is to introduce a dump load which can be switched in as the turbine approached rated speed, and switched out once the turbine has slowed. This speed control technique has been modelled in SIMULINK, where it was found to increase annual energy capture by over 50%, and has also been tested in field trials of an H-type Darrieus turbine where it has shown to be effective.

A second strand of the research work presented in this thesis focussed on extending the reach of the axial flux generator topology introduced in Chapter 2. This generator has been designed specifically for small-scale wind and water turbines and is particularly suited to small manufacturing companies because of its simple construction. In order to optimise the stator design of generator, the heat transfer mechanism was examined in some depth to improve the lumped parameter model used in the design process. It was found that fully exposing the stator, to force as much cooling air over the coils as possible, increased the surface heat transfer coefficient by 144% over an enclosed generator design. Further, it was found that the coils should be constrained to operate at the thermal limit of the winding rather then being constrained to an artificially imposed minimum acceptable efficiency. This is an important conclusion since many of the generators that have been integrated into turbine systems so far have been over-rated according to this criterion. A higher thermal limit can be achieved by abandoning the bobbin-wound construction and potting the coil directly into the stator; this increases the maximum armature temperature from 90 to 180°C and increases the power by 7%, albeit at a lower efficiency.

As larger generators are designed, however, the axial-flux topology becomes increasingly difficult to manage as the large magnetic closing forces cause the rotor plates to deflect, and this problem was investigated in some depth. By developing a structural finite element model of the generator, it was concluded that the critical loading phase occurs during assembly when only 3 simple supports were used to separate the rotor plates. Little thought had previously been given to assembly but the work done here shows this is critical and further support points must be provided for jacking during assembly.

A second important conclusion of the structural finite element work is that the simple axial flux generator topology is only viable up to a power rating of approximately 20kW, 100-200 rpm and beyond this point a radial flux configuration becomes advantageous because of its inherently stronger structure. Designing a radial flux machine that can be built easily at large diameters by a small Engineering company is not a trivial task and a substantial amount of the research time was devoted to this. A number of novel stator materials were tested including various types of steel wire and a composite made of steel shot in an Epoxy matrix. Of the materials tested it was found that 0.5mm mild steel wire was the most attractive due to its low hysteresis loss. There was a significant difference in the magnetic properties the wires that were tested and this may be problematic for a small Engineering company since, if the wrong wire is used, the core losses may become unacceptably high.

The design, manufacture and testing of the PM radial flux machine formed the bulk of research presented in Chapter 11. Two stator constructions were built: a wire-wound structure and an air-cored structure. In both machines novel manufacturing techniques were tested such as the use of MDF discs cut on a radius bar to form an epoxy mould, and the use of steel wire to form the stator and rotor back iron. It has been shown that this manufacturing technique is entirely feasible for small Engineering companies, and the resulting generator has acceptable core losses (6.9%). If a large volume of generators were manufactured, the stator wire could be made from a commercial grade electrical steel, which would reduce these losses still further.

It was also found that the inclusion of steel wire increased the generated EMF, and therefore the machine power, by approximately 40% over a fully air-cored structure. However, the wire-wound machine would have produce a 6% lower air gap flux

density then if commercial grade electrical steel laminations had been used, which corresponds to a similar drop in output power.

Two armature coil construction techniques were tested for the prototype generators: the first used a heat activated self-bonding wire to form a solid, homogenous, but flat, coil; the second used standard enamel coated copper wire to produce a coil which could be epoxied along two edges to form a flexible structure that was secured directly onto the inside radius of the stator. It was clear that the self-bonding wire produced a much more satisfactory coil with a higher packing factor. At large diameters the flatness of the coil would not significantly increase the air-gap of the machine either, making this technique the clear choice. Fully potting the coil is also vital for producing a robust structure and by doing this the heat transfer mechanism is not significantly compromised.

Tests on the two generators verified the design assumptions, with measured powers, voltages and efficiencies being within (3%) of predicted values. Lumped parameter and finite element thermal model were compared to the temperature rises observed in both generators. It was found that the finite element model gave reasonably accurate predictions of temperature rise where as the lumped parameter model gave slight overestimates. Since the design process relies on the lumped parameter model, this overestimate is to be welcomed as it will produce a more conservative design.

12.3 Further work

The work covered in this thesis could be extended in three main areas.

1) Extending the wind turbulence model. The turbulent wind model developed in Chapter 4 is only valid for time periods of a few minutes because it is based

around an average wind speed which is assumed to be constant, and this assumption only holds over this time frame. An interesting extension of this work would be to allow the average wind speed to change according to a Weibull distribution which could be inputted into the model. This would allow the model to be used in more versatile applications such as in studying the impact of micro wind turbines on low voltage networks.

2) Wind tunnel tests on the H-type Darrieus. Chapter 5 identified potential stall problems associated with H-type Darrieus turbines when connected to the grid through a Windy Boy grid-tie inverter. The research predicted that cambered blade sections were stable while symmetrical blade sections caused stalling, and it would be extremely interesting to test out this hypothesis in the wind tunnel.

3) Further structural analysis of the axial flux machine. Although the structural finite element work that was carried out on the axial flux generator made reasonably good predictions of the rotor plate deflections caused by the magnet forces, the deformation that occurred during assembly is not well understood and should be the subject of further modelling work. This will almost certainly have to be carried out if larger axial-flux machines (20kW, 100rpm) are to be designed.

Chapter 13

References

1. International Panel on Climate Change (IPCC) Fourth Assessment Report - Working Group I Report "The Physical Science Basis", 2007

2. Charlson, R.J., Ackerman, A.S., Bender, F.A.M. 'On the climate forcing consequences of the albedo continuum between cloudy and clear air'. Tellus Series B-Chemical and Physical Meteorology, Sep 2007. 59(4): p. 715-727.

3. Haupt, B.J. and Seidov D., 'Strengths and weaknesses of the global ocean conveyor: Inter-basin freshwater disparities as the major control'. Progress in Oceanography, 2007, 73(3-4): p. 358-369.

4. Alley, R.B. 'Wally was right: Predictive ability of the North Atlantic "Conveyor belt" hypothesis for abrupt climate change'. Annual Review of Earth and Planetary Sciences, 2007. 35: p. 241-272.

5. Historical coal data: Coal production, availability and consumption 1853 to 2006, Department of Trade and Industry, 2007 - www.ecdti.co.uk

6. Historical gas data: Gas production and consumption and fuel input 1882 to 2006 - Department of Trade and Industry, 2007 - www.ecdti.co.uk

7. 'The Energy Review: The Energy Challenge', Department of Trade and Industry, 2006.

8. 'The Energy Review: A Performance and Innovation Unit Report', Department of Trade and Industry, February 2002.

9. Lovelock, J., The Revenge of Gaia. 2006: Penguin Books Ltd.

10. International Panel on Climate Change (IPCC) Fourth Assessment Report - Working Group III Report, "Mitigation of Climate Change", 2007

11. European Union press release (Europa), June 2007 - http://europa.eu/pol/ener/overview_en.htm.

12. Energy White Paper: "Our energy future – creating a low carbon economy". Department of Trade and Industry, 2003.

13. Kyoto Protocol to the United Nations Framework Convention on Climate

Change, United Nations, 2005 - http://untreaty.un.org/English/notpubl/kyoto-en.htm

14. Pudjianto D., Zafiropoulos E., and Daoutis L., 'Methodology for Quantifying Economic and Environmental Benefits of MicroGrids', European Commission. July 2005.

15. Cipcigan L. and Taylor P. 'A Generic Model of a Virtual Power Station Consisting of Small-scale Energy Zones', 19th International Conference on Electricity Distribution, Vienna, Austria, 21-24 May, 2007.

16. Dutton A.G., Halliday J.A. and Blanch M.J., 'The feasiblitiy of Building Mounted/Integrated Wind Turbines (BUWTs)', Department of Trade and Industry and The Carbon Trust, 2003.

17. Kemsley R, Maloyd A, White S, Reidy A, Tayor P, 'Our energy challenge: power from the people. Microgeneration strategy', Department of Trade and Industry, 2006 - http://www.berr.gov.uk/files/file27575.pdf

18. 'Capacity Mapping and Market Scenarios for 2010 and 2020', The Carbon Trust and Mott McDonald, November 2003.

19. Milborrow, D., 'Assimilating wind'. IEE Review, 48(1): p. 9-13, Jan 2002.

20. Kemsley R, Maloyd A, White S, Reidy A, Tayor P, 'Potential for Micro Generation: study, and analysis of electricity stability issues', Econnect, October 2005.

21. Strbac, G., Jenkins N, Hird M, Djapic P, Nicholson G, 'Integration of operation of embedded generation and distribution networks', Manchester Centre for Electrical Energy, 2002

22. Scoraig Wind Electric - http://www.scoraigwind.com/index.html, last accessed 2007.

23. Warwick Urban Wind Trail Project, Interim Report - http://www.warwickwindtrials.org.uk/8.html, last accessed: 2007.

24. Bergey Wind turbines - http://www.bergey.com/, last accessed: 2007.

25. Carbon Concepts - www.carbonconcepts.co.uk, last accessed: 2007.

26. Rugged Renewables, 2005.

27. XCO_2 Vertical Axis Wind Turbine - http://www.quietrevolution.co.uk/, last

accessed: 2007.

28. Control Advanced Research Turbine (CART) 650kW, 2007 – http://www.nrel.gov/docs/fy03osti/32879.pdf

29. Kirke, B, 'Evaluation of self-starting vertical axis wind turbines for stand-alone applications', PhD Thesis, Griffith University, Australia, 2005.

30. Vergnet Wind Turbines, - http://www.vergnet.fr/V17/EN/Cadre.php?PRubrique=Edito&PCadre=P&PEcran=17&PCN=01&PLangue=EN, last accessed: 2007.

31. Solener - http://www.solener.com/fabricam_e.html, last accessed: 20072007.

32. Polinder, H, 'Design of a PM generator for the Turby, a wind generator for the built environment', 16th International Conference on Electrical Machines, Cracow, Poland, 5-8 September 2004.

33. Eoltec - http://www.eoltec.com/English/Main_en.htm, last accessed: 20072007.

34. Spooner, E. and Chalmers B.J., 'Torus - A Slotless, Toroidal-Stator, Permanent-Magnet Generator', IEE Proceedings-B Electric Power Applications, 139(6): p. 497-506, November 1992.

35. Bumby J and Martin R, 'Axial flux Permanent Magnet Air-cored Generator for Small-scale Wind Turbines', IEE Proceedings on Power Applications, 152(5), p.1065-1075, Sep 2005.

36. Kamper MJ, Wang RJ, and Rossouw FG, 'Analysis and Performance evaluation of axial flux air-cored stator permanent magnet machine with concentrated coils'. Proceedings from the International Electrical Machines and Drive Conference (IEMDC). 3-5 May 2007, Vol. 1., p13-20

37. SMA Windy Boy Grid-Connect Inverter – www.sma-america.com/windyboy.html#2500, last accessed: 2007

38. Mohan N, Undeland T, and Robbins W, 'Power electronics - converters, applications and design', 3rd edition, 2003, Published by Wiley. ISBN: 0-471-42908-2

39. Kloss A, 'A basic guide to power electronics', 1984 Published by John Wiley & Sons. ISBN: 0471904325

40. 'Illustrated history of wind power development' - http://telosnet.com/wind/20th.html, last accessed: 2007.

41. National Renewable Energy Laboratory (USA) - http://www.nrel.gov/wind/

42. Gipe P., 'Wind Power for Home, Farm, & Business', 2nd edition, 2004: Published by Chelsea Green, ISBN-10: 1931498148.

43. Harrion H, Hau E, and Snel H, 'Large Wind Turbines', 2000: Published by Wiley.

44. NOABL Wind speed database (DBERR) - http://www.dti.gov.uk/energy/sources/renewables/renewables-explained/wind-energy/page27326.html, last accessed: 2007

45. British Wind Energy Association (BWEA) - www.bwea.com, last accessed: 2007

46. Musgrove, P.J., 'Wind Energy-Conversion - An Introduction', IEE Proceedings-A-Science Measurement And Technology, 130(9): p. 506-516 1983.

47. Lun, I.Y.F. and Lam J.C., 'A study of Weibull parameters using long-term wind observations', Renewable Energy, 20(2): p. 145-153, June 2000.

48. Gupta, B.K., 'Weibull Parameters For Annual And Monthly Wind-Speed Distributions for 5 Locations in India', Solar Energy, 37(6): p. 469-471, 1986.

49. Dorvlo, A.S.S., 'Estimating wind speed distribution', Energy Conversion and Management, 43(17): p. 2311-2318, November 2002

50. Watson, GM., Halliday JA, Palutikof JP, Holt T, Barthelmie RJ, Coelingh JP, van Zuylen EJ, Cleijne JW, 'Predicting Off-shore Wind Energy Resources (Power). Rutherford Appleton Laboratory, July 2001.

51. The Carbon Trust - http://www.carbontrust.co.uk/default.ct, last accessed: 2007.

52. 'Micro-wind turbines in urban environments: an assessment', The Building Research Establishment Trust (report FB17), November 2007

53. Rankine RK, Chick JP, and Harrison GP, 'Energy and Carbon Audit of a Rooftop Wind Turbine'. Proceedings of the Institute of Mechanical Engineers Part A – Journal of Power and Energy, 2006, 220(A7): p643-654.

54. Betz A, in Wind-Engerie. 1919.

55. National Renewable Energy Laboratory (NREL) - http://www.nrel.gov/wind/pdfs/33450.pdf, Feb 2003

56. National Renewable Energy Laboratory (NREL) - http://www.nrel.gov/wind/pdfs/32748.pdf, Dec 2001

57. Gripe, P, 'Testing the Power Curves of Small Wind Turbines', WindStats Newsletter, 13(3), 2000.

58. Swift Wind Turbines - http://www.renewabledevices.com/swift/, last accessed: 2007.

59. Windsave - www.windsave.com, last accessed: 2007.

60. Bahaj AS, Myers L and James PAB, 'Urban energy generation: Influence of micro-wind turbine output on electricity consumption in buildings', Energy And Buildings, 39(2): p. 154-165, Feb 2007.

61. Watson S, 'Predicting the yield of micro-wind turbines in the roof-top urban environment.' 2007: Centre for Renewable Energy Systems Technology, Loughborough University.

62. Campbell N, Stankovic S, Graham M, Parkin P, Duijvendijk M, De Gruiter T, Behling S, 'Wind Energy for the Built Environment (Project WEB)', European Wind Energy Conference. Copenhagen, Denmark, 2-6 July 2001.

63. Bahrain World Trade Centre - http://bahrainwtc.com/, last accessed: 2007.

64. Aeolian Roof Wind Energy System - http://www.eunrg.com/product_3.htm, last accessed: 2007.

65. Clarke JA, Hensen JLM, Johnstone CM, McDonald I, 'On the use of Simulation in the Design of Embedded Energy Systems', ESRU, Department of Mechanical Engineering University of Strathclyde, Glasgow, 1999.

66. Phillips P, 'Influence of Building Geometry on Flow Conditions for Building Mounted Wind Turbines' MSc Thesis, Durham University, 2006.

67. Mertens S, van Kuik G, and van Bussel G, 'Performance of an H-Darrieus in the skewed flow on a roof', Journal Of Solar Energy Engineering-Transactions of the Asme, 125(4): p. 433-440, November 2003.

68. Mertens S, H Polinder, and Sidler HFA, 'TURBY: concept and realisation of a small VAWT for the built environment', EAWE/EWEA Special Topics Conference 'The Science of making Torque from Wind', Delft, The Netherlands, 19-21 April 2004.

69. Action Renewables - www.actionrenewables.org, last accessed: 2007.

70. The Low Carbon Building Programme - http://www.lowcarbonbuildings.org.uk/home/ lasted accessed: 2007.

71. The Energy Saving Trust - http://est.custhelp.com, lasted accessed: 2007.

72. West Wales Eco Centre - http://www.ecocentre.org.uk, lasted accessed: 2007.

73. Ofgem - gem.gov.uk/temp/ofgem/cache/cmsattach/17009_ofgem48.pdf?wtfrom=/ofgem/press/pressrelease-list.jsp. lasted accessed: 2007.

74. Green Energy - http://www.greenenergy.uk.com, lasted accessed: 2007.

75. Good Energy - http://www.good-energy.co.uk/, lasted accessed: 2007.

76. EDF energy - http://www.edfenergy.com, lasted accessed: 2007.

77. Equinox Energy - http://www.equinox-energy.co.uk/grid_connected_systems.htm, lasted accessed: 2007.

78. Wind and Sun - http://www.windandsun.demon.co.uk/, lasted accessed: 2007.

79. Proven wind turbines - http://www.provenenergy.com/, lasted accessed: 2007.

80. Sisterson D. and Frenzen P, 'Nocturnal boundary-layer wind maxima and the problem of wind power assessment', Environmental Science & Technology, 1978.

81. Wheldon J, 'Don't tell Dave, but wind turbines in cities won't keep a hairdryer running', article in The Daily Mail, 6 March, 2007.

82. Vaughan A, 'Renewable energy runs into turbulence on the home front', article in The Guardian, 21 December, 2006.

83. Slavin T, 'Lower bills may not be blowing in the wind', article in The Observer, 21 June, 2006.

84. 'Potential for Microgeneration Study and Analysis - Final Report' Department of Trade and Industry, 2005 - http://www.sd-commission.org.uk/publications/downloads/Micro-generationreport.pdf, last accessed: 2006.

85. Westlake AJG., 'Modelling, Dynamics and Control of a Permanent magnet Generator for Wind Power Applications' - PhD Thesis, Durham University,

1997

86. Leithead WE, 'Wind Turbine Control Systems Modelling and Design Phase I and II - Appendix D', Industrial Control Unit, University of Strathclyde, Glasgow, 1992

87. Nichita C, Luca D, Dakyo B, Ceanga E, 'Large band simulation of the wind speed for real time wind turbine simulators', IEEE Transactions On Energy Conversion, 17(4): p. 523-529, Dec 2002.

88. Welfonder E, Neifer R, and Spanner M, 'Development and experimental identification of dynamic models for wind turbines', Control Engineering Practice, 5(1): p. 63-73, January 1997

89. Stannard NJ and Bumby JR, 'Performance aspects of mains connected small scale wind turbines'. IET Generation, Transmission & Distribution, 1(2): p. 348-356, March 2007.

90. Stannard N, Bumby JR, Taylor P, Cipcigan LM, 'AC and DC aggregation effects of small-scale wind generators. IET Renewable Power Generation, 1(2): p. 123-130, 2007.

91. Van der Hoven I, 'Power Spectrum of Horizontal Wind Speed in the Frequency Range from 0.0007 to 900 Cycles per Hour', American Journal of Meteorology, 1957. 14: p. 160-164.

92. Davenport AG, 'Spectrum of horizontal gustiness near the ground in high winds', Quarterly Journal of the Royal Meteorological Society, 87(3): p. 194-211, 1961.

93. Kaimal JC, 'Turbulence spectra, Lebght scales and structure parameters in the stable surface layer', Boundary Layer Meterology, 4: p. 289-309, 1973.

94. Holley WE, 'Wind Turbulence Inputs for Horizontal Axis Wind Turbines'. Wind Turbine Dynamics Conference, Cleveland, Ohio, USA, 24-26 February 1981.

95. Spera D, 'Wind Turbine Technology'. Published by: ASME Press, 1994

96. Frandsen S, 'Flapwise extreme response of wind turbine blades to turbulence loading', BWEA Annual Conference, Glasgow, 10-13 July 1988.

97. Real time wind data from the Rutherford Appleton Laboratory, courtesy of Geoff Dutton, 2005.

98. Strum R and Kirk D, 'Contempory Linear Systems'. Published by PWS

Publishing Company, 1994.

99. Prudnikov AP, Brychkov YA, and Marichev OI, 'Integrals and Series', Vol. I. Published by: Gordon and Breach Science Publishers, 1992.

100. European Standard for Wind Loads – Eurocode EN 1991-1-4 WIND ACTIONS

101. Leithead WE, Delasalle S, and Reardon D, 'Role And Objectives of Control for Wind Turbines, IEE Proceedings-C Generation Transmission & Distribution, 138(2): p. 135-148, March 1991.

102. Leithead WE, 'Effective wind speed models for simple wind turbine simulations'. Proceedings of the 14th Annual BWEA Conference, Nottingham, March 25-27 1992, p.73-78.

103. Kristensen L, and Frandsen S, 'Model for the Power Spectra of the Blade of a Wind Turbine Measured from the Moving Reference Frame', Journal of Wind Engineering and Industrial Aerodynamics, 10: p. 249-262. Feb 1982.

104. El-Sayed AA, Hirsch C and Derdelinckx R, 'Dynamics of Vertical Axis Wind Turbines (Darrieus Type)'. International Journal of Rotating Machinery, 1995. 2(1): p. 33-41.

105. Manwell J. and Hunter R, 'Wind Diesel Systems'. Published by Cambridge University Press, UK, 1994.

106. Whisper Wind Turbine (manufactured by South West Wind) - http://www.windenergy.com/index_wind.htm, last accessed: 2007.

107. Bornay Wind Turbines - http://www.genasyspowersystems.co.uk/Bornay.htm, last accessed: 2007.

108. Ampair Wind turbine - http://www.ampair.com, last accessed: 2007.

109. Ropatec - http://www.ropatec.com/, last accessed: 2007.

110. Musgrove PJ, 'Variable Geometry Vertical Axis Windmill', Energy Digest, 1976. 5(6): p. 10-11.

111. Evans FC, Interlinked variable-pitch blades for windmills and turbines - US Patent Number 4299537. 1980: US.

112. MatWeb - Online materials database - http://www.matweb.com, last accessed 2007.

113. Ohta S, 'Temperature Classes of Electrical Insulators'. Three Bond Technical News, December 1985.

114. Campbell P, 'Principles of a permanent magnet-magnet axial-field dc machine'. Proceedings of IEE – Power,. 121(12): p. 1489-1494, December 1974

115. Strand 7 Finite Element Software - http://www.strand7.com/, last accessed: 2007.

116. Mueller MA, McDonald AS, and Macpherson DE, 'Structural analysis of low-speed axial-flux permanent-magnet machines'. IEE Proceedings-Electric Power Applications, 152(6): p. 1417-1426, November 2005.

117. Roark R, 'Roark's formulas for stress and strain'. 6th edition 1975, Published by: McGraw-Hill.

118. Spooner E, Gordon P, Bumby JR, French CD, 'Lightweight ironless-stator PM generators for direct-drive wind turbines'. IEE Proceedings-Electric Power Applications, 152(1): p. 17-26, January 2005.

119. Gordon P, 'Aspects of, and New Approaches to, the Design of Direct Drive Generators for Wind Turbines', PhD Thesis, Durham University, 2004.

120. de Vries E, 'Battle of the giants', article in New Energy Magazine for Renewable Energy. 2005. p. 54.

121. Enercon E-70 Tenchical description - http://www.suffolkcoastal.gov.uk/NR/rdonlyres/3125C3A5-232F-4406-8579-16341EA6927F/0/Appendix5BEnerconE70TechnicalDescription.pdf, last accessed: 2007.

122. Neuigkeiten - http://www.odenwaldwind.de/news/index.html. last accessed: 2007.

123. Open Hydro - http://www.openhydro.com/home.html. last accessed: 2007.

124. Cros M. and Viarouge P, 'New structures of polyphase claw-pole machines'. IEEE Transactions on Industry Applications, Jan-Feb 2004. 40(1): p. 113-120.

125. Schofield N, Canova A, Gruosso G, Repetto M, Ottella M, 'The application of soft magnetic composites to the design of tubular linear actuators'. International Journal of Applied Electromagnetics and Mechanics, 2004. 19(1-4): p. 225-229.

126. Cros M, Viarouge P, Chalifour Y, Figueroa J, 'A new structure of universal motor using soft magnetic composites'. IEEE Transactions on Industry

Applications, Mar-Apr 2004. 40(2): p. 550-557.

127. Jack AG, Mecrow BC, Dickinson PG, Stephenson D, Burdess JS, Fawcett N, Evans JT, 'Permanent-magnet machines with powdered iron cores and repressed windings'. IEEE Transactions on Industry Applications, Jul-Aug 2000. 36(4): p. 1077-1084.

128. De Wulf M, Anestiev L, Dupre L, Froyen L, Melkebeek J, 'Magnetic properties and loss separation in iron powder soft magnetic composite materials'. Journal of Applied Physics, May 2002. 91(10): p. 7845-7847.

129. Gilbert IP, Moorthy V, Bull SJ, Evans JT, Jack AG, 'Development of soft magnetic composites for low-loss applications'. Journal of Magnetism and Magnetic Materials, April 2002. 242: p. 232-234.

130. Myers HP, 'Introductory Solid State Physics'. 2nd edition Published by: Taylor & Francis, 1997

131. Guo YG, Zhu JG, Lin ZW, Zhon JJ, '3D vector magnetic properties of soft magnetic composite material'. Journal of Magnetism and Magnetic Materials, July 2006. 302(2): p. 511-516.

132. Say M. and Taylor E, 'Direct Current Machines'. Published by Pitman Publishing Ltd, 1980.

133. Finite Element Method Magnetics v. 3.4 (FEMM) written by Meeker D, http://femm.foster-miller.net/wiki/HomePage, last accessed 2004.

134. MIRAGE v. 1.0. Finite Element Software written by Meeker D, http://femm.foster-miller.net/wiki/HomePage, last accessed 2004

135. MatWeb - Material Property Data, www.matweb.com, last accessed: 2007.

136. Bumby J, Martin R, Mueller M, Spooner E, Brown NL, Chalmers BJ, 'Electromagnetic design of axial flux permanent magnet machines'. Proceedings of IEE – Electrical Power Applications, March 2004. 151(2): p. 151-160.

Appendix A

Details of micro and small-scale wind turbines currently on the market

Manufacture	Rated Power (W)	Rated turbine speed (RPM)	Cut-in speed (m/s)	Rated wind speed (m/s)	Diameter (m)	Swept Area (m^2)	Cp (max) e	Lamda (opt)
Air-X	400	2000	3.0	12.5	1.14	1.02	0.328	9.55
AreoCraft	120		3.0	9	1.20	1.13	0.238	
AreoCraft	240		3.0	9	1.65	2.14	0.251	
AreoCraft	500		3.0	9.5	2.40	4.52	0.210	
Atlantic Power Master	525		3.0	12	1.90	2.84	0.175	
Atlantic Power Master	760		3.0	12	1.91	2.85	0.252	
AWP	1500	350	2.7	11.1	3.60	10.18	0.176	5.94
Bergy	1000	490	2.5	11.1	2.50	4.91	0.243	5.78
Bergy	1500		3.6	12.5	3.20	8.04	0.156	
Bergy	10000	310	3.6	13.8	6.70	35.26	0.176	7.88
Bornay	250		3.0	11	1.35	1.43	0.214	
Bornay	600		3.5	11	2.00	3.14	0.234	
Bornay	1500		3.5	12	2.86	6.42	0.221	
Bornay	3000		3.5	12.5	4.00	12.57	0.200	
Bornay	6000		3.5	12	4.00	12.57	0.451	
Eoltec	6000	245	2.7	11.5	5.60	24.63	0.262	6.25
Gusto Energy	2000		3.5	13	3.20	8.04	0.185	
HWG	400		3.0	12.5	1.40	1.54	0.217	
Jacobs	15000	205	3.6	11.1	7.92	49.27	0.363	7.66
Power point	1000		3	12.5	2.19	3.77	0.222	
Power point	6000		3.0	12.5	5.00	19.63	0.255	
Proven	600	500	2.5	10	2.55	5.11	0.192	6.68
Proven	2500	300	2.5	12	3.50	9.62	0.246	4.58
Proven	6000	200	2.5	12.5	5.50	23.76	0.211	4.61
Proven	15000	160	2.5	12	9.00	63.62	0.223	6.28
Ropatec	750	350	2.0	14	1.50	2.25	0.198	1.96

Ropatec	1500	350	3.0	14	1.50	4.50	0.198	1.96
Ropatec	3000	90	2.0	14	3.30	7.26	0.246	1.11
Ropatec	6000	90	2.0	14	3.30	14.52	0.246	1.11
Rutland	720		3.0	12.5	1.69	2.24	0.269	
SuperWind	350	1300	3.5	12.5	1.20	1.13	0.259	6.53
SVIAB	750	800	3.0	12	2.40	4.52	0.157	8.38
SWP Lakota	900		2.7	13	2.10	3.46	0.193	
Synergy	360	400		11	2.70	5.73	0.077	5.14
Travere	1200	550	3.0	12.5	3.20	8.04	0.125	7.37
Travere	3000	500	3.0	12.5	3.60	10.18	0.246	7.54
Travere	7500	220	3.0	12.5	5.60	24.63	0.255	5.16
Turby	2500	124	4.0	13	1.99	5.97	0.311	4.00
Vaigunth Ener Tek	200	500	3.5	8	1.85	2.69	0.237	6.05
Vaigunth Ener Tek	500	310	3.0	8	3.00	7.07	0.226	6.09
Vaigunth Ener Tek	1000	250	3.5	8.2	4.00	12.57	0.236	6.39
Vaigunth Ener Tek	5000	166	3.5	9	6.80	36.32	0.308	6.57
West wind (cyclone)	200	420	3.0	8	2.00	3.14	0.203	5.50
West wind (cyclone)	300	330	3.0	8	2.30	4.15	0.230	4.97
West wind (cyclone)	500	460	3.0	8	2.60	5.31	0.300	7.83
West wind (cyclone)	1000	460	3.0	9	2.80	6.16	0.364	7.49
West wind (cyclone)	2000	480	3.0	10	3.00	7.07	0.462	7.54
West wind (cyclone)	3000		3.0	10	4.00	12.57	0.390	
West wind (cyclone)	5000		3.0	10	4.50	15.90	0.513	
West wind (cyclone)	7500		3.0	10	7.00	38.48	0.318	
West wind (cyclone)	10000		3.0	11	8.00	50.27	0.244	
Whisper 175	3200		3.1	12	4.26	14.25	0.212	
Whisper H40	900	1150	3.4	12.5	2.10	3.46	0.217	10.12
Whisper H80	1000	900	3.1	11.6	2.10	3.46	0.302	8.53
Wind Save	1000		2.9	12	1.75	2.41	0.393	

Appendix B

Derivation of the Nichita transfer function from the Von Karman power spectrum

A schematic of the wind turbulence signal shaping filter is shown below.

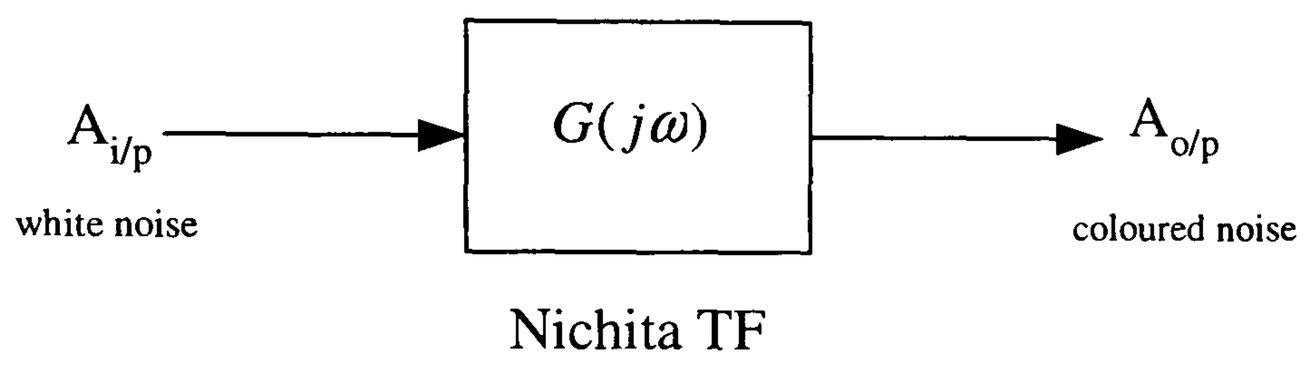

Figure B-1. Transfer function schematic

Since the system is linear, the output amplitude of the filter is related to the input by:

$$A_{o/p} = |G(j\omega)|.A_{i/p} \qquad [B\text{-}1]$$

This system is best depicted in the frequency domain as shown below. (The time series can be converted to a frequency series by using an FFT.) White noise, which has a uniform power per unit bandwidth, is passed through a transfer function which attenuates the signal at higher frequencies.

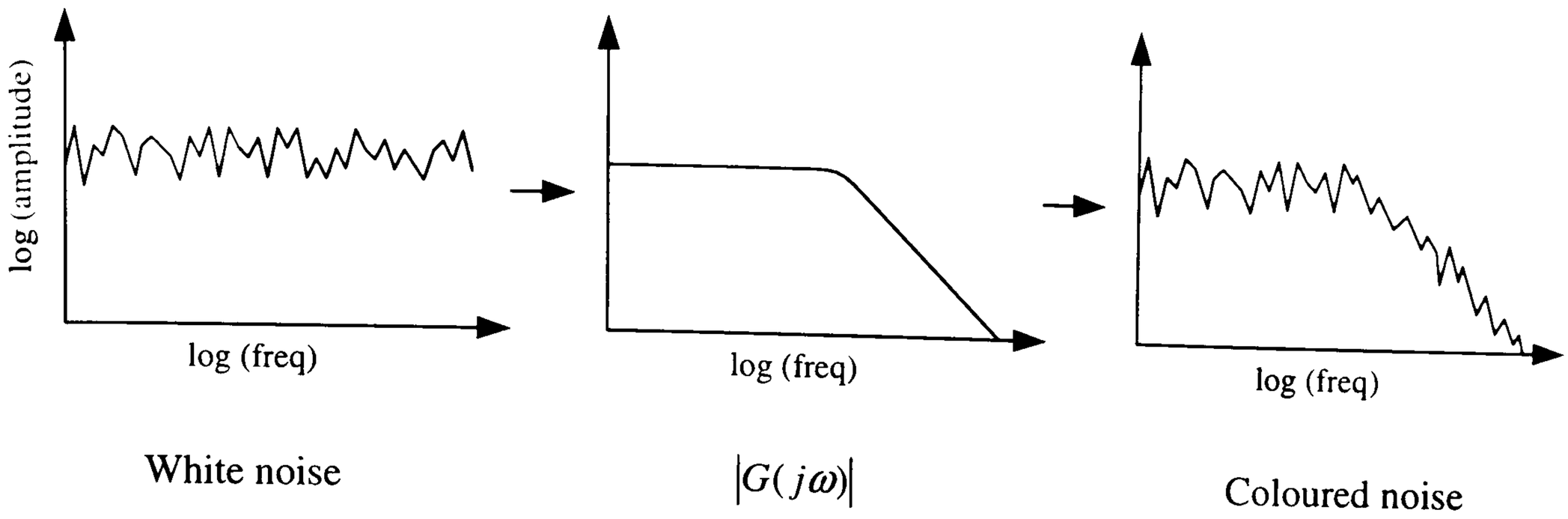

Figure B-2. Signal filter in frequency domain

The power gain of the system is given by:

$$P_{gain} = \left(\frac{A_{o/p}}{A_{i/p}} \right)^2 = |G(j\omega)|^2 \qquad [B\text{-}2]$$

The Nichita transfer function is:

$$G(s) = \frac{K_F}{(1 + sT_F)^{5/6}} \qquad [B\text{-}3]$$

Where K_F and T_F are the gain and time constants of the system. By replacing the Laplace operator with $j\omega$, the power gain becomes:

$$P_{gain} = |G(j\omega)|^2 = \left[\frac{K_F}{\left(\sqrt{1^2 + (\omega T_F)^2}\right)^{5/6}} \right]^2 = \frac{{K_F}^2}{\left(1 + (\omega T_F)^2\right)^{5/6}} \qquad [B\text{-}4]$$

Comparing equation [B-4] with the Von Karman power spectrum (equation [B-5]) shows the power gain of the system is consistent if $T_F = \frac{L}{V_{mean}}$ and $K_F \, \alpha \sqrt{T_F}$, which

is indeed the case (see equations [4-8] and [4-9]).

$$S_v(\omega) = 0.475\sigma_v^2 \frac{LV_{mean}^{-1}}{\left[1 + \left(\omega LV_{mean}^{-1}\right)^2\right]^{\frac{5}{6}}} \qquad \text{[B-5]}$$

In the SIMULINK model, the output of the signal shaping filter is scaled by the standard deviation of the turbulent wind, σ_u, which is proportional to the mean wind speed, and this produces the σ_u^2 term in equation [B-5]. (N.B. the coefficient in the above equation is part of K_F.)

Thus, if white noise is passed through the Nichita transfer function the resulting power attenuation will be identical to the Von Karman power spectrum.

Appendix C

Calculation of rotor plate closing forces

In the simplest case, the closing force between two magnets can be calculated by evaluating the Maxwell stress:

$$F_{mag\ pair} = \frac{1}{2}\frac{B_g^2}{\mu_0} \qquad [C\text{-}1]$$

In the axial flux generator the flux distribution varies sinusoidally in the circumferential across the face of the magnet (Figure C-1) and so the magnetic stress must be calculated by integrating the flux density over one pole pitch, (a flux density value at the mean axial position is taken). This gives the closing force experienced between one set of magnets; the total rotor plate closing force can be evaluated by multiplying by the number of magnets per disc.

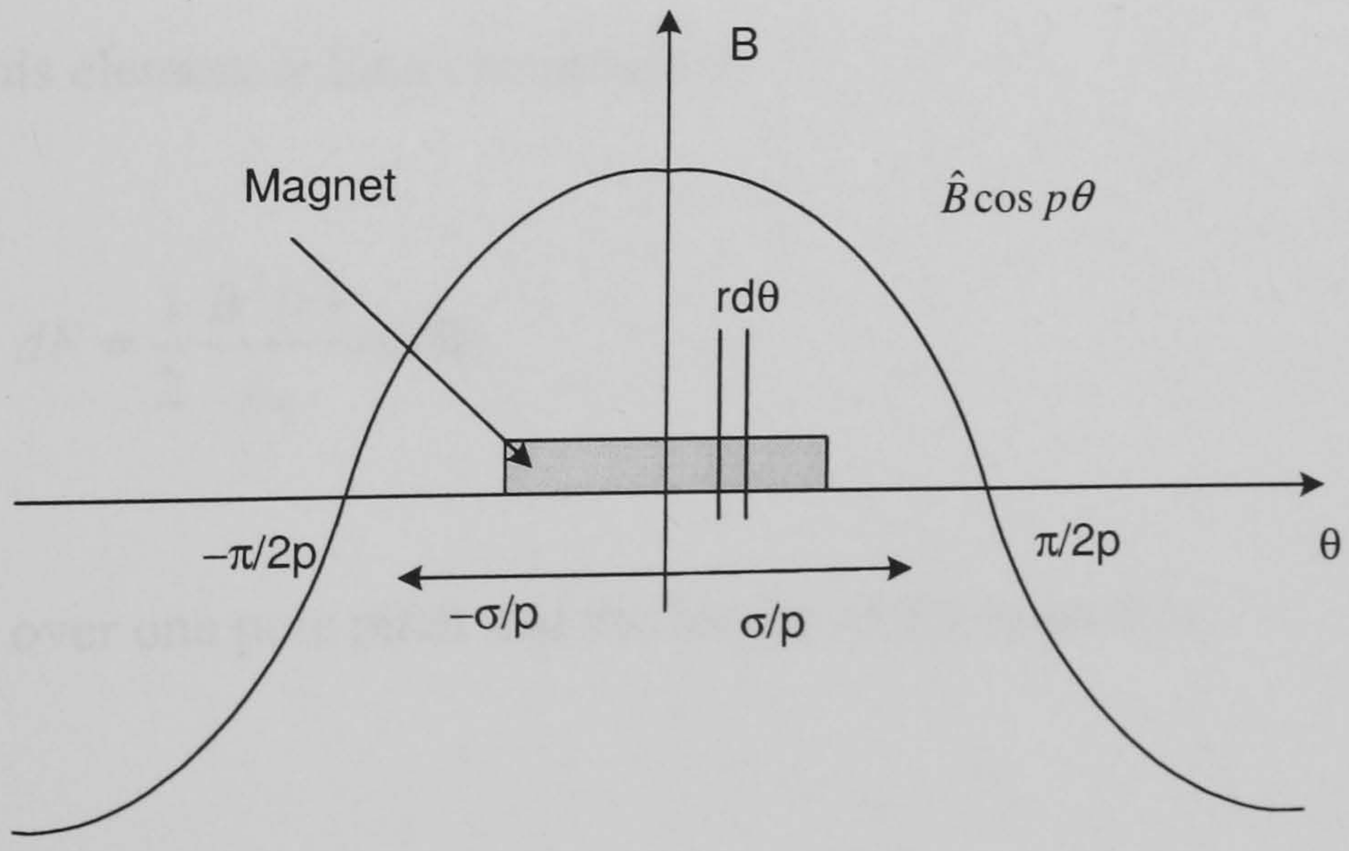

Figure C-1. Flux distribution across pole pitch

The magnet flux density is assumed to be sinusoidally distributed in the circumferential direction as

$$B(\theta) = \hat{B}\cos p\theta \qquad \text{[C-2]}$$

The trapezoidal magnet can be split into an element of area $rdrd\theta$ in the radial direction, Figure C-2.

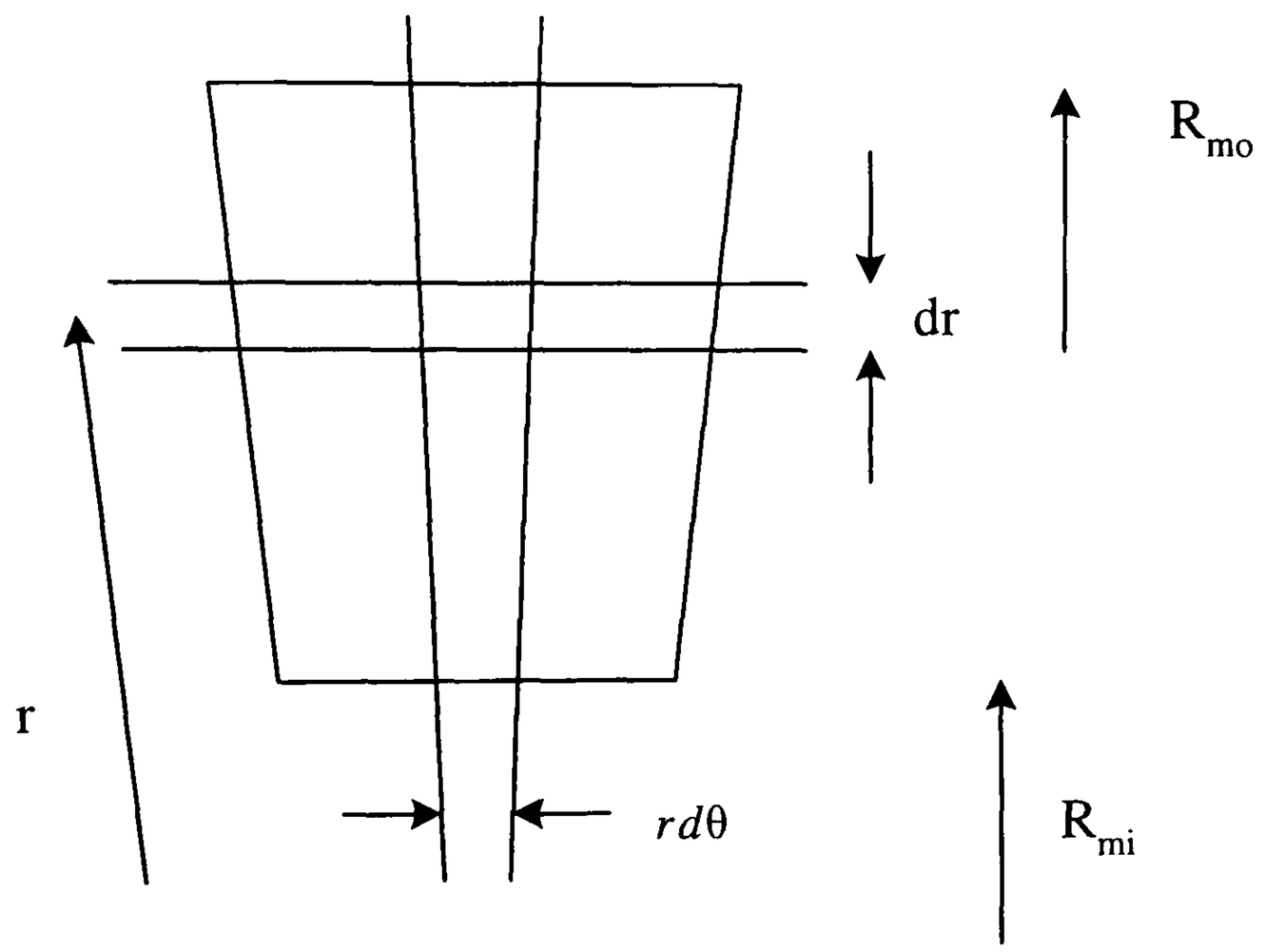

Figure C-2. Elemental area

The force on this element is then calculated as

$$dF = \frac{1}{2}\frac{B^2(r)}{\mu_0} rd\theta dr \qquad \text{[C-3]}$$

The total force over one pole pitch and the length of the magnet is

$$F_{mag\ pair} = \frac{1}{2}\frac{\hat{B}^2}{\mu_0}\int_{R_{mi}}^{R_{mo}}\int_{-\sigma/p}^{\sigma/p}(\cos^2 p\theta) r d\theta dr \qquad [C\text{-}4]$$

Evaluating this integral over one pole pitch i.e. $\sigma=\pi/2$ gives the closing force between a magnet pair as

$$F_{mag\ pair} = \frac{\pi}{4p}\frac{\hat{B}^2}{\mu_0} R_{mm} L_m \qquad [C\text{-}5]$$

Total closing force between the two rotor plates is then obtained by multiplying equation [C-5] by the number of poles *2p* to give

$$F = \frac{\pi}{2}\frac{\hat{B}^2}{\mu_0} R_{mm} L_m \qquad [C\text{-}6]$$

Appendix D

Generator design procedure

D.1 General design

The output power of a prospective generator design can be predicted using a spreadsheet design process. This allows dimensions of the generator to be varied to produce a design with the necessary power rating at the required speed and efficiency. A list of input parameters are shown in the table below.

Speed (RPM)	200
Number of magnets	24
Number of armature coils	18
Running clearance (mm)	3
Magnet thickness (radial) (mm)	10
Magnet width (circumferential) (mm)	40
Magnet depth (axial) (mm)	100
Magnet width/pole pitch ratio	0.62
Magnet binding tape thickness (mm)	0.5
Width of coil (circumferential) (mm)	25
Height of coil (radial) (mm)	8
Copper wire diameter (mm)	0.75
Number of parallel strands (lose wound)	1
Armature current density (A/mm^2)	4.0
Armature packing factor	0.51
Armature temperature (deg C)	100

Table 37. Input parameters to design spreadsheet

By defining the number of magnets and the magnet width/pole pitch ratio, the circumference of the rotor can be determined. The other geometric generator dimensions, such as the diameter of the stator, can then be referenced to the rotor, taking into account the running clearance, binging tape thickness and coil height. The

axial depth of the generator depends on the axial depth of the magnets, and from this the coil geometry can be defined. The number of coil turns, the coil resistance, the EMF and the coil inductance can also be calculated and these are described in sections D.2, D.3 and D.4. The current loading of the generator is determined by the heat transfer properties of the armature windings, and a lumped parameter and a finite element model of the coil winding have been developed to evaluate this. The heat transfer models are discussed in section 11.6. By predicting the generated EMF, coil current, resistance and reactance of the armature, the AC terminal voltage can be calculated according to the phasor diagram shown in Figure 11-8, and from this the total AC output power of generator can be found by summing the contributions of each phase. The DC output power may also be calculated by assuming the AC output is rectified using a standard 6-pulse rectifier; the voltage and current can then be calculated on the DC side of the rectifier according to equations [2-11] and [2-12]. A screen dump of the design spreadsheet for the 2kW, 200rpm wire-wound machine is shown in the figure below.

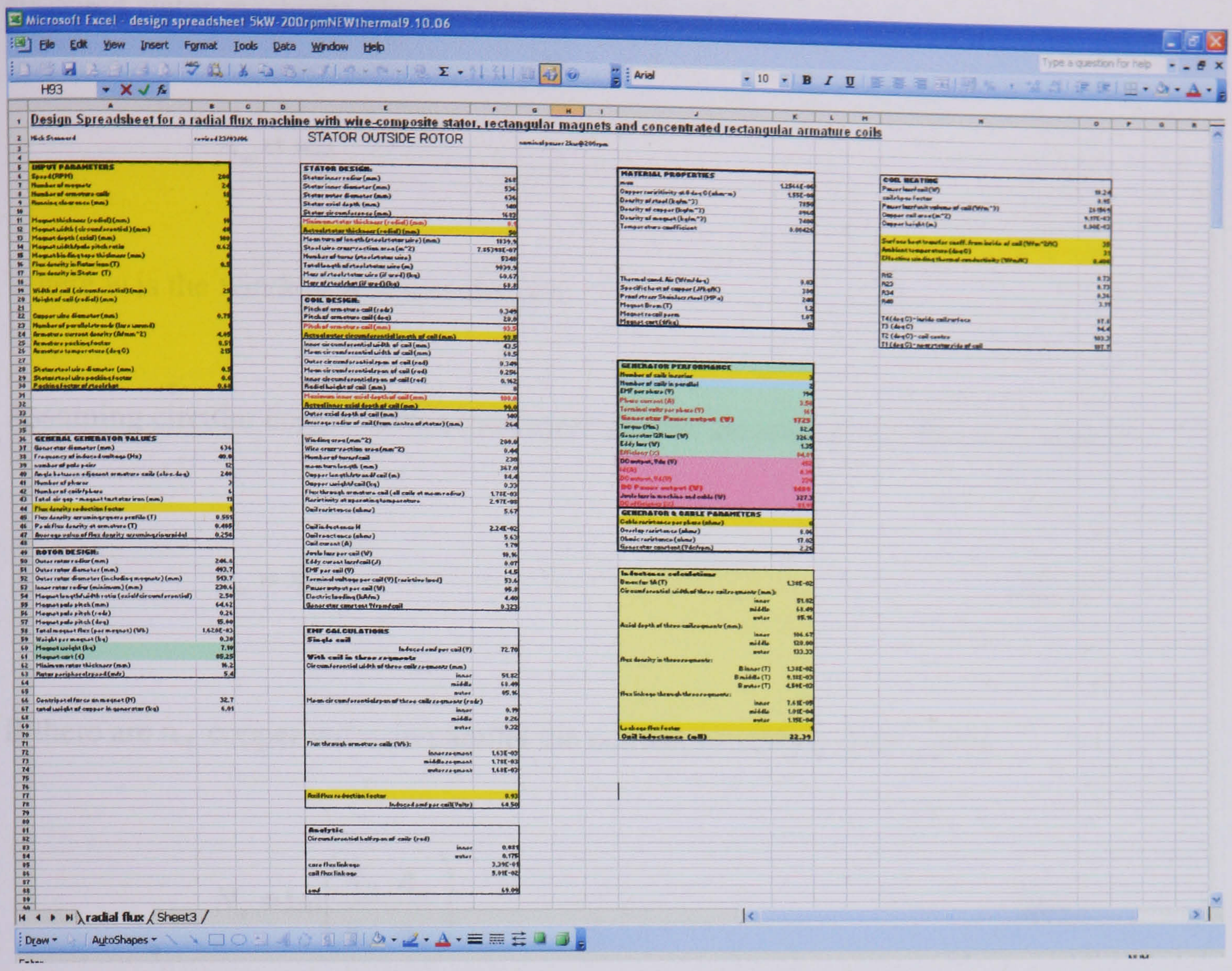

Figure D-1. 2kW,200rpm wire wound machine design spreadsheet

D.2 Armature coil design

The number of turns on the armature winding depends on the winding area, size of wire used and the number of strands connected in parallel (usually 1). The winding area is calculated as the cross-sectional area of the coil. In the case of the circular coil geometry, if the inside and outside radii of the armature coil and its height are defined, then the area available for the winding is:

$$A_w = (r_o - r_i)h \qquad \text{[D-2]}$$

In the case of rectangular coil geometry, appropriate for the radial flux wire-wound and

air-cored stator machines, the winding area is given by:

$$A_w = wh \qquad \text{[D-3]}$$

Where w is the winding width of the coil.

Assuming circular copper wire of diameter a_w then the area of one strand of wire is

$$a_w = \pi \frac{d_w^2}{4} \qquad \text{[D-3]}$$

If there are n_{sp} copper wires in parallel the number of turns in each coil is

$$N_c = \text{int}\left(\frac{k_p}{n_{sp}} \frac{A_w}{a_w} \right) \qquad \text{[D-4]}$$

where k_p is a defined copper packing factor.

The length of the winding is calculated by assuming all the turns are concentrated at the mean coil radius, r_m when the length of the mean turn for circular coils is

$$l_{mean} = 2\pi r_m \qquad \text{[D-5]}$$

and for rectangular coils is

$$l_{mean} = \tfrac{1}{2}(l_{outer} + l_{inner}).\tfrac{1}{2}(w_{outer} + w_{inner}) \qquad \text{[D-6]}$$

and the total length of wire in the coil is

$$l_{coil} = N_c l_{mean} \qquad \text{[D-7]}$$

The weight of an individual coil is now obtained from

$$M_{coil} = \rho_{cu} l_{coil} a_w n_c \qquad \text{[D-8]}$$

where ρ_{cu} is the density of copper.

The coil resistance is dependant on the length and size of copper wire used. It is also dependant on operating temperature.

The resistivity of copper is defined at 0°C so that at any other defined temperature it is given by

$$\rho_{cu} = \rho_0 (1 + \alpha T) \qquad \text{[D-9]}$$

where α is the temperature coefficient of resistance and T the armature operating temperature. T must be defined. The coil resistance follows from

$$R_{coil} = \rho_{cu} \frac{l_{coil}}{n_{sp} A_s} \qquad \text{[D-10]}$$

D.3 Coil induced EMF

In general terms, the EMF induced in a coil of wire by a changing magnetic field is:

$$E = \frac{d\lambda(t)}{dt} \text{ where } \lambda(t) = \hat{\lambda} \sin(\omega t) \qquad \text{[D-11]}$$

Therefore $$\frac{d\lambda(t)}{dt} = \omega\hat{\lambda}\cos(\omega t) \qquad [D\text{-}12]$$

$$E_{rms} = \frac{2\pi f}{\sqrt{2}}\hat{\lambda}\cos(\omega t) \qquad [D\text{-}13]$$

To calculate the induced EMF it is therefore only necessary to find the peak flux linkage, $\hat{\lambda}$, of a single coil since the electrical frequency of the generator is known. To do this two methods are outlined in the following sections. The first method assumes the flux density is constant in the radial direction across the coil; although this assumption may be considered accurate for the wire-wound machine it cannot be relied on for the air-cored machine since the flux path is essentially one large leakage field. To circumvent this problem a second method is outlined in section 0 which, although more complex, is analytically accurate.

D.4 Induced EMF in the wire wound stator machine

The peak flux linkage in the wire-wound machine can be found by assuming the flux density is constant in the radial direction and integrating the distribution across the coil span, σ_m, which is shown in the Figure below.

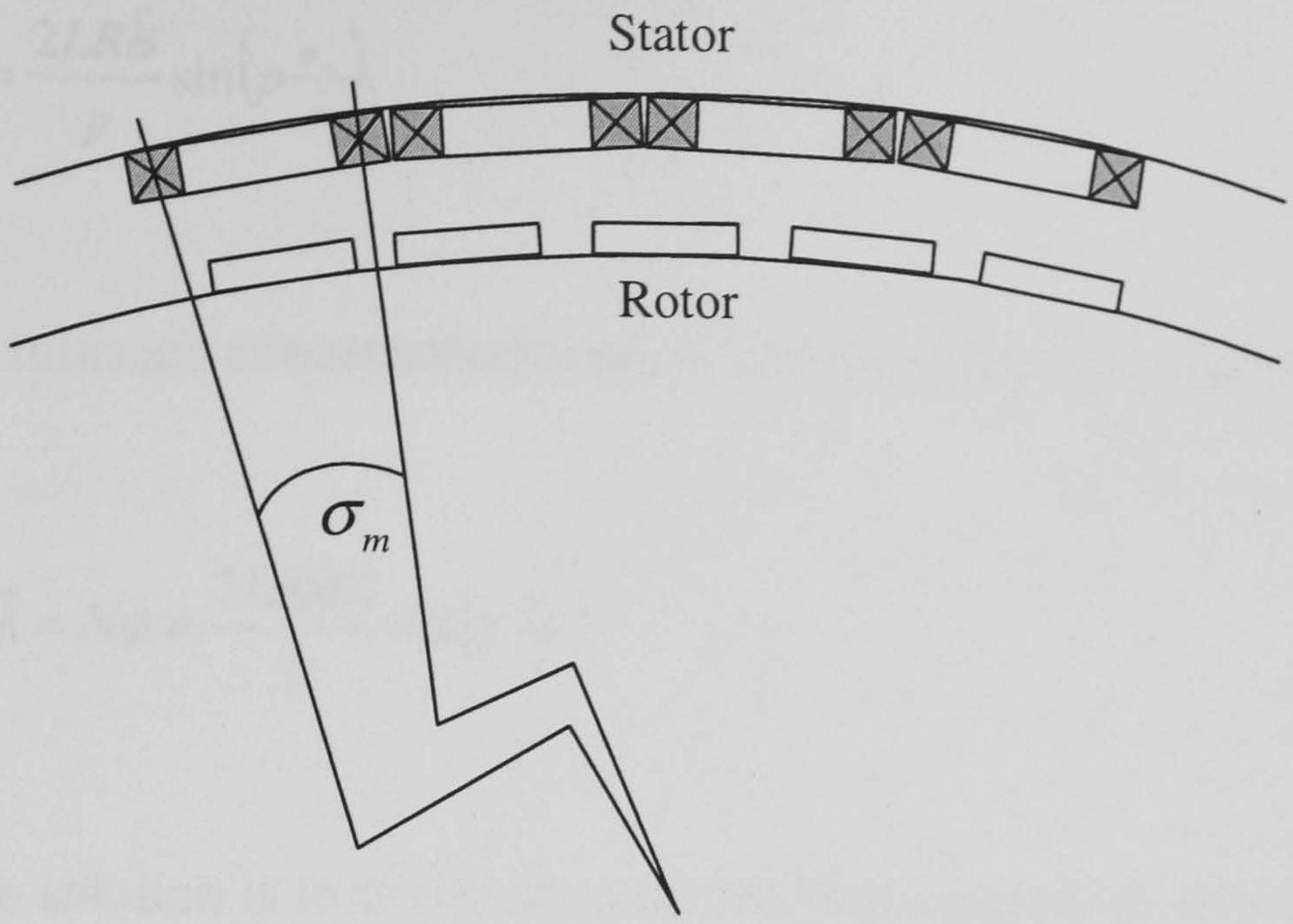

Figure D-2. Mean span of coil

In this analysis all turns are assumed to be concentrated at the mean coil radius. If the stator is 'unwrapped', the flux profile follows a sinusoidal distribution in the circumferential direction, as shown in Figure D-3.

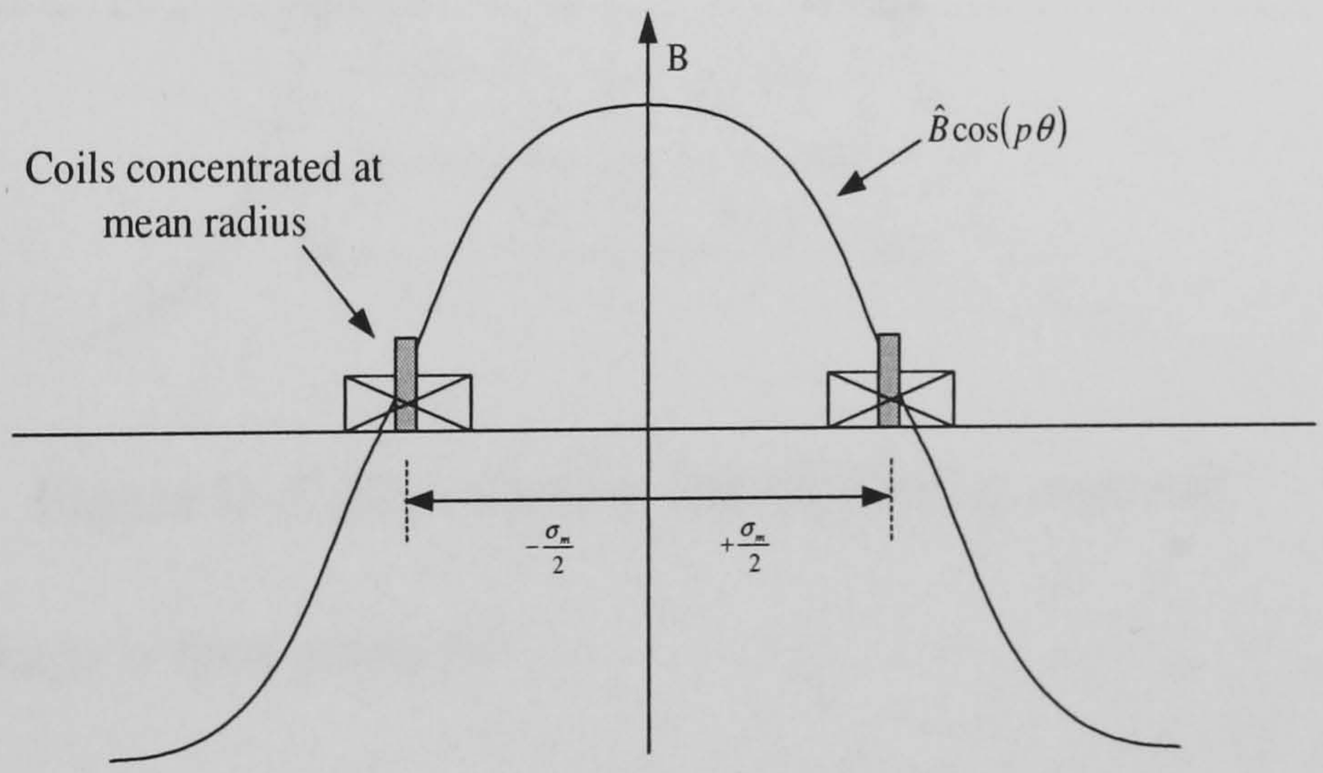

Figure D-3. Flux distribution through windings

The flux through the coil can be determined by:

$$\phi = L \int_{-\frac{\sigma_m}{2}}^{+\frac{\sigma_m}{2}} \hat{B}\cos(p\theta).(Rd\theta) \qquad \text{[D-14]}$$

$$= \frac{2LR\hat{B}}{p} \sin\left(p\frac{\sigma_m}{2}\right) \qquad \text{[D-15]}$$

Therefore, if all turns are concentrated at mean coil diameter, the peak flux linkage is:

$$\hat{\lambda} = N\phi = \frac{2LR\hat{B}N}{p} \sin\left(p\frac{\sigma_m}{2}\right) \qquad \text{[D-16]}$$

A more accurate solution is to divide the coil into three segments with an equal number of turns distributed between each segment, Figure D-4.

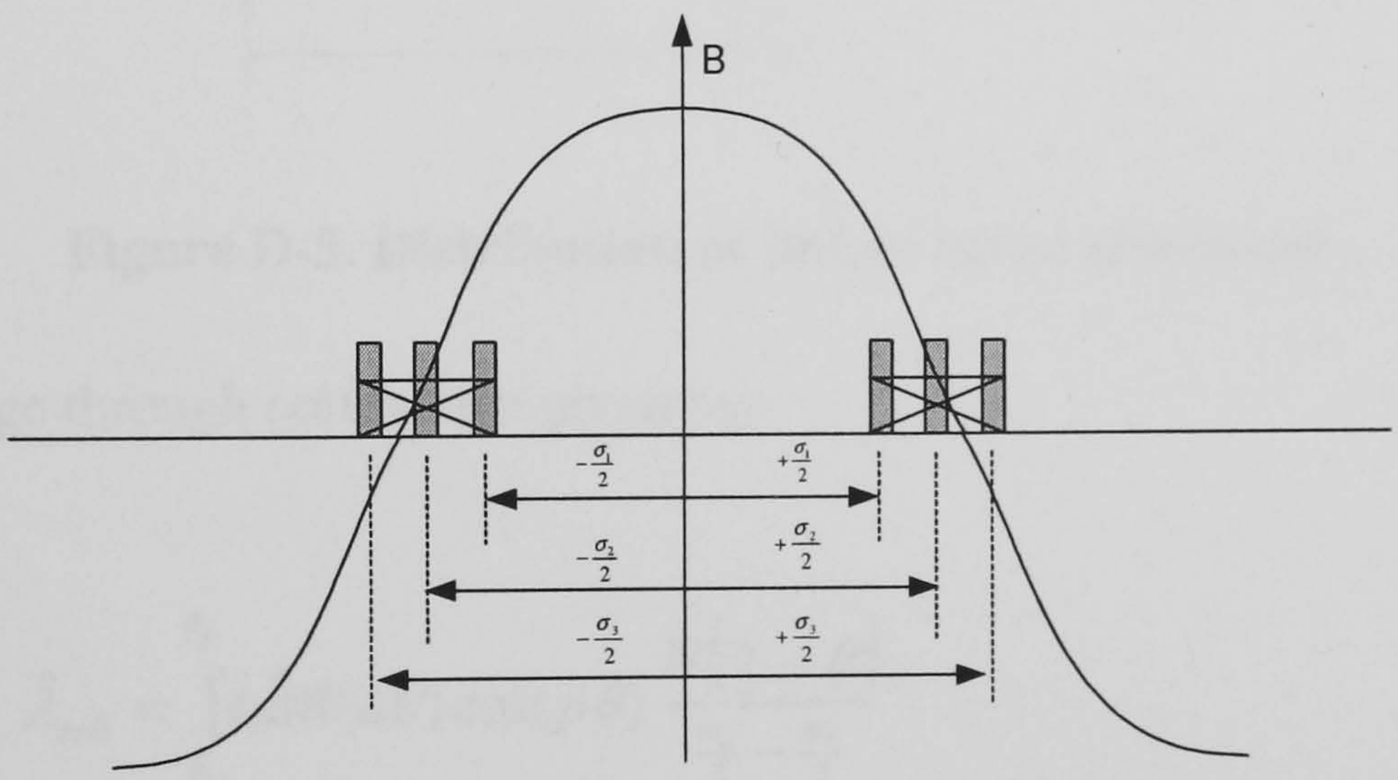

Figure D-4. Flux density distribution across coil

The peak flux linkage is then given by:

$$\hat{\lambda} = \frac{2LR\hat{B}}{p}\frac{N}{3}\left[\sin\left(p\frac{\sigma_1}{2}\right) + \sin\left(p\frac{\sigma_2}{2}\right) + \sin\left(p\frac{\sigma_3}{2}\right)\right] \qquad \text{[D-17]}$$

The correct analytical solution is given by summing the flux through the centre of the coil with the distributed flux passing through the coils. All turns link the flux though the centre of the coil which is given by:

$$\hat{\lambda}_{bore} = \frac{2LR\hat{B}N}{p}\sin\left(p\frac{\sigma_i}{2}\right) \qquad \text{[D-18]}$$

The flux linkage through the coil itself will vary with radius since there are fewer turns linking flux as one approaches the outer edge of the coil. The distribution of turns is shown below:

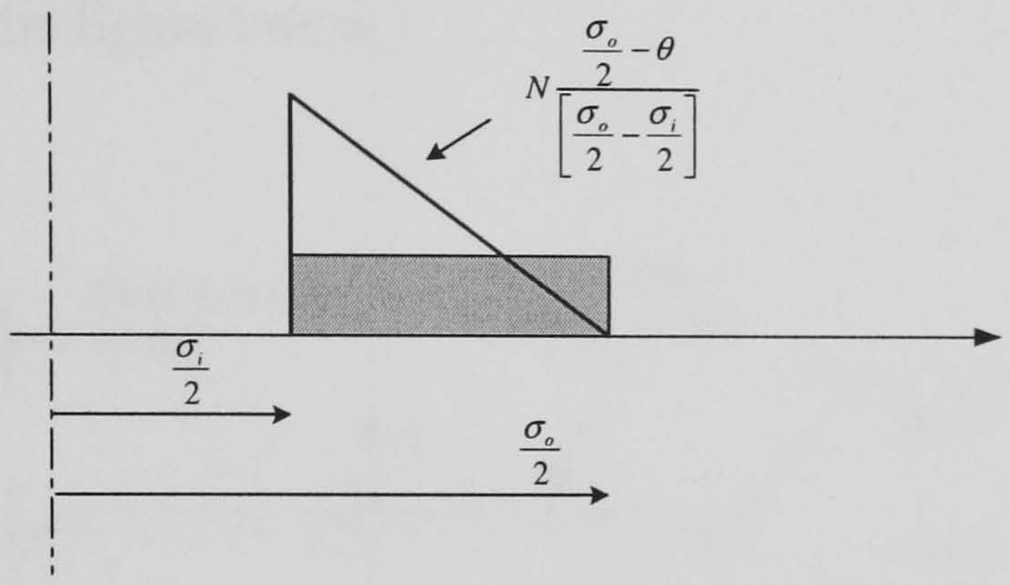

Figure D-5. Distribution of linked turns across coil

The flux linkage through coil is then given by:

$$\hat{\lambda}_{coil} = \int_{\frac{\sigma_i}{2}}^{\frac{\sigma_o}{2}} L\hat{B}R(d\theta)\cos(p\theta)\frac{N\left(\frac{\sigma_o}{2}-\theta\right)}{\frac{\sigma_o}{2}-\frac{\sigma_i}{2}} \qquad \text{[D-19]}$$

$$\hat{\lambda}_{coil} = \frac{L\hat{B}RN}{\frac{\sigma_o}{2}-\frac{\sigma_i}{2}}\left\{\frac{1}{p^2}\left(\cos p\frac{\sigma_i}{2}-\cos p\frac{\sigma_o}{2}\right)+\frac{1}{p}\left(\frac{\sigma_i}{2}-\frac{\sigma_o}{2}\right)\sin p\frac{\sigma_i}{2}\right\} \qquad \text{[D-20]}$$

The total peak flux linkage through the armature winding is then:

$$\hat{\lambda}_{total} = k\left(\hat{\lambda}_{bore}+\hat{\lambda}_{coil}\right) \qquad \text{[D-21]}$$

Where k is the flux reduction factor which is described below.

The method outlined above for calculating the induced EMF assumes the sinusoidal flux density profile is integrated over a fixed distance, L, in the axial direction. In reality, the flux density decays toward the edges of the magnet due to leakage, and this must be accounted for in the EMF calculations since the inner turns link slightly less flux then the outer ones. Because of this decay, the coils of the radial flux machines were designed to slightly overhang the magnets in order to reduce the axial length of the machine, as shown in the figure below.

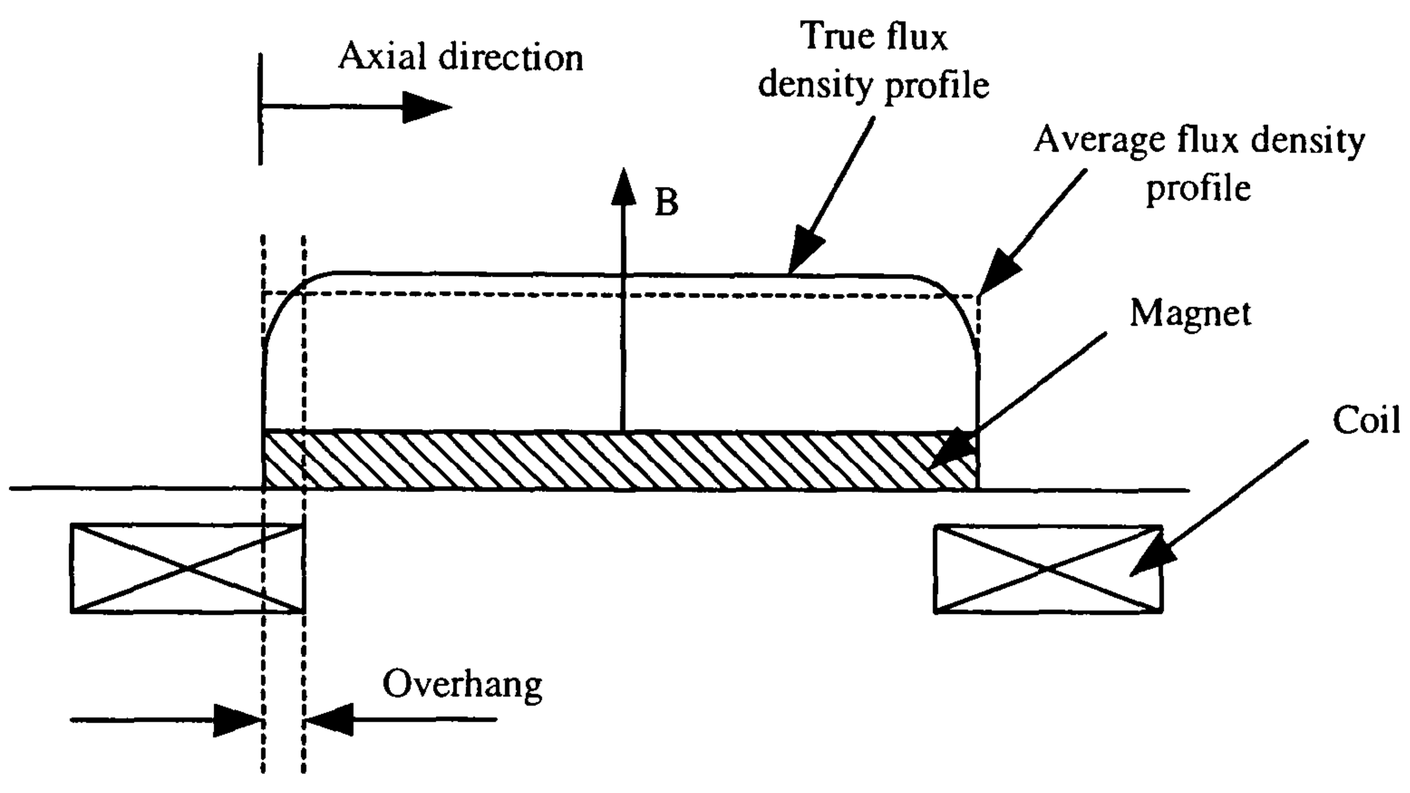

Figure D-6. Axial leakage field of magnet

In order to quantify this leakage field, the problem can be modelled in a finite element package [133] and the resulting flux density profile numerically integrated to establish an average flux value. The average value of flux density was found to be 93% of the peak value. By assuming that all the turns link this slightly lower value, the axial length, L, of integration could be taken as the entire length of the magnet.

D.5 Induced EMF in the air-cored machine

A second method has been developed to calculate the induced EMF in the armature winding using a 2D solution to Laplace's equation. This analytical solution must be used for the air-cored machine since it can no longer be assumed that the flux

density is constant across the armature coil in the radial direction. A detailed account the analytical solution is given in reference [136] with specific application to the axial flux generator in [35]. Its application to the radial flux topology considered here will be outlined below.

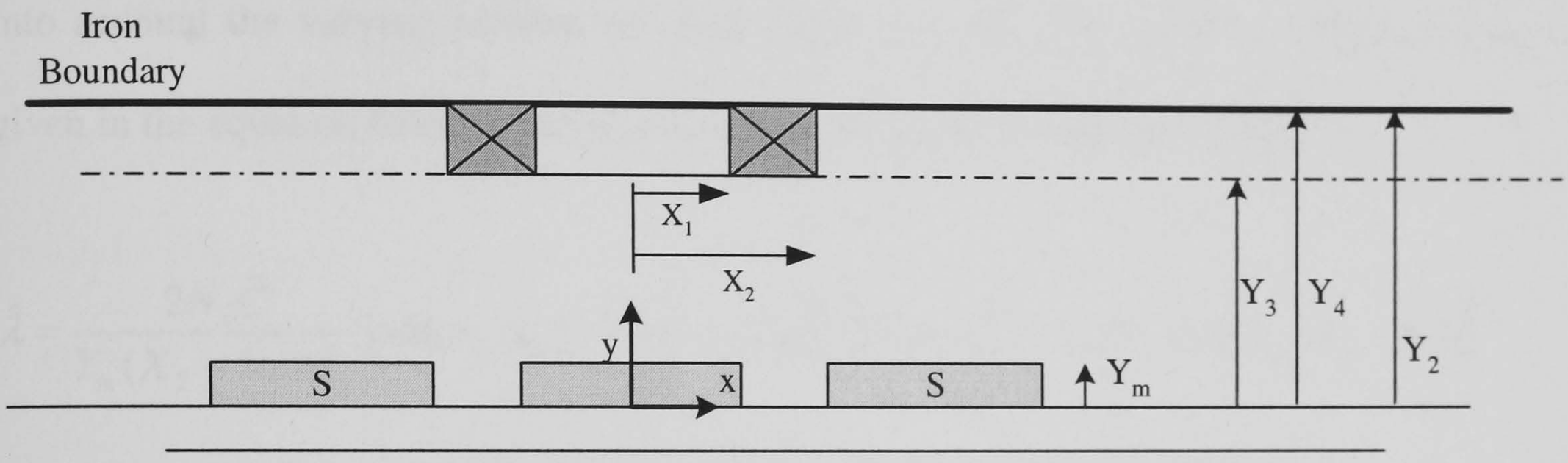

Figure D-7. Laplace's solution of radial flux topology

The radial flux topology is shown in schematic form in the Figure above. In the solution an iron boundary is assumed to exist behind the armature coil; in the design process this boundary is then moved out to infinity to replicate the true air-cored generator. The Laplace solution represents the permanent magnets as circumferentially distributed current sources of equivalent current density:

$$\hat{J}_n = \frac{8}{\pi}\bar{J}\delta \sin n\alpha = \frac{4}{\tau}\frac{B_{rem}}{\mu_0 \mu_{rec}} \sin\frac{n\pi}{2}\left(\frac{\tau_m}{\tau}\right) \qquad \text{[D-22]}$$

where $u_n = \dfrac{2\pi n}{\lambda} = \dfrac{\pi n_h}{\tau}$ [D-23]

Note that the wavelength is $\lambda = 2\tau$.

The flux density in the air gap is then:

$$B_{yn_h 2}(x) = \frac{\hat{J}_{n_h}\mu_0}{u_{n_h}} \frac{\sinh u_{n_h} Y_m}{\sinh u_{n_h} Y_2} \cosh u_{n_h}(Y_2 - y).\cos u_{n_h} x \qquad \text{[D-24]}$$

The flux linkage can be calculated by integrating the flux density across the coil in the circumferential direction in a similar manner to the method outlined above, which takes into account the varying number of turns across the coil. The resulting expression is given in the equation below and full details can be found in reference [136].

$$\hat{\lambda} = \frac{2N_c\hat{C}}{Y_m(X_2 - X_1)u_{n_h}^3}\left[\cos(u_{n_h}X_1) - \cos(u_{n_h}X_2)\right]\left[\sinh(u_{n_h}(Y_4 - Y_2)) - \sinh(u_{n_h}(Y_3 - Y_2))\right]$$

[D-25]

Where $\hat{C} = \frac{\hat{J}_{n_h}\mu_0}{u_n} \frac{\sinh(u_{n_h}t_m)}{\sinh(u_{n_h}Y_{eff})}$

In equation [D-25], X_1 is the inner coil radius, X_2 the outer coil radius, Y_3 the distance from the rotor to the bottom edge of the coil, Y_4 the distance from the bottom edge of the rotor to the top edge of the coil, Y_2 distance between the iron boundaries (this distance can be set to infinity in the case of the air cored machine).

A second method of determining the induced EMF can also be employed as a 'belt and braces' measure. The coil can be split into 3 layers in the radial direction and equation [D-24] used to predict the average flux density in each. Each of the layers can then be treated as a separate coil and sub-divided into 3 further segments in the circumferential direction and the contribution of each segment summed in an identical manner to that outlined in section D.4. A similar adjustment can also be made for the lower flux at the

ends of the magnets caused by the axial leakage field.

It was found that both methods of calculating the EMF produced almost identical results, with the 3 layer method being within 0.3% of the full analytical solution.

D.6 Coil inductance

The synchronous inductance of the armature winding is made up of two components: self inductance and mutual inductance. The self inductance of a coil is defined as the quantity of flux linkage created per unit of current passing through the coil:

$$L_{self} = \frac{\lambda}{i} \qquad \text{[D-26]}$$

Due to the high reluctance of the return path (see below), it is assumed that there is negligible mutual inductance between separate coils within the machine. For this reason the synchronous inductance of each coil is assumed to be identical to the self-inductance.

The following sections develop two methods of calculating the coil inductance: the first considers a segmented coil, the second uses a finite element method. Both methods are compared in section D.6.1.2.

D.6.1 Segmented coil method for inductance calculation

In order to calculate the self inductance of the armature winding in the wire-wound stator machine, it is assumed that the coil sits between two infinitely long iron boundaries and that all the flux travels through these boundaries without leakage, as

shown below.

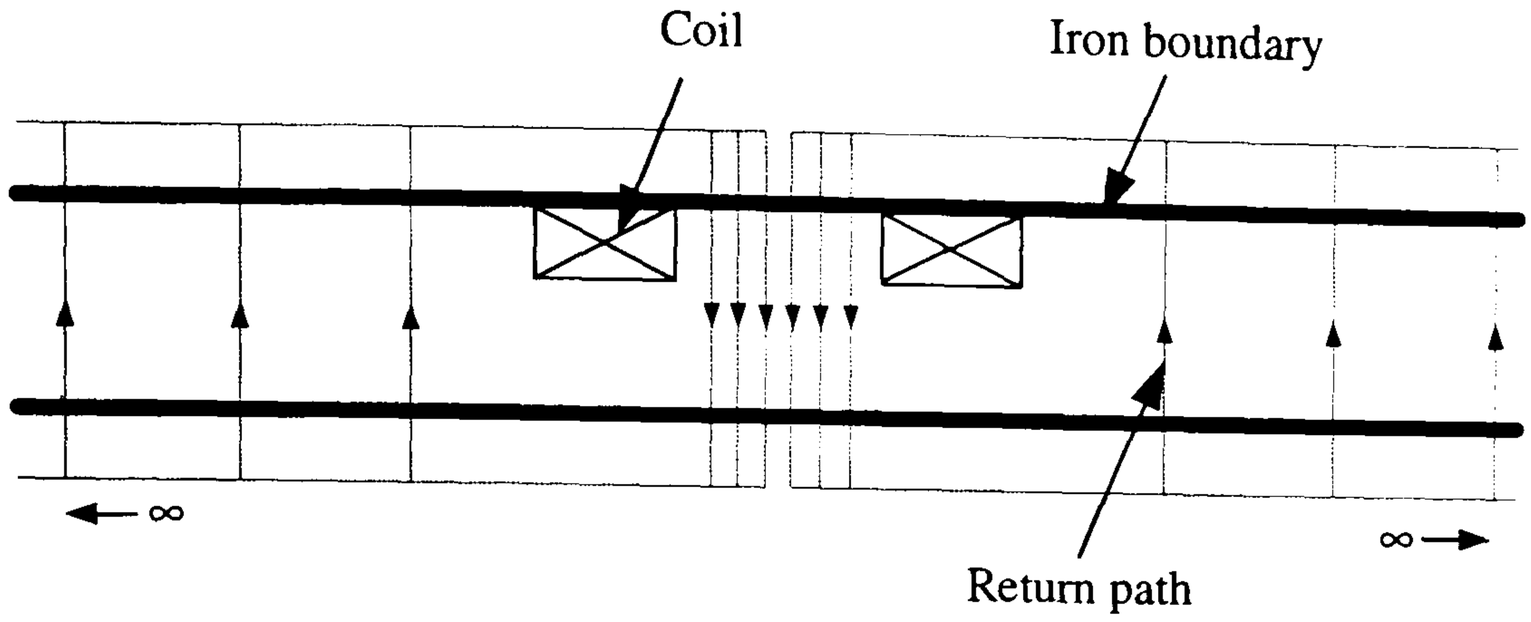

Figure D-8. Flux path for inductance calculation

If the iron boundary is assumed to have an infinite permeability, an equivalent circuit can be drawn:

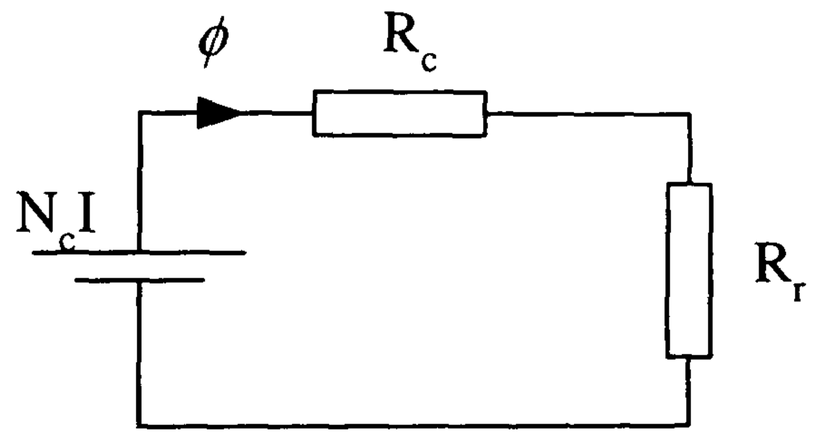

Figure D-9. Equivalent circuit

Where R_c is the reluctance of the path at the centre of the coil and R_r the reluctance of the return path. This may be ignored, however, since:

$$R_r = \frac{l_{return}}{\mu_0 A_{return}} \qquad [D\text{-}27]$$

As $A_{return} \to \infty$, $R_r \to 0$.

The total flux linking the coil can be estimated by splitting the coil into three equal segments and summing the contribution of each segment, assuming a linearly

distributed flux profile, as shown in Figure D-10.

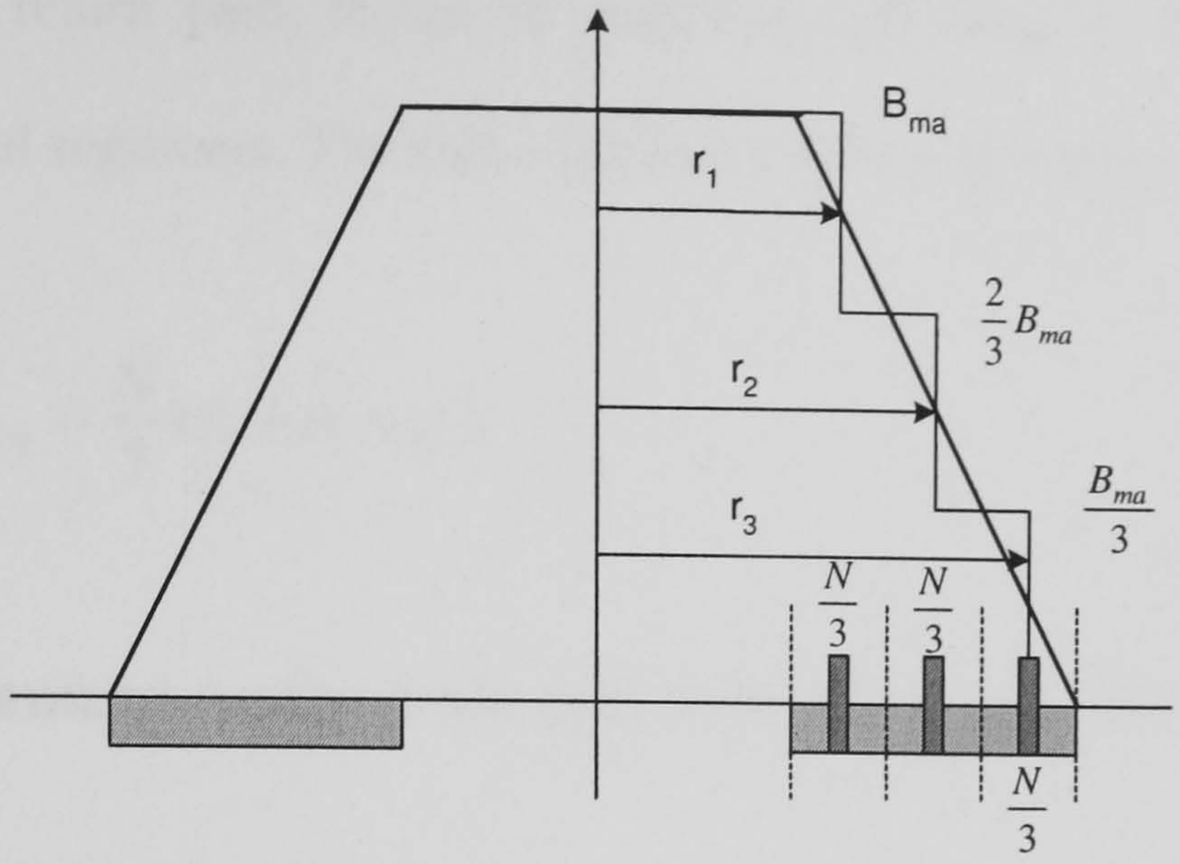

Figure D-10. Flux density across coil

The maximum flux density at the armature, B_{ma}, can be calculated from the equivalent circuit as:

$$B_{ma} = \mu_0 \frac{NI}{g} \qquad \text{[D-28]}$$

Where g is the total air gap between the two iron boundaries and is given by:

$$g = h + c + t_m + t_{binding} \qquad \text{[D-29]}$$

The flux through each of the three segments is given by:

$$\begin{aligned} \phi_1 &= A_1 B_1 \\ \phi_2 &= \phi_1 + A_2 B_2 \\ \phi_3 &= \phi_2 + A_3 B_3 \end{aligned} \qquad \text{[D-30]}$$

where $B_1 = B_{ma}, B_2 = \frac{2}{3} B_{ma}, B_3 = \frac{1}{3} B_{ma}$ and A_1, A_2 and A_3 are the areas of the three coil

segments.

Due to the long return path, it can be assumed that there is no mutual inductance between individual segments. The coil inductance is then given by:

$$L_{coil} = \frac{N}{3}(\phi_1 + \phi_2 + \phi_3) \qquad [D\text{-}31]$$

D.6.2 Finite element method for coil induction calculation

A two dimensional finite element package [133] can be used to predict the self-inductance of the armature winding in order to verify the 3-segment method. This can be done in the finite element package by placing the coil between two long iron boundaries to provide a semi-infinite flux return path. The FE method can also be extended to give a more accurate prediction of coil inductance by modelling the wire back iron in the generator using the same modelling technique that is described in Chapter 10.

The flux density profiles across the middle of the coil are compared in Figure D-11 for these three methods. In the three segment method the peak flux density is calculated according to equation [D-29], while in the two finite element plots the coil is placed between iron boundaries in the first case, and wire composite boundaries with identical composition to the generator in the second. In all three plots the flux density was calculated for a 1A armature current. The corresponding inductance predictions are shown in Table 38 along with the measured inductance which was calculated, along with the resistance, by passing an alternating current through each of the armature coils and measuring the real and reactive power consumed using a power analyser. These

values could then be equated to resistance and reactance since: $P=I^2R$ and $Q=I^2(\omega L)$.

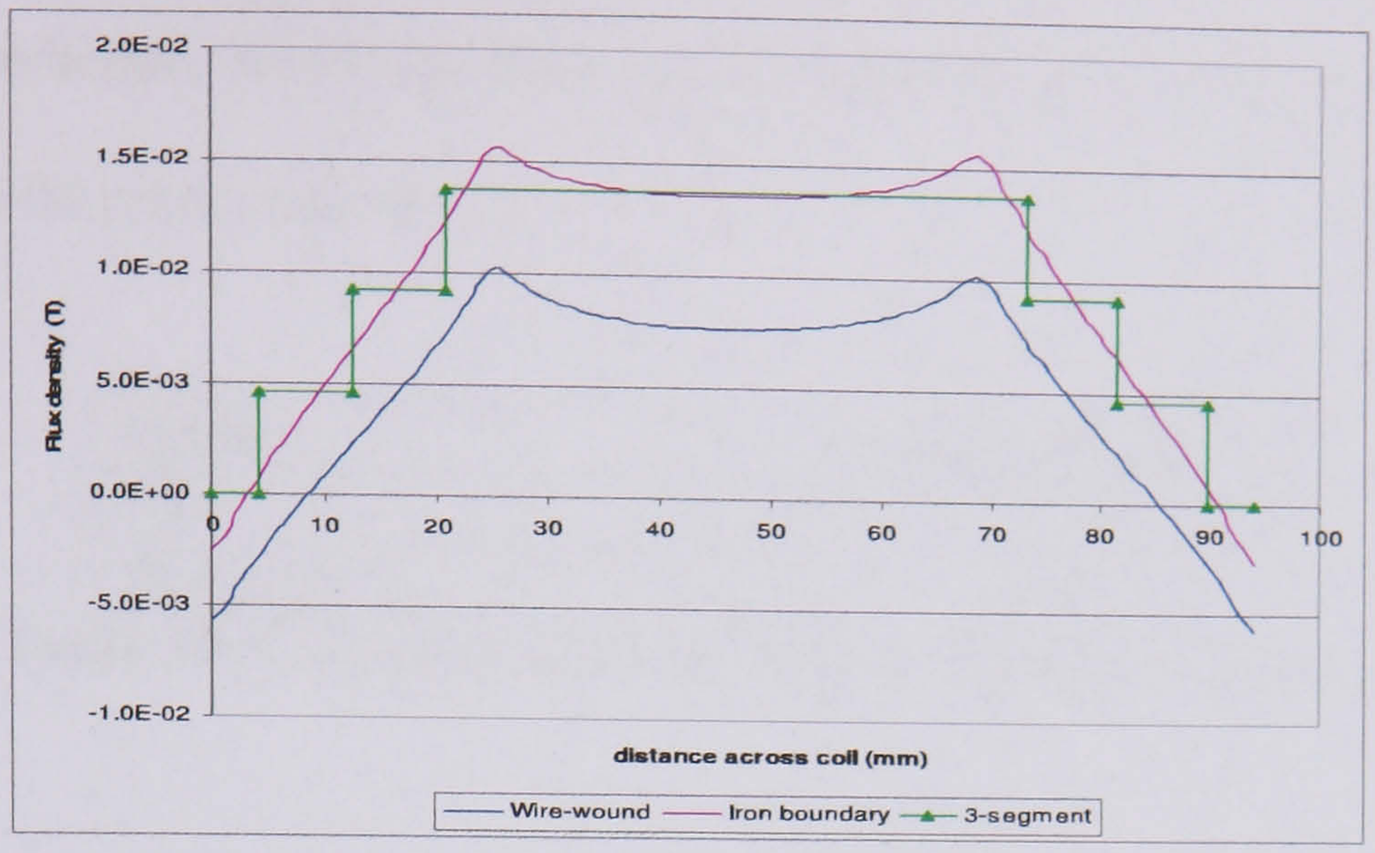

Figure D-11. Flux density profile through the centre of the coil

Method	Inductance (mH)
3-segment	22.4
FEA – iron boundary	22.6
FEA – wire stator	12.8
Measured	10.4

Table 38. Coil inductance for wire-wound stator machine

Figure D-11 shows the peak value of flux density from the 3-segment method compares favourably with the iron boundary method. In reality the coil sits between a wire-wound stator and rotor, however, and this lowers the flux density and produces a lower inductance value.

Table 38 shows that the 3-segment method produces a significant over-estimate of coil inductance. This method cannot therefore be relied on in the design process, as was the case with the axial-flux machine, and so the FEA using the wire-wound stator model was adopted in its place. The predicted inductance value, accounting for the wire-wound stator and rotor, is within 23% of the measured value which is acceptable for the design process.

A similar FE analysis can be used to predict the coil inductance of the air-cored machine and this is shown in the table below along with the measured value. As can be seen, the FE prediction, which has been again adopted in the design process, is in close agreement with the measured value.

Method	Inductance (mH)
FEA	11.6
Measured	11.9

Table 39. Coil inductance for air-cored stator machine

Appendix E

Heat transfer equations for the test generators

Lumped parameter models have been developed for the two coil construction methods tested in Chapter 11 and these are described below.

Heat loss is divided equally between each segment and is assumed to be concentrated at nodes 1, 2 and 3 (see Figure E-1). The thermal resistances linking the nodes depend on the distance between them, the thermal area and the material thermal conductivity. Heat transfer from nodes 4 and 0 to the cooling air is by convection.

The following assumptions have been made about the heat flow:

1. All heat flow is radial. Although some heat will leak into the centre of the coil, this air pocket is trapped by the coil binding tape in the wire-wound machine and is filled with epoxy in the air-cored machine, so the potential for cooling is greatly reduced.
2. The effect of the binding tape is neglected. Although the binding tape serves to slightly insulate the coil, the tape thickness is only 0.3 mm and so has been ignored.
3. All heat is removed by air passing over the inner surface of the coil, i.e. the coil is thermally insulated on the stator side. This is reasonable since the stator consists of a 60 mm thick ring of epoxy, which has an exceedingly low thermal conductivity (<1 $W/K/m^2$).

The heat transfer models and equivalent circuits for the wire-wound and air-cored machines are shown below.

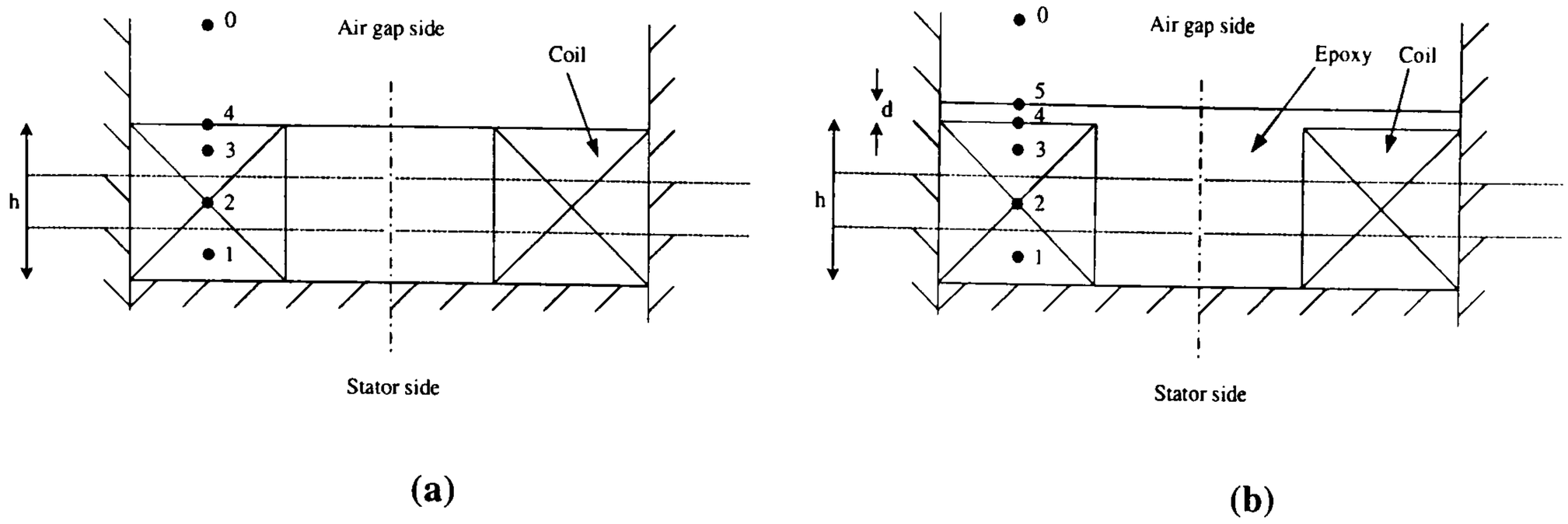

Figure E-1. Heat transfer in armature coil in (a) the simply attached coil construction and (b) the fully potted structure

The heat transfer model can be represented by an equivalent circuit, shown below.

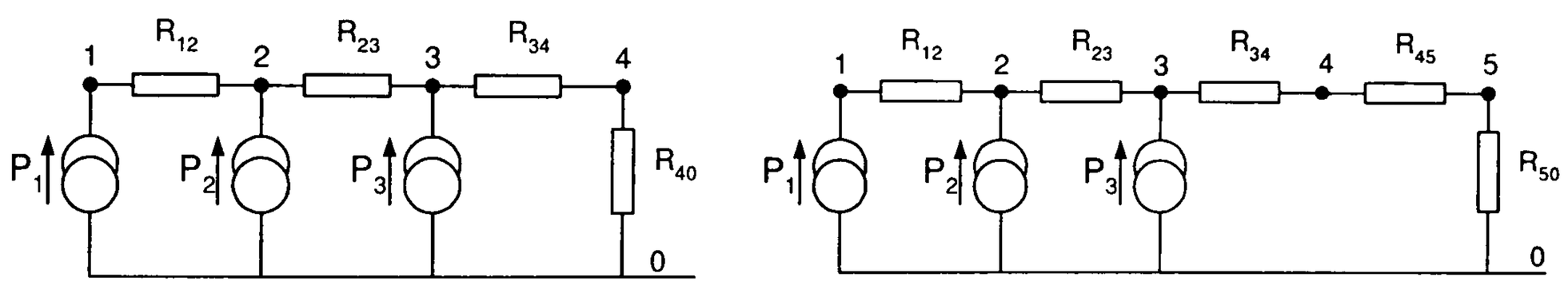

Figure E-2. Equivalent circuit for (a) the simply attached coil construction and (b) the fully potted structure

The thermal resistances are:

$$R_{12} = R_{23} = \frac{h}{3}\frac{1}{k_{wind} A_c} \qquad \text{[E-1]}$$

$$R_{34} = \tfrac{1}{2} R_{12} \qquad \text{[E-2]}$$

$$R_{40} = R_{50} = \frac{1}{h_s A_c} \qquad \text{[E-3]}$$

For the fully potted structure a fifth thermal resistance is required to account for the protective layer covering coils:

$$R_{45} = \frac{d}{k_{epoxy} A_c} \qquad \text{[E-4]}$$

The power dissipated in each segment of the coil is, by symmetry:

$$P_1 = P_2 = P_3 = \tfrac{1}{3} P \qquad \text{[E-5]}$$

For the simply attached coil construction, circuit analysis gives:

$$T_4 = PR_{40} + T_0 \qquad \text{[E-6]}$$

$$T_3 = PR_{34} + T_4 \qquad \text{[E-7]}$$

$$T_2 = \tfrac{2}{3} P\, R_{23} + T_3 \qquad \text{[E-8]}$$

$$T_1 = \tfrac{1}{3} PR_{12} + T_2 \qquad \text{[E-9]}$$

While for the fully potted structure, circuit analysis gives:

$$T_5 = PR_{50} + T_0 \qquad \text{[E-10]}$$

$$T_4 = PR_{45} + T_5 \qquad \text{[E-11]}$$

$$T_3 = P\,R_{34} + T_4 \qquad \text{[E-12]}$$

$$T_2 = \tfrac{2}{3} PR_{23} + T_3 \qquad \text{[E-13]}$$

$$T_1 = \tfrac{1}{3} PR_{12} + T_2 \qquad \text{[E-14]}$$